UNIVERSITÀ DI PARMA

UNIVERSITA' DEGLI STUDI DI PARMA

DOTTORATO DI RICERCA IN
"INGEGNERIA CIVILE E ARCHITETTURA"

CICLO XXXV°

A Study on Existing Prestressed Concrete Beams under Chloride-induced Corrosion

Coordinatore:
Chiar.mo Prof. Andrea Spagnoli

Tutore:
Chiar.ma Prof.ssa Beatrice Belletti

Dottorando: Lorenzo Franceschini

Anni Accademici 2019/2020 – 2021/2022

I would like to dedicate this thesis to my Family
that made all this possible

"In view of the large societal and economic impact of RC corrosion, there is no doubt about the urgent need for experts in the field of corrosion of steel in concrete (termed ''RC corrosion experts''). Ideally, this group of professionals has profound understanding about corrosion and concrete materials science that is universal enough to be applied to non-standard situations, i.e. situations where purely experience based approaches cannot be used. This group of professionals should also have sufficient background to write codes, standards, and technical rules to ensure durability for modern and future commercial products and construction technologies, guarantee proper applications of condition assessment methods, etc. Ideally, these corrosion experts have a university degree in civil engineering, materials science, chemistry followed by thorough and prolonged study of a corrosion subject such as in the form of a PhD thesis. The current situation, however, is that there are only relatively few professionals who had this sort of training."
(U. M. Angst, 2018)

Summary

Corrosion of steel reinforcements is nowadays considered as one of the leading causes of the durability and performance reduction of existing reinforced (RC) and prestressed (PC) concrete structures and infrastructures. Moreover, most of the structural and infrastructural heritage has already exceeded its service life and has been characterized by evident sign of deterioration. Concurrently, the effects associated with climate change seriously affect the durability of the existing heritage by interacting with the corrosion process. Global warming increases the frequency and the intensity of natural hazards, leading to the rising exposure of existing structures and infrastructures to severe structural damages, therefore, impacting the related structural vulnerability.

As a result, the combination of these factors leads to the structural capacity reduction of existing RC and PC members over time, sometimes causing unexpected failures due to the lack of bending, shear or anchorage resistance. These latter failures may occur without warning signs, resulting in a great potential for life losses and causing a significant economic impact. In this context, several buildings and PC bridges collapses have occurred worldwide, such as the well-known collapse of the Berlin Congress Hall in Germany and the more recent failure of the Polcevera Viaduct in Italy. These recent and past events have emphasized the urgent need for reliable and stringent maintenance protocols as well as simplified analytical models capable of assessing the residual structural capacity of deteriorating RC and PC members, making the corrosion topic of great interest among the scientific community. Despite the possible corrosion forms, in the case of PC members, the chloride-induced corrosion can lead to the worst consequences, since pitting can cause stress concentration and strain localization of prestressing wires, generally subjected to initial high mechanical stresses.

Although recent experimental, numerical and analytical studies have been conducted on RC members, the knowledge on PC structures subjected to corrosion is still uncertain and scarce. The primary reasons are as follow:

- *(i) Most of experimental research, concerning the analysis of the residual structural capacity of corroded members, have been performed by adopting the artificially accelerated process.*
- *(ii) Few studies have been focusing on the analysis of the longitudinal and sectional variability of corroded prestressing reinforcements.*

(iii) The scientific literature has revealed a scarcity of models investigating the residual mechanical behaviour of corroded prestressing strands.

(iv) Guidelines and codes, dealing with corrosion issues for the assessment of the residual service life of corroded structures, are not completed and fully validated.

First, to partially extend the current knowledge, the present Thesis investigates several naturally corroded PC beams subjected to 10 years of sea water wet-dry cycles. The study aims to evaluate the influence of corrosion on the residual structural performance. To this end, two un-corroded PC beam specimens were manufactured with the same type of concrete and curing conditions and subsequently tested to be a reference for the quantification of corrosion effects. During the mechanical three- and four-point bending tests, Digital Image Correlation (DIC) was performed by taking photos at each load step to investigate the displacement and strain fields evolution of each tested beam.

Second, the Thesis defines analytical constitutive laws for the prediction of the residual mechanical behaviour of corroded prestressing strands. To this end, 3D models of retrieved un-corroded and corroded strand samples were obtained by using a structured light 3D scanner. Afterwards, the sectional and longitudinal pitting morphology spatial variability was investigated by superimposing the un-corroded and corroded 3D models using the GOM Inspect software. Furthermore, tensile tests were performed for the models' calibration. Based on the experimental findings, two constitutive laws, namely CPS- and SCPS-models, were proposed to predict the tensile force-strain or stress-strain relationship of a corroded strand. Although the models are designed on different assumptions, the equivalent spring material model that reproduces the overall response of a corroded strand as the sum of wire contributions, which are assumed as springs working in parallel with each other, is adopted. On the one hand, the CPS-model assumes the cross-sectional loss of each wire as the main input parameter for the prediction of the ultimate strength and the ultimate strain decay by distinguishing between three pit type morphology configurations – denoted as hemispherical, half-moon and planar shape –. The SCPS-model, on the other hand, is a simplified version of the CPS-model designed for the daily engineering practice and conceived on a single input parameter that is the maximum penetration depth of the most corroded wire. This model is independent from the pit type morphology configurations and adopts a unique relationship for the ultimate strain decay. Furthermore, based on the sectional pitting morphology estimation, the model attributes a sectional average penetration depth to the remaining external wires via

a measurement-based-correlation, defined on the basis of the maximum penetration depth of the most corroded wire.

Finally, an analytical approach for assessing the residual flexural and shear capacity of corroded PC beams without transversal reinforcement is proposed. The model first quantifies the instantaneous and time-dependent prestressing losses associated with: (i) the concrete elastic contraction caused by the strand releasing, (ii) the steel relaxation over time, and (iii) the rheological effects of creep and shrinkage. Consequently, the corrosion parameters in terms of (i) average penetration depth of the remaining external wires, (ii) cross-sectional loss, and (iii) mass loss are calculated based on the corrosion pattern of the analyzed PC beam, estimated via visual inspection. Specifically, the model assumes the maximum penetration depth of the most corroded wire as unique input parameter, and defines four different corrosion scenarios. Afterwards, the SCPS-model is adopted to determine the residual mechanical properties of corroded strands. Furthermore, analytical models for the evaluation of the transmission length variation, and the ultimate bond strength decay induced by corrosion over time are introduced. Finally, the residual flexural and shear capacity of the investigated PC member are determined via equilibrium and compatibility conditions. On the one hand, a simplified moment-curvature diagram is proposed for the residual flexural capacity quantification. The Model Code 2010 Level II of approximation expression, on the other hand, is adopted for the shear capacity assessment of structural PC members without transversal reinforcement, opportunely modified to account for corrosion effects.

The accuracy and the effectiveness of the proposed models are validated through the comparison with experimental tests. Moreover, the SCPS-model reliability for the prediction of the residual mechanical response of corroded strands is evaluated based on the obtained results and the performed comparisons. In detail, a preliminary partial safety factor for the design strength of corroded strands is determined following the probabilistic estimation of the SCPS-model uncertainties. It is worth noting that the recommendations provided by the draft of the Model Code 2020 are adopted for the quantification of the uncertainties.

To conclude, the main observations, the future research as well as the needed improvements are outlined.

Sommario

La corrosione delle armature in acciaio è oggi considerata una delle principali cause di riduzione della durabilità e prestazione di strutture e infrastrutture esistenti in cemento armato (CA) e cemento armato precompresso (CAP). Inoltre, la maggior parte del patrimonio strutturale e infrastrutturale ha già superato la propria vita utile ed è caratterizzato da evidenti segni di deterioramento. Contemporaneamente, gli effetti associati al cambiamento climatico incidono seriamente sulla durabilità del patrimonio esistente, attraverso l'interazione con il processo di corrosione. Di fatto, il riscaldamento globale aumenta la frequenza e l'intensità dei rischi naturali, portando a una maggiore vulnerabilità delle strutture e delle infrastrutture esistenti a causa dell'esposizione crescente a gravi danni strutturali.

La combinazione di questi fattori induce, di conseguenza, la riduzione della capacità portante degli elementi in CA e CAP nel corso del tempo, causando - talvolta - cedimenti inaspettati dovuti alla mancanza di resistenza a flessione, a taglio o all'ancoraggio. Queste modalità di rottura possono avvenire senza segnali premonitori, inducendo un elevato rischio in termini di perdite di vite umane e determinando un significativo impatto economico. In questo contesto, negli ultimi decenni, numerosi crolli di edifici e ponti in CAP si sono verificati in tutto il mondo, come il ben noto crollo del Palazzo dei Congressi di Berlino in Germania e il più recente crollo del Viadotto Polcevera in Italia. Questi eventi recenti e passati hanno evidenziato l'urgente necessità di protocolli di manutenzione affidabili e rigorosi, nonché la formulazione di modelli analitici semplificati in grado di valutare la capacità strutturale residua di elementi strutturali deteriorati, promuovendo il tema della corrosione come un argomento di grande interesse per la comunità scientifica. A dispetto delle molteplici forme di corrosione possibili, nel caso di elementi in CAP, le conseguenze peggiori sono indotte dalla corrosione da cloruri, in quanto il pitting può causare concentrazioni tensionali e localizzazione delle deformazioni in fili da precompressione, che risultano abitualmente sottoposti a elevate sollecitazioni meccaniche iniziali.

Sebbene recenti studi sperimentali, numerici e analitici siano stati condotti su elementi in CA, le conoscenze riguardo strutture corrose in CAP si rivelano essere ancora incerte e limitate. I motivi principali sono i seguenti:

(i) La maggior parte delle ricerche sperimentali, riguardanti l'analisi della capacità strutturale residua di elementi corrosi, sono state eseguite adottando un processo di corrosione accelerato artificialmente.

(ii) Pochi studi si sono concentrati sull'analisi della variabilità longitudinale e sezionale delle armature di precompressione corrose.

(iii) La letteratura scientifica ha rivelato un numero insufficiente di modelli che studiano il comportamento meccanico residuo dei trefoli da precompressione corrosi.

(iv) Codici e linee guida, che trattano le problematiche della corrosione ai fini della valutazione della vita utile residua, non sono complete e opportunamente validate.

In primo luogo, al fine di estendere le attuali conoscenze, la presente tesi analizza travi in CAP corrose naturalmente e sottoposte a 10 anni di cicli di bagnatura e asciugatura con acqua di mare. Lo studio mira a indagare l'influenza della corrosione sulle prestazioni strutturali residue. A tal fine, due campioni non corrosi di travi in CAP sono stati realizzati con lo stesso tipo di calcestruzzo e condizioni di maturazione, successivamente testati per essere da riferimento per la quantificazione degli effetti associati alla corrosione. Durante le prove meccaniche a tre e quattro punti di carico, si è eseguita la tecnica della "Digital Image Correlation" (DIC), scattando foto ad ogni fase di carico, al fine della valutazione dell'evoluzione dei campi di spostamento e deformazione di ogni trave testata.

In secondo luogo, la tesi definisce legami costitutivi per la previsione del comportamento meccanico residuo dei trefoli da precompressione corrosi. A tal fine, i modelli 3D dei provini dei trefoli corrosi e non corrosi recuperati sono stati realizzati utilizzando uno scanner 3D a luce strutturata. Dopodiché, la variabilità spaziale della morfologia da pitting in direzione longitudinale e sezionale è stata esaminata attraverso la sovrapposizione dei modelli 3D corroso e non corroso utilizzando il software GOM Inspect. Successivamente, prove di trazione sui trefoli disponibili sono state eseguite per la calibrazione dei modelli. Sulla base dei risultati ottenuti, due legami costitutivi, denominati modello CPS e modello SCPS, sono stati proposti per prevedere la relazione forza-deformazione o tensione-deformazione di un trefolo corroso. Sebbene i due legami costitutivi vedano assunzioni differenti, entrambi adottano il modello a molla equivalente ("equivalent spring model"), il quale riproduce la risposta resistente complessiva del trefolo come la somma dei contributi dei singoli fili, assunti come molle che lavorano in parallelo tra loro. Da una parte, il modello CPS assume la perdita di sezione trasversale di ciascun filo come principale parametro di input per la previsione della resistenza e della deformazione ultima distinguendo tra tre configurazioni morfologiche del pit – conosciute come forma emisferica, semilunare e planare -. Il modello SCPS, d'altra parte, è una versione semplificata del modello CPS per la pratica ingegneristica quotidiana ed è

concepito sulla base di un unico parametro di input che è la massima profondità di penetrazione del filo più corroso. Tale modello è indipendente dalle possibili configurazioni morfologiche del pit e considera un'unica legge di decadimento per la previsione della deformazione ultima. Inoltre, sulla base dei risultati inerenti alla stima della morfologia da pitting sezionale, il modello attribuisce ai restanti fili esterni una profondità di penetrazione media attraverso una correlazione sperimentale definita in funzione della profondità di penetrazione massima del filo più corroso.

Infine, un approccio analitico è stato definito per la valutazione della capacità residua flessionale e di taglio di travi corrose in CAP prive di armatura trasversale. A tale scopo, il modello quantifica dapprima le perdite di precompressione istantanee e dipendenti dal tempo associate: (i) alla contrazione elastica del calcestruzzo dovuta al rilascio dei cavi da precompressione, (ii) al fenomeno di rilassamento dei trefoli nel tempo, e (iii) agli effetti reologici di ritiro e viscosità. Successivamente, i parametri di corrosione di (i) penetrazione media dei rimanenti fili esterni, (ii) sezione persa, e (iii) massa persa, sono calcolati sulla base del "corrosion pattern" della trave in CAP analizzata, definito tramite analisi visiva. In dettaglio, l'approccio assume la massima profondità del filo più corroso come unico parametro di input, e definisce quattro possibili scenari di corrosione, mentre Il modello SCPS viene assunto per la previsione della risposta meccanica residua dei trefoli corrosi. Ulteriormente, sono stati introdotti modelli analitici che stimano la variazione della lunghezza di trasmissione e il decadimento della resistenza ultima dovuta all'aderenza acciaio-calcestruzzo al variare del livello di corrosione. Infine, la capacità residua a flessione e a taglio dell'elemento in CAP è determinata tramite condizioni di equilibrio e compatibilità delle deformazioni. Da una parte, la capacità residua flessionale è valutata tramite la proposta di un legame semplificato per la definizione del diagramma momento-curvatura. D'altra parte, la capacità residua a taglio per elementi in CAP privi di armatura trasversale è stimata attraverso l'espressione fornita dal Model Code 2010 – livello II di approssimazione – opportunamente modificata per considerare gli effetti della corrosione.

L'accuratezza e le potenzialità dei modelli proposti sono stati validati tramite il confronto con prove sperimentali. Inoltre, i risultati ottenuti e i confronti condotti hanno permesso di valutare l'affidabilità dei modelli analitici proposti per la valutazione della risposta meccanica residua di trefoli corrosi. Nel dettaglio, la stima su base probabilistica delle incertezze di modello - associate all'utilizzo del modello SCPS - ha consentito la determinazione preliminare di un coefficiente parziale di sicurezza da adottare per la stima della resistenza di progetto di

trefoli corrosi. Vale la pena sottolineare che la quantificazione delle incertezze in gioco è stata condotta sulla base delle raccomandazioni fornite dal Draft del Model Code 2020.

In conclusione, sono state delineate le principali osservazioni, le ricerche future e i miglioramenti necessari.

List of Figures

Figures – Main Text

Figure 1-1 Research in Scopus-indexed journal concerning corroded RC and PC members: (a) trend of the number of publication in the period 1962-2022, and (b) scientific areas of research for corroded PC members. (https://www.scopus.com/). 1-4
Figure 1-2 Identification of countries as a function of the number of published works on corroded PC members, (https://www.scopus.com/). 1-5
Figure 1-3 Scheme of the all research activities. 1-10
Figure 2-1 Schematic representation of the electrochemical process of corrosion. 2-4
Figure 2-2 Corrosion mechanisms: (a) microcells and (b) macrocells. 2-7
Figure 2-3 Tuutti's model schematic representation from *fib* Bulletin 34 (2006). Reproduced from *fib* Bulletin 34 - Model code for service life design, page 91 - "Figure R1.1-1: Deterioration process of reinforcement corrosion and life design definition of limit states for basic scheme of the service life design" with permission from the International Federation for Structural Concrete (*fib*). 2-8
Figure 2-4 Carbonation-induced corrosion: focus on the penetration ingress of atmospheric carbon dioxide (CO_2) and example of carbonation front. 2-10
Figure 2-5 Chloride-induced corrosion: focus on the penetration ingress of chloride ions (Cl^-) and mechanism of corrosion. 2-12
Figure 2-6 Factors influencing the threshold concentration of chloride ions. 2-13
Figure 2-7 Classifications of corrosion forms. 2-16
Figure 3-1 Timeline of principal collapses and heavy damaged bridge from 1960. 3-3
Figure 3-2 Partial collapse of the Berlin Congress Hall, reproduced from (Plank et al., 1981). 3-4
Figure 3-3 Collapse of the Ynys-y-Gwas Bridge, (Woodward & Williams, 1988). Reproduced with permission from ICE Publishing. 3-5
Figure 3-4 Collapse of the Polcevera Viaduct. (https://theconversation.com/genoa-bridge-collapse-maintaining-these-structures-is-a-constant-battle-against-traffic-and-decay-101627). 3-6
Figure 3-5 Relevance of corrosion costs on the U.S. economy, reproduced from Angst (2018). 3-9

Figure 3-6 Schematic representation of IC methods: (a) soaking method, (b) part soaking method, (c) surface coating method and (d) embedded auxiliary electrode method, (J. Chen et al., 2020). Reproduced with permission from Elsevier. 3-13
Figure 3-7 Schematic representation of ACE method, (I. Khan et al., 2014). Reproduced with permission from Springer Nature. 3-14
Figure 3-8 Analysis of the mechanical behaviours investigated through experimental campaigns. 3-25
Figure 3-9 Analysis of the current density ranges in the case of IC method adoption. 3-26
Figure 3-10 Comparative example between corroded and un-corroded pre-tensioned PC beams, adapted from Rinaldi et al. (2010). 3-28
Figure 3-11 Highlights on the available 10 years old PC beams. 3-32
Figure 3-12 Approaches for the reproduction of the mechanical behaviour of prestressing strands: (a) equivalent bar model and (b) equivalent spring model. 3-34
Figure 3-13 Classification of corrosion type in the case of corroded reinforcements, adapted from (Andrade, 2021). Reproduced from the "Proceedings of CACRCS DAYS 2021: Capacity Assessment of Corroded Reinforced Concrete Structures" with permission from the International Federation for Structural Concrete (*fib*) 3-35
Figure 3-14 Hemispherical pit type morphology configuration for localized pitting corrosion. 3-36
Figure 3-15 Planar pit type morphology configuration for localized pitting corrosion. 3-37
Figure 3-16 Half-moon pit type morphology configuration for localized pitting corrosion. 3-37
Figure 3-17 Additional pit type morphology configurations introduced by: (a) Wang et al. (2020) and (b) Yoo et al. (2018; 2020). 3-39
Figure 3-18 Morphology configuration: (a) homogeneous corrosion and (b) pitting corrosion, adapted from CONTECVET manual (2001). 3-39
Figure 3-19 Tensile tests outcomes from analyzed experimental campaigns, expressed in terms of normalized ultimate strength, $f_{pu,corr}/f_{pu,0}$: (a) strand mass loss, and (b) strand section loss. 3-42
Figure 3-20 Tensile tests outcomes from analyzed experimental campaigns, expressed in terms of normalized ultimate strain, $\varepsilon_{pu,corr}/\varepsilon_{pu,0}$: (a) strand mass loss, and (b) strand section loss. 3-42
Figure 3-21 Decay relationships available in scientific literature for the prediction of: (a) ultimate strain, and (b) ultimate strength, adapted from Belluco et al. (2021). 3-43
Figure 3-22 Bilinear model for the stress-strain relationship of corroded and un-corroded strands. 3-44

Figure 3-23 Steps of the structural assessment of corroded members. 3-49
Figure 4-1 Beam details: (a) and (b) longitudinal configurations of two campaigns, (c) cross-section..... 4-4
Figure 4-2 Evaluation of concrete compressive strength: (a) concrete core samples, (b) compressive uniaxial test machine and (c) example of sample failure. 4-5
Figure 4-3 Detected surface defects of concrete. 4-7
Figure 4-4 Crack pattern of corroded PC beams. 4-8
Figure 4-5 Focus on the construction practice deficiency identified at (a) left and (b) right beam edges. 4-9
Figure 4-6 Test set-up for corrosion potential methodology..... 4-11
Figure 4-7 Corrosion potential maps along the overall length of each PC beam..... 4-12
Figure 4-8 Test set-up for linear polarization methodology – I_{corr} measurements..... 4-14
Figure 4-9 Main outcomes: (a) corrosion rate and (b) ohmic drop values. 4-15
Figure 4-10 Spectrophotometry XRF technique procedure: (a) retrieval of samples, (b) crumbling of concrete, (c) test arrangement and (d) chloride test execution. 4-17
Figure 4-11 Main outcomes from chloride tests. 4-18
Figure 4-12 Relationship between corrosion rate and ohmic drop. 4-19
Figure 4-13 Relationship between corrosion rate and chloride ions concentration. 4-20
Figure 5-1 Experimental test set-up: (a) three-point loading system and (b) four-point loading system. 5-4
Figure 5-2 Focus on loading system components: (a) steel plate under the loading point, (b) steel plate at supports and (c) servo-hydraulic actuator. 5-4
Figure 5-3 DIC methodology set-up: (a) ROI identification, (b) focus on high resolution digital camera and (c) focus on random high-contrast uniform speckle pattern. 5-6
Figure 5-4 Evaluation of corrosion level of prestressing reinforcements: (a) procedure of strands extraction after testing and (b) extracted reinforcements. 5-7
Figure 5-5 Failure analysis of PBN3P1 beam: (a) crack pattern, (b) corrosion patter – in the case of un-corroded beam is not available -, (c) beam at failure, (d) DIC analysis and (e) vertical displacement along the beam length for increasing load values. 5-11
Figure 5-6 Failure analysis of PB3P10 beam: (a) crack pattern, (b) corrosion patter, (c) beam at failure, (d) DIC analysis, and (e) vertical displacement along the beam length for increasing load values. 5-12

Figure 5-7 Failure analysis of PB3P11 beam: (a) crack pattern, (b) corrosion patter, (c) beam at failure, (d) DIC analysis and (e) vertical displacement along the beam length for increasing load values. 5-13
Figure 5-8 Experimental load-deflection curve from three-point bending tests for beam: (a) PBN3P1, (b) PB3P10 and (c) PB3P11. 5-14
Figure 5-9 Focus on detected shear failure modes: (a) Shear I and (b) Shear II. 5-18
Figure 5-10 Failure analysis of PBN4P2 beam: (a) crack pattern, (b) corrosion patter – in the case of un-corroded beam is not available -, (c) beam at failure, (d) DIC analysis and (e) vertical displacement along the beam length for increasing load values. 5-22
Figure 5-11 Failure analysis of PB4P5 beam: (a) crack pattern, (b) corrosion patter, (c) beam at failure, (d) DIC analysis and (e) vertical displacement along the beam length for increasing load values. 5-23
Figure 5-12 Failure analysis of PB4P6 beam: (a) crack pattern, (b) corrosion patter, (c) beam at failure, (d) DIC analysis and (e) vertical displacement along the beam length for increasing load values. 5-24
Figure 5-13 Failure analysis of PB4P7 beam: (a) crack pattern, (b) corrosion patter, (c) beam at failure, (d) DIC analysis and (e) vertical displacement along the beam length for increasing load values. 5-25
Figure 5-14 Failure analysis of PB4P8 beam: (a) crack pattern, (b) corrosion patter, (c) beam at failure, (d) DIC analysis and (e) vertical displacement along the beam length for increasing load values. 5-26
Figure 5-15 Failure analysis of PB4P9 beam: (a) crack pattern, (b) corrosion patter, (c) beam at failure, (d) DIC analysis and (e) vertical displacement along the beam length for increasing load values. 5-27
Figure 5-16 Failure analysis of PB4P13 beam: (a) crack pattern, (b) corrosion patter, (c) beam at failure, (d) DIC analysis and (e) vertical displacement along the beam length for increasing load values. 5-28
Figure 5-17 Failure analysis of PB4P14 beam: (a) crack pattern, (b) corrosion patter, (c) beam at failure, (d) DIC analysis and (e) vertical displacement along the beam length for increasing load values. 5-29
Figure 5-18 Experimental load-deflection curve from four-point bending tests for beam: (a) PBN4P2, (b) PB4P5, (c) PB4P6, (d) PB4P7, (e) PB4P8, (f) PB4P9, (g) PB4P13 and (h) PB4P14. 5-30
Figure 6-1 Step-by step procedure for the pitting morphology analysis. 6-6

Figure 6-2 Location of samples and relations with crack pattern. 6-9
Figure 6-3 Retrieved samples classified as a function of L_i: (a) twelve samples 450 mm long and (b) twelve samples 700 mm long. 6-10
Figure 6-4 Estimation of the weight loss Δ_2 in the case of sample PB11-L(196-266). 6-11
Figure 6-5 3D scanning system: (a) general overview of the final configuration and (b) focus on principal components. 6-12
Figure 6-6 Custom-made fixing elements: (a) 3D printer and (b) realized components. 6-13
Figure 6-7 GOM Inspect phase: (a) mesh repairing and (b) superimposition of corroded and un-corroded 3D models. 6-15
Figure 6-8 Focus on the analyzed corrosion parameters. 6-16
Figure 6-9 Calculation of number of pits as a function of different corrosion level: (a) low corrosion, (b) intermediate corrosion, and (c) high corrosion level. 6-17
Figure 6-10 Sectional analysis every 10 mm for the evaluation of pitting corrosion parameters. 6-18
Figure 6-11 Assumed pit type morphology configurations. 6-19
Figure 6-12 Maximum penetration depths classification: (a) adopting three different pit type morphology configurations, and (b) considering only Type 3 morphology. 6-20
Figure 6-13 Variability of penetration depth as a function of different corrosion levels..... 6-23
Figure 6-14 Pitting spatial variability of corroded samples unaffected by surface defects of concrete: (a) low, (b) intermediate and (c) high corrosion level. 6-25
Figure 6-15 Pitting spatial variability of corroded samples affected by surface defects of concrete: (a) with and (b) without the additional effect of construction practice deficiency..... 6-27
Figure 6-16 Correlations for the evaluation of $P_{max,long}/r_{outer}$ as a function of surface defects of concrete: (a) $P_{max,long}/r_{outer}$ vs n_{pits}/m, (b) $P_{max,long}/r_{outer}$ vs $P_{av,long1}/r_{outer}$ and (c) $P_{max,long}/r_{outer}$ vs η. 6-29
Figure 6-17 Sample PB9-L(12-82) distribution functions comparison: (a) PDF and (b) CDF. 6-34
Figure 6-18 Lognormal distributions for each corroded strands in terms of (a) PDF and (b) CDF. 6-35
Figure 6-19 Lognormal distribution function for the longitudinal maximum penetration depth, $P_{max,long}$, expressed in terms of PDF: (a) normal and (b) semilogarithmic scale. 6-36
Figure 6-20 Variability of residual cross-section of corroded strand as a function of corrosion level. 6-38

Figure 6-21 Comparison of corrosion parameters (P_x and A_{min}) for corroded samples retrieved from the left edge of beam PB4P14. 6-39
Figure 6-22 Focus on $P_{av,transv,i}$ calculation. 6-40
Figure 6-23 Regression trend for the prediction of the transversal pitting factor Ω_i. 6-42
Figure 6-24 Relationship between η and $P_{max,long}$. 6-45
Figure 6-25 Relationship between η and $P_{max,long}/r_{outer}$. 6-46
Figure 6-26 Relationship between η and $A_{min}/A_{p,0}$. 6-46
Figure 6-27 Relationship between $P_{max,long}$ and μ_{max}. 6-50
Figure 6-28 Relationship between μ_{max} and μ_{strand} 6-51
Figure 6-29 Focus on $P_{av,long3}$ calculation. 6-53
Figure 6-30 Pitting factor variability for: (a) $P_{av,long1}$, (b) $P_{av,long2}$ and (c) $P_{av,long3}$ measurements for increasing corrosion level expressed in terms of mass loss values, η. 6-55
Figure 6-31 Relationship between $P_{max,long}$ and $P_{av,long3}$. 6-56
Figure 7-1 Tensile test set-up at the Laboratory MastrLab of the Politecnico of Turin. 7-6
Figure 7-2 Focus on DIC methodology: (a) definition of ROI and speckle patter, and (b) example of post-processing of taken images by adopting Ncorr software. 7-6
Figure 7-3 Experimental stress-strain relationships for un-corroded samples. 7-8
Figure 7-4 Experimental stress-strain relationships for corroded samples. 7-10
Figure 7-5 Focus on the failure sequence of sample PB9-L(426-496). 7-11
Figure 7-6 Comparison of experimental data with outcomes available in scientific literature as a function of strand mass loss: (a) ultimate corroded strength, and (b) ultimate corroded strain. 7-13
Figure 7-7 Comparison of experimental data with outcomes available in scientific literature as a function of the cross-sectional loss of the most corroded wire: (a) ultimate corroded strength, and (b) ultimate corroded strain. 7-14
Figure 7-8 Flowchart of the main steps of the CPS-model. 7-19
Figure 7-9 Focus on the tri-linear response of the un-corroded wire. 7-20
Figure 7-10 Ultimate strain decay as a function of the cross-sectional loss of the most corroded wire: (a) pit type configuration 1, (b) pit type configuration 2 and (c) pit type configuration 3. 7-23
Figure 7-11 Ultimate strength decay as a function of the cross-sectional loss of the most corroded wire: (a) pit type configuration 1, (b) pit type configuration 2 and (c) pit type configuration 3. 7-25

Figure 7-12 Changing of the stress-strain relationship of a corroded wire for different corrosion levels.....7-26
Figure 7-13 Comparison between experimental and analytical predictions (CPS-model) of stress-strain relationships of un-corroded strands. 7-27
Figure 7-14 Comparison between experimental and analytical predictions (CPS-model) of stress-strain relationships of corroded strands. 7-30
Figure 7-15 Comparison of failure sequence for corroded strands evaluated from tensile test outcomes and predicted by adopting the CPS-model – sample PB9-L(12-82).....7-32
Figure 7-16 Comparison between experimental and analytical predictions for un-corroded and corroded strands belonging to Jeon et al (2019) work. 7-36
Figure 7-17 Comparison between experimental and analytical predictions for un-corroded and corroded strands belonging to Giriraju et al. (2022) work. 7-37
Figure 7-18 Flowchart of the main steps of the SCPS-model in comparison with the CPS-model. 7-48
Figure 7-19 Ultimate corroded strain decay, definition of the bi-linear trend. 7-51
Figure 7-20 Ultimate corroded cross-sectional area decay, definition of a bi-linear trend...7-53
Figure 7-21 Stress-strain relationship of a prestressing wire as a function of different corrosion levels: (a) un-corroded, (b) low corroded, (c) intermediate corroded, and (d) high corroded. 7-54
Figure 7-22 Equivalent spring model: residual mechanical response of a corroded strand considering different corrosion levels. 7-56
Figure 7-23 Comparison between experimental and analytical predictions – by adopting both the CPS- and SCPS-models – of the corroded strands belonging to the present research tensile tests outcomes. 7-64
Figure 7-24 Comparison between experimental and analytical predictions – by adopting both the CPS- and SCPS-models – of the corroded strands belonging Jeon et al. (2019) experimental activity. 7-65
Figure 7-25 Comparison of experimental and analytical results by adopting the CPS- and SCPS-models – in terms of : (a) ultimate strength, $f_{pu,corr,exp}/f_{pu,corr,an}$, and (b) ultimate strain, $\varepsilon_{pu,corr,exp}/\varepsilon_{pu,corr,an}$. 7-67
Figure 7-26 Focus on the SCPS-model uncertainties.....7-74
Figure 7-27 θ_i values for investigated corroded strands; orange line represents the perfect matching between experimental outcomes and analytical predictions. 7-78

Figure 7-28 Quantile plot by considering θ_i values for investigated corroded strands – adopting a Lognormal distribution function.....7-79
Figure 8-1 Flowchart of the main phases of the proposed analytical model.....8-2
Figure 8-2 Flexural and shear demand evaluation for three-point bending loading configuration. 8-5
Figure 8-3 Flexural and shear demand evaluation for four-point bending loading configuration. 8-7
Figure 8-4 Focus on the prestressing losses due to releasing of strands. 8-8
Figure 8-5 Flowchart for the quantification of corrosion effects. 8-13
Figure 8-6 Lognormal distribution function of maximum penetration depths for different corrosion scenarios: (a) PDF and (b) CDF with a focus on fractile value at 50%, $P_{max,0.5}$. ..8-15
Figure 8-7 Focus on the correspondence between cross-sectional loss and mass loss of a corroded strand along the visually inspected length, $L_{inspected}$. 8-17
Figure 8-8 Residual mechanical response of corroded strands having different corrosion levels. 8-18
Figure 8-9 Sectional residual mechanical response assignment to corroded strands as a function of PC beam corrosion pattern: example for beam PB3P11.....8-19
Figure 8-10 Normalized corroded transmission length according to the simplified approach proposed by Anaya et al. (2022). 8-22
Figure 8-11 Normalized bond strength decay laws.....8-26
Figure 8-12 Simplified constitutive law for concrete in compression and in tension. 8-27
Figure 8-13 SCPS-model for un-corroded prestressing strands. 8-28
Figure 8-14 Simplified quadrilinear trend for the definition of the sectional moment-curvature diagram of a prestressed concrete beam. 8-29
Figure 8-15 Corrosion scenarios and residual mechanical response of corroded strands by adopting SCPS-model: (a) low corrosion, (b) intermediate corrosion, and (c) high corrosion. 8-31
Figure 8-16 Identification of the cross-sectional failure cases: (a) Failure Case 1, (b) Failure Case 2, and (c) Failure Case 3. 8-32
Figure 8-17 Principle of superimposition: sectional contributions due to (i) prestressing force, (ii) moment due to prestressing and eccentricity of strands, and (iii) acting bending moment. 8-35
Figure 8-18 Geometrical definition of the equivalent shear depth, z^*.....8-37

Figure 8-19 Simplified moment-curvature diagram validation on experimental outcomes available in literature: (a) test set-up from Billet (1953), (b)-(e) specimens B5 to B12. 8-43
Figure 8-20 Simplified moment-curvature diagrams for corroded and un-corroded scenarios: (a) M-χ responses, and (b) strands and concrete strains vs corrosion levels. 8-48
Figure 8-21 Longitudinal strain at mid-height of the effective shear depth trend for corroded and un-corroded scenarios. 8-48
Figure 8-22 (a) Ultimate moment and cracking moment reduction, and (b) prestress level reduction for the different corrosion scenarios considered. 8-49
Figure 8-23 Comparison between longitudinal strains at mid-height of the effective shear depth for corroded and un-corroded scenarios. 8-53
Figure 8-24 Location of critical section for beams with pinned and fixed supports under point and uniform loading. 8-57
Figure 8-25 Failure mode and analytical prediction for the un-corroded beam PBN3P1 8-57
Figure 8-26 Failure mode and analytical prediction for the un-corroded beam PBN4P2 8-58
Figure 8-27 Failure mode and analytical prediction for the corroded beam PB3P11. 8-59
Figure 8-28 Failure mode and analytical prediction for the corroded beam PB4P6. 8-60
Figure 8-29 Failure mode and analytical prediction for the corroded beam PB4P7. 8-61
Figure 8-30 Comparison of ultimate load from experimental tests and analytical methods. 8-63
Figure 8-31 Analytical ultimate load percentage ratio (corroded/un-corroded) considering different corrosion levels. 8-64
Figure 8-32 Average vs design: (a) stress-strain of prestressing steel, (b) moment-curvature response. 8-66
Figure 8-33 Average vs design: predicted loads at failure of beams with un-corroded and corroded (mean and design) properties. 8-68
Figure 8-34 Ratio between design and mean loads at failure. 8-68
Figure A-1 Analysis of the mechanical behaviour investigated through experimental campaigns. xxxiv
Figure A-2 Analysis of the corrosion methods adopted in experimental campaigns to investigate the corrosion effects: (a) percentage subdivision and (b) range of current density in the case of IC method. xxxv

List of Tables

Tables – Main Text

Table 1-1 Outline of the *Thesis*. 1-11
Table 2-1 Chloride threshold values from codes and guidelines, adapted from (Ann & Song, 2007). 2-13
Table 3-1 Features of bridges and structures subjected to heavy damages or collapsed due to corrosion. 3-6
Table 3-2 State-of-the-Art on post-tensioned corroded PC beams: geometrical properties and reinforcements. 3-17
Table 3-3 State-of-the-Art on post-tensioned corroded PC beams: corrosion process, exposure environment, and beams failure mode. 3-20
Table 3-4 State-of-the-Art on artificially corroded pre-tensioned PC beams: geometrical properties and reinforcements. 3-22
Table 3-5 State-of-the-Art on naturally corroded pre-tensioned PC beams: geometrical properties and reinforcements. 3-23
Table 3-6 State-of-the-Art on artificially corroded pre-tensioned PC beams: corrosion process, exposure environment, and beams failure mode. 3-24
Table 3-7 State-of-the-Art on naturally corroded pre-tensioned PC beams: corrosion process, exposure environment, and beams failure. 3-25
Table 3-8 Corrosion amount measured during the experimental campaigns on corroded PC specimens: (left) artificially accelerated, and (right) from natural environment. 3-27
Table 3-9 State-of-the-Art on analytical models for the prediction of the residual mechanical response of corroded prestressing strand. 3-41
Table 3-10 Critical mass loss or cross-sectional loss threshold for the different available models. 3-44
Table 4-1 Corrosion potential measurements, E_{corr}. 4-12
Table 4-2 Corrosion rate and ohmic drop measurements. 4-16
Table 4-3 Chloride content measurements. 4-17
Table 5-1 Geometrical features of tested beams. 5-5
Table 5-2 Corrosion levels definition. 5-7

Table 5-3 Flexural response of tested beams: experimental outcomes from three-point bending tests. 5-10
Table 5-4 Shear response of tested beams: experimental outcomes from four-point bending tests. 5-21
Table 6-1 Classification of retrieved prestressing strands samples. 6-8
Table 6-2 Corrosion classification of corroded strands. 6-22
Table 6-3 Relevant corrosion parameters estimated from the pitting variability of corroded strands. 6-32
Table 6-4 Main statistical parameters of the Lognormal distribution function of each corroded strand. 6-37
Table 6-5 Longitudinal average penetration depths and corresponding pitting factors in the case of corroded strands. 6-57
Table 7-1 Tensile test outcomes in terms of ultimate tensile force, $T_{pu,corr,exp}$, ultimate strength, $f_{pu,corr,exp}$, and ultimate strain, $\varepsilon_{pu,corr,exp}$. The reported data consider also the un-corroded samples. 7-15
Table 7-2 Tensile test outcomes in terms of ultimate strength, $f_{pu,corr,exp}$, and ultimate strain, $\varepsilon_{pu,corr,exp}$, of un-corroded and corroded samples belonging to Jeon et al. (2019) and Giriraju et al. (2022) experimental activities. 7-34
Table 7-3 CPS-model predictions in terms of ultimate strength, $f_{pu,corr,an1}$, ultimate strain, $\varepsilon_{pu,corr,an1}$, normalized strength, $f_{pu,corr,exp}/f_{pu,corr,an1}$, and normalized strain, $\varepsilon_{pu,corr,exp}/\varepsilon_{pu,corr,an1}$. The reported data consider also the un-corroded samples. 7-39
Table 7-4 SCPS-model predictions in terms of ultimate strength, $f_{pu,corr,an2}$, ultimate strain, $\varepsilon_{pu,corr,an2}$, normalized strength, $f_{pu,corr,exp}/f_{pu,corr,an2}$, and normalized strain, $\varepsilon_{pu,corr,exp}/\varepsilon_{pu,corr,an2}$. The reported data consider also the un-corroded samples. 7-68
Table 7-5. β_{target} evaluation based on economic optimization. 7-72
Table 7-6 Main parameters of the probabilistic evaluation of the maximum penetration depth to be used as input parameter of the SCPS-model and updated $\boldsymbol{f_{pu,corr,an2}}$ predictions. 7-77
Table 7-7 SCPS-model: Shapiro-Wilk test of normality outcomes. 7-80
Table 8-1. Maximum and average pit depths for the different corrosion scenarios considered. 8-14
Table 8-2 Test set-up and geometrical features, Billet (1953). 8-42
Table 8-3 Mechanical properties of B5, B7, B9, and B12 specimens, Billet (1953). 8-42
Table 8-4 Comparison between experimental outcomes and analytical predictions obtained by adopting the proposed analytical model. 8-62

Table 8-5 Comparison between experimental outcomes and analytical predictions obtained by adopting the analytical approach proposed by Walraven (2020). 8-62
Table 8-6 Mechanical properties and partial safety factors assumed for concrete and prestressing steel. 8-66
Table 8-7 Comparison between analytical load at failure for beams with un-corroded and corroded (mean and design) properties. 8-67
Table A-1 State-of-the-Art on flexural and shear experimental behaviour of corroded RC beams. xxxi
Table A-2 State-of-the-Art on tensile tests and residual mechanical response of corroded rebars. xxxvi
Table A-3 Geometrical description of the maximum pit for each external wire and additional classification of the corresponding area loss due to pitting. xl
Table A-4 Cross-sectional loss, μ, of each external wire at the section where the longitudinal maximum pit depth, $P_{max,long}$, was measured. xliii

List of Symbols & Acronyms

Chapter 1

RC & PC	Reinforced Concrete and Prestressed Concrete
NaCl & $CaCl_2$	Sodium and calcium chloride
ASCE	American Society of Civil Engineers
FHWA	Federal Highway Administration
DIC	Digital Image Correlation
ASTM	American Society for Testing and Materials

Chapter 2

ISO	International Organization for Standardization
REDOX	Reduction and Oxidation reactions
OH^-	Hydroxyl ions
$Ca(OH)_2$	Calcium hydroxide
Fe	Iron atoms
Fe^{2+}	Ferrous ions
Fe^{3+}	Ferric ions
$Fe(OH)_2$	Ferrous hydroxides
$Fe(OH)_3$	Ferric hydroxides
Fe_20_3	Ferrous oxides
H_2O & O_2	Water and Oxygen

H^+	Hydrogen ions
Cl^-	Chloride ions
SLS	Serviceability Limit State
ULS	Ultimate Limit State
X, XC, XD, XS	Exposure classes
CO_2	Carbon dioxide
NaOH	Sodium hydroxides
KOH	Potassium hydroxides
Na_2CO_3	Sodium carbonates
K_2CO_3	Potassium carbonates
$CaCO_3$	Calcium carbonates
pH	Potential hydrogen
CO_3^{2-}	Carbonic acid
Na^+	Sodium ions
K^+	Potassium ions
Ca^{2+}	Calcium ions
HCO_3^-	Bicarbonates
$NaHCO_3$	Sodium bicarbonates
$KHCO_3$	Potassium bicarbonates
$Ca(HCO_3)_2$	Calcium bicarbonates
C_{crit}	Threshold concentration of chloride ions
$FeCl_2$	Ferrous chlorides
ACI	American Concrete Institute
BS	British Standard

CEB	Comité Euro-international du Béton
$C_3ACaCl_2.10H_2O$	Calcium chloroaluminate
C_3A	Tri calcium aluminate
GC	Galvanic Corrosion
EC	Erosion-Corrosion
CC	Crevice Corrosion
SCC	Stress-Corrosion Cracking
HE	Hydrogen Embrittlement
CF	Corrosion Fatigue
H^0	Molecular hydrogens
IPCC	Intergovernmental Panel on Climate Change
SRES	Special Report on Emissions Scenarios
RCP	Representative Concentration Pathway
RF	Radiative Force

Chapter 3

MCEER	Multidisciplinary Centre of Earthquake Engineering Research
UK	United Kingdom
GNP	Gross National Products
NACE	National Association of Corrosion Engineers International
GDP	Gross Domestic Product
NIST	National Institute of Standard and Technologies
IC	Impressed Current method

CID	Chloride Ion Diffusion method
ACE	Artificial Climate Environment method
t_{test}	Testing period
η	Mass loss
$M_{specimen}$	Molar mass of steel reinforcement
$n_{specimen}$	Steel valence
$C_{Faraday}$	Faraday constant
ξ	Constant for rebar types
SM	Soaking Method
PSM	Part Soaking Method
SCM	Surface Coating Method
EEM	Embedded auxiliary Electrode Method
I_{corr}	Current density
NAT	Natural corrosion
FPBT	Four-Point Bending Test
TPBT	Three-Point Bending Test
CFRP	Carbon Fibre Reinforced Polymers
h	Beam height
b	Beam width
m_0	Weight of un-corroded reinforcement
m_{corr}	Weight of corroded reinforcement
A_0	Un-corroded area (cross-section) of reinforcement
A_p	Area loss due to pitting
A_{min}	Minimum residual area (cross-section) of reinforcement

ϕ_t	Residual diameter of corroded reinforcement
ϕ_0	Un-corroded diameter of reinforcement
P_x	Radius loss
P_{corr}	Radius loss in the case of homogenous corrosion
P_{pit}	Radius loss – Pit depth – in the case of pitting corrosion
V_{corr}	Corrosion rate
t_p	Propagation period
α	Pitting factor
r	Un-corroded radius of reinforcement
p	Corrosion perimeter
M	Monotonic loading test (Appendix A.2)
C	Cyclic (Fatigue) loading test (Appendix A.2)
μ_{max}	Maximum cross-sectional loss
P_{max}	Maximum penetration depth
f_y	Yield strength of rebar (Appendix A.2)
f_u	Ultimate strength of rebar (Appendix A.2)
ε_u	Ultimate strain of rebar (Appendix A.2)
E_s	Elasticity modulus of rebar (Appendix A.2)
$E_{s,0}$	Un-corroded elasticity modulus of rebar (Appendix A.2)
$f_{y,corr}$	Yield strength of corroded rebar (Appendix A.2)
$f_{u,corr}$	Ultimate strength of corroded rebar (Appendix A.2)
$\varepsilon_{u,corr}$	Ultimate strain of corroded rebar (Appendix A.2)
$f_{y,0}$	Un-corroded yield strength of rebar (Appendix A.2)
$f_{u,0}$	Un-corroded ultimate strength of rebar (Appendix A.2)

$\varepsilon_{u,0}$	Un-corroded ultimate strain of rebar (Appendix A.2)
$f_{py,corr}$	Yield strength of corroded prestressing reinforcement
$f_{pu,corr}$	Ultimate strength of corroded prestressing reinforcement
$\varepsilon_{pu,corr}$	Ultimate strain of corroded prestressing reinforcement
$E_{p,0}$	Un-corroded elasticity modulus of prestressing reinforcement
μ_{av}	Average cross-sectional loss
μ_{crit}	Critical cross-sectional loss threshold
η_{crit}	Critical mass loss threshold
x	Thickness of concrete cover
C_0	Initial chloride content
$C(x,t)$	Chloride content at depth x and at time t
C_{sa}	Chloride content achieved at concrete surface
D_{cl}	Chloride diffusion coefficient
fib	Federation International du Béton
HCPW	High Council for Public Works

Chapter 4

L_{tot}	Beam total length
$\phi_{eq,0}$	Equivalent un-corroded diameter of prestressing reinforcement
r_{outer}	Un-corroded radius of external wire (7-wire prestressing strand)
r_{inner}	Un-corroded radius of internal wire (7-wire prestressing strand)
$A_{p,0}$	Un-corroded cross-section (Area) of prestressing reinforcement
$A_{w,inner,0}$	Un-corroded cross-section (Area) of internal wire

$A_{w,outer,0}$	Un-corroded cross-section (Area) of external wire
$\sigma_{p,0}$	Initial prestressing stress
$F_{p,0}$	Initial prestressing force
$A_{s,0}$	Un-corroded cross-section (Area) of rebar
e	Eccentricity of prestressing reinforcement evaluated from mid-height
f_{cm}	Average compressive strength of concrete
$f_{pu,0}$	Un-corroded ultimate strength of prestressing reinforcement
$\varepsilon_{pu,0}$	Un-corroded ultimate strain of prestressing reinforcement
PB	Prestressed Beam
E_{corr}	Corrosion potential
RE	Reference Electrode
CE	Counter Electrode
E_{OC}	Open Circuit Potential
R_p	Polarization resistance
i_{corr}	Current value – Current density
K	Ohmic drop
p.p.m.	Parts Per Million

Chapter 5

3D	Three Dimensional
L	Span length
LVDT	Linear Variable Displacement Transducer
d_1; d_2	Left and right distances between beam edge and support

a/d	Shear span-to-depth ratio
ROI	Region Of Interest
Ncorr	Software for MATLAB environment used for DIC analysis
LV-I; LV-II; LV-III	Corrosion levels of prestressing reinforcements from visual inspection
$P_{failure}$	Ultimate peak load from experimental testing
$\Delta_{failure}$	Ultimate deflection from experimental testing
$M_{failure}$	Ultimate bending moment from experimental testing
$S_{failure}$	Ultimate shear force from experimental testing
Shear I; Shear II	Types of shear failure mode observed from four-point bending tests

Chapter 6

L_i	Variable prestressing strand sample length (450 mm or 700 mm)
L_{scan}	Scanned length of corroded and un-corroded samples
Δ_1, Δ_2	Weight loss contributions according to ASTM G1-03 standard
n_{pits}	Number of pits measured for each corroded strand
P_y	Longitudinal extension of scanned pit
P_z	Transversal width of scanned pit
$P_{x,sectional}$	General sectional penetration depth of an external wire
$P_{max,sectional,i}$	Sectional maximum penetration depth of a corroded wire or strand
$P_{max,long}$	Longitudinal maximum penetration depth of a corroded wire or strand
A_{min}	Minimum residual cross-sectional area of a corroded strand
θ_1, θ_2 and θ_3	Corrosion angles for the different pit type morphology configurations
LV-A; LV-B; LV-C	Corrosion levels of prestressing reinforcements based on mass loss values

LV-A*; LV-B*	Updated corrosion levels of prestressing reinforcements based on mass loss values
$P_{av,long1}$; $P_{av,long2}$; $P_{av,long3}$	Longitudinal average penetration depths of a corroded strand
μ_{max}	Cross-sectional loss of the most corroded wire
μ_{strand}	Strand unit-section loss
α_1; α_2; α_3	Different longitudinal pitting factor expressions
Ω_i	Transversal (sectional) pitting factor
γ_i	Intensity factor for the evaluation of the transversal pitting factor
β_i	Transversal factor for the evaluation of the transversal pitting factor
$n_{external}$	Number of external wires making up the prestressing strand
$P_{av,transv}$	Sectional average penetration depth
$n_{sectional}$	Number of external wires, except for the most corroded wire
λ_x	Mean value of Lognormal distribution function
ζ_x	Standard deviation of Lognormal distribution function
$P_{x,0.95}$	Fractile value at 95% of the penetration depth by adopting a Lognormal distribution function
μ_x	Mean value of Lognormal distribution function expressed in mm
PDF	Probability Density Function
CDF	Cumulative Distribution Function

Chapter 7

CPS-model	Model for Corroded Prestressing Strands
SCPS-model	Simplified Model for Corroded Prestressing Strands
$f_{pu,corr,exp}$	Experimental ultimate strength of a corroded strand from tensile test
$\varepsilon_{pu,corr,exp}$	Experimental ultimate strain of a corroded strand from tensile test

$T_{p,exp}$	Experimental tensile force of a strand from tensile test
$T_{pu,corr,exp}$	Experimental tensile force of a corroded strand from tensile test
FEA	Finite Element Analysis
P_{inner}	Penetration depth of inner wire
$\varepsilon_{pp,0}$	Un-corroded strain in correspondence of the proportional limit
$f_{pp,0}$	Un-corroded strength in correspondence of the proportional limit
$\varepsilon_{py,0}$	Un-corroded yield strain of prestressing reinforcement
$f_{py,0}$	Un-corroded yield strength of prestressing reinforcement
μ_{lim}	Threshold critical cross-sectional loss
$f_{pu,corr}$	Ultimate strength of a corroded prestressing wire
$\varepsilon_{pu,corr}$	Ultimate strain of a corroded prestressing wire
$E'_{p,0}$	Un-corroded yielding modulus of prestressing reinforcement
$E''_{p,0}$	Un-corroded hardening modulus of prestressing reinforcement
$A_{w,outer,corr}$	Cross-sectional area of a corroded external wire
$A_{w,inner,corr}$	Cross-sectional area of a corroded inner wire
DUCT	Ductile failure mode of a corroded strand
BRIT	Brittle failure mode of a corroded strand
$\sigma(\varepsilon)$	Strand stress for a given epsilon
$\sigma_{w,i}$	Stress of the i^{th} wire making up the strand
$f_{pu,corr,an}$	Analytical ultimate strength of a corroded strand
$\varepsilon_{pu,corr,an}$	Analytical ultimate strain of a corroded strand
$f_{pu,corr,an1}$	Analytical ultimate strength of a corroded strand by adopting the CPS-model
$\varepsilon_{pu,corr,an1}$	Analytical ultimate strain of a corroded strand by adopting the CPS-model
CoC	Coefficient of Correlation

CV	Coefficient of Variation
$\sigma_{w,max}$	Stress of the most corroded wire
$\sigma_{w,av}$	Stress of the remaining external wires
$\sigma_{w,inner}$	Stress of the inner wire
Failure 1	Failure stage of the most corroded wire
Failure 2	Failure stage of the remaining external wires
$f_{pu,corr,an2}$	Analytical ultimate strength of a corroded strand at Failure 1 by adopting the SCPS-model
$\varepsilon_{pu,corr,an2}$	Analytical ultimate strain of a corroded strand at Failure 1 by adopting the SCPS-model
$T_{pu,corr,\mathrm{an2}}$	Analytical ultimate corroded tensile force at Failure 1 by adopting the SCPS-model
α_{Acorr}	Parameter that estimates the normalized residual cross-sectional area of the entire strand at Failure 1
$f_{pu,corr,an2,2}$	Analytical ultimate strength of a corroded strand at Failure 2 by adopting the SCPS-model
$\varepsilon_{pu,corr,an2,2}$	Analytical ultimate strain of a corroded strand at Failure 2 by adopting the SCPS-model
$T_{pu,corr,an2.2}$	Analytical ultimate corroded tensile force at Failure 2 by adopting the SCPS-model
α'_{Acorr}	Parameter that estimates the normalized residual cross-sectional area of the entire strand at Failure 2
DVM	Design Value Method
β_{target}	Reliability index for a 1-year reference period
$\gamma_{m,corr}$	Partial safety factor for corroded strand
$f_{pu,corr,des}$	Design tensile strength for a corroded prestressing strand
V_s	Coefficient of variation related to un-corroded material properties of prestressing steel
α	Sensitivity factor for 1-year reference period
CC	Consequence Class
μ_a and V_a	Mean value and the coefficient of variation of the uncertainty in geometrical properties
$\mu_{\theta R}$ and $V_{\theta R}$	Mean value and the coefficient of variation of the resistance model uncertainty
μ_{mod} and V_{mod}	Mean value and the coefficient of variation of the uncertainty related to the adoption of the SCPS-model

$\gamma_{m,un\text{-}corr}$	Un-corroded value of the proposed partial safety factor
ξ_{max}	Fractile value in correspondence of the maximum penetration depth
$\mu_{\xi max}$, $\sigma_{\xi max}$ and $V_{\xi max}$	Mean value, standard deviation, and coefficient of variation of the distribution of the fractile values, $\xi_{max,i}$
$\mu_{Pmax,sectional}$	Updated maximum penetration depth to be adopted as input parameter of the SCPS-model
θ_i	Ratio between experimental and analytical ultimate corroded strength
W	Shapiro-Wilk test statistic for normality
y_i	Random variable, i^{th}- observation
σ_{mod}	Standard deviation of the SCPS-model uncertainty

Chapter 8

P	Applied load
$P_{failure,an}$	Analytical load at failure
$\varepsilon_{p,0}$	Initial prestressing strain
$L_{t,0}$	Un-corroded transmission length of prestressing reinforcement
$L_{t,corr}$	Corroded transmission length of prestressing reinforcement
q	Distributed load
V_{d1} and V_{d2}	Shear contribution of the left and the right beam cantilevers
M_{d1} and M_{d2}	Bending contributions of the left and the right beam cantilevers
V_x	Shear reaction at left support
V_{Ed}	Acting shear force
M_{Ed}	Acting bending moment
N_{Ed}	Acting axial force
$\sigma_p(t)$	Prestressing stress after instantaneous and time-dependent losses

$\Delta\sigma_{p,el}$	Instantaneous loss due to the concrete elastic contraction caused by strand releasing
$\Delta\sigma_{p,rel}(t)$	Time-dependent loss due to the steel relaxation
$\Delta\sigma_{p,cr}(t)$	Time-dependent loss due to rheological creep effect
$\Delta\sigma_{p,shr}(t)$	Time-dependent loss due to rheological shrinkage effect
$\sigma_{p,s}$	General prestressing reinforcement stress
α_e	Ratio between the un-corroded moduli of elasticity of prestressing reinforcement and concrete
I_i	Cross-section second moment of Inertia
S	Cross-section first moment of Inertia
μ_p	Ratio between the initial prestressing stress, $\sigma_{p,0}$, and the un-corroded ultimate strength of the prestressing reinforcements, $f_{pu,0}$
$\varepsilon_{cc}(t,t_0)$	Creep strain
$\varphi(t,t_0)$	Creep coefficient
α_E	Coefficient that considers the aggregate type effect
$\varphi_{bc}(t,t_0)$	Basic creep coefficient
$\varphi_{dc}(t,t_0)$	Drying creep coefficient
$t_{0,adj}$	Adjusted age at loading in days
α_c	Coefficient that considers the cement type effect
$t_{0,T}$	Age of concrete at loading in days
Δt_i	Number of days where the temperature T prevails
$\beta_{dc}(f_{cm})$	Compressive strength contribution to drying creep coefficient
$\beta(\mathrm{RH})$	Relative humidity contribution to drying creep coefficient
$\beta_{dc}(t_0)$	$t_{0,adj}$ contribution to drying creep coefficient
$\beta_{dc}(t,t_0)$	Additional contribution to drying creep coefficient
$\varepsilon_{cs}(t,t_s)$	Total shrinkage strain
$\varepsilon_{cbs}(t)$	Basic shrinkage

$\varepsilon_{cds}(t,t_s)$	Drying shrinkage
t_s	Concrete age at the beginning of drying days
$\varepsilon_{cbs0}(f_{cm})$	Basic notional shrinkage coefficient
$\beta_{bs}(t)$	Time function for the basic shrinkage estimation
$\varepsilon_{cds0}(f_{cm})$	Notional shrinkage coefficient
β_{RH}(RH)	Relative humidity contribution to drying shrinkage
$\beta_{ds}(t\text{-}t_s)$	Time-development function for the drying shrinkage estimation
LV-0, LV-I, LV-II, LV-III	Corrosion levels (scenarios) considered in the analytical approach
$P_{max,0.5}$	Fractile value at 50% of the maximum penetration depth
$P_{av,0.5}$	Average penetration depth related to the Fractile value at 50% of P_{max}
$P_{inner,0.5}$	Inner wire penetration depth related to the Fractile value at 50% of P_{max}
$\mu_{0.5}$	Cross-section loss related to the Fractile value at 50% of P_{max}
$\eta_{0.5}$	Mass loss related to the Fractile value at 50% of P_{max}
$A_{w,outer,corr,0.5}$	Cross-sectional area of external wires related to the Fractile value at 50% of P_{max}
$A_{w,outer,corr,max,0.5}$	Cross-sectional area of the most corroded wire related to the Fractile value at 50% of P_{max}
$A_{w,outer,corr,av,0.5}$	Cross-sectional area of the remaining external wires related to the Fractile value at 50% of P_{max}
$A_{p,corr,0.5}$	Residual strand cross-sectional area related to the Fractile value at 50% of P_{max}
$L_{inspected}$	Visually inspected length of prestressing reinforcement
ρ_{steel}	Density of steel
τ_b	Ultimate bond stress
V_{det}	Slope coefficient for the quantification of the corroded transmission length
$\mu_{lim,Lt}$	Threshold cross-sectional loss for the quantification of the corroded transmission length
η_{lim}	Threshold mass loss for the quantification of the bond reduction
R	Normalized bond strength from pull-out tests on specimens with stirrups

R_1	Normalized bond strength from beam tests on specimens with stirrups
R_2	Normalized bond strength from pull-out tests on specimens without stirrups
$\sigma_{p,corr}(t)$	Prestressing stress affected by prestressing losses due to corrosion
$F_{p,corr}(t)$	Reduced prestressing force
E_c	Modulus of elasticity of concrete
ε_{c0}	Concrete strain at peak load
ε_{cu}	Ultimate concrete compressive strain
f_{ctm}	Average concrete tensile strength
G	Beam section centre of gravity
x	Cross-section neutral axis
$x_{i,j}$	Neutral axis associated to Failure case (i) 1,2, and 3 for Points (j) A', A, B, C, and D of the simplified moment-curvature diagram
ω_p	Un-corroded mechanical reinforcement ratio for prestressing reinforcement
ω_1, ω_3	Threshold un-corroded mechanical reinforcement ratios
λ	Reduction parameter associated to the "stress-block" of concrete in compression
$M_{p,0}$	Bending moment due to a prestressing force $F_{p,0}$ and an eccentricity e
$A_{p,0,tot}$	Overall un-corroded area of prestressing reinforcements
A_i	Total cross-sectional area
$M_{i,j}$	Bending moment associated to Failure case (i) 1,2, and 3 for Points (j) A', A, B, C, and D of the simplified moment-curvature diagram
$M_{A'}$, M_A, M_B, M_C, M_D	Bending moment associated to Points A', A, B, C, and D of the simplified moment-curvature diagram
$\sigma_{c,b}$	Concrete stress at the bottom layer of the beam cross-section
$\sigma_{c,t}$	Concrete stress at the top layer of the beam cross-section
$\chi_{i,j}$	Curvature associated to Failure case (i) 1,2, and 3 for Points (j) A', A, B, C, and D of the simplified moment-curvature diagram
$\chi_{A'}$, χ_A, χ_B, χ_C, χ_D	Curvature associated to Points A', A, B, C, and D of the simplified moment-curvature diagram
$\varepsilon_{x,i,j}$	Longitudinal strain at mid-height of the effective shear depth associated to Failure case (i) 1,2, and 3 for Points (j) A', A, B, C, and D of the simplified moment-curvature diagram

$\varepsilon_{x,A'}$, $\varepsilon_{x,A}$, $\varepsilon_{x,B}$, $\varepsilon_{x,C}$, $\varepsilon_{x,D}$	Longitudinal strain at mid-height of the effective shear depth associated to Points A', A, B, C, and D of the simplified moment-curvature diagram
z^*	Equivalent shear depth
$\omega_{p,corr}$	Corroded mechanical reinforcement ratio for prestressing reinforcement
$\omega_{1,corr}$, $\omega_{3,corr}$	Threshold corroded mechanical reinforcement ratios
$\varepsilon_{p,corr}$	Corroded strain due to prestressing
$x_{i,j,corr}$	Corroded neutral axis associated to Failure case (i) 1,2, and 3 for Points (j) A', A, B, C, and D of the simplified moment-curvature diagram
$M_{i,j,corr}$	Corroded bending moment associated to Failure case (i) 1,2, and 3 for Points (j) A', A, B, C, and D of the simplified moment-curvature diagram
$\chi_{i,j,corr}$	Corroded curvature associated to Failure case (i) 1,2, and 3 for Points (j) A', A, B, C, and D of the simplified moment-curvature diagram
$\varepsilon_{x,i,j,corr}$	Corroded longitudinal strain at mid-height of the effective shear depth associated to Failure case (i) 1,2, and 3 for Points (j) A', A, B, C, and D of the simplified moment-curvature diagram
V_{Rd}	Shear capacity
$V_{Rd,c}$	Concrete contribution to shear resistance
γ_c	Partial safety factor for concrete
k_v	Coefficient dependent on the longitudinal strain at mid-height of the effective shear depth, ε_x
k_{dg}	Coefficient for the size of the maximum aggregate particles effect
$V_{Rd,corr}$	Residual shear capacity
β	Amplification factor of the longitudinal strain at mid-height of the effective shear depth
$V_{Rd,c,end}$	Critical shear capacity at beam edges according to Eurocode 2 provision
α_I	Coefficient for the prestressing force transmission effect in pre-tensioned PC elements
$P_{failure,an,mean}$	Analytical load at failure by adopting mean material properties
$P_{failure,an,des}$	Analytical load at failure by adopting design material properties

Contents

Summary ..... **I**

Sommario ..... **V**

List of Figures ..... **IX**

List of Tables ..... **XVIII**

List of Symbols & Acronyms ..... **XXI**

Contents ..... **XXXVII**

1 Introduction **1-1**

1.1 Background and issue statement 1-1

1.2 Lacunae in the current knowledge 1-3

1.3 Research methodology and layout of the *Thesis* 1-7

2 Literature review on corrosion processes of steel reinforcement in concrete **2-1**

2.1 Highlights 2-1

2.2 Definitions 2-2

2.3 Mechanisms and processes 2-3

2.3.1 Carbonation-induced corrosion 2-9

2.3.2 Chloride-induced corrosion 2-11

2.4 Types of corrosion 2-15

2.4.1 Uniform or homogenous corrosion 2-17

2.4.2 Galvanic corrosion (GC) 2-17

2.4.3 Pitting corrosion 2-17

2.4.4 Crevice corrosion (CC) 2-18

2.4.5 Stress-corrosion cracking (SCC) 2-18

2.4.6 Corrosion fatigue (CF) 2-19

2.4.7 Hydrogen damage 2-19

2.5 Main effects 2-20

2.5.1 Corrosion of prestressing steel 2-22
2.6 Consequences of climate change on corrosion process 2-25
3 Literature review on corroded PC beams and reinforcements 3-1
3.1 Highlights 3-1
3.2 Historical collapses due to corrosion: a timeline 3-2
3.3 Cost of corrosion 3-8
3.4 Mechanical performance of corroded PC beams 3-11
3.4.1 Natural corrosion vs. Artificial accelerated process 3-11
3.4.1.1 Impressed Current (IC) method 3-12
3.4.1.2 Artificial Climate Environment (ACE) method 3-14
3.4.2 The residual response of PC beams 3-15
3.4.2.1 Post-tensioned PC beams 3-16
3.4.2.2 Pre-tensioned PC beams 3-21
3.4.2.3 Challenges and open issues 3-31
3.5 Mechanical behaviour of corroded prestressing reinforcements 3-33
3.5.1 Quantification of corrosion damage 3-34
3.5.2 Modelling of the tensile behaviour 3-40
3.5.2.1 Challenges and open issues 3-45
3.6 Current guidelines and codes for the structural assessment of corroded beams and reinforcements 3-47
4 Characterization of 10 year-old corroded PC beams 4-1
4.1 Highlights 4-1
4.2 Experimental program introduction 4-3
4.3 Naturally corroded PC beams description 4-4
4.3.1 Materials 4-5
4.4 Preliminary investigation 4-6
4.4.1 Visual inspection and concrete surface defects mapping 4-7
4.4.2 Indirect corrosion measurements 4-10
4.4.2.1 Corrosion potential mapping 4-10
4.4.2.2 Corrosion rate and ohmic drop measurements 4-13
4.4.2.3 Chloride moisture content estimation 4-16

4.5 Main observations....4-19

5 Experimental program on naturally corroded PC beams.....5-1

5.1 Highlights....5-1
5.2 Introduction....5-3
5.3 Experimental Procedure....5-3
5.3.1 Test set-up....5-3
5.3.2 Digital Image Correlation method....5-6
5.3.3 Estimation of corrosion level of prestressing reinforcements....5-7
5.4 Flexural performance of corroded PC beams....5-8
5.4.1 Main observations....5-15
5.5 Shear performance of corroded PC beams....5-16
5.5.1 Main observations....5-31

6 Evaluation of the pitting morphology of corroded strands 6-1

6.1 Highlights....6-1
6.2 Introduction....6-3
6.3 Corrosion measurements....6-5
6.3.1 Retrieval of corroded prestressing strand samples....6-7
6.3.2 Mass loss calculation: gravimetrical method....6-10
6.3.3 3D Scanning procedure and GOM Inspect software analysis....6-11
6.4 Results and Discussion....6-17
6.4.1 Classification of detected pits....6-17
6.4.2 Essential correlations for the assessment of corroded strands....6-23
6.4.2.1 Longitudinal variability analysis of corrosion parameters....6-23
6.4.2.2 Transversal pitting factor definition....6-40
6.4.3 Correlations between different corrosion damage assessment parameters....6-44
6.4.3.1 Penetration depth vs mass loss....6-44
6.4.3.2 Mass loss vs minimum residual cross-section....6-46
6.4.3.3 Cross-sectional loss vs strand-unit sectional loss....6-48
6.4.3.4 Maximum penetration depth vs cross-sectional loss of the most corroded wire....6-49
6.4.3.5 Wire unit cross-sectional loss vs strand unit cross-sectional loss....6-50
6.4.4 Overview on longitudinal pitting factor....6-52
6.4.4.1 Average penetration depth definition....6-53

6.4.4.2 Longitudinal pitting factor calculation 6-54
6.5 Main observations 6-58
7 Definition of constitutive laws for corroded strands 7-1
7.1 Highlights 7-1
7.2 Introduction 7-3
7.3 Tensile tests of prestressing strands 7-5
7.3.1 Experimental set-up 7-5
7.3.2 Stress-strain relationships of tested prestressing strands 7-7
7.4 CPS-model: refined model for the prediction of the residual stress-strain response of a corroded strand 7-16
7.4.1 Basic assumptions 7-16
7.4.2 Stress-strain relationship for un-corroded wires 7-20
7.4.3 Stress-strain relationship for corroded wires 7-22
7.4.4 Model validation 7-27
7.4.5 Main observations 7-41
7.5 Simplified model for the daily engineering practice: the SCPS-model 7-45
7.5.1 Basic assumptions 7-45
7.5.2 Main simplifications 7-49
7.5.2.1 Stress-strain relationship for corroded wires 7-53
7.5.3 Simplified expressions for daily engineering practice application 7-57
7.5.4 Model validation 7-62
7.5.5 Main observations 7-69
7.6 Partial safety factor for the design tensile strength of corroded strands 7-71
7.6.1 Description of adopted procedure 7-71
7.6.2 SCPS-model uncertainty quantification 7-73
7.6.2.1 Procedure for the probabilistic estimation of the maximum penetration depth 7-75
7.6.2.2 Estimation of the resistance model uncertainty 7-78
8 Analytical approach for the assessment of corroded PC beams 8-1
8.1 Highlights 8-1

8.2 Analytical model overview 8-2
8.3 Flexural and shear demand 8-5
8.4 Instantaneous and time-dependent prestressing losses evaluation 8-8
8.4.1 Losses due to releasing of strands 8-8
8.4.2 Losses due to steel relaxation and rheological creep and shrinkage effects 8-9
8.5 Effects of corrosion 8-13
8.5.1 Corrosion levels estimation 8-13
8.5.2 Evaluation of corrosion parameters 8-15
8.5.3 Residual mechanical properties of corroded prestressing strands 8-18
8.5.4 Reduced prestressing force 8-19
8.5.4.1 Transmission length variation 8-20
8.5.4.2 Ultimate bond strength reduction 8-23
8.6 Calculation of the residual flexural capacity 8-27
8.6.1 Simplified moment-curvature approach 8-29
8.6.1.1 Basic assumptions 8-29
8.6.1.2 Critical mechanical reinforcements ratios and cross-sectional failure cases 8-31
8.6.1.3 Analytical approach for the un-corroded scenario 8-33
8.6.1.4 Failure Case “1” 8-33
8.6.1.5 Failure Case “2” 8-38
8.6.1.6 Failure Case “3” 8-40
8.6.1.7 Analytical approach modification due to corrosion 8-44
8.7 Calculation of residual shear capacity 8-50
8.7.1 Assessment of PC elements without stirrups: a new proposal 8-50
8.7.1.1 Check on shear capacity at beam edges 8-54
8.8 Model validation 8-55
8.9 Main observations and drawbacks 8-64
8.9.1 Analytical model application by adopting design properties 8-66
9 General conclusions and Future research 9-1
9.1 Conclusions and observations 9-1
9.2 Future research and recommended improvements 9-5
9.2.1 Corrosion measurements and experimental tests on corroded PC elements 9-5
9.2.2 Pitting morphology analysis of corroded prestressing strands 9-6

9.2.3 Constitutive laws for the residual mechanical response of corroded strands 9-7
9.2.4 Analytical model for the assessment of the residual capacity of PC beams 9-8
9.2.5 Improvements of current codes and guidelines 9-9

References i

Appendix xxxi

A.1. Mechanical performance of corroded RC beams xxxi
A.2. Mechanical behaviour of corroded ordinary reinforcements xxxvi
A.3. Maximum pits features and area loss due to pitting classification xl
A.4. Cross-sectional loss evaluation of corroded external wire xliii

Acknowledgements xlv

Ringraziamenti xlvi

Curriculum Vitae (CV) xlvii

List of Publications xlviii

1 Introduction

1.1 Background and issue statement

Corrosion of steel reinforcements is nowadays considered as one of the leading causes of the durability and capacity reduction of existing reinforced (RC) and prestressed (PC) concrete structures and infrastructures. To date, the scientific and technical communities, in collaboration with private and public authorities, are conducting extensive research on the corrosion of RC and PC members in order to limit economic and human losses. In this context, detailed surveys carried out by the American Society of Civil Engineers (ASCE) and the Federal Highway Administration (FHWA) revealed that a high number of existing bridges in America (approximately 30% of the American bridges – similarly to other countries around the world, including Italy) have already exceeded their service life and have been characterized by evident sign of deterioration, (Federal Highway Administration, 2006). During the last decades, however, several buildings and bridges collapses have occurred worldwide. One only need to think of the Berlin Congress Hall in Germany, the Lowe's Motor Speedway Pedestrian Bridge in North Carolina, and the more recent Polcevera Viaduct in Italy. These examples emphasize the urgent need for reliable and efficient monitoring systems, stringent maintenance protocols, and simplified analytical models capable of assessing the residual structural capacity of deteriorating RC and PC members.

In general, two are the main types of corrosion that might affect RC and PC members: (i) chloride-induced corrosion, caused by the action of chloride ions contained in sea water or de-icing salts; and (ii) carbonation-induced corrosion, caused by the long-period action of carbon dioxide. The first type of corrosion, denoted as localized or pitting corrosion, is more likely to occur in marine, coastal or mountain environments, where the presence of sea water and salt aerosol are persistent and/or the use of de-icing salts is extensive (D. Li et al., 2019; F. Li et al., 2011). When chloride concentration reaches its threshold limit at reinforcements level, the concrete alkaline environment is affected and the passive layer that protects the reinforcement locally is destroyed, allowing, therefore, the pits to grow. In the case of PC members, the chloride-induced corrosion can lead to worse consequences, since pitting can cause stress concentration and fracture localization, (Elices et al., 2012; Sanchez et al., 2017). Carbonation-induced corrosion, on the other hand, is predominant in carbon dioxide-rich environments, such as densely populated areas, (U. M. Angst, 2018). In this urbanized area, the

combination of the exposure to carbon dioxide and chloride ions may cause even worst scenarios. Regardless of the corrosion type, the following effects are considered by the scientific community as the main issues associated with steel corrosion in concrete:

- Volume expansion due to formation of rust products, (Asami & Kikuchi, 2003; Zhao et al., 2011);
- Concrete damage such as swellings, delamination, cracking up to spalling of concrete cover, (Andrés A. Torres-Acosta & Castro-Borges, 2013; S. F. Zhang et al., 2011; Zhao et al., 2012, 2020);
- Reduction of cross-section of reinforcement, especially dangerous in the case of seven-wire prestressing strands having wires with small diameters, (L. Wang, Li, et al., 2020);
- Decay of ultimate mechanical properties of steel in terms of both ultimate strength and ductility, (A. A. Almusallam, 2001; Z. H. Lu et al., 2016; Ou et al., 2016);
- Bond decay between concrete and steel, (L. Wang et al., 2018).

As a result, all these factors contribute to reduce the structural capacity of existing RC and PC members over time, sometimes causing unexpected failures due to the lack of bending, shear, or anchorage resistance without warning signs.

Although several experimental research programs have been carried out over the last years, both to investigate the residual mechanical behaviour of corroded reinforcements (A. A. Almusallam, 2001; Ch Alk Apostolopoulos, 2007; Ch Alk Apostolopoulos et al., 2006; Cairns et al., 2005; Ou et al., 2016) and the residual flexural and shear capacity of corroded RC members (Soltani et al., 2019), only a limited number of experimental works have been conducted to investigate the same topics in the case of corroded prestressing strands and PC members. Among the few, Wang et al. (2020) and Jeon et al. (2019) proposed different analytical models for the prediction of the residual mechanical behaviour of corroded strands in terms of stress-strain relationships, while Rinaldi et al. (2010) and Recupero et al. (2019) tested a set of nine and eleven PC beams artificially corroded, respectively.

However, since natural corrosion requires a lengthy period of exposure to the aggressive environment, in most experimental research, corrosion is artificially triggered through impressed current or by adding a mixture of $CaCl_2$ or $NaCl$. In general, the artificially accelerated method produces different corrosion effects than those induced by the natural environmental attack on structures. As a result, according to Zhu (2011), the accelerated corrosion cannot actually represent the state of real corrosion, especially if the scientific community cannot unanimously agree on a current density value that should be applied in tests

to simulate natural corrosion. Therefore, the outcomes coming from different experimental works cannot be easily compared at this stage since they are conducted under different conditions.

Concurrently, the effects associated with global warming seriously affect and interact with the corrosion process. Indeed, global warming increases the frequency and the intensity of natural hazards, leading to the rising exposure of existing structures and infrastructures to severe structural damages, as highlighted by the "Global Assessment report", (United Nations Office for Disaster Risk Reduction, 2019). Moreover, it affects the rise in sea level and promotes heavy snows that may lead to the worsening of chloride-induced corrosion (United Nations Office for Disaster Risk Reduction, 2020). For example, after heavy snows, a larger amount of de-icing salts is needed to ensure the maintenance and operation of transport lines.

In the context of a great variability of corrosion processes related to possible exposure classes and different aggressive environments, as defined by EN 206 (CEN, 2014), this *Thesis* is focused on the assessment of existing naturally prestressed concrete beams subjected to 10 years of chloride-induced corrosion.

1.2 Lacunae in the current knowledge

Based on previous considerations, corrosion is a topical issue at both national and international level. However, to fill the gap between the available scientific knowledge on corrosion processes and its effects on structural performance, and the effective behaviour of corroded existing structures, further research efforts should be especially devoted to the analysis of corroded PC members. In this regard, Figure 1-1(a) reports the outcomes of a research conducted in Scopus-indexed journals concerning the number of scientific works published on corrosion of RC and PC structures and infrastructures from 1962 to 2022. When compared to scientific works on corroded RC members, it is undeniable that works on corroded PC members are scarce and scaled by a factor of four. However, from the engineering point of view, the relevance of the research topic is confirmed in Figure 1-1(b) where the engineering branch ranks first among the scientific areas for published works in the field of corrosion of PC elements. Finally, Figure 1-2 shows an additional focus on countries that are leading the way in the engineering study of corrosion of PC members and structures. China and the United States of America are first and second with a total number of publications equal to eight hundred fifty and seven hundred sixty-four, respectively. Nevertheless, taking into account the large disparity in terms of territorial extent, laboratory dimension as well as economic resources, Italy

holds a relevant seventh place with one hundred fifty-three published works just behind Japan and Germany.

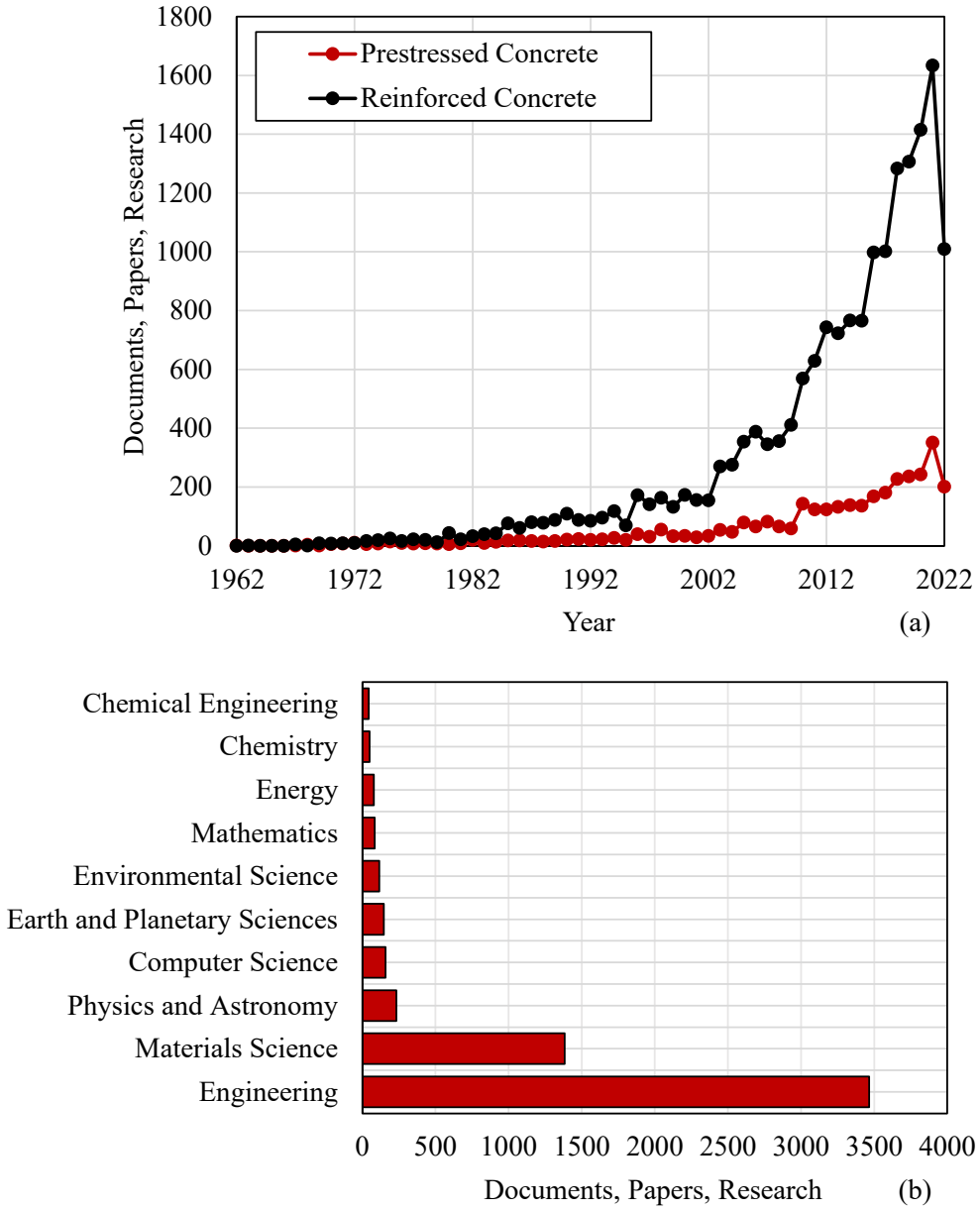

Figure 1-1 Research in Scopus-indexed journal concerning corroded RC and PC members: (a) trend of the number of publication in the period 1962-2022, and (b) scientific areas of research for corroded PC members. (https://www.scopus.com/).

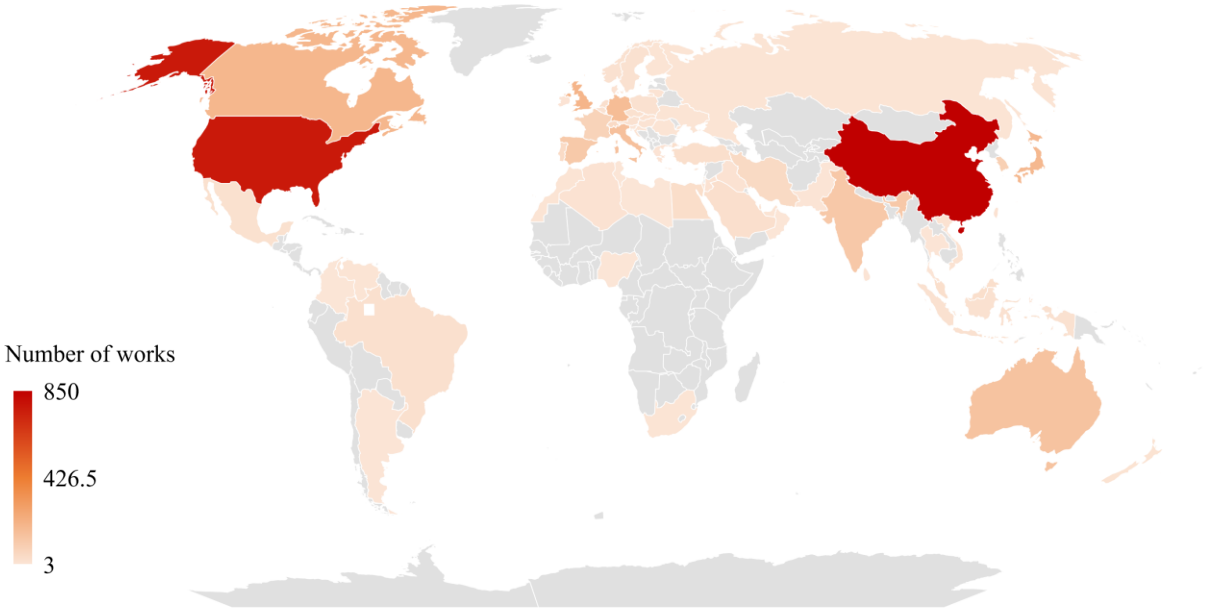

Figure 1-2 Identification of countries as a function of the number of published works on corroded PC members, (https://www.scopus.com/).

The main lacunae in the current scientific literature are summarized as follows:

- The knowledge on PC members against corrosion is still uncertain and, scarce experimental, numerical and analytical studies are available compared to RC members;
- Most of experimental research concerning the analysis of the residual structural capacity of corroded members have been performed with the accelerated process. This latter technique is not perfectly suitable to reproduce the natural corrosion process, which requires a long period of exposure. Furthermore, no agreement has been reached among scientific communities on the optimal current density to be applied during testing in order to better reproduce the natural corrosion process. As a result, more research on naturally corroded members is required to fully understand the behaviour of RC and PC members subjected to corrosion;
- The majority of experimental campaigns and available analytical models have been focused on the study and the prediction of the flexural resistance of corroded members, although the shear failure may lead to worse consequences due to its brittle and sudden nature. Therefore, special attention should be further addressed to the evaluation of the development of the shear failure mode of corroded PC members;

- Limited studies investigated the corrosion-induced ductility reduction. Ductility is a particularly relevant parameter of corroded reinforcements since directly influences the failure mode of the member. When the ultimate strain of corroded reinforcements reduces under a certain threshold limit, a change in the failure mode of the corroded member from ductile to brittle occurs. In this regard, shear failure is prone to occur in highly deteriorated members where the ductility of reinforcements is severely compromised by corrosion. Therefore, additional efforts should be further addressed to the evaluation of the effect of ductility reduction on failure mode change in corroded PC members;
- Despite several works have been carried out to investigate the pitting morphology of corroded deformed bars, few studies have been focusing on the analysis of the longitudinal and sectional variability of corroded prestressing reinforcements;
- In contrast to the comprehensive State-of-the-Art on the prediction of the residual mechanical properties of corroded rebars, the scientific literature lacks of models suitable for the prediction of the residual mechanical behaviour of prestressing strands. From the standpoint of engineering daily practice, the development and improvement of simplified models is crucial to allow a fast and reliable assessment of the capacity of corroded PC members and a more accurate estimation of the residual life of existing PC structures;
- Although, guidelines such as CONTECVET manual (2001) and Dura Crete Final Technical Report (2000) extensively treat the corrosion topic, they do not provide a fully validated analytical approach for the assessment and prediction of the residual service life of corroded structures;
- A simplified partial factor method for existing concrete structures has been proposed in *fib* Bulletin 80 (CEB-fip, 2016) even though it do currently not take into account reduced material characteristics of corroded members. Besides, Eurocodes only address the issue of corrosion and environmental deterioration of structures over time, without requiring any specific design or assessment. Therefore, to optimize the maintenance strategies of the existing structural heritage, simplified methods for design and assessment purposes – capable of using as input data the parameters measured from in-situ inspections and outputting the residual structural capacity and the residual life estimation of corroded PC members – are needed.

In order to extend the current knowledge of the corrosion of PC members, this *Thesis* aims to analyse the residual structural behaviour of several naturally corroded PC beams. Moreover, based on the evaluation of the pitting morphology of retrieved corroded samples, the *Thesis* proposes analytical approaches to predict the residual mechanical behaviour of corroded prestressing strands as well as a simplified analytical model to assess the residual service life of PC beams subjected to chloride-induced corrosion.

1.3 Research methodology and layout of the *Thesis*

In the present work, the chloride-induced corrosion of existing structures is evaluated through the analysis of naturally corroded prestressed concrete beams subjected to 10 years of sea water wet-dry cycles. To successively identify the impact of corrosion, two un-corroded PC beams specimens were manufactured with the same type of concrete and curing conditions. The scheme of the research activities is reported in Figure 1-3.

First, the concrete surface defects of each corroded PC beam were analysed. Since the PC beams were subjected to a corrosive environment for a long period, cracking of concrete caused by splitting phenomena as well as spalling of concrete cover (especially at beam edges) were observed and mapped. At the same time, indirect measurements of corrosion in terms of corrosion potential mapping, ohmic drop and corrosion rate were performed.

Second, mechanical experiments were carried out on corroded and un-corroded beams to study the residual structural performance of the members. During these mechanical tests, Digital Image Correlation (DIC) was performed by taking photos at each load step to successively investigate the strain fields evolution and to document the crack opening formation of each tested beam.

After the mechanical tests, the beams were dismantled and twenty-four prestressing strand samples – four un-corroded and twenty corroded – were extracted to be further analysed. The samples were cleaned and the mass loss was measured by adopting the gravimetrical method.

Third, 3D models – one for each corroded sample – were obtained by using a structured light 3D scanner. The spatial variability of corrosion distribution in terms of pitting morphology was then depicted sectionally and longitudinally along the entire sample length through the superimposition process of un-corroded and corroded 3D models by using the GOM Inspect software.

Tensile tests were performed to investigate the residual mechanical behaviour of corroded prestressing strands. Based on the findings, two analytical models, namely CPS- and SCPS-model, were proposed for predicting the tensile force-strain or stress-strain relationship of corroded strands. The models are based on different assumptions, however, both assume the equivalent spring material approach to predict the overall response of the corroded strand by summing the contributions of each wire. Both models were validated by comparing the analytical predictions to the experimental tensile test outcomes coming from the present research and the work carried out by Jeon et al. (2019).

Finally, an analytical approach for assessing the residual flexural and shear capacity of corroded PC beams without transversal reinforcement was defined. In detail, the analytical approach is based on a single input corrosion parameter, which is the maximum penetration depth of the most corroded wire.

The sections of the present research work concern:

- *Steel corrosion in concrete*: a general introduction to the corrosion phenomena with particular focus on the evaluation of corrosion typologies, mechanisms, and main effects on RC and PC structures. Furthermore, the correlation between the climate change issue and the worsening of corrosion effects is also discussed.
- *State-of-the-Art*: a literature investigation on the residual structural capacity of corroded PC beams, and the analysis of models for the prediction of the residual mechanical behaviour of corroded prestressing strands. Additionally, an overview of current standards and guidelines for the assessment of corroded elements is outlined.
- *Characterization of naturally corroded PC beams*: a description of the research program involving fourteen 10-years old naturally corroded PC beams coming from the refrigeration tower of a Spanish thermal power plant. This section focuses on the characterization of the available corroded specimens in terms of mapping of concrete surface defects – i.e., longitudinal splitting cracks, swellings, and spalling of concrete cover – as well as the performance of indirect measurements of corrosion, such as corrosion potential mapping, ohmic drop and corrosion rate. Moreover, the relationships between concrete surface defects and indirect measurements are investigated.
- *Residual structural performance analysis:* the residual flexural and shear capacity of naturally corroded PC beams are estimated in this section using three-point and four-point bending tests up to failure, carried out at the Instituto Eduardo Torroja in Madrid. Furthermore, displacement and strain fields are evaluated using DIC analysis;

experimental results are compared to the un-corroded reference beams; failure mode are analysed and the impact of corrosion level on the failure mode change from ductile to brittle are investigated.

- *Pitting morphology evaluation*: corroded prestressing strands are retrieved from the tested beams, samples cleaned according to ASTM G1-03 standard (2017) and gravimetrical measurements performed. Follows the 3D scanning of available corroded samples, the creation of 3D models using the GOM Inspect software and the post-processing of data aimed to examine the longitudinal and sectional pitting spatial variability of corroded seven-wire prestressing strands in terms of residual cross-section and penetration depth. Finally, several relationships between main pitting parameters and corrosion levels are proposed.

- *Mechanical behaviour of corroded strands*: coupled with the results from the tensile tests performed in collaboration with the Politecnico of Turin, two analytical models for the prediction of the residual stress-strain response of corroded strands are proposed. The first one, named CPS-model, assumes the cross-sectional loss of each wire as the main input parameter for the prediction of the ultimate strength and the ultimate strain decay. The CPS-model considers different decay laws as a function of three different pit type morphology configurations – hemispherical, half-moon and planar shape – and considers the un-corroded area of the overall strand for the final prediction of the stress-strain response. The second approach, named SCPS-model, is a simplified version of the CPS-model based on a single input parameter, which is the maximum penetration depth of the most corroded wire, and is designed for the daily engineering practice. The SCPS-model, which is independent from the possible pit type morphology configurations, adopts a single decay law for the ultimate strain and estimates a sectional average penetration depth for the remaining external wires as a function of the maximum penetration depth of the most corroded wire. Conversely to CPS-model, the SCPS-model considers the corroded area of the overall strand for the final prediction of the stress-strain response. For this purpose, a decay law of the residual cross-sectional area of the wire is also introduced.

  Both models are based on the equivalent spring material approach that consists in the evaluation of the residual response of the corroded strand through the sum of contributions of the seven wires that are considered as springs working in parallel with each other. A partially safety factor for corroded prestressing steel is finally

proposed for the estimation of the design strength of corroded strands by quantifying the SCPS-model uncertainty.

- *Analytical method*: based on the considerations highlighted in the previous sections and the simplified expressions derived, the work concludes with a simplified analytical model for the assessment and/or residual life prediction of corroded PC beams in terms of flexural and shear capacity estimation.
- *Conclusions and future research*: a summary of main findings, conclusions and research that require improvements are finally highlighted as the conclusive part of the present work.

In Table 1-1 is reported the schematic *Thesis* outline.

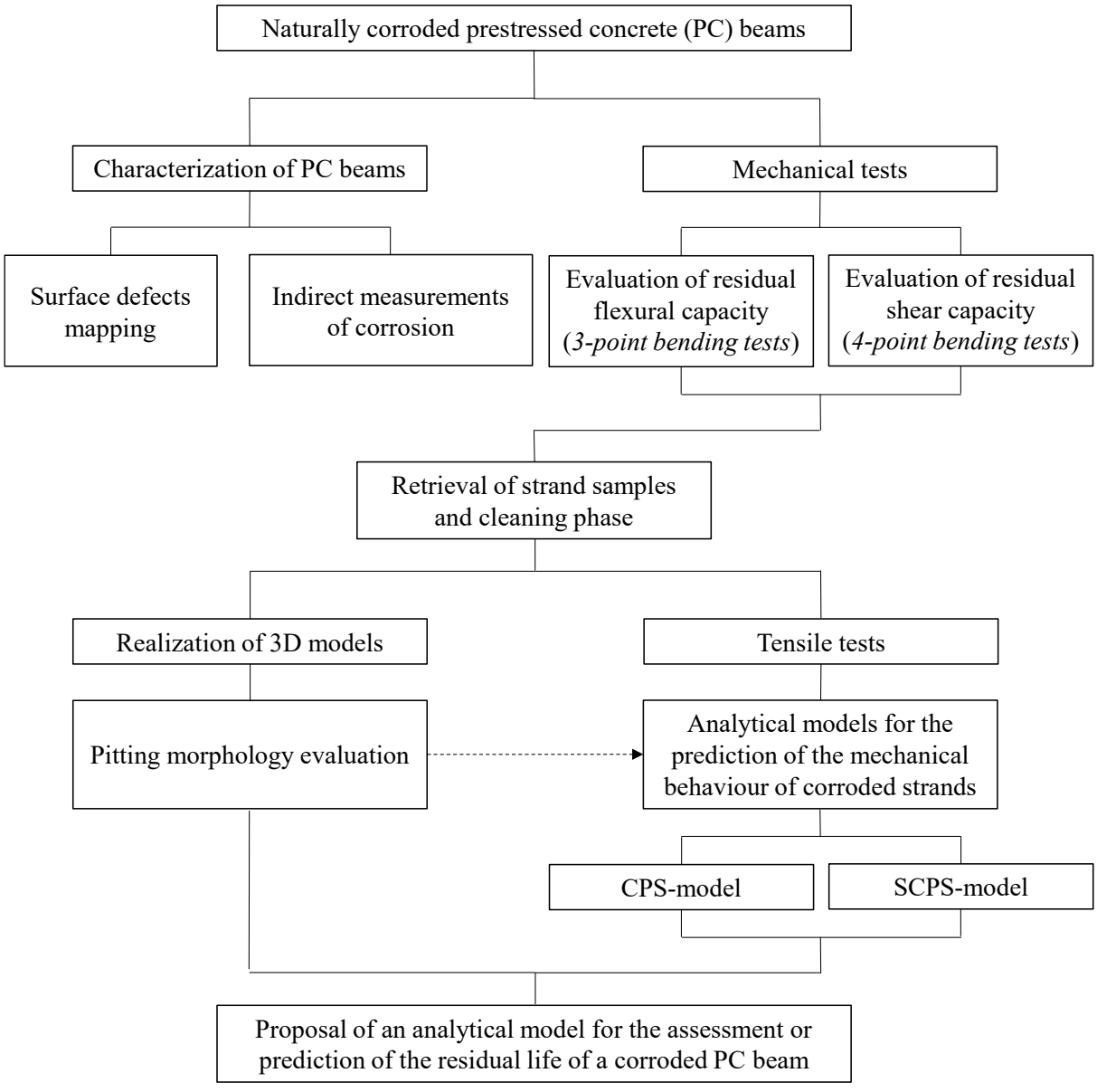

Figure 1-3 Scheme of the all research activities.

Table 1-1 Outline of the *Thesis*.

Chapter	Contents
1	General introduction: background; current lack of knowledge; layout of the *Thesis*.
2	Literature review on steel corrosion process of reinforcing steel embedded in concrete: definitions; mechanisms; types of corrosion; main effects on RC and PC structures; climate change effects.
3	Literature review on corroded PC beams and strands: historical collapses; cost of corrosion; experimental tests on post- and pre-tensioned PC beams aiming to study the residual structural capacity of corroded members; experimental tensile tests and analysis of the available material models for the prediction of the residual mechanical response of corroded prestressing strands; brief overview on current codes and guidelines.
4	Description of the research program involving fourteen naturally corroded PC beams: analysis of the environment that led to chloride-induced corrosion; characterization of the specimens in terms of concrete surface defects mapping and performance of indirect measurements of corrosion.
5	Analysis of the residual structural capacity: evaluation of load-deflection curves of corroded and un-corroded PC beams via three-point and four-point bending tests; performance of DIC analysis for the evaluation of displacements and strain fields; failure modes analysis.
6	Evaluation of the pitting morphology of corroded strands: retrieval of samples; cleaning procedure and gravimetrical measurements; 3D scanning phase; data processing by means of the GOM Inspect software through the superimposition of un-corroded and corroded 3D models; proposed relationships between analyzed corrosion damage parameters.
7	Constitutive laws for the prediction of the residual mechanical behaviour of corroded prestressing strands (stress-strain relationship): (i) refined model, CPS-model, based on the cross-sectional loss of each wire and pit type morphology configurations; (ii) simplified model for the daily engineering practice, SCPS-model, based on a single input parameter that is the maximum penetration depth of the most corroded wire. Partial safety factor estimation for the design strength of corroded strands.
8	Proposed analytical approach for the assessment and/or prediction of the residual life of corroded PC beams (without shear reinforcements); description of the main assumptions and model validation.
9	Conclusions and future research concerning corrosion of PC members and prestressing reinforcements.
Appendix A.1 and A.2	Literature review concerning experimental campaigns on corroded RC beams and tensile tests on corroded rebars.
Appendix A.3 and A.4	Experimental data on corrosion parameters in terms of maximum penetration depth and cross-sectional loss from pitting morphology study.

2 Literature review on corrosion processes of steel reinforcement in concrete

2.1 Highlights

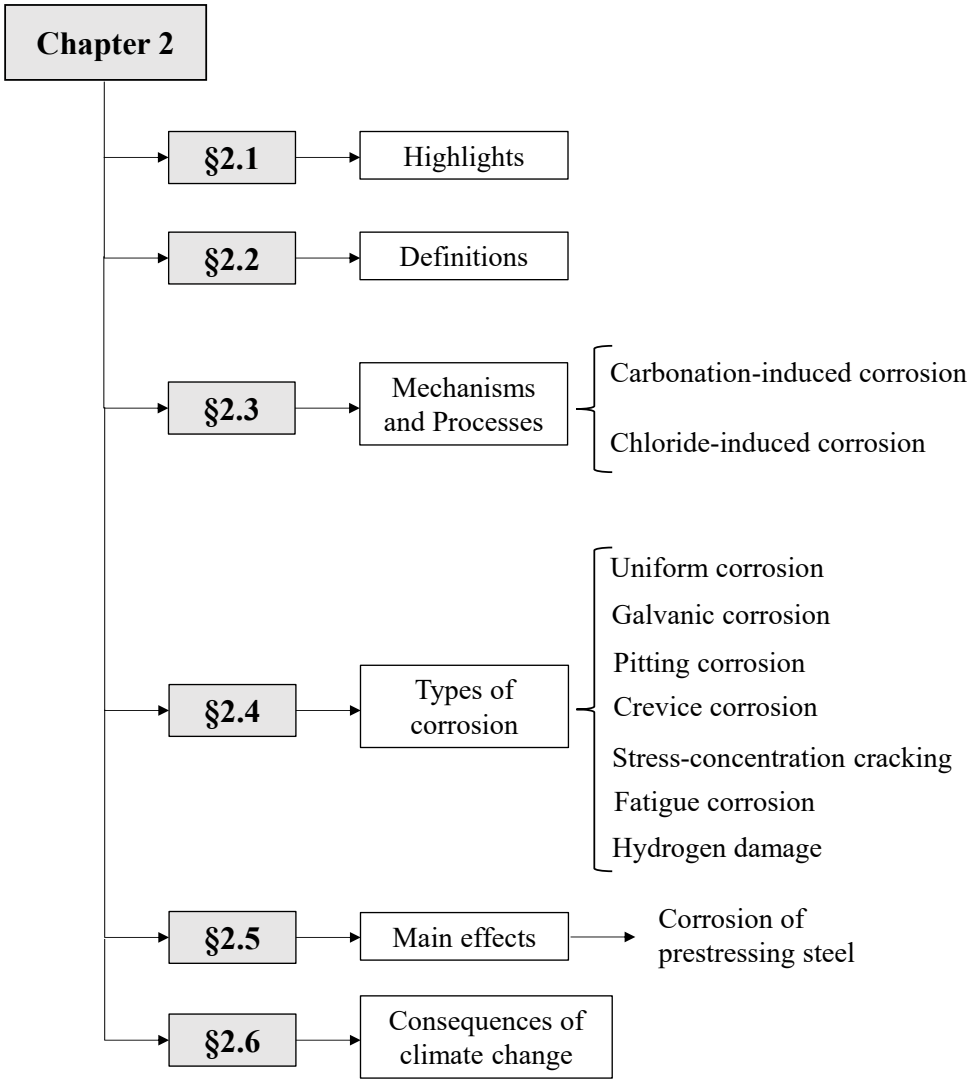

2.2 Definitions

From an etymological standpoint, the word "corrosion" shows a variety of historical influences. Its origins can derive (i) from the Middle English *corosioun* with the meaning of tissues' deterioration, (ii) from the Old French *corrosion*, or (iii) from the Latin *corrōsiōn* and (iv) *corrōsus* – past participle of corrōdere – which refers to the act of gnawing.

Over the last decades, several definitions of the word "corrosion" have been proposed worldwide. Some are strictly related to a type of corrosion which is specific to a field of research, whereas others are generic and easily attributed to several corrosion forms. In this context, the ISO 8044 standard (2020) defines corrosion as:

"a physicochemical interaction between a metallic material and its environment that results in changes in the properties of the metal, and that may lead to significant impairment of the function of the metal, the environment or the technical system, of which these form a part."

In general, corrosion is defined in scientific literature as a natural process where a metallic material, i.e. iron or steel, tends to interact with the surrounding environment by combining with other chemical elements, such as water and oxygen, to reach its lowest energy states. To achieve this condition, confined electrochemical reactions, known as oxidation and reduction reactions (abbreviated REDOX reactions), take place at metal surface. Therefore, the corrosion process is strongly influenced by the surrounding environment where reactions occur. For the abovementioned reason, a detailed description of the environment in terms of:

- Physical state: by distinguishing between gas, liquid, or solid state;
- Chemical composition: by defining the chemical elements that compose the environment and their concentrations;
- Temperature;
- Relative humidity;

turns out to be essential for accurately defining the corrosion process underway. In fact, as stated by Davis J. (2000):

"Corrosion is the deterioration of a metal and is caused by the reaction of the metal with the environment."

Finally, the term “aqueous corrosion” is used in literature to draw attention to the three main components essential for the initiation of the corrosion process, which are the presence of (i) a metal, (ii) moisture and (iii) oxygen.

2.3 Mechanisms and processes

In recent years, the growing interest of the scientific community on the topic of corrosion of RC and PC concrete structures has led to an in-depth understanding of corrosion mechanisms and processes, (Hansson et al., 2006).

Through the analysis of metals exposed to an atmospheric environment, three distinct behaviours can be identified:

- Immune behaviour: metals not susceptible to corrosion (*Noble Metals*) or other metals nobler than hydrogen cathodic reaction;
- Active behaviour: metals highly susceptible to corrosion but not able to restore their protective passive condition;
- Passive behaviour: metals, such as iron, susceptible to corrosion and characterized by insoluble rust products, that allow the formation of a protective layer that inhibits the development of further corrosion damages by reducing the corrosion attack to negligible values.

In detail, metals with an active or a passive behaviour tend to strictly interact with the surrounding environment to reach their lowest energy states, enabling the development of corrosion processes.

Corrosion is a natural process that converts a metal into a stable oxide, and it is subdivided into wet or dry corrosion. Electrochemical corrosion is a wet corrosion process that involves a series of complex electrochemical reactions that take place under the occurrence of certain conditions, such as (i) difference in energy level, (ii) presence of an electrolyte, and (iii) metallic connection.

In the case of corrosion of steel embedded in concrete, the deterioration process is favoured by the specific function performed by concrete. Under standard condition, concrete is a reliable environment and an excellent electrolyte characterized by high alkalinity of pore water and a pH of about 12.5. Concrete’s alkalinity is primarily determined by the presence of hydroxyl ions (OH^-) in the pore water, which results from the dissolution of calcium hydroxide ($Ca(OH)_2$) formed during the hydration process. This basic environment encourages the

formation of a passive layer of ferric oxide around steel reinforcements, which prevents further metal dissolution caused by corrosion.

According to Hunkeler (2005), five specific components must be simultaneously present to initiate and sustain the corrosion process of steel in reinforced and prestressed concrete, Figure 2-1:

- An anode, where corrosion takes place (a zone of the reinforcing steel);
- A cathode, which does not corrode and where the environment reduces (a zone of the reinforcing steel);
- An electrolyte, between the anodic and cathodic zones, with high conductivity that allows the electrons' flow (the concrete). The presence, even limited, of a water film to ensure ion mobility is necessary;
- A conductor in which electrons flow (the reinforcing steel);
- A sufficient level of moisture to complete the electrolytic condition of the cell.

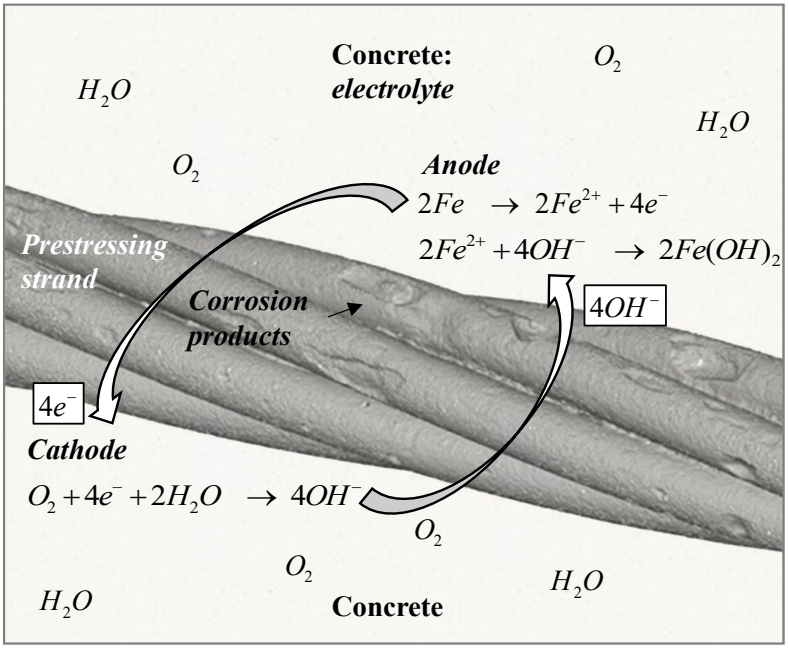

Figure 2-1 Schematic representation of the electrochemical process of corrosion.

When all the conditions are fulfilled, anodic and cathodic reactions take place, Figure 2-1. According to Eq. 2-1, the anodic reaction, also known as metal oxidation, implies the dissolution of iron atoms (Fe) in the surrounding water solution in the form of ferrous ions (Fe^{2+}) – if the supply of oxygen is scarce – or ferric ions (Fe^{3+}) – if oxygen is available – associated with the loss of one or more electrons.

$$2Fe \rightarrow 2Fe^{2+} + 4e^{-}$$
$$Fe^{2+} + O_2 + 2H^{+} \rightarrow Fe^{3+} + H_2O \quad \text{2-1}$$

Once the metal is oxidized and the free electrons migrate from the anodic to the cathodic zone due to the presence of a metallic connection, the cathodic reaction takes place. The latter involves the reduction of oxygen through the consumption of free electrons and water to form hydroxyl ions (OH^-), as expressed by Eq 2-2.

$$O_2 + 4e^{-} + 2H_2O \rightarrow 4OH^{-} \quad \text{2-2}$$

The electrochemical cell is completed by the charge flow undertaken by the movement of the hydroxyl ions from the cathode to the anode by diffusion. Thus, the coupling of oxidation and reduction reactions yields to the formation of ferrous ($Fe(OH)_2$) or ferric ($Fe(OH)_3$) hydroxides, according to Eq. 2-3.

$$2Fe^{2+} + 4OH^{-} \rightarrow 2Fe(OH)_2$$
$$2Fe^{3+} + 4OH^{-} \rightarrow 2Fe(OH)_3 \quad \text{2-3}$$

Thereafter, in the presence of a sufficient amount of moisture and oxygen, acid-base reactions may result in the conversion of ferrous and ferric hydroxides into ferrous oxide (Fe_20_3) with the consequent rust products formation, as briefly summarized in Eq. 2-4 to Eq. 2-6. As a result, a thin passive layer forms on the surface of steel reinforcements, which remains stable until the alkalinity of concrete pore water is not affected by the ingress of external aggressive agents such as carbon dioxide or chloride ions.

$$2Fe^{2+} + 4H_2O \rightleftharpoons 2Fe(OH)_2 + 4H^{+}$$
$$2Fe^{3+} + 6H_2O \rightleftharpoons 2Fe(OH)_3 + 6H^{+} \quad \text{2-4}$$

$$2Fe(OH)_2 \rightleftharpoons 2FeO + 2H_2O$$
$$2Fe(OH)_3 \rightleftharpoons 2FeO(OH) + 2H_2O \quad \text{2-5}$$

$$4Fe(OH)_2 + O_2 + 6H_2O \rightarrow 2Fe_2O_3.10H_2O$$
$$2FeO(OH) \rightleftharpoons Fe_2O_3 + H_2O \quad \text{2-6}$$

It is worth noting that, depending on the availability of oxygen and water, the oxidation of iron can produce a variety of rust products characterized by different colours and chemical reactions, as shown in Eqs. 2-7 – 2-12, (Fraczek, 1987; Popovics et al., 1983; Weizhong et al., 2010).

$$2Fe(OH)_2 + \tfrac{1}{2}O_2 \rightarrow Fe_2O_3.H_2O + H_2O \text{ (Red rust)} \quad 2\text{-}7$$

$$2Fe(OH)_2 + \tfrac{1}{2}O_2 + H_2O \rightarrow 2Fe(OH)_3 \text{ (Red rust)} \quad 2\text{-}8$$

$$3Fe(OH)_2 + \tfrac{1}{2}O_2 \rightarrow Fe_3O_4 + 3H_2O \text{ (Black rust)} \quad 2\text{-}9$$

$$2FeO + \tfrac{1}{2}O_2 + H_2O \rightarrow Fe_2O_3.H_2O \text{ (Red rust)} \quad 2\text{-}10$$

$$2FeO + \tfrac{1}{2}O_2 + 3H_2O \rightarrow 2Fe(OH)_3 \text{ (Red rust)} \quad 2\text{-}11$$

$$3FeO + \tfrac{1}{2}O_2 \rightarrow Fe_3O_4 \text{ (Black rust)} \quad 2\text{-}12$$

According to Rodriguez et al. (1999), six types of galvanic cells in the corrosion of steel embedded in concrete can be defined, each of which plays a key role in the corrosion process of steel reinforcements:

- Differential aeration cells;
- Differential surface conditions cells;
- Differential salt concentrations cells;
- Differential pH cells;
- Passive/active cells;
- Rusted/bright cells.

However, until the passive layer is provided, their effects are limited and inconsequential. Once the passive layer is broken down by aggressive agents, either locally or on a wide area, through the action of chloride ions (Cl^-) or due to carbonation of concrete, the passive-active transition occurs, and the corrosion process induced by galvanic cells becomes tangible. At this point, the six types of galvanic cells can be considered as different steps of the overall corrosion process.

Even though several types of corrosion cells have been defined in literature, the most significant distinction is between galvanic micro and macro cells, Figure 2-2. Microcells are characterized by a limited distance between the anode and the cathode in the microns order, Figure 2-2(a), whereas macrocells are distinguished by a significant distance between anodic and cathodic zone in the centimetres to meters order, Figure 2-2(b). As pointed out by Schiessel and Raupach (1997), several examples of macrocells can be found in daily engineering practice.

Indeed, macrocells can develop both on a single reinforcing rebar or prestressing strands as well as between different reinforcement layers where the metal connection between layers is provided by stirrups, Figure 2-2(b). Referring to existing RC and PC structures, macrocells occur in correspondence to cracks also. In these deteriorated areas the penetration of external aggressive agents such as chloride ions or carbon dioxide is enhanced, leading to the depassivation of steel reinforcement. The anodic reaction occurs in proximity of the crack, while the cathodic reaction develops on the same steel reinforcement within the distance between cracks, (Schiessl & Raupach, 1997), causing localized corrosion characterized by a high corrosion rate.

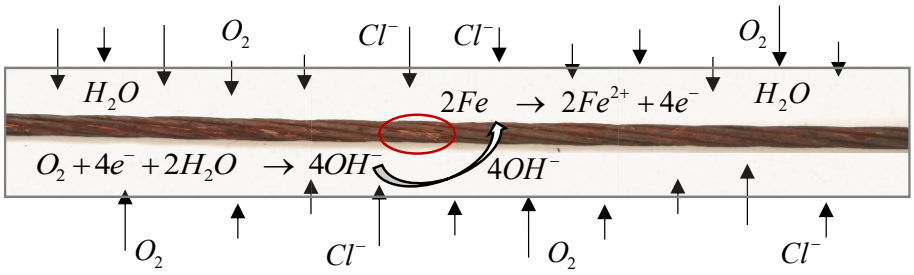

(a)

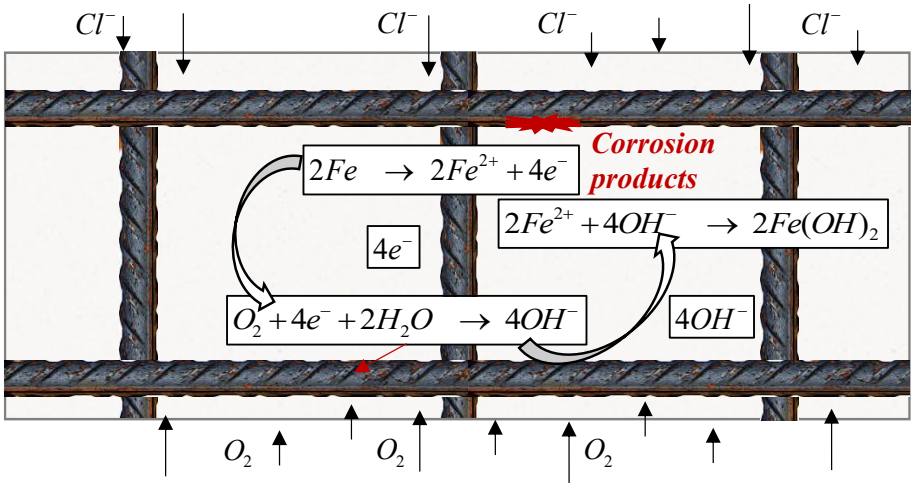

(b)

Figure 2-2 Corrosion mechanisms: (a) microcells and (b) macrocells.

Anyway it is worth noting that the overall corrosion process of steel embedded in concrete results from the combination of microcells and macrocells, (Fraczek, 1987).

In this framework, Tuutti (1982) distinguished the corrosion process into two main phases, named initiation period and propagation period, respectively, as shown in Figure 2-3.

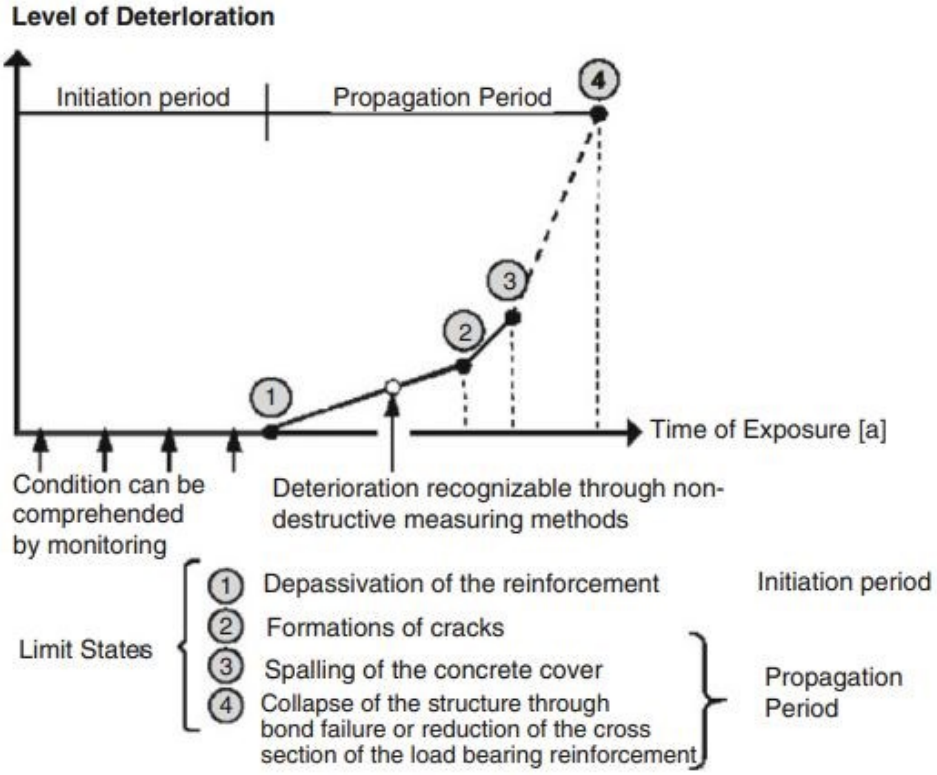

Figure 2-3 Tuutti's model schematic representation from *fib* Bulletin 34 (2006). Reproduced from *fib* Bulletin 34 - Model code for service life design, page 91 - "Figure R1.1-1: Deterioration process of reinforcement corrosion and life design definition of limit states for basic scheme of the service life design" with permission from the International Federation for Structural Concrete (*fib*).

The initiation period represents the time up to the depassivation of the steel reinforcement, while the propagation period is the time from the steel depassivation up to the reaching of a certain unacceptable level of deterioration, for example the Serviceability Limit State (SLS) or the Ultimate Limit State (ULS) of the analyzed structural member, (L. Franceschini et al., 2021). In terms of the initiation period, the scientific community agrees in identifying the carbonation of concrete and the chloride attack as the main processes that induce the depassivation of steel reinforcement through the transition from the passive to active stage of the corrosion process. The propagation period, conversely, refers to the development and progress of the corrosion process over time, which is controlled by its corrosion rate.

The corrosion rate is strongly conditioned by the surrounding environment where the analyzed RC or PC member is located. The EN 206 (CEN, 2014) defines four main exposure classes as function of possible aggressive environments:

1. No risk of corrosion or attack: X0;
2. Corrosion induced by carbonation: XC1 (dry or permanently wet environment), XC2 (wet, rarely dry), XC3 (moderate humidity), and XC4 (cyclic wet and dry);

3. Corrosion induced by chlorides other than from sea water: XD1 (moderate humidity), XD2 (wet, rarely dry), and XD3 (Cyclic wet and dry);
4. Corrosion induced by chlorides from sea water: XS1 (exposed to airborne salt but not in direct contact with sea water), XS2 (permanently submerged), and XS3 (tidal, splash and spry zones).

Furthermore, other aspects impact the corrosion rate, such as the fluid transport in concrete, which is promoted by three main mechanisms – diffusion, permeability and absorption –, oxygen and water availability, the type and the resistivity of concrete, the curing conditions, the cell polarization and the temperature.

2.3.1 Carbonation-induced corrosion

The carbonation of concrete, also known as *carbonation-induced corrosion*, is a natural process that occurs when the atmospheric carbon dioxide (CO_2) reacts with the alkalis in the pore water of concrete, generally sodium, potassium and calcium hydroxides ($NaOH$, KOH and $Ca(OH)_2$) to form sodium, potassium and calcium carbonates (Na_2CO_3, K_2CO_3, $CaCO_3$), (Zhou et al., 2015). The primary consequence of carbonation is a significant decrease of the alkalinity of concrete. Beyond the threshold pH value of 8.5, the protective passive layer becomes unstable and breaks down at the steel-concrete interface, allowing the steel reinforcement to corrode. Indeed, carbon dioxide has the ability to react with concrete without causing damage to it, but at the same time, it can also compromise steel reinforcement, Figure 2-4. In this context, the extension of the carbonation fronts as well as the penetration rate of carbon dioxide are influenced by:

- Cement types and concrete;
- Cement porosity and permeability;
- Concrete curing condition and compaction level;
- Water/cement ratio;
- Exposure condition: temperature, carbon dioxide concentration and its diffusion coefficient.
- Relative humidity: the ideal humidity level ranges between 25% and 75%. For values below 25% the carbonation process is trivial, whereas for values greater than 75%, moisture saturates the concrete capillaries by preventing carbon dioxide penetration, (ACI 201.2R-92). Additionally, for values between 60% and 95% the carbonation rate tends to increase linearly.

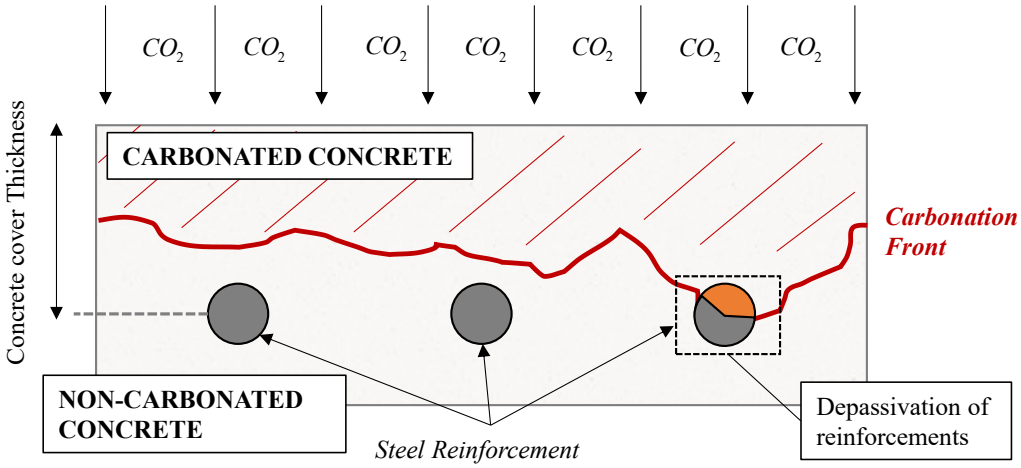

Figure 2-4 Carbonation-induced corrosion: focus on the penetration ingress of atmospheric carbon dioxide (CO_2) and example of carbonation front.

According to Hunkeler (2005), the first step of the carbonation-induced corrosion process consists in the formation of carbonic acid (CO_3^{2-}) from the dissolution of carbon dioxide in water, as expressed by Eq. 2-13.

$$CO_2 + H_2O \rightarrow 2H^+ + CO_3^{2-} \qquad 2\text{-}13$$

Concurrently, the alkaline components tend to dissolve in concrete pore water according to Eqs. 2-14 – 2-16.

$$NaOH \rightarrow Na^+ + OH^- \qquad 2\text{-}14$$

$$KOH \rightarrow K^+ + OH^- \qquad 2\text{-}15$$

$$Ca(OH)_2 \rightarrow Ca^{2+} + 2OH^- \qquad 2\text{-}16$$

Combining Eq. 2-13 with Eqs. 2-14 – 2-16, the full reactions can be summarized in Eqs. 2-17 – 2-19. During this phase, carbonates form and additional water is released by the reaction process. As a result, the consumption of hydroxyl ions (OH^-) causes a first significant decrease in the alkalinity of concrete, leading to a subsequent decrease in the pH value.

$$2NaOH + H_2O + CO_2 \rightarrow Na_2CO_3 + 2H_2O \quad 2\text{-}17$$

$$2KOH + H_2O + CO_2 \rightarrow K_2CO_3 + 2H_2O \quad 2\text{-}18$$

$$Ca(OH)_2 + H_2O + CO_2 \rightarrow CaCO_3 + 2H_2O \quad 2\text{-}19$$

With the continuation of the carbonation process, given the availability of additional water and carbon dioxide, a further reduction of pH is induced by the formation of soluble hydrogen carbonate, which produces the simultaneous presence of carbonic acid (CO_3^{2-}) and bicarbonate (HCO_3^-) in the concrete pore water, Eqs. 2-20 – 2-22.

$$Na_2CO_3 + H_2O + CO_2 \rightarrow 2NaHCO_3 \quad 2\text{-}20$$

$$K_2CO_3 + H_2O + CO_2 \rightarrow 2KHCO_3 \quad 2\text{-}21$$

$$CaCO_3 + H_2O + CO_2 \rightarrow Ca(HCO_3)_2 \quad 2\text{-}22$$

As a result, several parameters such as (i) temperature, (ii) cement alkali content, (iii) concrete hydration level, (iv) moisture content, and (v) CO_2 pressure, influence the final pH, (Hunkeler, 2005). From an assessment and design point of view, however, the concrete cover thickness of new and already existing structures in relation to the carbonation front depth represents the major risk of carbonation-induced corrosion, (Parrott, 1990). Indeed, for a fixed carbonation rate, a thinner concrete cover results in a shorter steel depassivation time and, consequently, an earlier start of the propagation phase. However, although carbonation-induced corrosion directly affects reinforcements' depassivation, influencing the end of the initiation period in Tuutti's model (1982), it is ineffective on the propagation period since it does not contribute to the corrosion rate.

2.3.2 Chloride-induced corrosion

The chloride ion attack, also known as *chloride-induced corrosion*, is generally considered as the most serious threat for the durability of RC and PC structures, (M. U. Khan et al., 2017; Zhou et al., 2015).

The main issue related to chloride ion attack is the local breakdown of the protective passive layer of steel reinforcements, Figure 2-5.

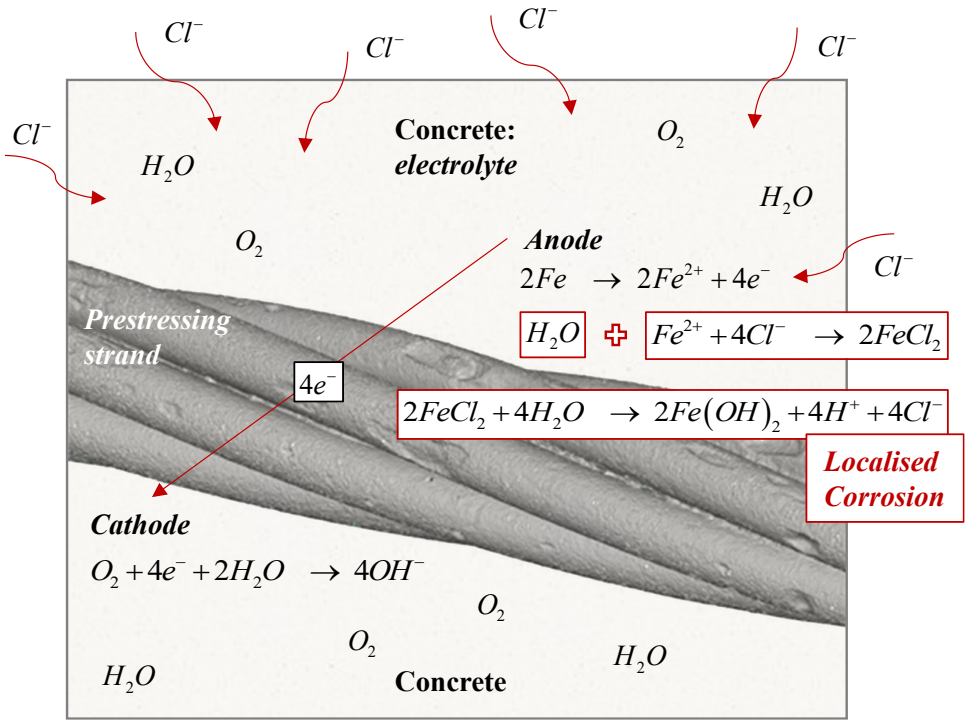

Figure 2-5 Chloride-induced corrosion: focus on the penetration ingress of chloride ions (Cl^-) and mechanism of corrosion.

When chloride ions reach a critical level of concentration at the steel-concrete interface, known as *threshold concentration of chloride ions* C_{crit}, galvanic microcells start to form, leading to localized corrosion, Figure 2-2(a). The threshold concentration is strictly related to the hydroxyl ions (OH^-) concentration in the concrete pore water, which affects the pH of the pore solution. Although there is no general agreement among scientific communities on a specific C_{crit} value, several codes and guidelines have prescribed maximum chloride contents, expressed as a percentage of the cement content of concrete, as reported in Table 2-1. Besides, as pointed out in the state of the art review carried out by Angst et al. (U. Angst & Vennesland, 2009; Ueli Angst et al., 2009), numerous scientific studies have been conducted in the last years to estimate the threshold chloride content sufficient to induce the onset of active corrosion under different exposure conditions. Anyway, since several factors influence the C_{crit} value, such as: (i) steel-concrete interface, (ii) binder type, (iii) steel surface condition, (iv) concentration of hydroxyl ions, (v) moisture content of the concrete, (vi) temperature, (vii) w/c ratio, (viii) oxygen availability, (ix) chemical composition of steel, and (x) electrical resistivity of concrete and (xi) cover thickness, a unique threshold value that disregards the exposure environment has not been derived (Ueli Angst et al., 2009). The scheme reported in Figure 2-6 shows the key issues related to the C_{crit} value determination. In detail, among the several exposure classes contemplated by the EN-206 (CEN, 2014), the wet and dry condition is

deemed to be the worst case scenario enhancing the chloride-induced corrosion process because of its ability to accelerate the diffusion by capillarity or by absorption of chloride ions within the concrete.

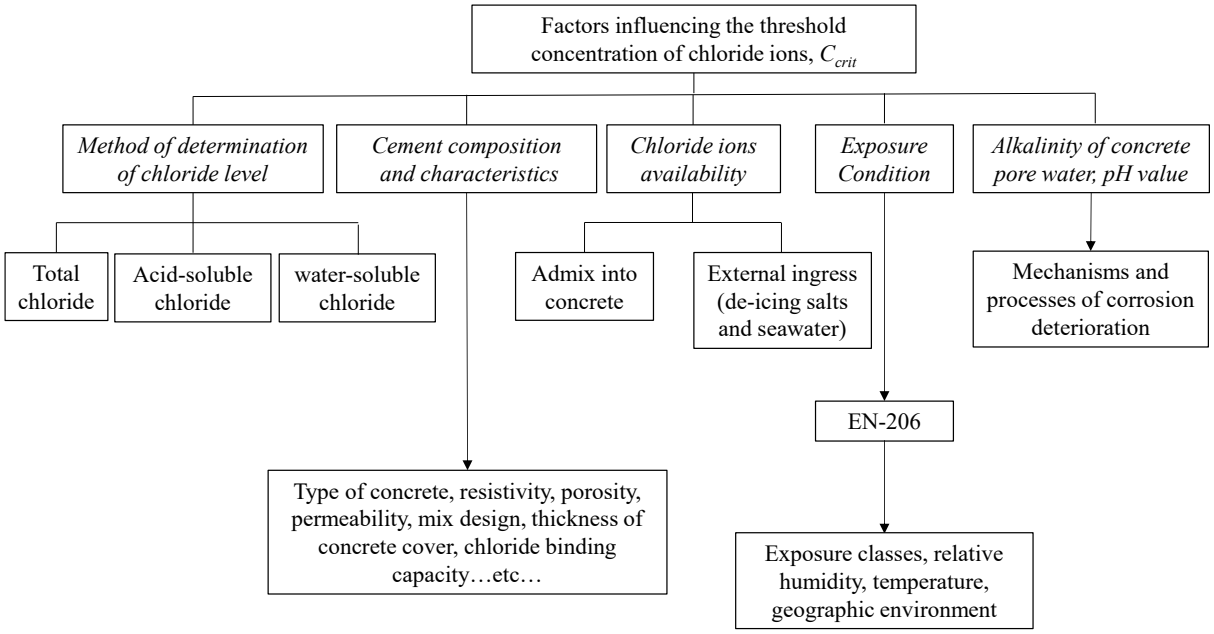

Figure 2-6 Factors influencing the threshold concentration of chloride ions.

Table 2-1 Chloride threshold values from codes and guidelines, adapted from (Ann & Song, 2007).

	Type of concrete			
Codes and Guidelines	**Reinforced Concrete (exposed to chloride)**	**Reinforced Concrete (dry or protect from moisture)**	**Prestressed Concrete**	**Other Reinforced Concrete**
BS 8110 (1985)	0.20	0.40	0.10	-
ACI 201 (1994)	0.10	-	-	0.15
ACI 357 (1994)	0.10	-	0.06	-
ACI 222 (1994)	0.20	-	0.08	-
CEB (1989)	-	-	-	0.2** and 0.4 (not carbonated)

**expressed in percentage of acid-soluble chlorides by cement weight

The mechanism of chloride-induced corrosion primarily interacts with the anodic reaction of a metal, (Montemor et al., 2003). After iron oxidation, chloride ions in concrete pore water react with available ferrous ions to form ferrous chlorides ($FeCl_2$), as reported in Eq. 2-23 and as shown in Figure 2-5.

$$Fe^{2+} + 4Cl^{-} \rightarrow 2FeCl_2 \qquad 2\text{-}23$$

Afterwards, given a sufficient amount of water, the gradual hydrolysis of ferrous chlorides brings to a decrease in pH, and to the concurrent formation of ferrous hydroxides ($Fe(OH)_2$) and the gradual release of chloride (Cl^-) and hydrogen ions (H^+). The result is the development of acid conditions, as highlighted in Eq. 2-24 – known as hydrogen embrittlement, Figure 2-5.

$$2FeCl_2 + 4H_2O \rightarrow 2Fe(OH)_2 + 4H^+ + 4Cl^- \qquad 2\text{-}24$$

The high availability of chloride ions causes an increase in corrosion rate, which results in a further reduction in pH and in an increased susceptibility of steel reinforcement to corrosion. It is crucial to note that chloride ions can be present in concrete pore water in different forms: (i) chloride ions bound to the cement matrix, (ii) chloride ions loosely-bound, and (iii) free chloride ions in pore solution from external ingress such as the use of unwashed marine aggregates or sands, extensive use of de-icing salts during winter periods, or chlorides from sea water. In this context, only free chlorides are responsible for the steel reinforcement deterioration, (Hope et al., 1985). Conversely, the formation of calcium chloroaluminate ($(Ca_2Al(OH)_6)Cl.2H_2O$ or $C_3ACaCl_2.10H_2O$, where C_3A stands for tricalcium aluminate) – which is a compound resulting from the hydration products of cement and chloride – tends to bind the chloride into concrete. In this configuration, the chloride ions are immobilized, meaning a reduction in the C_{crit} value and, as a result, a lower susceptibility of steel reinforcement to corrosion. The simultaneous presence of carbonation-induced corrosion, however, may cause an increased reduction of pH over time, leading to the instability of calcium chloroaluminate. This phenomenon involves the release of chloride ions, which bind in the cement matrix and causes a rapid increase in steel reinforcement corrosion vulnerability.

In general, the following negative effects of chloride ion penetration via diffusion, absorption and capillarity mechanisms can be summarized, (Hunkeler, 2005):

1. Breakdown of the protective passive layer at interface level between steel and concrete, enhancing the activation of corrosion process;
2. Reduction of the concrete alkalinity, i.e. reduction of pH value in the concrete pore water making the passive layer unstable;
3. Increase of the electrical conductivity of concrete;
4. Permeabilization of the passive layer to ferrous ions inducing anodic reactions without the breakdown of film protection.

2.4 Types of corrosion

According to different exposure environments, concrete properties, metal or alloy characteristics and structural design, corrosion may develop in various forms. As schematically reported in Figure 2-7, corrosion forms have been classified in literature based on:

- Nature of the corrodent: wet and dry corrosion process, (Davis, 2000);
- Appearance of corrosion damage and mechanism of attack: uniform corrosion, localized corrosion and mechanically-assisted corrosion; each category can be further subdivided into other specific corrosion forms.

Referring to the nature of corrodents, dry corrosion refers to processes that need the presence of high-temperature gases, whereas wet corrosion identifies the processes that request the presence of a liquid or a moisture for the development of REDOX reactions.

Surely, the classification based on the appearance of corrosion damage and the mechanism of attack is the most refined and the widely adopted. According to Mazumder (2020), four broad groups can be identified based on the nature of the environment: (i) electrochemical, (ii) chemical, (iii) biological and (iv) mechanically-assisted corrosion. Since electrochemical and mechanically-assisted corrosion can be considered as the main corrosion forms affecting aqueous corrosion of steel embedded in concrete, they will be discussed in details in the following paragraphs.

In terms of appearance of corrosion damage, which is generally determined by in-situ visual inspection or magnification techniques, electrochemical corrosion can be divided into two types: uniform corrosion and localized corrosion. This distinction consists in the extension of the steel region that cannot sustain passivity. Uniform corrosion is characterized by a uniform dissolution of steel along the reinforcement length that leads to a higher value of mass loss, whereas localized corrosion is distinguished by a local dissolution of steel caused by the formation of local anodes, resulting in a lower level of mass loss but an increased tensile stress in the reinforcements due to the cross-section area reduction induced by corrosion. Based on the extension and intensity of local attacks, localized corrosion can be further divided in macroscopic and microscopic corrosion, respectively. On the one hand, macroscopic corrosion includes (i) galvanic corrosion (GC), (ii) erosion-corrosion (EC), (iii) pitting corrosion, (iv) crevice corrosion (CC), (v) exfoliation, and (vi) dealloying corrosion. On the other hand, microscopic corrosion encloses (i) intergranular corrosion, (ii) stress-corrosion cracking (SCC), (iii) hydrogen embrittlement (HE), and (iv) corrosion fatigue (CF). Since the protective passive layer of steel reinforcement can be destroyed by the mutual action of applied mechanical forces

and an aggressive corrosive environment, stress-corrosion cracking, corrosion fatigue, hydrogen embrittlement and erosion-corrosion can be categorized as mechanically-assisted corrosion mechanisms.

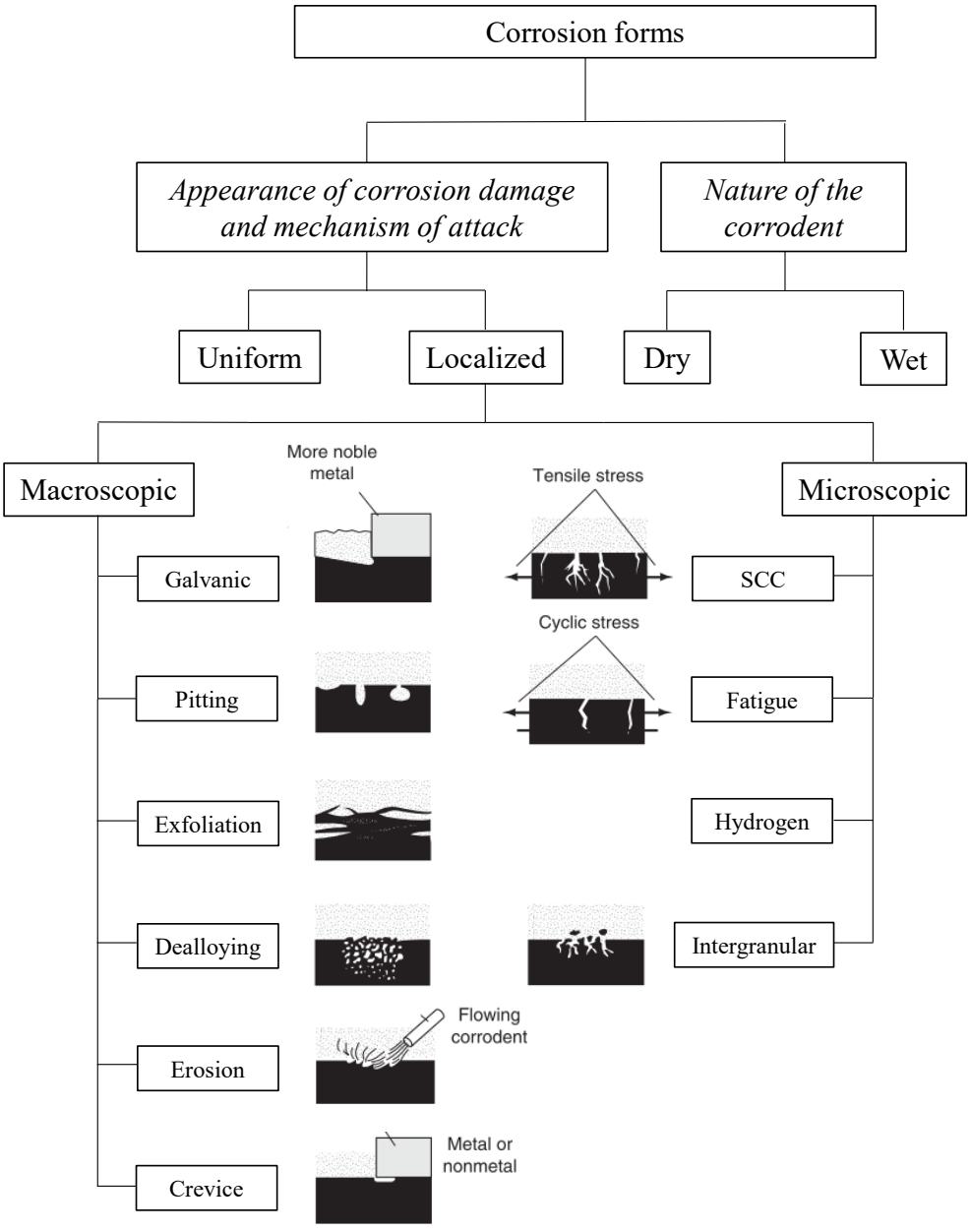

Figure 2-7 Classifications of corrosion forms.

2.4.1 Uniform or homogenous corrosion

Defined also as "general corrosion", uniform corrosion is caused primarily by the action of the atmospheric carbon dioxide penetration, i.e. carbonation-induced corrosion.

This type of corrosion is characterized by a uniform metal consumption along the entire length of the reinforcement and it is caused by the formation of several microcells placed closely together. Indeed, the proximity of two opposing charges causes metal to dissolve uniformly. In any case, general corrosion is considered as an ideal type of corrosion since – under normal circumstances, and particularly for corrosion of steel embedded in concrete – a level of non-uniformity takes place. During uniform corrosion, a number of anodes and cathodes are simultaneously and widely activated on the metal surface and the half-cell electrodes are constantly changing, resulting in a non-homogeneous metal consumption.

2.4.2 Galvanic corrosion (GC)

Galvanic corrosion is particularly influenced by concrete resistivity and results from the electric potential generated by the presence of:

- An electric connection of two different metals, inducing a potential difference;
- A conductive solution, usually sea water.

When the previous conditions are satisfied, the less *Noble* metal becomes the anode and starts to oxidate, whereas the other – the more *Noble* metal – becomes the cathode and corrodes slower. In more detail, the galvanic corrosion rate is determined by the ratio of anodic and cathodic areas. With the anodic area fixed, the galvanic corrosion rate increases as the cathodic area increases.

2.4.3 Pitting corrosion

Pitting corrosion is the most common type of chloride-induce corrosion, where pits are formed by the local breakdown of the protective passive layer of reinforcements. This corrosion type is distinguished by highly localized metal loss caused by the rapid increase in pit depth over time. In this scenario, the environment is unable to re-passivate the damaged areas and the corrosion process becomes self-accelerated and autocatalytic due to the reduction in pH value and the increased acidity of the environment caused by the high concentration of chloride ions in the pits' region. The danger of pitting corrosion stems from its ability to remain unnoticed until the corrosion process has progressed to the point of brittle failure of reinforcements.

Several pit type morphology configurations have been defined in literature. Roberge (2008) identified seven pit type morphology configurations: (i) narrow, (ii) shallow, (iii) elliptical, (iv) subsurface, (v) undercutting, (vi) horizontal grain attack, and (vii) vertical grain attack. Based on observations from specimens belonging to existing bridges, Jeon et al. (2019) defined three different pit type morphology configurations, named hemispherical shape, half-moon shape and planar shape, for the description of damage morphology induced by corrosion in strands. Additionally, Wang et al. (2020) classified 119 pits coming from prestressing strands artificially corroded by distinguishing between spheroidal, saddle and pyramidal pit type morphology configurations. Anyway, despite the several shapes previously outlined, the notorious morphology – generally adopted in codes and guidelines such as CONTECVET manual (2001) –, is the hemispherical configuration defined by Val and Melchers, (D. V. Val, 2007; V. Val & Melchers, 1997).

2.4.4 Crevice corrosion (CC)

Crevice corrosion is a particular form of pitting corrosion occurring in narrow openings. This form of corrosion generally takes place between metal-to-metal or metal-to-nonmetal elements.

Because of the differential aeration between the region inside and outside the narrow opening, favorable conditions for the development of the corrosion process – characterized by the presence of corrosive chloride solution – arise within a crevice. With the reduction in oxygen availability, the protective passive layer within the crevice cannot be maintained, leading to the onset of the corrosion process. The region inside the crevice acts as the anode of the corrosion process, while the environment region surrounding the crevice – richer in oxygen – acts as the cathode.

2.4.5 Stress-corrosion cracking (SCC)

Stress-corrosion cracking, abbreviated in literature with the acronym SCC, is one of the most common mechanically-assisted corrosion mechanisms, and it is particularly relevant in the case of PC structures with prestressing reinforcements subjected to high stress states.

SCC arises from the combination of internal or external static tensile stress and specific environmental conditions, and it is influenced by (i) mechanical variables, (ii) metallurgical variables, as well as (iii) environmental variables. In field application, stress-corrosion cracking

does not occur until a minimum stress value in the reinforcements is reached. However, as the corrosion process progresses, the reinforcement cross-section gradually shrinks, leading to the formation of cracks perpendicular to the applied stress. As previously stated, this corrosion form is particularly dangerous in the case of prestressing reinforcements, where even minor cross-sectional changes can cause failure due to the applied high stress state.

2.4.6 Corrosion fatigue (CF)

Corrosion fatigue is another relevant corrosion form classified as mechanically-assisted corrosion mechanism. This form of corrosion is caused by the combined action of a corrosive aggressive environment and the application of cyclic stresses to a metal.

The corrosion environment directly affects the susceptibility of a metal by increasing the cracking fatigue rate normally induced by the application of cyclic stress.

2.4.7 Hydrogen damage

Hydrogen damage is a term used in the literature to describe the reduction in load-carrying capacity caused by hydrogen action in conjunction with applied tensile or residual stresses. Three are the major types of hydrogen damage that can be defined: (a) hydrogen embrittlement (HE), (b) hydrogen-induced blistering, and (c) cracking from precipitation of internal hydrogen.

As previously reported in Eq. 2-24, hydrogen ions (H^+) are formed during corrosion process as a result of the gradual hydrolysis of ferrous chlorides. The hydrogen ions can then undergo two distinct processes depending on a number of variables. On the one hand, H^+ may recombine to form molecular hydrogen, which bubbles to the specimen surface, leading to a decrease in hydrogen concentration at the steel-concrete interface. On the other hand, hydrogen ion recombination may be hindered, favouring the latter's absorption in the metal material.

Among the three forms of hydrogen damage, hydrogen embrittlement can be considered the most relevant for steel corrosion embedded in concrete. This form takes place in acidic environments by the combination of high applied stress to steel and the specific cathode reaction reported in Eq. 2-25, which implies hydrogen atom formation from the reduction of hydrogen ions.

$$2H^+ + 2e^- \rightarrow 2H^0 \qquad 2\text{-}25$$

Subsequently, the molecular hydrogens (H^0) diffuse and dissolve in critical points of the steel – the most stressed ones. As a result of the gradual accumulation of hydrogen in stressed zones, cracking phenomena characterized by transgranular or intergranular form occur.

Hydrogen-induced blistering is favored by the precipitation of previously absorbed molecular hydrogen, at internal voids or laminations. Once a significant gas pressure arises and accumulates in the void regions just beneath the metal surface, it tends to lift up, causing internal cracks and metal surface bulging (blistering).

2.5 Main effects

Regardless of the possible types of corrosion, the scientific community agrees on the main effects associated to corrosion of steel embedded in concrete.

On the one hand, the oxidation of iron into ferrous ions involves the consumption and the degradation of steel reinforcements that primarily leads to:

- Reduction of cross-section of reinforcements, especially dangerous in the case of seven-wire prestressing strands with small diameter wires, (L. Wang, Li, et al., 2020);
- Decay of ultimate mechanical properties of steel in terms of both ultimate strength and ductility, (A. A. Almusallam, 2001; C. A. Apostolopoulos & Papadakis, 2008; Ch Alk Apostolopoulos et al., 2006; Cao et al., 2020; Cobo et al., 2011; Darmawan & Stewart, 2007; L. Franceschini et al., 2022; S. Imperatore & Rinaldi, 2016; Sun et al., 2018; L. Wang, Li, et al., 2020);
- Reduction in fatigue strength, (C. A. Apostolopoulos & Papadopoulos, 2007; Ch Alk Apostolopoulos, 2007; Department of Transportation, 1993; Fernandez et al., 2015; Kashani et al., 2015; S. Li, Tang, Gui, & Ma, 2017; W. Zhang et al., 2012).

These effects have a significant impact on the durability of existing RC and PC structures. The major consequence is the significant reduction of the overall structural load-carrying capacity of the corroded member induced by the reduced mechanical resistance, as well as an increased susceptibility of the reinforcement to brittle fracture instead of a hopeful ductile behaviour.

On the other hand, additional worsening effects are caused by the formation of rust products. Concrete cracking and surface defects result from the increasing action of pressure

forces at the steel-concrete interface caused by reinforcement volume expansion over time, which is induced by the complex electrochemical reactions of the corrosion process, (Asami & Kikuchi, 2003; Zhao et al., 2011). The consequences of concrete cracking are:

- Bond decay between concrete and steel, (A. A. Almusallam et al., 1996; Charis Alk Apostolopoulos et al., 2019; A. Castel et al., 2000b; Coronelli et al., 2019; Jiang et al., 2018a, 2018b; F. Li & Yuan, 2013; Lin et al., 2019, 2017; Ma et al., 2017, 2017; Mak et al., 2019; F. J. Tang et al., 2014; L. Wang et al., 2018; Y. Yang et al., 2019);
- Concrete damage such as swellings, delamination, and spalling of concrete cover, (Andrés A. Torres-Acosta & Castro-Borges, 2013; S. F. Zhang et al., 2011; Zhao et al., 2012, 2020).

The bond decay implies a further decrease of the overall structural load-carrying capacity of the corroded member by reducing its anchorage capacity and affecting its failure mode. Conversely, damage to concrete, especially in the form of longitudinal cracking at the reinforcement level up to concrete cover spalling, induces an increase in corrosion activity by establishing preferential pathways for the penetration of external corrosive agents.

As a result, the combination of some or all these factors contributes to the structural capacity reduction of existing RC and PC members over time, sometime causing unexpected failures due to the lack of bending, shear, or anchorage resistance without warning signs.

Additionally, the social consequences of corrosion include issues such as (i) public safety – which includes fires and explosion events triggered by the sudden collapse of structures and infrastructures –, and (ii) health of occupants of corroded structures – which includes pollution problems caused by the release of corrosion products or the release of escaping pollutants from corroded equipment.

2.5.1 Corrosion of prestressing steel

Since the present *Thesis* investigates and discusses chloride-induced corrosion of pre-tensioned prestressing reinforcements in the form of localized pitting corrosion, this section is addressed in evaluating its primarily effects in-depth.

According to the research conducted by Nurnberger (2002), pitting corrosion, stress-corrosion cracking, and hydrogen embrittlement are considered to be the most dangerous corrosion forms occurring in prestressing reinforcement and leading to premature failure without warning signs. In this context, three types of fracture were identified as a function of load conditions, prestressing reinforcement properties and corrosion processes:

1. Brittle fracture caused by the exceeding in residual load capacity. This type of failure is generally induced by localized pitting corrosion and hydrogen embrittlement;
2. Fracture caused by hydrogen that induces stress-corrosion cracking;
3. Fractures caused by fatigue.

In this context, corrosion of prestressing steel can be considered more serious than ordinary reinforcing steel for several reasons, (Lopes & Simões, 1999).

First, prestressing strands are subjected to high tensional states during their service life – ranging from 70% to 85% of their ultimate strength – and are characterized by small wire diameters. The combination of these two features yields prestressing reinforcements particularly prone to catastrophic rupture induced by pitting corrosion, especially when combined with fatigue load, stress corrosion cracking and hydrogen embrittlement, (F. Li et al., 2011). In particular, a small cross-section reduction caused by corrosion can turn into a significant decay in the mechanical properties of prestressing reinforcements, (Giriraju et al., 2022; Chi Ho Jeon et al., 2019; X. Liu et al., 2017; Z. H. Lu et al., 2016; L. Wang, Li, et al., 2020). Moreover, prestressing strands have a high surface area to volume ratio when compared to ordinary rebars, implying a larger surface area that may be affected by corrosion processes.

Second, corrosion significantly affects the fatigue resistance of prestressing reinforcements and fatigue life of deteriorated PC members. To address this issue, Li et al. (2017) experimentally investigated the combined action of chloride corrosion and fatigue through the analysis of twelve PC beams characterized by different actions combination, highlighting that the fatigue intensity increase plays a key role in the increase of the corrosion level of prestressing reinforcements. Moreover, Liu et al. (2017) and Jia et al. (2011) pointed out that the increase in corrosion level and loading cycles leads to the significant reduction of

both ultimate strength and ultimate strain of corroded prestressing wires. Yu et al. (2011) observed that the fatigue capacity of corroded PC beams reduces with the increase in corrosion level, resulting in higher deflection and crack widths. In this context, Liu et al. (2023) conducted an experimental campaign on thirteen PC beams artificially corroded and subsequently tested via high-cycle fatigue testing. The obtained results revealed that the fatigue life of the investigated PC beam is significantly affected and characterized by the fatigue fracture of the corroded tensile reinforcements that occurred at the minimum cross section where a severe corrosion pit was observed. Similar outcomes were also noticed by Zhang et al. (2016). Additionally, Su et al. (2022) proposed an analytical approach for the prediction of the fatigue life assessment of PC beams subjected to the combined action of corrosion and fatigue.

Third, bond decay and prestressing reduction due to corrosion has been documented in scientific literature by taking care to distinguish between pre-tensioned and post-tensioned corroded PC members, (Vereecken et al., 2021). Specifically, it is worth noting that the behavior of pre-tensioned PC members is more affected by bond between strand and concrete than post-tensioned one, where the prestressing force in strand is mainly transferred to the member by end anchorage system, (L. Wang et al., 2018). Similarly to ordinary rebars, the residual bond strength of pre-tensioned PC members is strongly influenced by (i) the concrete confinement reduction caused by the volume expansion of rust products and (ii) the transversal reinforcement cross-section reduction. However, the primarily difference with ordinary rebars consists in the prestressing strand twisting during the slip process. In this research field, Wang et al. (2017) first proposed a simplified model to describe the progressive bond degradation at steel-concrete interface by analyzing the experimental outcomes of 10 pull-out tests, characterized by corrosion level variability. According to the simplified model, the normalized bond strength remains constant until the reaching of a critical mass loss threshold of 6%, then, an exponential decay law was proposed. However, two years later, the same authors suggested a new model based on the experimental results obtained by performing beam tests on a total of nine pre-tensioned artificially corroded PC beams, (L. Wang et al., 2018). According to the improved model, an adjusted critical mass loss threshold of 5.25% and a following linear decay law were introduced. For completeness, Li & Yuan (2013) performed 12 pull-out tests, showing that the experimental bond-slip curve of corroded and un-corroded specimens changed due to corrosion. In fact, a tri-segments relationship was observed for the un-corroded scenario, which consisted of an ascending, a horizontal, and a descending branch; whereas the corroded bond-slip was only characterized by ascending and descending branches. Additionally, Imperatore et al. (2021) conducted several pull-out tests on corroded prestressing strands, noticing that a

significant reduction of the peak bond strength coupled to a variation in the shape of the curve occur.

In addition, further factors promoting corrosion in pre-tensioned PC members are listed in the following:

- Poor construction practice, such as inadequate concrete cover thickness, improper vibration of concrete, or use of poor quality concrete;
- Presence of chlorides from mix water or unwashed aggregates;
- Joints inadequately sealed and airtight and/or watertight.

Briefly mention to the post-tensioning technique, relevant aspects are the inadequate sealing of the duct as well as the mechanical performance and chemical composition of the grout components, where the use of unwashed marine aggregates or sands rich in chloride ions together with voids in the grout, may promote the chloride-induced corrosion, (X. Zhang, Wang, Zhang, & Liu, 2017a). Moreover, the presence of damage or holes in the duct accelerates the penetration of chloride ions caused by the use of de-icing salts or sea water, (National Physical Laboratory, 2020). In this regard, significant factors affecting corrosion in post-tensioned PC members are:

- Inadequate anchorage system protection;
- Poor construction practice;
- Inadequate sheathing and poor grouting;
- Poor quality duct, voids in the duct and/or non-watertight duct.

The deterioration of anchorage systems can lead to the sudden failure of PC members. Although the interaction between corrosion process and anchorage system type differs as a function of the adopted prestressing technique, similar features can be pointed out. Indeed, anchorage corrosion generally occurs due to the combination of direct ingress of chlorides and/or atmospheric carbon dioxide and the inadequate protection of the anchorage system, resulting in a significant decay of bond capacity that may cause the premature failure of the structural member, (A. A. Almusallam et al., 1996; Coronelli et al., 2019; Jiang et al., 2018a; L. Wang et al., 2018). To prevent this failure type, frequent visual inspection activities must be conducted in accordance with the maintenance protocol recommendations.

2.6 Consequences of climate change on corrosion process

Recently, climate change has become a crucial topic of debate among scientific communities worldwide, especially driven by the Intergovernmental Panel on Climate Change (IPCC), (2013, 2014). This phenomenon is triggered by global warming, which is generally recognized as the main cause of the worsening actions of natural weather events such as storms, heatwaves, hurricanes, and floodings.

Climate change evolution and related future risks are probabilistically predicted through one of the six potential greenhouse gas emission scenarios established in the Special Report on Emissions Scenarios (SRES), (Nakicenovic et al., 2000), named A1Fl (the most pessimistic) – RCP8.5 – RCP6.0 – RCP4.5 (the more realistic) – RCP2.6 – B1 (the most optimistic). The acronym RCP stands for Representative Concentration Pathway, while the following number is the approximate Radiative Forcing (RF), expressed in W/m^2. As defined by Nasr et al. (2019), the RF is a measure of the change in energy flux per surface area where positive values mean surface warming, whereas negative ones mean surface cooling. Under these scenarios, the uncertainties of climate change probabilistic predictions result particularly related to the estimated evolution of greenhouse gas emission.

Several are the effects associated with climate change over time; the main risks in the case of existing structures and infrastructures are two, (Nogal et al., 2021):

- The growth in intensity and frequency of natural hazards, which increases the risk of severe structural damage to new and existing structures and infrastructures, potentially resulting in economic and human losses, (United Nations Office for Disaster Risk Reduction, 2019). Therefore, structural loads, such as snow-load, wind-load, and thermal-load, subsequently increase in intensity and frequency, resulting in the overloading of existing structures and infrastructures.
- Durability reduction, which is affected by climate change-induced factors such as: (i) higher and lower precipitation in some regions, (ii) higher temperatures, (iii) increase and decrease in relative humidity, (iv) sea level rise (coastal and marine regions), (v) higher carbon dioxide concentration, and (vi) higher solar radiation. In this context, due to their long service life and the high exposure to natural hazards, bridges are considered as one of the most vulnerable infrastructure to climate change risks, (Kumar & Imam, 2013; Mondoro et al., 2018).

Referring explicitly to corrosion of RC and PC structures, climate change directly impacts the corrosion process by altering (i) the ambient temperature, (ii) the relative humidity, and (iii) the carbon dioxide concentration level. The proper evaluation of the corrosion risks triggered by climate change effects is then dependent on the geographical location, the adopted construction technique, the age of the structure, and the adopted maintenance strategies, (Sousa et al., 2020). Analyzing the durability issue, the decrease in relative humidity leads to the consequent increase in shrinkage losses, while creep losses are promoted by the lower relative humidity over land and the higher temperatures that accelerate the concrete creep rate of concrete, (Bažant & Panula, 1978; Vandamme et al., 2013).

The aggressiveness of carbonation-induced corrosion is determined by the availability of carbon dioxide (CO_2) and its penetration rate together with the temperature and the relative humidity of the environment. Temperature and relative humidity changes increase the rate of carbon dioxide penetration and accelerate the rate of REDOX reactions, such as CO_2 dissolution. According to the works conducted by Saha & Eckelman and Talukdar et al., (Saha & Eckelman, 2014; Talukdar et al., 2012), a 45% increase in carbonation depth values is expected by 2100 when compared to the year-2000 baseline by adopting the RCP8.5 scenario.

Chloride-induced corrosion appears to be less affected by climate change, even though changes in temperature and relative humidity have a significant impact on the diffusion coefficient of chloride ions as well as on its threshold concentration, C_{crit}. Among the potential extreme natural hazards caused by climate change, rising sea levels and heavy snows, are two major factors influencing chloride-induced corrosion (United Nations Office for Disaster Risk Reduction, 2020). According to EN 206 (CEN, 2014), the definition of the exposure classes depends on the proximity of structures and infrastructures to the sea. However, the appropriate exposure class may vary over time as due to climate change creating more aggressive environments. Moreover, the increased frequency of heavy snow events and freeze-thaw cycles requires the use of de-icing salts on a more frequent basis than in the past to ensure the maintenance and operation of transportation lines. To this subject, assuming the RCP8.5 greenhouse gas emission scenario and year-2000 baseline, a 15% increase in chloride concentration at reinforcement level is expected by 2100, (Xie et al., 2018). Furthermore, Bastidas-Arteaga et al. (E. Bastidas-Arteaga et al., 2010; E. Bastidas-Arteaga et al., 2013) predicted a lifetime reduction of RC structures of up to 18% and 31%, respectively, in terms of the period of corrosion initiation and the collapse of the structure.

3 Literature review on corroded PC beams and reinforcements

3.1 Highlights

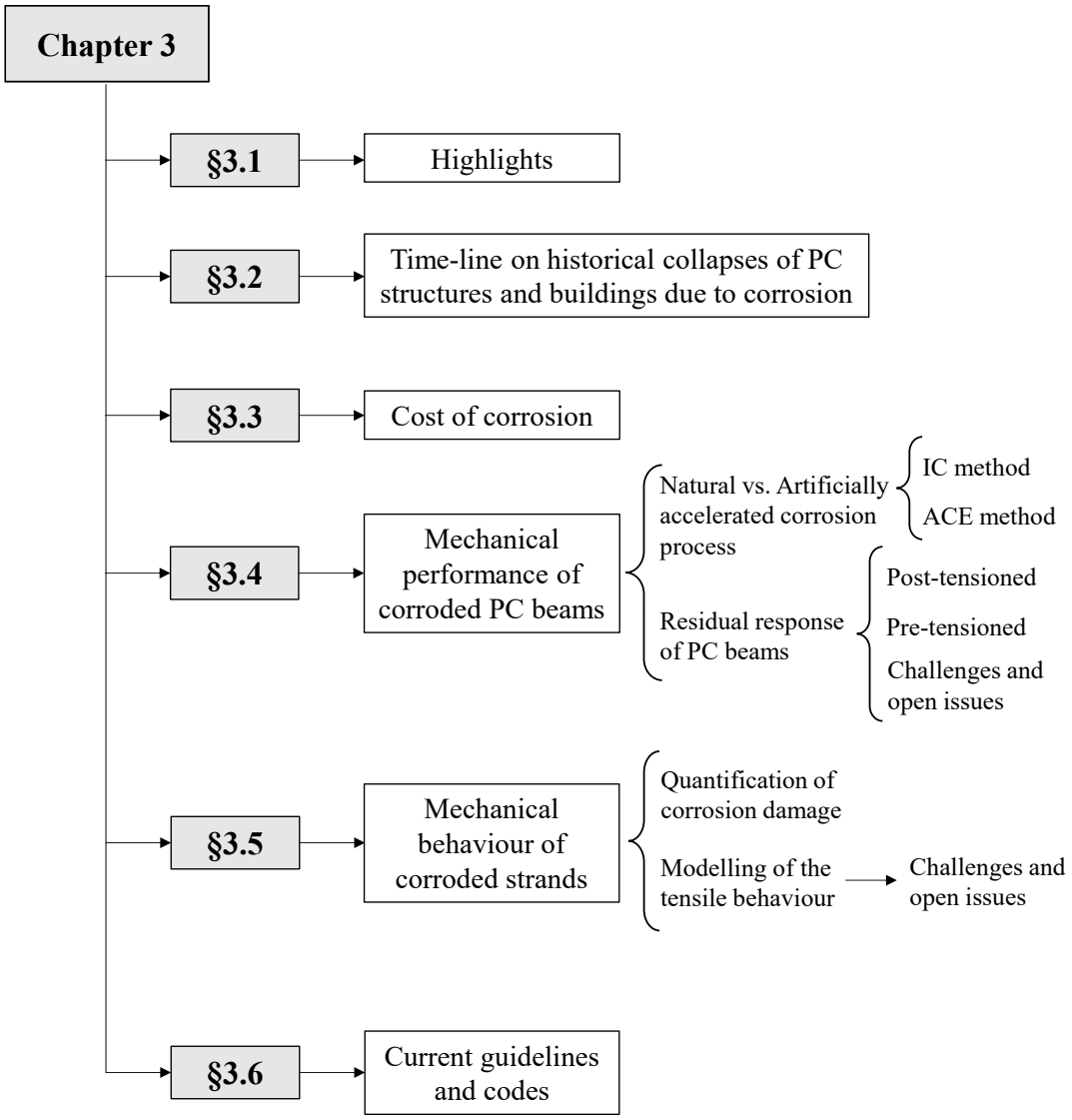

3.2 Historical collapses due to corrosion: a timeline

Since 2000, a total of one-hundred fifteen bridge collapses have been registered around the globe as a result of natural or man-made hazards – such as floods, storms, tsunamis, earthquakes, and vehicle impacts, (Deng et al., 2016). Conversely, some collapses occurred during regular bridge service life and under normal operating circumstances, generally with no significant warning signs, (Morgese et al., 2020). Referring to Imhof's database created in 2004 (Imhof, 2004), and containing three hundred forty-seven bridge failures during a period ranging from 1813 to 2004 – environmental deterioration was found to be the cause of 2.3% of the analyzed collapses. A technical report published in 2013 and sponsored by the Multidisciplinary Centre of Earthquake Engineering Research (G. C. Lee et al., 2013), stated that environmental deterioration was responsible for 6.3% of the 1062 bridge collapses occurred in USA between 1980 and 2012. Furthermore, a study conducted by Schießl & Mayer (2007) and readapted by the *fib* Bulletin 59 (2011) pointed out that the 69% of the bridges deterioration issues of German motorway network was due to corrosion; 66% induced by chloride attack and the remaining 3% by carbonation. Based on the available outcomes, it is evident how environmental deterioration – in particular corrosion – should be considered as a relevant failure cause.

Whitin this framework, the present *Thesis* identifies the collapses or the heavily damaged prestressed concrete bridges that have been recorded over the last sixty years, through the timeline shown in Figure 3-1. For the sake of completeness, Table 3-1 also reports the relevant information for each analyzed prestressed structure by listing: (i) the name, (ii) the reference country, (iii) the level of damage, (iv) the type of corrosion that caused the collapse, and (v) the number of fatalities and injuries – where N/A means that no data is available. Relevant references are provided for further information.

It is worth noting that the majority of the investigated bridges are post-tensioned and chloride-induced corrosion was the primary cause of heavy damage or even rupture of prestressing reinforcements. As observed in the previous chapter, the aggressive environment plays a fundamental role in the corrosion process. Indeed, bridges located in marine or coastal regions are constantly exposed to the presence of sea salt aerosol (hence chloride ions attack), while others are in damp environments typical of lagoon or river crossing areas, resulting in localized corrosion after relative short periods of exposure. Examples include the Santo Stefano Bridge in Italy, the Kure-tsubo Bridge in Japan, the Sorell Causeway Bridge in Australia and the Hamanatua Stream Bridge in New Zealand. Conversely, bridges located in mountain areas can suffer from the deteriorating effect caused by the extensive use of de-icing salts during the

winter period, which triggers the localized corrosion of reinforcements due to the percolation and diffusion of chloride ions, as happened with the Ynys-y-Gwas Bridge in Great Britain or the Polcevera Viaduct in Italy. Furthermore, other collapses, including the Silver Bridge in the US and the Berlin Congress Hall in Germany, failed due to stress corrosion cracking, which can be extremely dangerous in the case of prestressing reinforcements that are constantly subjected to high stress states throughout their service life (Schupack & Suarez, 1982).

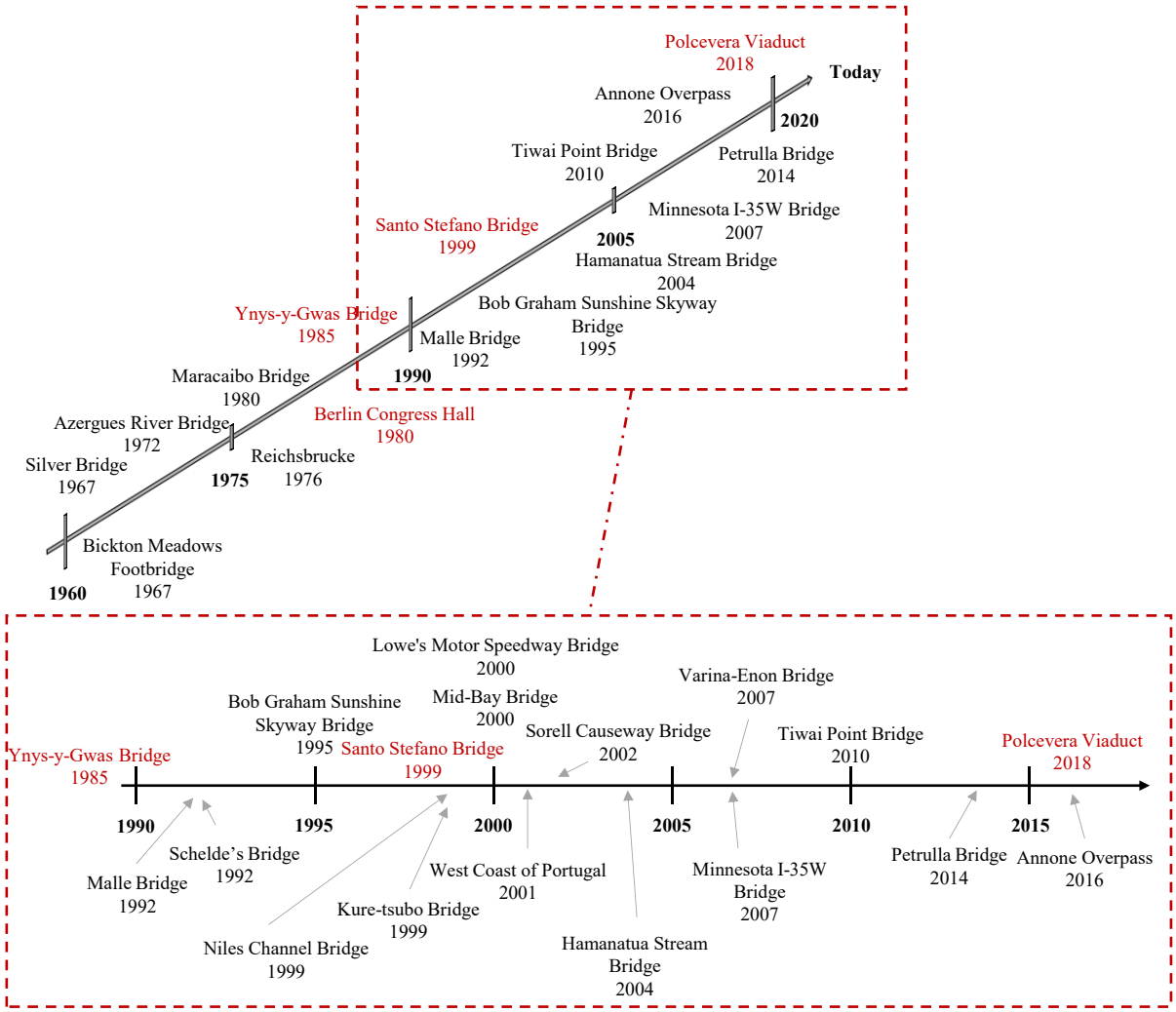

Figure 3-1 Timeline of principal collapses and heavy damaged bridge from 1960.

Despite some collapses occurred from 1960 to 1980, it was after the partially collapse of the Berlin Congress Hall and the total collapse of the Ynys-y-Gwas Bridge, that the scientific community became more interested in the corrosion of prestressed reinforcements. The sudden partial collapse of the roof of the Berlin Congress Hall, on May 21, 1980, after twenty-three years of service, had worldwide resonance because of the building historical and political significance. Indeed, the Congress Hall was gifted from the United States to Germany during

the 1956 International Exhibition for Construction as a symbol of freedom following World War II (Helmerich & Zunkel, 2014). The causes of the partial collapse of the roof, which resulted in one fatality and several injuries, were discovered in the failure of ten tendons presenting a high level of corrosion, particularly in the area near the final groove of the ring beam, Figure 3-2.

Conversely, the unexpected collapse of the Ynys-y-Gwas Bridge on December 4, 1985, after thirty-two years of service, was not only the first collapse of a PC highway bridge in the UK, but it also highlighted the major issues associated with corrosion of PC structures (Woodward & Williams, 1988). Indeed, after intensive investigation, severe corrosion of prestressing tendons was discovered to be one of the primary causes of the segmental post-tensioned deck collapse, Figure 3-3. The chloride-induced corrosion – probably caused by the percolation of de-icing salts and the use of dune sand in the mortar – was triggered by a combination of several bridge-condition-related issues:

- Ineffective waterproofing system (unable to limit the percolation of chloride ions of de-icing salt);
- Inadequate protection system of prestressing reinforcements (bad quality of grout);
- Corrosive environment (high humidity near the river);
- Poor workmanship;
- Presence of voids in the grouting.

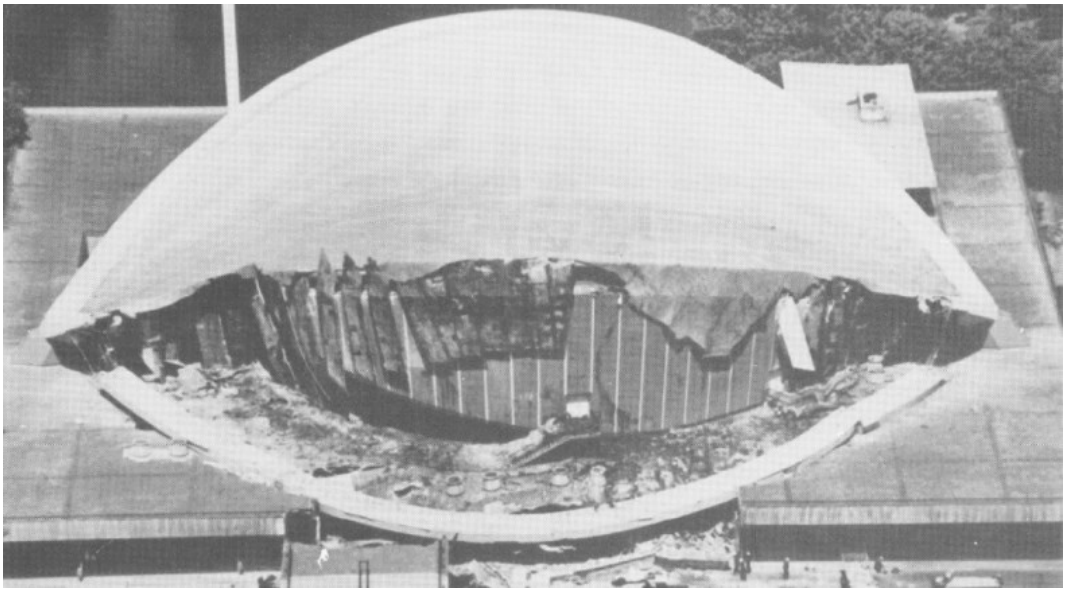

Figure 3-2 Partial collapse of the Berlin Congress Hall, reproduced from (Plank et al., 1981).

Figure 3-3 Collapse of the Ynys-y-Gwas Bridge, (Woodward & Williams, 1988).
Reproduced with permission from ICE Publishing.

Referring to Italy, the collapse of the Santo Stefano Bridge (1999) in Messina and the sudden collapse of the Polcevera Viaduct in Genoa on August 14, 2018, can be considered as the most significant collapses of the last two decades.

The first collapse shocked the scientific community not because of its catastrophic nature – the bridge collapsed under permanent loads when no vehicles were passing through – but because of its ability to highlight the vulnerability to corrosion of the Italian road network's viaducts and bridges. As pointed out by Colajanni et al. (2016), the use of precast PC segments with post-tensioned technologies is commonly used in Italy due to their structural flexibility. Therefore, the collapse of the Santo Stefano Bridge was a key event in the field of bridge engineering, prompting the drafting of new guidelines, ("Linee guida per la classificazione e gestione del rischio, la valutazione della sicurezza ed il monitoraggio dei ponti esistenti", Ministero delle Infrastrutture e della Mobilità Sostenibili, 2022), with the aim of ensuring high levels of safety and reliability of Italian viaducts and bridges through a careful evaluation and monitoring process for the periodic assessment of the deterioration level and relative remaining service life of Italian infrastructures. Conversely, the catastrophic collapse of the Polcevera Viaduct (Morandi's Bridge), which caused the death of forty-three people, had a global media impact since it was an important transport link that connected the Mediterranean Sea to several European countries and it was considered as a prestressed concrete masterpiece, Figure 3-4.

This failure generated heated discussion among engineers since the bridge already showed corrosion deficiencies after a short period of time from the inauguration, emphasising the importance of a monitoring control and retrofitting of some parts. Pier 11, indeed, was retrofitted by replacing the deteriorated suspending cables. The main reasons affecting the Polcevera viaduct collapse are still under investigation. Nevertheless, according to Nuti et al. (2020), Polcevera collapse can be considered as the first large-scale bridge failure that, in addition to other concomitant involved factors, was affected by the corrosion-induced structural capacity decay, which reduced the mechanical properties of prestressing reinforcements.

Figure 3-4 Collapse of the Polcevera Viaduct. (https://theconversation.com/genoa-bridge-collapse-maintaining-these-structures-is-a-constant-battle-against-traffic-and-decay-101627).

Table 3-1 Features of bridges and structures subjected to heavy damages or collapsed due to corrosion.

Reference	**Country**	**Name**	**Damage**	**Type of corrosion (fatalities)**
(G. C. Lee et al., 2013; Morgese et al., 2020)	US	*Silver Bridge*	Collapsed	Stress corrosion and fatigue corrosion (46 fatalities; 9 injuries)
(The National Academy of Science, 2000)	UK	*Bickton Meadows Footbridge*	Heavy Damaged	Chloride-corrosion
(Podolny, 1992)	France	*Azergues River Bridge*	Heavy Damaged	Chloride-corrosion
(Imhof, 2004)	AUT	*Reichsbrucke*	Collapsed	*N/A (1 fatality)
(Helmerich & Zunkel, 2014)	Germany	*Berlin Congress Hall*	Partially Collapsed	Stress corrosion (1 fatality + injuries)

(Imhof, 2004)	Venezuela	*Maracaibo Bridge*	Heavy Damaged	*N/A
(Woodward & Williams, 1988)	UK	*Ynys-y-Gwas Bridge*	Collapsed	Chloride-corrosion
(Youn & Kim, 2017)	Belgium	*Malle Bridge*	Collapsed	Chloride-corrosion
(Imhof, 2004)	Belgium	*Bridge Schelde*	Collapsed	*N/A
(Trejo et al., 2009)	Florida, US	*Bob Graham Sunshine Skyway Bridge*	Heavy Damaged	Chloride-corrosion
(Colajanni et al., 2016)	Messina, IT	*Santo Stefano Bridge*	Collapsed	Marine aerosol
(Tanaka Y. et al., 2001)	Japan	*Kure-tsubo Bridge*	Demolished	Coastal environment
(Pillai et al., 2010)	Florida, US	*Niles Channel Bridge*	Heavy Damaged	Salt-water
(El Menoufy & Soudki, 2014)	US	*Lowe's Motor Speedway Bridge*	Collapsed	Calcium chloride
(Pillai et al., 2010; Trejo et al., 2009)	Florida, US	*Mid-Bay Bridge*	Heavy Damaged	Chloride-corrosion
(Valiente, 2001)	ESP	*N/A	Heavy Damaged	Stress corrosion
(Costa & Appleton, 2002)	Portugal -	*N/A	Heavy Damaged	Chloride-corrosion
(Pape & Melcher, 2013)	Australia	*Sorell Causeway Bridge*	Demolished	Marine environment
(Bruce et al., 2008)	New Zealand	*Hamanatua Stream Bridge*	Damaged	Marine environment
(Hansen et al, 2007); (Pillai et al., 2010)	Virginia, US	*Varina-Enon Bridge*	Heavy Damaged	Chloride-corrosion
(Morgese et al., 2020; Salem & Helmy, 2014)	Minnesota, US	*Minnesota I-35W Bridge*	Collapsed	*N/A (13 fatalities+145 inj.)
(Rogers et al., 2012)	New Zealand	*Tiwai Point Bridge*	Demolished	Coastal environment
(Anania et al., 2018)	Licata, IT	*Petrulla Bridge*	Collapsed	Chloride-corrosion (4 injuries)
(Bazzucchi et al., 2018)	Lecco, IT	*Annone Overpass*	Collapsed	*N/A (1 fatality)
(Calvi et al., 2019; Morgese et al., 2020; Nuti et al., 2020)	Genoa, IT	*Polcevera Viaduct*	Collapsed	Marine environment (43 fatalities)

3.3 Cost of corrosion

The effects of corrosion can be: (i) direct, with a significant impact on the service life and ultimate structural capacity of a corroded member, or (ii) indirect, affecting administration of public and private authorities through corrosion costs for maintenance, repair, retrofitting and/or reconstruction of damaged structures and infrastructures.

Analyzing indirect effects, it has been estimated that the annual corrosion cost of a country ranges between 1% and 5% of the gross national product (GNP), (Javaherdashti, 2017). A similar situation has been depicted by a recent survey carried out by NACE International in 2016, (Koch et al., 2016), where the authors claimed that the global cost of corrosion is equal to $2.5 trillion, which corresponds approximately to the 3.4% of the global gross domestic product (GDP). In this ranking, Europe shows an alarming trend with a corrosion cost equal to 3.8% of its GDP. The industry sector is the most affected one with a cost of about $401 billion, followed by the services sector at $297 billion and agriculture at approximately $3.5 billion. Focusing on Italy, the service sector is the most severely impacted ($1.5 billion), followed by industry ($0.5 billion), while agriculture appears to be only marginally affected by corrosion issues ($0.04 billion).

According to the National Institute of Standard and Technologies (NIST), in collaboration with the Battelle Columbus Laboratories (1995), the corrosion cost of metals in the United States amounts to approximately $276 billion per year, which corresponds to 3.1% of the U.S. GDP, (Hansson, 2011; Kruger, 2011). In particular, the corrosion costs related to bridge heritage sum up to $8.3 billion per year, (Schmitt et al., 2009).

Sarcastically, the catastrophic financial burden caused by corrosion issues is clearly shown in Figure 3-5, which compares the U.S. direct costs related to corrosion – too often neglected in political debates – with the costs related to health issues such as smoking and obesity, or climate-related issue such as storms and hurricanes – which are, on the contrary, under the media spotlight, (U. M. Angst, 2018). The cost of a single intervention to repair corrosion-related damage can range from thousands of dollars, to repair a corroded electrical pylon or to renovate a parking deck corroded during its service life by the intensive use of de-icing salts, to millions of dollars for the reconstruction of a collapsed bridge or to ensure the safety of a nuclear power plant.

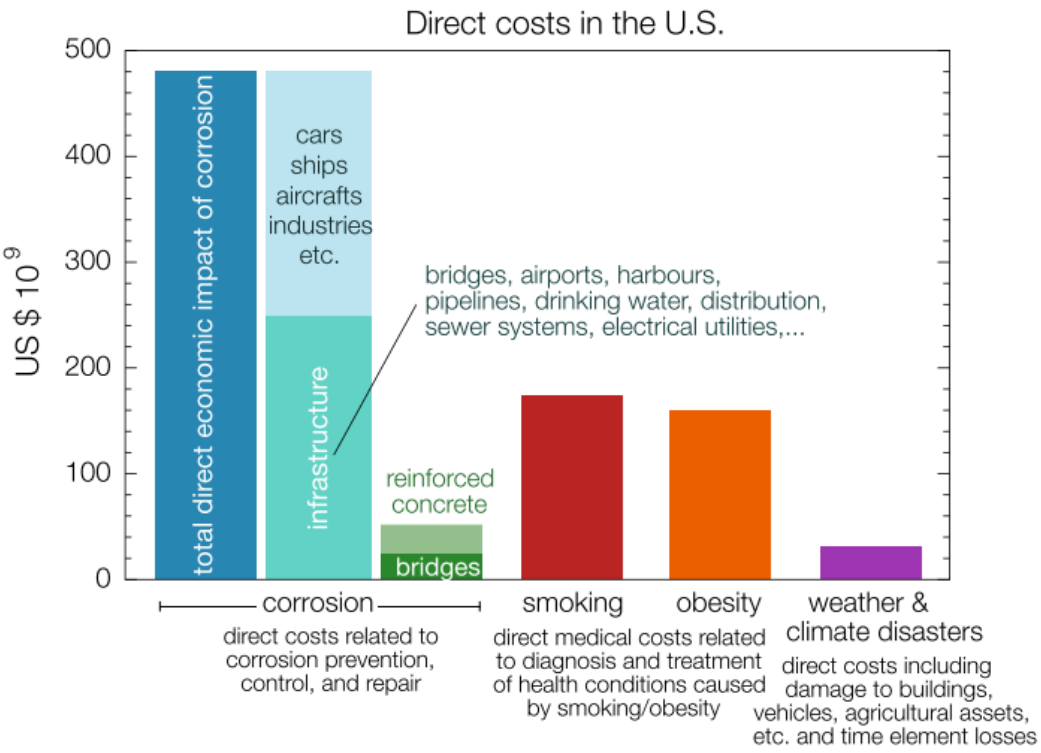

Figure 3-5 Relevance of corrosion costs on the U.S. economy, reproduced from Angst (2018).

In general terms, the following economic consequences influencing corrosion costs can be listed, (Davis, 2000):

- Preventive maintenance;
- Overdesign taking into account possible corrosion damage;
- Replacement, repair or retrofitting of corroded structures and infrastructures;
- Shutdown of structures and infrastructures due to corrosion evidence;
- Loss of efficiency, related to the partial use of a corroded structure or infrastructure (for example, a bridge partially closed to traffic);
- Damage to structures or infrastructure adjacent to collapsed ones due to corrosion issues.

Additionally, it is possible to identify several factors that positively or negatively influence corrosion costs. The main factors that help public and private authorities to decrease corrosion costs are (a) scientific research and increased knowledge concerning corrosion processes and mechanisms; (b) the application of new technology in construction and industrial sectors, allowing to prevention of corrosion; and (c) the proper application of new available methods to prevent and control corrosion such as inhibitors or coatings methodology. On the other hand, factors that cause the increase in corrosion costs are (a') the unchecked and unjustified extension of the service life of buildings and infrastructures; (b') deferred

maintenance, which allows the unhindered development of corrosion over time; and (c') the extensive urbanization in hostile and aggressive environments. To this end, a survey by the American Society of Civil Engineers (ASCE) and the Federal Highway Administration (FHWA) on the United States' bridge heritage revealed that 30% of existing bridges have already exceeded their service life, (Federal Highway Administration, 2006). Similarly, Polder et al. (2012) pointed out that the majority of Dutch bridges are approaching their 50 year service life. Thus, in the near future, the age profile of existing structures and infrastructure in developed countries will impact corrosion costs by increasing repair and maintenance costs, whereas emerging countries will face a significant expansion of structural heritage necessitating the design of durable new buildings and infrastructures, (U. M. Angst, 2018).

Finally, referring to climate change issues, it is important to note that an international study conducted by the United Nations Office for Disaster Risk Reduction entitled "Making Critical Infrastructure Resilient" (2020) discovered that European economic losses due to infrastructure damage as a consequence of extreme weather events amount to approximately €9.3 billion per year, with this figure expected to rise to €37 billion by 2080. In particular, extreme weather conditions have a significant impact on the transportation sector, resulting in an annual economic loss of approximately €0.8 billion.

3.4 Mechanical performance of corroded PC beams

3.4.1 Natural corrosion vs. Artificial accelerated process

In the aftermath of disasters or extreme events caused by corrosion, such as a RC or PC bridge collapse, intensive experimental campaigns are commonly conducted to study the mechanical behaviour and residual load-carrying capacity of RC and PC members subjected to carbonation-induced or chloride-induced corrosion.

From an experimental and laboratory point of view, chloride-induced corrosion can be naturally triggered or artificially accelerated by applying several techniques. Although specimens subjected to natural corrosion properly reproduce the effective degradation process undergone by the structural element during its service life, they turn out to be rare and difficult to find since they result from long experimental campaigns or are recovered from decommissioned structures such as bridges, power plants or buildings. Moreover, the outcomes obtained by testing naturally corroded specimens are strongly influenced by the actual environment, exposure time, aggressive agent concentration and type of corrosion involved, causing problems in the comparison of different experimental outcomes. When compared to natural corrosion, artificial accelerated corrosion can be performed within a short period of time. However, researchers generally agree that artificially accelerated methods produce different corrosion characteristics and effects on the investigated structural element than those induced by natural environmental attack, especially if high values of corrosion rate are adopted. The greatest constraint in the interpretation of the obtained results lies in the high variability induced by differences in dimensions and characteristics of the tested specimens, test conditions and methodologies applied.

According to the comparative review carried out by Feng et al. (2021), three groups of accelerated methods can be defined:

- Impressed Current (IC);
- Chloride Ion Diffusion (CID);
- Artificial Climate Environment (ACE).

In laboratory activities, IC method is the most commonly used technique to accelerate the corrosion process. The major benefit consists in the time saved in reaching the desired corrosion level through the application of an electrochemical potential between the anode and cathode regions of steel reinforcement. The ACE method involves the use of an appropriate chamber to simulate the splash and spray conditions of natural environments and, unlike the IC method, promotes corrosion by accelerating chloride ion ingress without the application of

current. Finally, the CID method is mainly applied to shorten the initiation period of the corrosion process by accelerating the chloride ions diffusion using an electric field, (Geng et al., 2008). However, since the CID method has no direct impact on the propagation phase of corrosion, only a limited number of studies have been carried out to evaluate its efficiency in reproducing the effects of the natural corrosion process. Due to their widespread use in laboratory-based experimental tests, the IC and ACE methods are examined further in the following paragraphs.

3.4.1.1 Impressed Current (IC) method

The IC method involves the use of a direct current power supply that induces corrosion in the reinforcements embedded in concrete by applying an electrochemical potential between anode and cathode. To this aim, the current power supply is regulated to apply a constant impressed current to the specimen, generally immersed into a $NaCl$ or $CaCl_2$ solution during the testing period, t_{test}. The $NaCl$ solution reproduces the effects associated to sea water, whereas the $CaCl_2$ solution can be adopted to investigate the use of de-icing salt consequences. The testing period varies from hours to months as a function of the desired corrosion level and it is calculated using Faraday's law, as shown in Eq. 3-1:

$$t_{test}\left[s\right] = \xi \frac{\eta \cdot n_{specimen} \cdot C_{Faraday}}{current\left[A\right] \cdot M_{specimen}} \qquad 3\text{-}1$$

where η is the desired mass loss after the corrosion process, $M_{specimen}$ is the molar mass of the steel reinforcement, $n_{specimen}$ is the steel valence, set equal to 2, $C_{Faraday}$ is the Faraday constant, equal to 96480 and ξ is a constant set equal to 1 for bare bars, and higher than 1 for the embedded specimens, (Imperatore et al., 2017).

Four IC methods have been defined in scientific literature as a function of the counter electrode position and electrolyte, named: (a) soaking method, (b) part soaking method, (c) surface soaking method, and (d) embedded auxiliary electrode method, (J. Chen et al., 2020). A schematic representation of each IC method is reported in Figure 3-6.

Regardless of the type of IC method adopted, the main advantages are:

(i) Time-saving due to the celerity of corrosion process compared to natural corrosion;

(ii) Applicability to full-scale specimens due to its adjustable nature obtained by using a current power regulator;

(iii) Control of corrosion rate by setting relevant parameters such as current density, salt solution concentration and external load.

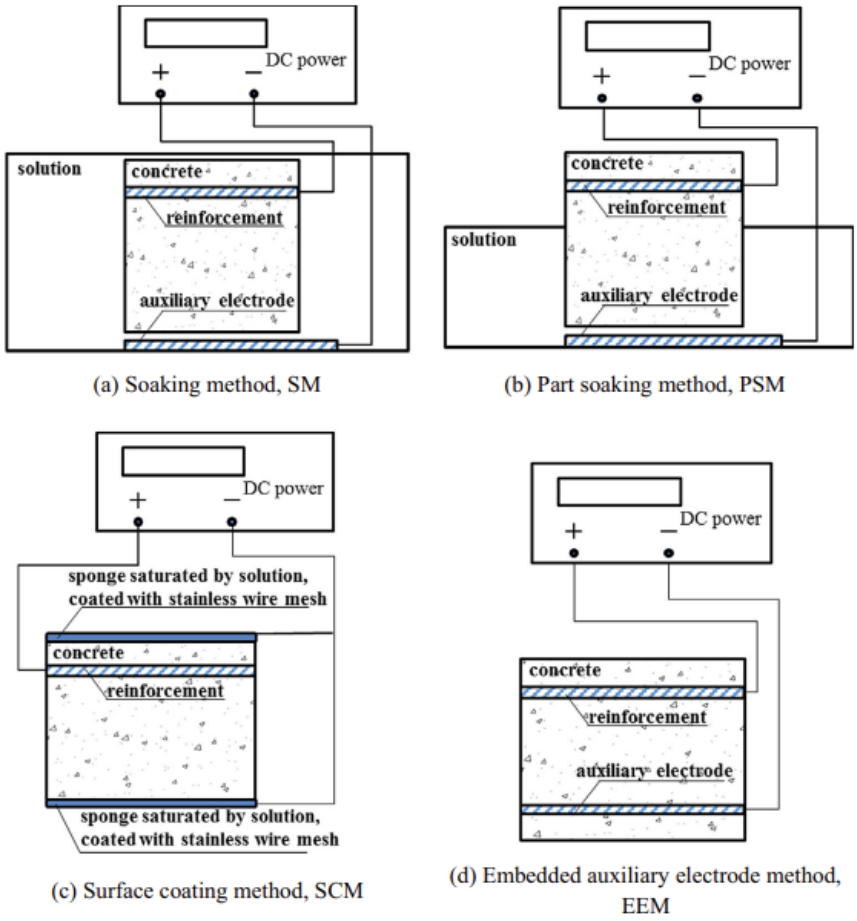

Figure 3-6 Schematic representation of IC methods: (a) soaking method, (b) part soaking method, (c) surface coating method and (d) embedded auxiliary electrode method, (J. Chen et al., 2020). Reproduced with permission from Elsevier.

Nonetheless, the biggest issue consists in the wide range of testing configurations, especially in the selection of the appropriate applied current density value, I_{corr}. Referring to scientific literature, the range of natural current density varies between 0.1 μA/cm^2 and 10 μA/cm^2 with some exceptional cases reaching a value equal to 100 μA/cm^2 due to the seasonal change in weather conditions, (Alonso et al., 1998). Conversely, in the case of artificially accelerated methods, a wider range in I_{corr} values varying between 0.04 μA/cm^2 to 900 μA/cm^2 for the studies conducted by Yang et al. (2018) and Hariche et al. (2012) is observed. The primary consequence is the inability of the IC method to actually reproduce the deterioration effects induced by natural corrosion when high current density values are applied. In light of this issue, Maaddawy and Soudki investigated the variability of reinforcement strain as a function of applied current density values varying from 100 μA/cm^2 to 500 μA/cm^2, (T. A. El Maaddawy & Soudki, 2003). The obtained outcomes showed that – for the same time of current application during test – higher reinforcement strain can be measured with the increase in

applied current density. Additionally, the same authors set the critical I_{corr} threshold value at 200 μA/cm^2 above which the crack pattern, in terms of crack width induced by corrosion, is strongly affected due to a more extensive rust expansion. Furthermore, according to Rodriguez et al. (1997), applied current density values higher than 100 μA/cm^2, which corresponds to ten times the current density measured in highly corroding concrete structures, tend to be ineffective in reproducing the morphology of localized pitting corrosion because of its tendency to induce uniform corrosion patterns in the reinforcements.

3.4.1.2 Artificial Climate Environment (ACE) method

Unlike the IC method, current density is not applied in the ACE method, leading to a more realistic representation of the natural diffusion process of chloride ions towards the embedded steel reinforcements.

During the ACE method, the tested specimens are placed into an environmental chamber that mimics natural exposure conditions by controlling temperature, relative humidity, and oxygen concentration. Furthermore, spray nozzles are installed – typically at the upper and lower corners of the environmental chamber – to recreate wet-dry cycles through salt-water spraying, (Yuan et al., 2007). For the sake of clarity, Figure 3-7 shows a schematic representation of the environmental chamber commonly adopted for conducting the ACE method. The major advantage in the use of the ACE methodology over the IC method consists in a more accurate representation of the natural corrosion process, especially for localized pitting corrosion.

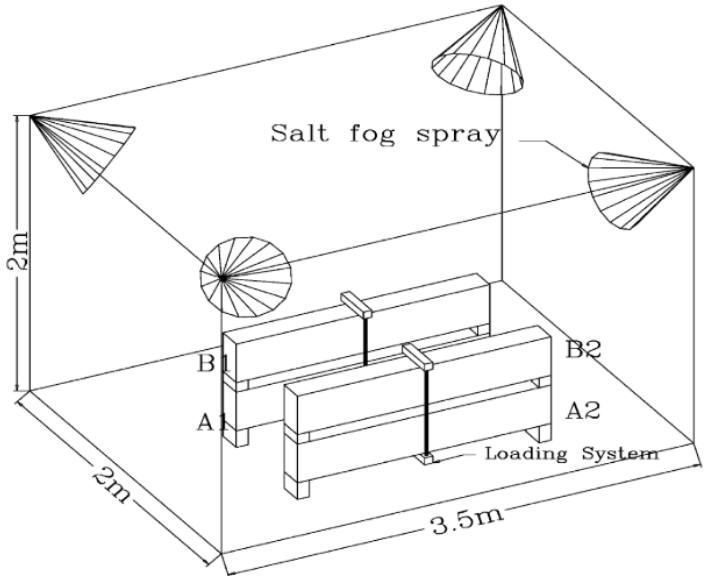

Figure 3-7 Schematic representation of ACE method, (I. Khan et al., 2014). Reproduced with permission from Springer Nature.

3.4.2 The residual response of PC beams

Despite numerous experimental works have been carried out on corroded RC beams, a scarcity of research has been devoted to providing information on the residual flexural and shear structural resistance of corroded PC beams.

Since the present *Thesis* deals with the evaluation of naturally corroded pre-tensioned PC beams, a general overview of the experimental tests conducted worldwide on corroded RC beams is reported in Appendix A.1. This latter lists the experimental campaigns conducted from 1990 to 2022, thereby extending the survey carried out by Soltani et al. (2019), to investigate the flexural and shear behaviour of corroded RC beams available in scientific literature. Referring to PC members, the State-of-the-Art proposes a first summary of the experimental research conducted on the residual flexural and shear capacity of post-tensioned PC beams, then the experimental campaigns conducted on pre-tensioned PC beams are analyzed in depth.

The decision to analyze the two prestressing techniques separately is based on (i) the different corrosion activation phenomena, (ii) the different resistant mechanisms of the two systems involved to respond to corrosion, and (iii) the different adopted anchorage systems, (Kioumarsi et al., 2021). On the one hand, corrosion in pre-tensioned beams causes the resistance and/or ductility decay due to the mutual reduction of reinforcement cross-section and bond strength, resulting in the subsequently reduction of the prestressing force. On the other hand, corrosion in post-tensioned beams can be marginally affected by bond reduction and may be influenced by grout injection defects.

Finally, challenges and open issues concerning the assessment of the residual load-carrying capacity of corroded PC beams is discussed.

3.4.2.1 Post-tensioned PC beams

To the best of the author's knowledge, 13 experimental works on post-tensioned PC beams have been conducted concerning the corrosion topic. Among them, only one research dealt with the analysis of two 34 year-old naturally corroded PC beams that during their service life were subjected to the severe coastal environment of the Kure-tsubo Bridge in Japan, (Tanaka Y. et al., 2001); whereas, the remaining studies investigated the corrosion effects by adopting the accelerated impressed current technique (IC) through the laboratory application of different current density values and exposure times.

As reported in Table 3-2, all of the experimental works tested scaled PC beams characterized by a rectangular cross-section with heigh, h, and width, b, ranging between 100 mm ÷ 400 mm and 200 mm ÷ 450 mm, respectively, except for the T-shape cross-section of the two naturally corroded beams retrieved from the Kure-tsubo Bridge. These latter had significant lengths, L, of 39.34 m and 21.15 m, respectively, while the beam length assumed in the other works varied between 1.6 ÷ 6.3 m.

In terms of reinforcements, seven-wires prestressing strands with an equivalent diameter of 15.2 mm were used in eight of the thirteen available experimental campaigns, while the 12.7 mm equivalent diameter was adopted in the experimental work by Youn & Kim (2006). In addition, the PC beams tested by Tanaka et al. (2001), Coronelli et al. (2009) and Minh et al. (2007) were reinforced with 5-mm, 8-mm and 9-mm prestressing wires, respectively. Top and bottom longitudinal reinforcements as well as stirrups with different spacing at bending and shear zones were generally used, except for the Serie-A beams in Minh et al. (2007) research, which were characterized by the sole presence of a linear 9-mm prestressing wire. The majority of laboratory tests investigated the residual load-carrying capacity of corroded PC beams by adopting a four-point bending loading scheme, except for the studies conducted by Recupero & Spinella (2019) and Jeon & Shim (Chi Ho Jeon & Shim, 2020), where the deteriorated behaviour of corroded beams was analyzed by adopting a three-point bending test set-up, Table 3-2. It is worth noting that these latter experimental activities were the only ones adopting multiple strands, placed in a singular prestressing cable.

Table 3-2 State-of-the-Art on post-tensioned corroded PC beams: geometrical properties and reinforcements.

Reference	N° of tested beams	Test set-up	Cross-section (*b*x*h*x*L* [cm])	Reinforcements
Tanaka et al. (2001)	2	FPBT	S3: 110(80) x 203 x 3934 (T-shape) S5: 60 x 138 x 2115 (I-shape)	Prestressing: S3: 9 x 44ϕ5 mm; S5: 4 x 42ϕ5 mm. Additional long. reinf.: yes. Stirrups: yes.
Youn & Kim (2006)	5	FPBT	15 x 30 x 400	Prestressing: 1 ϕ12.7 mm (7-wires). Additional long. reinf.: Top: 2ϕ13 mm Bottom: 2ϕ13 mm. Stirrups: ϕ5 / 300 mm.
Minh et al. (2007)	13	FPBT	10 x 20 x 200 10 x 30 x 160	Prestressing: Series-A = ϕ9.3 mm – Linear; Series-H = ϕ9.3 mm - Parabolic. Additional long. reinf.: Series-A = NO; Series-H = 4ϕ6 mm. Stirrups: Series-A = NO; Series-H: 7ϕ6 / 200 mm.
Coronelli et al. (2009)	4	FPBT	15 x 20 x 300	Prestressing: Single wire: ϕ8 mm. Additional long. reinf.: Top: 3ϕ6 mm Bottom: 2ϕ6 mm. Stirrups: ϕ6 mm.
Castel et al. (2012)	*Considers the experiment tests conducted by Young & Kim and added NLFEA			
Yanhong Zheng (2013)	9	FPBT	15 x 30 x 260	Prestressing: 1 ϕ15.2 mm (7-wires). Additional long. reinf.: Top: 2ϕ12 mm Bottom: 2ϕ16 mm and 2ϕ22 mm (L6). Stirrups: ϕ8 / 100 mm (shear zone) and ϕ8 / 200 mm (bending zone).
Zhang et al. (2017)	8	FPBT	15 x 22 x 200	Prestressing: 1 ϕ15.2 mm (7-wires). Additional long. reinf.: Top: 2ϕ12 mm Bottom: 2ϕ8 mm. Stirrups: ϕ8 / 90 mm.
Recupero and Spinella (2019)	12	TPBT	40 x 25 630	Prestressing: 4 ϕ15.2 mm (7-wires). Additional long. reinf.: Top: 2ϕ18 mm Bottom: 2ϕ18 mm. Stirrups: ϕ8 / 80 mm (shear zone) and ϕ8 / 100 mm (bending zone).
Jeon and Shim (2020)	5	TPBT	28 x 38 x 310	Prestressing: 3 ϕ15.2 mm (7-wires) - parabolic profile. Additional long. reinf.: Top: 2ϕ13 mm Bottom: 2ϕ10 mm . Stirrups: ϕ10 / 90 mm.
Wang L. et al. (2020)	8	FPBT	16 x 45 x 300	Prestressing: 1 ϕ15.2 mm (7-wires) - parabolic profile. Additional long. reinf.: Top: 2ϕ10 mm Bottom: 2ϕ25 mm. Stirrups: ϕ6 / 50 mm (support zone) and ϕ6 / 200 mm (bending zone).

Dai et al. (2021)	6	FPBT	20 x 35 x 400	Prestressing: 1 ϕ15.2 mm (7-wires) - straight profile. Additional long. reinf.: Top: 3ϕ10 mm Bottom: 3ϕ16 mm. Stirrups: ϕ8 with variable spacing.
Qian Qian Yu et al. (2022)	6	FPBT	15 x 30 x 260	Prestressing: 1 ϕ15.2 mm (7-wires) - straight profile. Additional long. reinf.: Top: 2ϕ12 mm Bottom: 2ϕ16 mm or 2ϕ22 mm. Stirrups: ϕ8 with variable spacing.
Yang et al. (2022)	4	FPBT	16 x 45 x 300	Prestressing: 1 ϕ15.2 mm (7-wires) - parabolic profile. Additional long. reinf.: Top: 2ϕ10 mm Bottom: 2ϕ25 mm. Stirrups: ϕ8 with variable spacing.

*N/A = not available data, *b* = width, *h* = height, *L* = Longitudinal length, ϕ = diameter [mm], FPBT = four-point bending test, and TPBT = three-point bending test.

Table 3-3 collects the main features of the available corroded post-tensioned PC beams regarding the corrosion process, the exposure environment, and the residual mechanical response of the analyzed PC beams in terms of observed failure mode. However, due to the great scattering in experimental results – caused by the combination of a limited number of experimental tests and the adoption of different geometrical beam dimensions, reinforcement ratios (number of strands, presence of stirrups with different spacing and additional longitudinal reinforcements), type of deterioration process (natural vs. accelerated methods), material properties, presence of sustained load, exposure environments and test set-up, it was not possible to clearly define and quantify the corrosion effects on the structural resistance of the tested beams. Nevertheless, common experimental evidence can be outlined as follows:

- *Structural performance reduction*: corrosion led to a noticeable reduction in flexural and shear load-carrying capacity in terms of ultimate load, deflection and ductility, favoured by the presence of grouting deficiencies, Youn & Kim (2006). As expected, PC beams with corroded strands near the support did not show meaningful flexural behavioural changes, conversely, corroded strands, placed at mid-span, showed relevant load-bearing capacity reduction, Jeon and Shim (2020). In the case of multiple strands, the load-carrying capacity decay was proportional to the number of strands or wires broken.
- *Crack pattern*: the number of cracks and the space between adjacent bending cracks increased with the increase in corrosion level, Yanhong Zheng (2013). Moreover, it was also discovered that the presence of external forces could aggravate cracks induced by reinforcements corrosion, Tanaka et al. (2001).

- *Stiffness reduction*: the initial stiffness prior to flexural cracking was slightly affected by corrosion; while the post-cracking stiffness was significantly reduced, Zhang et al. (2017).
- *Failure mode*: Low or absent corrosion levels induced a ductile (flexural) failure mode often characterized by concrete crushing and vertical flexural cracks in the proximity of loading points. This type of failure involved a progressive ductility reduction without relevant load-carrying capacity decay. High corrosion level, on the contrary, induced a brittle (shear) failure mode characterized by the development of diagonal cracks from the loading points toward the supports and the occurrence of strand rupture. This type of failure showed a significant decrease in both ductility and load-carrying capacity. Differently from homogeneous corrosion, localized corrosion led to non-uniform corrosion patterns along the overall beam length, resulting in asymmetrical crack patterns and failure modes. In addition, since stirrups were in an outermost position compared to prestressing reinforcements, they suffered earlier deterioration due to a premature exposure to aggressive agents. Thus, the shear resistance of corroded PC beams and their relative failure modes were found to be directly impacted by transverse reinforcement corrosion level.

Table 3-3 State-of-the-Art on post-tensioned corroded PC beams: corrosion process, exposure environment, and beams failure mode.

Reference	Corrosion process	Exposure environment	Failure mode
Tanaka et al. (2001)	NAT (34 years)	Severe coastal environment (Japan: Kure-tsubo Bridge)	S3: too corroded to sustain its self-weight (bending failure); S5: crushing of concrete
Youn & Kim (2006)	IC (- μA/cm^2)	*N/A	PC-1, PC-4, and C-1 Bending PC-2 and PC-3 bending + wire failures
Minh et al. (2007)	IC: Series-A: 0.7A Series-H: 0.57A	Chloride-induced corrosion	All in bending with concrete crushing
Coronelli et al. (2009)	IC (- μA/cm^2)	*N/A	All in bending, except for 1 beam in shear
Castel et al. (2012)	-	-	-
Yanhong Zheng (2013)	IC (200 μA/cm^2)	Chloride-induced corrosion	Corrosion ratio < 0.08: crushing of concrete in compression zone; Corrosion ratio > 0.08: rupture of corroded strands
Zhang et al. (2017)	IC (180 μA/cm^2 or 0.4A)	5% saline solution	The failure mode changes from ductile (concrete crushing) to brittle (wire rupture) with the increase of corrosion level (threshold cross-sectional loss equal to 27%)
Recupero and Spinella (2019)	IC (- μA/cm^2)	Chemical and acid solution	All beams are designed to achieve a ductile - bending failure: characterised by crushing of concrete
Jeon and Shim (2020)	IC (- μA/cm^2)	3.5% *NaCl* solution: the strands were corroded before casting	CB2-CB4 and RB5: concrete crushing; CB1: concrete crushing after rupture of six wires
Wang L. et al. (2020)	IC (270 μA/cm^2)	10% saline solution	For all corroded beams, the critical shear cracks occurred in the corroded shear span and extended from the supports to the loading points
Dai et al. (2021)	IC (2 μA/cm^2)	5% *NaCl* solution mass fraction of cement	S0 and R0: concrete crushing; S1: strand fractured in the end anchorage region but failed dure to concrete crushing; S2-S4: failed due to the main crack on the concrete surface exceeded the critical width
Qian Qian Yu (2022)	IC (200 μA/cm^2)	5% *NaCl* solution	L2 and L3: bending failure due to concrete crushing; L1, L4, L5 and L6: bending failure due to strand rupture
Yang et al. (2022)	IC (- μA/cm^2)	5% *NaCl* solution	All beams (B1, B2, B3 and B4) experienced shear-compression failure

3.4.2.2 Pre-tensioned PC beams

Similarly to corroded post-tensioned PC beams, Table 3-4 and Table 3-5 report the geometrical and reinforcement features of the pre-tensioned corroded PC beams available in scientific literature, by distinguishing between PC beams subjected to artificially accelerated corrosion processes or natural environment, respectively. In addition, Table 3-6 and Table 3-7 illustrate: (i) the corrosion process, (ii) the exposure environment, and (iii) the observed failure mode of each analyzed PC beam.

The database contains 16 papers; four of them analyzed full-scale corroded PC beams retrieved from dismissed bridges and exposed to natural environments for different periods of time, whereas the remaining twelve analyzed scaled laboratory specimens by adopting the IC technique.

Rectangular cross-sections with heigh, h, and width, b, ranging respectively between 100 mm ÷ 250 mm and 200 mm ÷ 450 mm were adopted, except for T-shape cross-sections tested in the experimental works conducted by El Menoufy and Soudki (2014), ElBatanouny et al. (2015), Rogers et al. (2012) and Pape and Melchers (2013). The length of the scaled specimens varied between 2.6 m ÷ 5.0 m, while Rogers et al. (2012) and Pape and Melchers (2013) tested the full-scale PC beams with an overall beam length equal to 18 m and 13 m, respectively. Although a variety of wires and prestressing diameters were used, as shown in Table 3-4, 7-wires prestressing strands with an equivalent diameter equal to 12.7 mm were widely adopted. It is worth noting that all experimental activities adopted multiple prestressing strands, except for the studies conducted by El Menoufy and Soudki (2014) and Dai et al. (2020), who investigated the effect of a single corroded strand having an equivalent diameter of 12.7 mm and 15.2 mm, respectively. Top and bottom longitudinal reinforcements, as well as stirrups – sometimes having different spacing at shear and bending zones – were also present. Finally, it is emphasized that all experimental research were carried out by using four-point bending tests to evaluate the residual flexural and shear structural resistance of corroded pre-tensioned PC beams, except for the three-point bending test set-up used by Dasar et al. (2016).

Table 3-4 State-of-the-Art on artificially corroded pre-tensioned PC beams: geometrical properties and reinforcements.

Reference	N° of beams	Test set-up	Cross-section (*bxhxL* [cm])	Reinforcements
Rinaldi et al. (2010)	9	FPBT	20 x 30 x 300	Prestressing: Top: 1 ϕ12 mm (7-wires) Bottom: 2 ϕ12 mm (7-wires). Additional long. reinf.: Top: 2ϕ10 mm Bottom: 2ϕ10 mm. Stirrups: ϕ8 / 200 mm.
Li et al. (2010) - in Chianese, from (Kioumarsi et al., 2021)	5	FPBT	15 x 20 x 260	Prestressing: *N/A. Additional long. reinf.: *N/A. Stirrups: *N/A.
El Menoufy and Soudki (2014)	7 (2 with CFRP)	FPBT	40(10) x 30 x 360 (T-shape)	Prestressing: 1 ϕ12.7 mm (7-wires). Additional long. reinf.: Top: 5ϕ8 mm. Stirrups: ϕ10 / 75 mm (shear zone) and none (bending zone).
ElBatanouny et al. (2015)	8	FPBT	61(15.2) x 38.1 x 498 (T-shape)	Prestressing: 2 ϕ13 mm (7-wires). Long. reinf.: Top Flange = 4ϕ10 mm. Stirrups: ϕ10 / 240 mm (U-shape).
Zhang et al. (2016)	13	FPBT	15 x 30 x 270	Prestressing: 2 wires ϕ7 mm. Additional long. reinf.: Top: 2ϕ10 mm Bottom: 2ϕ12,14,16 mm. Stirrups: ϕ10 / 100 mm (shear zone) and ϕ10 / 200 mm (bending zone).
Liu and Fan (2019)	10	FPBT	15 x 25 x 220	Prestressing: 2 ϕ12.7 mm (7-wires). Additional long. reinf.: Top: 2ϕ14 mm Bottom: 2ϕ14 mm. Stirrups: 7ϕ6 / 100 mm.
Liu et al. (2019), from (Kioumarsi et al., 2021)	5	*N/A	15 x 30 x 270	Prestressing: *N/A. Additional long. reinf.: *N/A. Stirrups: *N/A.
Yang et al. (2020)	6	FPBT	25 x 45 x 360	Prestressing: 3 ϕ12.7 mm (7-wires). Additional long. reinf.: Top: 3ϕ18 mm Bottom: 2ϕ10 mm. Stirrups: ϕ8 / 50 mm (shear zone) and ϕ8 / 100 mm (bending zone).
Liu et al. (2020), from (Kioumarsi et al., 2021)	5	FPBT	15 x 25 x 220	Prestressing: *N/A. Additional long. reinf.: *N/A. Stirrups: *N/A.
Benenato et al. (2020)	2	FPBT	20 x 30 x 300	Prestressing: Top: 1 ϕ12 mm (7-wires) Bottom: 2 ϕ12 mm (7-wires). Additional long. reinf.: Top: 2ϕ10 mm Bottom: 2ϕ10 mm. Stirrups: ϕ8 / 100 mm (shear zone) and ϕ8 / 200 mm (bending zone).
Dai et al. (2020)	8	FPBT	13 x 15 x 200	Prestressing: 1 ϕ15.2 mm (7-wires). Additional long. reinf.: Top: 2ϕ8 mm Bottom: 2ϕ6 mm. Stirrups: ϕ6 / 100 mm.

Liu et al. (2023)	13	FPBT	15 x 30 x 270	Prestressing: 2 ϕ7 mm (prestressing wires). Additional long. reinf.: Top: 2ϕ10 mm Bottom: 2ϕ12, 14 or 16 mm. Stirrups: ϕ8 / 100 mm (shear zone) and ϕ8 / 200 mm (bending zone).

*N/A = not available data, *b* = width, *h* = height, *L* = Longitudinal length, ϕ = diameter [mm], FPBT = four-point bending test, and TPBT = three-point bending test.

Table 3-5 State-of-the-Art on naturally corroded pre-tensioned PC beams: geometrical properties and reinforcements.

Reference	**N° of beams**	**Test set-up**	**Cross-section (*b*x*h*x*L* [cm])**	**Reinforcements**
Mircea et al. (1994)	38	FPBT	15 x 15 x 320 12 x 18 x 320	Prestressing: 3 wires ϕ5 mm, 2 x 7ϕ2.5 mm, 2 x 7ϕ3 mm. Additional long. reinf.: Top: 2ϕ8 mm. Stirrups: yes, but not specified.
Rogers et al. (2012)	19	FPBT	82.6(25.4) x 68.6 x 1800 (T-shape)	Prestressing: 12 ϕ12.7 mm (7-wires). Additional long. reinf.: 9ϕ12.7 mm (7-wires), Top reinf: 2ϕ15.9 mm. Stirrups: ϕ9.5 / 380 mm.
Pape and Melchers (2013)	3	FPBT	61.3(22.9) x 68.7 x 1300 (T-shape)	Prestressing: 2 x 18 x ϕ5 mm wire. Additional long. reinf.: Top: 4ϕ6 mm Bottom: 2ϕ9 mm. Stirrups: ϕ6 / 200 mm; Top: C-reinforcement ϕ6 / 100 mm.
Dasar et al. (2016)	2	TPBT	15 x 30 x 240	Prestressing: round wires of ϕ2-2.9 mm. Additional long. reinf.: *N/A. Stirrups: ϕ10 / 100 mm.

*N/A = not available data, *b* = width, *h* = height, *L* = Longitudinal length, ϕ = diameter [mm], FPBT = four-point bending test, and TPBT = three-point bending test.

Table 3-6 State-of-the-Art on artificially corroded pre-tensioned PC beams: corrosion process, exposure environment, and beams failure mode.

Reference	Corrosion process	Exposure environment	Failure mode
Rinaldi et al. (2010)	IC, only bottom strands 0.4A	Chloride-induced corrosion	Bending due to concrete crushing and shear with wires rupture
Li et al. (2010) - in Chianese, from (Kioumarsi et al., 2021)	IC (- μA/cm^2)	3% *NaCl* into the mass fraction of cement	Concrete crushing and rupture of strands
El Menoufy and Soudki (2014)	IC (2 μA/cm^2)	Salt-bearing concrete with 2.1% chloride concentration by mass of cement	All beams characterised by rupture of the strands
ElBatanouny et al. (2015)	IC (- μA/cm^2)	*NaCl* solution	All the specimens failed for: (a) strand rupture, or (b) excessive residual deflection; C3-04 beam failed due to concrete spalling
Zhang et al. (2016)	IC (100 μA/cm^2)	5% *NaCl* solution	9 beams failed in the constant moment region at the location of the main crack, except one
Liu and Fan (2019)	IC (- μA/cm^2)	De-icing salt solution for 120 days, $CaCl_2$ and $MgCl_2$ in a concentration of 5%	Changing in failure mode from bending to shear
Liu et al. (2019), from (Kioumarsi et al., 2021)	IC (- μA/cm^2)	*N/A	Changing in failure mode from bending to shear
Yang et al. (2020)	IC (150 μA/cm^2)	Wet-dry cycles: 4 days wet by means of a sponge soaked in 5% *NaCl* + 3 days dry	The failure of corroded beams showed unexpected brittle characteristics
Liu et al. (2020), from (Kioumarsi et al., 2021)	IC (- μA/cm^2)	*N/A	Bending
Benenato et al. (2020)	IC (350 μA/cm^2)	3% *NaCl* solution	Un-corroded beam failed under the combination of concrete crushing and buckling of the compressed reinforcement; The corroded one collapsed due to slight concrete crushing and wires rupture
Dai et al. (2020)	IC, 0.1A	5% *NaCl* solution	Bending induced by concrete crushing in the compression zone
Liu et al. (2023)	IC (100 μA/cm^2)	5% *NaCl* solution	All beams failed due to fatigue fracture of corroded prestressing wires and/or rebars

Table 3-7 State-of-the-Art on naturally corroded pre-tensioned PC beams: corrosion process, exposure environment, and beams failure.

Reference	Corrosion process	Exposure environment	Failure mode
Mircea et al. (1994)	NAT (10-12 years)	Natural urban; Natural marine; Chloride and nitrogen industrial; laboratory conditions.	Bending
Rogers et al. (2012)	NAT (42 years)	Chloride: regular presence of wind-blow salt spry (Tiwai Point Bridge, New Zealand)	Some beams in bending, others showed a pure web shear crack followed by concrete crushing.
Pape and Melchers (2013)	NAT (45 years)	Aggressive marine environment (Sorell Causeway Bridge, Australia)	Beam A: bending; Beam B: shear (rupture of wires); Beam C: shear (rupture of wires).
Dasar et al. (2016)	NAT (35 years)	Marine environment 20 years + 15 years at *PARI* Institute	Bending

A total of 153 beams were analyzed. Referring to the 16 scientific papers reviewed, 56% studied the corrosion influences on the flexural structural capacity of pre-tensioned PC beams, 25% analysed the residual shear structural capacity, whereas the remaining 19% investigated the fatigue capacity, as shown graphically in Figure 3-8.

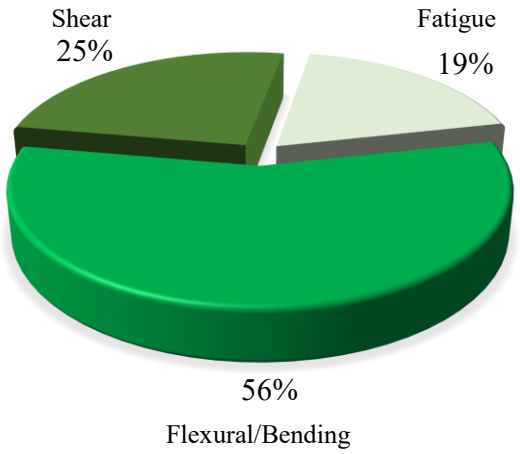

Figure 3-8 Analysis of the mechanical behaviours investigated through experimental campaigns.

The 75% of experimental tests were performed by adopting the impressed current (IC) method – 12 experimental programs –, whereas the remaining 25% conducted experimental programs on PC specimens coming from natural environments – 4 experimental programs. Indeed, only the experimental research carried out by Mircea et al. (1994), Rogers et al. (2012),

Pape and Melchers (2013) and Dasar et al. (2016) estimated the residual load-bearing capacity of several naturally corroded PC beams. As shown in Figure 3-9, 16.67% of the experimental campaigns – carried out through the application of the IC method – adopted current density, I_{corr}, values ranging between 100 μA/cm^2 and 400 μA/cm^2, whereas 25% used I_{corr} values lower than 100 μA/cm^2, as suggested by Rodriguez et al. (1997) and Alonso et al. (1998), who set this current density threshold value as the critical condition to be fulfilled to avoid rapid and undesirable corrosion effects. Unfortunately, the remaining 58.33% of the available experimental research did not provide the used I_{corr} value, except for Rinaldi et al. (2010) and Dai et al. (2020), who performed the artificially accelerated process by imposing a constant amperage of 0.4A and 0.1A, respectively.

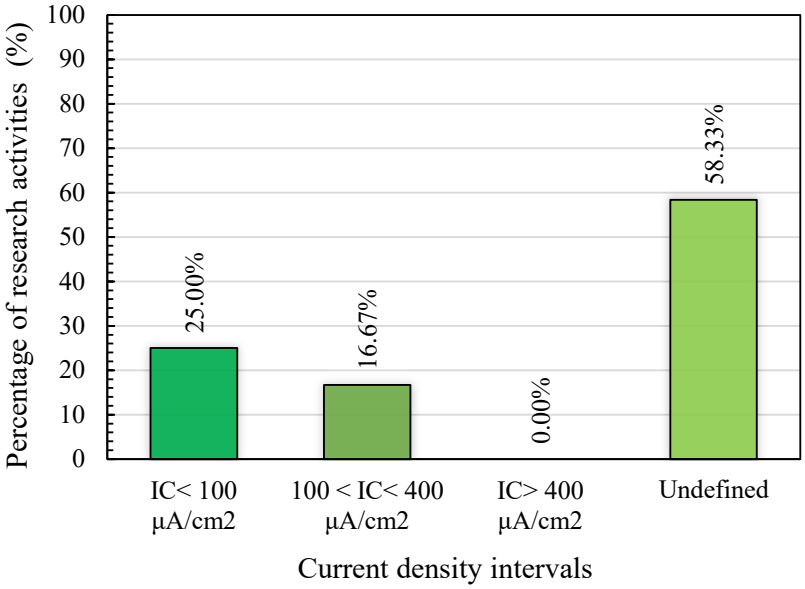

Figure 3-9 Analysis of the current density ranges in the case of IC method adoption.

In general terms, the experimental activities conducted on naturally corroded PC beams tend to quantify corrosion damage of prestressing reinforcement through the cross-sectional loss measurement, while the studies carried out on artificially corroded PC beams commonly measured the reinforcement mass loss by performing the gravimetrical method. In detail, Table 3-8 reports the mass loss range and the maximum cross-sectional loss measured during the experimental activities for the investigated experimental programs in the case of artificially accelerated and naturally corroded specimens, respectively.

Table 3-8 Corrosion amount measured during the experimental campaigns on corroded PC specimens: (left) artificially accelerated, and (right) from natural environment.

Reference	Corrosion amount: Mass loss
Rinaldi et al. (2010)	7%, 14%, and 20%
Li et al. (2010) - in Chianese, from (Kioumarsi et al., 2021)	0.0-2.87%
El Menoufy and Soudki (2014)	2.5%, 5%, 10%
ElBatanouny et al. (2015)	0.0-12.80%
Zhang et al. (2016)	0.013-0.056
Liu and Fan (2019)	*N/A
Liu et al. (2019), from (Kioumarsi et al., 2021)	0.0-4.00%
Yang et al. (2020)	0.0-30.07%
Liu et al. (2020), from (Kioumarsi et al., 2021)	0.0-10.20%
Benenato et al. (2020)	7.00%
Dai et al. (2020)	0.0-14.69%
Liu et al. (2023)	Variable: longitudinally determined via 3D scanning analysis

Reference	Corrosion amount: Cross-section loss
Mircea et al. (1994)	*N/A
Rogers et al. (2012)	Variable with a maximum value up to 60%
Pape and Melchers (2013)	Beam B: up to 57% Beam C: up to 64%
Dasar et al. (2016)	*N/A

Based on the outcomes of pre-tensioned corroded PC beams, the following experimental evidence – in addition to those previously mentioned in paragraph 3.4.2.1 – can be outlined:

- *Structural performance reduction*: several studies found out that with the increase in corrosion level (expressed in terms of mass loss or cross-sectional loss) the overall behaviour of corroded pre-tensioned PC beams is strongly affected in terms of both ultimate load-carrying capacity and ductility reduction. For the sake of clarity, examples of typical bending moment – mid-span displacement response for un-corroded and corroded pre-tensioned PC beams are reported in Figure 3-10, by reproducing the experimental test results obtained by Rinaldi et al. (2010). The outcomes show the significant flexural capacity reduction of corroded PC beams in comparison with the un-corroded one. Specifically, for a mass loss of approximately 20%, a flexural decay of about 65% is observed. Moreover, increasing the corrosion level, a severe ductility reduction is also pointed out.

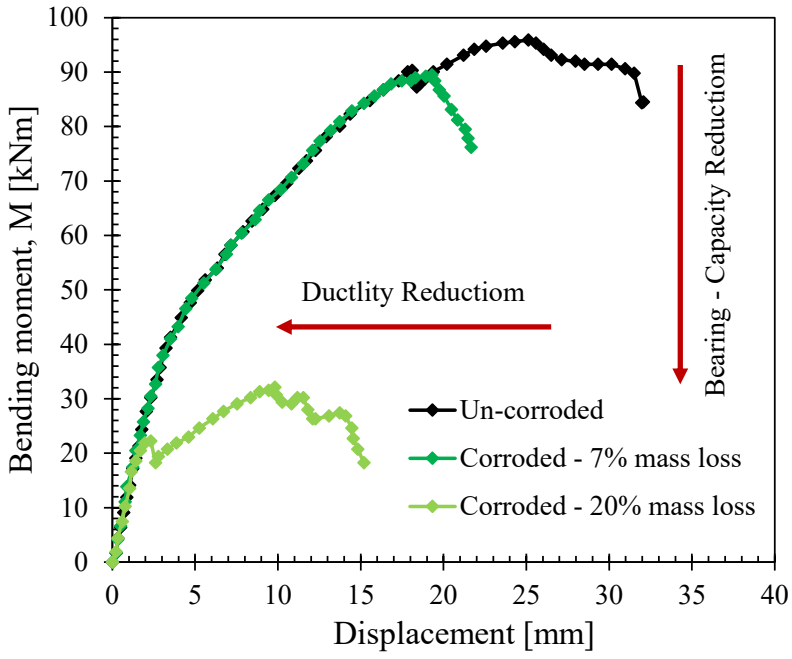

Figure 3-10 Comparative example between corroded and un-corroded pre-tensioned PC beams, adapted from Rinaldi et al. (2010).

In general, studies additionally showed the decrease in ultimate beam deflection and the increase in the crack width for increasing corrosion level. Finally, the residual structural resistance of corroded PC beams is strongly

impacted by the bond decay at the steel-concrete interface. To this end, Dai et al. (2020) validated the bond decay model proposed by Wang et al. (2016). According to this model, bond strength results practically unaffected up to a mass loss percentage of 6.6%; thereafter, once the critical threshold is exceeded, bond strength decreases until it reaches the total de-bonding of prestressing reinforcements for a mass loss percentage of 34%;

- *Crack pattern*: Dasar et al. (2016) pointed out that pre-cracking plays a key role in the corrosion process of prestressing reinforcements and in the consequent residual structural performance of corroded PC beams. Indeed, pre-cracking leads to a tangible decrease in beams load-carrying capacity by allowing the early ingress of external aggressive agents during the structural element service life.
- *Failure mode*: as with post-tensioned PC beams, the increase in corrosion level, influences the failure mode of pre-tensioned PC beams, which turns from ductile to brittle. In detail, two distinct transitional behaviours of corroded PC beams can be experimentally pointed out: (i) a ductile-brittle transition associated to the reduction of the flexural non-linear behaviour of a corroded beam for increasing corrosion level, or (ii) a ductile-brittle transition associated to the change in failure mode from bending to shear. According to Rinaldi et al. (2010) and Benenato et al. (2020), the first transition occurs when the mass loss percentage of reinforcements reaches 7%. When this threshold is reached, the prestressing reinforcement behaviour changes from ductile – characterized by strand yielding – to brittle – characterized by strand rupture. Additionally, by analyzing localized corrosion, it was demonstrated that the first wire fracture takes place at the minimum cross-section where corrosion pits have formed, Liu et al. (2023). As a result, it may happen that, as the corrosion level increases, PC beams fail at the minimum cross-section of one of the corroded prestressing strands, which may not be subjected to the maximum action.
- *Effect of the level of prestressed load*: the mass loss of prestressing strands results accelerated by the applied prestress level. Indeed, as observed by Dai et al. (2020), by gradually increasing the strands prestress level from 0 to 75%, the measured average mass loss value tends to increase, reaching an increment of 37% for a prestress level of 75%.

- *Effect of sustained load*: According to Yang et al. (2020), the combination of corrosion and sustained loads induced higher prestressing force losses. In the case of severely corroded strands, a decrease in prestressing force, resulted in wider transverse cracks. Additionally, the presence of sustained loads increased the risk of a pronounced localized corrosion, which directly favoured the mechanical properties decay of prestressing strands, inducing a significant reduction in the residual structural performance of corroded PC beams.
- *Fatigue loading*: the combination of corrosion and fatigue loading induced a significant reduction in the ultimate deflection capacity and the initial stiffness of severely corroded PC beams, Zhang et al. (2016) and Liu et al. (2019). Moreover, a shortening of the post-yielding branch of the beam residual structural response was also observed. In detail, as demonstrated by Liu et al. (2023), all investigated PC beams – tested by performing high-cycle fatigue testing – failed due to fatigue fracture of corroded rebars and/or prestressing wires at the minimum cross sections where a severe corrosion pit was documented.

3.4.2.3 Challenges and open issues

A general overview of the experimental campaigns on corroded RC and PC beams available in literature has been provided. Following a comprehensive State-of-the-Art review concerning naturally and artificially corroded RC beams reported in Appendix A.1, two comprehensive databases on post-tensioned and pre-tensioned corroded PC beams were defined to analyze the main issues affecting the residual structural response of deteriorated PC beams.

Although useful findings were outlined, several drawbacks associated to corrosion issue need to be further discussed and studied:

I. The corrosion phenomenon of prestressing reinforcement must be thoroughly investigated. In comparison to the massive amount of experimental activities carried out on corroded RC beams (55 papers), only a limited number of studies have been conducted on corroded PC beams (13 papers on post-tensioned beams and 16 papers on pre-tensioned beams) to evaluate their residual flexural and shear response. In this framework, only few papers provided experimental data on the residual shear capacity of corroded PC beams by testing artificially corroded specimens commonly reinforced with stirrups. However, relevant structures such as power plants or buildings built prior to the implementation of new seismic recommendations might have been constructed without the presence of stirrups. Special research efforts should therefore be devoted to filling the gap in experimental works dealing with the analysis of the residual shear capacity of naturally corroded PC beams without transverse reinforcement.

II. Because its faster execution, the artificially accelerated impressed current technique (IC method) was implemented in the majority of experimental research conducted on the corrosion of PC beams. Although the experimental period was significantly reduced, the great discrepancy between natural corrosion and electrochemically-induced corrosion outcomes was found to be a critical aspect in the proper evaluation and quantification of corrosion effects. Therefore, regardless of the longer testing time, more experimental campaigns should be planned to analyze specimens retrieved from buildings or bridges subjected to natural environments. To date, only 5 works (1 for post-tensioned PC beams and 4 for pre-tensioned PC beams) studied the residual structural performance of naturally corroded PC beams from marine, coastal or nitrogen environments.

III. The limited number of experimental tests on corroded PC beams combined with the specimen's variability in geometrical dimensions, reinforcement ratios, type of deterioration process, material properties, effect of sustained load, exposure environments and test set-up, led to a large dispersion of experimental outcomes, making the comparison of obtained results rather challenging. Moreover, the tested specimens have been usually scaled with a thinner concrete cover. As a result, non-negligible size effects could influence the obtained results: (i) by inducing shorter initiation period – by reducing the needed time of aggressive agents to reach the reinforcements – or (ii) by influencing the corrosion propagation along the overall beam length – which means smaller specimens and therefore a more homogeneous corrosion level along the beams length.

IV. Zhu (2014) highlighted the urgent need to conduct experimental programs that study the corrosion topic from the corroded specimen's retrieval (natural corrosion) or casting (artificial corrosion) to the proposal of simplified models useful in daily engineering practice. These programs should include a preliminary analysis of the crack pattern and an evaluation of specimens' residual structural response. Moreover, a follow-up phase suitable for quantifying the reinforcement corrosion level and a data post-processing phase aimed at proposing measurement-based correlations describing the trends of the main corrosion parameters as a function of the change in the corrosion level, must be considered. Currently, the majority of experimental activities investigate these corrosion issues separately, resulting in conclusions that frequently differ or disagree.

In light of the deficiencies identified above, the present *Thesis* examines an experimental campaign involving the assessment of naturally corroded pre-tensioned PC beams subjected to constant sea water wet-dry cycles over the course of their 10 years of service, showing signs of chloride-induced corrosion, Figure 3-11.

Figure 3-11 Highlights on the available 10 years old PC beams.

3.5 Mechanical behaviour of corroded prestressing reinforcements

Despite the availability in the literature of several works on tensile testing and the subsequent prediction of corroded rebars stress-strain relationships, only a limited number of studies on the same topics have been conducted with regard to corroded prestressing reinforcements. To this end, Appendix A.2 reports a general overview of the experimental tensile tests and analytical models for corroded ordinary reinforcements. The current State-of-the-Art intends to highlight all scientific works undertaken in the prediction of the residual stress-strain response of corroded rebars by presenting a comprehensive list of the research realized from 2000 to 2022, thus extending the survey conducted by Vanama & Ramakrishnan (2020). Conversely, the following paragraphs propose a detailed State-of-the-Art of the several pit type morphology configurations available in scientific literature and the most accredited constitutive laws for the prediction of the residual mechanical properties of corroded prestressing strands.

In the present section, two of the main effects induced by corrosion are investigated:

- The reinforcement cross-section reduction;
- The mechanical properties reduction.

Indeed, the main mechanical properties affected by corrosion are the ultimate strength and the ultimate strain of reinforcements. In this latter framework, two main approaches can be defined:

(i) The *equivalent bar* approach, Figure 3-12(a): that reproduces the prestressing strand behaviour as a reinforcement rebar, as proposed by Wang et al. (2020) and Zhang X. et al. (2017);

(ii) The *equivalent spring* approach, Figure 3-12(b): that reproduces the behaviour of the overall strand by summing the individual contributions of each wire, which are considered as springs working in parallel with each other, as proposed by Lu et al. (2016), Zhang et al. (2019), and Jeon et al. (2019).

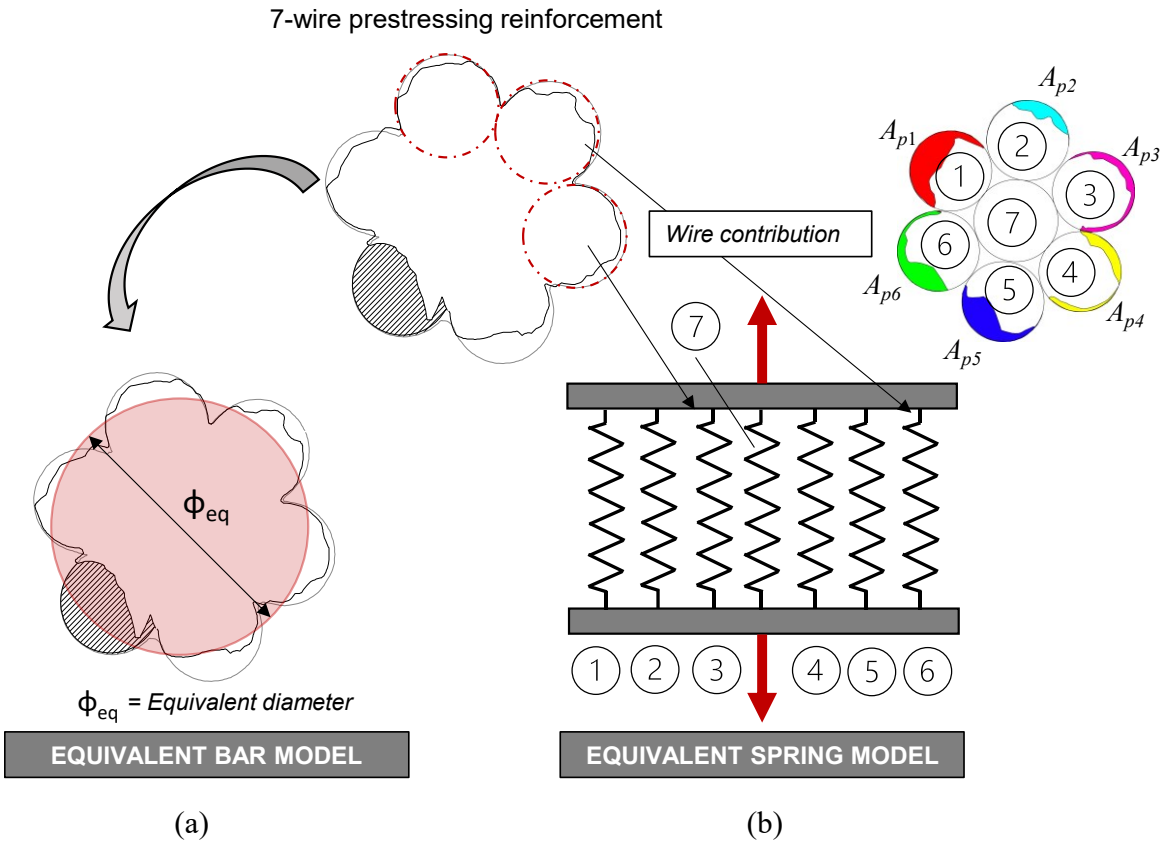

Figure 3-12 Approaches for the reproduction of the mechanical behaviour of prestressing strands: (a) equivalent bar model and (b) equivalent spring model.

3.5.1 Quantification of corrosion damage

Corrosion was shown to be closely related to the nature of the surrounding environment in which the structural element is placed. Although the corrosion process of a corroded rebar and a prestressing strand generally differs, some preliminary considerations concerning the quantification of corrosion damage for prestressing strands can be extrapolated from the analysis of ordinary rebars. To this end, the single prestressing wire composing the strand should be treated as a singular ordinary rebar.

According to Andrade (2021), reinforcement corrosion can be initially simply classified as either homogeneous or localized corrosion, as shown in Figure 3-13. Homogeneous corrosion can be further divided into symmetric or asymmetric deterioration depending on the direction of the aggressive front. In general terms, homogeneous corrosion begins with an asymmetric morphology since it is easier for aggressive agents to reach the reinforcement in a zone closer to the outer beam side, characterized by a thinner concrete cover. Once the aggressive agent has affected the entire reinforcement perimeter, the morphology

configuration may change to symmetric. However, it is worth noting that the ideal symmetric corrosion cannot be achieved since the reinforcement side that corrodes first, usually shows a higher deterioration if compared to the back reinforcement side. Conversely, localized corrosion can be further divided into local or pitting corrosion based on the longitudinal and transversal pit dimensions. Regardless of the type of morphology corrosion, the failure mode of the corroded reinforcement can be ductile or brittle depending on the corrosion level – expressed in terms of residual diameter –, exposure condition, aggressivity of external agents and load regime (static or cyclic).

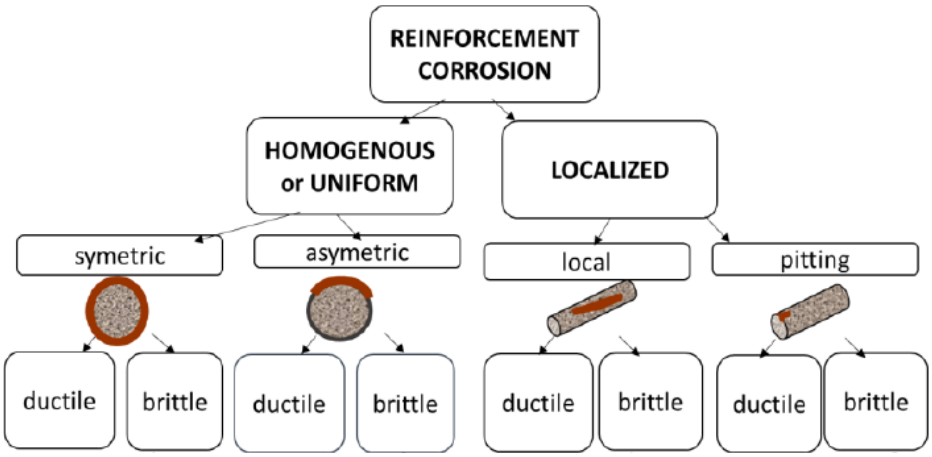

Figure 3-13 Classification of corrosion type in the case of corroded reinforcements, adapted from (Andrade, 2021). Reproduced from the "Proceedings of CACRCS DAYS 2021: Capacity Assessment of Corroded Reinforced Concrete Structures" with permission from the International Federation for Structural Concrete (*fib*).

Two are the main parameters that are generally used in scientific literature to predict the residual mechanical response of corroded prestressing strands:

I. The mass loss, η, which is measured by adopting the gravimetrical method described by the ASTM G1-03 standard (2017) and calculated according to the expression reported in Eq. 3-2:

$$\eta = \frac{m_0 - m_{corr}}{m_0} \qquad 3\text{-}2$$

where m_0 and m_{corr} are the weight of the un-corroded and corroded reinforcement samples, respectively.

II. The cross-sectional loss, μ, which is evaluated sectionally through Eq. 3-3:

$$\mu = \frac{A_0 - A_{\min}}{A_0} = 1 - \frac{A_{\min}}{A_0} = \frac{A_p}{A_0} \qquad 3\text{-}3$$

where A_0 is the un-corroded area of the prestressing strand, and A_p and A_{min} are the area loss and the residual area due to pitting, respectively.

From a general perspective, mass loss measurement better reflects the average corrosion level of the reinforcement along its entire length. Therefore, η can be considered as a reliable parameter for the estimation of homogeneous corrosion. The cross-sectional loss measurement, on the contrary, better reproduces the effects of localized corrosion, such as pitting corrosion. Additionally, several authors pointed out that mass loss measurement might be very challenging to perform during in-situ inspections, because it requires the weighing of the corroded reinforcement which needs to be extracted from the structural member, (Chi Ho Jeon et al., 2019; X. Liu et al., 2017; L. Wang, Li, et al., 2020); conversely, the assessment of the minimum residual cross-section can be measured using non-destructive techniques, such as radiography, X-ray scans, endoscopic inspections, or magnetic fields methods, (C. H. Yoo et al., 2020).

The sectional radius or diameter loss of corroded prestressing wires is assumed to be the key factor in the mass loss and cross-sectional loss evaluation. Since several corrosion scenarios can be identified, different pit type morphology configurations have been defined in the last few years for estimating the cross-sectional loss, especially with regards to localized pitting corrosion.

First, Val & Melchers (2007; 1997) defined a hemispherical pit type morphology configuration, as shown in Figure 3-14, where the area loss caused by pitting, A_{p1}, is calculated on the basis of geometrical relationships, as expressed in Eq. 3-4:

$$A_{p1} = 2r^2\left(\vartheta_1 - 2\sin\vartheta_1\cos\vartheta_1\right) \qquad \vartheta_1 = arc\cos\left(1-\frac{P_x}{2r}\right) \qquad 3\text{-}4$$

where P_x is the maximum pit depth measured and r is the un-corroded reinforcement radius.

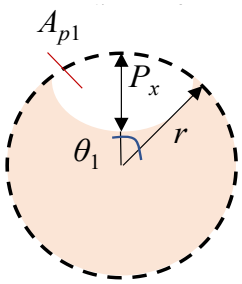

Figure 3-14 Hemispherical pit type morphology configuration for localized pitting corrosion.

Second, Hartt and Lee (2016) introduced a planar pit morphology configuration, as reported in Figure 3-15, where the area loss due to pitting, A_{p3}, is calculated according to Eq. 3-5:

$$A_{p3} = r^2\left(\vartheta_3 - \sin\vartheta_3\cos\vartheta_3\right) \qquad \vartheta_3 = arc\cos\left(1-\frac{P_x}{r}\right) \qquad 3\text{-}5$$

where P_x is the maximum pit depth measured and r is un-corroded reinforcement radius.

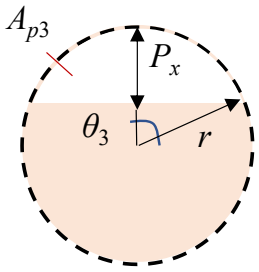

Figure 3-15 Planar pit type morphology configuration for localized pitting corrosion.

Finally, Jeon et al. (2019) adopted three different pit type morphology configurations. In addition to the hemispherical shape, introduced by Val & Melchers (2007; 1997), and the planar shape, defined by Hartt and Lee (2016), the authors considered an intermediate pit type morphology configuration, denoted as half-moon shape. The third morphology is reported in Figure 3-16 and the expression for the calculation of the related area loss, A_{p2}, is given by Eq. 3-6:

$$A_{p2} = r^2\left(2\vartheta_2 - \pi - 2\sin\vartheta_2\cos\vartheta_2\right) \qquad \vartheta_2 = arc\cos\left(-\frac{P_x}{2r}\right) \qquad 3\text{-}6$$

where P_x is the maximum pit depth measured and r is the usual un-corroded reinforcement radius.

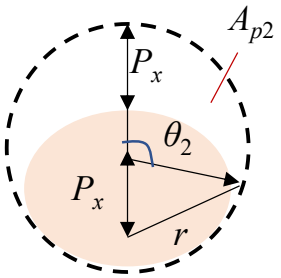

Figure 3-16 Half-moon pit type morphology configuration for localized pitting corrosion.

For the sake of completeness, it is worth noting that additional pit type morphology configurations were defined by Wang et al. (2020) and Yoo et al. (2018; 2020). As shown in Figure 3-17(a), Wang and co-authors defined three pit shapes, named spheroidal, saddle and pyramidal, based on a geometric morphology analysis of one-hundred nineteen pits measured from nineteen strands artificially corroded through the ACE method. According to the authors, the formation of these different configurations was related to the presence of many micro-crystal clusters of pearlitic grain characterized by different electrochemical properties in prestressing strands. However, no mathematical formulations were provided for the geometrical calculation of the three shapes, making it difficult to apply any of these configurations for pitting spatial variability analysis and pit classification.

Yoo and co-authors introduced additional formulations for the estimation of the cross-sectional loss as a function of the corrosion perimeter, p, as shown in Figure 3-17(b), to overcome the issue related to the maximum penetration depth measurement of corroded strands along a large area during in-situ inspections of a bridge in service. This latter can be measured by means of an endoscope, or borescope, inserted through a small hole created ad hoc in the duct. A correlation between maximum penetration depth and corrosion perimeter was then established, as expressed by Eq. 3-7. Furthermore, the area loss caused by pitting, A_{p4}, was calculated through geometrical relationships in accordance with Eqs. 3-8 – 3-11.

$$\frac{p}{2\pi r} = \left(\frac{P_x}{r} \right)^{0.49} \tag{3-7}$$

$$\vartheta_a = \frac{p}{2r} = \pi \left(\frac{P_x}{r} \right)^{0.49} \tag{3-8}$$

$$\vartheta_b = arc\cos\left(1 + \frac{P_x^{\,2} - 2rP_x}{2s\left(s - \left(r - P_x\right)\right)} \right) \tag{3-9}$$

$$s = r + \frac{P_x^{\,2} + 2rP_x\cos\vartheta_a}{2r\left(1 - \cos\vartheta_a\right) - 2P_x} \tag{3-10}$$

$$A_{p4} = r^2\left(\vartheta_a - \sin\vartheta_a\cos\vartheta_a\right) - s^2\left(\vartheta_b - \sin\vartheta_b\cos\vartheta_b\right) \quad 0 \le \vartheta_a \le \pi \tag{3-11}$$

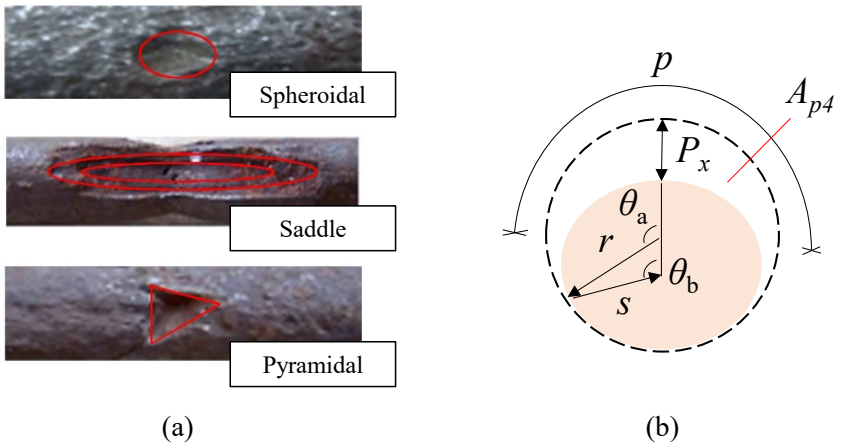

Figure 3-17 Additional pit type morphology configurations introduced by: (a) Wang et al. (2020) and (b) Yoo et al. (2018; 2020).

In addition, CONTECVET manual (2001) proposed two different pit type morphology configuration in the case of homogeneous and pitting corrosion, as reported in Figure 3-18. These circular shapes can be geometrically defined once the diameter loss is estimated through the expression reported in Eq. 3-12:

$$\phi_t = \phi_0 \left(1 - P_x\right) = \phi_0 \left(1 - V_{corr} t_p \alpha\right) \qquad 3\text{-}12$$

where ϕ_t and ϕ_0 are the corroded and the un-corroded diameters, P_x is the radius loss, which results equal to P_{corr} for homogeneous corrosion and equal to P_{pit} for localised pitting corrosion, V_{corr} is the corrosion rate, t_p is the propagation time after depassivation of the reinforcement, and α is the pitting factor. The biggest difference consists in the definition of the pitting factor α, which is recommended equal to 2 and 10 by the manual in the case of homogeneous and pitting corrosion, respectively.

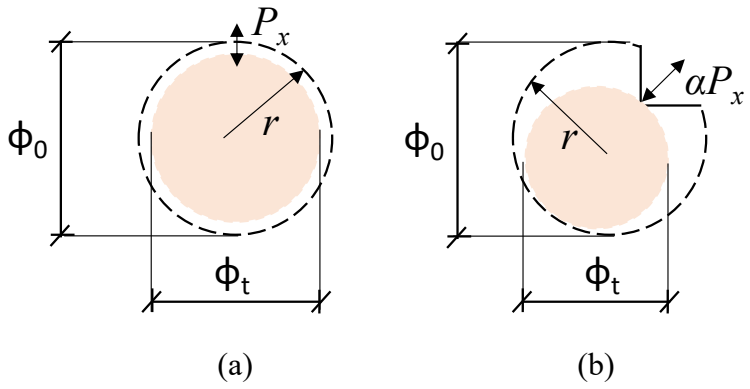

Figure 3-18 Morphology configuration: (a) homogeneous corrosion and (b) pitting corrosion, adapted from CONTECVET manual (2001).

3.5.2 Modelling of the tensile behaviour

To investigate the corrosion effects on the residual mechanical response of corroded strands, Table 3-9 outlines common features and differences through the comparison of various experimental programs and proposed stress-strain relationships.

All the available scientific research performed tensile tests on corroded prestressing strands with a diameter of 15.2 mm and subjected to different corrosion levels. The different corrosion levels were achieved following natural corrosion or throughout the IC and ACE artificial accelerated techniques. During the execution of the IC method, a current density value equal to 100 $\mu A/cm^2$ was applied to artificially reproduce the natural corrosion effects, whereas for the ACE method a salt fog with a 5% *NaCl* solution together with a constant temperature and relative humidity was adopted.

After the retrieval of samples from natural corroded members or the conduction of the artificial corrosion process, each experimental program performed tensile tests on one or more samples characterized by the absence of corrosion signs in order to establish the reference un-corroded mechanical properties. Furthermore, corroded collected specimens were also tensile tested, and their residual mechanical response was then evaluated. To this end, Figure 3-19 and Figure 3-20 report experimental tensile test results in terms of normalized ultimate strength, $f_{pu,corr}/f_{pu,0}$, and normalized ultimate strain, $\varepsilon_{pu,corr}/\varepsilon_{pu,0}$, of the available samples as a function of both strand mass loss and strand section-loss.

Referring to constitutive law proposal, the corrosion parameters usually adopted for the prediction of the residual mechanical response of corroded strands were (i) the maximum cross-sectional loss, μ_{max}, and (ii) the mass loss, η. Specifically, η values were measured by adopting the gravimetrical method described by ASTM G1-03 standard (2017), whereas μ_{max} values were experimentally evaluated through (i) 3D scanning techniques or (ii) CAD analysis. In the experimental campaign conducted by Jeon et al. (2019), the maximum cross-sectional loss was geometrically evaluated on the basis of the maximum penetration depth of the most corroded external wire, P_{max}, which was experimentally measured by means of a pit depth gauge instrument.

Table 3-9 State-of-the-Art on analytical models for the prediction of the residual mechanical response of corroded prestressing strand.

Constitutive law / Main features	Lu et al. (2016)	Zhang X. et al. (2017)	Zhang W. et al. (2019)	Jeon et al. (2019)	Wang et al. (2020)
Experimental Program					
Number of corroded samples, (un-corroded)	12 (2)	7 (3)	Tests on wires	13 (3)	18 (1)
Equivalent diameter of strands, (mm)	15.2	15.2	15.2	15.2	15.2
Type of corrosion	IC	ACE	IC	NAT (chloride)	ACE
Characteristics of artificial corrosion	100 μA/cm^2	Salt fog (5% salt solution)	100 μA/cm^2	-	By using a wet sponge
Maximum strand/wire cross-sectional loss, (%)	-	Strand: 27.5%	Wire: 31.4%	Wire: 20.3%	Strand: 27.5%
Maximum strand mass loss, (%)	Strand: 20.4%	-	-	-	-
Tensile test: test speed	0.2 kN/s (force control)	1 mm/min until failure first wire; 2 mm/min for the residual capacity	*N/A	5 mm/min (displacement control)	1 mm/min (displacement control)
Constitutive law: stress-strain relationship features					
Main parameter of the model	Mass loss (strand)	Section loss (strand)	Section loss (wire)	Section loss (wire)	Section loss (strand)
Type of approach	*Spring model*	*Equivalent bar*	-	*Spring model*	*Equivalent bar*
Elasticity modulus variability	*V*	*X*	*X*	*X*	*X*
Regression trend: ultimate strain	Exponential	Linear in intervals	Linear in intervals	Exponential in intervals	Linear in intervals
Regression trend: ultimate strength	Linear	Linear in intervals	Linear	Linear	Linear in intervals
Relationship between $f_{pu,corr}$ and $\varepsilon_{pu,corr}$	Independent	Dependent	Independent	Independent	Independent
Stress-strain relation	Bilinear	Bilinear	Bilinear	Bilinear	Bilinear
Reference Area for Tensile Load	Un-corroded	*N/A	Average corroded area	Un-corroded	Minimum corroded area
Model validation	*V*	*V*	*V*	*V*	*V*

* IC = Impressed Current method, ACE = Artificial Climate Environment method, NAT = natural corrosion, N/A = not available, *V* = taken into account, and *X* = neglected, $f_{pu,corr}$ = ultimate corroded strength, and $\varepsilon_{pu,corr}$ = ultimate corroded strain.

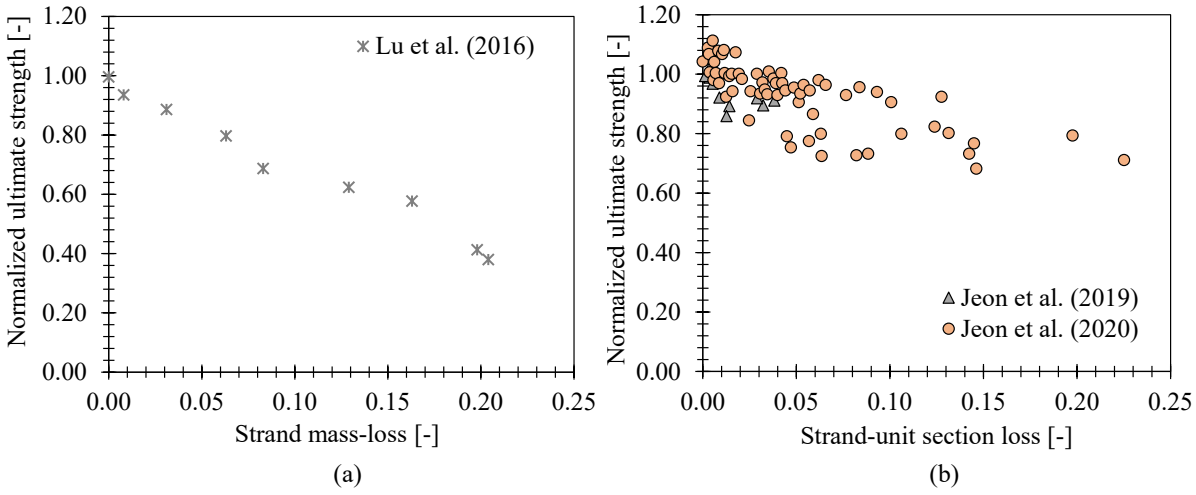

Figure 3-19 Tensile tests outcomes from analyzed experimental campaigns, expressed in terms of normalized ultimate strength, $f_{pu,corr}/f_{pu,0}$: (a) strand mass loss, and (b) strand section loss.

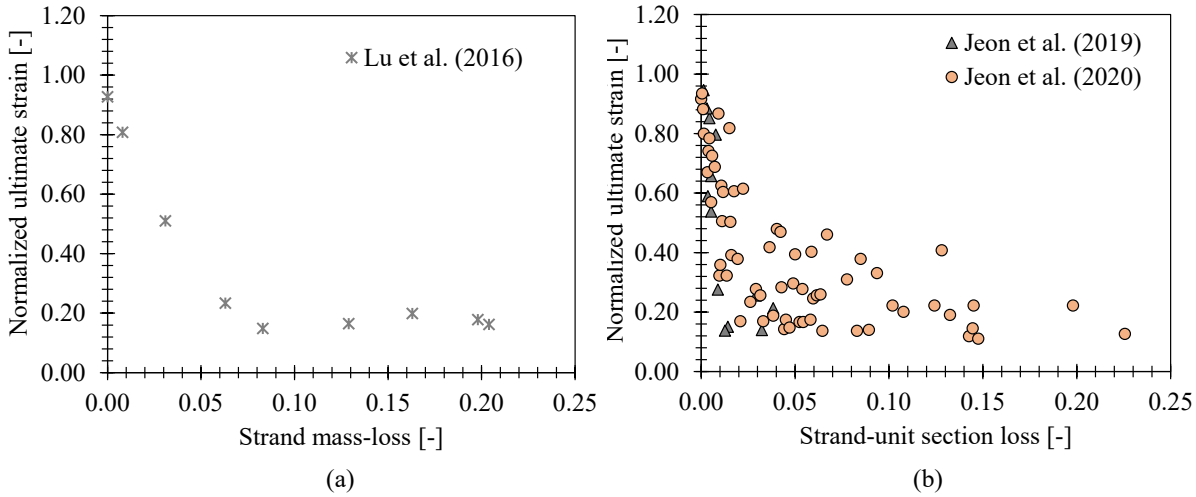

Figure 3-20 Tensile tests outcomes from analyzed experimental campaigns, expressed in terms of normalized ultimate strain, $\varepsilon_{pu,corr}/\varepsilon_{pu,0}$: (a) strand mass loss, and (b) strand section loss.

Although the majority of models expressed the ultimate strength and ultimate strain decay relationships as a function of μ_{max} values, Lu et al. (2016) and Zhang W. et al. (2019) models adopted the mass loss, η, and the average cross-sectional loss, μ_{av}, as the main input parameters, respectively. To appreciate the differences, Figure 3-21 graphically reports the available ultimate strength and ultimate strain decay relationships as a function of the corrosion parameter adopted by the model. From an analytical point of view, significant discrepancies between the ultimate strength and the ultimate strain decay relationships emerged from the comparison of the different models, as highlighted in Figure 3-21.

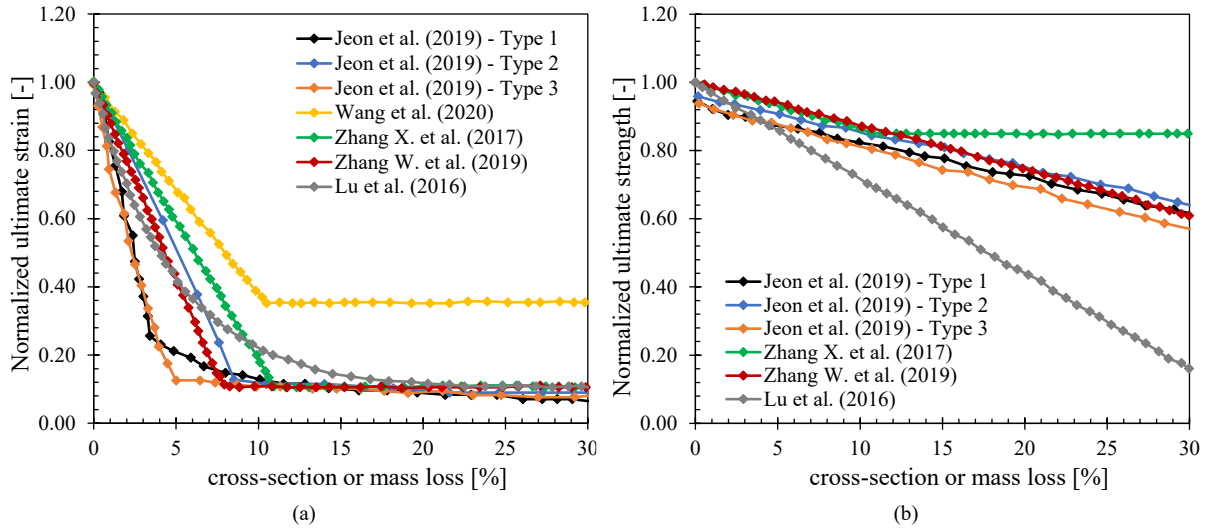

Figure 3-21 Decay relationships available in scientific literature for the prediction of: (a) ultimate strain, and (b) ultimate strength, adapted from Belluco et al. (2021).

Specifically, Belluco et al. (2021) pointed out that the ultimate strength decay relationships were obtained by dividing the ultimate tensile load with the remaining cross-sectional area.

Despite the differences highlighted in Figure 3-21, all models adopted a bilinear trend for the description of the stress-strain response of un-corroded and corroded prestressing strands, as expressed by the relationship reported in Eq. 3-13 and shown in Figure 3-22:

$$\sigma(\varepsilon)=\begin{cases} E_{p,0}\varepsilon & \varepsilon \le \varepsilon_{py,corr} \quad \mu \le \mu_{crit} \\ f_{py,corr}\left(\varepsilon-\varepsilon_{py,corr}\right)\dfrac{f_{pu,corr}-f_{py,corr}}{\varepsilon_{pu,corr}-\varepsilon_{py,corr}} & \varepsilon_{py,corr} < \varepsilon \le \varepsilon_{pu,corr} \\ E_{p,0}\varepsilon \quad \varepsilon \le \varepsilon_{py,corr} \quad \mu > \mu_{crit} \end{cases}$$

3-13

where $f_{py,corr}$ stands for the corroded yield strength, considered to be 0.85 times the ultimate corroded strength $f_{pu,corr}$, and $\varepsilon_{py,corr}$ is the corroded yield strain, considered to be the ratio between the corroded yield strength, $f_{py,corr}$, and the elasticity modulus of prestressing reinforcements, $E_{p,0}$.

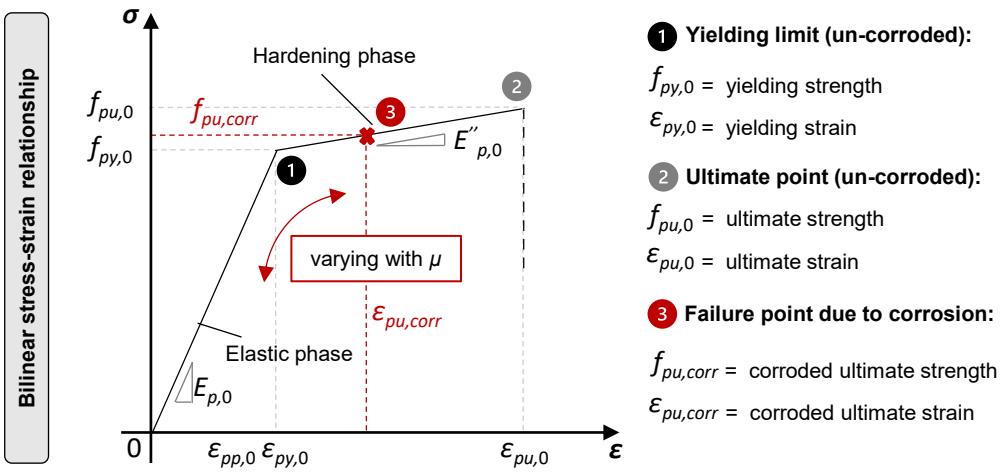

Figure 3-22 Bilinear model for the stress-strain relationship of corroded and un-corroded strands.

Referring to Eq. 3-13, the critical cross-sectional loss or mass loss, $\mu_{crit} - \eta_{crit}$, is regarded as a fundamental parameter for defining the residual stress-strain relationship of a corroded prestressing strand. In the residual response of the corroded wire/strand, this latter value corresponds to the threshold value above which the hardening phase cannot develop. For this reason, it represents the critical stage at which the failure mode of the corroded wire/strand turns from ductile to brittle. In this regard, each model proposed a different threshold value, as reported in Table 3-10.

Table 3-10 Critical mass loss or cross-sectional loss threshold for the different available models.

Constitutive law / Main features	Lu et al. (2016)	Zhang X. et al. (2017)	Zhang W. et al. (2019)	Jeon et al. (2019)	Wang et al. (2020)
Critical cross-sectional loss / mass loss	8%	11%	8%	Type 1: 3.6% Type 2: 8.5% Type 3: 5.1%	10.40%

Additionally, it is worth noting that the elastic modulus, $E_{p,0}$, generally considered unaffected by corrosion, has been set equal to its un-corroded value, except for Lu et al. (2016) model in which a damage factor was introduced. Finally, in light of the several pit type morphology configurations previously described in paragraph 3.5.1, it is important to emphasize that – in the case of prestressing strands composed by multiple wires – the pit type morphology analysis and the related cross-sectional loss measurement, μ, were conducted: (i) at the wire level, when the equivalent spring approach was adopted, and (ii) at the entire strand section level, when the equivalent bar approach was considered, Figure 3-12.

3.5.2.1 Challenges and open issues

A State-of-the-Art of the tensile tests performed on corroded prestressing strands has been proposed. To achieve this, experimental programs and analytical models available in scientific literature for the prediction of the residual mechanical properties of corroded prestressing strands have been analyzed and briefly compared.

Based on the literature review outcomes, the following drawbacks and open issues can be identified:

- Similarly to the experimental research conducted on corroded PC beams, just a limited number of tensile test research have been conducted on corroded prestressing strands. Additionally, most of the available experimental data belongs to tensile testing of samples that were artificially corroded by adopting the IC or the ACE techniques. Only one experimental work examined naturally corroded samples retrieved from an existing bridge which had been exposed to a marine environment during its whole service life. As a result, further experimental campaigns on naturally corroded strands are needed in order to extend the database of available experimental outcomes. Furthermore, new data could be useful to calibrate and validate analytical and numerical models capable of predicting the residual capacity of corroded strands, in terms of both resistance and ductility, as well as their corresponding failure mode.
- Although several efforts have been devoted to the assessment of the residual response of PC members and related prestressing reinforcement affected by corrosion, the topic still needs to be further studied. Indeed, a lack of data has been observed in the scientific literature on the comparison between natural pitting corrosion characterization and mechanical test results in terms of ultimate strength and ultimate strain of corroded prestressing strand. For example, the model proposed by Jeon et al. (2019) was based on the response of wires determined from non-linear finite element analyses.
- No clear guidelines are available for the in-situ assessment of corroded existing structures and detailed procedures and validated models to be adopted for the prediction of the residual mechanical response of corroded strands are not defined. Therefore, the engineering daily practice is hindered by the lack of well-consolidated simplified formulations and analytical models that investigate the uncertainties in the correlation between the damage induced by corrosion and the residual mechanical response of corroded prestressing

strands. To fill this gap, a detailed analysis of the longitudinal and sectional pitting spatial variability of corroded strands should be carefully conducted to identify the key corrosion parameters that affect the residual behaviour of corroded reinforcements.

- Because of the different corrosion techniques adopted, associated with a variability in the current density applied in the case of IC method, the mechanical properties results obtained from tensile testing varied from study to study. Moreover, even though the proposed analytical models usually assumed the same bilinear trend for the description of the residual stress-strain relationship of a corroded strand, different input parameters, such as mass loss or maximum and average cross-sectional loss, were used in the estimation of ultimate residual mechanical properties. This variability is confirmed by the different regression relationships for the ultimate mechanical properties decay proposed by the different authors. As a result, new reliable constitutive models based on simple input parameters – easily measurable during in-situ inspection – and simplified expressions – quickly applicable in daily engineering practice – should be provided. Once simplified stress-strain relationships are available, assessment analytical methods capable of inputting the results of in-situ inspections and outputting the residual mechanical capacity and the residual life estimation of a corroded member should be provided to optimize the maintenance strategies of the existing structural heritage.

In this framework, the present *Thesis* analyzes several naturally corroded prestressing strands extracted from full-scale PC beams with the aim to:

- Investigate the characteristics of the pitting spatial variability of corroded strands;
- Propose correlations able to provide the input parameters for the definition of both refined and simplified constitutive laws, useful in the prediction of the residual stress-strain relationship of a corroded strand.

3.6 Current guidelines and codes for the structural assessment of corroded beams and reinforcements

To date, prestressed concrete is globally recognized as a viable building and infrastructural system that, if compared to reinforced concrete, provides numerous advantages, such as design flexibility, longer spans, increased ultimate load-carrying capacity and in-service performance. However, corrosion durability problems continue to be documented not only in Italy but all over the word. Due to the strategical importance of PC structures, such as bridges, power plants and tanks, the scientific community needs to develop practical methodologies for determining the remaining service life of these damaged structural elements. According to Figure 3-23, there are three main steps to be considered for a detailed assessment of a corroded member:

I. Definitions of corrosion process and mechanism: this mostly pertains to durability issues caused by aggressive agents diffusion towards embedded reinforcements and the related estimation of the corrosion initiation period, (Tuutti, 1982);
II. Evaluation and quantification of corrosion effects: this mainly refers to the estimation of the propagation period of the corrosion process through the development of simplified measurement-based correlations and analytical constitutive laws that relate corrosion parameters to the residual mechanical response of reinforcements;
III. Prediction of the residual service life: this is pursued through the introduction of simplified analytical models capable of reproducing the deteriorated behaviour of a structural member with a relative margin of safety.

Prior to the introduction of Eurocode 1992-1-1(CEN-EC2) in 2004, durability was not considered a significant issue in building standards. Indeed, it was believed that for reinforced concrete structures, a proper concrete cover thickness was sufficient to shield reinforcements from the ingress of aggressive agents – such as chloride ions and carbon dioxide – which are responsible for the activation of corrosion processes. Following the occurrence of several collapses of deteriorated structures worldwide, the necessity to improve the scientific knowledge on corrosion topic became clear. In this regard, a significant step forward was introduced by the CONTECVET manual (*A Validated User's Manual for Assessing the Residual Life of Concrete Structures*) in 2001. This guideline was developed on real case studies and provided a step-by-step procedure for the evaluation of the residual service life of structural

elements in the case of both homogeneous or localized corrosion through the application of simplified or detailed methods.

Concerning the estimation of the initiation period, *fib* Bulletin 34 (2006) and *fib* Bulletin 76 (2015) presented approved durability related models by accurately treating the environmental factors that lead to concrete and embedded reinforcements degradation. These models differ for the chloride-induced or the carbonation-induced corrosion. Since the present work focuses on the analysis of prestressed beams and strands exposed to chloride attack, exclusively the model inherent to this type of corrosion is briefly mentioned.

The chloride concentration diffusion model, commonly known as Fick's second law of diffusion, was proposed for estimating the initiation time, through the expression reported in Eq. 3-14:

$$C_{crit} = C\left(x = c, t\right) = C_0 + \left(C_{s,a} - C_0\right)\left[1 - erf\,\frac{c - \Delta x}{2\sqrt{D_{cl}t}}\right] \qquad 3\text{-}14$$

where, C_{crit} is the critical chloride content, $C(x,t)$ is the chloride content at depth x from the concrete surface at a certain time t (years), x is the concrete cover thickness (mm), C_0 is the initial chloride content (%), C_{sa} is the achieved surface chloride content (%), which can be for example evaluated from scientific literature according to the DuraNet report (Helland et al., 2003) in function of the height above sea level, and D_{cl} is the chloride diffusion coefficient of the concrete, which significantly varies as a function of the exposure condition.

Referring to the quantification of corrosion effects and subsequent evaluation of deteriorated members' service life, no codes or guidelines are currently available, except for the procedure defined by the CONTECVET manual, which is based on the prediction of the penetration depth of corroded reinforcements as a function of the propagation period and the representative current density. On the one hand, the propagation period can be easily calculated once the initiation period is estimated and the carbonation front or the chloride profile are known. On the other hand, the representative current density can be evaluated by adopting monitoring techniques or in-situ measurements. In the lack of direct measurements, the CONTEVECT manual provides potential current density ranges to consider as a function of the actual environmental exposure class, as defined in EN206, (CEN, 2014). Once the penetration depth is known, the corrosion effects and the residual service life of the deteriorated structural element can be evaluated.

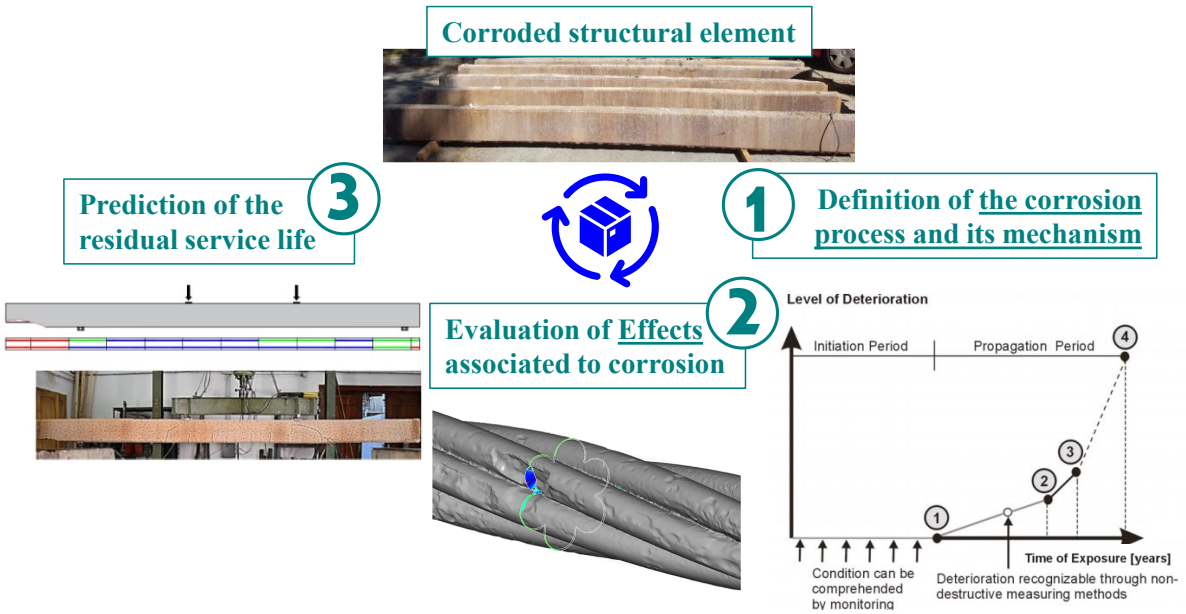

Figure 3-23 Steps of the structural assessment of corroded members.

In recent years, more research activities on the structural assessment of corroded members are ongoing. For example, the new guidelines for existing bridges within the Italian roadway network, entitled "Linee Guida per la classificazione e gestione del rischio, la valutazione della sicurezza ed il monitoraggio dei ponti esistenti", has been published, (Ministero delle Infrastrutture e della Mobilità Sostenibili, 2022). This document derives from the work carried out by the High Council for Public Works (HCPW), which appointed a technical committee to select a number of case-study bridges for an early application of the guidelines, (Cosenza et al., 2020).

This document proposes a multi-level approach aimed to the classification, risk and safety assessment, and monitoring of existing bridges. The first step consists in collecting of available information (technical reports and drawings), and maintenance protocols. The second step involves a report production concerning the detect structural (e.g., corrosion) and non-structural damage (e.g., expansion joints) by conducting a visual inspection of the bridge. At this stage, structural, geotechnical, hydraulic, and seismic hazard parameters should be considered for a simplified risk assessment. Consequently, a preliminary and/or more detailed safety check is performed to establish the safety level of the construction as well as the monitoring protocol by considering the risk class of the investigated bridge, through a multi-level approach to define prioritization schemes for the bridge network.

In addition, as part of the Italian national PRIN and Reluis projects, several research groups are conducting extensive research on the structural assessment of corroded reinforced and prestressed concrete members, such as bridge girders, dapped-end-beams, etc...

Finally, at an international level, the new version of the *fib* model Code 2020 will be published soon, which will include sections devoted to corrosion.

4 Characterization of 10 year-old corroded PC beams

4.1 Highlights

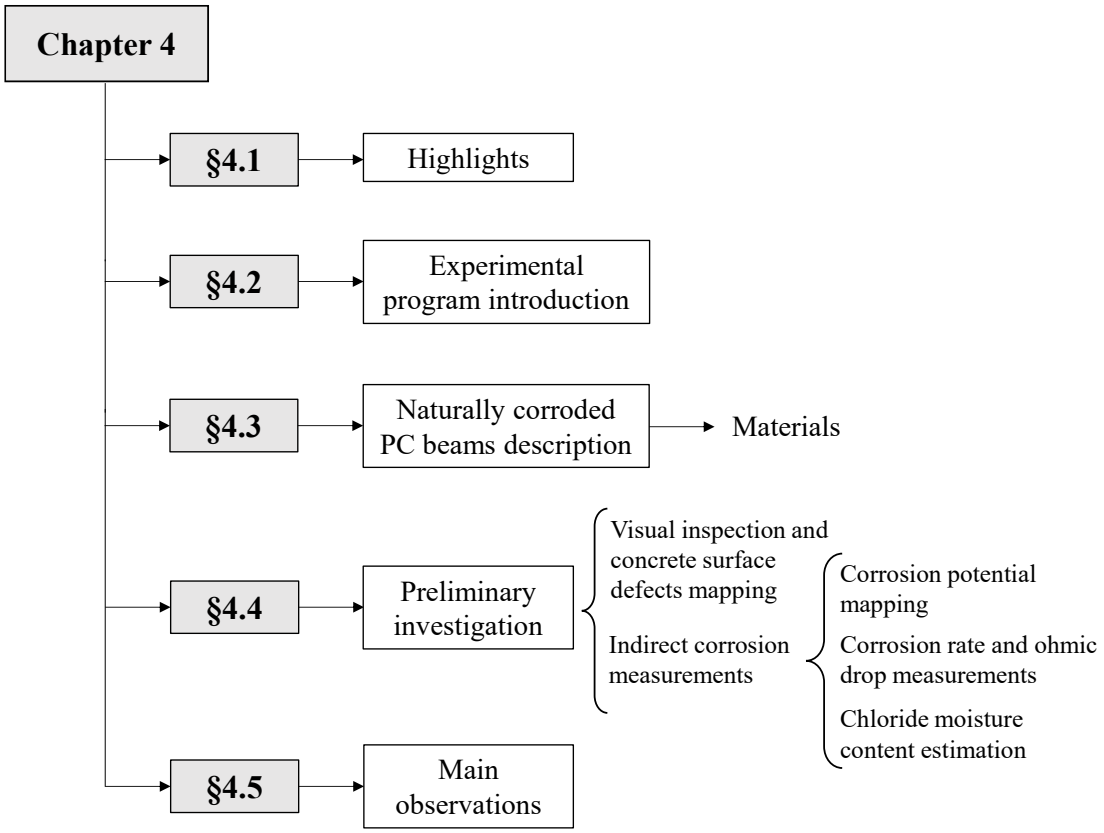

IMPORTANT NOTES: The topics covered in this chapter directly refers to statements, figures and results published by the author in the below mentioned works available in scientific literature:

- **Franceschini L.**, Belletti B., Tondolo F. & Sanchez J. (2022). *Study on the probability distribution of pitting for naturally corroded prestressing strands accounting for surface defects*. Buildings, 12, 1732. https://doi.org/10.3390/buildings12101732

- **Franceschini L.**, Belletti B., Sanchez J. & Tondolo F. (2022). *Dependency of pitting corrosion spatial variability on crack pattern of prestressed concrete members*. Proceedings of the 14th *fib* PhD Symposium, 5th – 7th September 2022, Rome, Italy.

4.2 Experimental program introduction

The present experimental program has been conducted by the University of Parma in collaboration with the Instituto de Ciencias de la Construcción Eduardo Torroja of Madrid (Spain) and the Politecnico of Turin (Italy).

A comprehensive study of a series of fourteen full-scale PC beams coming from a refrigeration tower of a Spanish thermal power plant was carried out. During their 10 years of service, the beams had been subjected to continuous sea water wet-dry cycles, as evidenced by the presence of chloride-induced corrosion. As a result, the owner of the power plant decided to dismantle the deteriorated beams and to bring them to the Eduardo Torroja laboratory for testing. Two experimental campaigns were performed from March 2018 to June 2019. During the first campaign – conducted from March to June 2018 – eight corroded and two un-corroded PC beams were tested, whereas the remaining six were analyzed during the second campaign – conducted from March to June 2019. All the beams were characterized by the same reinforcement and geometrical dimensions, while two un-corroded beams were especially fabricated with the same cement, concrete and curing conditions of the corroded ones to be used as a reference for the evaluation of corrosion effects. It is worth noting that two un-corroded and ten out fourteen naturally corroded PC beams are analyzed in the present *Thesis*.

4.3 Naturally corroded PC beams description

All full-scale PC beams had a rectangular cross-section with a width, b, and heigh, h, equal to 150 mm and 300 mm, respectively. The total length, L_{tot}, varied for beams belonging to the first and second campaign and was equal to 5.44 m and 5.21 m, as shown in Figure 4-1. The longitudinal and transversal thickness of concrete cover, measured from the centroid of reinforcements at the top and bottom of the concrete cross-section, were equal to 40 mm and 50 mm. The bottom of the beam was prestressed with two 7-wire prestressing strands (type 1/2S) having an equivalent diameter, $\phi_{eq,0}$, equal to 12.9 mm and a constant winding pitch. The seven wires were cold-drawn with homogeneous cross-sectional area. The six external wires and the core wire had a radius equal to 2.13 mm (r_{outer}) and 2.19 mm (r_{inner}), respectively. The un-corroded cross-sectional area of the strand was equal to 100 mm^2, $A_{p,0}$, while the area of inner, $A_{w,inner,0}$, and outer, $A_{w,outer,0}$, wires were equal to 15 mm^2 and 14.22 mm^2. The initial prestressing stress, $\sigma_{p,0}$, was equal to 1408 MPa, resulting in a total initial prestressing force, $F_{p,0}$, of 281.60 kN. The top of the beam was reinforced with two steel ribbed bars with a diameter equal to 5 mm having an un-corroded cross-section, $A_{s,0}$, equal to 19.63 mm^2. In addition, no transversal reinforcement was provided and an eccentricity, e, of prestressing reinforcement from the mid-height of the PC beam equal to 100 mm was measured. For the sake of clarity, Figure 4-1 highlights beam configurations and reinforcement details.

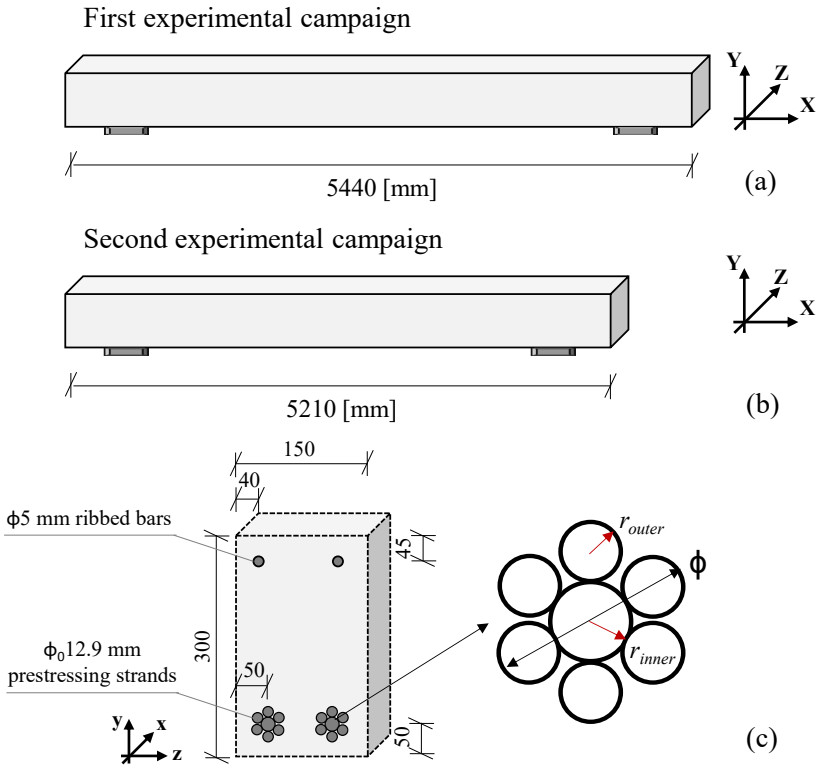

Figure 4-1 Beam details: (a) and (b) longitudinal configurations of two campaigns, (c) cross-section.

4.3.1 Materials

After failure testing, twenty-five concrete core samples with dimensions of 100 mm x 50 mm (height x core diameter) were extracted from the corroded PC beams to evaluate the cylindrical concrete compressive strength, Figure 4-2(a). Afterwards, compressive uniaxial tests under force-control were performed using an Automax 5 machine, working at a load rate of 0.6 MPa/s, as reported in Figure 4-2(b)-(c). Based on the obtained test results, an average concrete compressive strength, $f_{cm,}$ equal to 45.4 MPa was calculated.

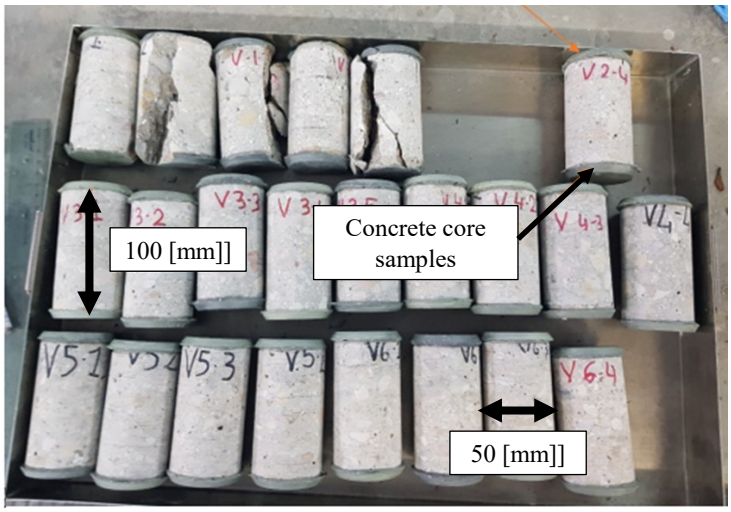

(a)

(b)

(c)

Figure 4-2 Evaluation of concrete compressive strength: (a) concrete core samples, (b) compressive uniaxial test machine and (c) example of sample failure.

Referring to the mechanical properties of un-corroded reinforcements, top longitudinal rebars had a yield strength, $f_{y,0}$, and an ultimate strength, $f_{u,0}$, equal to 450 MPa and 500 MPa, respectively. Moreover, the ultimate strain, $\varepsilon_{u,0}$, was equal to 18%, while the elasticity modulus, $E_{s,0}$, was 195 GPa. Although prestressing strands are analyzed in detail in the following chapters, it is already possible to disclose that an un-corroded ultimate strength, $f_{pu,0}$, and an un-corroded ultimate strain, $\varepsilon_{pu,0}$, equal to 1901.75 MPa and 5.1% respectively, were experimentally measured from tensile testing of four samples showing no signs of corrosion. An elastic modulus, $E_{p,0}$, equal to 195 GPa has been assumed.

4.4 Preliminary investigation

Referring to scientific literature, many efforts have been devoted to the study of experimental correlations, in which the concrete surface damage, especially in the form of crack width measurement, is related to the corrosion level of embedded reinforcements, (Al-Harthy et al., 2011; Andrade et al., 1993; Audenaert et al., 2009; Chernin et al., 2012; François & Arliguie, 1999; Koteš, 2013; Pedrosa & Andrade, 2017). Indeed, an early detection of surface damage can facilitate the in-situ technical assessment of corroded structures and may avoid high maintenance costs and significantly limit sudden collapses, traffic disruptions and fatalities that would take place in the case of severely deteriorated structures. In this context, longitudinal splitting cracks, swellings, and spalling of concrete cover can be considered typical warning signs of the ongoing corrosion process. Therefore, the analysis of these types of surface defects plays a key role in the prediction of the remaining service life of a corroded member and provides useful information for the identification of the most deteriorated parts of the structural element that urgently need retrofitting or strengthening interventions. However, considering PC members, a lack of scientific studies in this research field has been observed. To fill this gap, in the present chapter, all corroded PC beams were firstly visually inspected by identifying and mapping any concrete surface defects. Subsequently, indirect corrosion measurement such as (i) corrosion potential mapping as well as (ii) ohmic drop, (iii) corrosion rate and (iv) chloride content measurements were conducted only on corroded beams belonging to the second experimental campaign to preliminary describe the different behaviour of cracked and un-cracked regions of corroded PC beams. In detail, an identifying code in the form – PB*w* – was used to distinguish the analyzed corroded beams, where PB stands for Prestressed Beam and *w* is a number indicating the name of the beam. The numbers vary from 5 to 8 and from 9 to 14

for beams belonging to the first and second campaign, respectively. Furthermore, the letter N is added after the acronym PB to identify the un-corroded specimens.

4.4.1 Visual inspection and concrete surface defects mapping

As a first step, corroded PC beams were visually inspected to detect areas potentially affected by corrosion damages, where critical brittle failures might be more likely to occur. As highlighted in Figure 4-3, the most common concrete surface defects were:

(i) Swelling;

(ii) Crazing;

(iii)Spalling of concrete cover;

(iv)Longitudinal cracks induced by splitting of concrete.

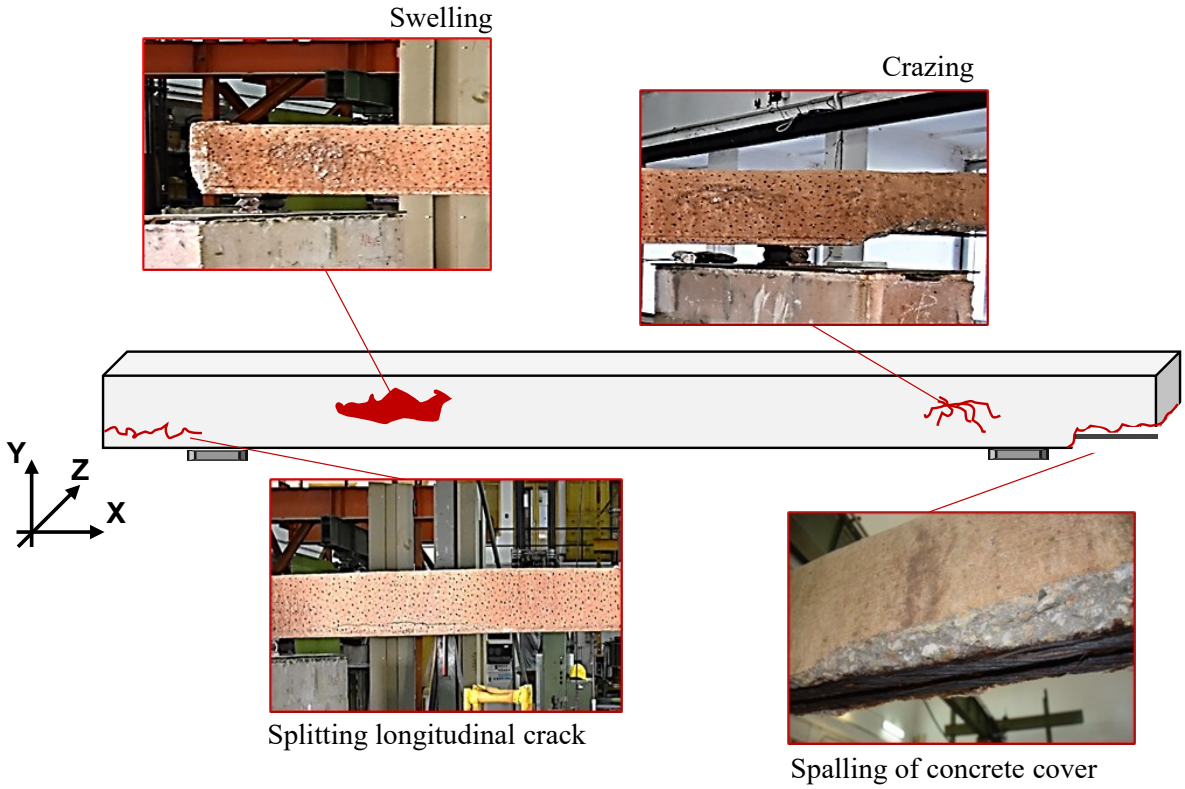

Figure 4-3 Detected surface defects of concrete.

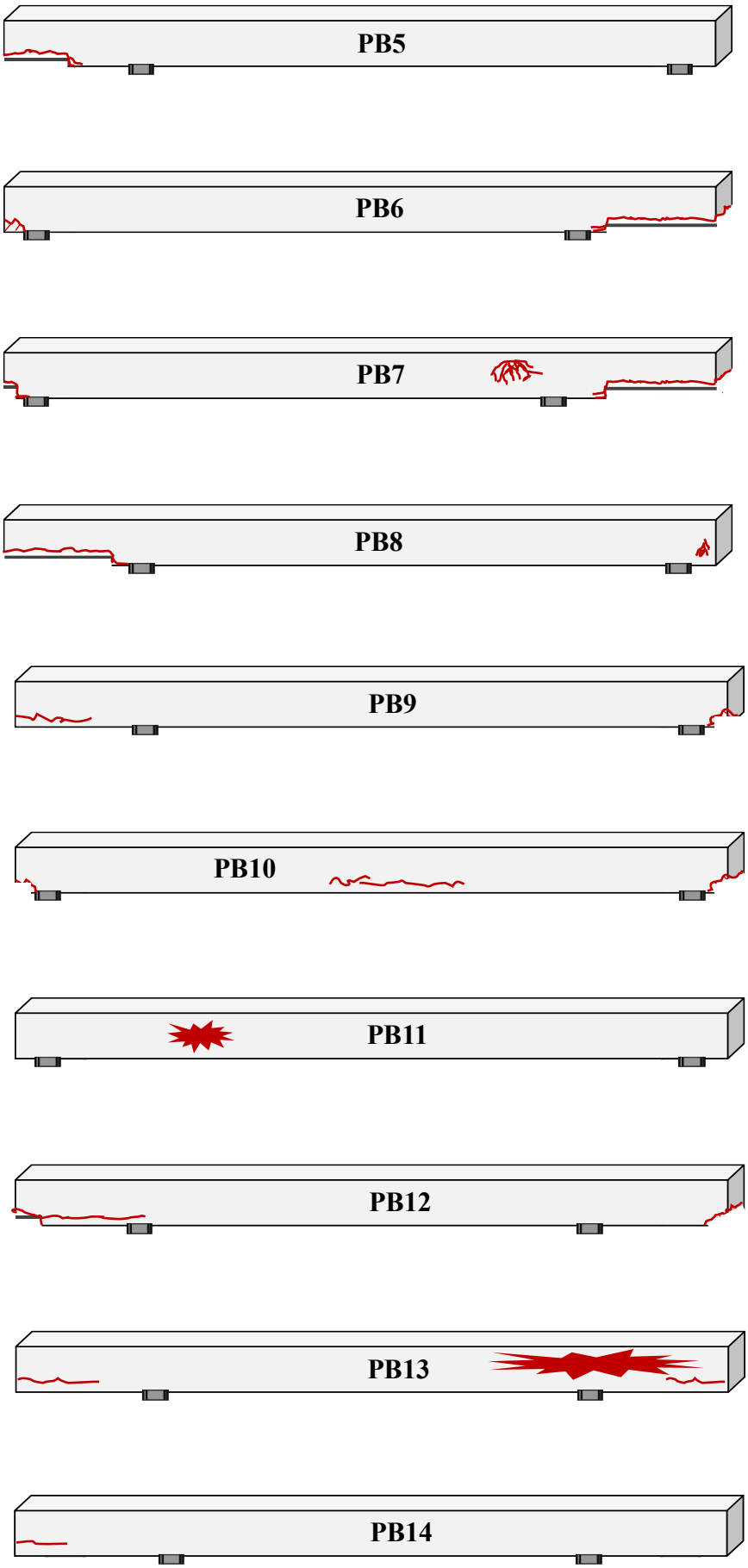

Figure 4-4 Crack pattern of corroded PC beams.

Additionally, Figure 4-4 reports the crack patterns of each corroded beam, where the main surface defects are drawn in red in their exact location. As expected, un-corroded beams did not show any corrosion damage and are not indicated in Figure 4-4. In detail, swelling of concrete was detected at top-left and top-right side of beam PB11 and PB13, respectively, whereas, concrete crazing was observed at top-right side and at right edge of beams PB7 and PB8. Beams PB9, PB12, PB13 and PB14 showed longitudinal cracks in correspondence of prestressing reinforcements at one or both beam edges, characterized by various crack extensions. Conversely, beam PB10 showed a significant longitudinal crack at mid-span. Finally, with the exception of beams PB11, PB13 and PB14, all beams exhibited spalling of concrete cover at one or both beam edges.

During beam characterization, a construction practice deficiency consisting in the lack of prestressing reinforcements protection was observed at all beam edges, as shown in Figure 4-5. This latter was identified as the primary cause of beam corrosion damage since it caused the uncovering of prestressing reinforcements and significantly promoted the penetration of chloride ions during the wet-dry cycles.

(a) (b)

Figure 4-5 Focus on the construction practice deficiency identified at (a) left and (b) right beam edges.

Since crack opening was not measured before testing in the present experimental campaigns, a direct comparison between crack widths and corresponding reinforcement corrosion levels cannot be performed. Nevertheless, a new experimental campaign on further corroded PC beams – coming from the same thermal power plant and characterized by the same exposure condition – has been planned to investigate the crack opening issue with the aim to provide useful relationships to be applied in the assessment of deteriorated structural members.

4.4.2 Indirect corrosion measurements

Concurrently with the visual inspection activity, corroded PC beams belonging to the second campaign were subjected to indirect corrosion measurements in terms of (a) mapping of the corrosion potential, E_{corr}, (b) ohmic drop, and (c) corrosion rate, I_{corr}, at the level of prestressing reinforcements by adopting GECOR10 instrument. According to RILEM recommendations, (Alonso C. et al. 2004), these types of measurements are suitable for the characterization and the on-site conditions assessment of RC and PC members since they can be applied in any condition by ensuring temperature higher than 0°C and pre-wetting the concrete surface before the measurement. The main drawback consists in the possibility to measure the closer reinforcement layer facing the counter electrode only. Nevertheless, since the investigated PC beams were characterized by the absence of transversal reinforcement layer, they were unaffected by this limitation. In addition, chloride moisture content, Cl^-, was evaluated by conducting chloride tests as described in the procedure of Chinchón-Payá et al. (2021).

4.4.2.1 Corrosion potential mapping

The potential mapping of embedded reinforcements is a measurement technique that evaluates the electromotive force, or the voltage conducted by reinforcement surface, which is commonly considered as a useful parameter in identifying areas potentially affected by corrosion. Indeed, during the corrosion process, anodic and cathodic regions form at steel-concrete interface, causing a difference in the electrochemical potential and leading to the consequent current flow in the electrolyte (concrete). The measurement of electrochemical potential differences along the overall beam length allows to identify the regions more prone to corrosion. Since the method is based on the local electrochemical potential measurement, it results effective for the estimation of the corrosion probability of both homogeneous and localized deterioration processes. However, the main drawback is that the adopted technique does not allow for a quantitative measurement of either corrosion rate or corrosion damage level.

The set-up consists of: (i) a high impedance voltmeter, (ii) a reference electrode, (iii) the actual reinforcement, which corrosion tendency must be evaluated, and (iv) the concrete environment. In detail, the circuit was realized by connecting the prestressing reinforcement, embedded in concrete environment, to the positive pole of the high impedance voltmeter and the reference electrode to the negative one, as shown in Figure 4-6. From the practical in-situ

activity point of view, the measurement was performed by detecting the electrochemical potential (voltage) of the prestressing strand with respect to a reference electrode placed in contact with the concrete surface by using a sponge soaked in water and with a copper sulphate electrode. Since prestressed concrete beams were analyzed, the usual copper / saturated copper sulfate electrode (Cu / $CuSO_4$), which consists of a copper bar immersed in a saturated solution of copper sulfate, set in contact with the external environment by means of a porous septum, of wood or ceramic material, was adopted.

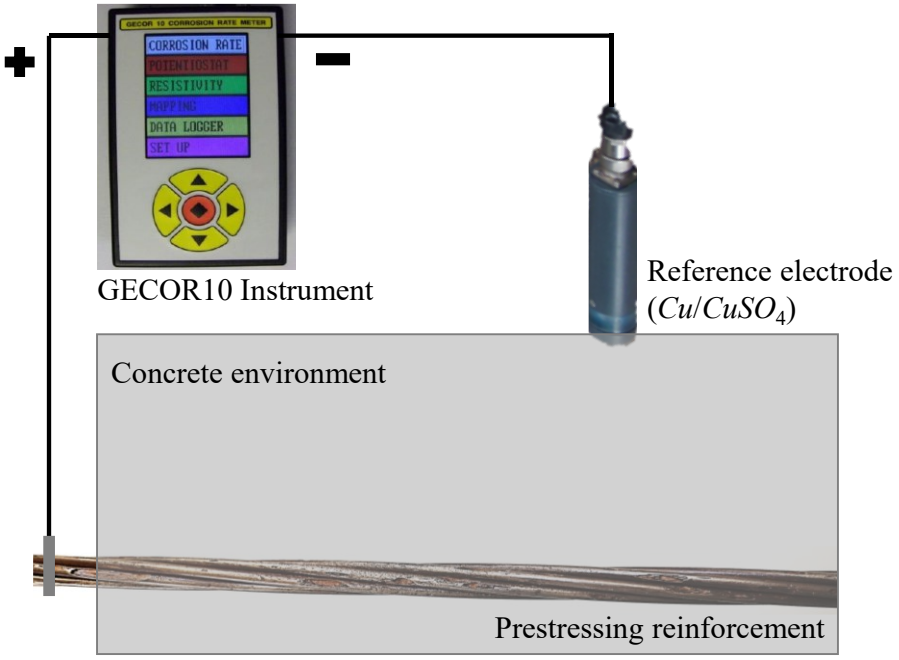

Figure 4-6 Test set-up for corrosion potential methodology.

Generally, E_{corr} values higher than -200 mV represent a probability of absence of corrosion greater than 90%, E_{corr} values ranging between -200 mV and -350 mV correspond to uncertainties about the presence of corrosion (about 50% of probability), whereas E_{corr} values lower than -350 mV stand for a corrosion probability greater than 90%. Figure 4-7 shows the corrosion potential maps of each investigated beam, where orange and red colours are used for regions with an intermediate and a high probability of corrosion, respectively. Moreover, the experimental E_{corr} values measured at mid-span and at the left and right side at a distance of 300 mm from beam edges are reported in Table 4-1.

As a result, a high probability of corrosion was generally measured along the overall beams extension. Moreover, the higher E_{corr} values coincided with the beam regions characterized by the presence of longitudinal splitting cracks, as highlighted in the dashed red box in Figure 4-7.

Table 4-1 Corrosion potential measurements, E_{corr}.

Beam Specimen	E_{corr} left edge	E_{corr} mid-span	E_{corr} right edge
PB9	-577.70	-296.80	-450.80
PB10	-480.10	-644.30	-414.00
PB11	-431.40	-282.50	-233.30
PB12	-530.30	-382.30	-457.70
PB13	-514.60	-364.10	-401.60
PB14	-511.50	-330.00	-390.80

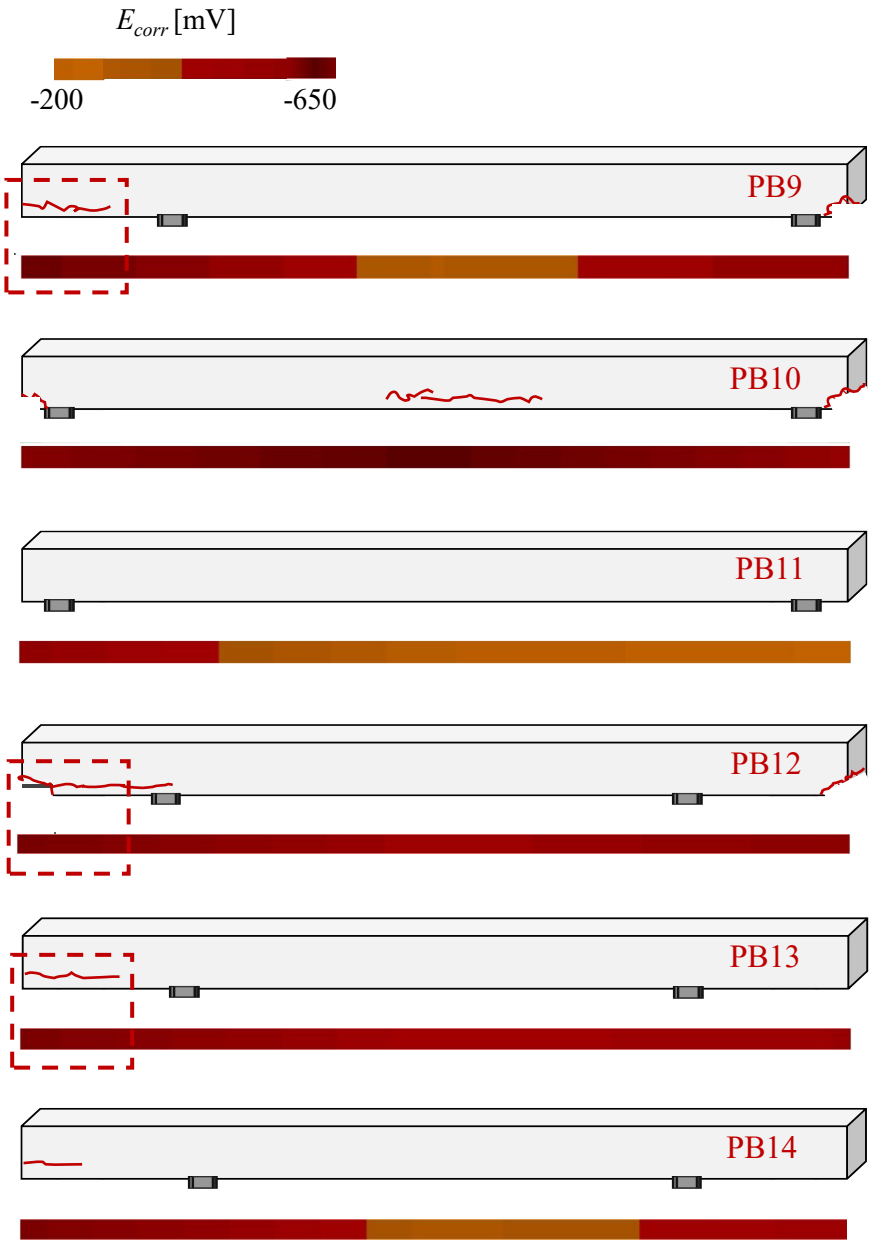

Figure 4-7 Corrosion potential maps along the overall length of each PC beam.

4.4.2.2 Corrosion rate and ohmic drop measurements

At the same location in which E_{corr} values were measured, i.e. beam mid-span and right and left edges, corrosion rate and ohmic drop values were estimated by using GECOR10 instrument, as reported in Table 4-2.

Corrosion rate measurement was carried out by adopting the linear polarization resistance technique. In general terms, the polarization resistance, R_p, of a reinforcement embedded in concrete is defined as the ratio between applied voltage, ΔE, and the step of current, ΔI, (Alonso et al. 2004) – multiplied by the exposed metallic area. This methodology consists in the alteration of prestressing reinforcement electrochemical potential through the application of an external current. The linear polarization technique allows to evaluate the corrosion rate of the reinforcement without significantly changing its potential. The set-up consists of: (i) the actual reinforcement for which the corrosion rate must be measured, also known as working electrode, (ii) a reference electrode, denoted as RE, (iii) a counter electrode, denoted as CE, that delivers current during the test, (iv) the concrete environment, and (v) a potentiostat that imposes a certain potential for the polarization of the prestressing reinforcement, as highlighted in Figure 4-8. The presence of three electrodes is fundamental since it allows for simultaneous potential control and current measurement of the working electrode by avoiding interferences from other electrochemical events that may be present in the cell. Once the reinforcement is polarized – generally within a small potential range around its free corrosion potential, E_{OC}, equal to ±10 mV – the relationship between potential and external current is almost linear. In particular, it is worth noting that the open circuit potential, E_{OC}, is the potential difference between the metal working electrode and the RE when immersed in the electrolyte. For the sake of completeness, the entire test procedure can be summarized in the following steps:

1. Evaluation of the open circuit potential, E_{OC};
2. Application of an electrochemical potential, E, of about -10 mV of the previously defined E_{OC};
3. Scanning at a slow scan rate until an electrochemical potential of about +10 mV of E_{OC} is reached;
4. Current measurement, i;
5. Calculation of the slope that graphically relates the applied electrochemical potential and the measured current → $\Delta E/\Delta i = R_p$ (*true polarization resistance*),
6. Adoption of the Stern-Geary relationship for R_p conversion into corrosion current density, i_{corr};

7. Estimation of the corrosion rate (non-uniform corrosion current in the case of localized pitting attack), I_{corr}, from the related i_{corr}.

In detail, according to the theory proposed by Stern and Geary (1957), the corrosion current density can be evaluated as the ratio between the simplified constant B, which for reinforcement embedded in concrete is assumed equal to 26 mV, (Andrade & Gonzalez, 1978), and the polarization resistance, R_p, (Ωcm^2) according to the expression highlighted in Eq. 4-1.

$$i_{corr}\left[\frac{\mu A}{cm^2}\right] = \frac{B}{R_p} = \frac{26[mV]}{R_p[\Omega cm^2]} \qquad 4\text{-}1$$

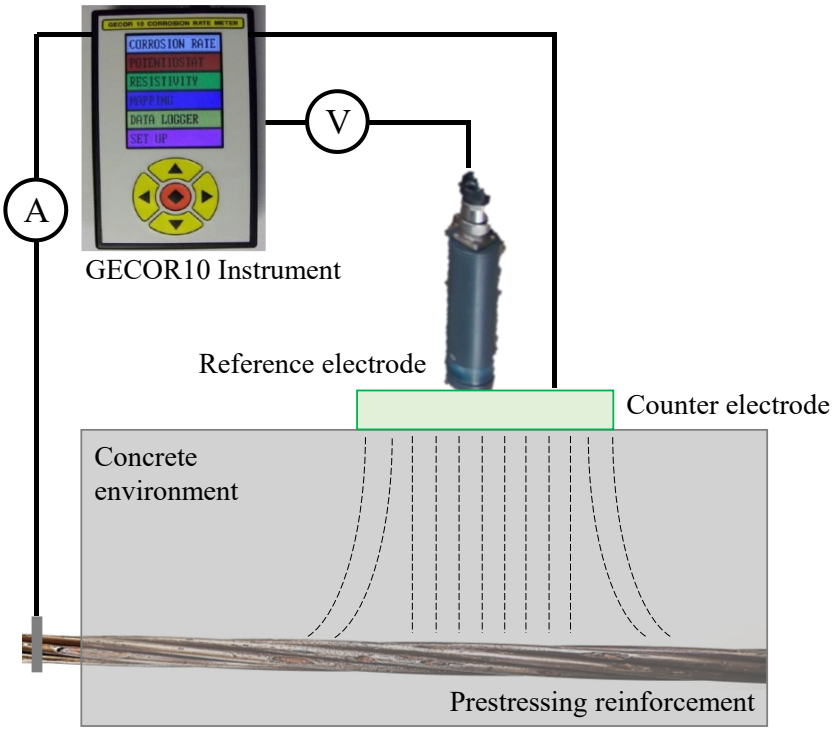

Figure 4-8 Test set-up for linear polarization methodology – I_{corr} measurements.

Considering corrosion rate measurements, which are expressed in a logarithmic scale in Figure 4-9(a), values higher than 0.2 μA/cm^2 were obtained, except for beam PB11. These latter values resulted beyond the established threshold of corrosion activation set equal to 0.1 μA/cm^2, (*CONTECVET*, 2001). Moreover, from the comparison between crack patterns – reported in Figure 4-4 – and the obtained corrosion rate values, I_{corr} higher than 0.5 μA/cm^2 were registered in correspondence of the presence of longitudinal cracks. Thus, a more severe corrosion level was expected for strand samples belonging to these critical deteriorated zones.

During the same procedure, also the ohmic drop, *K*, was evaluated and the obtained values are shown in Figure 4-9(b) and reported in Table 4-2. According to the outcomes, ohmic drop values ranged between 5 kΩ and 15 kΩ, except for beam PB11 that highlighted values higher than 30 kΩ. Since the geometry of the ohmic drop measurements was similar for all beams, this parameter can be considered to be directly related to the resistivity of concrete and the differences in values can be attributed mainly to the moisture content in the concrete itself. Indeed, higher values of ohmic drop imply high concrete resistivity and therefore probable low corrosion damages of the prestressing reinforcements.

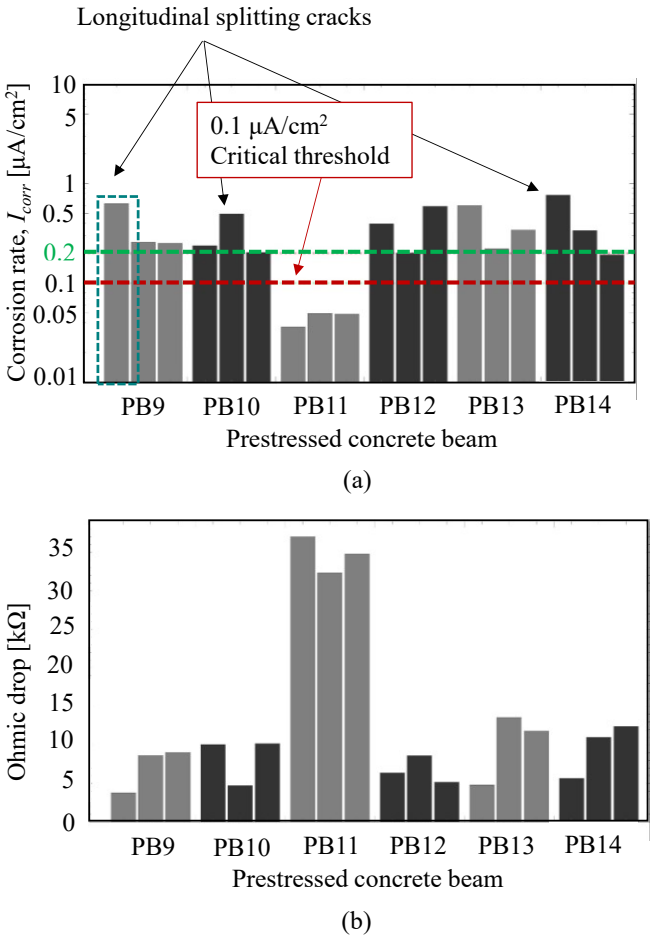

Figure 4-9 Main outcomes: (a) corrosion rate and (b) ohmic drop values.

Table 4-2 Corrosion rate and ohmic drop measurements.

Beam specimen	Left edge		Mid-span		Right edge	
	I_{corr} (μA/cm²)	K (kΩ)	I_{corr} (μA/cm²)	K (kΩ)	I_{corr} (μA/cm²)	K (kΩ)
PB9	0.630	3.79	0.257	8.65	0.250	9.04
PB10	0.239	10.04	0.499	4.74	0.204	10.15
PB11	0.036	37.06	0.049	32.31	0.049	34.75
PB12	0.394	6.34	0.202	8.59	0.592	5.15
PB13	0.605	4.80	0.222	13.54	0.345	11.81
PB14	0.768	5.65	0.339	10.96	0.194	12.37

4.4.2.3 Chloride moisture content estimation

At the Instituto Eduardo Torroja of Madrid, chloride tests were conducted by adopting a spectrophotometry XRF technique on concrete samples extracted from the same locations where corrosion potential and corrosion rate were previously evaluated. This method, also known as X-ray fluorescence spectroscopy, is a non-destructive technique that – through the study of X-ray fluorescence – allows the analysis of the elemental (chemical) composition of concrete samples, once sample atoms are excited by X-rays and high-energy gamma.

The overall testing procedure is schematically highlighted in Figure 4-10 and can be summarized in the following steps:

1. Retrieval of small concrete samples from tested corroded PC beams, Figure 4-10(a);
2. Crumbling of concrete samples with a mortar, Figure 4-10(b);
3. Samples setting and arrangement in the testing machine, Figure 4-10(c);
4. Execution of chloride test by means of DELTA portable XRF gun, data collection and post-processing on a portable computer, Figure 4-10(d).

As a result, the spectrophotometry XRF technique returned the value of chloride content of the analyzed sample expressed in *p.p.m.* (Parts Per Million), as reported in Table 4-3. Thereafter, knowing the cement density – set equal to 2200 kg/m^3 – and the cement content – established equal to 350 kg/m^3 –, the content of chloride ions, $\%CL^-$, expressed as a function of cement content percentage was estimated according to Eq. 4-2 and reported in Table 4-3:

$$\%CL^{-} = \frac{\frac{p.p.m.}{0.85} \cdot density(cement)}{\frac{1000}{content(cement)}} \qquad 4\text{-}2$$

Table 4-3 Chloride content measurements.

Beam specimen	Left edge		Mid-span		Right edge	
	Cl^- (*p.p.m.*)	Cl^- (%cem)	Cl^- (*p.p.m.*)	Cl^- (%cem)	Cl^- (*p.p.m.*)	Cl^- (%cem)
PB9	10575	7.82	2190	1.62	2967	2.19
PB10	3436	2.54	9921	7.34	2875	2.13
PB11	3193	2.36	3380	2.50	3520	2.60
PB12	3553	2.63	3294	2.40	3848	2.85
PB13	3775	2.79	3468	2.56	3303	2.44
PB14	4406	3.26	5293	3.91	3771	2.79

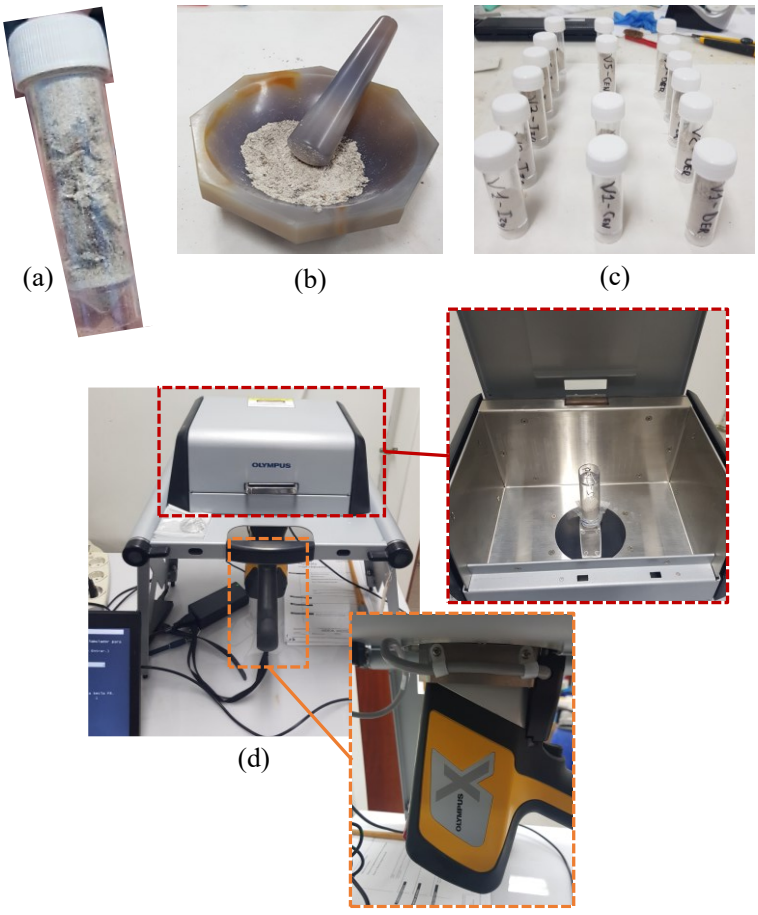

Figure 4-10 Spectrophotometry XRF technique procedure: (a) retrieval of samples, (b) crumbling of concrete, (c) test arrangement and (d) chloride test execution.

The tests were conducted according to the Spanish standard EHE08, (Ministry of Public of Works, 2008), which defines a critical threshold of chloride content of 0.6%cem. Based on the obtained results, the measured chloride content varied between a minimum value equal to 1.62%cem, evaluated at mid-span of beam PB9, and maximum values equal to 7.82%cem and 7.34%cem, evaluated at the right edge of beam PB9 and at mid-span of beam PB10, respectively. Therefore, it was demonstrated that the presence of chloride ions was abundant inside the investigated beams and played a significant role in inducing corrosion damage. In particular, it was observed that the value of chloride content also varied significantly along the beam length, being especially affected by beam regions characterized by longitudinal splitting cracks, as shown in Figure 4-11. Indeed, the average chloride content – considering all analyzed PC beams – was about 2.5%cem, except for two values with chloride content close to 8%cem. These anomalous measurements – in correspondence of the left edge of beam PB9 and at mid-span of beam PB10 – were strongly impacted by the presence of remarkable longitudinal cracks that allowed chloride ions to penetrate directly into concrete during the wet-dry cycles and to concentrate at prestressing strands level after a limited period of time if compared to beam regions where the concrete cover was undamaged.

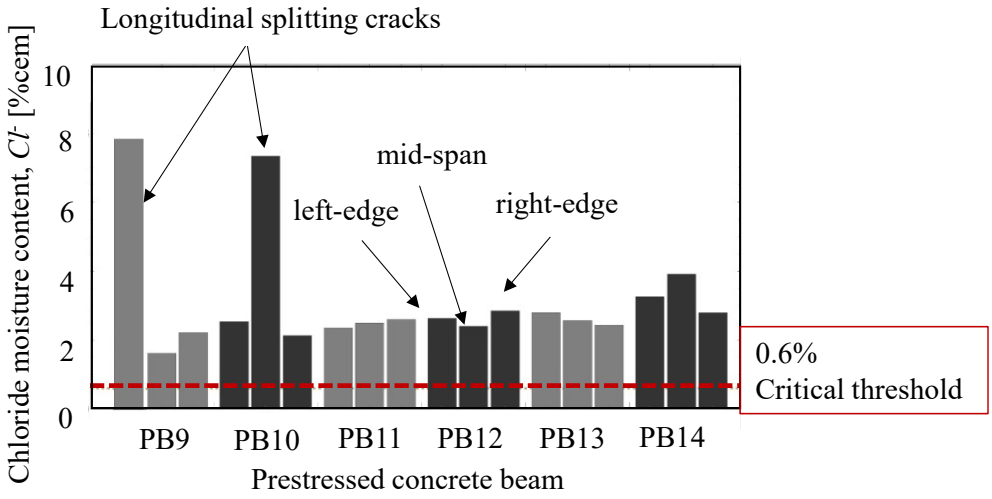

Figure 4-11 Main outcomes from chloride tests.

4.5 Main observations

By comparing the different investigated parameters, a good correlation between corrosion rate and ohmic drop was defined, as shown in Figure 4-12 and expressed by the exponential relationship reported in Eq. 4-3.

$$I_{corr} = 0.6862e^{-0.081K} \qquad 4\text{-}3$$

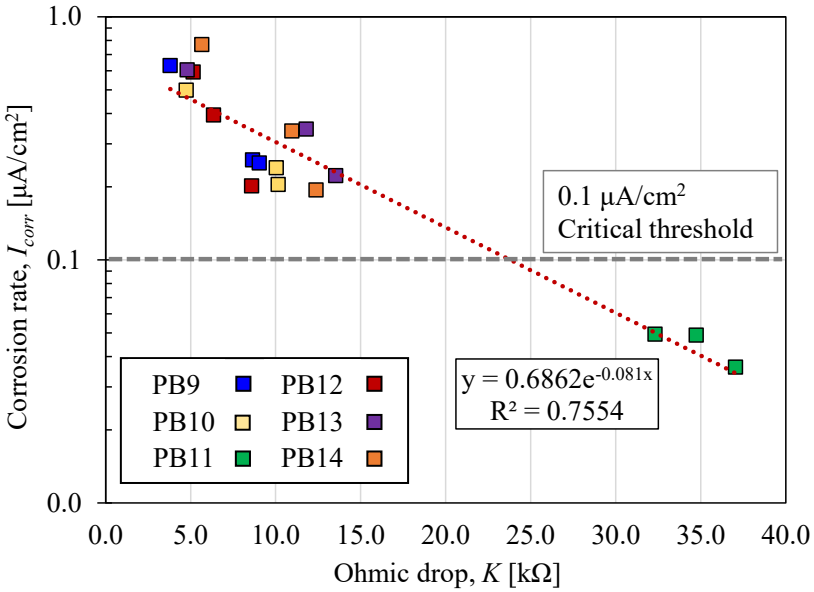

Figure 4-12 Relationship between corrosion rate and ohmic drop.

In particular, with the increase in measured ohmic drop (or concrete resistivity), a rapid decrease in corrosion rate was observed. The present correlation results particularly useful in understanding the different behaviour of beam PB11 and justifying the measured I_{corr} values lower than 0.1 µA/cm^2. The lower corrosion susceptibility of beam PB11 was also confirmed in Figure 4-13 by the comparison between I_{corr} values and percentage of chloride content, where for the I_{corr} values – lower than 0.1 µA/cm^2 – chloride concentration close to 2.5%cem were measured.

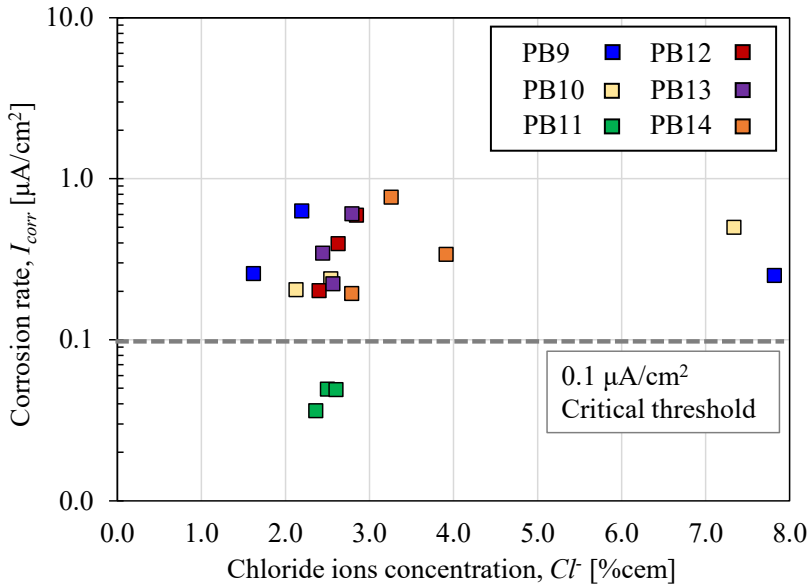

Figure 4-13 Relationship between corrosion rate and chloride ions concentration.

Finally, some preliminary remarks on the corroded PC beams can be outlined:

- Significant concrete surface defects were observed during the visual inspection. Spalling of concrete cover and longitudinal splitting cracks were found to be the most severe damages enhancing the chloride-induced corrosion process over the beams' service life (10 years). In addition, strand deterioration was facilitated by the lack of prestressing reinforcement protection at beam edges, which left strands free to corrode during the refrigeration wet-dry cycles of the thermal power plant.
- From the corrosion potential mapping, a high probability of corrosion was detected along the overall length of each corroded beam.
- Corrosion rate values, I_{corr}, higher than 0.1 µA/cm^2 – corresponding to the established threshold of corrosion activation – were measured for all beams by adopting the linear polarization technique, except for beam PB11 that showed particularly high concrete resistivity.
- Chloride tests, carried out by adopting the spectrophotometry XRF technique, revealed that the analyzed concrete samples were rich in chloride, Cl^-, as confirmed by chloride concentration levels considerably exceeding the standard threshold of 0.6%cem.
- Beam regions characterized by the presence of longitudinal splitting cracks formed at prestressing reinforcements level showed: (i) higher E_{corr} values in the range of -500 mV, and (ii) I_{corr} values higher than 0.5 µA/cm^2. Moreover, anomalous

chloride content concentration of about 8%cem were measured at the left beam end side of beam PB9 and at mid-span of beam PB10. These evidence highlighted that the investigated PC beams were strongly affected by the presence of remarkable longitudinal cracks, which most probably allowed chloride ions to penetrate directly into concrete during the wet-dry cycles and to quickly concentrate at the level of prestressing strands after a limited period of time.

- From the comparison of several investigated parameters, an exponential relationship between corrosion rate and ohmic drop experimental measurements was defined. In particular, based on the obtained data, a lower corrosion level is expected for beam PB11.

5 Experimental program on naturally corroded PC beams

5.1 Highlights

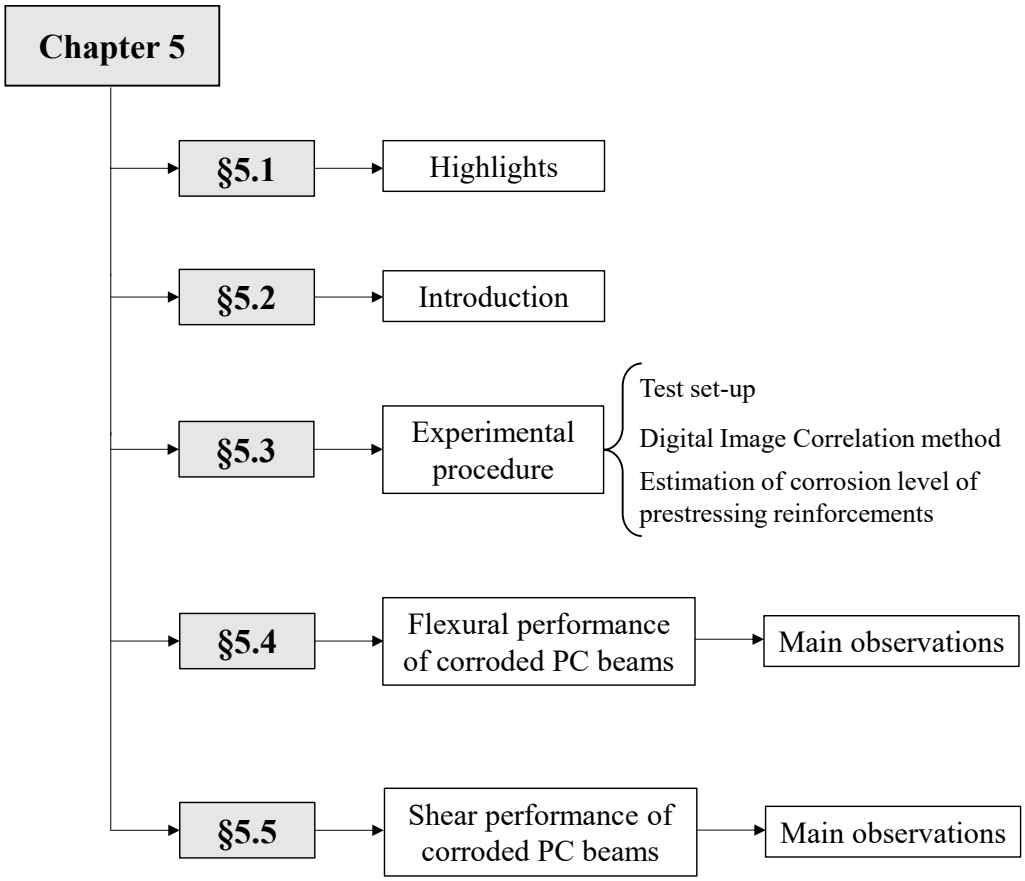

IMPORTANT NOTES: The topics covered in this chapter directly refers to statements, figures and results published by the author in the below mentioned works available in scientific literature:

- Belletti B., Rodriguez J., Andrade C., **Franceschini L.**, Sanchez J. & Vecchi F. (2020). *Experimental tests on shear capacity of naturally corroded prestressed beams*. Structural Concrete, pp. 1-17. https://doi.org/10.1002/suco.202000205

- Vecchi F., Belletti B., **Franceschini L.**, Andrade C., Rodriguez J. & Sanchez J. (2020). *Flexural test on prestressed beams exposed to natural chloride action*. Proceedings of the *fib* CACRCS Days 2020: *Capacity Assessment of Corroded Reinforced Concrete Structures*, 1st – 4th December 2020, venue on-line, Italy, pp: 205-212.

Specifically, the experimental tests on corroded PC beams were conducted at the Instituto Eduardo Torroja of Madrid. Furthermore, the test results were taken to be discussed in the present work from the Master Thesis of Stefano Zambonini from the University of Parma, entitled “Influence of corrosion in the prestressed concrete beams: experimental test and non-linear finite element analysis” and Alessandro Corrente from the University of Parma, entitled “Experimental study on corroded prestressed concrete beams”.

5.2 Introduction

As previously pointed out in the State-of-the-Art section, a lack of experimental tests concerning the investigation of the residual flexural and shear performance of naturally full-scale corroded PC beams was observed in the scientific literature. To fill the gap, the present chapter first studies the flexural capacity of two corroded (PB10 and PB11) and one un-corroded (PBN2) PC beams by performing three-point bending tests up to failure. Subsequently, the shear capacity of seven corroded (PB5, PB6, PB7, PB8, PB9, PB13 and PB14) and one un-corroded (PBN1) PC beams is also investigated by adopting four-point bending tests procedure.

During the above-mentioned tests, load-deflection curves were recorded, and the Digital Image Correlation (DIC) methodology was employed to analyze the 3D displacement and principal tensile strain fields of each tested beam with the aim of deeply investigate their failure mode. After an accurate description of the experimental program, the corrosion effects on flexural and shear capacity, ductility and change in failure mode are discussed and the main observations are drawn. To this end, the prestressing reinforcements were extracted from each beam after testing and classified through a visual inspection to estimate their corrosion level.

The testing of beam PB12 was hindered by technical issues that did not allow the recording of the related load-deflection response. Although the relations between corrosion effects and the residual mechanical response of the beam could not be studied, the visual inspection of the prestressing reinforcements was conducted to increase the number of corroded strands to be subsequently analyzed.

5.3 Experimental Procedure

5.3.1 Test set-up

Three simply supported beams – one un-corroded and two corroded – were loaded in a three-point loading system up to failure under load-control condition to evaluate the corrosion-induced decay of flexural capacity, as shown in Figure 5-1(a). The load was applied at a mid-distance between supports ($L/2$) by adopting a servo-hydraulic actuator with a nominal maximum capacity equal to 200 kN, Figure 5-2; whereas the deflection was measured using a Linear Variable Displacement Transducer (LVDT), placed at the bottom of the beam in correspondence of the loading point. Steel plates with dimensions equal to 70 x 250 x 8 mm – placed at supports and at load point application – completed the loading-controlled system, as

highlighted in Figure 5-2. To evaluate the corrosion-induced decay of shear capacity, the remaining PC beams – seven corroded and one un-corroded – were tested in a four-point loading system up to failure, Figure 5-1(b). In this case, the same experimental test set-up was adopted, with the exception of two symmetrical loads applied at a distance of $L/3$ from the supports by means of a steel beam used for load distribution, as in Figure 5-1.

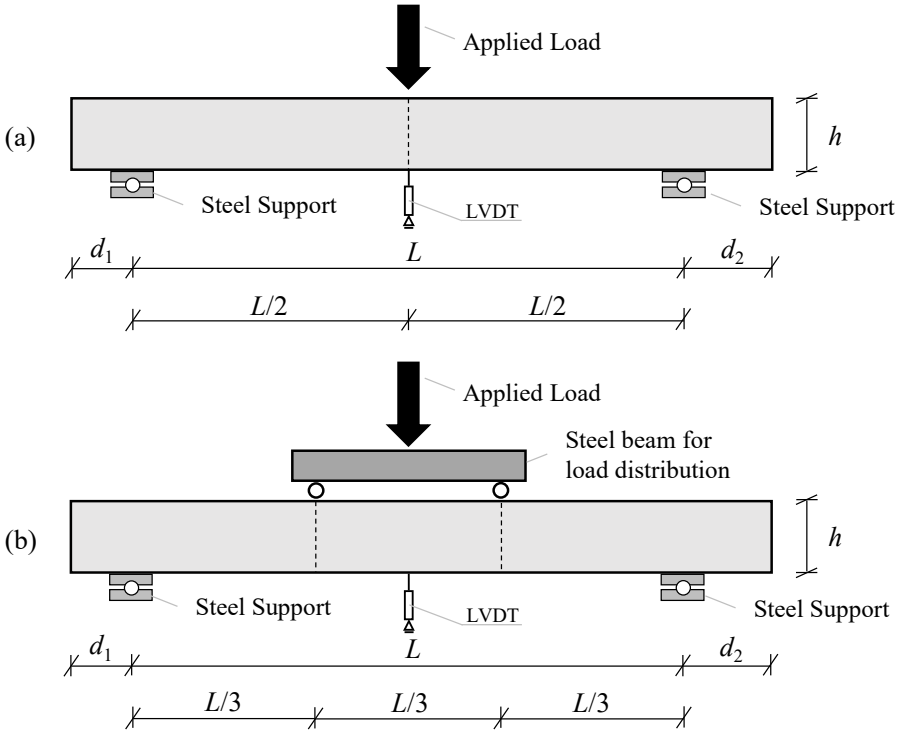

Figure 5-1 Experimental test set-up: (a) three-point loading system and (b) four-point loading system.

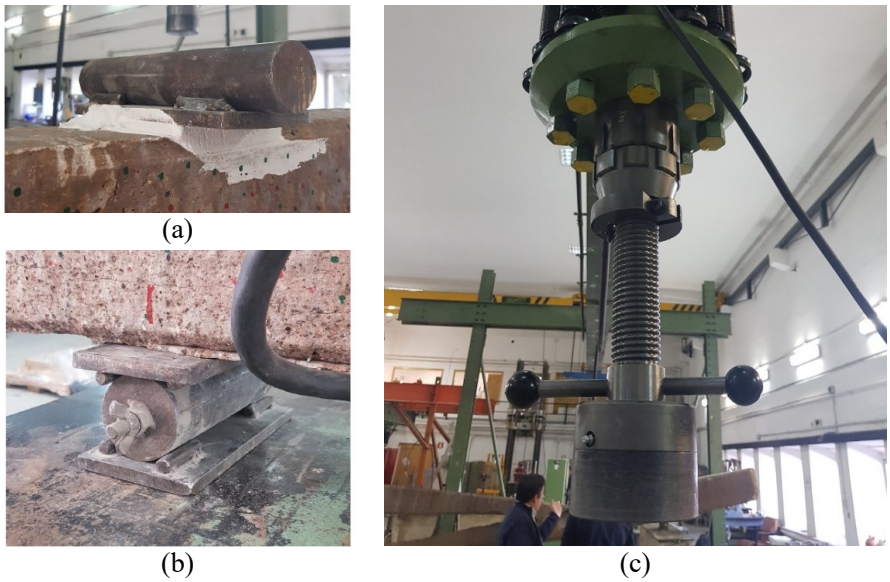

Figure 5-2 Focus on loading system components: (a) steel plate under the loading point, (b) steel plate at supports and (c) servo-hydraulic actuator.

Based on the visual inspection outcomes, the distance between supports, L, was not assumed fixed for all tests but varied depending on the concrete surface damages previously detected, such as the presence of longitudinal splitting cracks or spalling of concrete cover. Therefore, referring to the four-point bending tests, the loading points were not applied symmetrically to the overall beam length, L_{tot}, since the distances between beam edges and supports, d_1 and d_2, varied according to the corrosion damage. To standardize the tests, the supports were respectively assumed to be at a distance of 200 mm from the beam edges in the case of absence of corrosion damage, or 200 mm from the end of the damage in the case of concrete surface corrosion evidence. For the sake of completeness, Table 5-1 summarizes, for each analyzed beam, the main loading set-up dimensions and, in the case of four-point bending tests, reports the shear span-to-depth ratios, a/d, where the shear span a is set equal to $L/3$ and d is assumed equal to 250 mm. Moreover, the beam identification code was updated by adding a term representing the applied loading scheme after the acronym PB: 3P or 4P for three-point or four-point bending test set-up, respectively.

Table 5-1 Geometrical features of tested beams.

Beam Specimen	d_1 **[mm]**	L **[mm]**	d_2 **[mm]**	a/d **[-]**
Three-point bending tests: residual flexural performance				
PBN3P1	200	5040	200	-
PB3P10	250	4710	250	-
PB3P11	250	4710	250	-
Four-point bending tests: residual shear performance				
PBN4P2	200	5040	200	6.7
PB4P5	980	4260	200	5.7
PB4P6	200	4240	1000	5.7
PB4P7	200	4100	1140	5.5
PB4P8	1340	3900	200	5.2
PB4P9	950	4060	200	5.4
PB4P13	1000	3210	1000	4.3
PB4P14	1100	3110	1000	4.1

5.3.2 Digital Image Correlation method

To complete the test set-up, the DIC methodology was adopted to monitor the nonlinear behavior of the PC beams during the loading to failure phase and to subsequently obtain full 3D displacement and principal strain fields. In detail, the DIC procedure was based on:

I. The application of a uniform high-contrast speckle pattern to the beam surfaces – by using speckles colored red, green, black and blue – within a Region of Interest, named ROI, Figure 5-3(a)-(c). The ROI had dimensions *h* x *L* with a heigh, *h*, equal to 300 mm and a variable longitudinal length depending on the beam distance between supports, *L*, Figure 5-3(a);

II. The usage of a lighting device for constant illumination during testing to avoid interferences caused by the shadow effect;

III. The adoption of a high-resolution digital camera, which in the present experimental program was a Nikon D7200 having 24.72 million pixels installed on a tripod at a distance of approximately 3 m from the analyzed beam, Figure 5-3(b);

IV. The images elaboration by means of the open source 2D software package Ncorr, (Blaber et al., 2015; Schreier H et al., 2009), which works in MATLAB environment.

The post-processing phase of the DIC analysis consisted in the comparison between the reference image representing the undeformed shape of the beam – captured before the application of the load – and the images representing the deformed shape of the beam – captured every 5 kN load increment. Finally, displacement and strain values were obtained by overlapping the images of the undeformed and deformed beams.

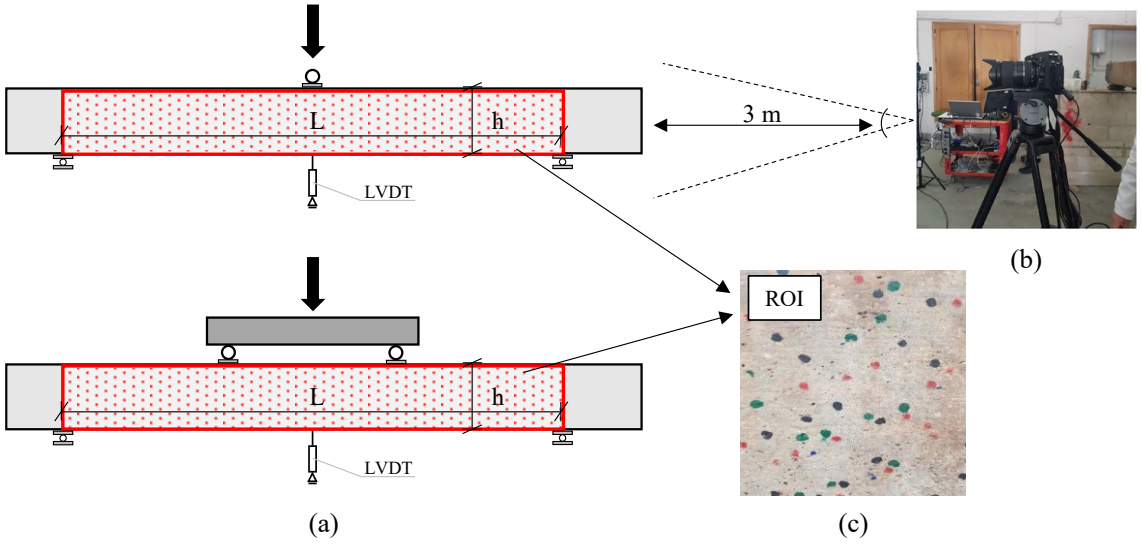

Figure 5-3 DIC methodology set-up: (a) ROI identification, (b) focus on high resolution digital camera and (c) focus on random high-contrast uniform speckle pattern.

5.3.3 Estimation of corrosion level of prestressing reinforcements

Following the loading tests, the prestressing reinforcements were extracted from the corresponding PC beams and visually classified to estimate the corrosion level, Figure 5-4. The classification was conducted every 500 mm length and the corrosion level was assumed to be approximately uniform for each piece of strand. In detail, three different corrosion levels, denoted as LV-I, LV-II, and LV-III, were preliminary defined for the evaluation of the corrosion pattern along the overall beam length, where blue, green and red colours were adopted to identify low, intermediate, and high corrosion level, respectively, as reported in Table 5-2.

Table 5-2 Corrosion levels definition.

Corrosion level	Adopter colour	Classification example (from visual inspection)
LV-I		
LV-II		
LV-III		

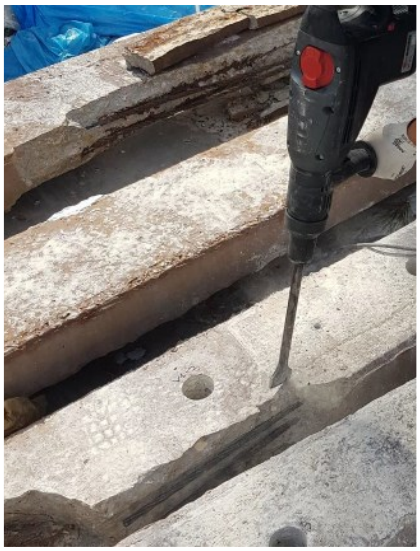

(a)

(b)

Figure 5-4 Evaluation of corrosion level of prestressing reinforcements: (a) procedure of strands extraction after testing and (b) extracted reinforcements.

5.4 Flexural performance of corroded PC beams

Analyzing the behaviour of beams PBN3P1, PB3P10 and PB3P11 after the testing phases (three-point bending), interesting considerations can be pointed out in terms of:

- *Failure Mode*: Shear and anchorage failures did not occur during testing. All the analyzed beams, in fact, failed in bending, as shown in Figure 5-5 – Figure 5-6 – Figure 5-7. In particular, the un-corroded PBN3P1 and the corroded PB3P11 failed due to concrete crushing under the loading point. Unlike PBN3P1, which failed in a ductile way after reinforcement yielding, PB3P11 failure was characterized by the rupture of prestressing strands at mid-span, as shown in Figure 5-7(c). PB3P10 failure was prematurely induced by splitting phenomena at prestressing reinforcements level, which led to spalling of the concrete cover at the bottom part of the beam in correspondence with the loading point and the related main flexural crack. Despite the extent of the failure, no rupture of prestressing reinforcements was recorded.
- *Crack pattern at failure*: For both corroded and un-corroded beams the crack pattern consisted of vertical cracks forming at mid-span. Specifically, PBN3P1 and PB3P11 beams were characterized by multiple vertical cracks of varying size in the region of constant bending moment, as highlighted in Figure 5-5(c) – Figure 5-7(c); whereas, PB3P10 beam showed a remarkable single vertical crack under the loading point, Figure 5-6(c), accompanied by longitudinal splitting cracks occurring at the level of both top reinforcement and bottom prestressing strands. It is worth noting that longitudinal splitting cracks at strands level were already noticed during the first visual inspection, as shown in Figure 5-6(a), and worsened during the loading phase.
- *Corrosion pattern after testing*: As shown in Figure 5-6(b) – Figure 5-7(b), the maximum corrosion level of strands was observed at mid-span in correspondence to the maximum applied bending moment for both corroded beams PB3P10 and PB3P11. The un-corroded reference beam, as expected, was unaffected by corrosion; therefore, no corrosion pattern was provided for PBN3P1 beam in Figure 5-5.
- *Residual load-deflection response*: The reference beam PBN3P1 showed the highest mechanical response in terms of (i) load-carrying capacity – equal to 70.14 kN – (ii) ultimate deflection at peak load – equal to 72.96 mm – and (iii) ductility – showing a significant nonlinear behaviour, as reported by the experimental curve in Figure 5-8(a). PB3P10 showed a premature brittle failure characterized by a peak load of 17.00 kN and an ultimate deflection at peak load of 6.4 mm, without showing any plastic

behaviour, as reported in Figure 5-8(b). Finally, PB3P11 exhibited a reduced sign of ductility with a peak load of 62.00 kN and an ultimate deflection of 23.81 mm, as reported in Figure 5-8(c). Since un-corroded and corroded PC beams were characterized by different distances between supports, L, a direct comparison of peak loads at failure could not be performed. To this end, the evaluation of the ultimate bending moment, $M_{failure}$, was conducted according to Eq. 5-1:

$$M_{failure} = \frac{P_{failure}}{2}\frac{L}{2} = \frac{P_{failure}L}{4} \qquad 5\text{-}1$$

where $P_{failure}$ is the ultimate load recorded during the three-point bending test and L represents the distance between the supports. Based on the obtained results, the ultimate bending moment of the un-corroded PBN3P1 resulted equal to 88.4 kNm, while $M_{failure}$ for corroded beams was equal to 20.0 kNm and 73.0 kNm for PB3P10 and PB3P11, respectively. Therefore, a reduction of ultimate bending moment of 77.38% and 17.42% for PB3P10 and PB3P11was calculated using the un-corroded beam as a reference. For the sake of clarity, Table 5-3 summarises the main experimental outcomes of the tested beams in terms of (i) peak load, (ii) ultimate deflection, (iii) corresponding ultimate bending moment, and (iv) observed failure mode. In detail, by comparing the residual response and the crack pattern of the tested corroded beams, it can be affirmed that the brittle behaviour of beam PB3P10 compared to beam PB3P11 was probably caused by the reduction of the effective depth due to the concrete spalling under the loading point. Moreover, the widespread extension of severely corroded prestressing reinforcements, as shown by the corrosion pattern in Figure 5-6(b), might have induced a higher reduction in the cross-section of prestressing strands and bond decay, promoting the significant decrease in the load-bearing capacity of beam PB3P10. Furthermore, a high chloride content approximately equal to 8% was previously measured at mid-span during the beam PB3P10 characterization phase. It is worth mentioning that PB3P11 was the corroded beam that – during the characterization phase – showed higher resistivity values and lower corrosion rate with respect to other corroded beams. This evidence had preliminary suggested a lower corrosion level, hence, a higher residual mechanical resistance of beam PB3P11, as confirmed by the loading test.

- *DIC analysis*: the data post-processing was performed by means of Ncorr software to better describe the sequence of the events that occurred during the test and to obtain additional information on the maximum principal strain fields of the tested beams. The analyzed load phases are marked by symbols in the load-deflection curves reported in

Figure 5-8, while the evolution of the principal strain fields of each tested beam is shown in Figure 5-5(d) and Figure 5-7(d), with the only exception of beam PB3P10, for which it was not possible to record images useful to be processing due to its sudden failure. Based on the obtained results, a similar evolution of maximum principal strain fields was observed for beams PBN3P1 and PB3P11. Referring to PBN3P1, initial vertical crack occurred at mid-span, under the loading point, for an applied load of 50 kN and a deflection of 17.36 mm. Then, with the increase in the applied load, the flexural cracks became more sizeable. The last recorded image of the beam, taken before its failure, corresponds to a load of 65 kN and a deflection of 42.20 mm, where multiple vertical cracks equally spaced were recorded. For beam PB3P11, the first cracks started to develop after applying a vertical load equal to 45 kN. Thereafter, as the load increased, the cracks propagated with a smaller spacing if compared to the un-corroded PBN3P1. The maximum principal strains, plotted at a load of 50 kN, became more pronounced and extended from the bottom to the top of the beam. Finally, the last recorded image refers to an applied load of 60 kN and a deflection of 21.00 mm. At this loading stage, it is possible to observe how the majority of the vertical cracks developed in correspondence to the highest corrosion level (LV-III) – already detected from the visual inspection of the prestressing reinforcements. The evolution of the vertical displacements of each tested beam as the applied load increases are shown in Figure 5-5(c), Figure 5-6(c) and Figure 5-7(c).

Table 5-3 Flexural response of tested beams: experimental outcomes from three-point bending tests.

Beam specimen	$P_{failure}$ **[kN]**	$\Delta_{failure}$ **[mm]**	$M_{failure}$ **[kNm]**	**Failure mode**
PBN3P1	70.14	72.96	88.40	Bending due to top concrete crushing and yielding of prestressing reinforcements.
PB3P10	17.00	6.40	20.00	Sudden brittle failure with the formation of a single vertical crack under the loading point.
PB3P11	62.00	23.81	73.00	Bending due to top concrete crushing with rupture of bottom prestressing strands.

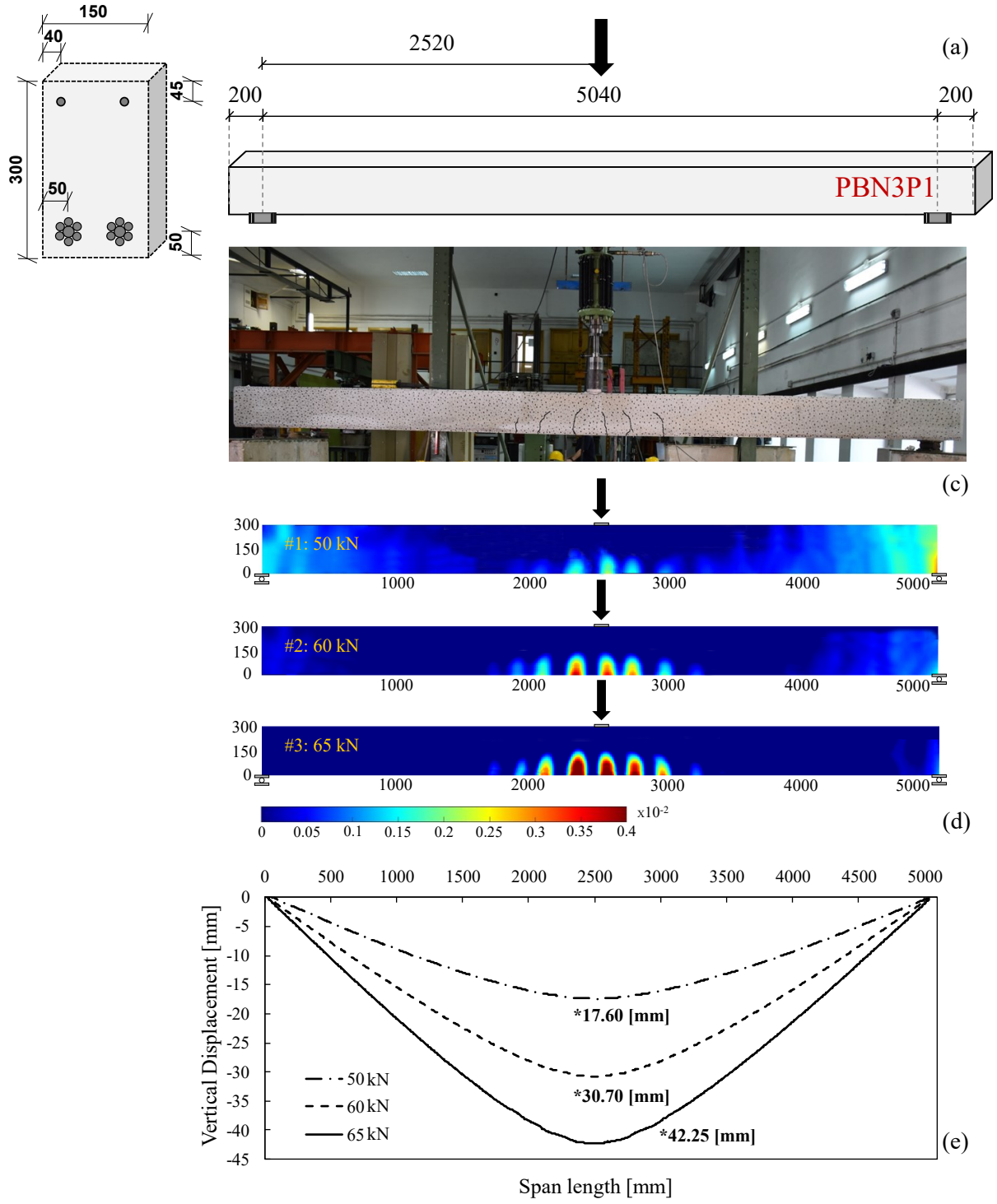

Figure 5-5 Failure analysis of PBN3P1 beam: (a) crack pattern, (b) corrosion patter – in the case of un-corroded beam is not available -, (c) beam at failure, (d) DIC analysis and (e) vertical displacement along the beam length for increasing load values.

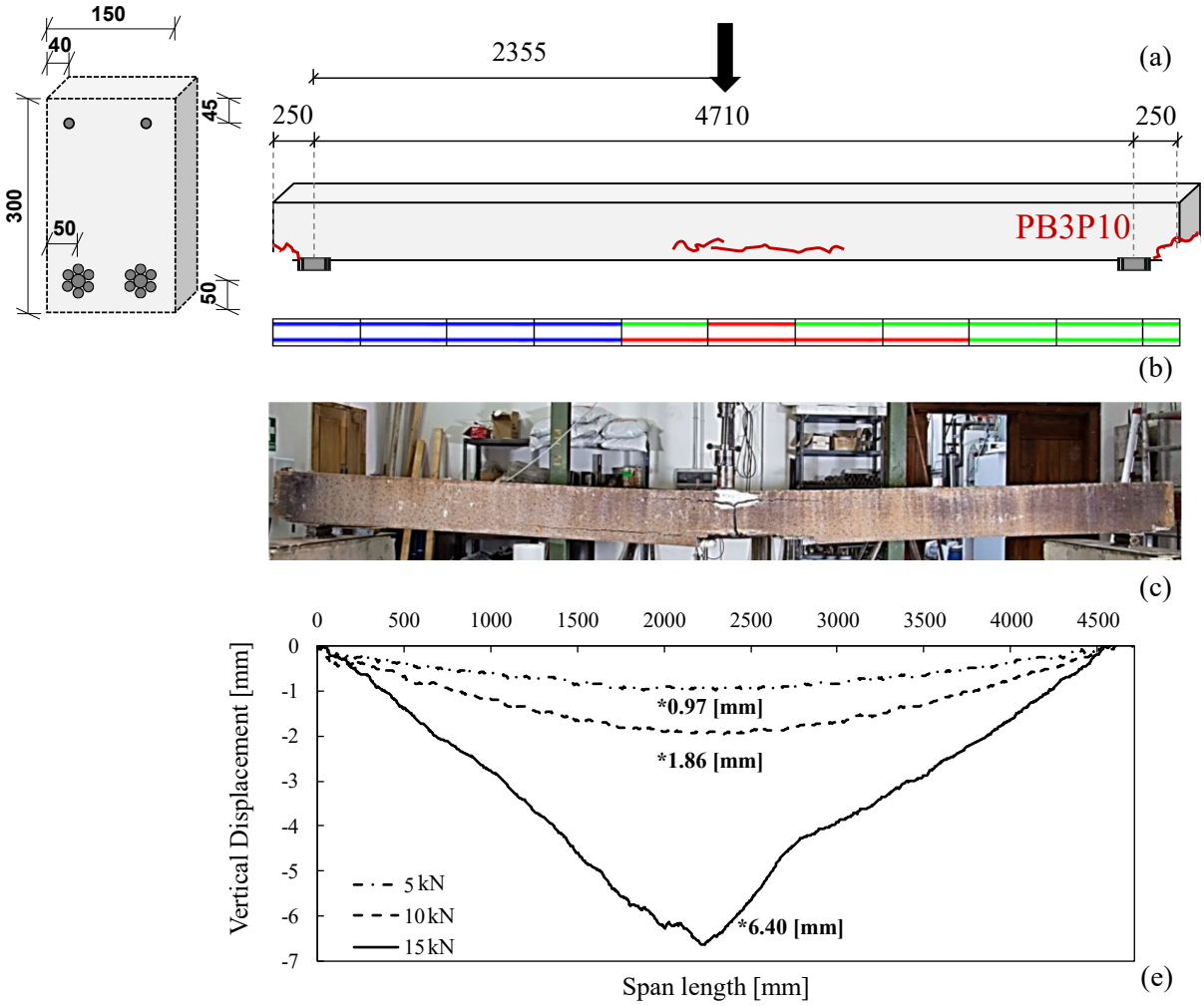

Figure 5-6 Failure analysis of PB3P10 beam: (a) crack pattern, (b) corrosion patter, (c) beam at failure, (d) DIC analysis, and (e) vertical displacement along the beam length for increasing load values.

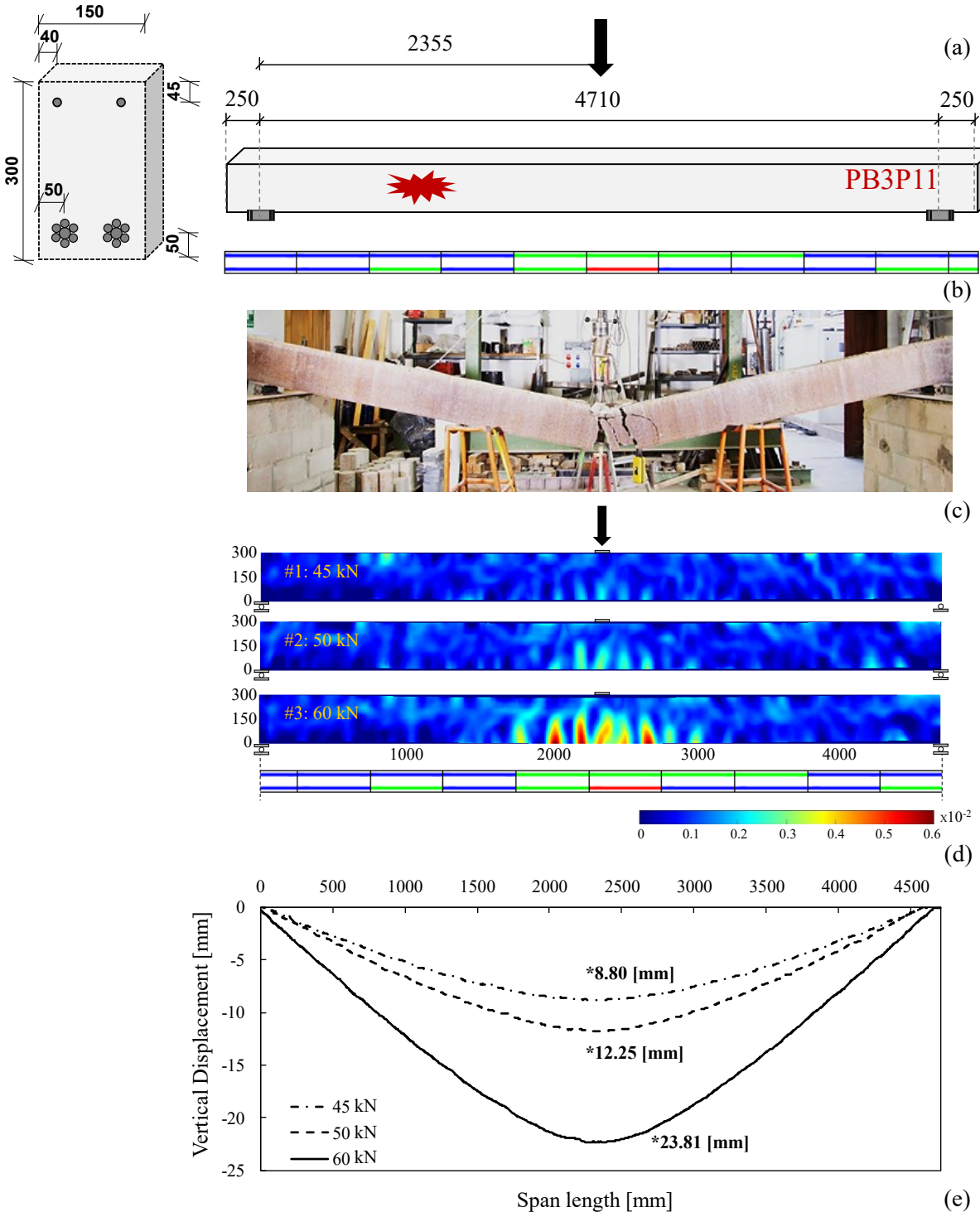

Figure 5-7 Failure analysis of PB3P11 beam: (a) crack pattern, (b) corrosion patter, (c) beam at failure, (d) DIC analysis and (e) vertical displacement along the beam length for increasing load values.

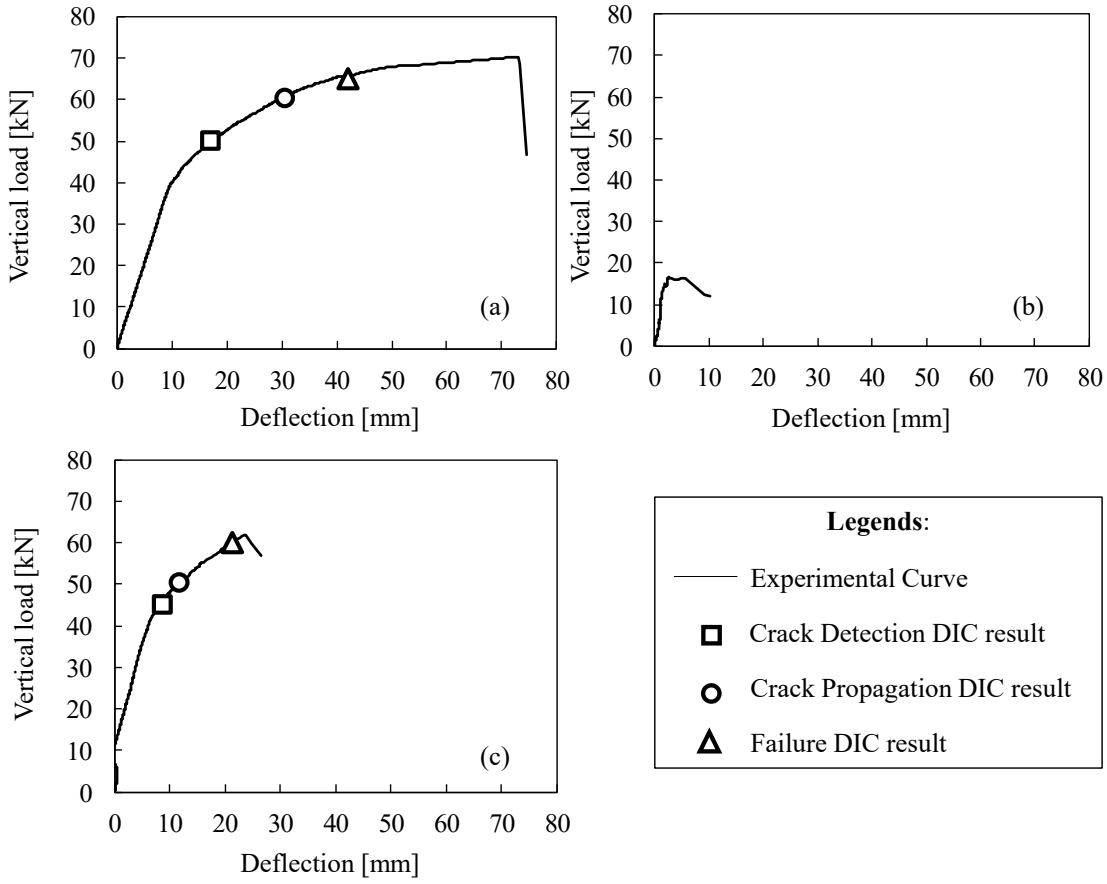

Figure 5-8 Experimental load-deflection curve from three-point bending tests for beam: (a) PBN3P1, (b) PB3P10 and (c) PB3P11.

5.4.1 Main observations

The experimental results obtained from the three-point bending tests on two naturally corroded PC beams and one un-corroded control specimen are discussed in the present section. In particular, the residual flexural mechanical behaviour of corroded specimens have been deeply investigated through the DIC methodology and by performing a visual classification of the corrosion level (corrosion pattern) of the extracted prestressing reinforcements. Based on the correlations between the residual mechanical response, the maximum principal strain fields evolution, the observed failure modes and the corrosion and crack patterns of each tested beam, the following main observations can be outlined:

- Overall, the un-corroded beam PBN3P1 showed the best mechanical performance. With regards to the corroded beams PB3P10 and PB3P11, it was observed a remarkable reduction in terms of ultimate bending moment (load-carrying capacity), deflection and ductility. Specifically, the ultimate bending moment of beams PB3P10 and PB3P11 decreased by 77.38% and 17.42%, respectively, compared to the reference beam PBN3P1. In this context, as hypothesized after the beams characterization phase, beam PB3P11 resulted to be less affected by the corrosion process due to its higher concrete resistivity and lower corrosion rate values when compared to the other corroded beam, leading to a significant residual mechanical performance characterized by the presence of a remarkable non-linear behaviour.
- The visual inspection conducted on the extracted prestressing reinforcements confirmed that the highest corrosion level occurred in correspondence to the presence of concrete surface defects, such as longitudinal splitting cracks or spalling of concrete cover at beam edges. This experimental evidence highlighted the high risk associated with concrete defects at the level of prestressing reinforcements, especially in the case of PC beams characterized by the absence of transverse reinforcement. Indeed, as demonstrated by the residual mechanical behaviour of beam PB3P10, longitudinal splitting cracks may primarily cause the debonding of prestressing reinforcements and induce a sudden failure mode.

5.5 Shear performance of corroded PC beams

Referring to un-corroded RC beams, the shear resistance can be evaluated from the combination of two mechanisms denoted as (i) beam action and (ii) arch action. The first action requires interaction at concrete-steel interface, referred to as bond action, and develops with a variable tensile force on the reinforcement with an almost constant level arm. In detail, in the case of RC beams without transversal reinforcement, a key role for shear resistance is played by the concrete tensile strength at the web. The second action is marginally affected by the bond interaction and develops with a variable lever arm and constant tensile force on the reinforcement. However, to bear the tie action in the arch, a proper anchorage is required at the end of the beam.

Among the experimental works available in literature, Leonhardt (1965) investigated un-corroded RC beams without transversal reinforcements demonstrating that the shear span-to-depth ratio, a/d, is a crucial parameter governing the shear failure mode. More precisely, the shear failure mechanism changes according to the following a/d intervals:

- For $3 < a/d < 7$: beam action failure occurs at – or shortly after – the application of the diagonal cracking load;
- For $2 < a/d < 3$: arch action failure occurs due to shear compression or flexural tension failure of the compression zone above diagonal cracking load;
- For $a/d < 2$: arch action failure occurs due to crushing/splitting of concrete.

As stated by Park & Paulay (1975), an a/d equal to 7 can be considered as the threshold value at which the flexural capacity of the beams is not attained and shear governs the design of the structural member.

Considering the seven corroded and one un-corroded PC beams analyzed in the present section, the ranges of shear span-to-depth ratios previously described for RC beams without transversal reinforcement cannot be directly adopted to schematize the shear failure modes resulting from the four-point bending tests. Four are the main factors that impacted the shear performance of the investigated PC beams:

1. The additional arch action mechanism generated by the application of the prestressing force at an eccentricity, e, equal to 100 mm from the centre of the transversal cross section of the PC beam;
2. The severe corrosion damage showed in some parts of the prestressing reinforcements, which led to strain localisation, reduction in bond resistance, rust products formation with consequent volume expansion, and decrease in

mechanical properties of reinforcements. Therefore, changing the "general" resisting mechanisms by reducing/increasing their effects along the beam length;

3. The occurrence of bond decay, causing a reduction in the beam and arch action mechanisms;
4. The decrease of concrete compressive strength – induced by prestressing force reduction.

To summarize, the main corrosion effects that significantly affected the shear mechanism and the related residual shear resistance of corroded PC beams without transversal reinforcements were the cross-sectional reduction of prestressing reinforcements, the decrease of prestressing force, and the bond decay.

Figure 5-10 to Figure 5-18 show the experimental outcomes of the four-point bending tests conducted at the Instituto Eduardo Torroja of Madrid. Based on experimental evidence, interesting considerations can be made in terms of:

- *Failure mode and crack pattern at failure*: two types of failure modes, denoted as Shear I and Shear II, were experimentally observed. Shear I failure mode involved a shear-bending interaction, Figure 5-9(a). Initially, in the central region of the beam between the load points where a constant bending moment was applied, bending vertical cracks formed from the bottom side towards compression reinforcements. Thereafter, diagonal shear cracks developed in the shear span where constant shear force was applied. Finally, the diagonal cracks abruptly propagated once the position of the loading steel plate was reached, causing the sudden beam collapse. As reported in Table 5-4 and shown in Figure 5-10(c) – Figure 5-11(c) – Figure 5-12(c) – Figure 5-14(c) – Figure 5-16(c), and Figure 5-17(c), PB4P5, PB4P6, PB4P8, PB4P13 and PB4P14 beams failed according to Shear I mode. Shear II failure mode was unaffected by shear-bending interaction and was characterized by the formation of a single diagonal shear crack that suddenly developed in correspondence of the most damaged shear span of the corroded PC beam, Figure 5-9(b). Beams PB4P7 and PB4P9 failed according to Shear II failure mode, as shown in Figure 5-13(c) and Figure 5-15(c). When comparing the two failure modes, Shear I appeared to be more ductile than Shear II and could be anticipated by the yielding of prestressing reinforcements without resulting in a bending failure mode.

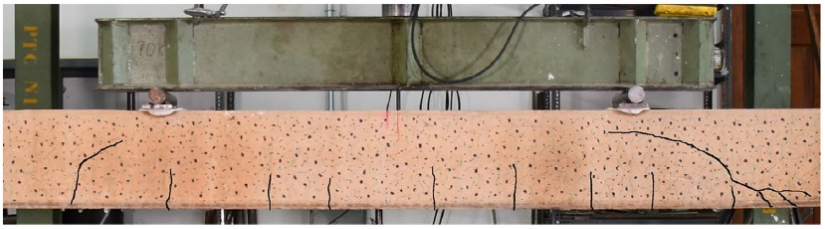

(a)

(b)

Figure 5-9 Focus on detected shear failure modes: (a) Shear I and (b) Shear II.

Analyzing the crack pattern at failure, the Shear I failure mode of the un-corroded beam PBN4P2 was almost symmetrical with respect to the mid-span of the beam; conversely, PB4P5, PB4P6, PB4P8, PB4P13 and PB4P14 crack patterns showed a more pronounced diagonal crack in correspondence to the shear span affected by the highest corrosion level, as highlighted by the corrosion pattern reported in Figure 5-10(b) – Figure 5-11(b) – Figure 5-12(b) – Figure 5-14(b) – Figure 5-16(b), and Figure 5-17(b). Similarly to Shear I failure mode, the Shear II failure mode of beam PB4P7 was governed by a single diagonal crack formed in correspondence to the shear span affected by the highest corrosion level, Figure 5-13(b); on the contrary, beam PB4P9 failed on the opposite side where the highest corrosion level of strands was not recorded, Figure 5-15(b). In this latter case, the crack patterns showed the additional formation of an extended horizontal crack at the level of prestressing strands, probably caused by bond failure. It is indeed known that Kani's tooth model requires that the bending moment, which is produced by bond force in strands, is in equilibrium with bending resistance of the cantilevered teeth, (Kani, 1966). The debonding of strands could be caused by splitting cracks induced by dowel action mechanisms, activated by shear transfer. As a matter of fact, in beams without transversal reinforcement, the dowel action mechanism is limited by tensile strength of concrete, (Park & Paulay, 1975).

- *Residual load-deflection response*: Table 5-4 reports the main experimental test outcomes in terms of (i) ultimate load-carrying capacity, (ii) ultimate deflection, and

(iii) failure mode. Since, each tested beam was characterized by a different shear span-to-depth ratio, the ultimate shear failure loads, $S_{failure}$, and ultimate bending moments, $M_{failure}$, were calculated according to Eqs 5-2 – 5-3 and reported in Table 5-4 in order to compare – at least in terms of loading – the obtained results.

$$S_{failure} = \frac{P_{failure}}{2} \quad 5\text{-}2$$

$$M_{failure} = \frac{P_{failure}}{2}\frac{L}{3} = \frac{P_{failure}L}{6} \quad 5\text{-}3$$

The comparison clearly shows that the corrosion process significantly reduced the ultimate load-carrying capacity and ductility of the tested corroded beams. Due to the different a/d ratios, no comparisons could be made with respect to mid-span deflections.

Referring to the load-deflection curves of each tested beam shown in Figure 5-18, the higher ductility of the un-corroded PC beam PBN4P2 in comparison with the ductility of corroded beams was highlighted, not only because this beam had the highest shear span-to-depth ratio, equal to 6.7, but also because stress localization due to corrosion effects did not occur. Analyzing Figure 5-18(b)-(f), it can be also observed how the beneficial effect of prestressing on the shear performance of corroded beams was strongly impacted by corrosion. Furthermore, the reduced tensile resistance of the strands caused a more pronounced interaction between flexural and shear mechanisms. Indeed, where strands were corroded, larger flexural crack opening widths developed, causing detrimental effects on the aggregate interlock mechanism, (Park & Paulay, 1975). Conversely, considering Figure 5-18(g)-(h), it was pointed out that the load-deflection curves of beams PB4P13 and PB4P14 reached the highest shear capacity and the lowest ultimate displacement because of the lowest shear span-to-depth ratios, equal to 4.3 and 4.1, respectively. As confirmed by Kani's comb model, cracked beams, having low values of shear span-to-depth ratios, can form a tied arch that can support loads even after the failure of cantilevered teeth, (Collins & Mitchel, 1997).

From a theoretical point of view, a more rigid elastic response was expected for beams PB4P5 to PB4P9 due to their a/d ratios ranging between 5.2 and 5.7 – if compared to the un-corroded beam a/d ratio equal to 6.7. In reality, however, the reduction in ultimate load-carrying capacity and ductility of corroded beams not only depended on lower a/d ratios but also on the detrimental effects induced by corrosion. To support

the previous consideration, the shear performance of beams PB4P5 and PB4P6 was compared. As a result, although both beams had the same shear span-to-depth ratios equal to 5.7 and failed in Shear I mode, the higher corrosion level of beam PB4P6 beam caused a slightly lower resistance and ductility compared to beam PB4P5 (89.39 kN and 34.06 mm vs. 90.21 kN and 35.20 mm). Similarly, the shear span-to-depth ratios of beams PB4P7 and PB4P9 – equal to 5.5 and 5.4, respectively – were lower than shear span-to-depth ratios of beams PB4P5 and PB4P6. Therefore, lower ultimate displacement values of beams PB4P7 and PB4P9 – of 29.66 mm and 27.88 mm, respectively – were expected. However, the lower peak load values of beams PB4P7 and PB4P9 – of 81.74 kN and 80.00 kN, respectively – compared to beams PB4P5 and PB4P6 could be caused by corrosion damage.

- *DIC analysis*: in agreement with the scientific works carried out by Campana et al. (2013), Huber et al. (2016) and Cavagnis et al. (2018), that adopted the DIC methodology for the evaluation of the shear failure process of RC members without transversal reinforcements, the present study implemented the DIC technique for the analysis of the maximum principal strain fields and the evolution of deformed displacement profiles of each beam for increasing applied loads, as shown from Figure 5-10(d) to Figure 5-17(d). For the sake of clarity, it is worth noting that the DIC contour plots did not have the same scale but varied in order to appreciate the crack pattern development of each investigated beam. Additionally, the analyzed load steps were marked by symbols in each load-deflection curve reported in Figure 5-18. Based on the obtained results, the maximum principal strain values were in good agreement with the observed crack patterns. The DIC analysis confirmed that the critical diagonal shear crack always developed in correspondence of the highest corrosion level of prestressing reinforcements, except for beam PB4P9 that probably failed due to the occurrence of sudden debonding issues. Moreover, the type of failure mode experimentally observed was also confirmed by the DIC analysis performed for the load step closest to the experimental ultimate load-carrying capacity recorded for each beam. In particular, in the case of beams PB4P13 and PB4P14, the DIC analysis clearly highlighted the presence of bending vertical cracks – not easily visible to the naked eye during the experimental tests – prior to the beam collapse induced by the development of a critical diagonal shear crack, revealing a Shear I failure mode.

  Finally, the DIC analysis was also adopted to measure the vertical displacements and the deformed shapes of the tested beams for different values of applied load, as shown

in Figure 5-10(e) to Figure 5-17(e). Generally, parabolic symmetrical trends of vertical displacement were measured with respect to the mean distance between supports, except for beams PB4P5, PB4P7 and PB4P9. For these latter beams, a non-symmetrical profile of the deformed shape and a significant displacement localization was observed where the critical shear diagonal cracks occurred. This discontinuity could be induced by the occurrence of a sudden bond failure, as demonstrated by the formation of longitudinal splitting cracks – visible to the naked eye – at the level of prestressing reinforcements when the beam collapsed, which led to the tangible increase of beam vertical displacements. Nevertheless, the debonding of prestressing reinforcements in the case of corrosion can be induced by several factors affecting the shear transfer mechanisms such as spalling of concrete cover, longitudinal splitting cracks or the reduction of both dowel action effect and tensile force of strands. Therefore, further studies should be devoted to analyzing the bond resistance of corroded PC beams in depth.

Table 5-4 Shear response of tested beams: experimental outcomes from four-point bending tests.

Beam specimen	***a/d*** **[-]**	$P_{failure}$ **[kN]**	$\Delta_{failure}$ **[mm]**	$M_{failure}$ **[kNm]**	$S_{failure}$ **[kN]**	**Failure mode**
PBN4P2	6.7	98.47	120.70	82.71	49.24	Shear I
PB4P5	5.7	90.21	35.20	64.05	45.11	Shear I
PB4P6	5.7	89.39	34.06	63.17	44.70	Shear I
PB4P7	5.5	81.74	29.66	55.86	40.87	Shear II
PB4P8	5.2	100.06	28.69	65.04	50.03	Shear I
PB4P9	5.4	80.00	27.88	54.13	40.00	Shear II
PB4P13	4.3	127.45	23.70	68.19	63.73	Shear I
PB4P14	4.1	145.90	22.30	75.62	72.95	Shear I

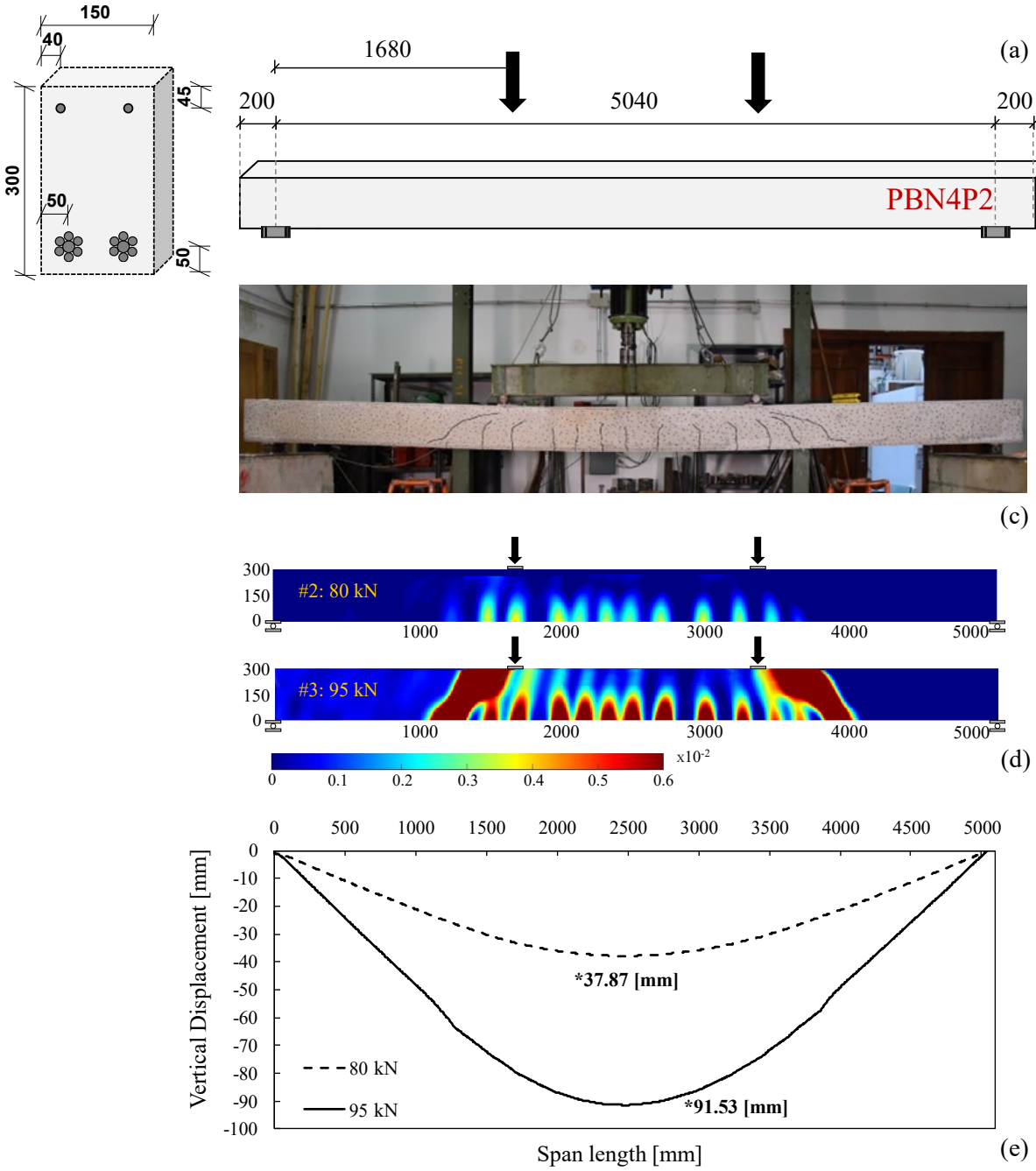

Figure 5-10 Failure analysis of PBN4P2 beam: (a) crack pattern, (b) corrosion patter – in the case of un-corroded beam is not available -, (c) beam at failure, (d) DIC analysis and (e) vertical displacement along the beam length for increasing load values.

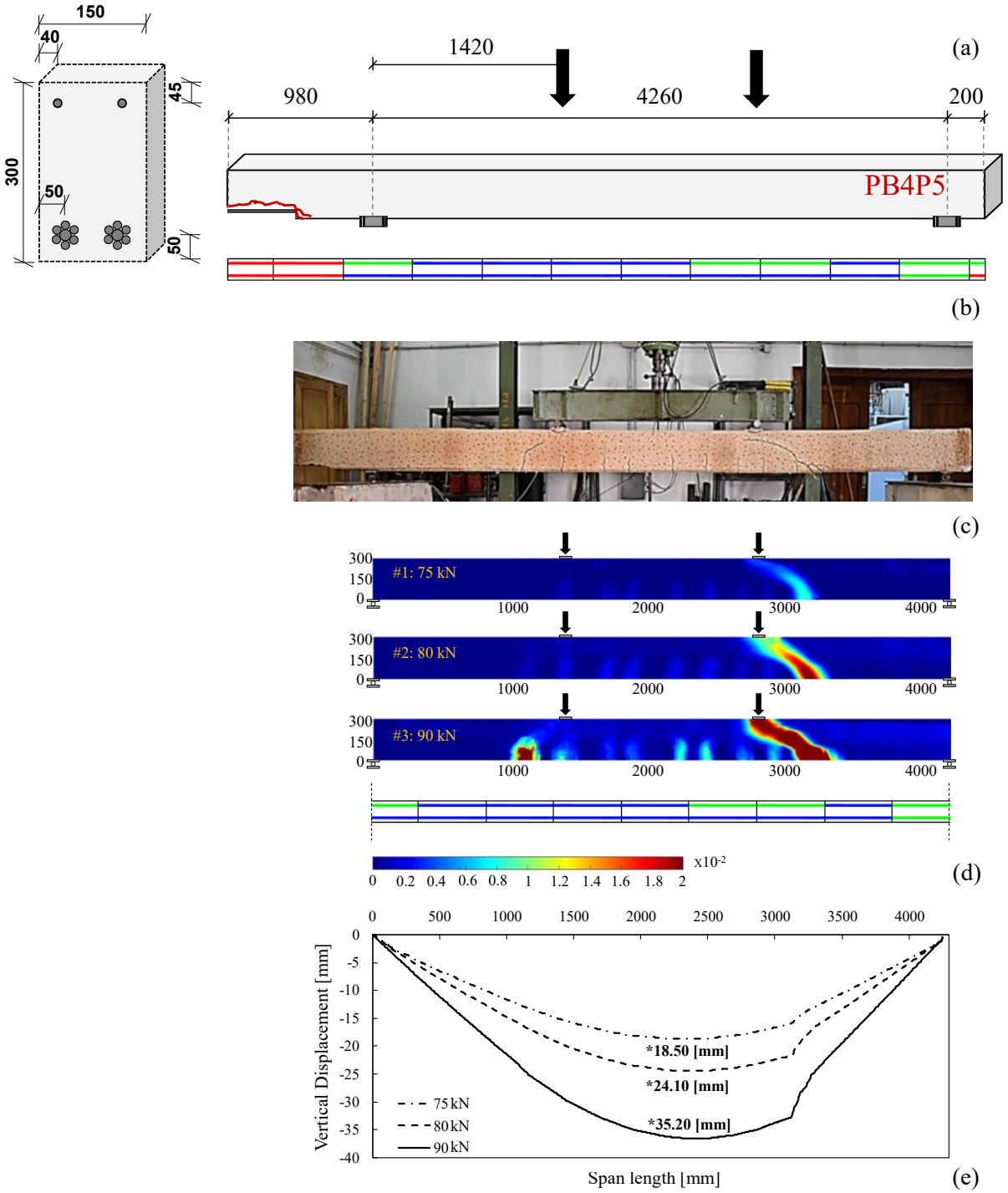

Figure 5-11 Failure analysis of PB4P5 beam: (a) crack pattern, (b) corrosion patter, (c) beam at failure, (d) DIC analysis and (e) vertical displacement along the beam length for increasing load values.

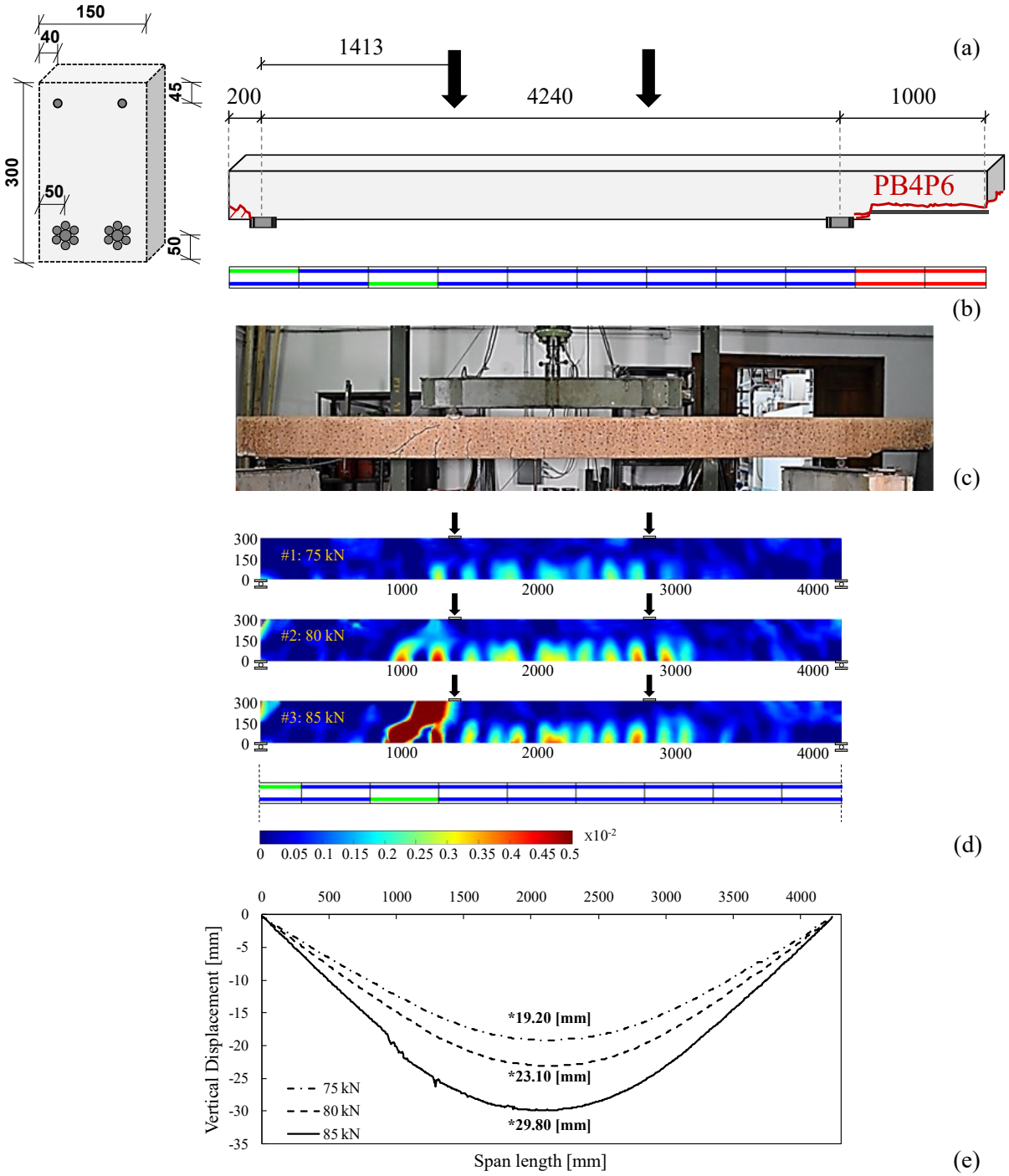

Figure 5-12 Failure analysis of PB4P6 beam: (a) crack pattern, (b) corrosion patter, (c) beam at failure, (d) DIC analysis and (e) vertical displacement along the beam length for increasing load values.

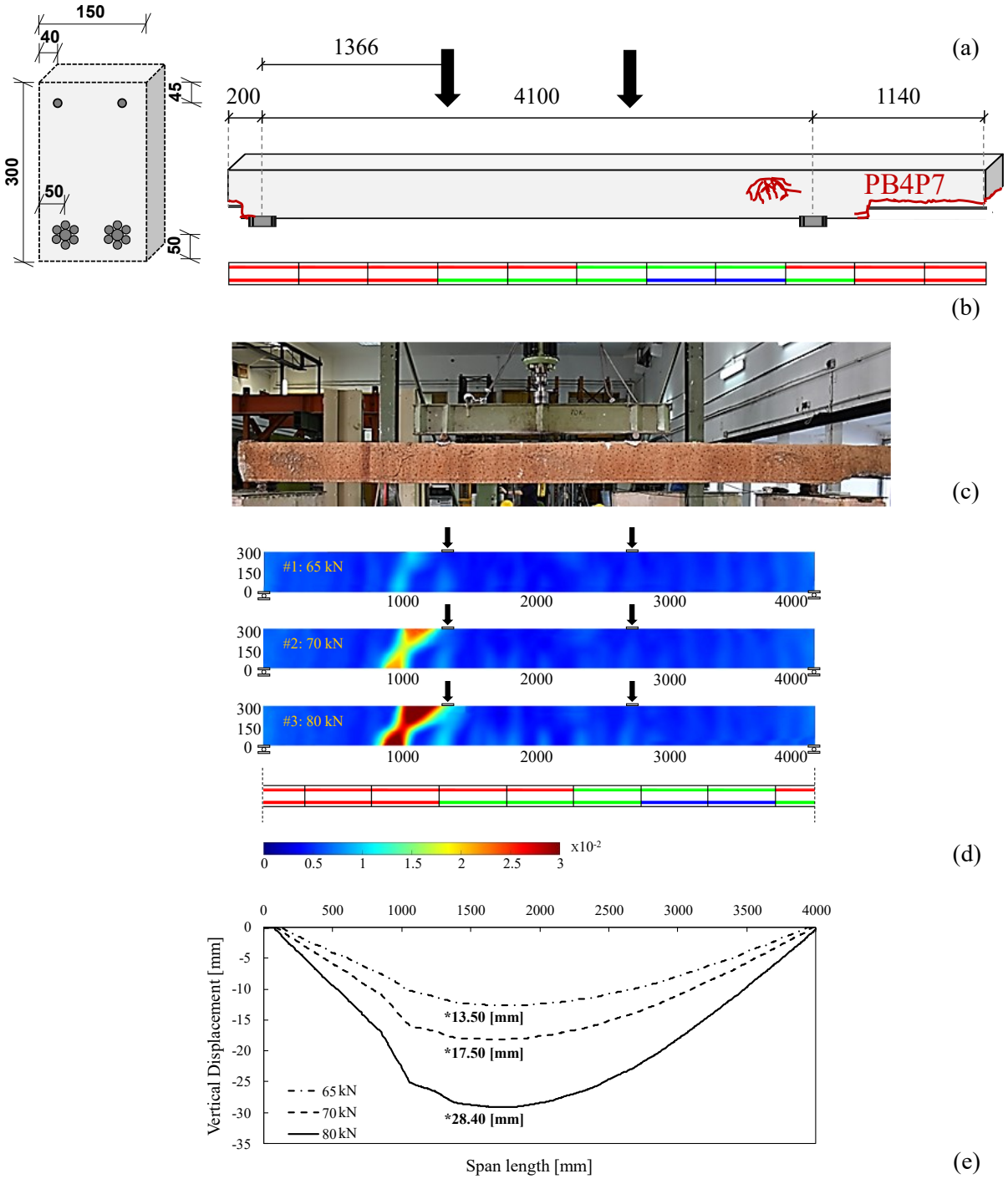

Figure 5-13 Failure analysis of PB4P7 beam: (a) crack pattern, (b) corrosion patter, (c) beam at failure, (d) DIC analysis and (e) vertical displacement along the beam length for increasing load values.

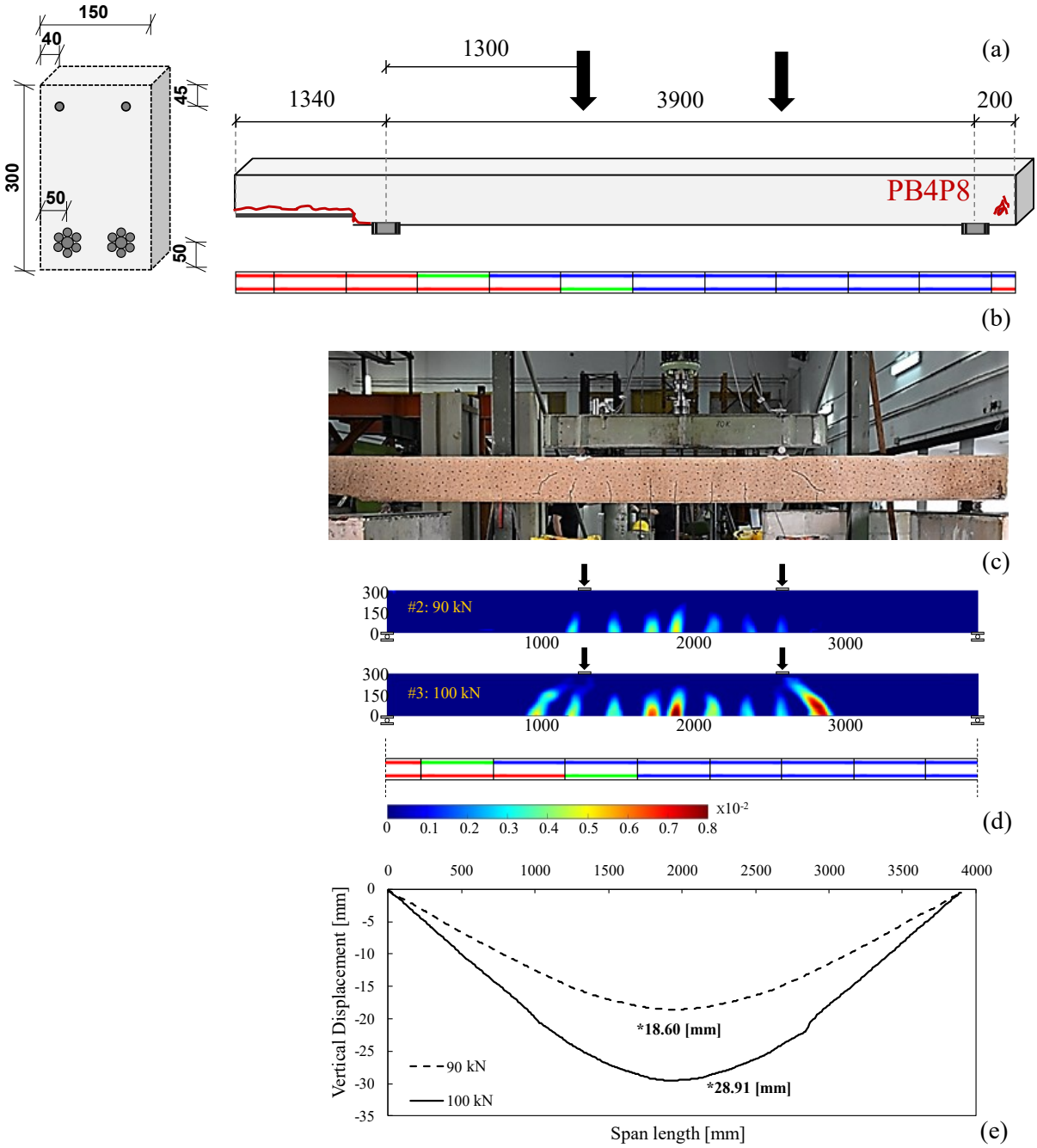

Figure 5-14 Failure analysis of PB4P8 beam: (a) crack pattern, (b) corrosion patter, (c) beam at failure, (d) DIC analysis and (e) vertical displacement along the beam length for increasing load values.

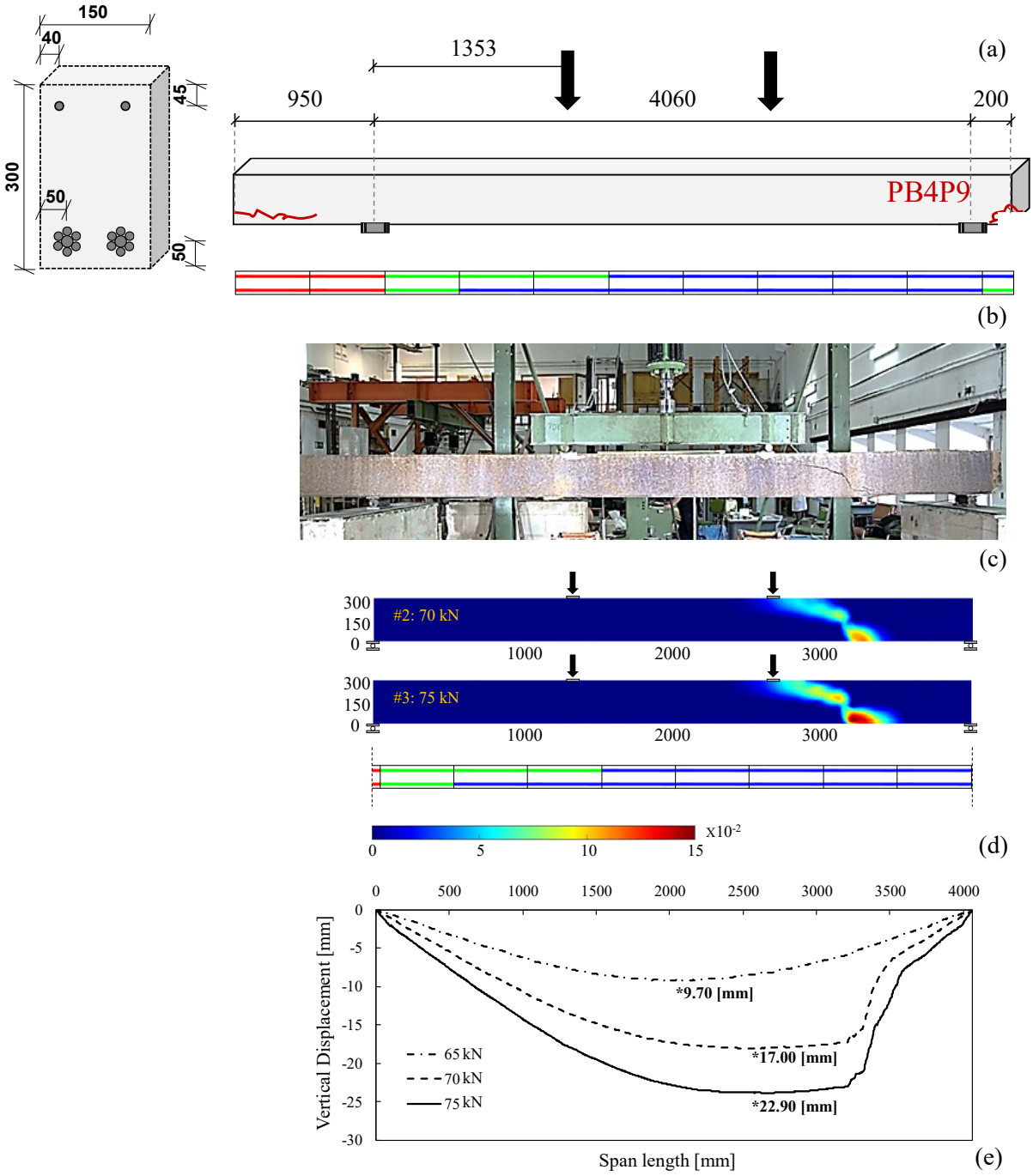

Figure 5-15 Failure analysis of PB4P9 beam: (a) crack pattern, (b) corrosion patter, (c) beam at failure, (d) DIC analysis and (e) vertical displacement along the beam length for increasing load values.

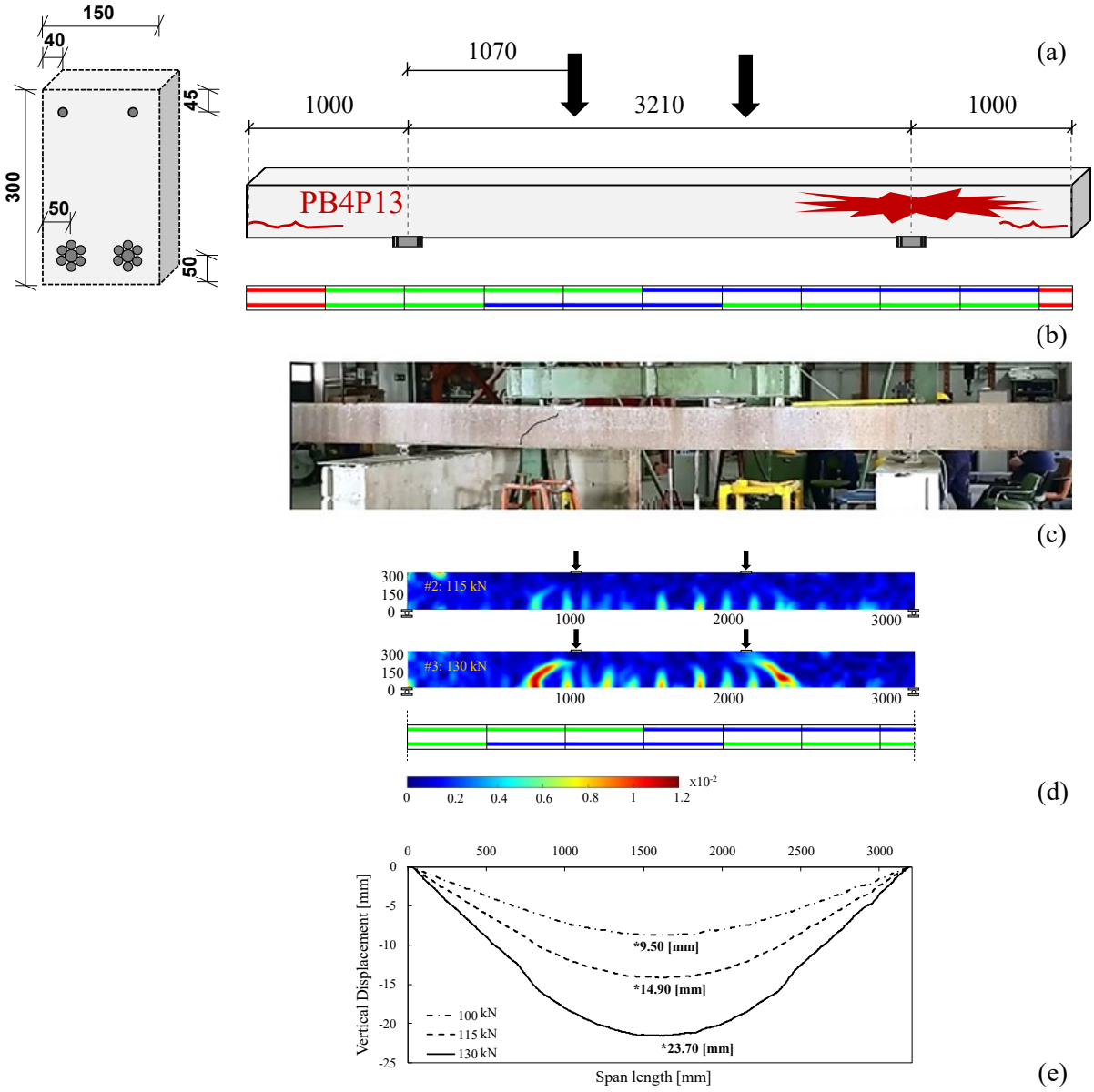

Figure 5-16 Failure analysis of PB4P13 beam: (a) crack pattern, (b) corrosion patter, (c) beam at failure, (d) DIC analysis and (e) vertical displacement along the beam length for increasing load values.

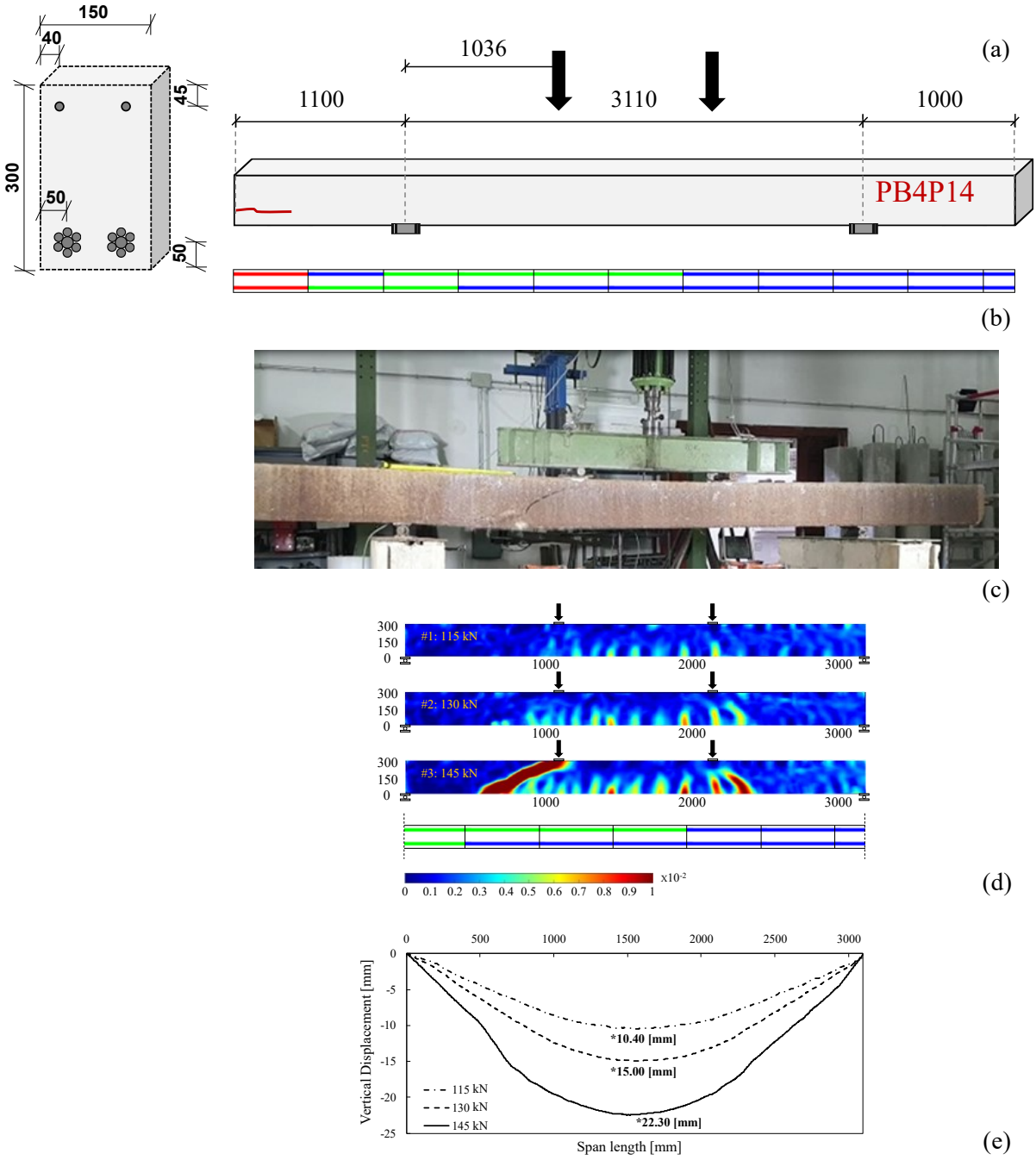

Figure 5-17 Failure analysis of PB4P14 beam: (a) crack pattern, (b) corrosion patter, (c) beam at failure, (d) DIC analysis and (e) vertical displacement along the beam length for increasing load values.

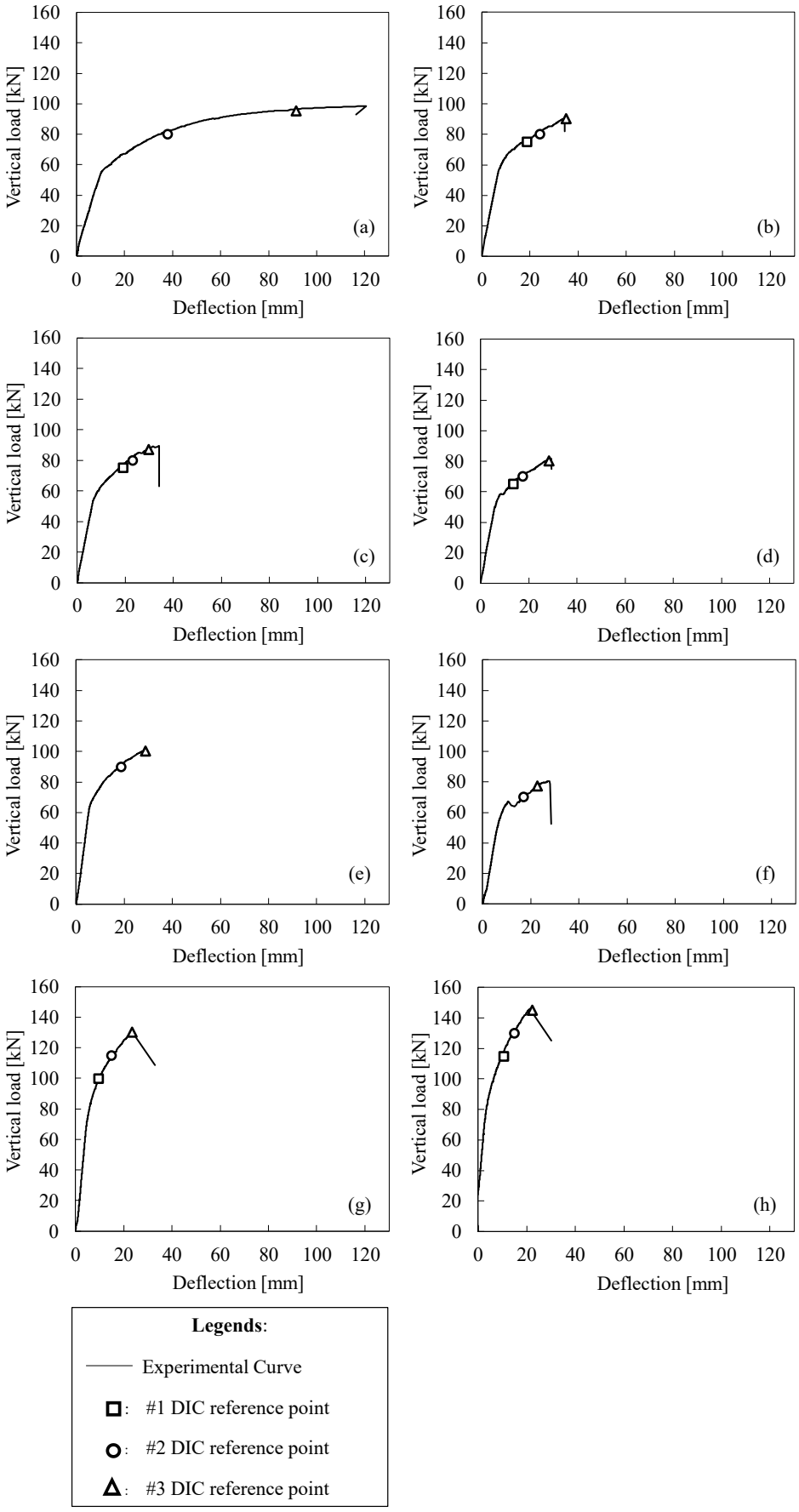

Figure 5-18 Experimental load-deflection curve from four-point bending tests for beam: (a) PBN4P2, (b) PB4P5, (c) PB4P6, (d) PB4P7, (e) PB4P8, (f) PB4P9, (g) PB4P13 and (h) PB4P14.

5.5.1 Main observations

This section summarises the experimental results obtained from the four-point bending tests on seven naturally corroded PC beams and one un-corroded control specimen. As in the previous residual flexural capacity evaluation of corroded PC beams, the mechanical shear behaviour of corroded specimens without transversal reinforcements was thoroughly investigated by conducting the DIC methodology and by performing a visual classification of the corrosion level of the extracted prestressing reinforcements. Based on the obtained outcomes, the following main observations can be highlighted:

- Although the tested beams were characterized by different shear span-to-depth ratios, two failure modes, denoted as Shear I and Shear II, were defined. In this context, the governing parameters were the variable shear span-to-depth-ratio and the corrosion levels of the prestressing reinforcements and their longitudinal spatial variability along the beam length.
- Shear I mode was characterized by a shear-bending interaction prior to failure. Indeed, bending vertical cracks developed before the occurrence of a diagonal shear crack that led to the beam collapse. On the contrary, Shear II mode showed the presence of a single diagonal crack that formed from the loading steel plate towards the prestressing reinforcement. Nevertheless, bond decay due to chloride-induced corrosion at prestressing steel–concrete interface might have played a relevant role in the shear failure mode of severely corroded PC beams, as highlighted by the sudden drops visible in the vertical displacement diagrams of beams PB4P5, PB4P7 and PB4P9.
- The corrosion level distribution of prestressing reinforcements, especially in the region between supports, plays a fundamental role in the shear failure mode of corroded PC beams without transversal reinforcements. In fact, the critical diagonal crack that led to the beam collapse, usually developed in correspondence to the highest recorded corrosion level of strands, except for beam PB4P9, which failure – however – was strongly affected by bond decay. In addition, the occurrence of diagonal cracks having significant crack opening widths induced detrimental effects on the residual shear performance by reducing the aggregate interlock contribution.
- In general, it was observed that the strain localization induced by prestressing strands deterioration may lead to premature beam failure. Indeed, for corroded PC beams with similar a/d ratios, the residual shear resistance decreased with increasing strand corrosion level. Therefore, if compared to the un-corroded specimen, a tangible

reduction in terms of ultimate load-carrying capacity, ultimate deflection, and ductility was commonly detected for corroded PC beams, as visible in Figure 5-18.

6 Evaluation of the pitting morphology of corroded strands

6.1 Highlights

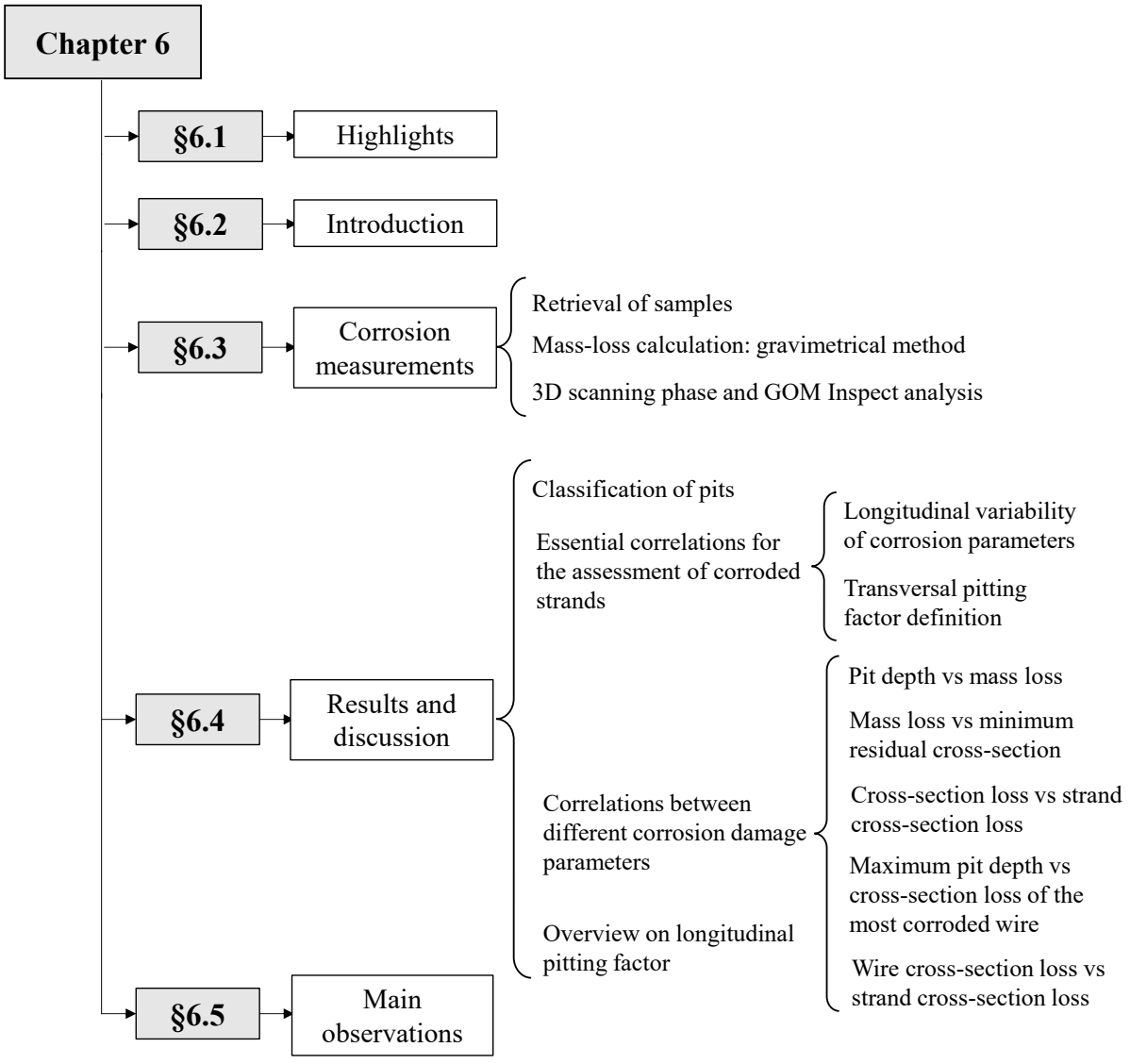

IMPORTANT NOTES: The topics covered in this chapter directly refers to statements, figures and results published by the author in the below mentioned works available in scientific literature:

- **Franceschini L.**, Belletti B., Tondolo F. & Sanchez J. (2022). *Study on the probability distribution of pitting for naturally corroded prestressing strands accounting for surface defects*. Buildings 12, 1732. https://doi.org/10.3390/buildings12101732

- Vecchi F., **Franceschini L.**, Tondolo F., Belletti B., Sanchez J. & Minetola P. (2021). *Corrosion morphology of prestressing steel strands in naturally corroded PC beams*. Construction and Building Materials, 296, pp. 1-20. https://doi.org/10.1016/j.conbuildmat.2021.123720

- **Franceschini L.**, Belletti B., Sanchez J. & Tondolo F. (2022). *Dependency of pitting corrosion spatial variability on crack pattern of prestressed concrete members*. Proceedings of the 14th *fib* PhD Symposium, 5th – 7th September 2022, Rome, Italy.

- **Franceschini L.**, Vecchi F., Tondolo F., Belletti B., Sanchez, J. & Minetola, P. (2021). *Variability in section loss and maximum pit depth of corroded prestressing wires*. 1st Conference of the European Association on Quality Control of Bridges and Structures – EUROSTRUCT2021, 29th August – 1st September, Padova, Italy.

Specifically, the experimental tensile tests on corroded and un-corroded prestressing strands were conducted at the Politecnico of Turin. Furthermore, the 3D scanning procedure and cleaning phase of corroded strands were performed by Anna Scuncia from the University of Parma during her Master Thesis, entitled “Study of strands of naturally corroded prestressed concrete beams”

6.2 Introduction

Over the last years, the scientific community has shown an increased interest in the pitting morphology spatial variability mainly due to its importance in the evaluation of the residual performance of existing structures and to the significant role of its corrosion parameters in guidelines and codes. To this aim, the accurate estimation of corrosion effects has been pursued to prevent and avoid catastrophic structural failures and to ensure the safety of existing structures and infrastructures. In this context, a proper evaluation of the pitting morphology plays a key role for the quantification of corrosion parameters, such as mass loss (η), cross-sectional loss (μ), and maximum penetration depth (P_{max}), that commonly govern the residual mechanical behaviour of corroded reinforcements. However, as previously mentioned for the experimental campaigns conducted on the prediction of the residual mechanical properties of deteriorated reinforcements, a larger amount of studies have been carried out on reinforcing rebars instead of prestressing strands, (Akpanyung & Loto, 2019; A. Apostolopoulos et al., 2013; Caines et al., 2013; Finozzi et al., 2018; González et al., 1995; Li et al., 2019; A. A. Torres-Acosta & Martnez-Madrid, 2003; Yu et al., 2015b). Among the few works investigating prestressing strands characteristics, worth mentioning is Yoo et al. (2020), who studied forty naturally corroded samples retrieved from prestressed concrete box-girder bridges located near Seoul, in the Republic of Korea, and proposed correlations between the measured penetration depths and the cross-sectional losses of the forty-nine investigated sections. Another work from Darmawan and Stewart (2007) introduced a probabilistic approach for estimating the penetration depth and pitting spatial variability of corroded prestressing wires and strands subjected to an artificially accelerated corrosion process.

Besides, as previously discussed in section 3.5.1, several pit type morphology configurations have been introduced for the detailed quantification of sectional corrosion damage. Nevertheless, the simplified hemispherical shape has been widely adopted in scientific literature to easily estimate the area loss due to pitting, (D. V. Val, 2007). However, referring to numerical simulations, other pit type morphology configurations, such as the ellipsoid configuration introduced by Hou & Song (2015), can be implemented to better reproduce the associated corrosion effects. Still, as highlighted by Wang et al. (2020), the quantification of pitting morphology spatial variability might lead to inconsistent results if conducted on the evaluation of the only penetration depth. As a result, both longitudinal and transversal pitting variability must be analyzed to accurately describe the overall damage induced by the chloride-induced corrosion process on prestressing reinforcements. To this goal, twenty-four seven-wire

strands – coming from the previously tested naturally corroded PC beams – were first retrieved. Second, the pitting morphology was investigated by adopting a structured light 3D scanner and measured pits were classified in terms of maximum penetration depth, longitudinal dimension, and transversal width. Thereafter, several corrosion parameters such as mass loss, area loss due to pitting, residual cross-sectional area and cross-sectional loss of external corroded wires were measured and discussed using the GOM Inspect software. Moreover, the pitting factor of naturally corroded strands was studied for the first time by considering both longitudinal and transversal variability. Finally, new correlations between the main investigated corrosion parameters were identified in order to provide useful tools for the in-situ inspection of existing structures as well as to propose simplified expressions conceived for the daily engineering practice of current codes and guidelines.

6.3 Corrosion measurements

The experimental procedure adopted for the analysis of the pitting morphology spatial variability of corroded prestressing strands is described. In particular, five main phases can be outlined:

- Retrieval of corroded prestressing strand samples from previously tested PC beams;
- Mass loss, η, calculation through the adoption of the gravimetrical method described by the ASTM G1-03 standard, (*ASTM G1-03. Standard Practice for Preparing, Cleaning, and Evaluating Corrosion Test Specimens.*, 2017);
- 3D scanning of available samples by using the 3D structured laser scanner of the GOM ATOS series;
- Measurement of corrosion parameters through the superimposition principle of corroded and un-corroded 3D models of analyzed samples conducted by means of the GOM Inspect software;
- Data post-processing for the provision of useful relationships to better estimate pitting morphology effects on corroded strand with a particular focus on the evaluation of the main corrosion parameters that should be considered in design and maintenance procedures of codes and guidelines as directly impacting the residual mechanical response of corroded reinforcements.

For the sake of clarity, Figure 6-1 briefly summarises the adopted step-by-step procedure.

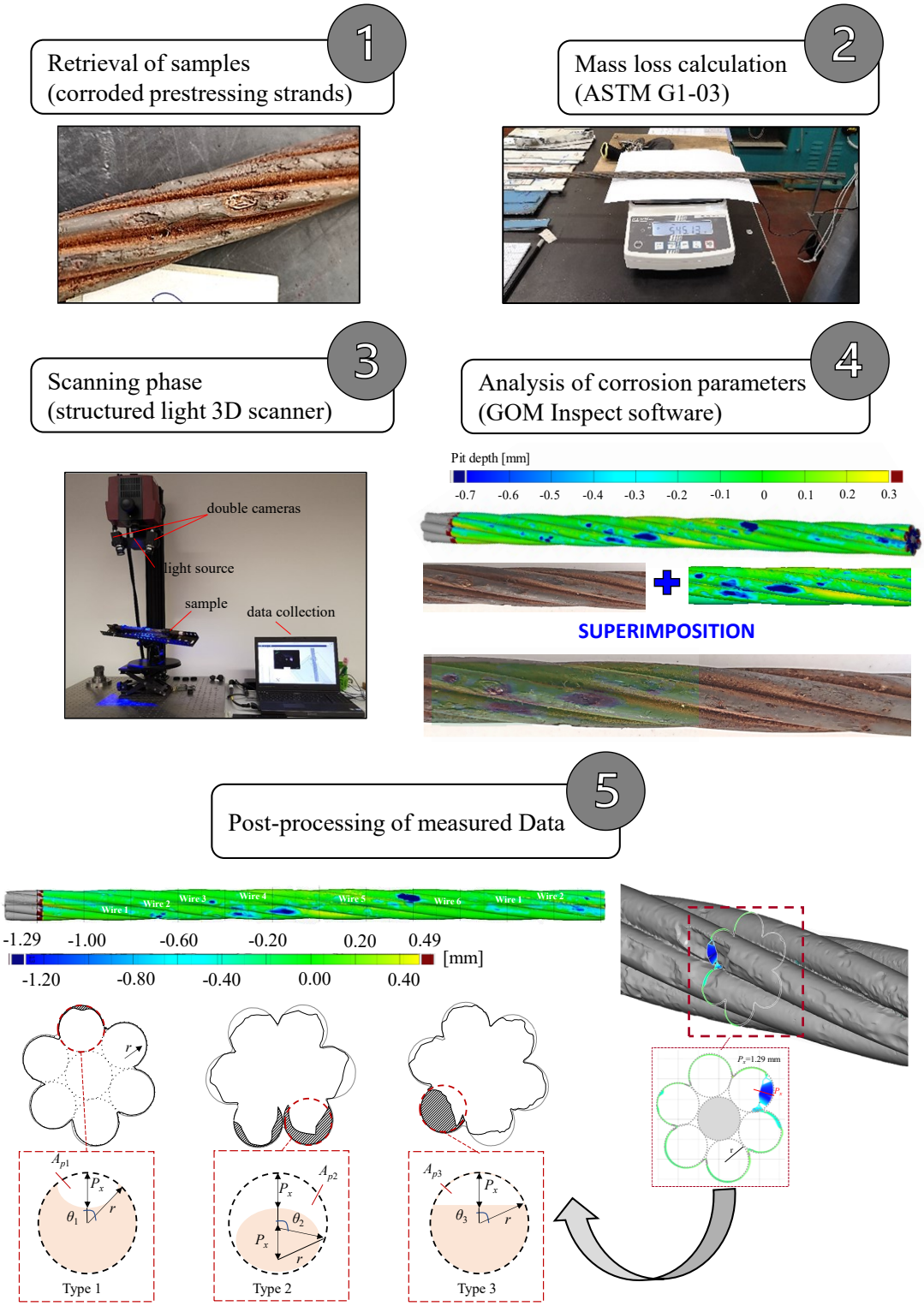

Figure 6-1 Step-by step procedure for the pitting morphology analysis.

6.3.1 Retrieval of corroded prestressing strand samples

After residual load-carrying capacity tests, the prestressing strands of each corroded beam were extracted and the corrosion pattern of each beam was drawn. Thereafter, a total of twenty-four prestressing strands samples – four from each beam – was retrieved from different beam positions. To distinguish the available samples, an identifying code – similar to the one adopted for corroded PC beams classification – was introduced. The code is in the form – PB*w*-L(*yy-zz*) or PB*w*-R(*yy-zz*) – where PB stands for Prestressed Beams, *w* is the number ranging from 9 to 14 which identifies the name of the tested beam belonging to the second experimental campaign, the letter L or R refers to the left or right cross-section position of the prestressing reinforcement from which the sample was retrieved, and the coordinates in brackets, *yy-zz*, identify the position of the sample along the beam length – from the left edge side to the right one – by defining its initial and final abscissa.

The available corroded strands were first classified as a function of the sample length, L_i, as shown in Figure 6-3. Indeed, twelve samples were 450 mm long, whereas the remaining twelve were 700 mm long. Considering corrosion evidence, the twenty-four samples were further classified through a visual inspection by distinguishing between three corrosion levels (low, intermediate and high). The samples belonging to the low corrosion level, denoted as LV-I, were characterized by small and localized pits; the samples from the intermediate level, denoted as LV-II, had bigger and widespread pits; finally the ones classified with high corrosion level, denoted as LV-III, showed deep and oversized pits, covering a large region of the external wire surface with a significant rust products formation. During the visual inspection, four samples – PB9-R(428-473), PB11-L(5-75), PB12-R(358-403) and PB14-L(455-500) – were found to be unaffected by corrosion signs and consequently they were assumed as un-corroded reference samples.

For the sake of completeness, Figure 6-2 shows the position from which the corroded samples were retrieved, further distinguishing between samples belonging to or not belonging to beam regions characterized by the presence of concrete surface defects, denoted as “cracked” and “un-cracked” regions, respectively. Moreover, Table 6-1 provides the following information for each sample: (i) the corresponding identifying code, (ii) the length, L_i, (iii) the level of corrosion established from visual inspection, and (iv) info regarding the presence or absence of concrete surface defects.

Table 6-1 Classification of retrieved prestressing strands samples.

Sample ID	L_i [mm]	L_{scan} [mm]	*Corrosion level (visual inspection)*	Presence/absence of surface defects
PB9-L(12-82)	700	500	LV-III	*cracked*
PB9-L(426-496)	700	500	LV-II	*un-cracked*
PB9-R(15-60)	450	250	LV-III	*cracked*
PB9-R(428-473)	450	250	LV-I	**un-corroded**
PB10-L(138-208)	700	500	LV-I	*un-cracked*
PB10-L(445-515)	700	500	LV-II	*un-cracked*
PB10-R(32-102)	700	500	LV-II	*un-cracked*
PB10-R(287-332)	450	250	LV-II	*cracked*
PB11-L(5-75)	700	500	LV-II	**un-corroded**
PB11-L(196-266)	700	500	LV-II	*un-cracked*
PB11-R(6-51)	450	250	LV-I	*un-cracked*
PB11-R(273-318)	450	250	LV-II	*un-cracked*
PB12-L(12-82)	700	500	LV-III	*cracked*
PB12-L(124-169)	450	250	LV-II	*un-cracked*
PB12-R(100-170)	700	500	LV-II	*un-cracked*
PB12-R(358-403)	450	250	LV-I	**un-corroded**
PB13-L(1-46)	450	250	LV-II	*cracked*
PB13-L(108-178)	700	500	LV-II	*un-cracked*
PB13-R(0-70)	700	500	LV-III	*cracked*
PB13-R(70-115)	450	250	LV-II	*un-cracked*
PB14-L(10-55)	450	250	LV-III	*cracked*
PB14-L(455-500)	450	250	LV-I	**un-corroded**
PB14-R(2-72)	700	500	LV-III	*cracked*
PB14-R(77-122)	450	250	LV-II	*un-cracked*

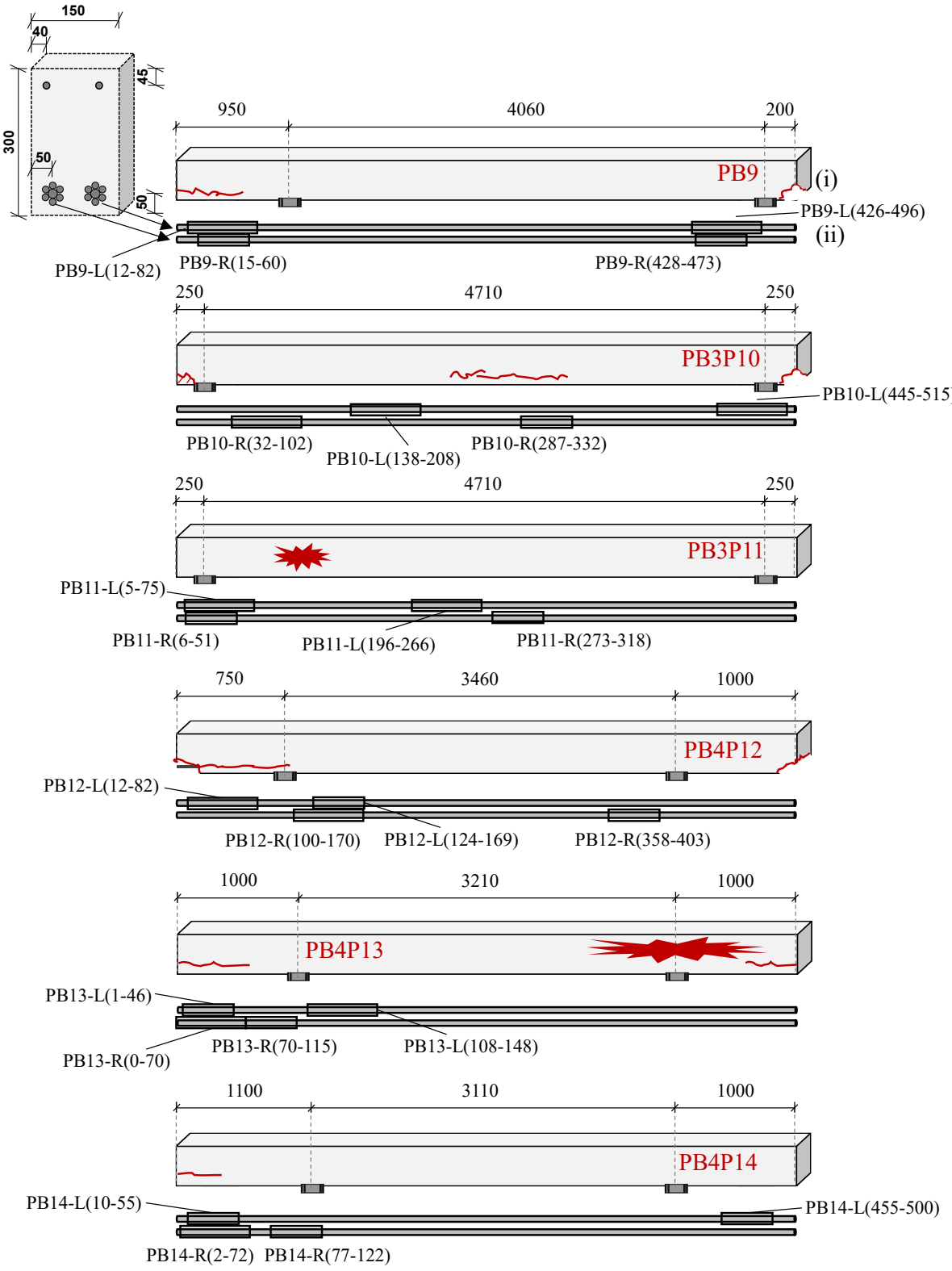

Figure 6-2 Location of samples and relations with crack pattern.

(a) (b)

Figure 6-3 Retrieved samples classified as a function of L_i: (a) twelve samples 450 mm long and (b) twelve samples 700 mm long.

6.3.2 Mass loss calculation: gravimetrical method

Following visual inspection, the mass loss, η, of each corroded sample was calculated by adopting the gravimetrical method proposed in the ASTM G1-03 standard (2017). For this purpose, a digital scale with an accuracy of 0.01 g was adopted for the weighing of corroded and un-corroded samples. According to this method, the mass loss of a corroded strand was defined through the expression previously reported in its basic form in Eq. 3-2 and recalled in Eq. 6-1 in its updated version:

$$\eta = \frac{m_0 - m_{corr}}{m_0} = \frac{m_{uc}L_i - \left(m_0 - \left(\Delta_1 + \Delta_2\right)\right)}{m_{uc}L_i} = \\ = \frac{m_{uc}L_i - \left(m_{uc}L_i - \left(\Delta_1 + \Delta_2\right)\right)}{m_{uc}L_i} = \frac{\left(\Delta_1 + \Delta_2\right)}{m_{uc}L_i} \quad \text{6-1}$$

where m_0 is the mass of the un-corroded sample (g) and it is defined as the product between m_{uc}, which is the highest weight per unit length measured for the reference un-corroded sample PB14-L(455-500) – equal to 0.7994 g/mm – and L_i, which is the previously calculated sample length (mm); whereas m_{corr} is the mass of the corroded sample and it is calculated as the difference between m_0 and the total weight loss caused by corrosion, which is evaluated as the sum of Δ_1 and Δ_2. In detail, Δ_1 is the weight loss due to first handling, while Δ_2 is the weight loss estimated during the cleaning procedure of the corroded sample. As indicated by the ASTM G1-03 standard, this latter was evaluated through a sequence of cleaning cycles conducted by using a steel brush. A bilinear trend – identified by lines AB and BC – having different slopes, was plotted interpolating the weight loss variation, Δ_i, calculated at each cleaning cycle of a

corroded sample. As shown in Figure 6-4, a large amount of rust products was removed during the first cleaning cycle, leading to a significant Δ_i value – line AB. After the second one, the increase in Δ_i values were less evident since the rust products removed were gradually decreasing at each cleaning cycle, as demonstrated by the smoother slope of line BC. As a result, the final value of Δ_2 (g) was estimated at the intersection point between line AB and line BC, as shown by the blue star in Figure 6-4. Finally, the mass loss value, η, of each investigated corroded sample is reported in Table 6-2.

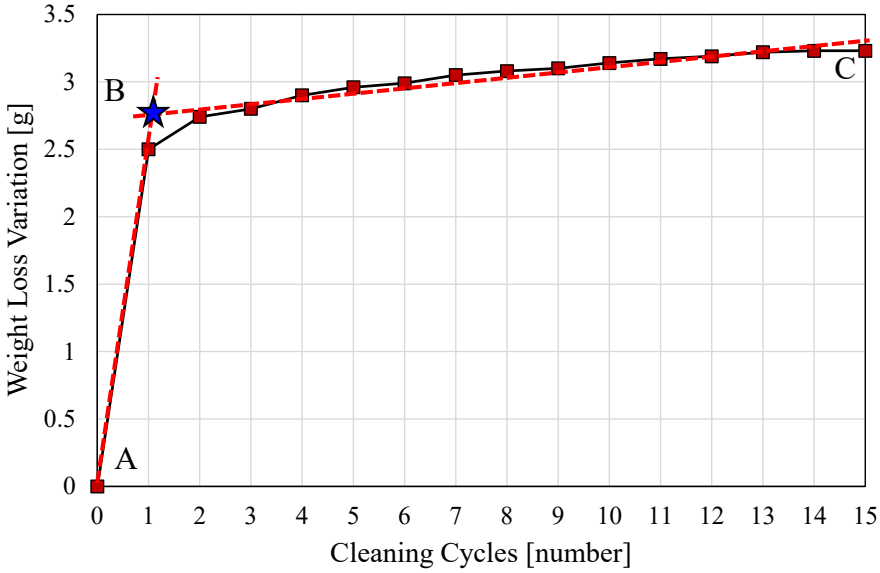

Figure 6-4 Estimation of the weight loss Δ_2 in the case of sample PB11-L(196-266).

6.3.3 3D Scanning procedure and GOM Inspect software analysis

The following phase involved the 3D scanning of the twenty-four available strand samples using a 3D structured light laser scanner of the ATOS series. The overall set-up, highlighted in Figure 6-5, consisted in:

- A custom-made fixing system composed of a metal support plate and two bearings of ABS material, realized ad-hoc using a 3D printer, which allowed to fix samples with variable lengths and to rotate each sample along its longitudinal axis during the scanning phase, Figure 6-5(a);
- Reference octagonal prisms supports realized with the help of a 3D printer using PLA filaments, Figure 6-5 (b);

- The ATOS Compact 3D structured light scanner with two 2-megapixel cameras measuring the 3D coordinates of each point of the sample surface by applying the triangulation principle, Figure 6-5(a);
- A portable computer with a data acquisition system receiving the 3D scanner data in the form of ".STL format" and reproducing the virtual model of the sample geometry. The model consisted of tessellated surfaces made up of triangles created from a cloud of points scattered in space resulting from the 3D scanning activity.

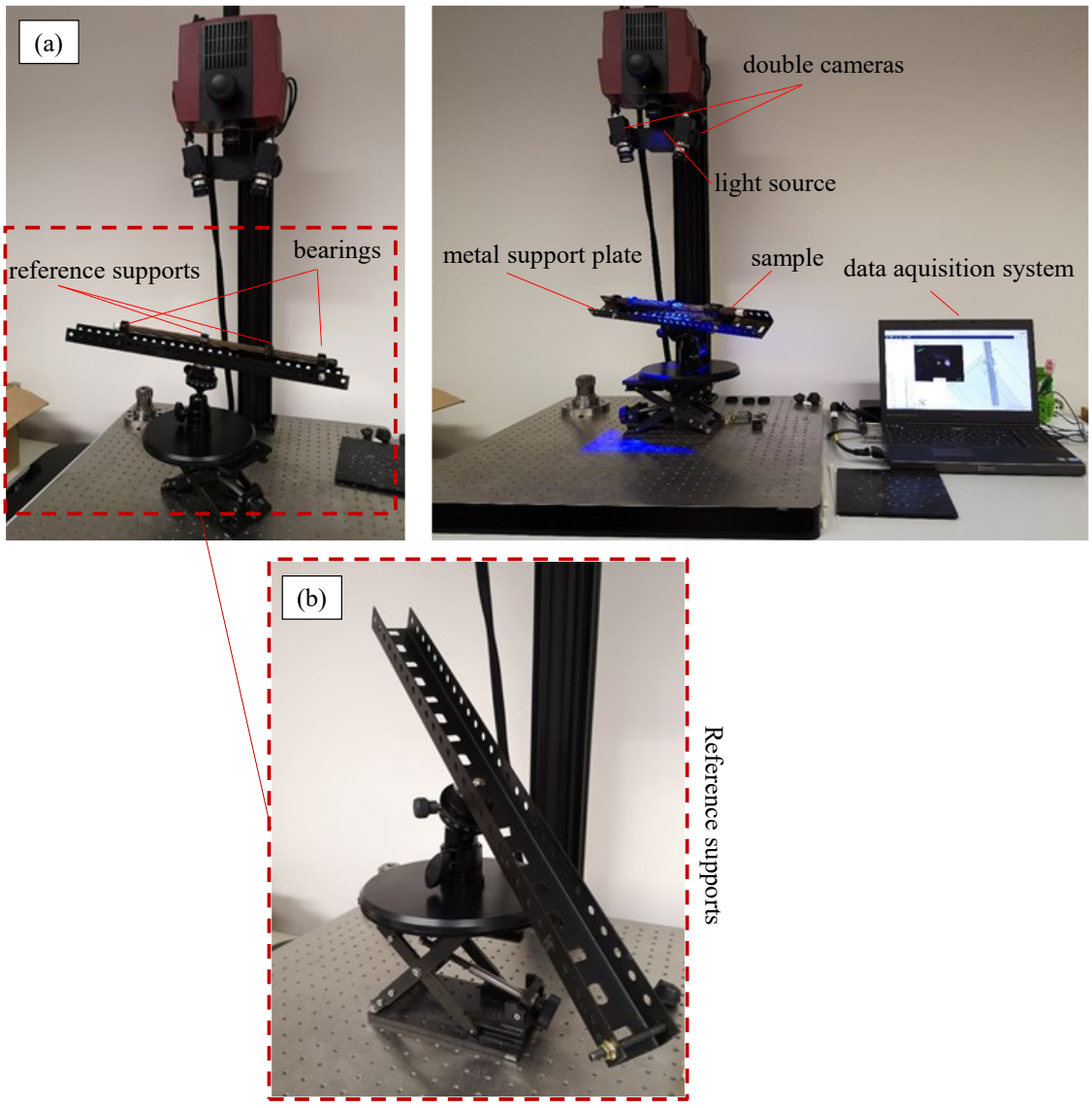

Figure 6-5 3D scanning system: (a) general overview of the final configuration and (b) focus on principal components.

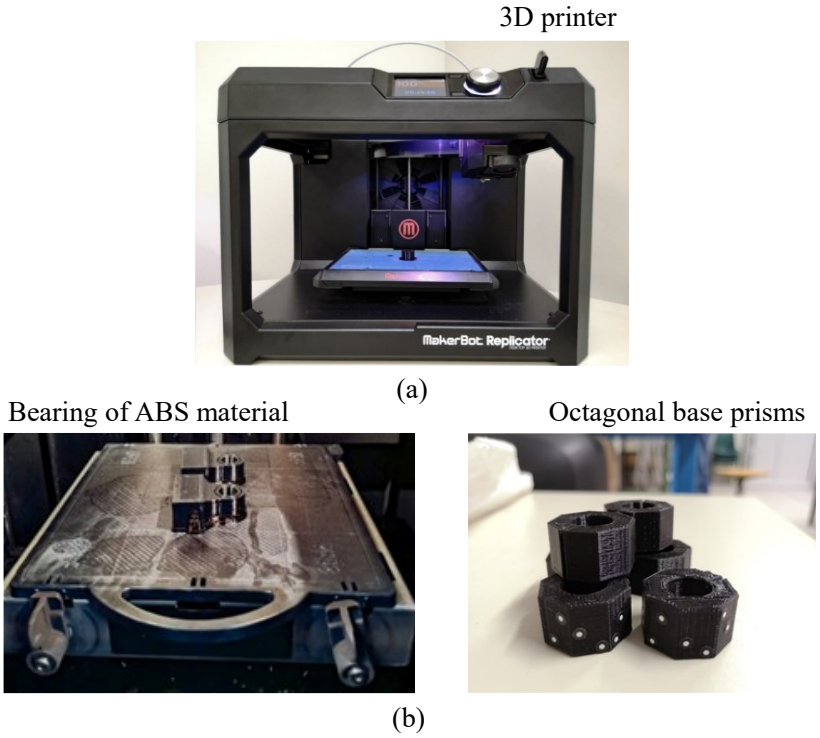

Figure 6-6 Custom-made fixing elements: (a) 3D printer and (b) realized components.

First, the sample was thoroughly cleaned in order to remove impurities and poor traces. Second, a thin layer of the opaque-reflection agent Metal Service MR® 2000 Anti-Reflex L was uniformly applied to the sample surface to reduce the typical metal reflection and to enhance sample contrast in the images captured by the 3D stereoscopic cameras. In support of this, the study conducted by Iuliano & Minetola (2009) demonstrated the faithfulness and reliability of scanning measurements when anti-reflection agents were used. Third, the sample was positioned in the working volume of the 3D scanner, making use of the custom-made fixing system. The working volume of the ATOS Compact scanner was 125 mm x 90 mm x 90 mm and its length measurement error was smaller than 0.020 mm as per the acceptance test of VDI/VDE 2634 Part 3 guideline. Next, round adhesive markers of 1.5 mm diameter with a central white circle were placed on the faces of the octagonal prisms to create a network of fixed reference points that allowed the GOM scan software to automatically align the data from multiple scans into the same cartesian reference system. Finally, a cloud of points was recorded during the scanning phase, which the scanning software converted into tessellated surfaces using triangles. The virtual model of the real geometry was then exported in .STL format to be further updated and analyzed with the GOM Inspect software.

As reported in Table 6-1, the scanned length, L_{scan}, varied for strand samples with total lengths of 450 mm or 700 mm. In detail, the scanned length of each sample was reduced by 100 mm on both end sides to account for the presence of the gripping system during the subsequent tensile testing. As a result, the final L_{scan} resulted equal to 250 mm and 500 mm.

To confirm the usefulness and the accuracy of the adopted procedure, Li et al. (2017) and Tahershamsi et al. (2017) pointed out that the 3D scanning technique is considered by the scientific community as the most precise technique for the evaluation of the geometrical parameter of pitting corrosion since it avoids the shortcomings of other available methods such as (i) weight loss, (ii) vernier caliper and (iii) drainage method, ensuring low cost, high efficiency and high precision measurements. The main drawback is that only the surfaces of the six outer wires can be scanned, with no possibility of detecting the corrosion damage of the central wire as well as the inner surfaces of the external wires. Nevertheless, as confirmed by the visual inspection prior to and after the tensile test procedure, these regions of the corroded samples did not show any significant sign of corrosion; they can therefore be considered as un-corroded in the following discussion as they did not alter the obtained results.

The final step consisted in the GOM Inspect software analysis. To this end, the virtual model generated by the 3D scanning procedure was first imported into the software for the mesh repairing phase, which involved the filling in of small holes and the removal of noise points, Figure 6-7(a). Subsequently, 3D models of corroded and un-corroded samples were superimposed to measure the variation of the main geometric parameters affecting pitting corrosion, as shown in Figure 6-7(b). In detail, this last step was enabled by the use of the best-fit algorithm implemented in the GOM Inspect software for aligning the scan data from the corroded sample with respect to the reference one. For this purpose, the roto-translation matrix was iteratively computed by the software in order to minimize the error associated with the alignment and superimposition steps. The measuring accuracy of the GOM Inspect has been certified by the German PTB Institute of the American NIST Institute. However, technical errors caused by an optical occlusion occurred during the scanning phase of samples PB10-R(32-102) and PB11-R(273-318); therefore some corrosion parameters could not be properly measured and were neglected in the comparison of the obtained experimental data.

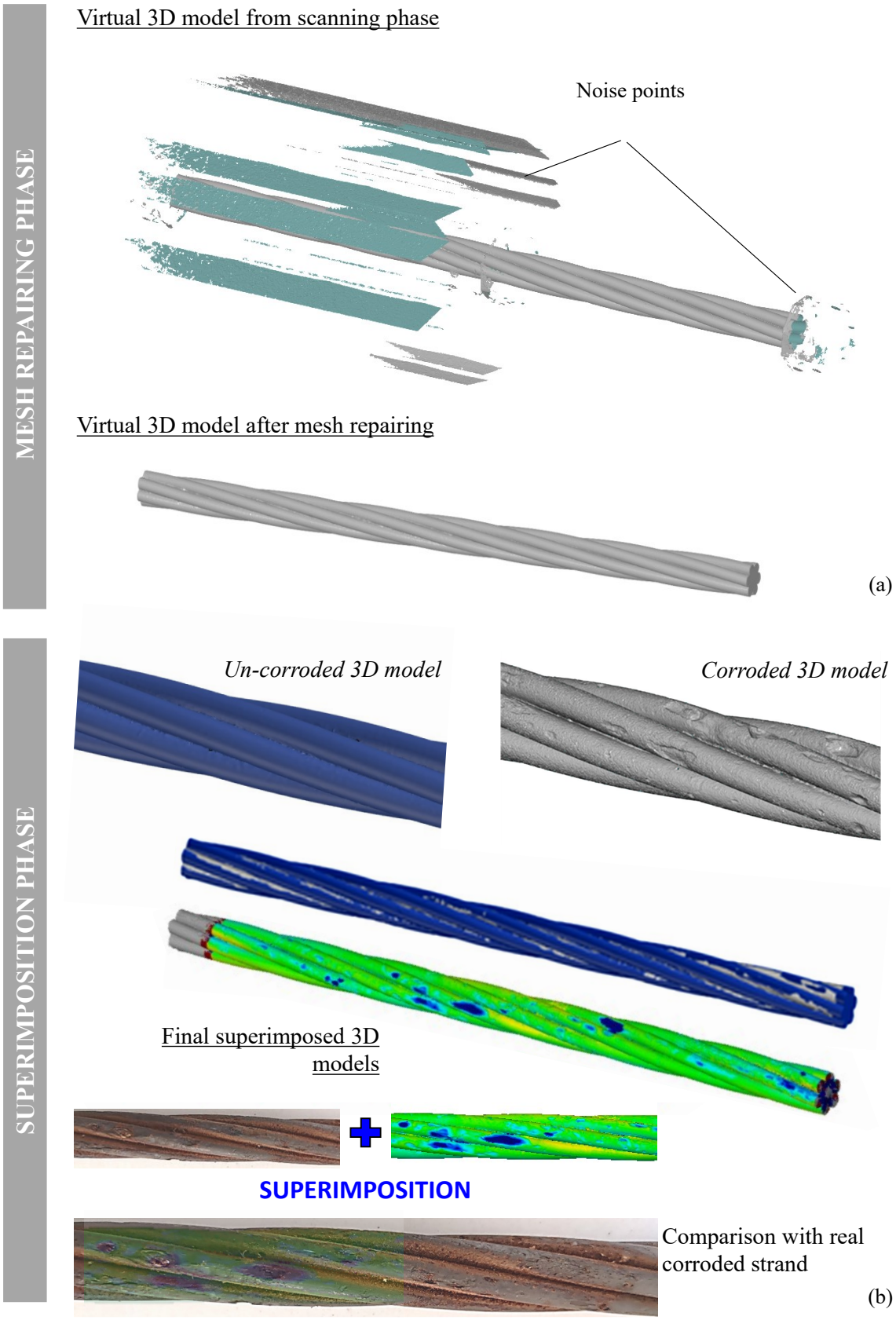

Figure 6-7 GOM Inspect phase: (a) mesh repairing and (b) superimposition of corroded and un-corroded 3D models.

Based on the software performance, the following parameters were analyzed to correctly assess the impact of chloride-induced corrosion on the behaviour of corroded prestressing reinforcements:

- Number of pits, n_{pits}, and their distribution along the sample length;
- Pit shape in terms of longitudinal extension, P_y, and transversal width, P_z;
- Pit penetration depth, P_x, with a particular focus on the measurement of its maximum value evaluated longitudinally along the overall sample length, $P_{max,long}$, or sectionally, $P_{max,sectional}$;
- Area loss caused by pit, A_p;
- Minimum, A_{min}, residual cross-sectional area of the strand.

For the sake of clarity, Figure 6-8 highlights the meaning of the investigated parameters.

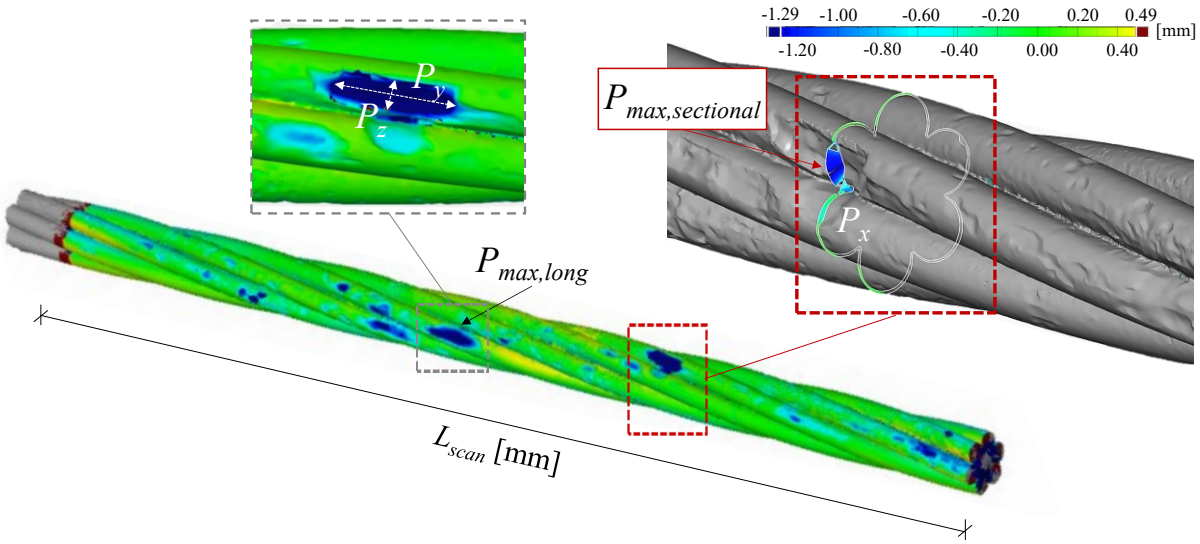

Figure 6-8 Focus on the analyzed corrosion parameters.

6.4 Results and Discussion

6.4.1 Classification of detected pits

Since four of the twenty-four retrieved strands were assumed to be un-corroded reference samples due to the absence of corrosion signs, and the scanning phase of two corroded samples (PB10-R(32-102) and PB11-R(273-318)) was characterized by technical issues, a total of 18 corroded prestressing strands were investigated in-deep.

First, the number of pits, n_{pits}, along the overall sample length was quickly determined by comparing corroded and un-corroded 3D models, as shown in Figure 6-9.

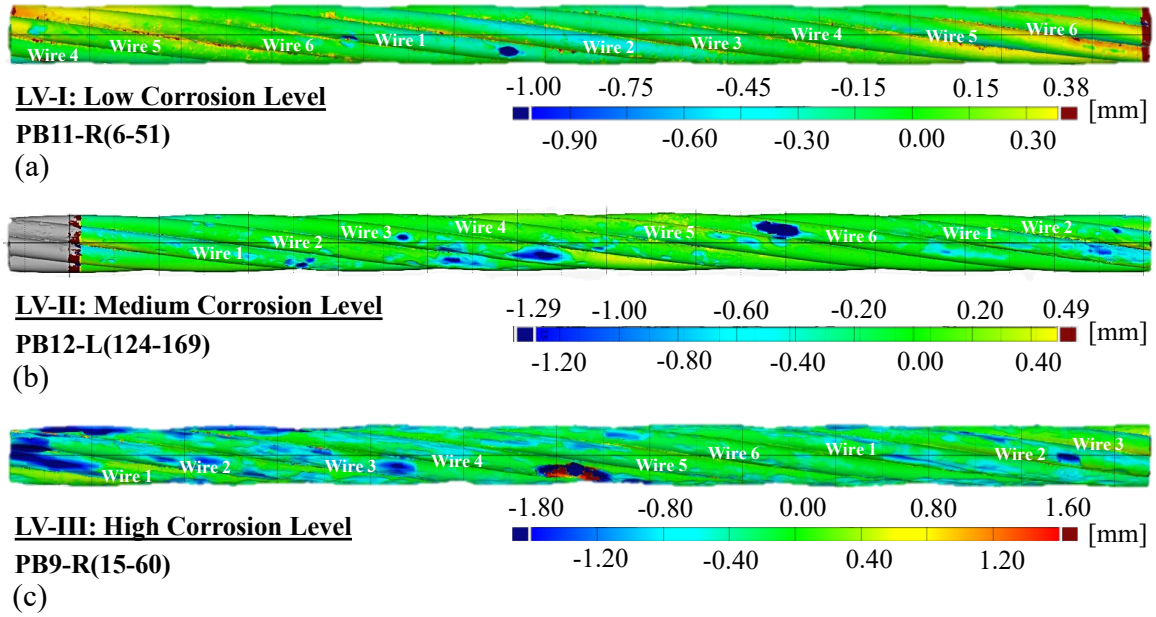

Figure 6-9 Calculation of number of pits as a function of different corrosion level: (a) low corrosion, (b) intermediate corrosion, and (c) high corrosion level.

To compare data from corroded samples of different lengths, the number of counted pits, n_{pits}, was normalized by dividing it by the scanned length, L_{scan}. The results – expressed as the number of pits per meter, n_{pits}/m, – are reported in Table 6-2. Since the analyzed samples were seven-wire prestressing strands with six external wires, a maximum of six pits with different penetration depths, P_x, could be measured at each section. Afterwards, a sectional analysis was performed every 10 mm on each corroded sample by adopting the approach outlined by Li et al. (2017), as shown in Figure 6-10.

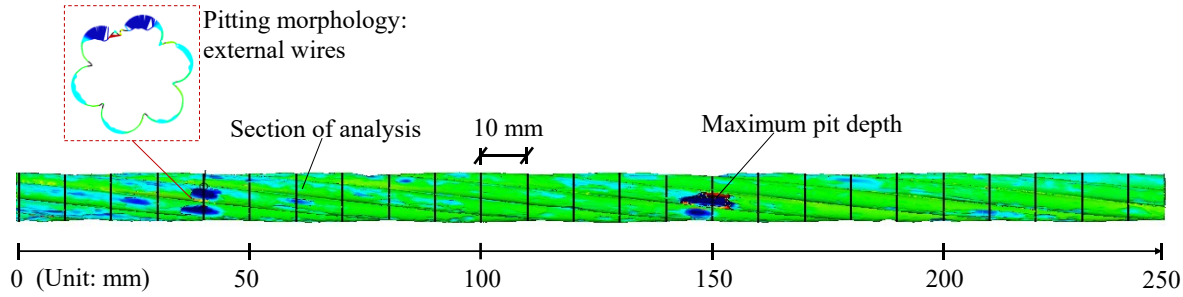

Figure 6-10 Sectional analysis every 10 mm for the evaluation of pitting corrosion parameters.

The maximum penetration depth has been considered by the scientific community as one of the main parameters influencing the residual mechanical behaviour of corroded rebars and/or prestressing strands. Therefore, an accurate classification of the maximum pit of each external wire (for the 18 collected samples) was carried out by measuring the penetration depth, $P_{max,sectional}$, and the pit shape in terms of P_y and P_z, Figure 6-8. The acquired results are reported in Appendix A.3 for completeness. Furthermore, since Jeon et al. (2019) stated that the failure of a corroded strands is governed by the failure of the most corroded wire where the maximum penetration depth is measured, the corresponding value of $P_{max,long}$ of each analyzed sample is reported in Table 6-2.

Additionally, the maximum pit of each external wire was classified by comparing the experimentally measured area loss caused by pitting, A_p, with the three pit type morphology configurations introduced by Jeon et al. (2019), as shown in Figure 6-11. The three morphologies, denoted as hemispherical, half-moon and planar, were identified with Type 1, Type 2 and Type 3, respectively. Moreover, the corresponding analytical area losses, A_{pi}, were assessed through Eqs. 6-2 to 6-4:

$$A_{p1} = 2r_{outer}{}^2\left(\vartheta_1 - 2\sin\vartheta_1\cos\vartheta_1\right) \qquad \vartheta_1 = arc\cos\left(1-\frac{P_x}{2r_{outer}}\right) \qquad 6\text{-}2$$

$$A_{p2} = r_{outer}{}^2\left(2\vartheta_2 - \pi - 2\sin\vartheta_2\cos\vartheta_2\right) \qquad \vartheta_2 = arc\cos\left(-\frac{P_x}{2r_{outer}}\right) \qquad 6\text{-}3$$

$$A_{p3} = r_{outer}{}^2\left(\vartheta_3 - \sin\vartheta_3\cos\vartheta_3\right) \qquad \vartheta_3 = arc\cos\left(1-\frac{P_x}{r_{outer}}\right) \qquad 6\text{-}4$$

where r (r_{outer}) is the radius of the un-corroded external wire – equal to 2.13 mm –, π is the Archimedes' constant considered equal to 3.14, and θ_1, θ_2 and θ_3 are the corrosion angles for each different pit shape.

An extensive geometrical analysis of the 101 measured pits can be found in Appendix A.3, including: (i) the experimental area loss due to pitting assessed with the GOM Inspect software, (ii) the analytical values of the area loss calculated by adopting the three different pit type morphology configurations, and (iii) the final classification. For the sake of clarity, Table 6-2 summarizes the measured area loss for the overall maximum pit of each corroded sample together with the corresponding pit type classification.

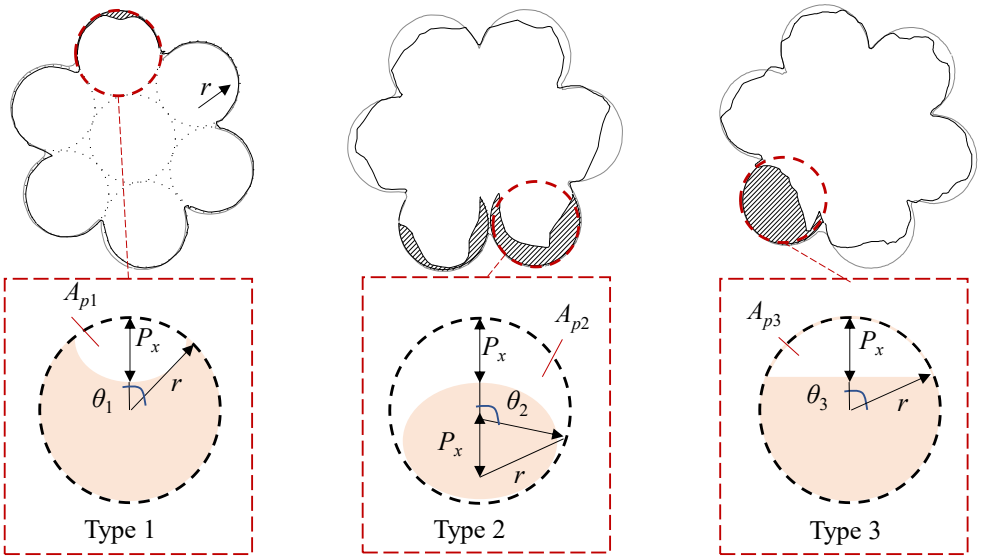

Figure 6-11 Assumed pit type morphology configurations.

Based on the obtained results, 46.5% and 47.5% of the pits were classified as Type 1 and Type 3, respectively, whit the remaining 6% classified as Type 2. When comparing the detected pit type morphology configurations with the three corrosion levels adopted, it could be observed that Type 1 and Type 3 configurations occurred with varying dimensions, especially in the case of intermediate and high corrosion levels, Figure 6-9(b) and (c). In addition, pits measured from samples having low corrosion levels were mostly classified as Type 1, Figure 6-9(a), while Type 2 configuration was mainly observed in samples having high corrosion levels. By tracking the maximum penetration depths against the corresponding estimated area losses, it was evident that a good fitting of Type 1 and Type 3 pits was obtained by adopting Eq. 6-2 and Eq. 6-4, respectively, as highlighted in Figure 6-12(a). On the contrary, a great dispersion of results occurred for Type 2 pits fitted by using Eq. 6-3, which led to an approximate interpolation of the experimental data. Referring to Figure 6-12(a), most of the pits analyzed had maximum penetration depth and area loss values ranging from 0.5 mm to 1.5

mm and 0.5 mm^2 to 5.00 mm^2, respectively. Moreover, only Type 1 and Type 3 pits recorded a penetration depths higher than 1.6 mm.

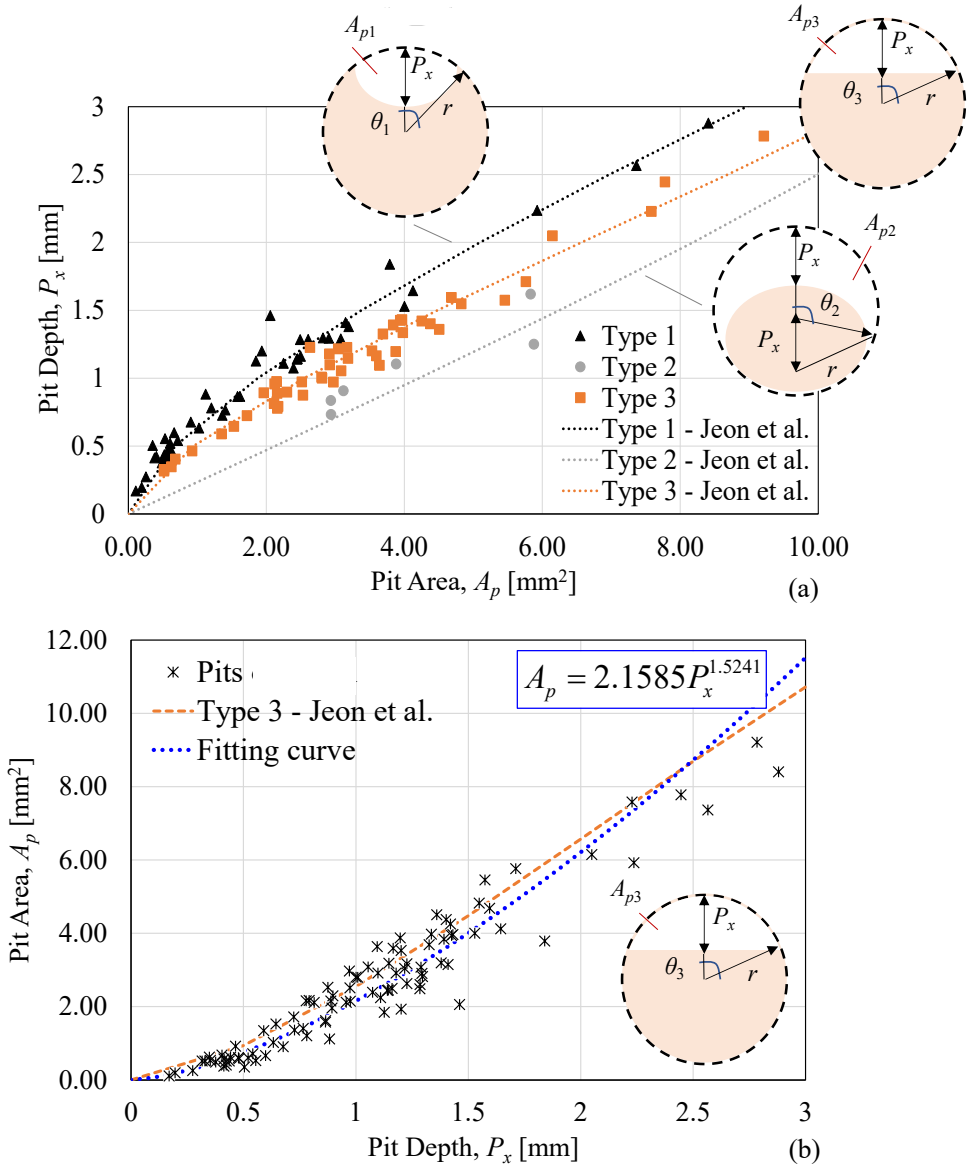

Figure 6-12 Maximum penetration depths classification: (a) adopting three different pit type morphology configurations, and (b) considering only Type 3 morphology.

Although these latter configurations can be expressed through different analytical expressions, their classification during in-situ inspection can be challenging, especially in the case of a high corrosion level, as the two morphologies tend to be quite similar. Given the rarity of Type 2 configuration, it was proposed to adopt the unique Type 3 for the estimation of the area loss, A_p, of all measured pits to avoid assessment errors, as illustrated in Figure 6-12(b). To validate the proposal, the percentage error committed in assuming Type 3 expression instead of using the previously estimated pit type morphology configuration was calculated and

reported – for the overall maximum pit of each corroded sample – in Table 6-2. As a result, a generally safe prediction of the A_p value was obtained with an overestimation of the actual experimental area loss ranging between 7% and 55% with an average overestimation of around 30%. In the case of unsafe predictions, i.e. underestimation of the actual experimental area loss, the average percentage error of the estimated value was limited to 10.60%.

In addition, regardless of the actual pit type morphology configurations, a new exponential relationship for estimating the area loss caused by pitting was achieved through the regression analysis of the experimental data as a function of the measured penetration depth, P_x, as shown in Figure 6-12(b) and reported in Eq. 6-5.

$$A_p = 2.1585 P_x^{1.5241} \qquad 6\text{-}5$$

The faithfulness and the accuracy of the proposed relationship was confirmed by the coefficient of correlation, R^2, equal to 0.913.

Based on the satisfactory fitting of data and taking into account the uncertainties associated with the identification of the actual pit type morphology configuration, the use of Type 3 expression as well as the proposed relationship reported in Eq. 6-5 can be considered as viable technical solutions to be applied during in-situ inspections and daily engineering practice for the preliminary estimation of the area loss due to pitting, A_p.

Table 6-2 Corrosion classification of corroded strands.

Sample ID	η [%]	n_{pits}/m [-]	$P_{max,long}$ [mm]	A_p [mm^2]	*Pit classification*	*Percentage error assuming Type 3 expression* [%]
PB9-L(12-82)	17.30	550	1.71	5.76	3	7.14
PB9-L(426-496)	2.80	22	0.42	0.51	1	-43.44
PB9-R(15-60)	21.50	576	2.78	9.21	3	-7.05
PB9-R(428-473)*	-	-	-	-	-	-
PB10-L(138-208)	2.40	16	0.59	1.35	3	11.39
PB10-L(445-515)	6.30	*N/A	2.45	7.78	3	-8.83
PB10-R(32-102)**	2.20	-	-	-	-	-
PB10-R(287-332)	8.00	250	2.88	8.41	1	-21.87
PB11-L(5-75)*	-	-	-	-	-	-
PB11-L(196-266)	2.90	130	1.40	4.38	3	6.67
PB11-R(6-51)	2.00	40	0.98	2.15	3	-14.62
PB11-R(273-318)	4.80	68	1.26	3.34	3	-
PB12-L(12-82)	14.20	476	1.55	4.82	3	3.00
PB12-L(124-169)	4.30	200	1.23	3.17	3	-7.23
PB12-R(100-170)	5.30	148	1.00	1.98	1	9.08
PB12-R(358-403)*	-	-	-	-	-	-
PB13-L(1-46)	7.60	340	1.16	2.50	1	-26.06
PB13-L(108-178)	4.30	*N/A	1.84	3.79	1	-55.53
PB13-R(0-70)	11.40	522	1.38	3.19	1	-25.15
PB13-R(70-115)	4.60	212	1.01	2.80	3	7.91
PB14-L(10-55)	14.70	592	2.24	5.92	1	-27.86
PB14-L(455-500)*	-	-	-	-	-	-
PB14-R(2-72)	11.60	354	1.23	2.63	3	-29.19
PB14-R(77-122)	3.82	60	0.54	0.71	1	-47.73

*un-corroded sample, **technical issues

6.4.2 Essential correlations for the assessment of corroded strands

6.4.2.1 Longitudinal variability analysis of corrosion parameters

6.4.2.1.1 Penetration depth

The longitudinal variability of the measured penetration depth of each corroded sample was analyzed using the GOM Inspect software.

In general, it was observed how pits formed randomly along the overall sample length as a function of the different chloride concentrations at prestressing reinforcement level; in this context, the measured penetration depths varied significantly in adjacent sections, as shown in Figure 6-13 for samples PB9-R(15-60), PB10-R(287-332), PB11-R(6-51), and PB12-L(124-169). This experimental evidence complemented other scientific studies – such as those conducted by Valor et al. (2010) and Murer & Buchheit (2013) – which supported the randomness of chloride-induced corrosion of reinforcing steel rebars embedded in concrete. In particular, the penetration depth was found to increase with increasing corrosion level, as shown in Figure 6-13 in the case of mass loss values of 2%, 4.3%, 8% and 21.5% for samples PB11-R(6-51), PB12-L(124-169), PB10-R(287-332) and B9-R(15-60), respectively.

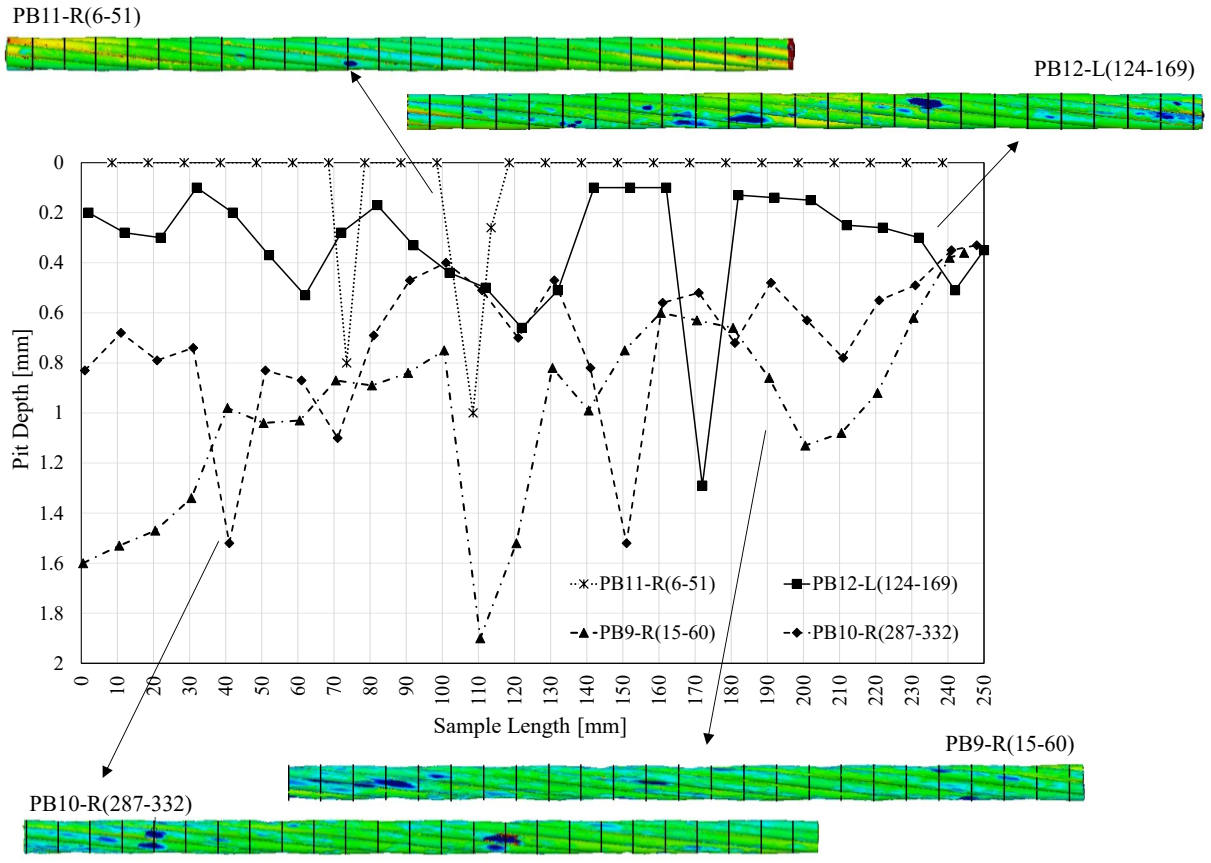

Figure 6-13 Variability of penetration depth as a function of different corrosion levels.

6.4.2.1.2 Penetration depth variability as a function of concrete surface defects

To investigate the consequences induced by the presence or absence of concrete surface defects, the longitudinal pitting spatial variability of corroded strands was analyzed, distinguishing between cracked and un-cracked beam regions, as reported in Table 6-1. To this aim, the measured penetration depth, P_x, of each scanned pit was normalized by dividing it by the un-corroded radius of the external wire, r_{outer}, (P_x/r_{outer}).

Referring to corroded samples retrieved from beam regions unaffected by concrete surface defects, Figure 6-14 depicts the rising severity of the spatial variability of longitudinal pitting morphology with the increase in corrosion level. Indeed, as the corrosion level increased, also the maximum and average penetration depth of the analyzed samples increased. To this end, an average longitudinal penetration depth, $P_{av,long1}$, defined as the mathematical average of scanned pits measured along the entire sample length, was calculated according to Eq. 6-6.

$$P_{av,long1} = \frac{\sum_{1}^{n_{pits}} P_{x,i}}{n_{pits}} \qquad 6\text{-}6$$

Then, a maximum normalized longitudinal penetration depth, $P_{max,long}/r_{outer}$, equal to 0.66, 0.86 and 0.74 was measured for low, intermediate and high corrosion level, respectively, as highlighted by the red markers in Figure 6-14. Moreover, an average normalized longitudinal penetration depth, $P_{av,long1}/r_{outer}$ – this time highlighted in Figure 6-14 by the green dashed lines – equal to 0.10, 0.17 and 0.25 was calculated for low, intermediate and high corrosion level, respectively. This great variability of penetration depth values occurring at different sections confirms the randomness of the chloride-induced corrosion. In particular, although the aggressiveness of corrosion was particularly high in PB11-R(273-318) and PB13-L(1-46), the presence of at least one un-corroded section was always identified.

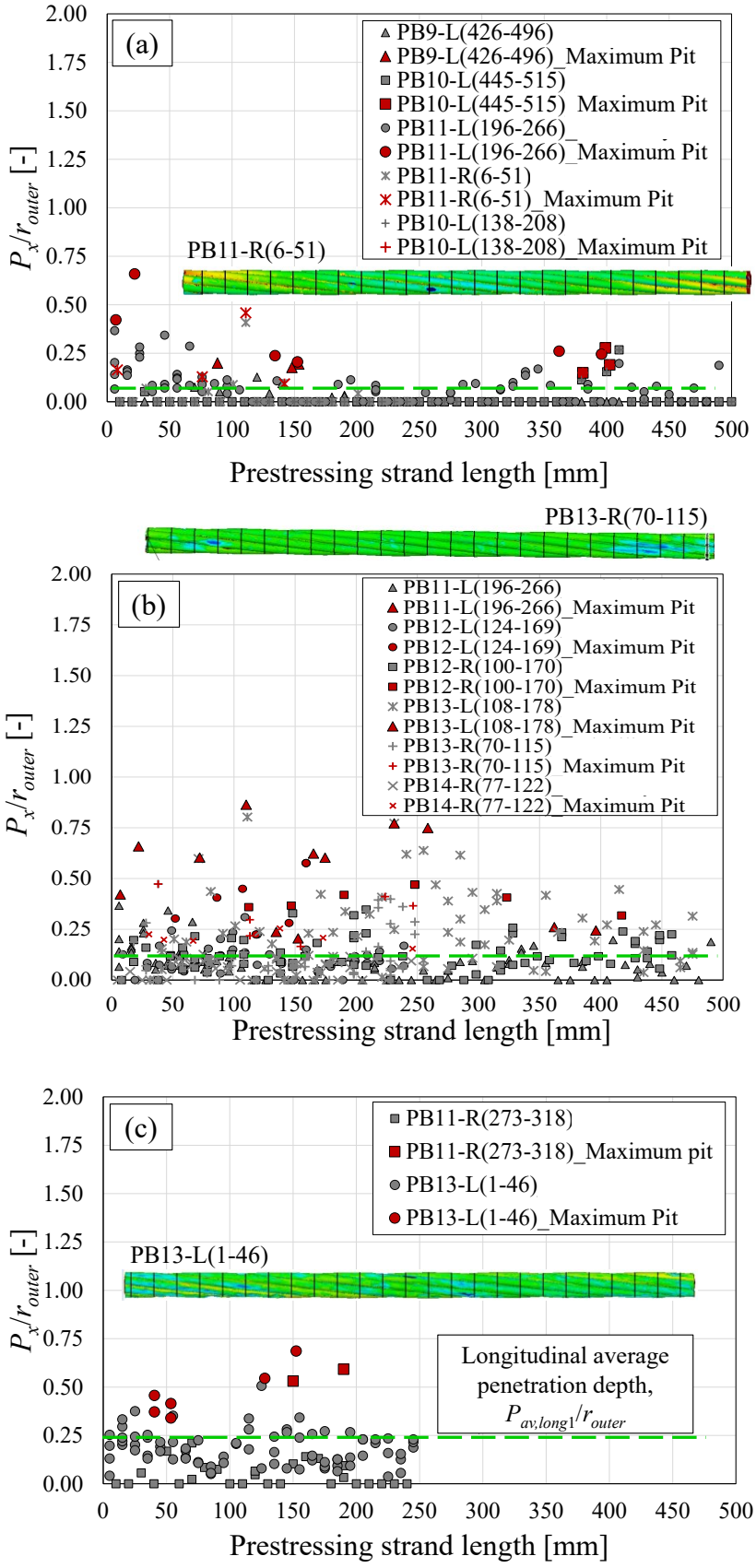

Figure 6-14 Pitting spatial variability of corroded samples unaffected by surface defects of concrete: (a) low, (b) intermediate and (c) high corrosion level.

The analysis of samples retrieved from beam regions affected by concrete surface defects in the form of longitudinal splitting cracks, revealed a significant increase in pitting spatial variability in terms of measured maximum penetration depth, $P_{max,long}/r_{outer}$, as well as uniformity and severity of the longitudinal damage pattern, i.e. average longitudinal penetration depth, $P_{av,long1}/r_{outer}$, as shown in Figure 6-15. Compared to the previously analyzed samples, a normalized average penetration depth, $P_{av,long1}/r_{outer}$, of more than 0.25 and a normalized maximum penetration depth, $P_{max,long}/r_{outer}$, of up to 1.25 were measured.

In addition, samples from "cracked" regions were classified further by differentiating them according to the different beam position in which concrete surface defects occurred, i.e. (i) at beam centreline or (ii) at the beam edges, as highlighted in Figure 6-15(a) and Figure 6-15(b). The different behaviour of the corroded samples is strictly associated to the construction practice deficiency highlighted at beam edges during the characterization phase. In fact, in the first scenario, which was characterized by the presence of longitudinal splitting cracks at mid-span, chloride ions could only rapidly migrate towards the prestressing strands due to the presence of concrete surface defects, Figure 6-15(a). The second scenario, conversely, was influenced by a combination of surface defects and construction practice deficiency that caused chloride ions to diffuse both through the longitudinal crack and from the end side of the PC beam due to the direct contact between aggressive agents and unprotected prestressing reinforcements, Figure 6-15(b). From the comparison of the two chloride ions diffusion scenarios, a significant difference in the pitting spatial variability of related corroded samples was clearly observed. Sample PB10-R(287-332) – subjected to the first chloride ions diffusion scenario – exhibited a uniform damage pattern with similar P_x/r_{outer} values in adjacent sections. Samples subjected to the second chloride ions diffusion scenario showed a non-uniform damage pattern along the entire length of the corroded strand, with deeper pits located near the beam edges due to the previously mentioned combined action. Furthermore, unlike samples retrieved from beam regions unaffected by concrete surface defects, all of the analyzed sections were affected by pitting, highlighting the greater aggressiveness of the corrosion process. In this regard, the obtained results were in line with the experimental findings of Chen et al. (2020), which showed the presence of deeper pits, greater volume loss and a more homogeneous spatial variability of pitting morphology from the analysis of 66 rebars subjected to chloride-induced corrosion for more than 3 years.

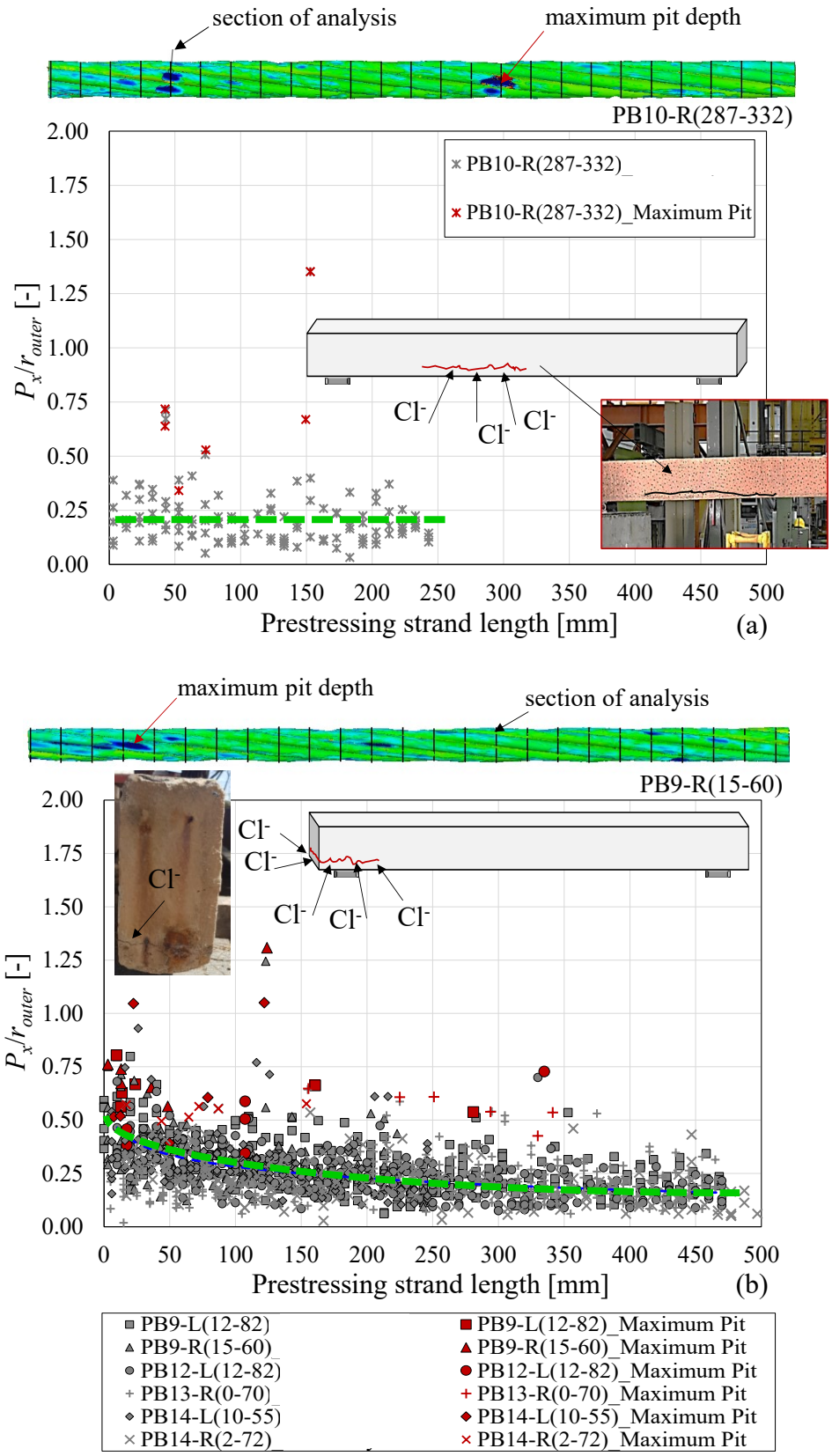

Figure 6-15 Pitting spatial variability of corroded samples affected by surface defects of concrete: (a) with and (b) without the additional effect of construction practice deficiency.

Subsequently, measurement-based-correlations were provided for the prediction of the normalized maximum penetration depth, $P_{max,long}/r_{outer}$, as a function of the number of pits per meter, n_{pits}/m, the normalized average longitudinal penetration depth, $P_{av,long1}/r_{outer}$, and the mass loss, η. The latter expressions were found to simultaneously take into account the effects associated with the corrosion process and the presence or absence of concrete surface defects.

As shown in Figure 6-16, a trilinear trend – discretized into (i) un-cracked, (ii) transition, and (iii) cracked phase – was defined for all proposed correlations, as expressed in Eqs. 6-7 to 6-9, Eqs. 6-10 to 6-12, and Eqs. 6-13 to 6-15. In particular, it is worth noting that experimental data of samples PB10-L(445-515) and PB13-L(108-178) were excluded from the definition of correlations due to outliers.

Un-cracked phase
$$\frac{P_{\max,long}}{r_{outer}} = 0.0061\frac{n_{pits}}{m} \qquad 0 \le \frac{n_{pits}}{m} < 85 \qquad \text{6-7}$$

Transition phase
$$\frac{P_{\max,long}}{r_{outer}} = 0.00037\frac{n_{pits}}{m} + 0.47 \qquad 85 \le \frac{n_{pits}}{m} < 350 \qquad \text{6-8}$$

Cracked phase
$$\frac{P_{\max,long}}{r_{outer}} = 0.0017\frac{n_{pits}}{m} \qquad \frac{n_{pits}}{m} \ge 350 \qquad \text{6-9}$$

Un-cracked phase
$$\frac{P_{\max,long}}{r_{outer}} = 5.65\frac{P_{av,long1}}{r_{outer}} \qquad 0 \le \frac{P_{\max,long}}{r_{outer}} < 0.5 \qquad \text{6-10}$$

Transition phase
$$\frac{P_{\max,long}}{r_{outer}} = 1.003\frac{P_{av,long1}}{r_{outer}} + 0.411 \qquad 0.5 \le \frac{P_{\max,long}}{r_{outer}} < 0.6 \qquad \text{6-11}$$

Cracked phase
$$\frac{P_{\max,long}}{r_{outer}} = 3.19\frac{P_{av,long1}}{r_{outer}} \qquad 0.6 \le \frac{P_{\max,long}}{r_{outer}} \le 2.0 \qquad \text{6-12}$$

Un-cracked phase
$$\frac{P_{\max,long}}{r_{outer}} = 0.1237\eta \qquad 0 \le \frac{P_{\max,long}}{r_{outer}} < 0.5 \qquad \text{6-13}$$

Transition phase
$$\frac{P_{\max,long}}{r_{outer}} = 0.0159\eta + 0.4359 \qquad 0.5 \le \frac{P_{\max,long}}{r_{outer}} < 0.6 \qquad \text{6-14}$$

Cracked phase
$$\frac{P_{\max,long}}{r_{outer}} = 0.058\eta \qquad 0.6 \le \frac{P_{\max,long}}{r_{outer}} \le 2.0 \qquad \text{6-15}$$

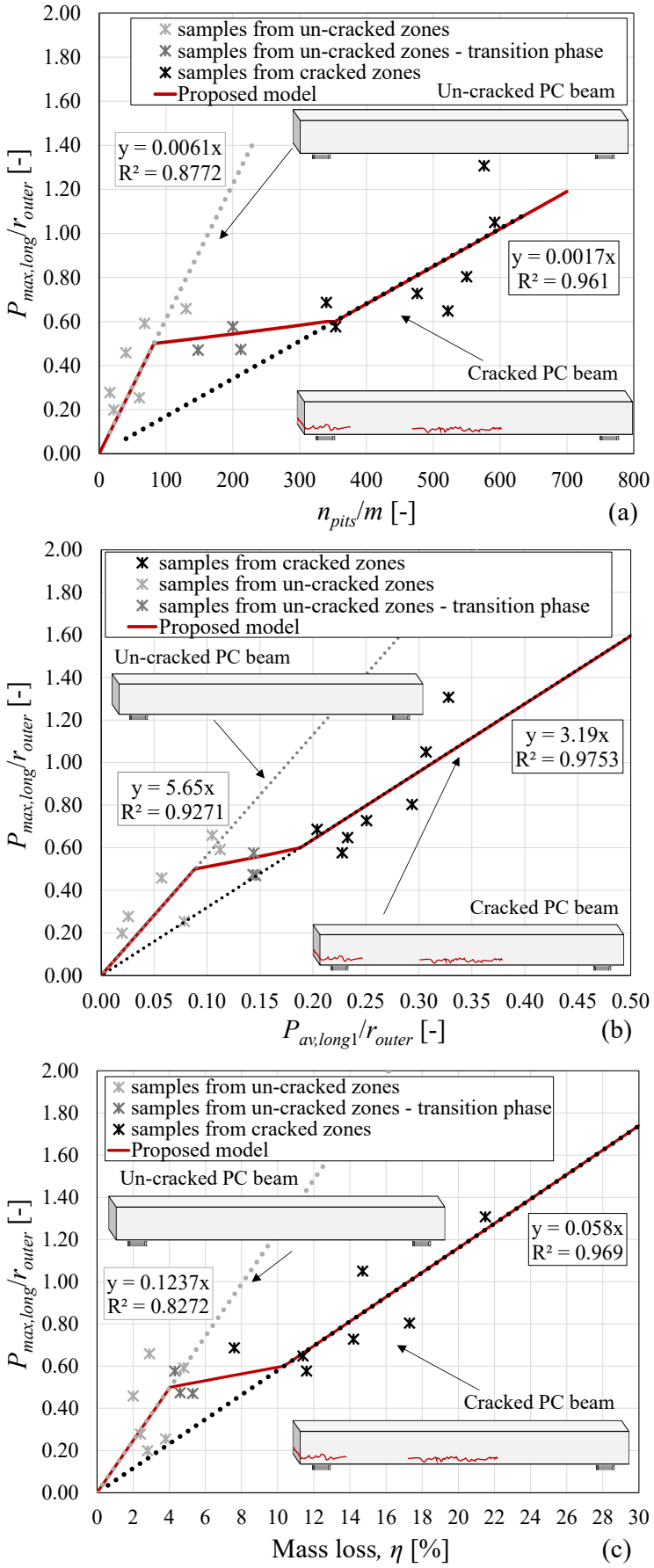

Figure 6-16 Correlations for the evaluation of $P_{max,long}/r_{outer}$ as a function of surface defects of concrete: (a) $P_{max,long}/r_{outer}$ vs n_{pits}/m, (b) $P_{max,long}/r_{outer}$ vs $P_{av,long1}/r_{outer}$ and (c) $P_{max,long}/r_{outer}$ vs η.

In general terms, during the first phase, the diffusion of chloride ions towards the prestressing reinforcements was inhibited by the presence of the un-cracked concrete cover, leading to the formation of small and localized pits. The ingress of chloride ions was then facilitated by the onset of concrete cracking, causing a pronounced increase in n_{pits}/m as well as in the number of section affected by corrosion, implying a rapid increase in $P_{av,long1}/r_{outer}$ and η. Simultaneously, the increase in maximum penetration depth was less pronounced with maximum pits usually occurring in correspondence of damaged beam regions or where a construction practice deficiency was detected. Finally, during the advanced cracked phase, the deteriorated concrete cover provided no barrier to the diffusion of chloride ions, resulting in a significant increase of all the examined corrosion parameters in terms of $P_{max,long}/r_{outer}$, n_{pits}/m, η, and $P_{av,long1}/r_{outer}$. In particular, it is interesting to note how mass loss values, η, higher than 10% were obtained in the case of corroded samples extracted from beam regions affected by concrete surface defects. Going into detail, $P_{max,long}/r_{outer}$ values of 0.0 and 0.5 were set as the upper and lower boundary limit of the un-cracked phase of the proposed relationships. These latter represent the absence of corrosion and the attainment of a deterioration level equivalent to $^1/_4$ of the external wire diameter, ϕ_{outer}, respectively. The upper boundary limit of the transition phase was similarly assumed at a $P_{max,long}/r_{outer}$ values of 0.6, which corresponds to the reaching of a deterioration level of approximately $^1/_3$ of the external wire diameter, ϕ_{outer}. In addition, n_{pits}/m threshold limits equal to 85 and 350 were defined in correspondence with $P_{max,long}/r_{outer}$ values of 0.5 and 0.6, respectively. For the same $P_{max,long}/r_{outer}$ values, threshold limits of η equal to 4% and 10% were calculated. These thresholds were generally defined on the basis of the best-fit of experimental outcomes. Furthermore, a $P_{max,long}/r_{outer}$ value equal to 2.0 was set as the upper boundary of the cracked phase for all correlations, representing the complete deterioration of the external wire ($P_{max,long}/r_{outer} = 2 = \phi_{outer}$).

The accuracy of the proposed relationship was confirmed by the good fitting of experimental data, as expressed by the coefficient of correlations, R^2, obtained for the un-cracked and cracked phases reported in Figure 6-16. From a general point of view, the proposed relationships are intended to light interest in the different behaviour between cracked and un-cracked PC members. Although these relationships should be further validated through the analysis of additional corroded prestressing strands, the preliminary outcomes clearly demonstrate the key role played by the presence of concrete surface defects in the modification of pitting morphology spatial variability of naturally corroded strands. In this context, particular attention should be paid to the identification of possible construction practice or design

deficiencies of the analyzed structural member as well as the different pathways that chloride ions can follow throughout the diffusion process towards the prestressing reinforcements. Of course, further studies should also be conducted to analyze PC beams subjected to different exposure conditions.

Table 6-3 Relevant corrosion parameters estimated from the pitting variability of corroded strands.

Sample ID	$P_{max,long}/r_{outer}$ [-]	$A_{min}/A_{p,0}$ [-]	$P_{av,long1}/r_{outer}$ [-]	μ_{max} [%]	μ_{strand} [%]
PB9-L(12-82)	0.80	0.788	0.29	37.58	21.28
PB9-L(426-496)	0.20	0.975	0.02	3.67	2.49
PB9-R(15-60)	1.31	0.794	0.33	69.20	20.58
PB9-R(428-473)	Un-corroded	-	-	-	-
PB10-L(138-208)	0.28	0.970	0.03	8.39	3.09
PB10-L(445-515)	1.20	0.859	0.20	59.61	14.04
PB10-R(32-102)	-	-	-	-	
PB10-R(287-332)	1.35	0.874	0.24	59.60	12.60
PB11-L(5-75)	Un-corroded	-	-	-	-
PB11-L(196-266)	0.66	0.938	0.10	28.66	6.30
PB11-R(6-51)	0.46	0.987	0.06	17.51	1.33
PB11-R(273-318)	0.59	0.953	0.11	23.48	-
PB12-L(12-82)	0.73	0.817	0.25	36.85	18.27
PB12-L(124-169)	0.58	0.949	0.14	23.96	5.14
PB12-R(100-170)	0.47	0.960	0.15	15.20	3.94
PB12-R(358-403)	Un-corroded	-	-	-	-
PB13-L(1-46)	0.69	0.954	0.20	22.85	4.62
PB13-L(108-178)	0.86	0.936	0.28	34.38	6.40
PB13-R(0-70)	0.65	0.858	0.23	27.02	14.19
PB13-R(70-115)	0.47	0.951	0.14	20.23	4.87
PB14-L(10-55)	1.05	0.833	0.31	53.06	16.69
PB14-L(455-500)	Un-corroded	-	-	-	-
PB14-R(2-72)	0.58	0.876	0.23	23.69	11.60
PB14-R(77-122)	0.25	0.987	0.08	4.99	1.33

6.4.2.1.3 Penetration depth probabilistic analysis

This section investigates the probabilistic analysis of the penetration depths measured for each corroded strand, adopting the sectional analysis every 10 mm. In detail, the probability distribution functions commonly used in the literature – i.e. Normal, Lognormal and Gumbel Extreme-value distributions – were first selected to fit the available experimental data in terms of both probability density function, PDF, and cumulative distribution function, CDF, reported in Figure 6-17 for sample PB9-L(12-82). From the comparison, the Lognormal distribution function was found to be the most suitable distribution for describing the spatial variability of longitudinal pitting morphology. For the sake of completeness, the general expression of Lognormal distribution is reported in Eq. 6-16:

$$f_X(x) = \frac{1}{\sqrt{2\pi}\zeta_x x}\exp\left[-\frac{1}{2}\left(\frac{\ln x - \lambda_x}{\zeta_x}\right)^2\right] \qquad 6\text{-}16$$

where λ_x and ζ_x are, respectively, the mean value and the standard deviation of the adopted distribution function, which outcomes are reported in Table 6-4 for each analyzed corroded sample. Table 6-4 also displays the main statistical parameters of the obtained distributions in terms of mean value, μ_x, and fractile value at 95%, $P_{x,0.95}$.

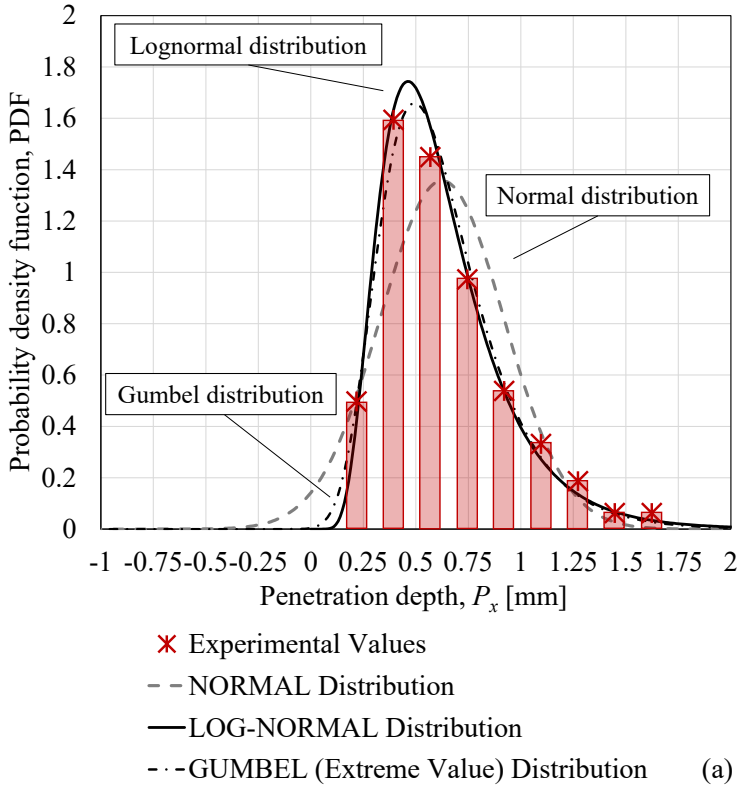

(a)

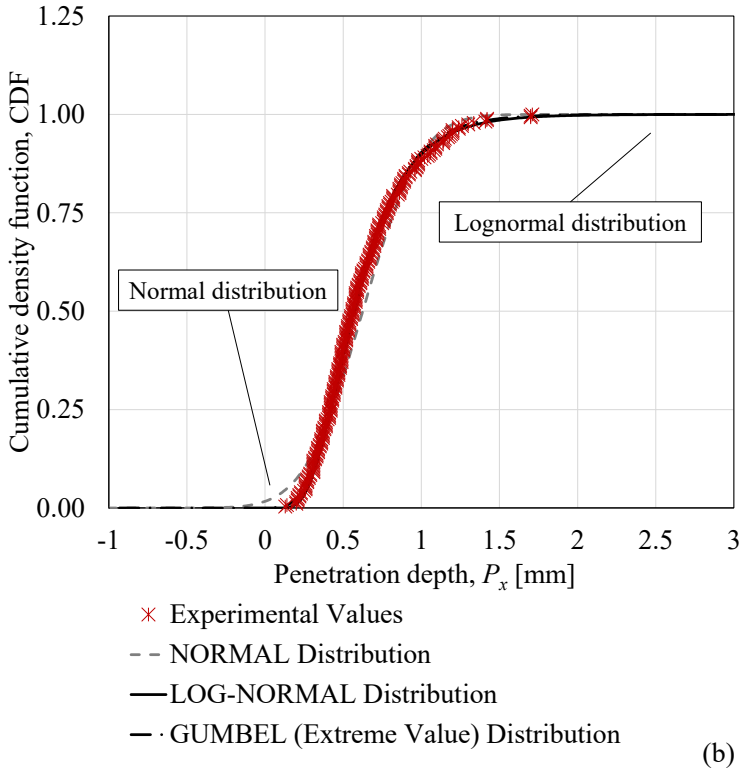

(b)

Figure 6-17 Sample PB9-L(12-82) distribution functions comparison: (a) PDF and (b) CDF.

Furthermore, Figure 6-18 summarizes the PDF and CDF of each corroded strand. By carefully analyzing the obtained distributions, it was confirmed that samples characterized by low corrosion damage showed shallow and small-size pits generally widely spaced along the sample length. Vice versa, as the corrosion level increased, the measured pits appeared randomly with varying size and penetration depth, reaching over-sized dimensions and a widespread diffusion for high corrosion levels.

Similarly to the procedure described for the probabilistic analysis of the measured penetration depths of each corroded strand, the Normal, Lognormal and Gamma distribution functions were subsequently adopted to investigate the maximum measured values of longitudinal penetration depth, $P_{max,long}$, reported in Figure 6-19. The Lognormal distribution function was found to be the most suitable curve for the probabilistic description of the maximum longitudinal penetration depth, as illustrated in Figure 6-19 by the PDF plots expressed in normal and semilogarithmic scale. In this regard, the statistical parameters of mean value, $\mu_{x,max}$, and variance, σ_{max}, were calculated to be 0.51 and 0.308, respectively. As a result, future research can be devoted to the proposal of new structural reliability methods on the basis of the obtained probabilistic results, providing useful tools for the assessment of corroded prestressing strands and existing deteriorated structures.

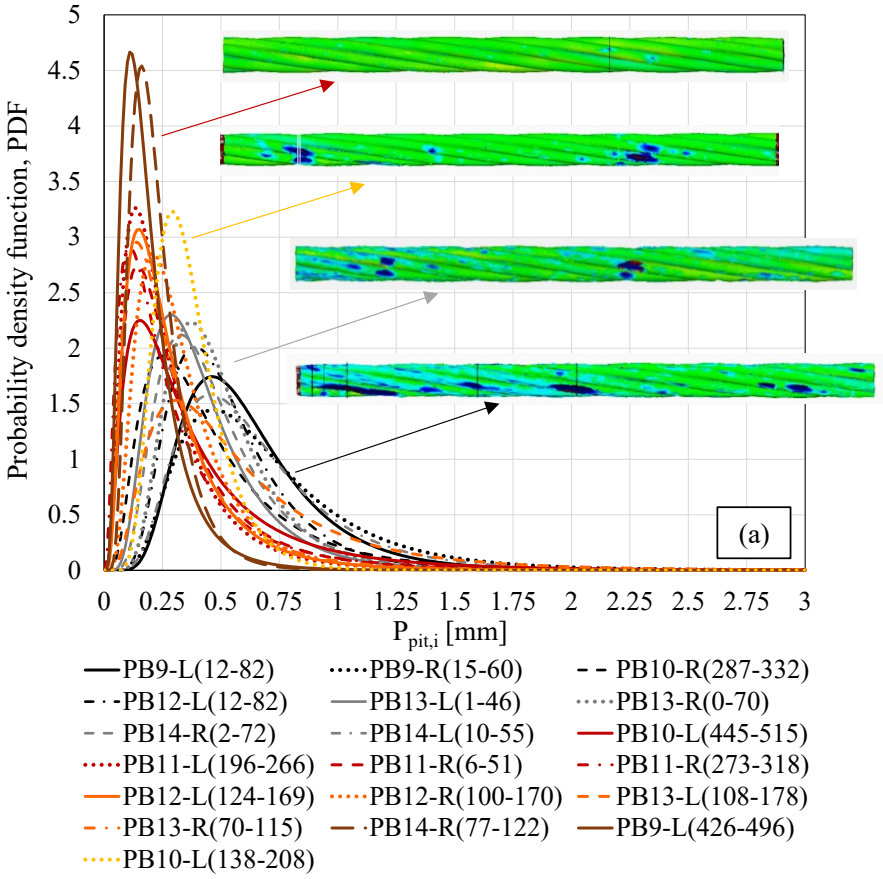

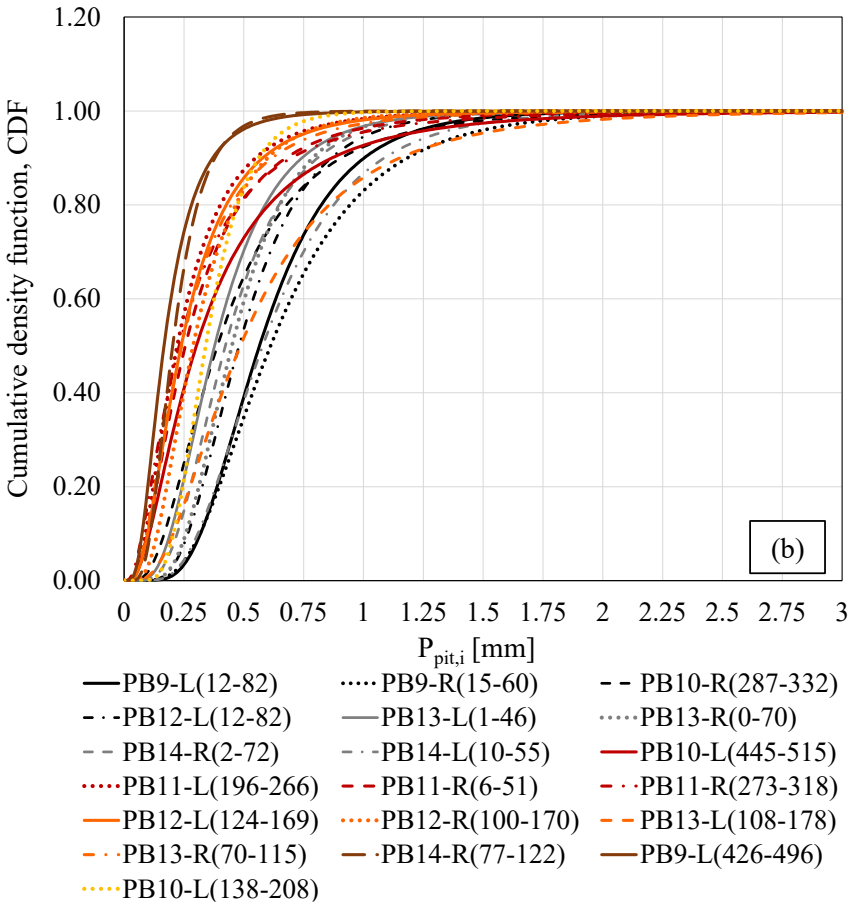

Figure 6-18 Lognormal distributions for each corroded strands in terms of (a) PDF and (b) CDF.

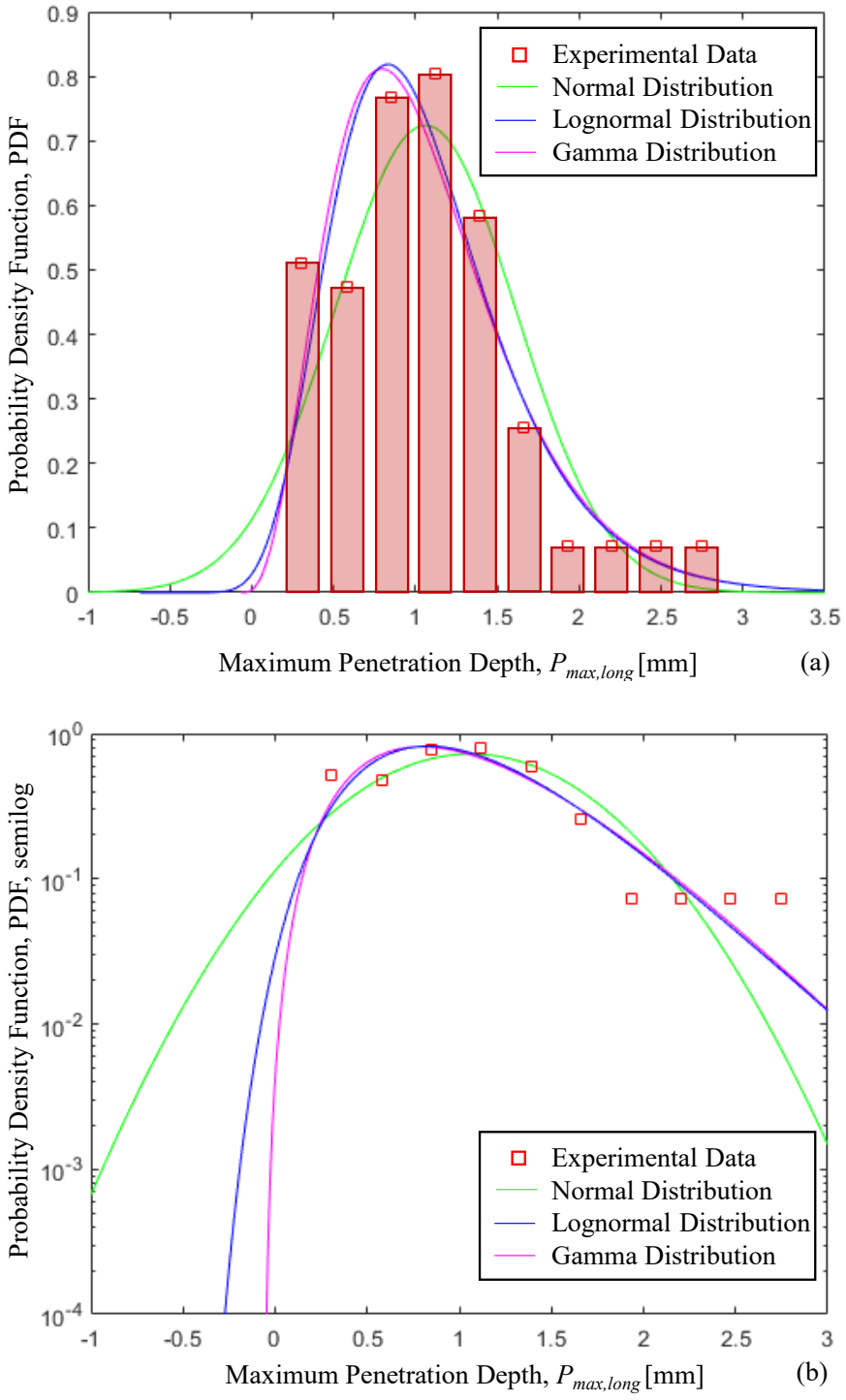

Figure 6-19 Lognormal distribution function for the longitudinal maximum penetration depth, $P_{max,long}$, expressed in terms of PDF: (a) normal and (b) semilogarithmic scale.

Table 6-4 Main statistical parameters of the Lognormal distribution function of each corroded strand.

Sample ID	λ_x [-]	ζ_x [-]	μ_x [mm]	$P_{x,0.95}$ [mm]
PB9-L(12-82)	-0.57	0.45	0.57	1.18
PB9-L(426-496)	-1.79	0.62	0.16	0.46
PB9-R(15-60)	-0.49	0.51	0.61	1.43
PB9-R(428-473)	Un-corroded			
PB10-L(138-208)	-1.08	0.39	0.34	0.65
PB10-L(445-515)	-1.20	0.82	0.30	1.17
PB10-R(32-102)	-	-	-	-
PB10-R(287-332)	-0.94	0.66	0.39	1.15
PB11-L(5-75)	Un-corroded			
PB11-L(196-266)	-1.51	0.71	0.22	0.71
PB11-R(6-51)	-1.36	0.76	0.25	0.89
PB11-R(273-318)	-	-	-	-
PB12-L(12-82)	-0.73	0.46	0.48	1.02
PB12-L(124-169)	-1.43	0.69	0.24	0.74
PB12-R(100-170)	-1.24	0.57	0.29	0.74
PB12-R(358-403)	Un-corroded			
PB13-L(1-46)	-0.97	0.53	0.38	0.90
PB13-L(108-178)	-0.72	0.67	0.49	1.47
PB13-R(0-70)	-0.80	0.44	0.45	0.92
PB13-R(70-115)	-1.43	0.74	0.24	0.81
PB14-L(10-55)	-0.55	0.49	0.58	1.30
PB14-L(455-500)	Un-corroded			
PB14-R(2-72)	-0.86	0.50	0.42	0.97
PB14-R(77-122)	-1.60	0.49	0.20	0.45

6.4.2.1.4 Residual cross-section

The residual cross-section, A_{min}, of each corroded sample were also analyzed using the GOM Inspect software. The residual cross-sectional area tended to decrease as the corrosion level increased, as shown in Figure 6-20. An unpredictability of A_{min} was observed in adjacent sections along the overall length of the analyzed corroded samples. It is worth noting that the difference between the un-corroded cross-sectional area measured using the GOM Inspect software – equal to 106.9 mm^2 – and the actual one – equal to 100 mm^2 in the case of a 7-wire prestressing strand with an equivalent diameter of 12.9 mm – was related to the inability of the 3D laser scanner to measure the empty space between adjacent wires. Furthermore, the maximum pit depth did not always occur in correspondence with A_{min}. To this end, three corroded samples belonging to the same region of the beam PB4P14 were compared in terms of both penetration depth and residual cross-sectional area variation. As evidenced by red and blue markers in Figure 6-21, the maximum pit depth and the residual cross-sectional area of sample PB14-L(10-55) occurred in the same section, while their position varied significantly from samples PB14-R(2-72) and PB14-R(77-122). This evidence is in contrast with the experimental findings on corroded rebars and depends on different contribution of external wires. Indeed, in correspondence of the maximum penetration depth recorded for the most corroded wire, the remaining wires can be characterized by different corrosion levels, resulting in a strong variability of A_{min} values.

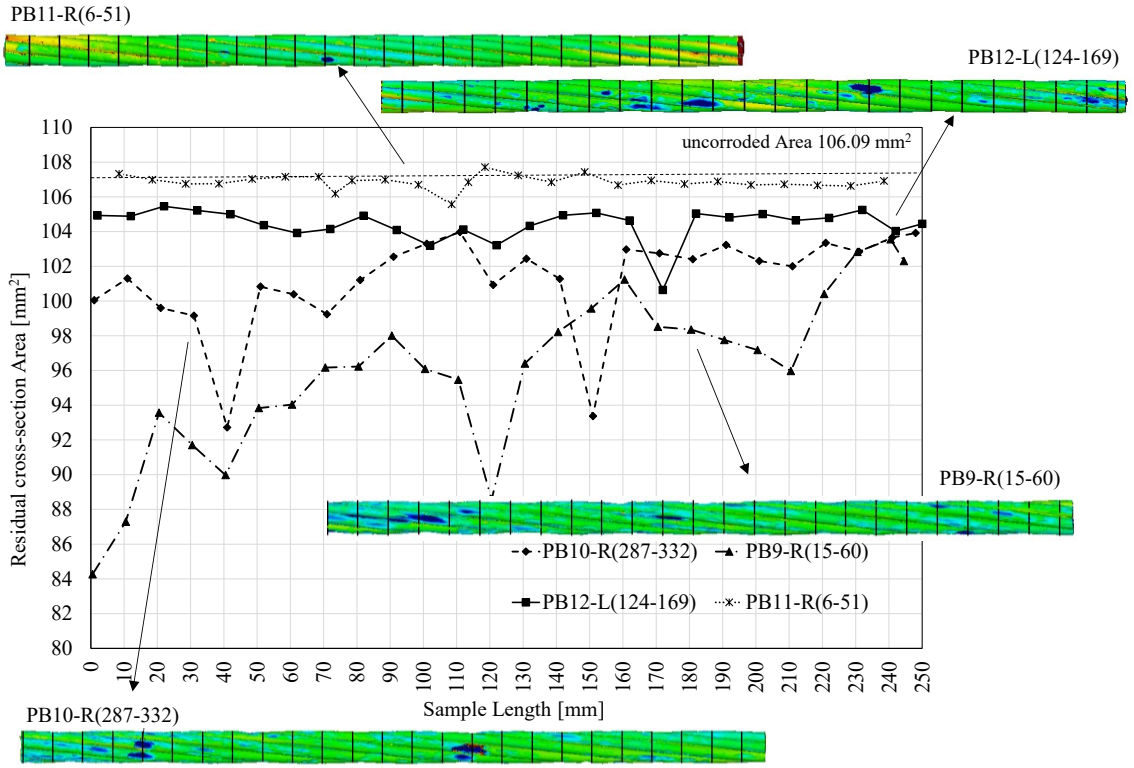

Figure 6-20 Variability of residual cross-section of corroded strand as a function of corrosion level.

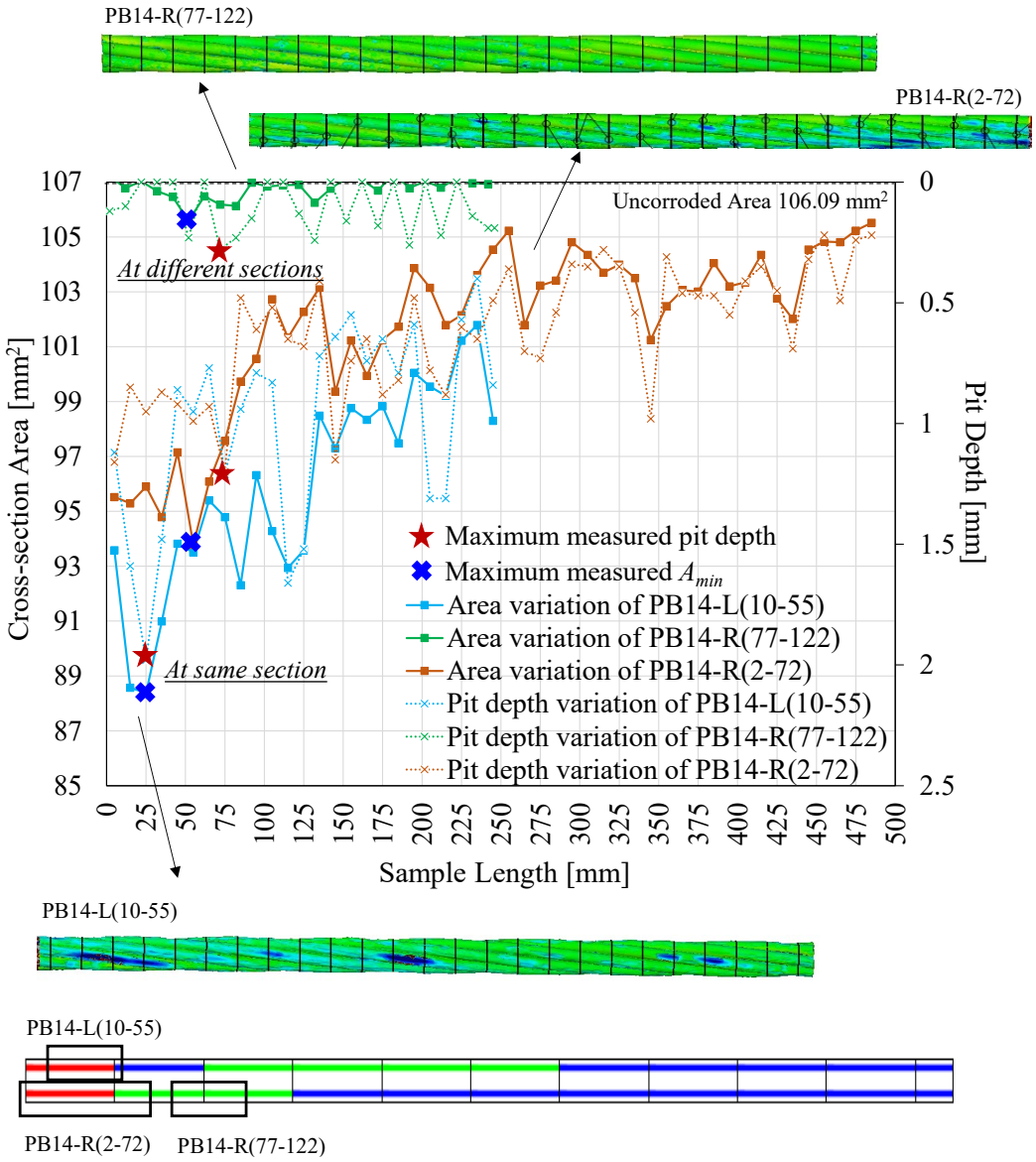

Figure 6-21 Comparison of corrosion parameters (P_x and A_{min}) for corroded samples retrieved from the left edge of beam PB4P14.

6.4.2.2 *Transversal pitting factor definition*

In the present research, since the sectional maximum penetration depth, $P_{max,sectional,i}$, varied along the sample length, as demonstrated by 3D scanning results, a transversal pitting factor was defined to characterize the sectional spatial variability of the analyzed corroded strands. The transversal pitting factor, Ω_i, is a sectional value and is a useful parameter for determining the sectional corrosion condition of the external wires of a corroded strand. Therefore, considering that a sectional analysis was conducted every 10 mm, a total of twenty-five or fifty Ω_i values were measured for each analyzed corroded strand on the basis of the two different scanned lengths, L_{scan}, reported in Table 6-1.

The sectional average penetration depth, $P_{av,transv,i}$, of each corroded strand at each analyzed section was calculated as the mathematical average of the sectional penetration depths, $P_{x,sectional,i}$, of the external wires with the only exception of the sectional maximum penetration depth neglection, $P_{max,sectional,i}$, according to Eq. 6-17 and as highlighted in Figure 6-22:

$$P_{av,transv,i} = \frac{\sum_{1}^{n_{sectional}} P_{x,sectional,i}}{n_{sectional}} \qquad 6\text{-}17$$

where $n_{sectional}$ is set equal to 5 and represents the number of external wires, except for the most corroded one.

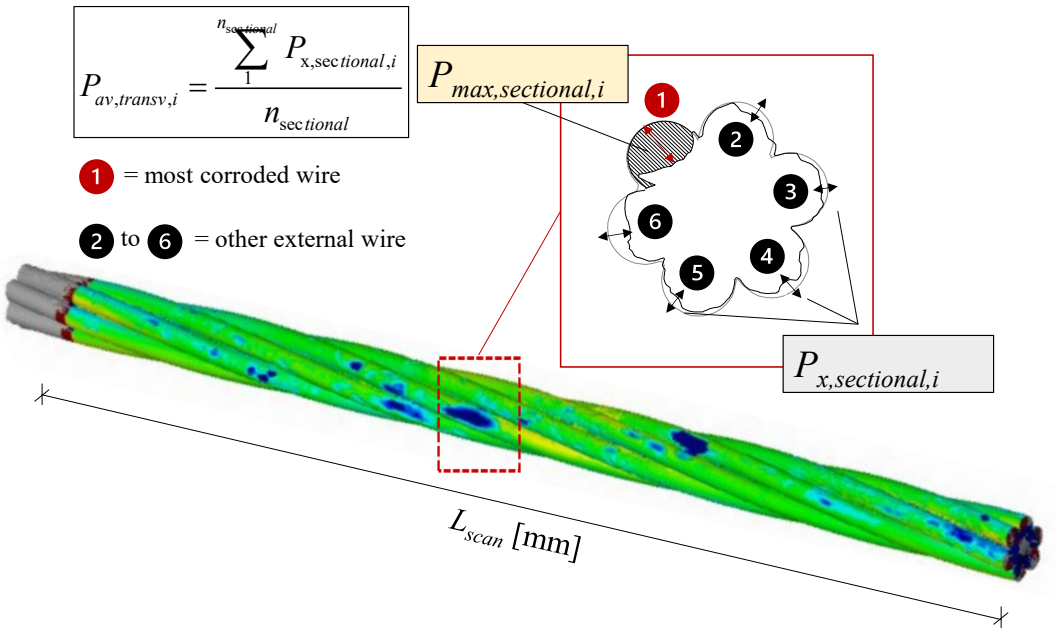

Figure 6-22 Focus on $P_{av,transv,i}$ calculation.

The transversal pitting factor, Ω_i, was defined as the product of two parameters, named as intensity factor γ_i and transversal factor β_i, as expressed in Eq. 6-18.

$$\Omega_i = \gamma_i \cdot \beta_i = \frac{P_{\max,sectional,i}}{2r_{outer}} \frac{\frac{P_{av,transv,i}}{r_{outer}}}{\frac{P_{\max,sectional,i}}{r_{outer}}} = \frac{P_{\max,sectional,i}}{2r_{outer}} \frac{\frac{\sum_{1}^{n_{sectional}} \frac{P_{x,sectional,i}}{n_{sectional}}}{r_{outer}}}{\frac{P_{\max,sectional,i}}{r_{outer}}} = \quad 6\text{-}18$$

$$= \frac{\frac{\sum_{1}^{n_{sectional}} \frac{P_{x,sectional,i}}{n_{sectional}}}{r_{outer}}}{2} = \frac{\sum_{1}^{n_{sectional}} \frac{P_{x,sectional,i}}{n_{sectional}}}{2r_{outer}}$$

The transversal pitting factor Ω_i ranged between 0 and 1.0, where 0 represents the un-corroded scenario, and 1.0 represents the entire deterioration of the external wires in the analyzed section. Specifically, the intensity factor γ_i, which identifies the sectional corrosion level, was defined as the ratio between the maximum sectional penetration depth, $P_{max,sectional,i}$, and two times the radius of the external un-corroded wire, r_{outer} (wire diameter). The factor γ_i ranged between 0 and 1.0, whit 0 representing the un-corroded scenario, and 1.0 being the critical scenario where the external wire is completely corroded ($P_{max,sectional,i}$ = 2 times r_{outer}). Besides, the transversal factor β_i was evaluated as the ratio of the normalized sectional values of average and maximum penetration depth, $P_{av,transv,i}$ and $P_{max,sectional,i}$, respectively. The factor β_i ranged also between 0 and 1.0, where 0 stands for the un-corroded scenario and 1.0 represents the homogeneous corrosion scenario. As a matter of fact, regardless of γ_i value at the investigated section, for a β_i value of 1.0, all the external wires had the same sectional penetration depth, which results equal to $P_{max,sectional,i}$.

After processing the experimental data obtained from the sectional analysis of each corroded sample, a quadratic regression trend was proposed for the prediction of Ω_i as a function of the normalized maximum sectional penetration depth, $P_{max,sectional,i}/r_{outer}$, as expressed in Eq. 6-19 and graphically shown in Figure 6-23:

$$\Omega_i = 0.189\left(\frac{P_{\max,sectional,i}}{r_{outer}}\right)^2 + 0.125\left(\frac{P_{\max,sectional,i}}{r_{outer}}\right) \quad 6\text{-}19$$

where an upper boundary limit of $P_{max,sectional,i}/r_{outer}$ was set equal to 2.0, which corresponds to the entire deterioration of the external wire scenario.

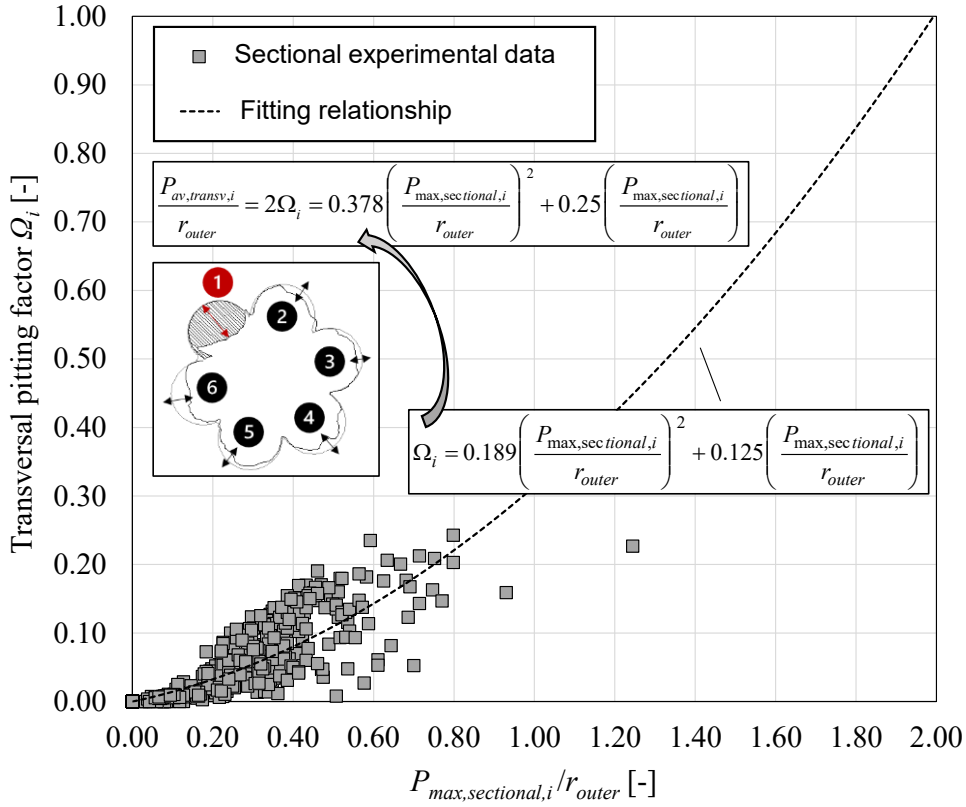

Figure 6-23 Regression trend for the prediction of the transversal pitting factor Ω_i.

The effectiveness of the proposed correlation consisted in the definition of a simplified expression for the sectional analysis of corroded prestressing reinforcements that allowed the prediction of the average sectional penetration depth of corroded external wires, $P_{av,transv,i}$, as a function of a single parameter, that is the sectional maximum penetration depth, $P_{max,sectional,i}$, as highlighted by Eq. 6-20. Furthermore, the use of the proposed correlation enabled to partially overcome the issue related to the in-situ assessment of prestressing reinforcement. Indeed, after the removal of the concrete cover, in-situ measurements are generally performed on outward external wires only, with no opportunity to identify the actual condition of hidden wires. Vice versa, once the maximum penetration depth is known the average sectional penetration depth, in the form $P_{av,transv,i}/r_{outer}$, can be predicted by adopting the relationship proposed in Eq. 6-20. To this end, it is worth noting that the highest corrosion level is commonly detected in the outward region of reinforcements, which is more exposed to aggressive agents and environments.

$$\frac{P_{av,transv,i}}{r_{outer}} = 2\Omega_i = 0.378\left(\frac{P_{\max,sectional,i}}{r_{outer}}\right)^2 + 0.25\left(\frac{P_{\max,sectional,i}}{r_{outer}}\right) \qquad 6\text{-}20$$

Finally, referring to Figure 6-23, it is possible to observe how the dispersion of experimental data varies as the maximum sectional penetration depth, $P_{max,sectional,i}/r_{outer}$, increases. In detail, taking into account different ranges of $P_{max,sectional,i}/r_{outer}$, the following considerations can be outlined:

- For the range $0.0 < P_{max,sectional,i}/r_{outer} < 0.2$: low Ω_i values with limited dispersion of experimental data were measured, indicating a lower sectional corrosion level of the external wires with respect to the most corroded one;
- For the range $0.2 < P_{max,sectional,i}/r_{outer} < 0.5$: the measured Ω_i values increased with the increase in $P_{max,sectional,i}/r_{outer}$, showing a relevant dispersion of experimental data. Indeed, different corrosion levels of external wires were detected, highlighting the great variability and randomness of corrosion attack in transversal (sectional) direction.
- For the range $0.5 < P_{max,sectional,i}/r_{outer} < 0.8$ (experimental maximum measured value): even though the absolute value of the parameter Ω_i still increased with the increase in $P_{max,sectional,i}/r_{outer}$, the experimental data dispersion obtained was lower if compared to the previously analyzed range. As a result, for high corrosion levels, it was confirmed that the corrosion attack became more homogeneous and diffuse in both transversal and longitudinal directions of a corroded strand.

6.4.3 Correlations between different corrosion damage assessment parameters

6.4.3.1 Penetration depth vs mass loss

To investigate the behaviour of corroded prestressing strands in depth, a relationship between mass loss, η, and maximum longitudinal penetration depth – whether or not in its normalized form (i) $P_{max,long}$ in Table 6-2 or (ii) $P_{max,long}/r_{outer}$ in Table 6-3 – was first analyzed. To this end, the available corroded samples were further divided into three groups based on their mass loss value, Table 6-2. According to Lu et al. (2016), the low corrosion level, denoted as LV-A, varied between η values equal to 0% and 2%; the intermediate corrosion level, denoted as LV-B, ranged between η values equal to 2% and 10%, whereas the high corrosion level, denoted as LV-C, referred to η values higher than 10%. Figure 6-24 shows that an univocal trend correlating the two corrosion parameters could not be defined; on the contrary, different linear regression trends were established for each corrosion level analyzed, as expressed by Eqs. 6-21 to 6-23.

$$P_{\max,long} = 0.0601\eta \quad \text{6-21}$$

$$P_{\max,long} = 0.2804\eta \quad \text{6-22}$$

$$P_{\max,long} = 0.1206\eta \quad \text{6-23}$$

Based on the obtained results, a wide dispersion of available data was observed, especially for samples belonging to LV-A and LV-B. In the case of LV-A, the scatter of the results was most likely caused by the small number of corroded samples, emphasizing the need for additional experimental research with the goal of expanding the available data. Conversely, with regards to LV-B, the data dispersion was already noticed in scientific literature in the case of corroded reinforcing rebars. In this context, Li et al. (2019) argued that $P_{max,long}$ values can better reflect the severity of localized pitting corrosion, whereas η values better suited to represent the average or homogeneous corrosion. Indeed, small scattered pits with low values of maximum pit depth or limited deep pits with high values of maximum pit depth can both return the same mass loss. Finally, a good data interpolation was obtained when looking at LV-C. This latter experimental evidence is associated with the tendency of pitting corrosion to distribute more evenly along the sample length as the corrosion level increases, resulting in a better fit of experimental data.

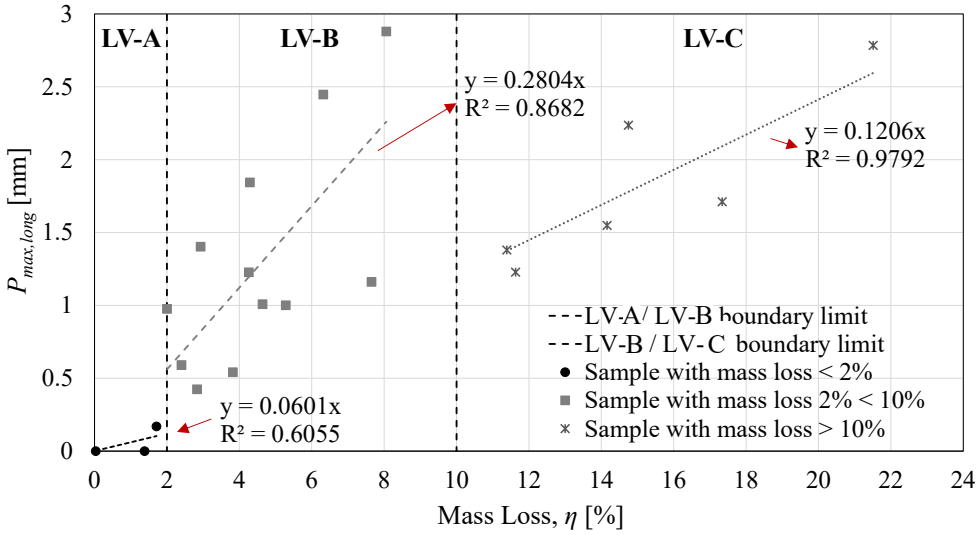

Figure 6-24 Relationship between η and $P_{max,long}$.

Investigating the relationship between η and $P_{max,long}/r_{outer}$ – highlighted in Figure 6-25 – a new analytical expression consisting of two branches was proposed, as also reported in Eq. 6-24 and Eq. 6-25. First, two groups of corroded samples, denoted as LV-A* and LV-B*, were identified by distinguishing between samples with a mass loss value lower or higher of 5%. Second, regression analyses were performed to best-fit the experimental data from the two different groups. Both groups were then discretized by adopting a linear and a parabolic trend, respectively. Finally, a critical mass loss threshold of 4.15% was determined as the intersection point of the two analytical trends.

$$\frac{P_{\max,long}}{r_{outer}} = 0.1212\eta \qquad 6\text{-}24$$

$$\frac{P_{\max,long}}{r_{outer}} = 0.002\eta^2 - 0.0076\eta + 0.5 \qquad 6\text{-}25$$

As a result, a good interpolation of the available data was obtained. In particular, the proposed expressions were able to capture the change in behaviour of corroded strands with high mass loss values. In addition, the power of the proposed relationships lay in the direct correlation of two of the main corrosion parameters adopted in the scientific literature to predict the residual mechanical properties of corroded prestressing strands.

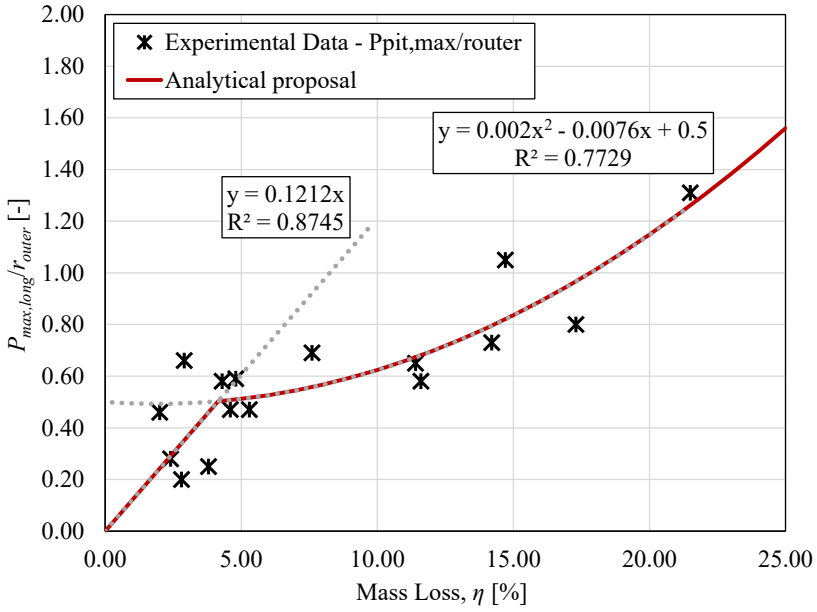

Figure 6-25 Relationship between η and $P_{max,long}/r_{outer}$.

6.4.3.2 Mass loss vs minimum residual cross-section

In addition, the correlation between mass loss, η, and minimum residual cross-section of the corroded prestressing strands, A_{min}, was investigated. The measured A_{min} values, in particular, were normalized by dividing them by the un-corroded cross-section of the entire strand, $A_{p,0}$, as reported in Table 6-3. Considering the coefficient of correlation, R^2, equal to 0.877, a satisfying relationship was established, as shown in Figure 6-26.

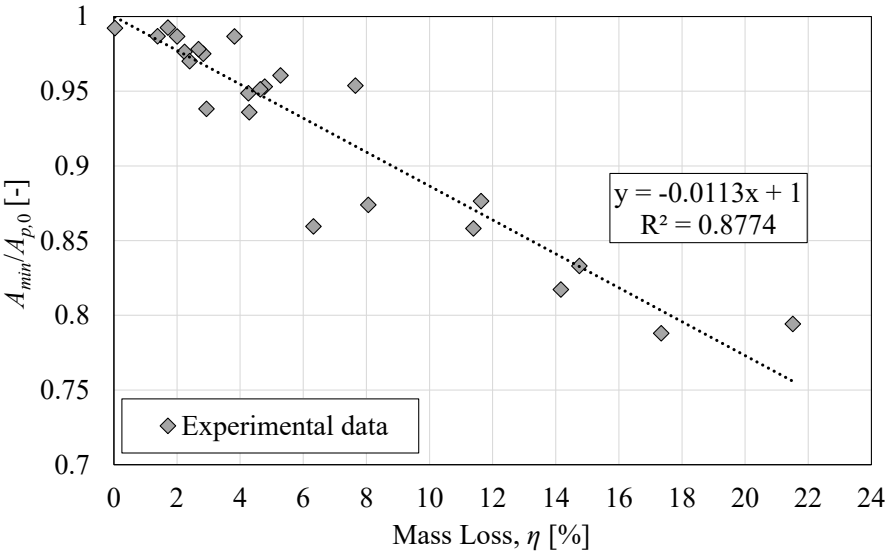

Figure 6-26 Relationship between η and $A_{min}/A_{p,0}$.

Based on the available data, the normalized minimum residual cross-section tended to decrease linearly with the increase in mass loss values, η, according to the expression showed in Eq. 6-26. In this framework, similar experimental findings were outlined in the scientific literature by other authors through the analysis of reinforcing steel rebars, (D. Li et al., 2019), and deformed steel bars, (F. Tang et al., 2014), subjected to chloride attack. Therefore, even in the case of corroded prestressing strands, the minimum residual cross-sectional area was discovered to be an important material damage parameter to be considered in the analysis of chloride-induced corrosion.

$$\frac{A_{\min}}{A_{p,0}} = -0.0113\eta + 1 \qquad 6\text{-}26$$

6.4.3.3 Cross-sectional loss vs strand-unit sectional loss

To thoroughly investigate the chloride-induced corrosion effects on seven-wire prestressing strands, other significant corrosion parameters besides η, $P_{max,long}/r_{outer}$, $P_{av,long1}/r_{outer,}$ and n_{pits}/m, were investigated on the basis of the GOM Inspect measurements:

1. The wire cross-sectional loss, μ, with particular focus on its maximum value in the case of the most corroded wire, μ_{max}, evaluated in correspondence of the measured maximum penetration depth;
2. The strand unit-sectional loss, μ_{strand}.

In general terms, the cross-sectional loss, μ, of a corroded wire was calculated according to Eq. 6-27:

$$\mu = \frac{A_p}{A_{w,outer,0}} = \frac{A_{w,outer,0} - A_{w,\min}}{A_{w,outer,0}} = 1 - \frac{A_{w,\min}}{A_{w,outer,0}} \qquad 6\text{-}27$$

where A_p is the previously calculated area loss due to pitting (Table 6-2 and appendix A.3) and $A_{w,outer,0}$ is the un-corroded cross-section (area) of the external wire and $A_{w,min}$ is the minimum residual cross-section of the corroded wire. In the case of a seven-wire prestressing strand, the cross-sectional loss of the most corroded wire, μ_{max}, was proven to be one of the most relevant parameters for the estimation of the residual mechanical properties, as demonstrated by the work carried out by Jeon et al. (2019). Therefore, the measured μ_{max} values for the investigated corroded samples were measured and reported in Table 6-3. In addition, the cross-sectional losses of each external wire – in correspondence to the section where the maximum penetration depth, $P_{max,long}$, was identified – were reported in Appendix A.4.

The strand-unit section loss, μ_{strand}, was defined as the sum of the wire cross-sectional losses, μ_i, evaluated at the same section, according to Eq. 6-28:

$$\mu_{strand} = \frac{\sum_{1}^{n} A_{p,i}}{A_{p,0}} \qquad 6\text{-}28$$

where $A_{p,0}$ is the un-corroded cross-section (area) of the prestressing strand, $A_{p,i}$ is the i^{th} area loss due to pitting of a wire at the analyzed section and n is the number of wires composing the strand – set equal to 7. For the sake of completeness, the strand-unit section loss, μ_{strand}, – evaluated in correspondence of the section at which the $P_{max,long}$ was identified – were reported in Table 6-3.

6.4.3.4 Maximum penetration depth vs cross-sectional loss of the most corroded wire

The relationship between the maximum longitudinal penetration depth, $P_{max,long}$, and the corresponding cross-sectional loss of the most corroded wire, μ_{max}, has been analyzed in the present paragraph. In particular, the experimental data obtained from the GOM Inspect measurements were adopted to further extend the validity of the analytical expression proposed by Wang et al. (2020). In their study, Wang et al. (2020) initially defined a logarithmic trend between $P_{max,long}$ and μ_{max} based on the regression analysis of experimental data obtained from the morphological investigation of 119 pits measured from corroded strands belonging to PC beams subjected to several years of wet-dry conditions, adopting an artificial climate box. However, the proposed correlation – depicted in Figure 6-27 and reported in Eq. 6-29 – was approximately fitting the experimental data, resulting in a large discrepancy between actual values and analytical predictions, as confirmed by the coefficient of correlation, R^2, equal to 0.49. Furthermore, the most corroded wire's cross-sectional loss value was only 33.4%.

$$P_{\max,long} = 0.531\ln\left(\mu_{\max}\right) + 0.02 \qquad 6\text{-}29$$

Similarly to the procedure adopted by Wang et al. (2020), an exponential relationship was first established between the two analyzed corrosion parameters on the basis of the new experimental outcomes reported in Table 6-3. The accuracy of the exponential trend – showed in Figure 6-27 and reported in Eq. 6-30 – was confirmed by the high R^2 value of 0.97. Moreover, unlike the experimental campaign conducted by Wang et al. (2020), the domain of application of Eq. 6-30 was expanded to a measured experimental μ_{max} value equal to 69.20%.

$$P_{\max,long} = 3.4221\mu_{\max}^{0.6695} \qquad 6\text{-}30$$

Subsequently, combining all the experimental data, the exponential relationship, given in Eq. 6-31, was determined and plotted with a black dotted line in Figure 6-27.

$$P_{\max,long} = 3.9262\mu_{\max}^{0.5852} \qquad 6\text{-}31$$

As a result, although the accuracy of the analytical prediction was significantly impacted by the data scattering measured in Wang et al. (2020) experimental work, the updated exponential trend resulted in an improvement of scientific knowledge in terms of: (i) increase of available experimental data from naturally corroded prestressing strands and (ii) improvement of the coefficient of correlation, R^2, of the original correlation, from 0.49 to 0.53. In this regard, the dispersion of data measured by Wang et al. (2020) can be attributed to two

concurrent factors: (i) the adoption of a different corrosion process, in this case the use of the ACE method instead of natural corrosion, and (ii) the adoption of a manual measurement procedure for the maximum penetration depth instead of an accurate 3D scanning technique.

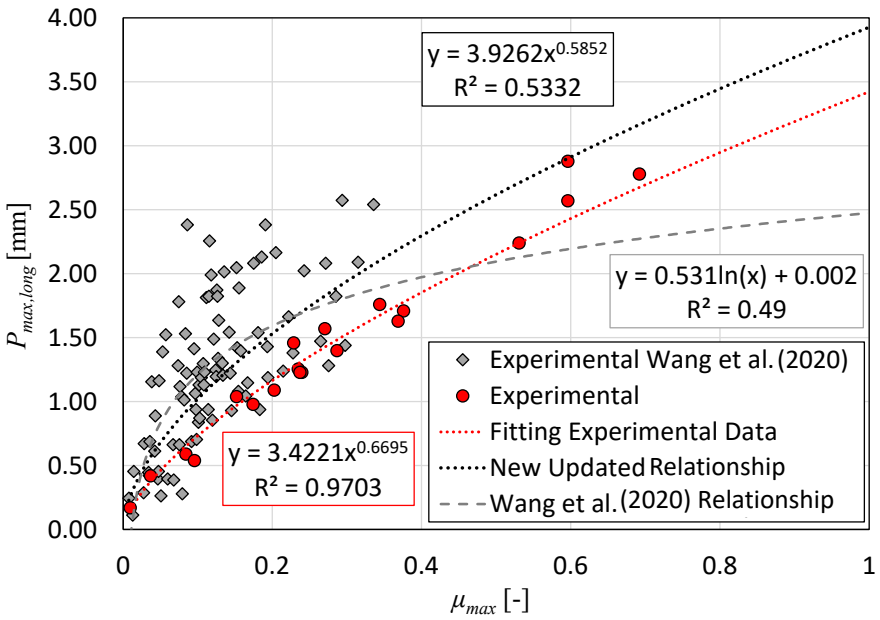

Figure 6-27 Relationship between $P_{max,long}$ and μ_{max}.

6.4.3.5 Wire unit cross-sectional loss vs strand unit cross-sectional loss

Further discussions concerned the relationship between the cross-sectional loss of the most corroded wire, μ_{max}, and the cross-sectional loss of the overall strand, μ_{strand}.

As shown in Figure 6-28, the measured experimental data – reported in Table 6-3 – were adopted to extend the original relationship proposed by Jeon et al. (2020). Specifically, the polynomial trend, reported in Eq. 6-32, was established from the analysis of corroded prestressing strands retrieved from naturally corroded dismantled bridges and was limited to μ_{max} and μ_{strand} values of approximately 35% and 10%, respectively. Thanks to the new data from the present research, an updated exponential version of the relationship, as expressed in Eq. 6-33, was proposed in which the domain of application was extended up to μ_{max} and μ_{strand} values of 69.20% and 21.28%, respectively.

$$\mu_{\max} = 26093\mu_{strand}^{5} - 12227\mu_{strand}^{4} + 1954.80\mu_{strand}^{3} - 140.35\mu_{strand}^{2} + 7.03\mu_{strand} \quad 6\text{-}32$$

$$\mu_{\max} = 1.9018\mu_{strand}^{0.7794} \quad 6\text{-}33$$

As a result, for a cross-sectional loss of the most corroded wire, μ_{max}, equal to 100%, corresponding to the deterioration of the entire external wire, a cross-sectional loss of the overall strand, μ_{strand}, of approximately 43% was predicted. Furthermore, it was demonstrated how, as the cross-sectional loss of the most corroded wire increased, the remaining wires could also be affected by different corrosion levels, leading to an exponential reduction of the cross-sectional loss of the overall strand. Therefore, once the most corroded wire is completely deteriorated, the contributions provided by the remaining wires are a fundamental resource for the residual mechanical behaviour of a corroded prestressing strand.

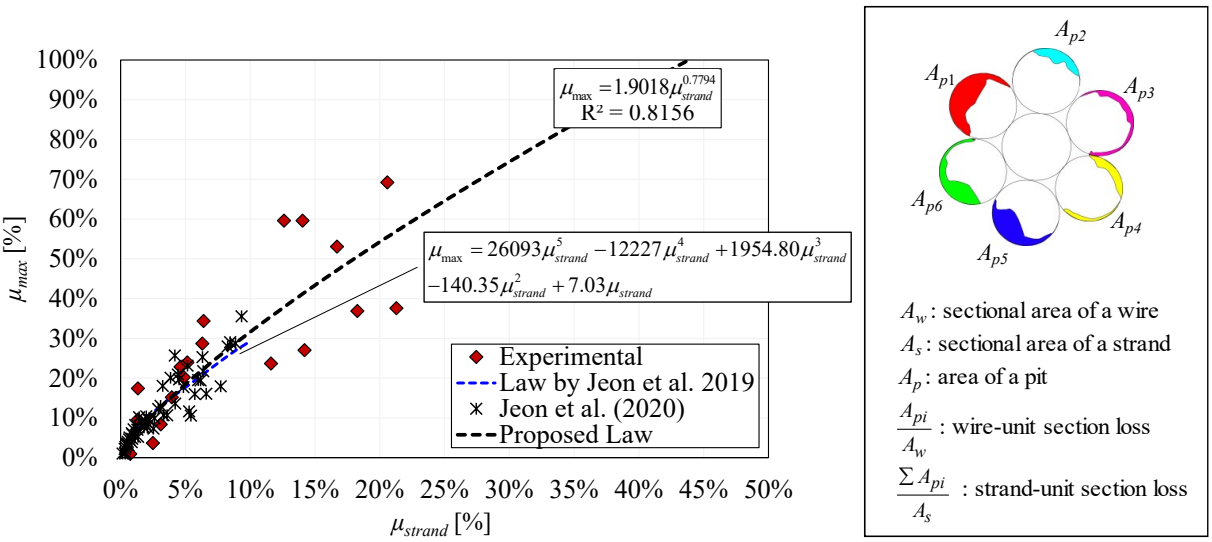

Figure 6-28 Relationship between μ_{max} and μ_{strand}.

6.4.4 Overview on longitudinal pitting factor

In the scientific literature, the longitudinal pitting factor is generally defined as the ratio between the maximum longitudinal penetration depth and the average penetration depth based on a homogeneous corrosion attack. Over the past decades, several experimental studies on corroded RC specimens have been conducted worldwide to investigate the pitting factor variability, revealing a significant dispersion of experimental outcomes. First, Tuutti (1982) observed a pitting factor range between 4 and 10 by conducting a two-year experimental campaign during which reinforcing rebars were subjected to accelerated corrosion by means of an external voltage source of approximately 1 V. Then, Apostolopoulos et al. (2013) compared the behaviour of reinforcements embedded in concrete and bare bars exposed to the same corrosion level (expressed in terms of mass loss). The outcomes revealed a greater aggressiveness of pitting corrosion in the case of embedded reinforcements, especially in terms of maximum penetration depth and pit planar dimensions. In detail, a pitting factor range from 4 to 8 was measured for B500c bars embedded in concrete cylinders previously placed in a salt-spray exposure chamber. Furthermore, Gonzalez et al. (1995) defined pitting factor values ranging from 2.7 to 8.9 in the case of natural corrosion and from 5.9 to 16.1 in the case of accelerated corrosion.

A lack of experimental studies was observed on the same topic in the case of corroded prestressing strands. In fact, Darmawan and Stewart research (2007) investigated the pitting factor of several prestressing wires and strands previously subjected to an accelerated corrosion process using a current density of 80 $\mu A/cm^2$. The outcomes revealed pitting factor ranging from 8.5 to 10.9 and from 8.1 to 11.0 in the case of prestressing wires and strands, respectively. To fill this gap, the present research analyzed the pitting factors of naturally corroded prestressing strands for the first time, with the aim of providing useful data for an accurate description of the pitting spatial variability of this particular type of reinforcements.

Hereafter, longitudinal pitting factors were defined to characterize the longitudinal spatial variability of the analyzed corroded strands. The longitudinal pitting factor, α, is unique to each corroded strand and is a useful factor to identify the axial corrosion condition. In this regard, three different expressions for the longitudinal pitting factor have been proposed in the following paragraph on the basis of three different methods for quantifying the average longitudinal penetration depth.

6.4.4.1 Average penetration depth definition

In addition to the previously estimated $P_{av,long1}$, two new definitions of the average longitudinal penetration depth, denoted as $P_{av,long2}$ and $P_{av,long3}$, were introduced as expressed in Eq. 6-34 and Eq. 6-35.

$$P_{av,long2} = \frac{\phi_{eq,0}}{2}\left[1-\left(1-\frac{\eta}{100}\right)^{0.5}\right] \quad 6\text{-}34$$

$$P_{av,long3} = \frac{\sum_{1}^{n_{external}} P_{\max,long,i}}{n_{external}} \quad 6\text{-}35$$

$P_{av,long2}$ was calculated as a function of the mass loss value, η, of each corroded strand, where $\phi_{eq,0}$ corresponds to the un-corroded equivalent diameter of the seven-wire prestressing strand; whereas, $P_{av,long3}$ was calculated as the average value of the six, $n_{external}$, maximum penetration depths measured for each external wire, $P_{max,long,i}$, through the GOM Inspect analysis, as shown in Figure 6-29. The latter parameter, in particular, was evaluated to simultaneously account for the contributions of external wires in the overall response of a corroded strand.

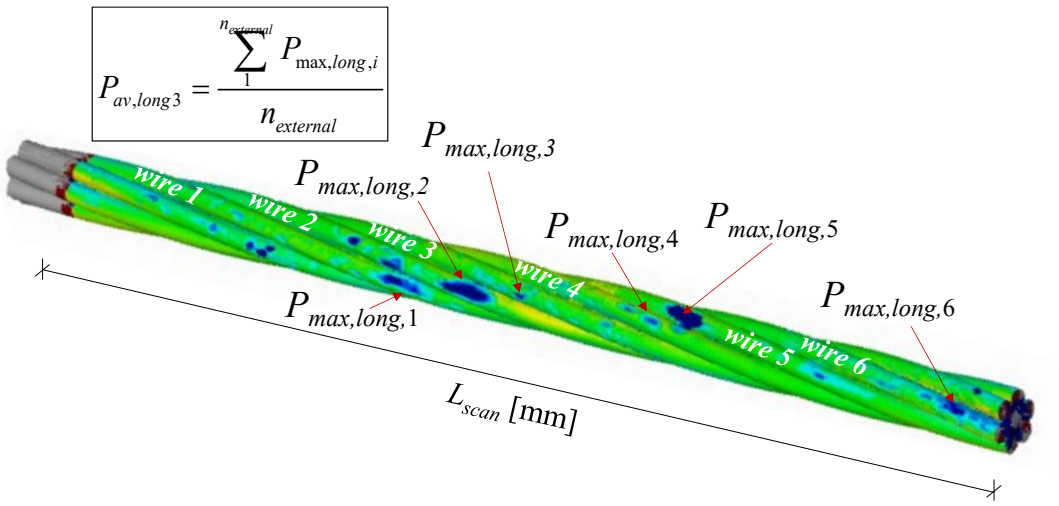

Figure 6-29 Focus on $P_{av,long3}$ calculation.

For the sake of completeness, the normalized values of $P_{av,long2}/r_{outer}$ and $P_{av,long3}/r_{outer}$ are obtained by dividing $P_{av,long2}$ and $P_{av,long3}$ values for the un-corroded radius of the external wire, r_{outer} , as reported in Table 6-5.

6.4.4.2 Longitudinal pitting factor calculation

Based on the different expressions of the previously determined average penetration depths, $P_{av,long1}$, $P_{av,long2}$, and $P_{av,long3}$, as many longitudinal pitting factor values, denoted as α_1, α_2, and α_3, were estimated. As previously stated, the longitudinal pitting factor was defined as the ratio between the maximum penetration depth, assumed to be $P_{max,long}$, and the average penetration depth calculated as a function of the mass loss value as if the corrosion was homogeneous. Therefore, the "*classic"* version of the longitudinal pitting factor was calculated according to Eq. 6-36 – with i equal to 2 – by adopting $P_{av,long2}$ values. Conversely, different interpretations of pitting factor – α_1 and α_3 – were proposed through Eq. 6-36 – with i equal to 1 and 3 – by using $P_{av,long1}$ and $P_{av,long3}$ values, respectively. Nevertheless, the calculated longitudinal pitting factors were always greater than 1.0 and were inconsistent over time, varying as a function of the corrosion level of the analyzed sample.

$$\alpha_i = \frac{P_{\max,long}}{P_{av,long,i}} \quad for \quad i = 1,2,3 \qquad 6\text{-}36$$

Referring to the average longitudinal penetration depth evaluated as the mathematical average of detected pits, $P_{av,long1}$, the measured pitting factors varied between 2.53 to 10.84. As shown in Figure 6-30(a), for low corrosion levels, the pits were localized along the sample length and a significantly disparity was generally observed between sectional and average penetration depths, leading to α_1 values close to 10. Conversely, as the corrosion level increased, the sectional difference in penetration depth, and consequently α_1 values, decreased, leading to α_1 values between 4 and 2. Once again, the reduction in pitting factor was strictly related to the appearance of multiple pits with variable penetration depths along the overall sample length, which yield to a more homogeneous longitudinal corrosion pattern as the corrosion level increased. Analyzing the variability of the pitting factor based on the average longitudinal penetration depth, $P_{av,long2}$, estimated as a function of η values, a range of α_2 from 2.92 to 15.11 was obtained, as shown in Figure 6-30(b). This range was comparable to the one (2.7 to 8.9) indicated by Gonzalez et al. (1995) in the case of naturally corroded reinforcing rebars. Nevertheless, having compared the obtained outcomes to the range (8.1-11.0) reported by Darmawan and Stewart (2007) for artificially corroded prestressing strands, a greater dispersion of measurements was noted. The observed discrepancy was attributable to the adopted corrosion process, which was natural instead of artificially accelerated.

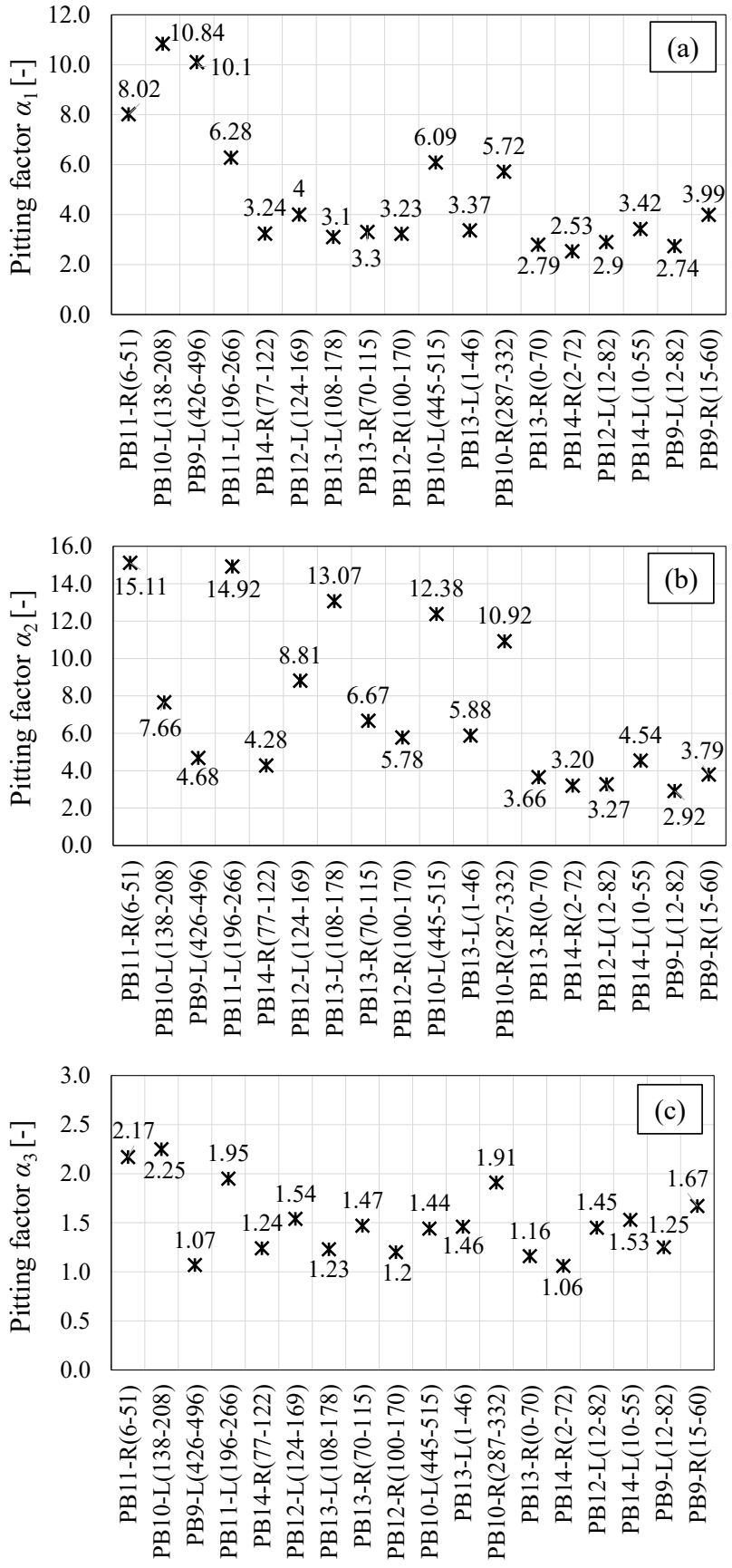

Figure 6-30 Pitting factor variability for: (a) $P_{av,long1}$, (b) $P_{av,long2}$ and (c) $P_{av,long3}$ measurements for increasing corrosion level expressed in terms of mass loss values, η.

Finally, considering $P_{av,long3}$ measurements, it was observed how the maximum longitudinal penetration depth increased with the increase in corrosion level. In particular, a linear regression trend, with a coefficient of correlation R^2 of 0.969, was established to fit the available data. As a result, regardless of the corrosion level of each analyzed strand, the maximum longitudinal penetration depth, $P_{max,long}$, was discovered to be 1.506 times the longitudinal average penetration depth, expressed in the form $P_{av,long3}$, as shown in Eq. 6-37 and Figure 6-31.

$$P_{\max,long} = \frac{1}{0.6638} P_{av,long3} = 1.506 P_{av,long3} \qquad 6\text{-}37$$

The calculated pitting factors ranged between 1.06 and 2.25. For sample PB14-R(2-72), the low α_3 value was caused by the presence of six deep pits on the external surface of adjacent wires. Since pits having a similar penetration depth were detected on all external wires, the maximum and average penetration depths were similar, resulting in a pitting factor close to 1. On the contrary, sample PB10-L(138-208) showed the highest α_3 value equal to 2.25. In this particular sample, three external wires were classified as un-corroded, while the other three showed a low corrosion level with pit depths ranging from 0.1 mm to 0.4 mm. Since the highest corrosion area was located in a single wire, showing only one pit depth of 0.59 mm, a tangible difference between maximum and average penetration depth was calculated.

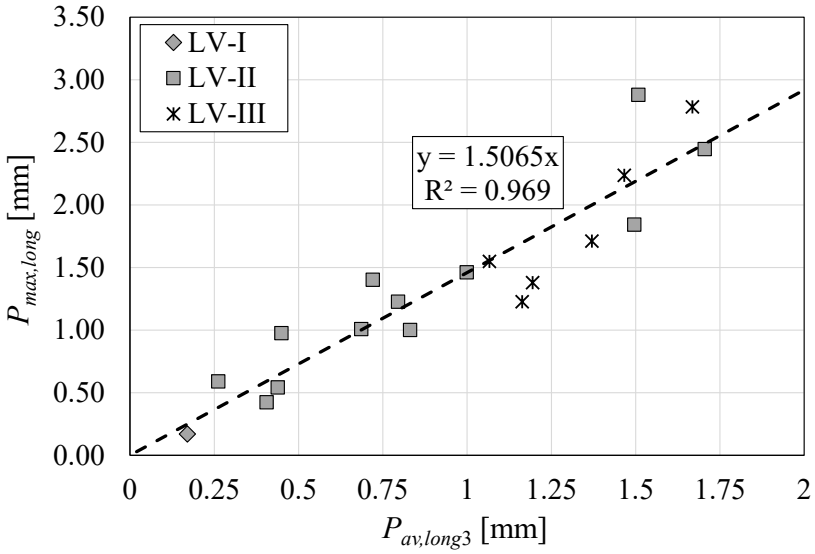

Figure 6-31 Relationship between $P_{max,long}$ and $P_{av,long3}$.

Table 6-5 Longitudinal average penetration depths and corresponding pitting factors in the case of corroded strands.

Sample ID	$P_{av,long2}/r_{outer}$ [-]	$P_{av,long3}/r_{outer}$ [-]	α_1 [-]	α_2 [-]	α_3 [-]
PB9-L(12-82)	0.27	0.64	2.74	2.92	1.25
PB9-L(426-496)	0.04	0.19	10.10	4.68	1.07
PB9-R(15-60)	0.35	0.78	3.99	3.79	1.67
PB9-R(428-473)	Un-corroded				
PB10-L(138-208)	0.04	0.12	10.84	7.66	2.25
PB10-L(445-515)	0.10	0.80	6.09	12.38	1.44
PB10-R(32-102)	-	-	-	-	-
PB10-R(287-332)	0.12	0.71	5.72	10.92	1.91
PB11-L(5-75)	Un-corroded				
PB11-L(196-266)	0.04	0.34	6.28	14.92	1.95
PB11-R(6-51)	0.03	0.21	8.02	15.11	2.17
PB11-R(273-318)	-	-	-	-	-
PB12-L(12-82)	0.22	0.50	2.90	3.27	1.45
PB12-L(124-169)	0.07	0.37	4.00	8.81	1.54
PB12-R(100-170)	0.08	0.39	3.23	5.78	1.20
PB12-R(358-403)	Un-corroded				
PB13-L(1-46)	0.12	0.47	3.37	5.88	1.46
PB13-L(108-178)	0.07	0.70	3.10	13.07	1.23
PB13-R(0-70)	0.18	0.56	2.79	3.66	1.16
PB13-R(70-115)	0.07	0.32	3.30	6.67	1.47
PB14-L(10-55)	0.23	0.69	3.42	4.54	1.53
PB14-L(455-500)	Un-corroded				
PB14-R(2-72)	0.18	0.54	2.53	3.20	1.06
PB14-R(77-122)	0.06	0.21	3.24	4.28	1.24

6.5 Main observations

To accurately evaluate the chloride-induced corrosion effects on the spatial variability of longitudinal and transversal pitting morphology of prestressing strands, a total of twenty-four samples (twenty corroded and four un-corroded) were retrieved from six naturally corroded PC beams subjected to 10 years of sea water wet-dry cycles. The overall procedure consisted of five main phases. First, a visual inspection and classification of available samples was conducted based on (i) the sample length, (ii) the detected corrosion level, and (iii) the presence or absence of concrete surface defects in the region of the beam where the samples were retrieved. Subsequently, the mass loss calculation carried out adopting the ASTM G1-03 standard procedure, the 3D scanning of corroded and un-corroded samples as well as the post-processing of data performed using the GOM Inspect software were individually conducted. The experimental data, obtained from the superimposition of 3D models of corroded and un-corroded strands and the sectional analysis conducted every 10 mm of each corroded sample, were then analyzed and several observations and useful correlations between the main investigated corrosion damage parameters were proposed, supported by a careful comparison with the data available to date in the scientific literature. The main results are summarized as follows:

- A total of 101 scanned pits were geometrically classified in terms of area loss due to pitting, A_p, adopting three pit type morphology configurations, referred to as (i) hemispherical (Type 1), (ii) half-moon (Type 2) and (iii) planar (Type 3), respectively. According to the findings, 46.5%, 6%, and 47.5% of pits were classified as Type 1, Type 2, and Type 3, respectively. Furthermore, regardless of the possible pit type morphology configuration, two analytical expressions were proposed for the prediction of the area loss due to pitting, A_p, as a function of the increasing corrosion level expressed in terms of measured penetration depth, P_x. The proposed relationships aim to overcome the issue related to the proper evaluation of the actual pit type morphology configuration during in-situ measurements, resulting in more accurate and less time-consuming operations.
- Considering the outcomes of the pitting morphology longitudinal variability, penetration depth and minimum residual cross-sectional area, A_{min}, were found to be random variables along the sample length. In particular, it was discovered that in the case of prestressing reinforcements, the maximum penetration depth and the minimum residual cross-section may not occur at the same location due to the effects

associated with the different corrosion levels exhibited by external wires. Furthermore, the 3D scanning procedure and the cleaning phase of corroded samples – conducted in the present research – revealed that the inner wire was un-corroded since it did not show any corrosion signs.

- The effect induced by the presence of concrete surface defects on the longitudinal spatial variability of pitting morphology was investigated. On the one hand, samples belonging to beam regions unaffected by surface defects displayed a random corrosion pattern with a strong localization of pits. On the other hand, the presence of surface defects induced a significant increase in the corrosion level of prestressing reinforcements in terms of both maximum longitudinal penetration depth, $P_{max,long}$, and uniformity of damage pattern, expressed in terms of average longitudinal penetration depth, $P_{av,long1}$. In the case of longitudinal splitting cracks, all analyzed sections revealed corrosion signs in one or more external wires showing pitting damage.

  Furthermore, the role of a construction practice deficiency consisting in the lack of prestressing reinforcements protection at all beam edges was analyzed. As a result, preferential pathways promoting the chloride ions attack through direct contact of external aggressive agents and prestressing reinforcements, were developed, leading to a more aggressive chloride-induced corrosion at the beam edges, characterized by deeper and more diffusely distributed pits. Additionally, the effects of concrete surface defects were considered in the definition of three-linear measurement-based-correlations for predicting the maximum penetration depth of the most corroded wire as a function of different corrosion parameters, such as mass loss (η), average longitudinal penetration depth ($P_{av,long1}$), and detected number of pits per meter (n_{pits}/m), respectively. The proposed relationships are essential for a preliminary description of the differences in behaviour between cracked and un-cracked PC members.

  - For a complete description of the pitting morphology, the pitting factor of naturally corroded prestressing strands was investigated for the first time by considering its transversal (sectional) variability. The transversal pitting factor, Ω_i, was defined as the product of two parameters, named intensity factor γ_i and transversal factor β_i. Based on experimental Ω_i measurements performed by adopting the GOM Inspect software, a simplified approach was proposed for the prediction of the average sectional penetration depth $P_{av,transv,i}$ of external wires as a function of the maximum

one $P_{max,sectional,i}$. The proposed correlations, specifically stated in the dedicated paragraph, were conceived to partially overcome the problems associated with the in-situ assessment of embedded prestressing reinforcements in existing structures. In fact, only exposed external wires can be visually inspected on-site, without any possibility to deeply identify the actual corrosion damage of hidden wires. On the contrary, the application of the proposed correlation enables the prediction of the average sectional penetration depth, in the form $P_{av,transv,i}/r_{outer}$, as a function of the single $P_{max,sectional,i}/r_{outer}$ measurement.

- Finally, the variability of penetration depths along the sample length were evaluated by adopting different probability distribution functions, such as Normal, Lognormal, Gamma, and Gumbel extreme-values distributions. Based on the obtained results, the Lognormal function provided the best fitting of experimental data in terms of both probability density function, PDF, and cumulative distribution function, CDF, respectively. As previously pointed out, new structural reliability methods on the basis of the obtained probabilistic results might be proposed.
- In addition, correlations between different corrosion damage assessment parameters were defined. These latter should be considered as useful tools for the comparison and the correlation of different experimental campaigns.
- In light of the following chapter, concerning the proposal of constitutive laws for the prediction of the residual response of corroded prestressing strands, some of the proposed correlations are essential for the proper estimation of reduced stress-strain relationships.

7 Definition of constitutive laws for corroded strands

7.1 Highlights

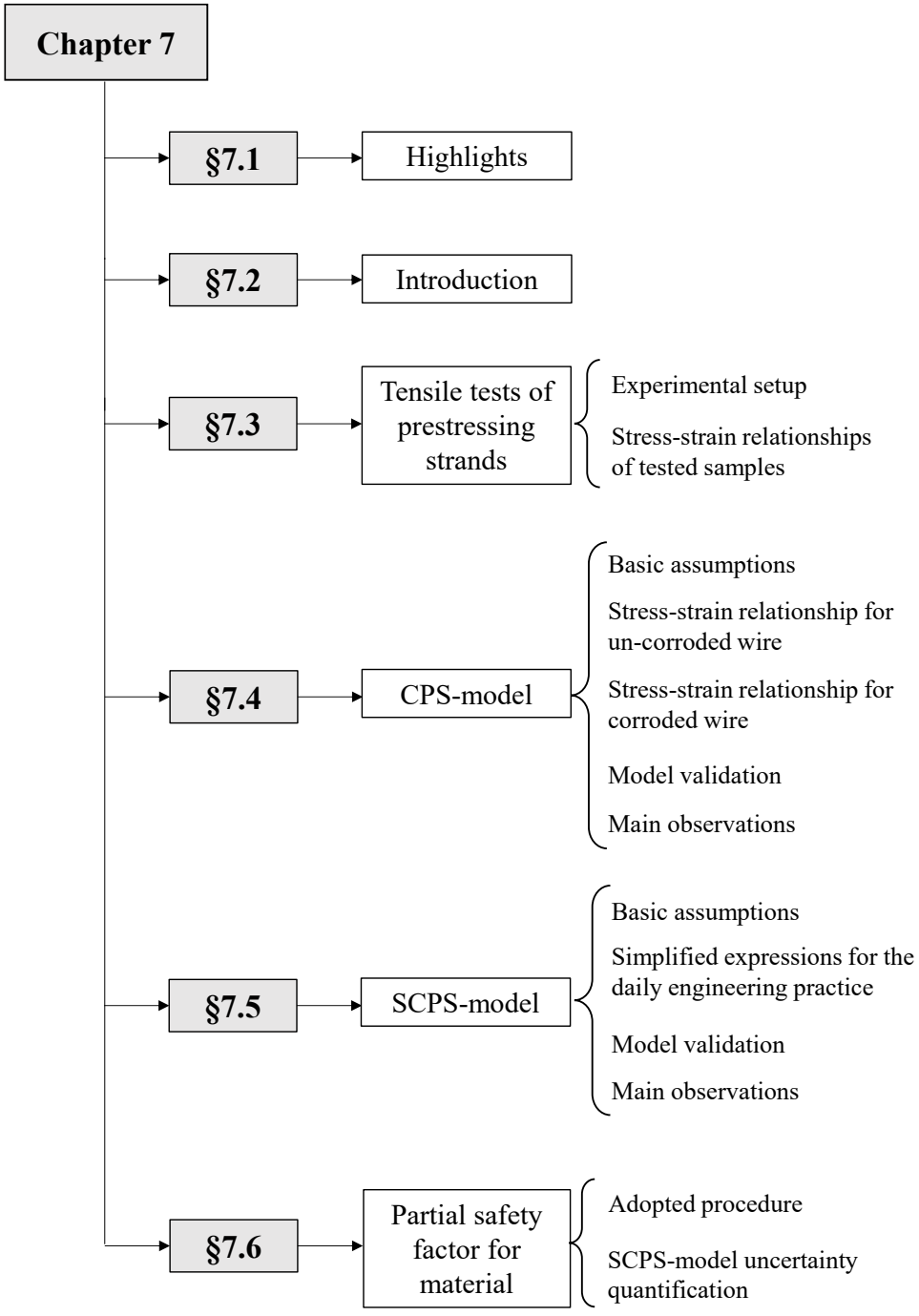

IMPORTANT NOTES: The topics covered in this chapter directly refers to statements, figures and results published by the author in the below mentioned works available in scientific literature:

- **Franceschini L.**, Vecchi F., Tondolo F., Belletti B. & Sanchez J. (2022). *Mechanical behaviour of corroded strands under chloride attack: a new constitutive law*. Construction and Building Materials, 316: 125872. https://doi.org/10.1016/j.conbuildmat.2021.125872

- **Franceschini L.**, Belletti B., Tondolo F. & Sanchez J. (2022). *A simplified stress-strain relationship for the mechanical behaviour of corroded prestressing strands: the SCPS-model*. Structural Concrete. https://doi.org/10.1002/suco.202200170

- **Franceschini L.**, Botte W., Caspeele R., Belletti B., Tondolo F. & Sanchez J. (2023). *Partial safety factor for the design strength prediction of naturally corroded prestressing strands*. Proceedings of the 14th International Conference on Application of Statistics and Probability in civil engineering (ICASP14), 9th – 13th July 2023, Dublin, Ireland. *abstract accepted & paper submitted.*

- **Franceschini L.**, Vecchi F., Belletti B., Tondolo F. & Sanchez J. (2021). *SCPS-Model: a Simplified Stress-strain Model for Corroded Prestressing Strands*. Proceedings of the *fib* CACRCS Days 2021: *Capacity Assessment of Corroded Reinforced Concrete Structures*, 30th November – 3rd December 2021, venue on-line, Italy, pp: 73-77.

7.2 Introduction

As extensively discussed in Chapter 3, a limited number of studies have been conducted to define a stress-strain constitutive law for corroded prestressing strands. To date, the state of the art has addressed the prediction of the tensile response of corroded prestressing strands according to two different approaches:

- By evaluating the corroded strand as a rebar;
- By estimating the overall behaviour of the corroded strand by summing the wires contributions (equivalent spring model).

Regarding the first approach, Zona et al. (2008), Wang et al. (2020), and Lu et al. (2016) proposed a simplified elastic-hardening model. As for the second approach, Jeon et al. (2019) proposed an equivalent spring model, while Zhang et al. (2019) established a stochastic stress-strain relationship for corroded prestressing wires based on a random generation of cross-sectional areas. Considering the uncertainty of the available models and the lack of scientific studies comparing natural pitting corrosion characterization with mechanical test outcomes, such as prestressing strands strength and ductility, the prediction of the residual mechanical response of corroded strands requires further efforts and investigation.

To fill the gap, tensile tests were first conducted at the Politecnico of Turin on the available corroded and un-corroded prestressing strands to evaluate their residual mechanical response. Then, within the framework of the equivalent spring model, a refined sectional stress-strain relationship, named CPS-model, was defined based on the pit type morphology configurations and the cross-sectional losses of the corroded wires. Although the proposed CPS-model has been successfully validated on the experimental stress-strain relationships from the present research and the studies conducted by Jeon et al. (2019) and by Giriraju et al. (2022), its application in daily engineering practice may be limited by the complexity of expressions, the number of corrosion parameters involved and the practical difficulty of conducting an in-situ visual classification of the actual pit type morphology configuration. Therefore, an additional simplified stress-strain relationship, named SCPS-model, was proposed.

The SCPS-model is based exclusively on the maximum penetration depth of the most corroded wire and remains independent from the classification of the pit type morphology and from cross-sectional or mass loss measurement. Moreover, simplified expressions were introduced for the prediction of the ultimate corroded strain, and an average penetration depth was attributed to the remaining external wires, based on the results of the spatial variability of pitting corrosion obtained in Chapter 6. From the model validation outcomes, the SCPS-model

proved to be a useful tool for engineers in current practice due to its reliable predictions of the residual mechanical properties of corroded strands.

Finally, referring to the draft Model Code 2022 recommendations, a partial material safety factor was evaluated for the first time for defining the ultimate design strength of a corroded prestressing strand to be used in the assessment of existing PC members. In detail, the proposed partial safety factor takes into account several uncertainties related to: (i) geometrical properties, (ii) mechanical properties of un-corroded prestressing steel, and (iii) failure mode. In addition, to account for the corrosion effects, the resistance SCPS-model uncertainties associated with maximum penetration depth measurement and ultimate corroded mechanical properties prediction were estimated. Although the adopted procedure could be improved with the future availability of additional experimental outcomes on corroded prestressing strands, the preliminary proposed partial safety factor should be considered as a useful tool for a reliable and time-efficient assessment of the residual capacity of corroded PC members.

7.3 Tensile tests of prestressing strands

7.3.1 Experimental set-up

To investigate the residual mechanical behaviour of the 18 available corroded prestressing strands in terms of (i) failure sequence, (ii) ultimate corroded strength, $f_{pu,corr,exp}$, and (iii) ultimate corroded strain, $\varepsilon_{pu,corr,exp}$, tensile tests were conducted at the MastrLab Laboratory of the Politecnico of Turin. Furthermore, additional 4 tensile tests were performed on un-corroded strand samples to preliminary define the ultimate mechanical properties in terms of un-corroded ultimate strength, $f_{pu,0}$, and un-corroded ultimate strain, $\varepsilon_{pu,0}$.

To accurately record the wires failure sequence, the tensile tests were conducted under displacement-controlled procedure, adopting a universal testing machine with a maximum capacity of 250 kN, as shown in Figure 7-1. The fixing system consisted of two grips, which clamped the ends of the analyzed sample, and a customized bracing element realized with the combined use of epoxy resin cast in steel tubes, which prevented the strand-ends from being damaged and slipping during loading, Figure 7-1. The test set-up was completed by the DIC system – previously defined in Section 5.3.2 – for the analysis of the strain field evolution of the investigated sample evaluated through the post-processing of images taken upon achieving predefined loading stages, as in Figure 7-2. A high-resolution digital camera NikonD90 was adopted for image recording, whereas the strand external surface was white painted and a high-contrast black speckle pattern was applied alongside the ROI of the tested strand for a length equal to L_{scan}, as shown in Figure 7-2(a). Similar to the procedure conducted for the study of the displacement and the principal strain fields of corroded PC beams, the open source software package Ncorr was used to analyze the strain field evolution through the comparison of the reference image of the unloaded strand and the images of the elongated sample – acquired at each loading stage, Figure 7-2(b). To validate the efficiency of the DIC measurements, an axial extensometer with a gauge length of 25 mm was further adopted to directly measure the strand elongation during the first loading stages. Although the extensometer was removed at a relative low loading stage to avoid instrumental damage and to ensure workers safety in the event of a sudden strand breakage, the comparison between recorded experimental values and DIC predictions for samples PB9-L(12-82), PB10-L(445-515), and PB11-R(6-51) revealed an excellent agreement. In particular, the outcomes allowed to assume an elasticity modulus, $E_{p,0}$, of 195 GPa, as highlighted in Figure 7-4.

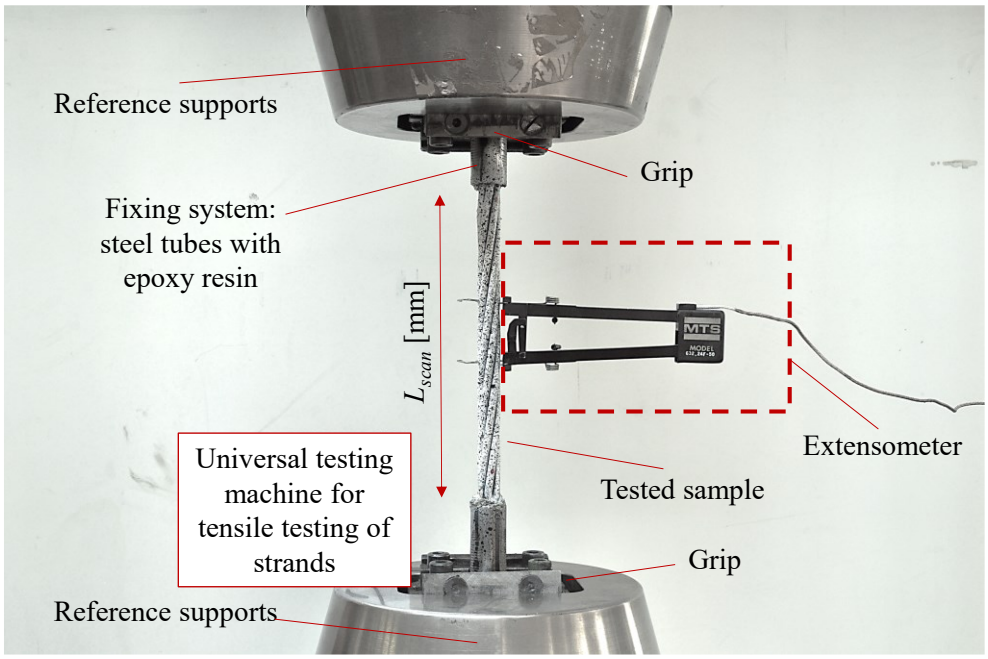

Figure 7-1 Tensile test set-up at the Laboratory MastrLab of the Politecnico of Turin.

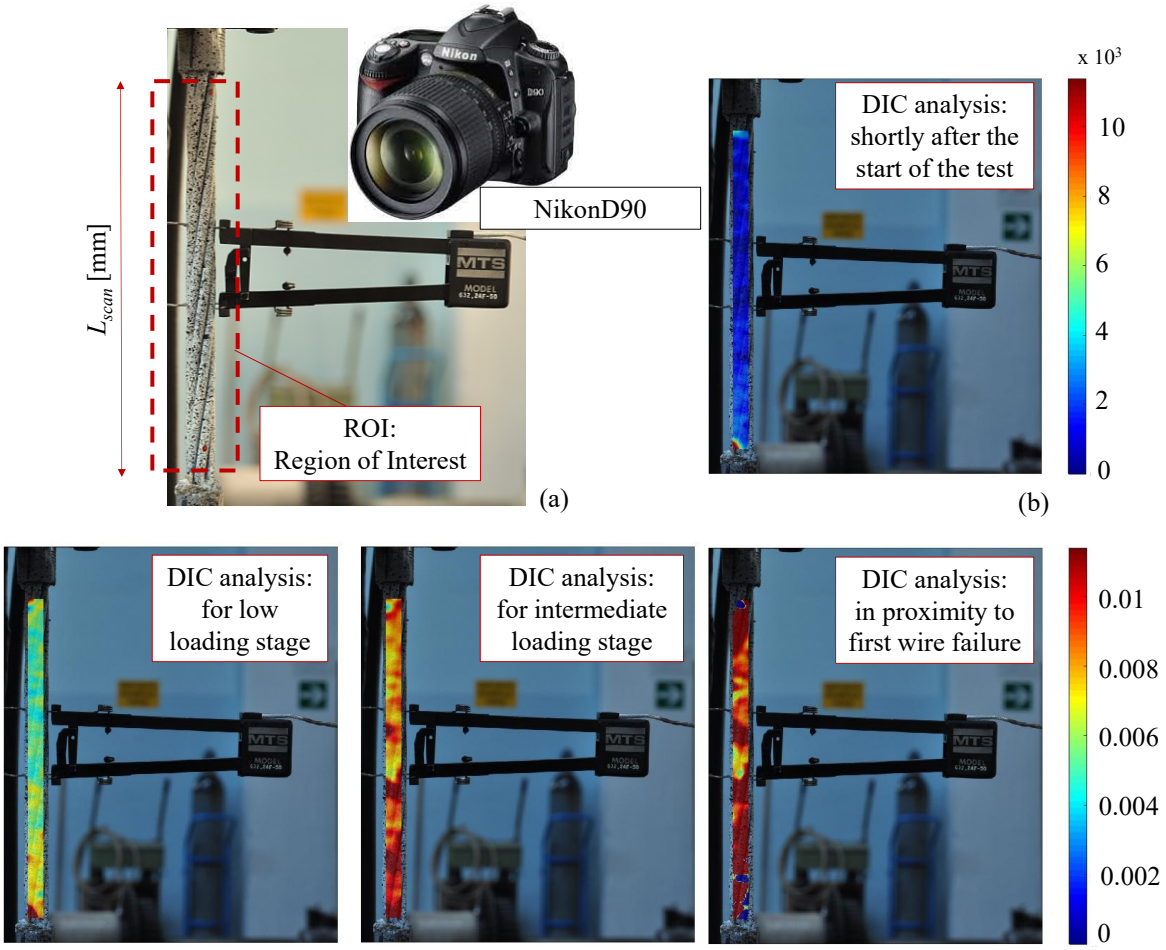

Figure 7-2 Focus on DIC methodology: (a) definition of ROI and speckle patter, and (b) example of post-processing of taken images by adopting Ncorr software.

7.3.2 Stress-strain relationships of tested prestressing strands

Following tensile testing, the experimental force-strain relationships of the analyzed samples were evaluated by combining the load recorded during the displacement-control procedure with the strain field evolution obtained from the DIC analysis. Subsequently, dividing the experimental tensile force, $T_{p,exp}$, by the un-corroded cross-section of the prestressing strand, $A_{p,0}$, previously assumed to be 100 mm^2, the experimental stress was calculated and the corresponding stress-strain relationships were defined, as depicted in the graph in Figure 7-3 and Figure 7-4 for un-corroded and corroded samples, respectively.

Analyzing the obtained stress-strain relationships, it was evident how, as the corrosion level of prestressing strand samples increased, a significant decay in ultimate mechanical properties in terms of both ultimate strength and ultimate strain occurred. In particular, the hardening phase in the stress-strain relationships was no longer visible for high corrosion level, resulting in a severe decay of ductility and the inevitable brittle failure of corroded prestressing strands. For low corroded samples, a residual hardening phase characterized by reduced ductility as well as reduced ultimate corroded strength, $f_{pu,corr,exp}$, was observed, resulting in a residual plastic behaviour of corroded prestressing strands. Nevertheless, regardless of the corrosion level of each tested sample, the elasticity modulus was marginally affected by chloride-induced corrosion, as previously pointed out by Zhang et al. (2019).

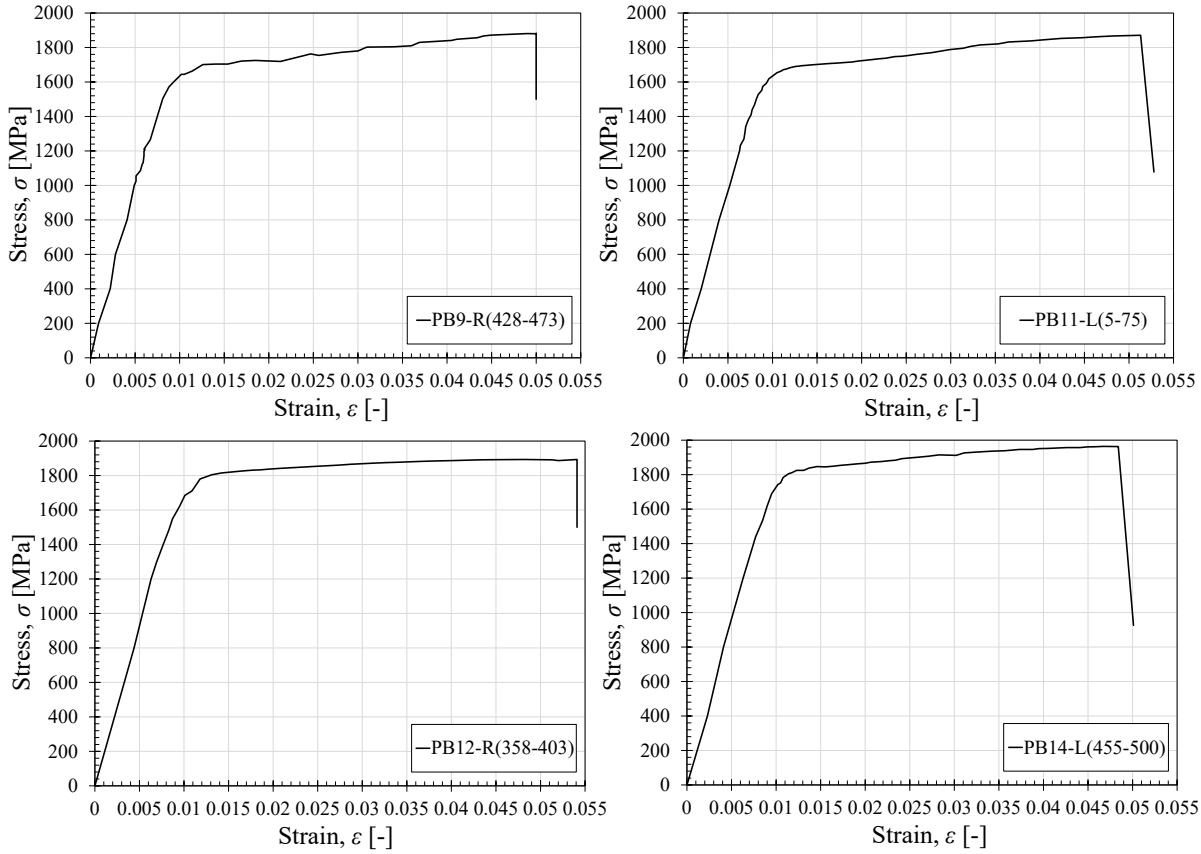

Figure 7-3 Experimental stress-strain relationships for un-corroded samples.

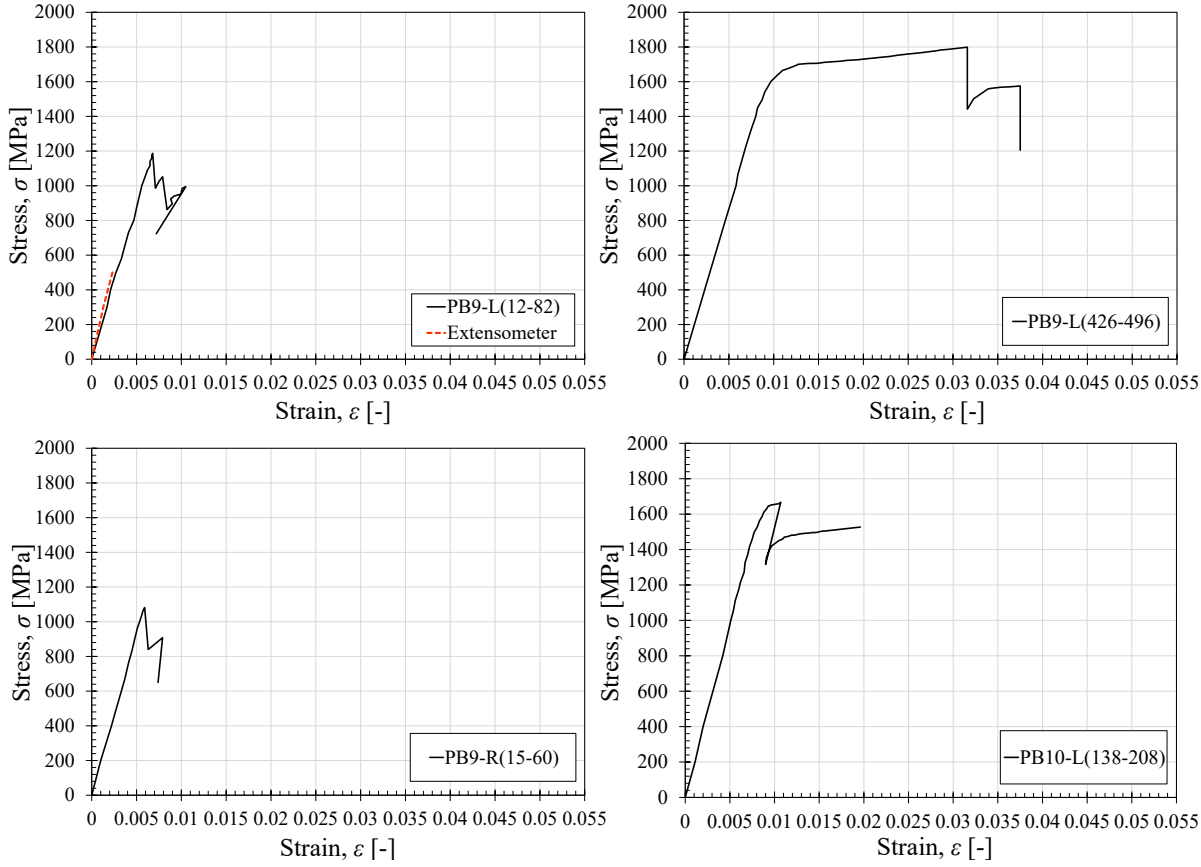

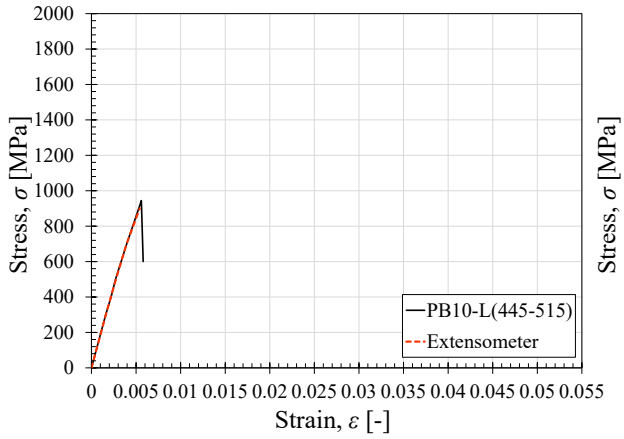
Stress, σ [MPa]
Strain, ε [-]
PB10-L(445-515)
Extensometer

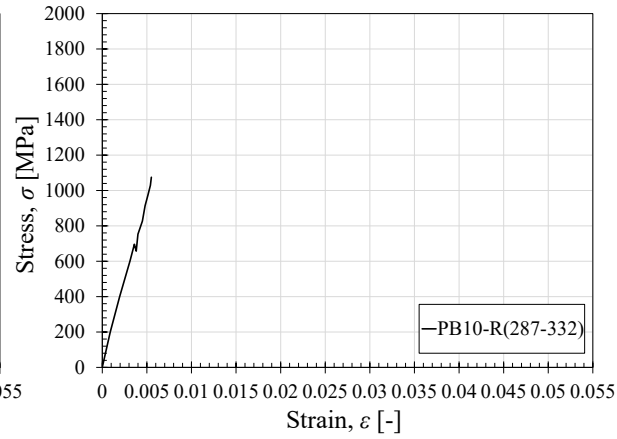
Stress, σ [MPa]
Strain, ε [-]
PB10-R(287-332)

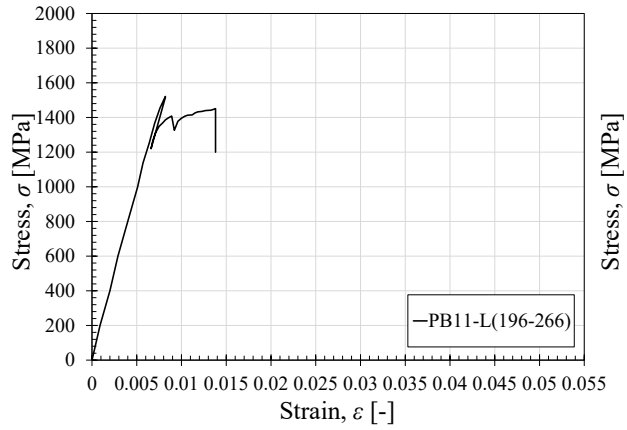
Stress, σ [MPa]
Strain, ε [-]
PB11-L(196-266)

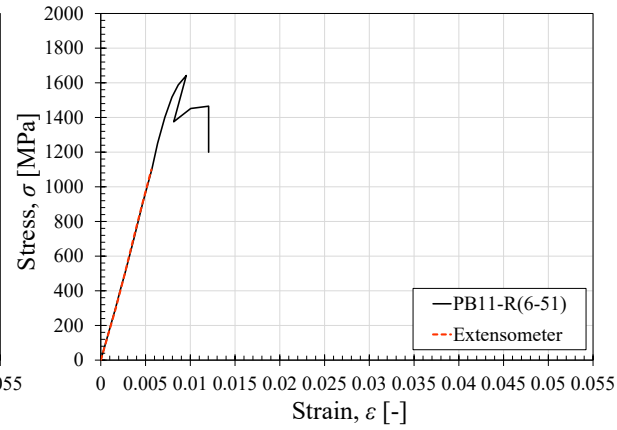
Stress, σ [MPa]
Strain, ε [-]
PB11-R(6-51)
Extensometer

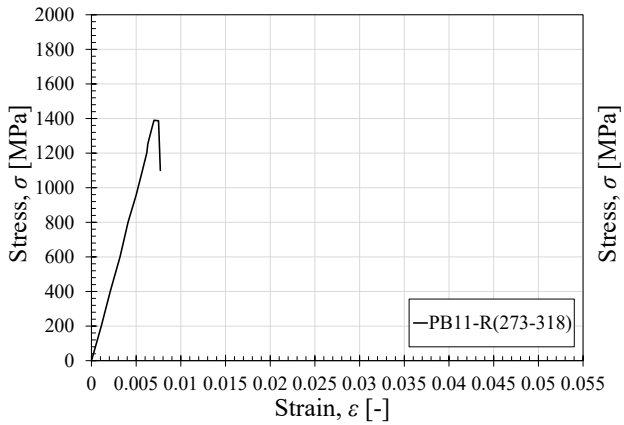
Stress, σ [MPa]
Strain, ε [-]
PB11-R(273-318)

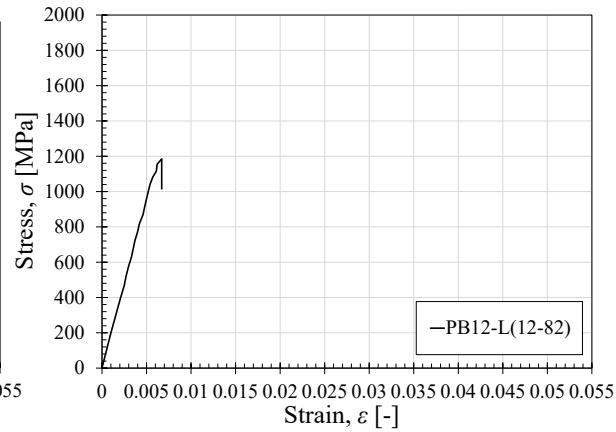
Stress, σ [MPa]
Strain, ε [-]
PB12-L(12-82)

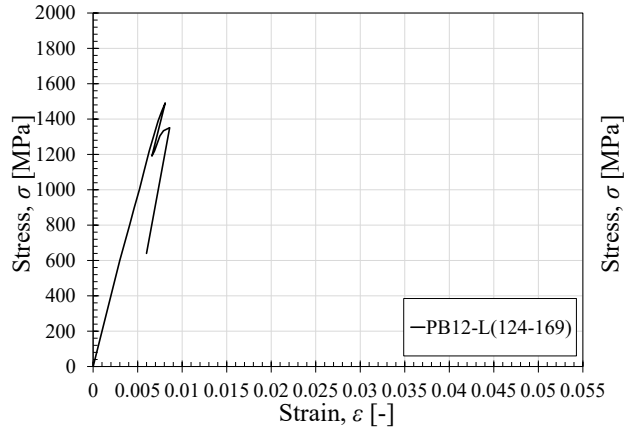
Stress, σ [MPa]
Strain, ε [-]
PB12-L(124-169)

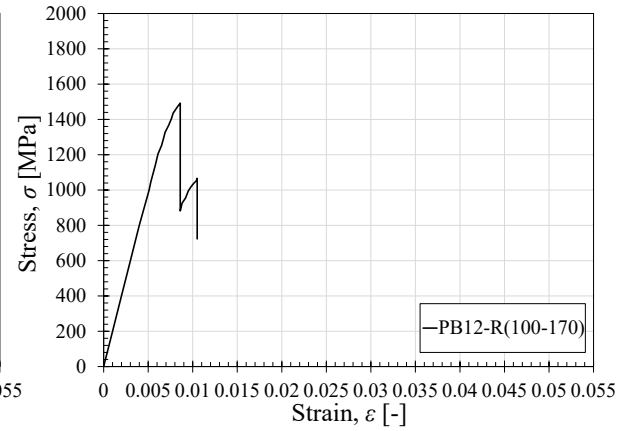
Stress, σ [MPa]
Strain, ε [-]
PB12-R(100-170)

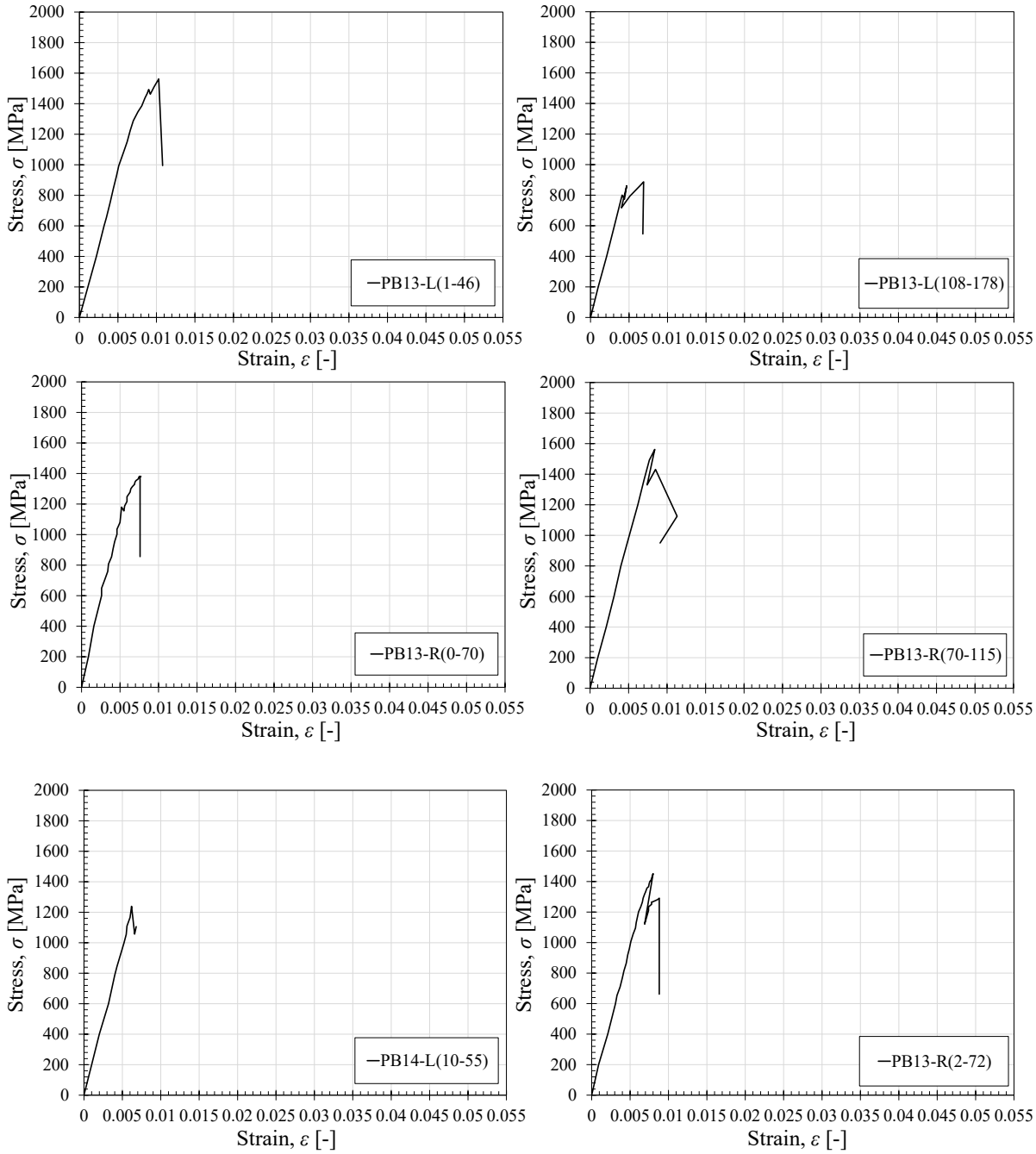

Figure 7-4 Experimental stress-strain relationships for corroded samples.

Although the adopted displacement-control procedure allowed for the failure sequences of the different corroded prestressing wires to be identified, as shown in Figure 7-5 by the subsequent drop-offs in the stress-strain relationship of sample PB9-L(426-496), the conventional failure of each corroded strand is assumed to occur in correspondence with the rupture of the most corroded wire, as stated by Jeon et al. (2019). This critical point coincides with the first recorded drop in the stress-strain relationship of each analyzed strand and occurred

at the section where the maximum longitudinal penetration depth, $P_{max,long}$, was measured during the pitting morphology analysis – point 1 in Figure 7-5.

For the sake of completeness, Table 7-1 reports the experimental ultimate tensile force, $T_{pu,corr,exp}$, the experimental ultimate corroded strength, $f_{pu,corr,exp}$, as well as the experimental ultimate corroded strain, $\varepsilon_{pu,corr,exp}$, evaluated at this conventional failure point. Since technical issues occurred during the tensile testing of sample PB14-R(77-122), the corresponding experimental outcomes are neglected in the following calculations and are not reported in Table 7-1.

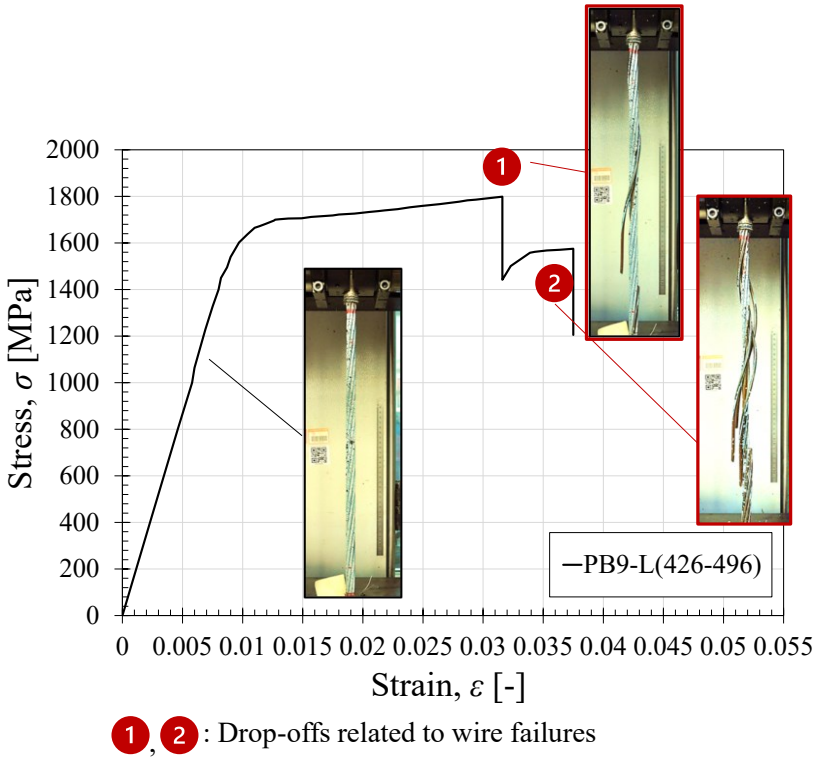

Figure 7-5 Focus on the failure sequence of sample PB9-L(426-496).

To validate the accuracy and faithfulness of the obtained results, the normalized values of $f_{pu,corr,exp}$ and $\varepsilon_{pu,corr,exp}$ were compared with experimental data coming from other research activities available in the scientific literature. First, the new data were expressed as a function of the strand mass loss, η, and compared with the experimental outcomes belonging to the work conducted by Lu et al. (2016), as highlighted in Figure 7-6. Second, considering the cross-sectional loss of the most corroded wire, μ_{max}, the same data were compared with the experimental outcomes belonging to Jeon et al. (2020; 2019) works, as reported in Figure 7-7. It is worth noting that $f_{pu,corr,exp}$ and $\varepsilon_{pu,corr,exp}$ values were normalized by dividing for the un-

corroded value of the ultimate strength, $f_{pu,0}$, and ultimate strain, $\varepsilon_{pu,0}$, respectively. These latter parameters, which resulted equal to 1901.75 MPa ($f_{pu,0}$) and 5.1% ($\varepsilon_{pu,0}$), were defined as the mathematical average of the tensile tests outcomes of the four un-corroded samples shown in Figure 7-3.

As attested by Figure 7-6 and Figure 7-7, the obtained experimental data were in good agreement with the outcomes from other research activities. In detail, the decay trend of the normalized ultimate corroded strength, $f_{pu,corr,exp}/f_{pu,0}$, as a function of both mass loss and cross-sectional loss of the most corroded wire was well fitted by linear regression expressions having R^2 values of 0.978 and 0.993, as expressed in Eq. 7-1 and Eq. 7-2, respectively.

$$\frac{f_{pu,corr,\exp}}{f_{pu,0}} = 1 - 2.828\eta \qquad 7\text{-}1$$

$$\frac{f_{pu,corr,\exp}}{f_{pu,0}} = 1 - 1.75448\mu_{\max} \qquad 7\text{-}2$$

Conversely, a lower fitting of experimental data was observed when analyzing the decay trend of the normalized ultimate corroded strain, $\varepsilon_{pu,corr,exp}/\varepsilon_{pu,0}$, where exponential expressions with R^2 values of 0.727 and 0.896 were derived, as expressed in Eq. 7-3 and Eq. 7-4 as a function of mass loss and cross-sectional loss variation, respectively. As a result, it can be stated that – fixing the mass loss of a corroded strand or the cross-sectional loss of the most corroded wire – the ultimate strain decay was remarkably higher than the ultimate strength decay. The residual ductility of corroded strands was therefore found to be significantly influenced by the corrosion process, being a key parameter governing the transition of the wire failure mode from ductile to brittle. In fact, as previously highlighted in Figure 7-4, the stress-strain relationship of highly corroded strands was characterized only by a linear-elastic phase, whereas the slightly corroded ones showed a residual hardening phase.

$$\frac{\varepsilon_{pu,corr,\exp}}{\varepsilon_{pu,0}} = 0.09337e^{\frac{0.0561}{0.02366+\eta}} \qquad 7\text{-}3$$

$$\frac{\varepsilon_{pu,corr,\exp}}{\varepsilon_{pu,0}} = 0.0899e^{\frac{0.06538}{0.02715+\mu_{\max}}} \qquad 7\text{-}4$$

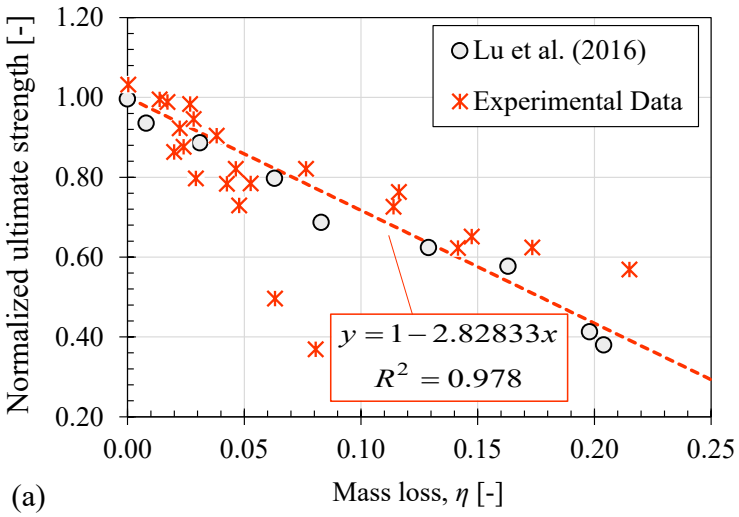

(a)

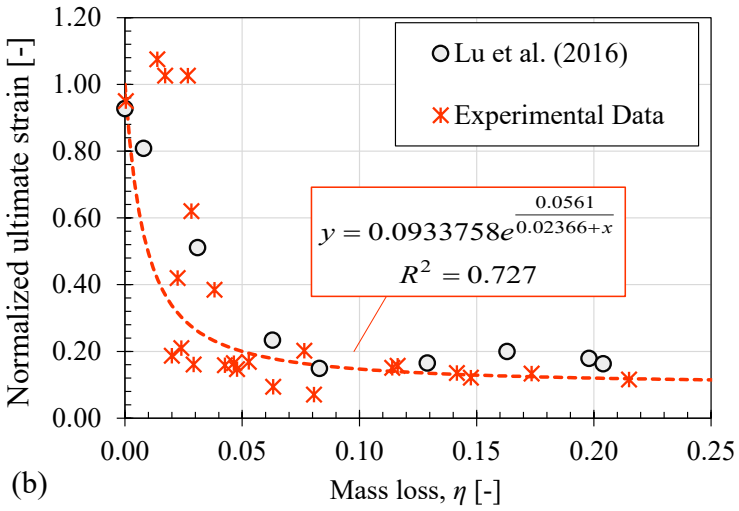

(b)

Figure 7-6 Comparison of experimental data with outcomes available in scientific literature as a function of strand mass loss: (a) ultimate corroded strength, and (b) ultimate corroded strain.

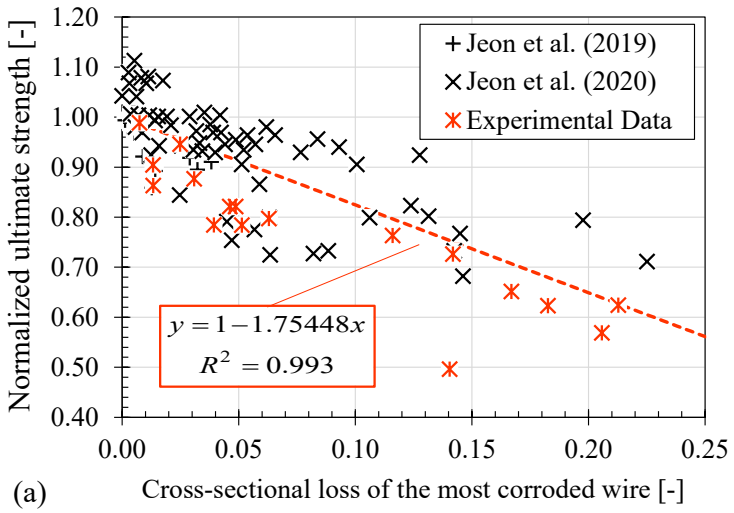

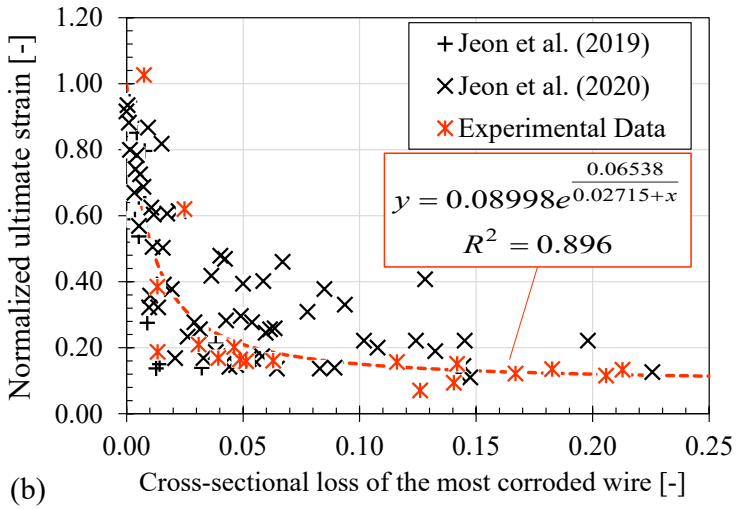

Figure 7-7 Comparison of experimental data with outcomes available in scientific literature as a function of the cross-sectional loss of the most corroded wire: (a) ultimate corroded strength, and (b) ultimate corroded strain.

Table 7-1 Tensile test outcomes in terms of ultimate tensile force, $T_{pu,corr,exp}$, ultimate strength, $f_{pu,corr,exp}$, and ultimate strain, $\varepsilon_{pu,corr,exp}$. The reported data consider also the un-corroded samples.

Sample ID	$T_{pu,corr,exp}$ [kN]	$f_{pu,corr,exp}$ [MPa]	$\varepsilon_{pu,corr,exp}$ [-]	Failure mode
PB9-L(12-82)	118.69	1186.90	0.0068	BRIT
PB9-L(426-496)	179.90	1799.00	0.0316	DUCT
PB9-R(15-60)	108.20	1082.00	0.0059	BRIT
PB9-R(428-473)	188.00	1880.00	0.0500	DUCT (un-corr.)
PB10-L(138-208)	166.70	1667.00	0.0107	DUCT
PB10-L(445-515)	94.40	944.03	0.0056	BRIT
PB10-R(32-102)	-	-	-	-
PB10-R(287-332)	69.60	696.00	0.0036	BRIT
PB11-L(5-75)	187.10	1871.00	0.0513	DUCT (un-corr.)
PB11-L(196-266)	151.60	1516.00	0.0082	BRIT
PB11-R(6-51)	164.20	1642.00	0.0095	BRIT
PB11-R(273-318)	138.70	1387.00	0.0075	BRIT
PB12-L(12-82)	118.50	1185.00	0.0069	BRIT
PB12-L(124-169)	149.10	1491.00	0.0081	BRIT
PB12-R(100-170)	149.20	1492.00	0.0086	BRIT
PB12-R(358-403)	189.30	1893.00	0.0541	DUCT (un-corr.)
PB13-L(1-46)	156.20	1562.00	0.0103	DUCT
PB13-L(108-178)	86.10	861.00	0.0047	BRIT
PB13-R(0-70)	138.10	1381.00	0.0077	BRIT
PB13-R(70-115)	156.20	1562.00	0.0084	BRIT
PB14-L(10-55)	123.90	1239.00	0.0062	BRIT
PB14-L(455-500)	196.30	1963.00	0.0484	DUCT (un-corr.)
PB14-R(2-72)	145.20	1452.00	0.0080	BRIT
PB14-R(77-122)	-	-	-	-

7.4 CPS-model: refined model for the prediction of the residual stress-strain response of a corroded strand

By combining the experimental data on the residual mechanical properties of corroded strands obtained from the tensile tests of the 18 corroded strands previously analyzed with the Finite Element Analysis (FEA) results provided by Jeon et al. (2019), a refined constitutive model was proposed for predicting the residual stress-strain response of a corroded strand, updating the equivalent spring model proposed by Jeon et al. (2019). The main steps of the proposed model, named CPS-model, which stands for "model for Corroded Prestressing Strands," were highlighted in the flowchart shown in Figure 7-8.

7.4.1 Basic assumptions

In general, the CPS-model was developed on the following fundamental assumptions:

I. **Input parameters:** The CPS-model is able to reproduce the entire failure sequence of a corroded strand by considering a different corrosion level for each wire. To this end, the input parameters of the sectional model are the maximum penetration depth of the corroded external wires and the preliminary visual classification of the pit type morphology configuration for each external corroded wire, which is to be selected between hemispherical (Type 1) – half-moon (Type 2) or planar (Type 3) shape, respectively. In addition, the un-corroded mechanical properties of the analyzed strands in terms of $f_{pu,0}$, $\varepsilon_{pu,0}$ and $E_{p,0}$ as well as the un-corroded radius of the external, r_{outer}, and internal, r_{inner}, wires must be provided. Although the CPS-model also allows a corrosion level to be attributed to the inner wire, from experimental evidence this latter parameter is assumed as un-corroded. Therefore, a maximum penetration depth of 0.0 was set for the inner wire, P_{inner}. In this context, further experimental studies on naturally corroded strands, showing corrosion damage of the inner wire, should be conducted to determine appropriate correlations describing the pitting morphology variability and the decay trend of the mechanical properties of the inner wire for different corrosion levels.

II. **Equivalent spring model:** The CPS-model predicts the residual mechanical response of a corroded strand based on the equivalent spring model. As previously described in the State-of-the-Art section (Chapter 3), the equivalent spring model reproduces the overall response of a corroded strand as the sum of wire contributions, which are assumed as springs acting in parallel with each other. According to Jeon et al. (2020),

when a spring (wire) fails, a reduction of approximately 1/7 of the entire strand tensile strength is expected because of the uniform stress distribution in each wire.

III. **Conventional failure mode:** Although the CPS-model allows the prediction of the wires' failure sequence, for a safe engineering assessment, the conventional failure of the overall strand is assumed in correspondence of the failure of the most corroded wire at the section where the maximum longitudinal penetration depth is measured, $P_{max,long}$. If a refined analysis is needed, the CPS-model generates a series of drop-offs, each reflecting the occurrence of a corroded wire rupture.

IV. **Pitting morphology:** The CPS-model classifies pits according to the three pit type morphology configurations introduced in Section 6.4.1 and denoted as hemispherical (Type 1) – half-moon (Type 2) and planar (Type 3) shape, respectively. Once each corroded pit in the section of analysis has been classified, the corresponding area loss due to pitting, $A_{p,i}$, is evaluated according to the expressions reported in Eqs. 6-2 to 6-4. Subsequently, the cross-sectional area loss of each wire, μ, is calculated by adopting Eq. 6-27.

V. **Stress-strain behaviour:** The CPS-model assumes a tri-linear relationship for representing the stress-strain behaviour of un-corroded and slightly corroded wires, according to the Ramberg-Osgood model, (Zhan et al., 2016). The tri-linear trend consists of: (a) an elastic phase ranging from (0; 0) to ($\varepsilon_{pp,0}$; $f_{pp,0}$), a yielding phase from ($\varepsilon_{pp,0}$; $f_{pp,0}$) to ($\varepsilon_{py,0}$; $f_{py,0}$), and a hardening phase from ($\varepsilon_{py,0}$; $f_{py,0}$) to ($\varepsilon_{pu,0}$; $f_{pu,0}$), as reported in Eq. 7-5. Conversely, for intermediate and high corroded wires the tri-linear trend is reduced to a bi-linear or a linear trend depending on the cross-sectional loss, μ, of the analyzed wire as described at point (VI).

VI. **Threshold limit of plastic behaviour:** Analyzing tensile test outcomes in terms of ultimate strain decay, the CPS-model defines a critical cross-sectional loss threshold, μ_{lim}, – one for each of the three different assumed pit-type morphology configurations – at which the hardening phase in the stress-strain relationship of a corroded wire no longer develops. Therefore, for a cross-sectional loss of a corroded wire, μ, higher than the critical value, μ_{lim}, the hardening phase disappears, while the presence of the yielding phase depends on the ultimate strength value, $f_{pu,corr}$. If $f_{pu,corr}$ is higher than the stress at the end of the elastic stage, $f_{pp,0}$, the yielding stage develops, and the stress-strain relations of a corroded wire can be expressed by a bi-linear model. Otherwise, the stress-strain response of the corroded wire is characterised by the presence of the elastic phase alone. In detail, the elastic ($E_{p,0}$), yielding ($E'_{p,0}$), and hardening ($E''_{p,0}$) modulus are

assumed to be unaffected by corrosion and are set equal to their un-corroded values. Therefore, starting from the estimated ultimate corroded strength of each wire, $f_{pu,corr}$, evaluated according to point (VII), and considering the tri-linear trend introduced at point (V) and (VI), the corresponding ultimate strain, $\varepsilon_{pu,corr}$, is estimated, as described at point (VIII).

VII. **Ultimate corroded strength:** The CPS-model evaluates the ultimate strength of each corroded wire, $f_{pu,corr}$, as a function of the corresponding cross-sectional loss, μ. Once again, different expressions for the ultimate strength decay were defined according to the three different pit type morphology configurations considered.

VIII. **Ultimate corroded strain:** The CPS-model evaluates the ultimate strain, $\varepsilon_{pu,corr}$, in correspondence to the ultimate strength calculated as per point (VII) by adopting exponential relationships – one for each of the three different pit-type morphology configurations considered.

IX. **Wire-cross section:** The CPS-model determines the tensile resistance of the entire strand as the product of the ultimate corroded strength of each wire evaluated at point (VII) times the corresponding un-corroded cross-sectional area. The effectiveness of the proposed assumption is ensured by the prediction of the ultimate corroded strength of each analyzed wire based on the corresponding cross-sectional loss. Indeed, the geometrical effect related to the cross-section reduction induced by the corrosion process is implicitly accounted.

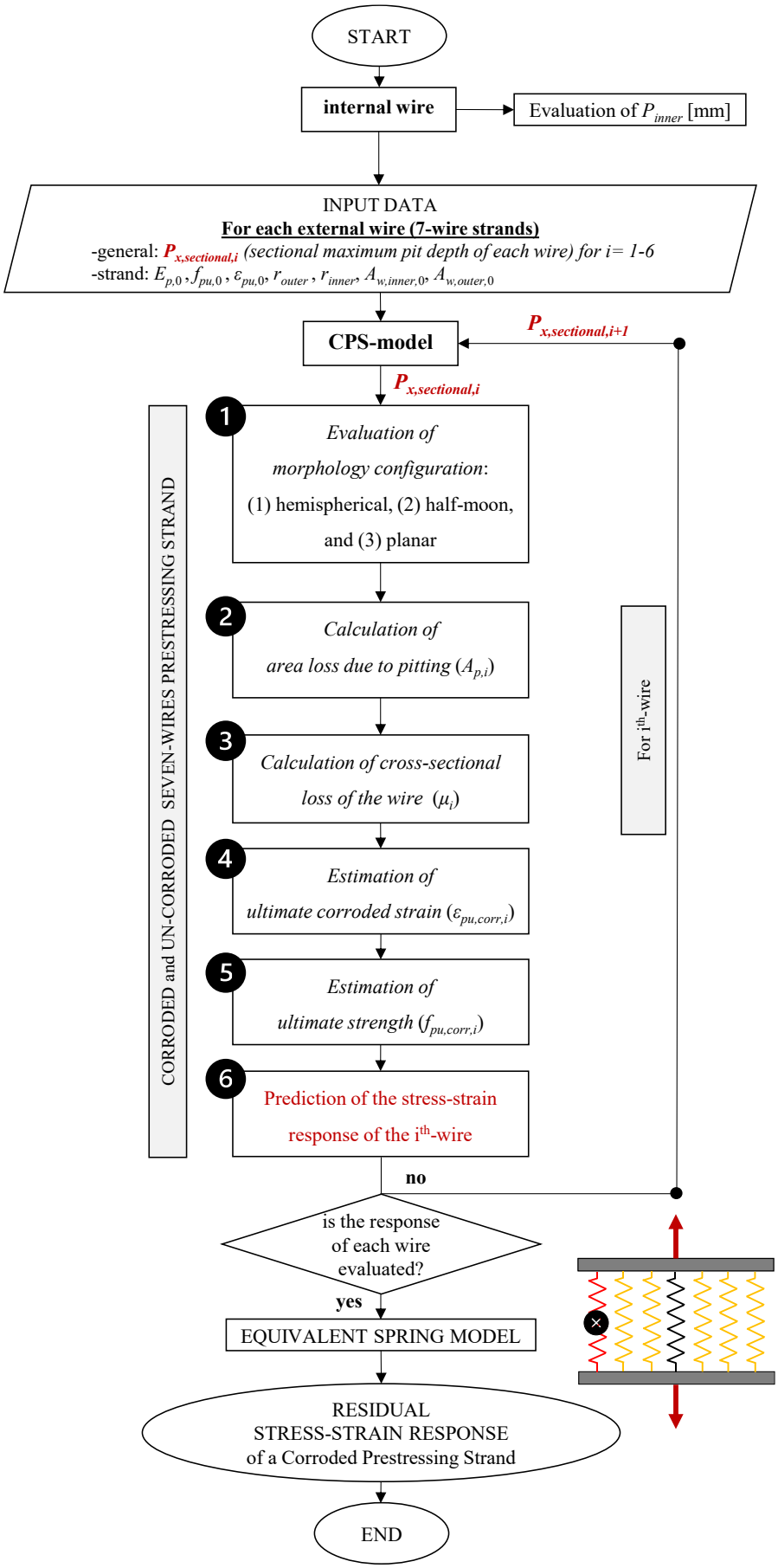

Figure 7-8 Flowchart of the main steps of the CPS-model.

7.4.2 Stress-strain relationship for un-corroded wires

As previously stated in Section 7.4.1 point (V), the stress-strain response of an un-corroded wire was defined by adopting a tri-linear trend that simplified the relationship proposed by Ramberg-Osgood, as expressed in Eq. 7-5 and illustrated in Figure 7-9:

$$\sigma_w(\varepsilon)=\begin{cases}\varepsilon E_{p,0} & \varepsilon \le \varepsilon_{pp,0}\\ \varepsilon_{pp,0}E_{p,0}+E'_{p,0}\left(\varepsilon-\varepsilon_{pp,0}\right) & \varepsilon_{pp,0}<\varepsilon\le\varepsilon_{py,0}\\ \varepsilon_{pp,0}E_{p,0}+E'_{p,0}\left(\varepsilon_{py,0}-\varepsilon_{pp,0}\right)+E''_{p,0}\left(\varepsilon-\varepsilon_{py,0}\right) & \varepsilon_{py,0}<\varepsilon\le\varepsilon_{pu,0}\\ 0 & \varepsilon>\varepsilon_{pu,0}\end{cases} \quad 7\text{-}5$$

where $\sigma_w(\varepsilon)$ represents the wire stress for a given strain, ε; whereas $\varepsilon_{pu,0}$, $f_{pu,0}$ and $E_{p,0}$ are the un-corroded mechanical properties previously determined as the average values of the tensile test outcomes conducted on the four un-corroded samples, resulting equal to 5.1%, 1901.75 MPa, and 195 GPa, respectively. Furthermore, according to Eq. 7-6 and Eq. 7-7, a yielding ($E'_{p,0}$) and a hardening ($E''_{p,0}$) modulus of 109 GPa and 5.47 GPa were estimated.

$$E'_{p,0}=\frac{f_{py,0}-f_{pp,0}}{\varepsilon_{py,0}-\varepsilon_{pp,0}} \quad 7\text{-}6$$

$$E''_{p,0}=\frac{f_{pu,0}-f_{py,0}}{\varepsilon_{pu,0}-\varepsilon_{py,0}} \quad 7\text{-}7$$

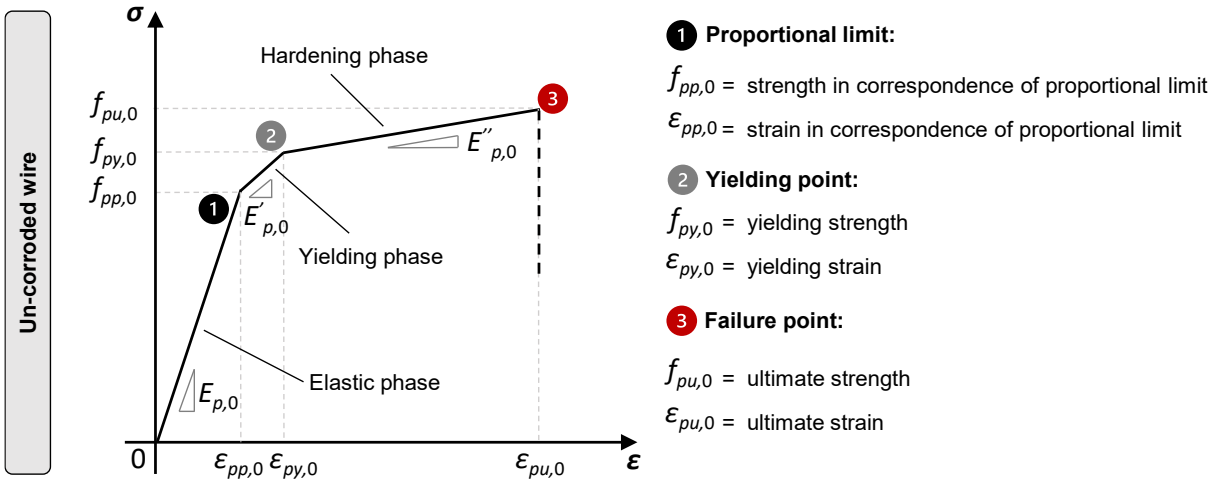

Figure 7-9 Focus on the tri-linear response of the un-corroded wire.

As highlighted in Figure 7-9, three different phases can be identified:

- An *elastic phase*, that ranges between the origin of the stress-strain relationship, denoted by the initial coordinates (0; 0), and the proportional limit ($\varepsilon_{pp,0}$; $f_{pp,0}$);
- A *yielding phase*, which runs from the proportional limit ($\varepsilon_{pp,0}$; $f_{pp,0}$) to the yielding point ($\varepsilon_{py,0}$; $f_{py,0}$);
- A *hardening phase*, that ranges between the yielding point ($\varepsilon_{py,0}$; $f_{py,0}$) and the failure point ($\varepsilon_{pu,0}$; $f_{pu,0}$).

According to the Probabilistic Model Code, (JCSS, 2001), the strength in correspondence to the proportional limit, $f_{pp,0}$, was established as 0.7 times the un-corroded ultimate strength, $f_{pu,0}$, as expressed in Eq. 7-8. The corresponding ultimate strain, $\varepsilon_{pp,0}$, on the contrary, was calculated as the ratio between the strength in correspondence to the proportional limit, $f_{pp,0}$, and the un-corroded elasticity modulus, $E_{p,0}$, as reported in Eq. 7-9. Based on the previously calculated un-corroded ultimate mechanical properties values, the strength and the strain in correspondence to the proportional limit were 1331.22 MPa and 0.665%, respectively.

$$f_{pp,0} = 0.7 f_{pu,0} \tag{7-8}$$

$$\varepsilon_{pp,0} = \frac{f_{pp,0}}{E_{p,0}} = \frac{0.7 f_{pu,0}}{E_{p,0}} \tag{7-9}$$

Finally, considering the yielding phase, the yielding point was defined in accordance with the Probabilistic Model Code, (JCSS, 2001). The yielding strain, $\varepsilon_{py,0}$, was fixed to 1% and the yielding strength, $f_{py,0}$, was assumed to be 0.882 times the un-corroded ultimate strength, $f_{pu,0}$, as highlighted in Eq. 7-10. It is worth noting that the JCSS defines the yielding strength of a prestressing wire as 0.85 times its ultimate strength, $f_{pu,0}$; however, – in the present research – this latter factor was updated to a value of 0.882 based on the experimental tensile test outcomes.

$$f_{py,0} = 0.882 f_{pu,0} \tag{7-10}$$

7.4.3 Stress-strain relationship for corroded wires

Once the general behaviour of the un-corroded wire was defined, the prediction of the residual stress-strain response of a corroded wire was evaluated as a function of two main parameters: (i) the critical cross-sectional loss, μ_{lim}, and (ii) the ultimate corroded strain, $\varepsilon_{pu,corr}$, of the analyzed wire, as expressed in Eq. 7-11.

$$\sigma_w(\varepsilon)=\begin{cases}\mu<\mu_{\lim} & \begin{cases}\varepsilon E_{p,0} & \varepsilon\le\varepsilon_{pp,0}\\ \varepsilon_{pp,0}E_{p,0}+E'_{p,0}\left(\varepsilon-\varepsilon_{pp,0}\right) & \varepsilon_{pp,0}<\varepsilon\le\varepsilon_{py,0}\\ \varepsilon_{pp,0}E_{p,0}+E'_{p,0}\left(\varepsilon_{py,0}-\varepsilon_{pp,0}\right)+E''_{p,0}\left(\varepsilon-\varepsilon_{py,0}\right) & \varepsilon_{py,0}<\varepsilon\le\varepsilon_{pu,corr}\\ 0 & \varepsilon>\varepsilon_{pu,corr}\end{cases}\\ \mu\ge\mu_{\lim} & \begin{cases}\varepsilon E_{p,0} & \varepsilon\le\varepsilon_{pp,0}\\ \varepsilon_{pp,0}E_{p,0}+E'_{p,0}\left(\varepsilon-\varepsilon_{pp,0}\right) & \varepsilon_{pp,0}<\varepsilon\le\varepsilon_{pu,corr}\\ 0 & \varepsilon>\varepsilon_{pu,corr}\end{cases}\\ & \begin{cases}\varepsilon E_{p,0} & \varepsilon\le\varepsilon_{pu,corr}\\ 0 & \varepsilon>\varepsilon_{pu,corr}\end{cases}\end{cases}$$

7-11

The critical cross-sectional loss threshold value, μ_{lim}, which marks the brittle failure of a corroded wire, varied depending on the configuration of the pit type morphology considered and was established from the analysis of the ultimate corroded strain decay expressed as a function of the cross-sectional loss of the most corroded wire, μ_{max}. To this end, the tested corroded strands were first divided into samples showing a brittle (BRIT) or a ductile (DUCT) behaviour at failure, as reported in Table 7-1. Second, the maximum longitudinal penetration depth, $P_{max,long}$, was identified using the GOM Inspect software and the maximum pit was assigned to one of the three adopted morphological configurations. Once the area loss due to pitting, A_p, was measured based on the selected pit shape, the cross-sectional loss of the most corroded wire, μ_{max}, was then determined. Finally, by combining the experimental values of the ultimate corroded strain, $\varepsilon_{pu,corr,exp}$, belonging to the present research and the data coming from Jeon et al. (2019) study, three different decay trends of $\varepsilon_{pu,corr}$ were established as a function of the cross-sectional loss of the most corroded wire – one for each pit type morphology configuration taken into account, as shown in Figure 7-10 in terms of $\varepsilon_{pu,corr}/\varepsilon_{pu,0}$.

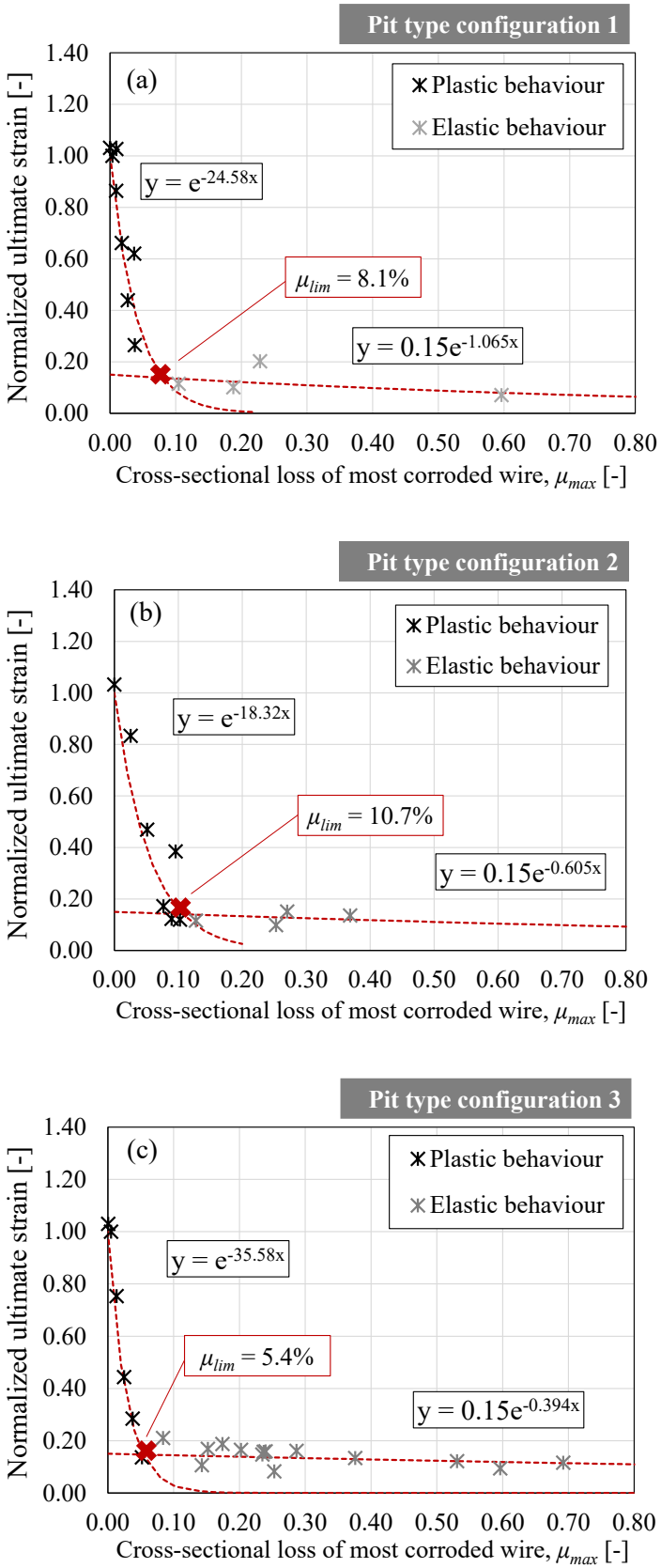

Figure 7-10 Ultimate strain decay as a function of the cross-sectional loss of the most corroded wire: (a) pit type configuration 1, (b) pit type configuration 2 and (c) pit type configuration 3.

For each pit type morphology configuration, the ultimate strain decay was discretized by adopting two different exponential trends, determined by distinguishing between BRIT (elastic behaviour) and DUCT (plastic behaviour) samples. In general, the first branch highlighted a strong ultimate strain decay for low cross-sectional losses, μ. On the contrary, the second branch revealed that the ultimate strain decreased less sharply with the increase in cross-sectional loss, as also noticed by Wang et al. (2020). In detail, the critical cross-sectional loss threshold, μ_{lim}, was evaluated at the intersection point of the two exponential trends, the red cross in Figure 7-10, resulting equivalent to 8.1%, 10.7% and 5.4% for pit morphology configuration Type 1, Type 2, and Type 3, respectively.

The ultimate corroded strain, $\varepsilon_{pu,corr}$, was calculated through Eq. 7-12:

$$\varepsilon_{pu,corr} = \begin{cases} \mu < \mu_{\lim} & \varepsilon_{py,0} + \dfrac{f_{pu,corr} - f_{py,0}}{E''_{p,0}} \quad f_{py,0} < f_{pu,corr} \le f_{pu,0} \\ \mu \ge \mu_{\lim} & \begin{cases} \varepsilon_{pp,0} + \dfrac{f_{pu,corr} - f_{pp,0}}{E'_{p,0}} & f_{pp,0} < f_{pu,corr} \le f_{py,0} \\ \dfrac{f_{pu,corr}}{E_{p,0}} & f_{pu,corr} < f_{pp,0} \end{cases} \end{cases} \qquad 7\text{-}12$$

where μ and μ_{lim} are the actual and the critical cross-sectional loss threshold of the analyzed wire, while $f_{pu,corr}$ is the ultimate corroded strength of the corroded wire. Similarly to $\varepsilon_{pu,corr}$, the decay of the normalized ultimate strength, $f_{pu,corr}/f_{pu,0}$, was evaluated as a function of the cross-sectional loss of the most corroded wire, μ_{max}. As shown in Figure 7-11, three different exponential trends were determined by adapting the available experimental data and by modifying the expressions originally proposed by Jeon et al. (2019). The main changes consisted of: (i) modifying the data fitting trend from linear to exponential, and (ii) assuming a predefined value of the ratio $f_{pu,corr}/f_{pu,0}$ set equal to 1.0 for the un-corroded scenario, i.e. for a cross-sectional loss of 0.0. As a result, the ultimate corroded strength, $f_{pu,corr}$, was evaluated according to Eq. 7-13, Eq. 7-14, and Eq. 7-15 for pit type configuration 1, 2, and 3, respectively.

$$f_{pu,corr} = f_{pu,0} \cdot e^{-1.588\mu_{\max}} \qquad 7\text{-}13$$

$$f_{pu,corr} = f_{pu,0} \cdot e^{-1.377\mu_{\max}} \qquad 7\text{-}14$$

$$f_{pu,corr} = f_{pu,0} \cdot e^{-1.035\mu_{\max}} \qquad 7\text{-}15$$

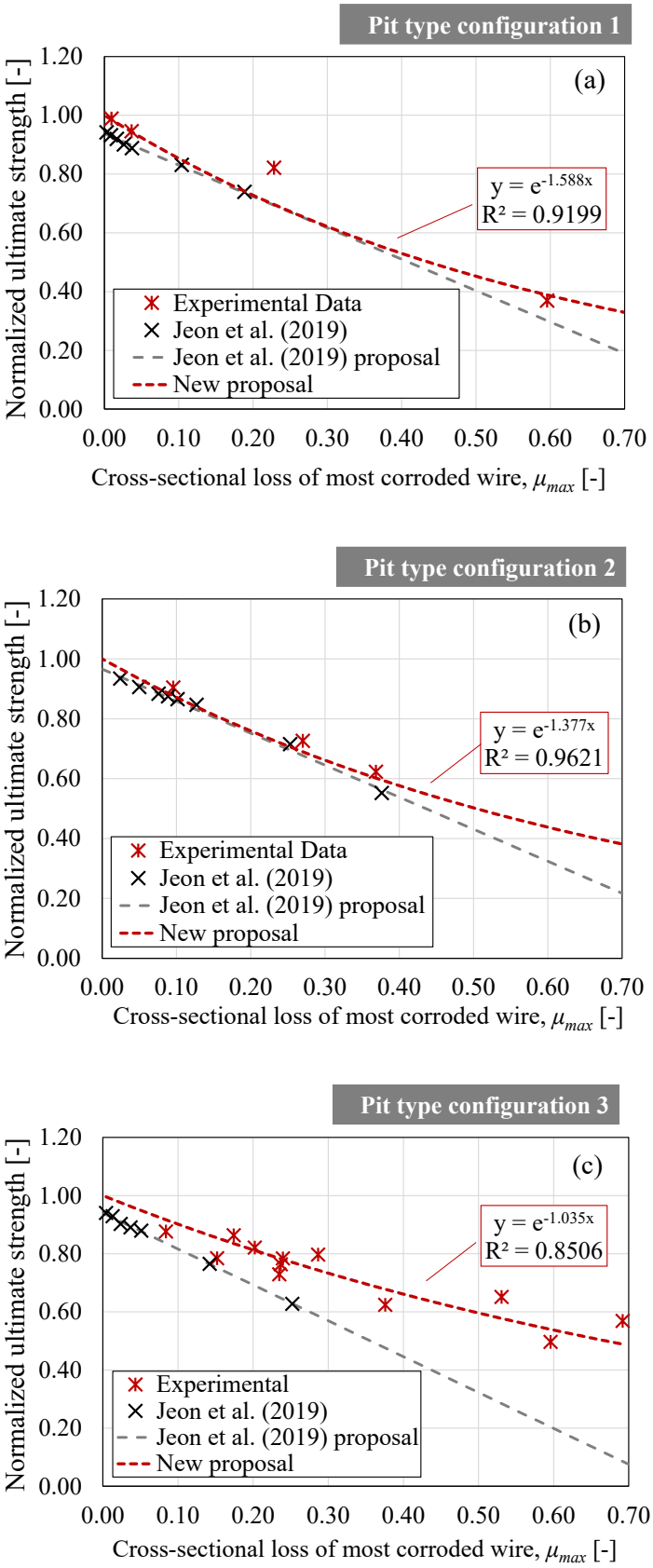

Figure 7-11 Ultimate strength decay as a function of the cross-sectional loss of the most corroded wire: (a) pit type configuration 1, (b) pit type configuration 2 and (c) pit type configuration 3.

Once the wire contributions were individually estimated by adopting the procedure described in Sections 7.4.2 and 7.4.3 in the case of un-corroded or corroded wires, the equivalent spring model was finally adopted according to Eq. 7-16 to predict the overall response of the investigated corroded prestressing strand, as in Figure 7-12:

$$\sigma(\varepsilon)=\frac{\sum_{i=1}^{6}\left(\sigma_{w,i}(\varepsilon)A_{w,outer,0}\right)+\sigma_{w,i}(\varepsilon)A_{w,inner,0}}{\sum_{i=1}^{6}\left(A_{w,outer,0}\right)+A_{w,inner,0}}=\frac{\sum_{i=1}^{6}\left(\sigma_{w,i}(\varepsilon)A_{w,outer,0}\right)+\sigma_{w,i}(\varepsilon)A_{w,inner,0}}{A_{p,0}} \qquad 7\text{-}16$$

where $\sigma(\varepsilon)$ represents the strand stress for a given strain, ε, whereas $\sigma_{w,i}$ is the stress of the ith wire composing the strand. Moreover, $A_{w,outer,0}$ and $A_{w,inner,0}$ are the un-corroded cross-sectional areas of external and internal wire, respectively, while $A_{p,0}$ is the un-corroded cross-sectional area of the entire strand.

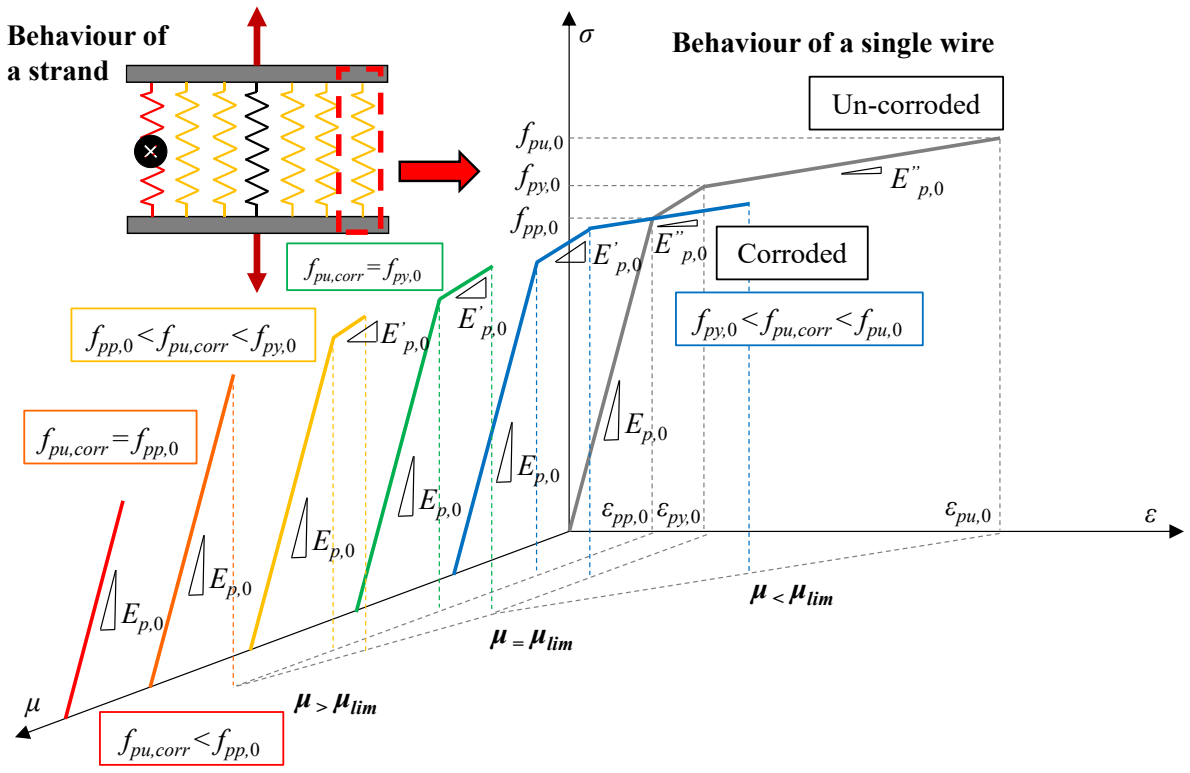

Figure 7-12 Changing of the stress-strain relationship of a corroded wire for different corrosion levels.

7.4.4 Model validation

Considering the cross-sectional losses of each corroded wire reported in Appendix A.4 – evaluated within the section where the maximum longitudinal penetration depth was measured –, the analytical stress-strain relationships of un-corroded and corroded strands were established by adopting the CPS-model, as reported in Figure 7-13 and Figure 7-14, respectively.

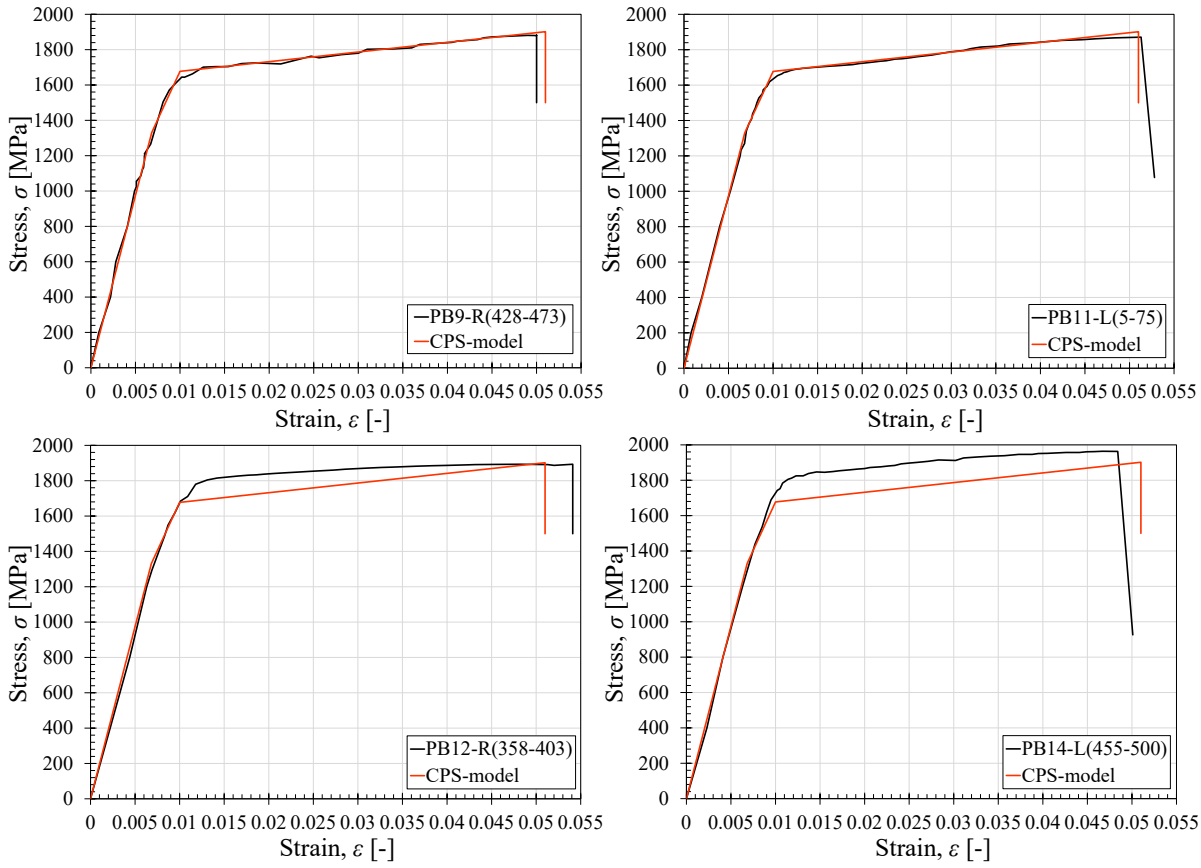

Figure 7-13 Comparison between experimental and analytical predictions (CPS-model) of stress-strain relationships of un-corroded strands.

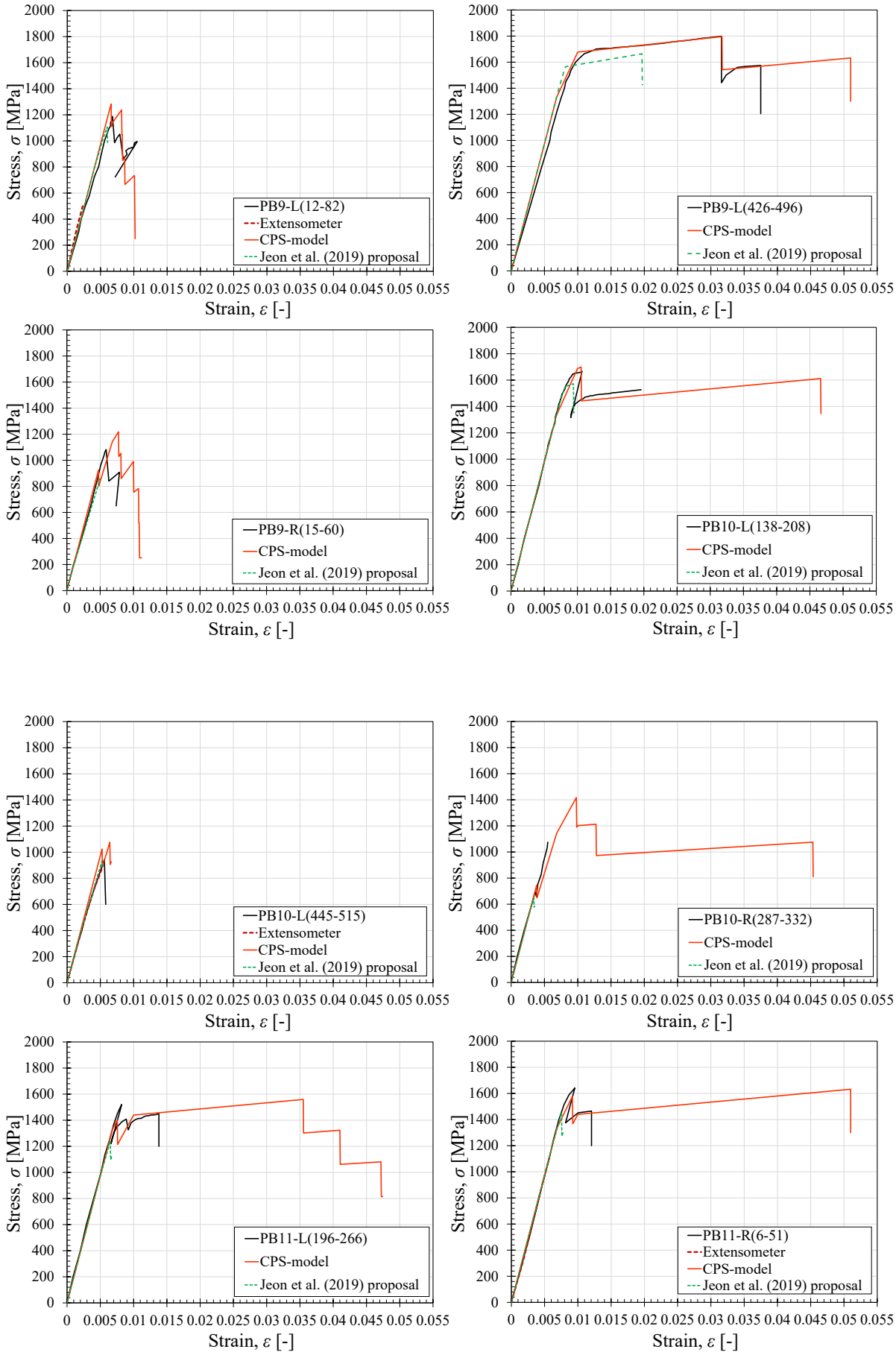
Stress, σ [MPa]
Strain, ε [-]
PB9-L(12-82)
Extensometer
CPS-model
Jeon et al. (2019) proposal
PB9-L(426-496)
PB9-R(15-60)
PB10-L(138-208)
PB10-L(445-515)
PB10-R(287-332)
PB11-L(196-266)
PB11-R(6-51)

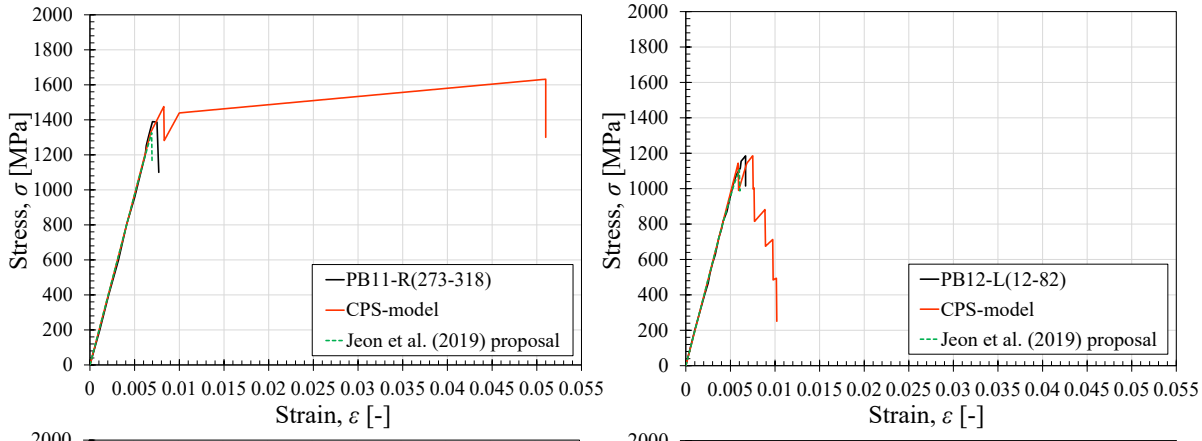
Stress, σ [MPa]
Strain, ε [-]
PB11-R(273-318)
CPS-model
Jeon et al. (2019) proposal

Stress, σ [MPa]
Strain, ε [-]
PB12-L(12-82)
CPS-model
Jeon et al. (2019) proposal

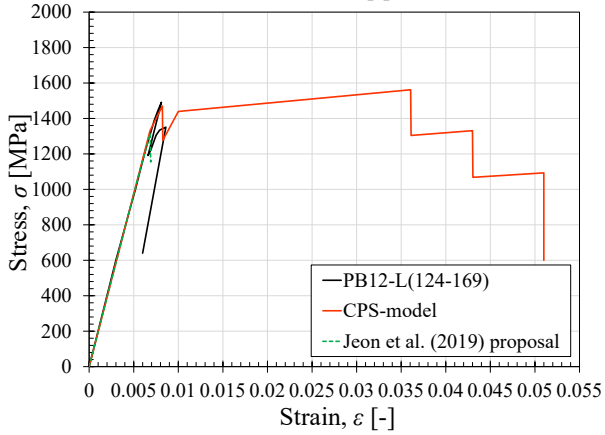
Stress, σ [MPa]
Strain, ε [-]
PB12-L(124-169)
CPS-model
Jeon et al. (2019) proposal

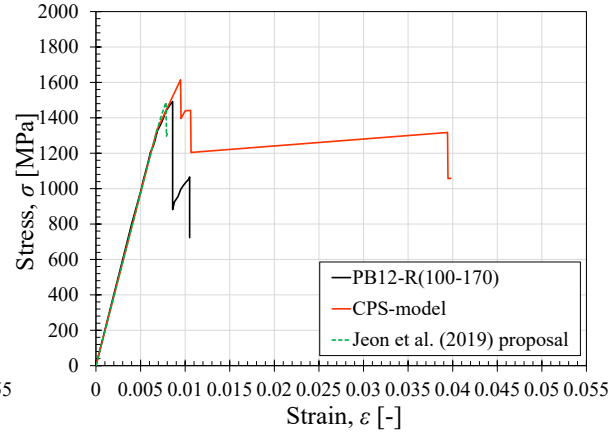
Stress, σ [MPa]
Strain, ε [-]
PB12-R(100-170)
CPS-model
Jeon et al. (2019) proposal

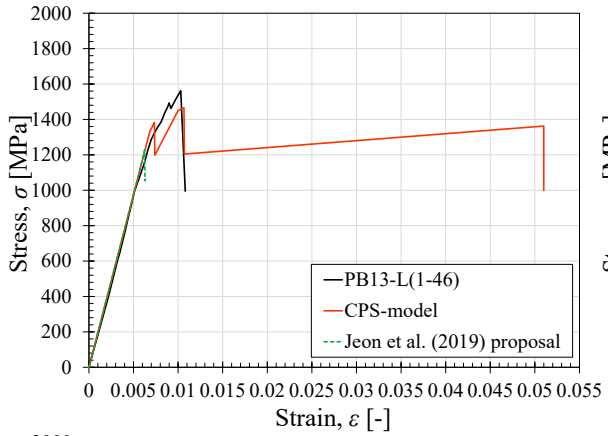
Stress, σ [MPa]
Strain, ε [-]
PB13-L(1-46)
CPS-model
Jeon et al. (2019) proposal

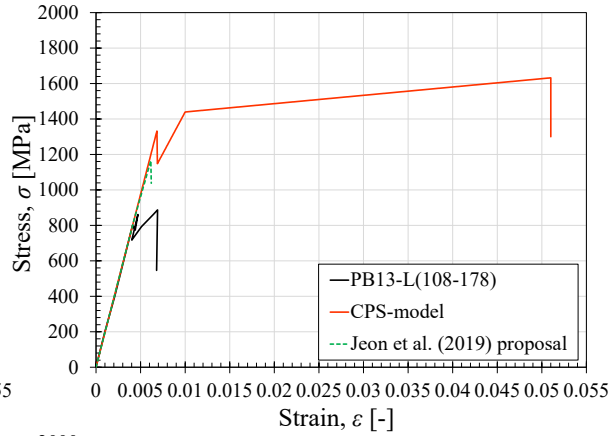
Stress, σ [MPa]
Strain, ε [-]
PB13-L(108-178)
CPS-model
Jeon et al. (2019) proposal

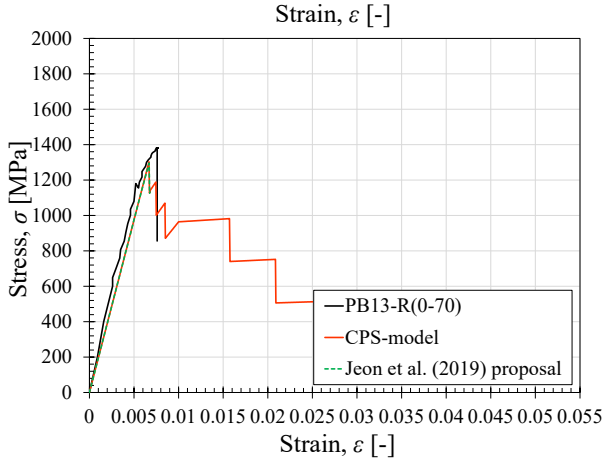
Stress, σ [MPa]
Strain, ε [-]
PB13-R(0-70)
CPS-model
Jeon et al. (2019) proposal

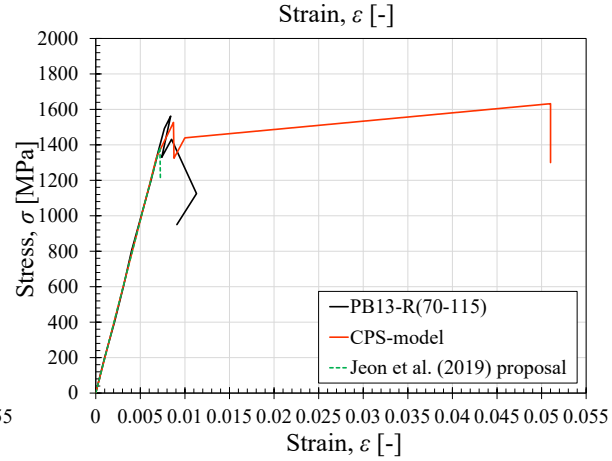
Stress, σ [MPa]
Strain, ε [-]
PB13-R(70-115)
CPS-model
Jeon et al. (2019) proposal

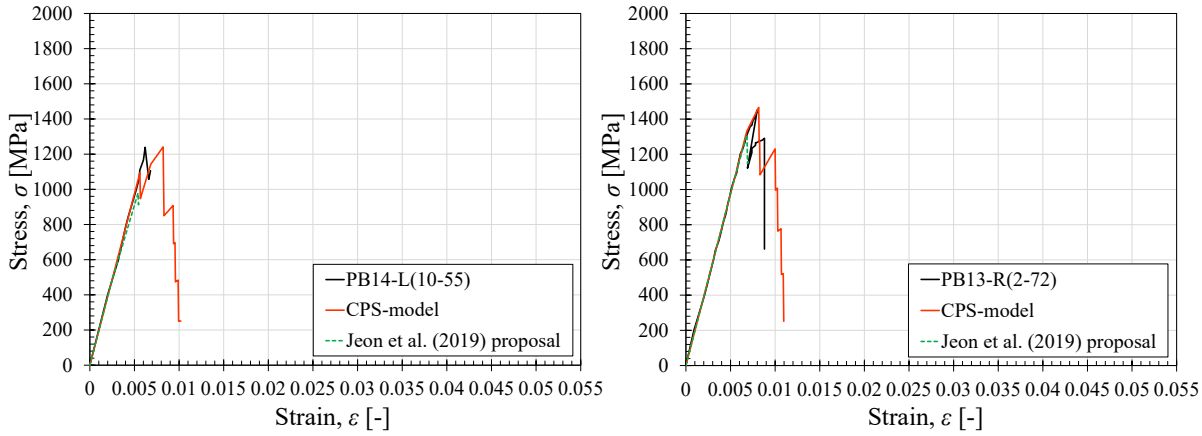

Figure 7-14 Comparison between experimental and analytical predictions (CPS-model) of stress-strain relationships of corroded strands.

Based on the obtained results, it is clear how the CPS-model can allow refined prediction of the stress-strain relationship of un-corroded and corroded strands. As previously mentioned, the conventional failure mode of the proposed model was assumed to correspond to the failure of the most corroded wire, which consisted in the first recorded drop in the corresponding stress-strain relationship. When comparing the experimental outcomes with the analytical predictions – reported in Figure 7-13 and Figure 7-14 – a significant correspondence in terms of both ultimate corroded strength and ultimate corroded strain was revealed for each investigated sample, with the exception of samples PB9-R(15-60), PB13-L(1-46), and PB13-L(108-178). In the case of samples PB9-R(15-60) and PB13-L(1-46), it was registered a slight (safer) underestimation of the ultimate corroded strength, while a significant overestimation of both ultimate corroded strength and strain was recorded for sample PB13-L(108-178), probably induced by a previous underestimation of the measured maximum penetration depth. For the sake of completeness, the predicted ultimate corroded strength, $f_{pu,corr,an1}$, and ultimate corroded strain, $\varepsilon_{pu,corr,an1}$, obtained for each investigated sample by adopting the CPS-model were reported in Table 7-3.

Furthermore, as previously stated, the CPS-model was able to reproduce the wires' failure sequence of the investigated corroded strands, as highlighted by the several drops visible for each stress-strain relationship in Figure 7-14. To be noted that the failure sequence is strictly dependent on the number of corroded wires and, since the CPS-model is a sectional model, it only reproduces the failure sequence of the wires at the section where the maximum penetration depth was measured. However, it frequently happened that the wire failures, occurring after the rupture of the most corroded wire, took place in different sections with respect to the section

where the maximum penetration depth was measured. Therefore, the failure sequence – predicted by using the CPS model – turned out to be theoretical and generally different from the experimental one, unless it is ensured that the remaining external wires in the analyzed section are characterized by the maximum penetration depths measured along their entire sample length. To confirm the previous considerations, the failure sequence of sample PB9-L(12-82), reported in Figure 7-15, was analyzed in depth. A good correspondence was observed between experimental and analytical prediction of the most corroded wire rupture. Since the second and the third wire ruptures occurred in different sections than in the one in which the maximum pit was measured, the experimental and analytical stress-strain relationships tended to be no longer overlapping. This issue is particularly relevant in the analysis of prestressing reinforcements due to the presence of multiple wires, whereas it is negligible in the evaluation of ordinary reinforcements. Indeed, for ordinary rebars, the maximum penetration depth and the maximum cross-sectional loss always take place in the same region, which is also where the reinforcement failure is most prone to occur. Therefore, considering a sectional analysis, the CPS-model was discovered to be able to reproduce the failure sequence of all the corroded wires composing the strand once their cross-sectional loss was known. However, when the experimental tensile test outcomes were compared to the analytical predictions, the stress-strain responses obtained by adopting the CPS-model tended to differ from the real ones after the rupture of the most corroded wire due to the longitudinal variability of the pitting morphology of the external wires. This experimental evidence confirmed the assumption of selecting the rupture of the most corroded wire as the conventional failure mode of the overall prestressing strand. As a result, although the corroded strand may show higher residual ultimate strength and ductility due to the contribution of the remaining wires, the CPS-model allows engineers to make accurate and reliable predictions of the residual mechanical properties to be adopted for the in-situ assessment of corroded PC structural members. Moreover, Figure 7-14 graphically demonstrates the improvement provided by the application of the CPS-model in the prediction of the residual stress-strain relationship of a corroded strand over the use of Jeon et al. (2019) constitutive law proposal.

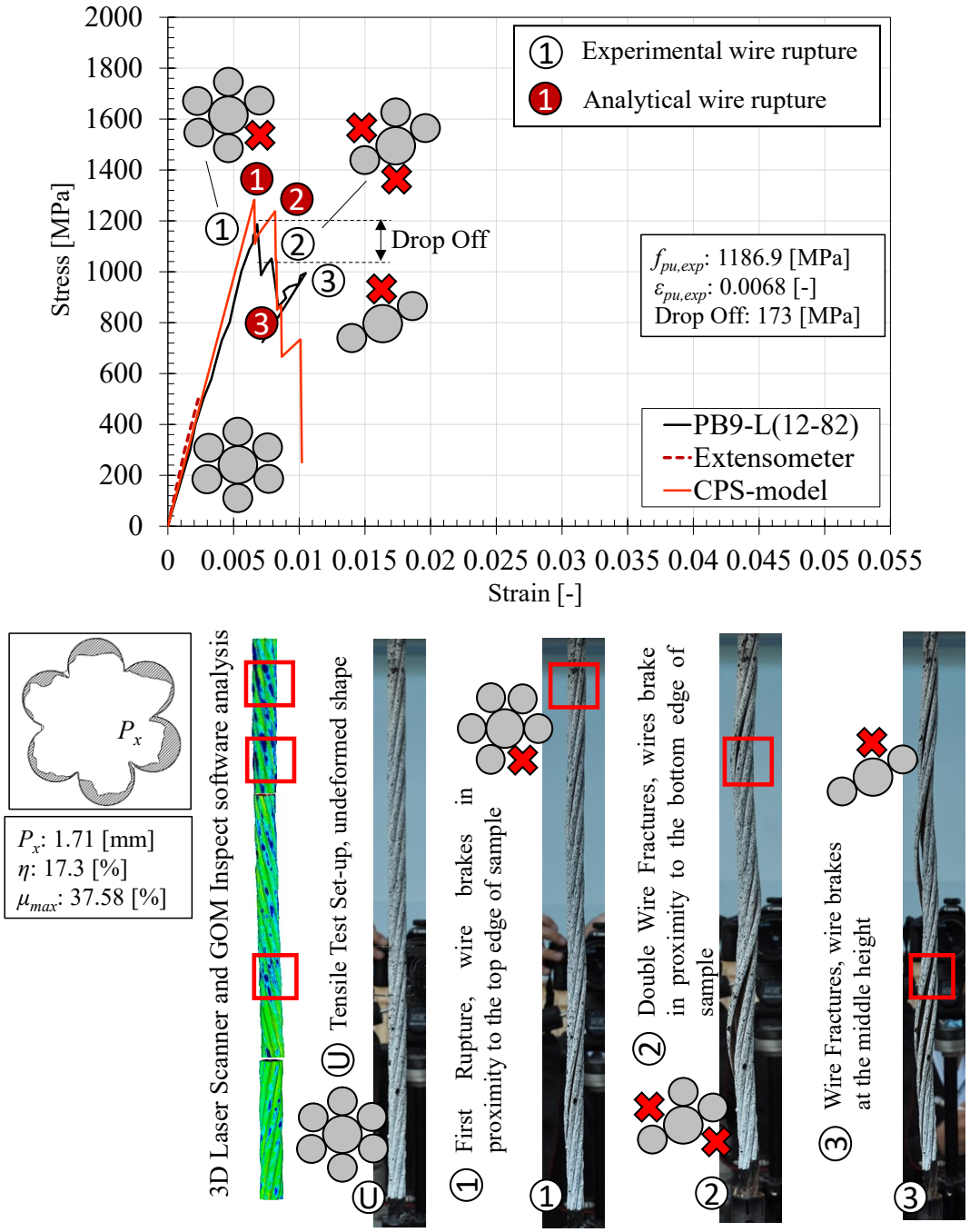

Figure 7-15 Comparison of failure sequence for corroded strands evaluated from tensile test outcomes and predicted by adopting the CPS-model – sample PB9-L(12-82).

To further validate the CPS-model, the proposed procedure was adopted to compare the experimental tensile test outcomes and the analytical predictions of corroded prestressing strands coming from other research activities available in scientific literature. In detail, a total of 15 samples (1 un-corroded and 14 corroded) belonging to the experimental works conducted by Jeon et al. (2019) and Giriraju et al. (2022) were additionally analyzed. For the sake of completeness, the experimental ultimate corroded strength, $f_{pu,corr,exp}$, and the ultimate corroded strain, $\varepsilon_{pu,corr,exp}$, of the investigated samples are reported in Table 7-2; while the comparison between experimental tensile test outcomes and the CPS-model analytical predictions are shown in Figure 7-16 and Figure 7-17 for Jeon et al. (2019) and Giriraju et al. (2022) samples, respectively.

Based on the obtained results, accurate or slightly safer predictions were achieved through the application of the CPS-model. Nevertheless, a modest overestimation of the experimental stress-strain response was noted for samples CS8 and CS10. Once again, the improvements made by adopting the CPS-model over Jeon et al. (2019) proposal for the prediction of the residual stress-strain relationship of corroded strands are highlighted in Figure 7-16. Although the CPS-model provided similar predictions to those of Jeon et al. (2019) for high corroded strands – for example samples CS3, CS4, CS7 and CS9 – it led to a marked improvement in the prediction of the residual mechanical response of intermediate or low corroded strands, such as CS1, CS2, CS6, CS11 and CS12.

Table 7-2 Tensile test outcomes in terms of ultimate strength, $f_{pu,corr,exp}$, and ultimate strain, $\varepsilon_{pu,corr,exp,}$ of un-corroded and corroded samples belonging to Jeon et al. (2019) and Giriraju et al. (2022) experimental activities.

Sample ID	$f_{pu,corr,exp}$ **[MPa]**	$\varepsilon_{pu,corr,exp}$ **[-]**
CS1	1857.53	0.0655
CS2	1880.82	0.0694
CS3	1691.42	0.0158
CS4	1668.31	0.0128
CS5	1580.56	0.0097
CS6	1729.03	0.0200
CS7	1739.79	0.0189
CS8	1890.17	0.0383
CS9	1670.72	0.0108
CS10	1844.79	0.0435
CS11	1897.91	0.0563
CS12	1919.07	0.0639
NC-1	1968.10	0.0681
C-1	1710.40	0.0068
C-2	969.90	0.0067

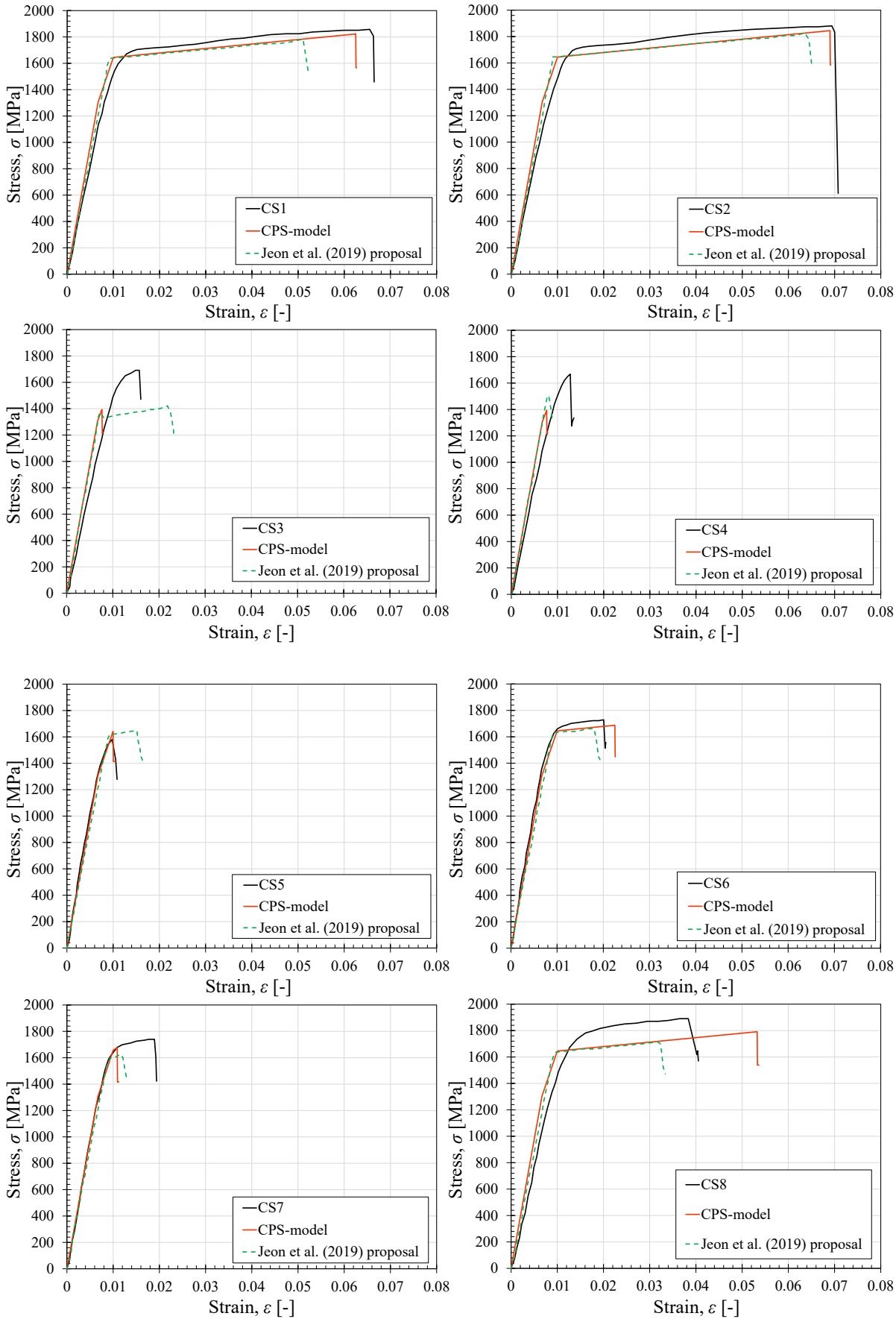
Stress, σ [MPa]
Strain, ε [-]
CS1
CPS-model
Jeon et al. (2019) proposal
CS2
CPS-model
Jeon et al. (2019) proposal
CS3
CPS-model
Jeon et al. (2019) proposal
CS4
CPS-model
Jeon et al. (2019) proposal
CS5
CPS-model
Jeon et al. (2019) proposal
CS6
CPS-model
Jeon et al. (2019) proposal
CS7
CPS-model
Jeon et al. (2019) proposal
CS8
CPS-model
Jeon et al. (2019) proposal

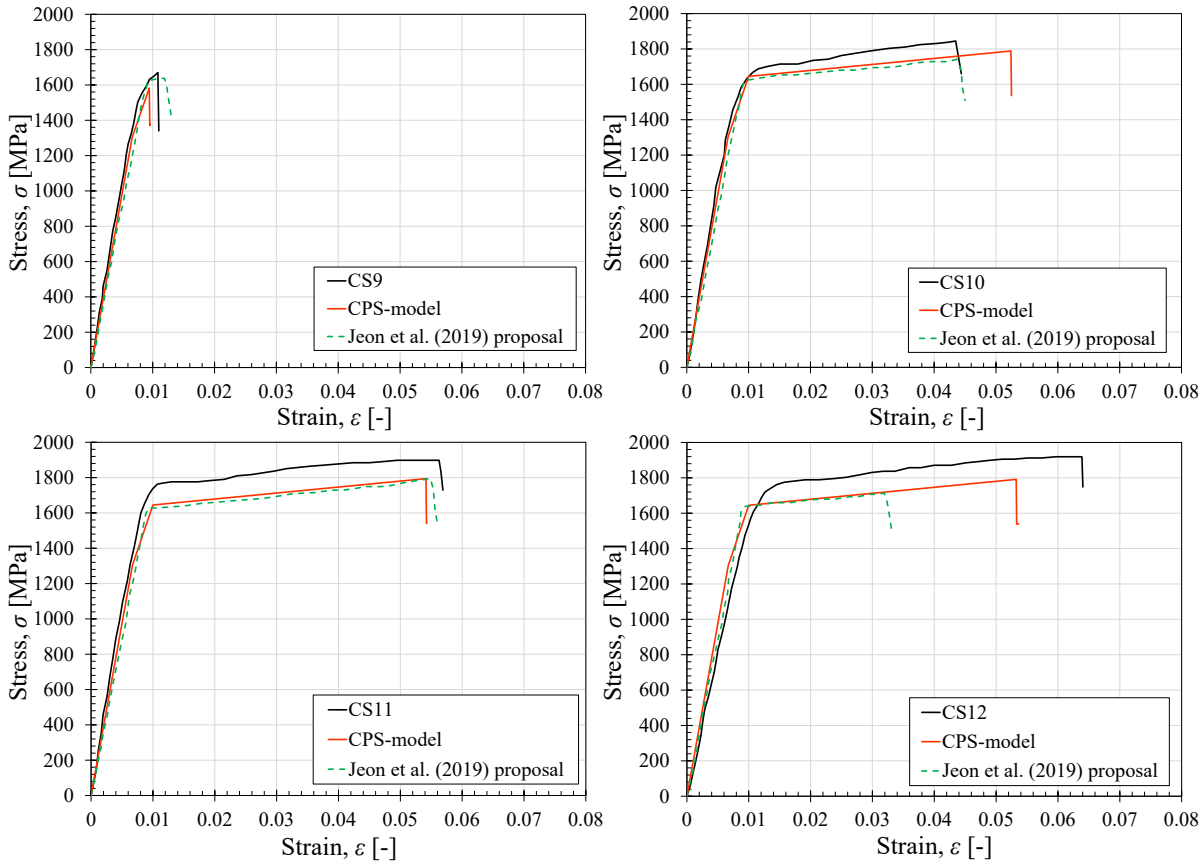

Figure 7-16 Comparison between experimental and analytical predictions for un-corroded and corroded strands belonging to Jeon et al (2019) work.

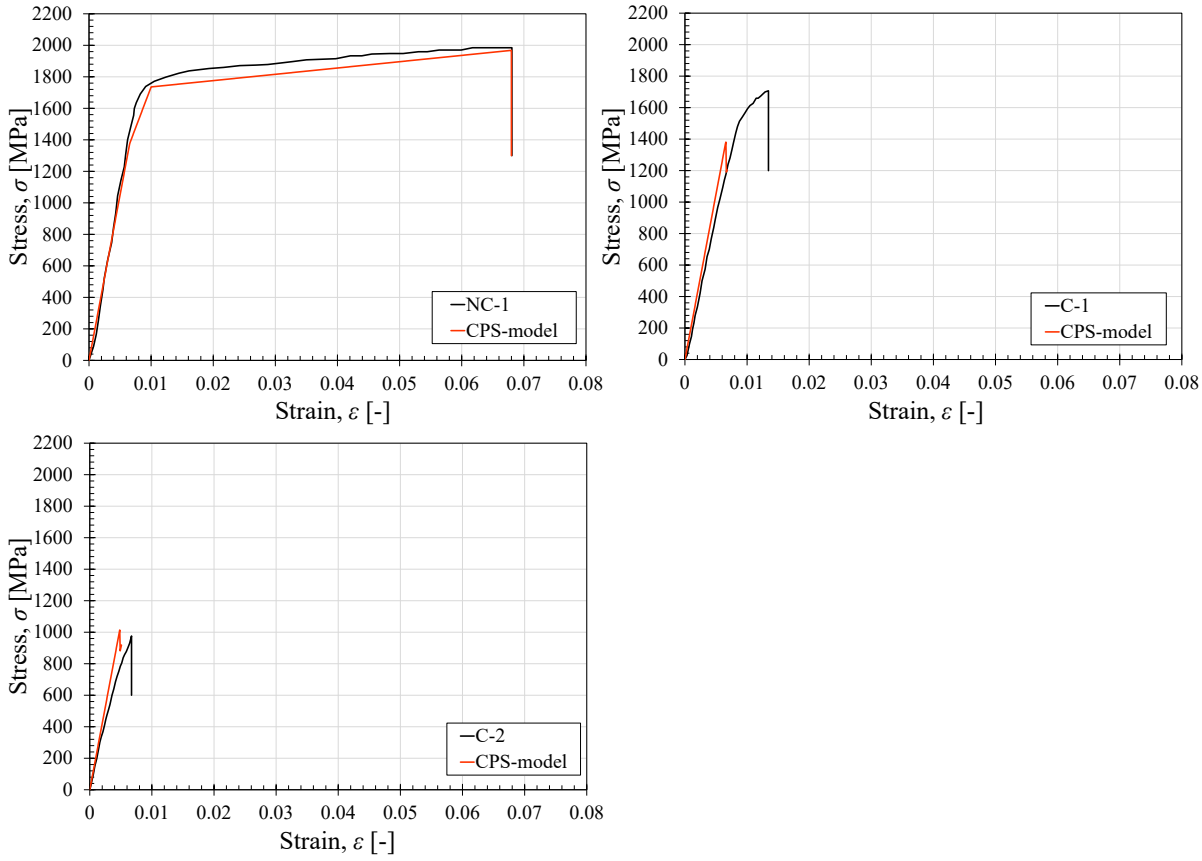

Figure 7-17 Comparison between experimental and analytical predictions for un-corroded and corroded strands belonging to Giriraju et al. (2022) work.

To determine the CPS-model performance, a statistical analysis of the 37 analyzed samples was conducted by investigating the normalized ratio between the experimental outcomes and the analytical predictions in the form $f_{pu,corr,exp}/f_{pu,corr,an1}$ and $\varepsilon_{pu,corr,exp}/\varepsilon_{pu,corr,an1}$, as reported in Table 7-3. Despite a relevant degree of agreement between experimental data and analytical predictions in the case of ultimate corroded strength, a grater scatter in the ultimate corroded strain was noted. Nevertheless, the CPS-model predictions were commonly observed to be conservative, thus providing a margin of safety in the evaluation of the residual mechanical behaviour of corroded prestressing strands – as confirmed by the mean values of ultimate corroded strength and strain ratio, $f_{pu,corr,exp}/f_{pu,corr,an1}$ and $\varepsilon_{pu,corr,exp}/\varepsilon_{pu,corr,an1}$, which were found to be 1.02 and 1.06, respectively.

Furthermore, the accuracy and the effectiveness of the CPS-model were confirmed through the estimation of the Coefficient of Correlation, CoC, and the calculation of the Coefficient of Variation, CV, which was assessed as reported in Eq. 7-17. CoC is a statistical parameter commonly adopted to evaluate the degree of correlation of two data sets, expressed by a linear relationship. In fact, CoC values equal to 1.0 denote a perfect correlation, i.e. a direct

relationship, of the two analyzed variables or data sets; whereas CoC values close to 0.0 represents the absence of relationship between the analyzed data. Adopting the CPS-model, CoC values equal to 0.92 and 0.98 were respectively obtained from the investigation of ultimate corroded strength and ultimate corroded strain ratios, resulting in a strong correlation between experimental outcomes and analytical predictions. CV is a parameter – expressed in percentage (%) – defined as the ratio between the standard deviation and the average value (mean) of the analyzed data, as in Eq. 7-17, indicating the accuracy of a statistical estimation. In particular, for decreasing CV values tending to 0.0, more precise predictions are obtained. For the CPS-model predictions, CV values of 9.52% and 20.01% were calculated for the ultimate corroded strength and the ultimate corroded strain ratios, respectively.

$$CV = \frac{S\tan dard \quad Deviation}{Mean \quad Value} \cdot 100 \qquad 7\text{-}17$$

Finally, it is important to emphasize that the CPS-model validation was conducted by considering all of the experimental tensile tests outcomes available in scientific literature, which provide the necessary input parameters for the application of the proposed model, i.e. cross-sectional loss (μ_{max}) and pit type morphology configuration (Type 1, Type 2 or Type 3) of the most corroded wire. Therefore, to further validate the CPS-model, additional tensile tests on corroded prestressing strands are strongly recommended. Indeed, new experimental data would be fundamental to improve the proposed regression relationships and, as a result, to improve and refine the conducted statistical analysis.

Table 7-3 CPS-model predictions in terms of ultimate strength, $f_{pu,corr,an1}$, ultimate strain, $\varepsilon_{pu,corr,an1}$, normalized strength, $f_{pu,corr,exp}/f_{pu,corr,an1}$, and normalized strain, $\varepsilon_{pu,corr,exp}/\varepsilon_{pu,corr,an1}$. The reported data consider also the un-corroded samples.

Sample ID	$f_{pu,corr,an1}$ [MPa]	$\varepsilon_{pu,corr,an1}$ [-]	$f_{pu,corr,exp}/f_{pu,corr,an1}$ [-]	$\varepsilon_{pu,corr,exp}/\varepsilon_{pu,corr,an1}$ [-]
PB9-L(12-82)	1282.90	0.0066	0.93	1.03
PB9-L(426-496)	1795.90	0.0317	1.00	1.00
PB9-R(15-60)	924.90	0.0047	1.17	1.26
PB9-R(428-473)	1901.75	0.0515	0.99	0.97
PB10-L(138-208)	1698.40	0.0105	0.98	1.02
PB10-L(445-515)	1024.30	0.0053	0.92	1.06
PB10-R(32-102)	-	-	-	-
PB10-R(287-332)	745.90	0.0038	0.94	0.95
PB11-L(5-75)	1901.75	0.0515	0.98	1.00
PB11-L(196-266)	1401.40	0.0075	1.08	1.09
PB11-R(6-51)	1578.50	0.0092	1.04	1.03
PB11-R(273-318)	1470.70	0.0082	0.94	0.91
PB12-L(12-82)	1143.70	0.0059	1.04	1.17
PB12-L(124-169)	1470.30	0.0082	1.01	0.99
PB12-R(100-170)	1615.10	0.0095	0.92	0.91
PB12-R(358-403)	1901.75	0.0515	1.00	1.05
PB13-L(1-46)	1382.80	0.0073	1.13	1.41
PB13-L(108-178)	1322.70	0.0068	0.65	0.69
PB13-R(0-70)	1302.80	0.0068	1.06	1.13
PB13-R(70-115)	1526.40	0.0087	1.02	0.97
PB14-L(10-55)	1093.90	0.0056	1.13	1.11
PB14-L(455-500)	1901.75	0.0515	1.03	0.94
PB14-R(2-72)	1466.00	0.0082	0.99	0.98
PB14-R(77-122)	-	-	-	-
NC-1	1968.10	0.068	1.00	1.00
C-1	1380.87	0.0072	1.24	0.94

C-2	1013.88	0.0052	0.96	1.29
CS1	1822.59	0.0625	1.02	1.05
CS2	1844.68	0.0690	1.02	1.01
CS3	1394.02	0.0076	1.21	2.07
CS4	1394.04	0.0076	1.20	1.68
CS5	1634.41	0.0099	0.97	0.98
CS6	1687.00	0.0224	1.02	0.89
CS7	1676.31	0.0109	1.04	1.74
CS8	1791.36	0.0532	1.06	0.72
CS9	1582.39	0.0094	1.06	1.15
CS10	1788.31	0.0523	1.03	0.83
CS11	1794.15	0.0540	1.06	1.04
CS12	1791.36	0.0532	1.07	1.20
		Mean Value:	1.02	1.06
		Standard Deviation:	0.10	0.21
		CoC [-]:	0.92	0.98
		CV [%]:	9.53	20.01

*Samples CS3 was neglected in the statistical analysis since considered as an outlier.

7.4.5 Main observations

In the present section, a constitutive law, named CPS-model, was proposed for prestressing strands subjected to chloride-induced corrosion, upgrading the equivalent spring model previously provided by Jeon et al. (2019). To this aim, the regression trends for the prediction of the ultimate corroded strength and the ultimate corroded strain of corroded prestressing strands were revised by considering the tensile test outcomes coming from the analysis of the available samples. In particular, the main input parameters of the proposed model, which are the cross-sectional losses and the pit type morphology configurations classification of the wires composing the strand in the section where the maximum penetration depth was recorded, were derived from the pitting morphology spatial variability previously conducted.

As a result, the main outcomes concerning the application of the proposed CPS-model can be summarized as follows:

- The faithfulness of the obtained tensile test outcomes was confirmed by comparing the results with a database collecting tensile test data available in the scientific literature in terms of ultimate strength and ultimate strain as a function of two different corrosion parameters, i.e. the mass-loss of a corroded strand and the cross-sectional loss of the most corroded wire. The results revealed a good agreement between the new experimental data and tensile test findings from earlier studies.
- The stress-strain behaviour of an un-corroded prestressing strand was reproduced by a three-linear trend, established on the basis of the Ramberg-Osgood model. Specifically, the ultimate mechanical properties in terms of $\varepsilon_{pu,0}$, $f_{pu,0}$ and $E_{p,0}$ were defined as the mathematical average of the four tensile tests performed on un-corroded strand samples; whereas the elastic, yielding and hardening phase boundary limits, i.e. the points ($\varepsilon_{pp,0}$; $f_{pp,0}$) and ($\varepsilon_{py,0}$; $f_{py,0}$), were evaluated according to the Probabilistic Model Code provisions, (JCSS, 2001).
- Based on the experimental tensile test outcomes, ultimate strength and ultimate strain decays were evaluated as a function of the cross-sectional loss of the most corroded wire, combining the new experimental data and the experimental results coming from Jeon et al. (2019) research activity. Therefore, by distinguishing between three different pit type morphology configurations, denoted as Type 1, Type 2, and Type 3, new exponential relationships were proposed for the assessment of the ultimate strength and the ultimate strain – one for each morphology type considered.

Thereafter, a critical cross-sectional loss threshold, μ_{lim}, which limited the development of the hardening phase in the stress-strain relationship and denotes the failure mode change from ductile to brittle of the analyzed corroded wire was established. The μ_{lim} resulted equal to 8.1%, 10.7% and 5.4% for Type 1 – Type 2, and Type 3 pit morphology configuration, respectively.

- Considering the updated expressions for the evaluation of the ultimate corroded strength and the ultimate corroded strain, as well as the established μ_{lim} values, the constitutive law for the prediction of the residual stress-strain relationship of a corroded prestressing strand was proposed. As described in the section on basic assumptions, the CPS-model is based on the equivalent spring approach, which defines the response of the overall strand as the sum of the wire contributions behaving as springs working in parallel with each other. In detail, the most relevant features of the proposed model are: (i) the conventional failure mode of a corroded strand – assumed to be governed by the rupture of the most corroded wire in the section where the maximum penetration depth was measured – and (ii) the model's ability to reproduce the wires' failure sequence.
- Finally, the effectiveness and accuracy of the proposed model were verified by comparing the experimental tensile test outcomes with the analytical stress-strain predictions for a total of 37 available prestressing strands coming from the present research (22 samples) and from the experimental activities conducted by Jeon et al. (2019) (12 samples) and Giriraju et al. (2022) (3 samples). Based on the obtained results, the application of the CPS-model allowed the prediction of the residual stress-strain relationship. In addition, the good matching between experimental data and analytical predictions was confirmed by the statistical analysis conducted on the overall set of available samples in terms of ultimate corroded strength, $f_{pu,corr,exp}/f_{pu,corr,an1}$, and ultimate corroded strain, $\varepsilon_{pu,corr,exp}/\varepsilon_{pu,corr,an1}$, ratios. Furthermore, the accuracy of the proposed CPS-model compared to the adoption of Jeon et al. (2019) proposal is graphically depicted in Figure 7-14 and Figure 7-16.

Although the CPS-model should be considered as an important step forward for the refined prediction of the residual mechanical response of a corroded prestressing strand, there are several drawbacks and limitations that call for further investigation:

- First, an operational procedure for in-situ sampling and measuring of the main corrosion parameters of corroded wires should be established in order to operationally apply the proposed model to in service degraded PC members. In this regard, the scientific literature indicated possible non-destructive techniques to be applied for the measurement of corrosion parameters directly during in-situ inspections. Yoo et al. (2020), for example, stated that radiography, X-rays, endoscopic inspection, or magnetic field methods could all be adopted to properly identify prestressing strands defects along the overall length of a PC element and to evaluate the location of the most corroded section. In addition, Wang et al. (2020) identified other possible non-destructive techniques for the evaluation of the strand unit cross-sectional loss, such as the acoustic emission method, the half-cell potential, or the linear polarization resistance. Once the minimum cross-sectional loss is known, a local removal of the concrete cover thickness would allow the evaluation of the main corrosion parameters of the corroded wires composing the strand in the section where the maximum longitudinal penetration depth, $P_{max,long}$, has been identified. In this context, advancements in miniaturized laser scanning techniques are welcomed for this purpose, as well as to limit concrete cover removal around the detected defect with digital measurement of corrosion parameters other than the estimation of the outer radius of external wires, thereby avoiding gross errors due to the operator's measuring activity. Non-destructive methods, however, are not the main focus of the present research and will not be discussed further.
- Second, since the CPS-model is based on the actual evaluation of pit type morphology configurations as well as the accurate measurement of the cross-sectional loss of the several corroded wires in the section where $P_{max,long}$ was measured, the model application can be severely limited in everyday engineering practice. To overcome this issue, a simplified version of the CPS-model is introduced in the next section, called SCPS-model, which stands for "Simplified model for Corroded Prestressing Strands". The simplified version will be based on a single input parameter, namely the maximum penetration depth of the most corroded wire, which can be easily measured during in-situ inspection. In fact, once the most corroded section is known, the maximum penetration depth can be measured directly

by means of technical instrumentation such as a pit depth gauge or a portable laser scanner, without performing destructive tests on the existing structural elements. This is especially true since the most corroded wire is generally located in the outer part of the prestressing strand embedded in concrete, which is more exposed to the chloride ion attack induced by the diffusion process of external agents. Therefore, following the concrete cover removal in the region of interest, the maximum penetration depth of the most corroded wire – the only input parameter – can be measured through a time-saving in-situ procedure.

- Third, the CPS-model is limited to the prediction of the residual mechanical response of a single corroded prestressing strand. Further efforts should be devoted into developing a simplified model capable of estimating the residual mechanical properties of multiple corroded strands characterized by different corrosion levels. Indeed, in the case of existing structures, such as bridges or tanks, several prestressing strands are generally present in the same section, providing a key contribution in the load-carrying capacity of the structural member. Therefore, it is necessary to provide a useful simplified analytical model that accurately estimates the residual mechanical response of the investigated structural member without leading to overly conservative predictions based on the estimate residual mechanical response of a single corroded strand.

7.5 Simplified model for the daily engineering practice: the SCPS-model

Although the CPS-model proved to be a powerful tool for the prediction of the residual stress-strain relationship of a corroded strand to be applied for refined analyses, disadvantages mainly related to the number of corrosion parameters involved and the need to visually classify the pit type morphology of each corroded wire were highlighted. Therefore, despite the high efficiency shown by the CPS-model, its application in the daily engineering practice may be hindered due to the time-consuming procedure to be conducted in rapid in-situ inspections. To overcome these technical issues, a simplified version of the proposed CPS-model, named SCPS-model, was defined. The SCPS-model was designed to provide accurate and conservative predictions of the residual mechanical response of corroded strands. To this end, the new version has been based on a single input parameter, namely the maximum penetration depth of the most corroded wire, and it has been developed to be independent from: (i) the pit type morphology classification and (ii) the evaluation of corrosion parameters such as the mass loss, η, of a corroded strand or the cross-sectional loss, μ, of corroded wires.

Hereafter, the basic assumptions and the main simplifications adopted with respect to the CPS-model are discussed in more detail; moreover, the SCPS-model is validated using the experimental tensile test outcomes coming from the present research – previously introduced in Section 7.3 – and the experimental activity conducted by Jeon et al. (2019).

7.5.1 Basic assumptions

For the sake of clarity, Figure 7-18 flowchart compares the main steps of the SCPS-model with those of the previously analyzed CPS-model. In detail, the SCPS-model was designed on the following basic assumptions:

I. **Input parameters:** Unlike the CPS-model, the input parameter of the SCPS-model is unique and consists of the maximum penetration depth of the most corroded wire at the section of analysis, $P_{max,sectional}$. Similar to the CPS-model, however, the SCPS-model neglects the friction behaviour between wires. Additionally, the wires failure sequence is reproduced by attributing an average penetration depth, $P_{av,transv}$, to the remaining external wires, which is estimated as a function of both $P_{max,sectional}$ and the transversal pitting factor, Ω_i, through Eq. 6-20.

II. **Equivalent spring model:** Both the CPS and SCPS models assume the equivalent spring approach for predicting the residual mechanical response of the entire corroded strand. In detail, the spring contribution that reproduces the behaviour of the most corroded wire is governed by $P_{max,sectional}$; whereas the five contributions associated to the remaining external wires behave similarly and their stress-strain relationship is determined by $P_{av,transv}$. Like in the CPS-model, due to the absence of corrosion signs, the inner wire is assumed as un-corroded and characterized by a P_{inner} equal to 0.0.

III. **Conventional failure mode:** As with the CPS-model, the conventional failure mode of the entire strand is assumed to occur in correspondence to the rupture of the most corroded wire. However, in the case of more refined analyses, the SCPS-model is also able to reproduce the failure sequence of all the wires composing the strand. The main simplification consists in assuming all the external wires, except for the most corroded one, having the same corrosion level, estimated as a function of the single input parameter of the SCPS-model, which is $P_{max,sectional}$. For the application of the proposed model in the daily engineering practice, simplified expressions have been defined for the accurate and time-saving assessment of the residual mechanical response of a corroded strand.

IV. **Pitting morphology:** In contrast to the CPS-model, the SCPS-model remains independent from the classification of pits. Moreover, the SCPS-model is independent from corrosion parameter calculations such as the mass loss of a corroded strand or the cross-sectional losses of corroded wires. The simplified model is designed to be dependent only on the maximum penetration depth of the most corroded wire and pitting morphology outcomes are introduced in the form of transversal pitting factor to assign an average penetration depth to the remaining external wires.

V. **Stress-strain behaviour:** Both CPS and SCPS models assume a tri-linear relationship for representing the stress-strain behaviour of un-corroded and low corroded wires, according to the Ramberg-Osgood model, (Zhan et al., 2016). The tri-linear trend consists of: (a) an elastic phase ranging from (0; 0) to ($\varepsilon_{pp,0}$; $f_{pp,0}$), a yielding phase from ($\varepsilon_{pp,0}$; $f_{pp,0}$) to ($\varepsilon_{py,0}$; $f_{py,0}$) and a hardening phase from ($\varepsilon_{py,0}$; $f_{py,0}$) to ($\varepsilon_{pu,0}$; $f_{pu,0}$). By contrast, for intermediate and high corroded wires the tri-linear trend reduces to a bi-linear or even a linear trend as a function of the normalized value of maximum penetration depth, $P_{max,sectional}/r_{outer}$, of the analyzed wire as described in point (VII).

VI. **Threshold limit of plastic behaviour:** Differently from the CPS-model, which limits the development of the hardening phase – in the stress-strain relationship of a corroded

wire – to the achievement of the critical cross-sectional loss threshold, μ_{lim}, the SCPS-model prevents the development of the hardening phase for a normalized critical threshold value of the maximum penetration depth, $P_{max,sectional}/r_{outer}$, equal to 0.33, that corresponds to approximately 1/6 of the un-corroded wire diameter, ϕ_{outer}.

VII. **Ultimate corroded strength:** The SCPS-model evaluates the ultimate corroded strength, $f_{pu,corr}$, in correspondence to the ultimate corroded strain, $\varepsilon_{pu,corr}$, evaluated as shown in point (VIII).

VIII. **Ultimate corroded strain:** In contrast to the CPS-model, the SCPS-model estimates the ultimate corroded strain decay via a bi-linear relationship expressed as a function of $P_{max,sectional}/r_{outer}$. According to the SCPS-model assumptions, the stress-strain relationship of corroded and un-corroded wires is equivalent; the only difference lies in the cut-off point, established at the achievement of the previously determined ultimate corroded strain, $\varepsilon_{pu,corr}$. In particular, for low corroded wires having $P_{max,sectional}/r_{outer}$ values lower than 0.33 (critical threshold value), a tri-linear stress-strain relationship with a reduced hardening phase is adopted. Conversely, a bi-linear relationship is assumed for intermediate corroded wires having $P_{max,sectional}/r_{outer}$ values ranging between 0.33 and 0.86; whereas, for the high corroded ones with $P_{max,sectional}/r_{outer}$ values between 0.86 and 2.00, a linear relationship is adopted. The scenario of a complete deterioration of the external wire occurs for the upper boundary limit with a $P_{max,sectional}/r_{outer}$ value of 2.00, which corresponds to the entire deterioration of the wire diameter, ϕ_{outer}.

IX. **Wire-cross section:** Unlike the CPS-model, which calculates the tensile resistance of a corroded strand by multiplying the ultimate corroded strength by the un-corroded cross-sectional area of the wire, the SCPS-model considers the residual cross-section of the corroded wire, $A_{w,outer,corr}$. In fact, as stated in point (VII), the SCPS-model predicts the ultimate corroded strength, while the cross-sectional area reduction is estimated by adopting a bi-linear decay relationship dependent on $P_{max,sectional}/r_{outer}$.

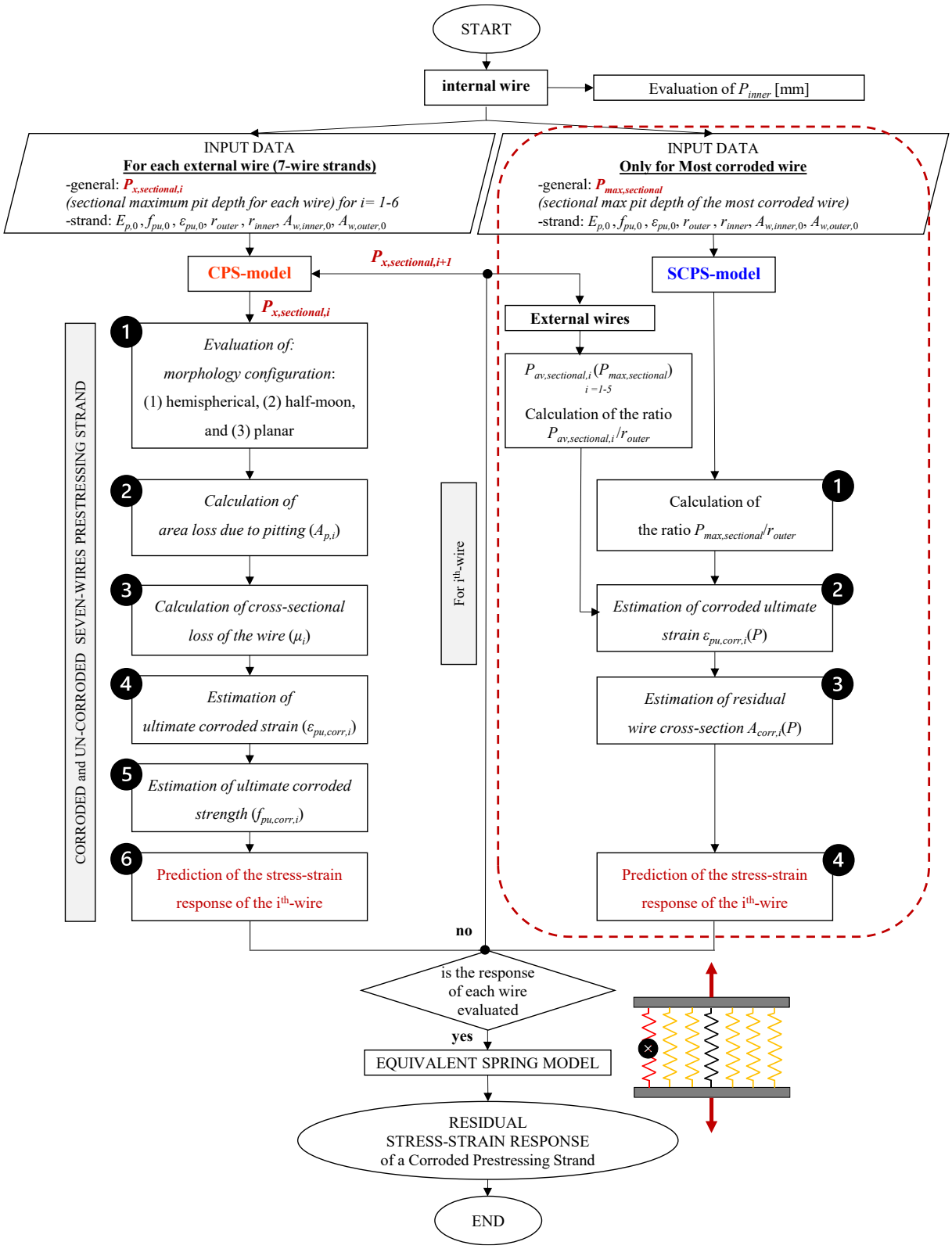

Figure 7-18 Flowchart of the main steps of the SCPS-model in comparison with the CPS-model.

7.5.2 Main simplifications

The SCPS-model is a simplified sectional model designed to depend on a single input parameter, $P_{max,sectional}$. As previously pointed out, this corrosion parameter can be easily measured during in-situ inspection and results independent from the morphological classification of the pit type. In addition, the measurement of $P_{max,sectional}$ does not require destructive testing on in service structural elements, with the only exception of the local removal of concrete cover in proximity to the section of analysis. Given the chloride ion diffusion process, the highest corrosion level of prestressing reinforcements embedded in concrete generally occurs in their outer region and, indeed, can be observed in-situ by adopting non-destructive techniques. After determining the critical section, the maximum penetration depth can be measured by adopting technical instruments such as the pit depth gauge instrument or a more accurate portable laser scanner.

A further simplification consists in the estimation of the average sectional penetration depth, $P_{av,transv}$, to be attributed to the remaining external wires. To this end, $P_{av,transv}$ was evaluated as a function of the measured $P_{max,sectional}$ by adopting the transversal pitting factor relationship, Ω_i, previously introduced in Section 6.4.2.2 and re-called in Eq. 7-18 for clarity. As shown in Figure 6-23, the transversal pitting factor trend was determined by investigating the sectional pitting morphology variability of the available corroded strands by adopting the GOM Inspect software. Although the inner wire was assumed to be un-corroded for the investigated corroded strands, future research is planned to investigate corroded prestressing strands having high corrosion level and corroded inner wire with the aim of establishing a new correlation between the sectional maximum penetration depth, $P_{max,sectional}$, of the most corroded wire and the corresponding sectional penetration depth of the inner wire, P_{inner}.

$$P_{av,transv} = 2\Omega_i r_{outer} = \left[0.378\left(\frac{P_{\max,sectional}}{r_{outer}} \right)^2 + 0.25\left(\frac{P_{\max,sectional}}{r_{outer}} \right) \right] r_{outer} \qquad 7\text{-}18$$

Finally, the ultimate corroded strain decay of a corroded wire is estimated by adopting a bi-linear trend expressed as a function of the normalized maximum penetration depth, $P_{max,sectional}/r_{outer}$, as shown in Figure 7-19. Similarly to the CPS-model, the bi-linear trend was established by post-processing the experimental data, $\varepsilon_{pu,corr,exp}$, from the present research and the experimental activity conducted by Jeon et al. (2019) with a particular focus on:

1. Subdividing the available $\varepsilon_{pu,corr,exp}$ data into two groups: (a) samples failing in a ductile mode or (b) samples failing in a brittle mode;

2. Normalizing the $\varepsilon_{pu,corr,exp}$ outcomes to compare experimental tensile test data on corroded strands having different un-corroded mechanical properties, i.e. un-corroded ultimate strain ($\varepsilon_{pu,0}$) or un-corroded yielding strain ($\varepsilon_{py,0}$), respectively;
3. Performing linear regression analyses on the available data, distinguishing between ductile and brittle wire behaviour.

Based on the obtained results, the bi-linear relationship predicting the ultimate corroded strain, $\varepsilon_{pu,corr}$, of a corroded wire was defined, as expressed in Eq. 7-19 and Eq. 7-20.

$$\begin{cases} \dfrac{\varepsilon_{pu,corr}-\varepsilon_{py,0}}{\varepsilon_{pu,0}-\varepsilon_{py,0}} = 1-3.03\dfrac{P_{\max,sectional}}{r_{outer}} & 0.0 < \dfrac{P_{\max,sectional}}{r_{outer}} < 0.33 \\ \dfrac{\varepsilon_{pu,corr}}{\varepsilon_{py,0}} = 1-0.599\left(\dfrac{P_{\max,sectional}}{r_{outer}}-0.33\right) & 0.33 \le \dfrac{P_{\max,sectional}}{r_{outer}} \le 2.00 \end{cases} \quad 7\text{-}19$$

$$\varepsilon_{pu,corr} = \begin{cases} \left[\left(1-3.03\dfrac{P_{\max,sectional}}{r_{outer}}\right)\left(\varepsilon_{pu,0}-\varepsilon_{py,0}\right)\right]+\varepsilon_{py,0} & 0.0 < \dfrac{P_{\max,sectional}}{r_{outer}} < 0.33 \\ \left(1-0.599\left(\dfrac{P_{\max,sectional}}{r_{outer}}-0.33\right)\right)\varepsilon_{py,0} & 0.33 \le \dfrac{P_{\max,sectional}}{r_{outer}} \le 2.00 \end{cases} \quad 7\text{-}20$$

As shown in Figure 7-19, a critical threshold of normalized sectional maximum penetration depth, $P_{max,sectional}/r_{outer}$, equal to 0.33 was identified. This critical value is equivalent to a wire deterioration of approximately 1/6 of the wire's external diameter, ϕ_{outer}, and represents the threshold value upon which the hardening phase of the stress-strain relationship of a corroded wire cannot develop further, thus resulting in the change of the wire's failure mode from ductile to brittle. Moreover, a lower and an upper boundary limit of $P_{max,sectional}/r_{outer}$ of 0.0 and 2.00 were established. The lower boundary limit represents the un-corroded scenario; the upper one corresponds to the deterioration of the entire wire. Furthermore, it is worth noting that the proposed bi-linear trend for ultimate corroded strain decay was validated up to $P_{max,sectional}/r_{outer}$ experimental values equal to 1.40, as evidenced by the continuous black line drawn in the elastic behaviour trend in Figure 7-19.

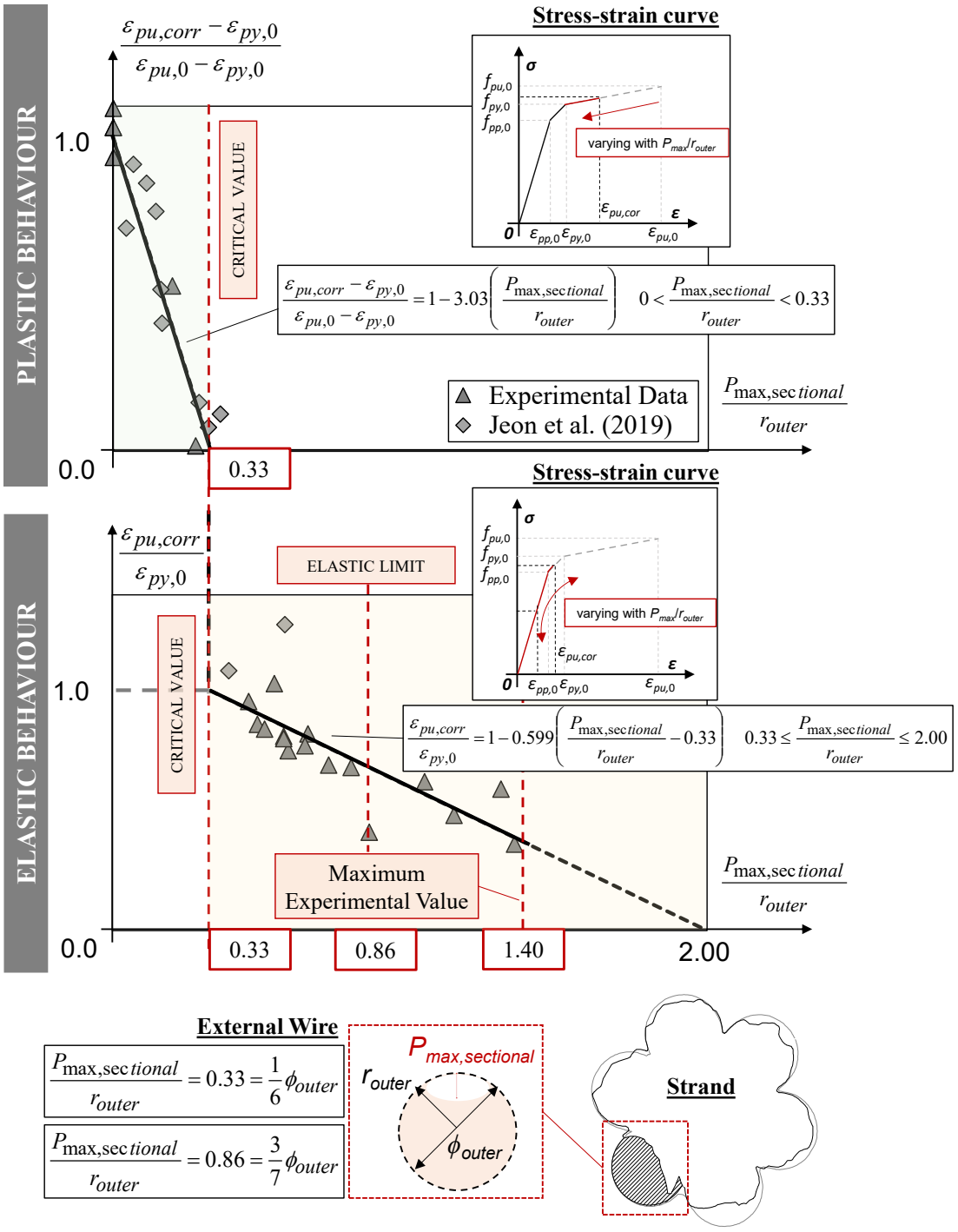

Figure 7-19 Ultimate corroded strain decay, definition of the bi-linear trend.

Similar to the procedure adopted for the prediction of the ultimate corroded strain, the residual cross-sectional area decay was additionally determined, as shown in Figure 7-20. For this purpose, a bi-linear relationship was proposed as a function of the normalized maximum penetration depth, $P_{max,sectional}/r_{outer}$, as expressed in Eq. 7-21 and Eq. 7-22.

$$\begin{cases} \dfrac{A_{w,outer,corr}}{A_{w,outer,0}} = \left(1 - 0.303\dfrac{P_{\max,sectional}}{r_{outer}}\right) & 0.0 < \dfrac{P_{\max,sectional}}{r_{outer}} < 0.33 \\ \dfrac{A_{w,outer,corr}}{A_{w,outer,0}} = \left[0.9 - 0.539\left(\dfrac{P_{\max,sectional}}{r_{outer}} - 0.33\right)\right] & 0.33 \le \dfrac{P_{\max,sectional}}{r_{outer}} \le 2.00 \end{cases} \quad 7\text{-}21$$

$$A_{w,outer,corr} = \begin{cases} \left(1 - 0.303\dfrac{P_{\max,sectional}}{r_{outer}}\right) A_{w,outer,0} & 0.0 < \dfrac{P_{\max,sectional}}{r_{outer}} < 0.33 \\ \left[0.9 - 0.539\left(\dfrac{P_{\max,sectional}}{r_{outer}} - 0.33\right)\right] A_{w,outer,0} & 0.33 \le \dfrac{P_{\max,sectional}}{r_{outer}} \le 2.00 \end{cases} \quad 7\text{-}22$$

Furthermore, the upper and lower boundary limits as well as the critical threshold value $P_{max,sectional}/r_{outer}$ were assumed to be identical to the ones previously adopted for the ultimate corroded strain decay, resulting equal to 0.0, 2.0, and 0.33, respectively. Since the wire un-corroded cross-sectional area, $A_{w,outer,0}$, differed from the present experimental campaign and from the research activity conducted by Jeon et al. (2019), the experimental values of the residual cross-sectional area, $A_{w,outer,corr}$, were normalized by dividing them by the corresponding un-corroded values, $A_{w,outer,0}$, equal to 14.22 mm^2 and 19.62 mm^2, respectively.

Specifically, for the critical threshold value $P_{max,sectional}/r_{outer}$ equal to 0.33, a normalized residual cross-sectional area, $A_{w,outer,corr}/A_{w,outer,0}$, of 0.90 was determined by using Eq. 7-22. In this context, considering the strain localization effect caused by cross-sectional loss pointed out by Chen et al. (2020) and Haefliger & Kaufmann (2022), a similar normalized residual cross-sectional area for ordinary corroded reinforcement can be determined. According to the latter, a critical cross-sectional loss was established as a function of the reinforcement un-corroded yield ($f_{y,0}$) and ultimate ($f_{u,0}$) strengths based on equilibrium conditions established between the undamaged and damaged parts, as briefly reported in Eq. 7-23. The procedure took also into account the effect associated with the ratio between the ordinary reinforcing bars undamaged (l_{uc}) and damaged (l_c) part lengths. Such effect may be implemented in the SCPS-model in future research.

$$A_{s,0}f_{y,l_{uc}} = (1-\varsigma_{crit})A_{s,0}f_{u,l_c} \rightarrow \varsigma_{crit} = 1 - \frac{f_{y,0}}{f_{u,0}} \quad 7\text{-}23$$

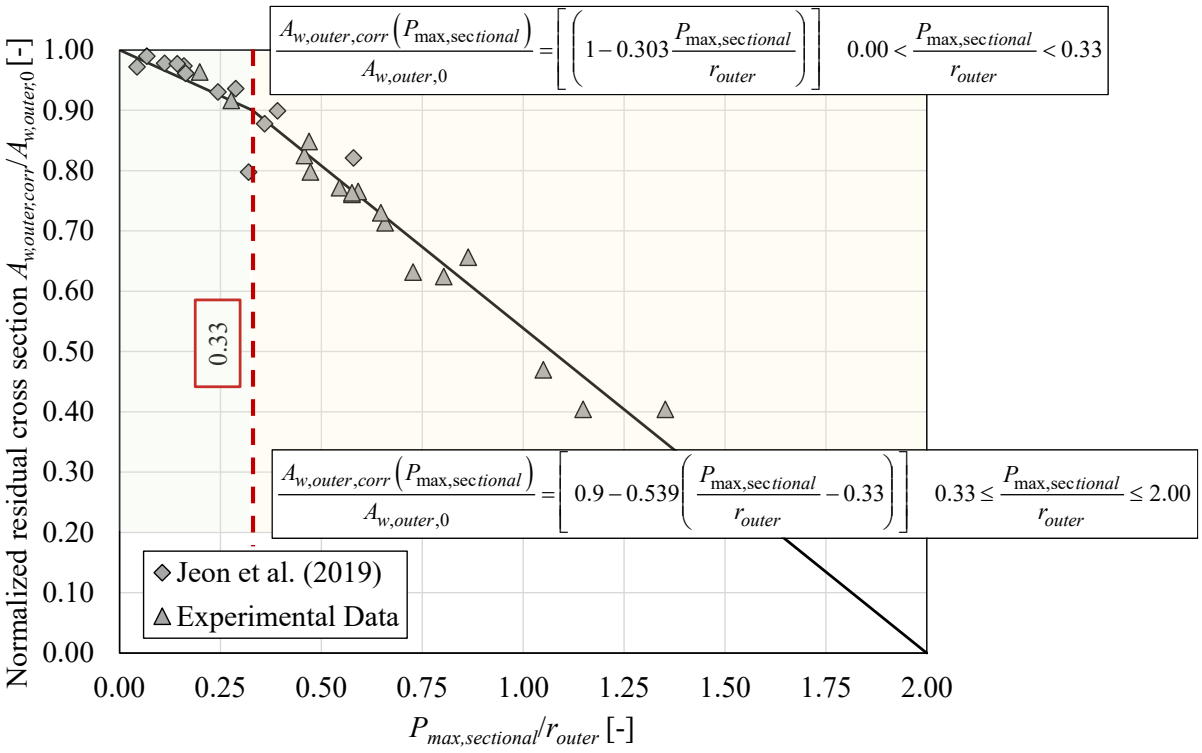

Figure 7-20 Ultimate corroded cross-sectional area decay, definition of a bi-linear trend.

7.5.2.1 Stress-strain relationship for corroded wires

Assuming the same behaviour of the un-corroded wire previously defined for the CPS-model, Figure 7-21(a), the residual stress-strain response of a corroded wire was predicted for the SCPS-model through Eq. 7-24 as a function of two main parameters: (i) the normalized maximum penetration depth of the most corroded wire and (ii) the ultimate corroded strain, $\varepsilon_{pu,corr}$, of the analyzed wire, estimated according to Eq. 7-19 or Eq. 7-20.

$$\sigma_w(\varepsilon) = \begin{cases} \dfrac{P_{\max,sectional}}{r_{outer}} < 0.33 \\ \varepsilon_{pu,corr} > \varepsilon_{py,0} \end{cases} \begin{cases} \varepsilon E_{p,0} & \varepsilon \le \varepsilon_{pp,0} \\ \varepsilon_{pp,0}E_{p,0} + E'_{p,0}\left(\varepsilon - \varepsilon_{pp,0}\right) & \varepsilon_{pp,0} < \varepsilon \le \varepsilon_{py,0} \\ \varepsilon_{pp,0}E_{p,0} + E'_{p,0}\left(\varepsilon_{py,0} - \varepsilon_{pp,0}\right) + E''_{p,0}\left(\varepsilon - \varepsilon_{py,0}\right) & \varepsilon_{py,0} < \varepsilon \le \varepsilon_{pu,corr} \\ 0 & \varepsilon > \varepsilon_{pu,corr} \end{cases}$$

$$\varepsilon_{pu,corr} \le \varepsilon_{py,0} \begin{cases} 0.33 \le \dfrac{P_{\max,sectional}}{r_{outer}} < 0.86 \\ 0.86 \le \dfrac{P_{\max,sectional}}{r_{outer}} \le 2.00 \end{cases} \begin{cases} \varepsilon E_{p,0} & \varepsilon \le \varepsilon_{pp,0} \\ \varepsilon_{pp,0}E_{p,0} + E'_{p,0}\left(\varepsilon - \varepsilon_{pp,0}\right) & \varepsilon_{pp,0} < \varepsilon \le \varepsilon_{pu,corr} \\ 0 & \varepsilon > \varepsilon_{pu,corr} \end{cases}$$

7-24

In more detail, Figure 7-21 shows how the behaviour of a corroded wire varies depending on the different levels of corrosion. According to Eq. 7-24, low corroded wires, characterized by $P_{max,sectional}/r_{outer}$ values lower than the critical threshold value of 0.33, develop a residual hardening phase, resulting in a reduced tri-linear trend of the mechanical response, as in Figure 7-21(b). When the critical value is exceeded, the wire behaviour changes from ductile to brittle and the hardening phase in the residual stress-strain relationship does not develop. As a result, a bi-linear trend is assumed for intermediate corroded wires until the $P_{max,sectional}/r_{outer}$ value does not exceed a second critical value equal to 0.86, as shown in Figure 7-21(c). This additional threshold limit of $P_{max,sectional}/r_{outer}$ is equivalent to a wire deterioration of approximately 3/7 of the wire's external diameter, ϕ_{outer}, and represents the critical value upon which the yielding phase of the stress-strain relationship of a corroded wire cannot develop. Lastly, when $P_{max,sectional}/r_{outer}$ values are higher than 0.86, only a linear-elastic trend of the residual stress-strain relationship of a corroded wire is adopted, as highlighted in Figure 7-21(d).

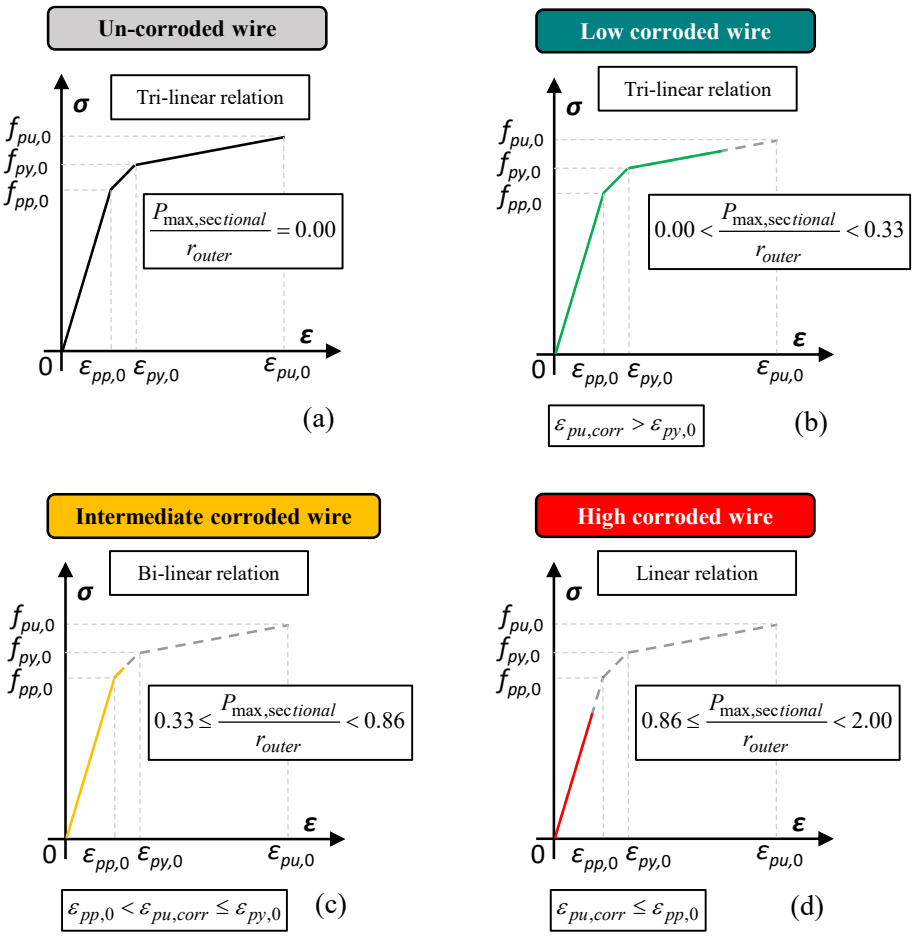

Figure 7-21 Stress-strain relationship of a prestressing wire as a function of different corrosion levels: (a) un-corroded, (b) low corroded, (c) intermediate corroded, and (d) high corroded.

Once the contribution of each wire is estimated, the equivalent spring model is used to predict the overall response of the corroded prestressing strand through Eq. 7-25:

$$\sigma(\varepsilon) = \frac{\sigma_{w,\max}(\varepsilon, P_{\max}) A_{w,outer,corr}(P_{\max}) + 5 \cdot \sigma_{w,av}(\varepsilon, P_{av}) A_{w,outer,corr}(P_{av}) + \sigma_{w,inner}(\varepsilon, P_{inner}) A_{w,inner,corr}(P_{inner})}{\sum_{i=1}^{6}\left(A_{w,outer,0}\right) + A_{w,inner,0}} = \frac{\sigma_{w,\max}(\varepsilon, P_{\max}) A_{w,outer,corr}(P_{\max}) + 5 \cdot \sigma_{w,av}(\varepsilon, P_{av}) A_{w,outer,corr}(P_{av}) + \sigma_{w,0}(\varepsilon) A_{w,inner,0}}{A_{p,0}}$$

7-25

where $\sigma(\varepsilon)$ represents the strand stress for a given strain, ε, whereas $\sigma_{w,max}$, $\sigma_{w,av}$ and $\sigma_{w,inner}$ are the stresses of the most corroded wire, the remaining external wires and the inner wire, respectively. In particular, P_{max} and P_{av} stand for $P_{max,sectional}$ and $P_{av,transv}$. Moreover, $A_{w,outer,0}$ and $A_{w,inner,0}$ represent the un-corroded cross-sectional areas of the external and internal wires, while $A_{p,0}$ is the un-corroded cross-sectional area of the entire strand. In this context, $\sigma_{w,inner}$ and $A_{w,inner,corr}$ – for the present case study – were considered equal to $\sigma_{w,0}(\varepsilon)$ and $A_{w,inner,0}$ because the inner wire was found to be un-corroded by the experimental findings, meaning a null maximum penetration depth of the inner wire, P_{inner}. The residual cross-sectional area of the external wire, $A_{w,outer,corr}$, was calculated for each wire through Eqs. 7-21 and 7-22.

For the sake of clarity, Figure 7-22 shows the application of the equivalent spring model for the evaluation of the residual stress-strain relationships of a corroded strand by varying its corrosion level, expressed in terms of $P_{max,sectional}/r_{outer}$. Similarly to the CPS-model, the conventional failure mode of the entire strand was assumed for the SCPS-model to be governed by the failure of the most corroded wire, characterized by the maximum sectional penetration depth, $P_{max,sectional}$. However, differently from the CPS-model, the SCPS-model attributes an average penetration depth, $P_{av,transv}$, to the remaining external wires; as a result, the five springs reproducing the behaviour of the remaining external wires fail simultaneously.

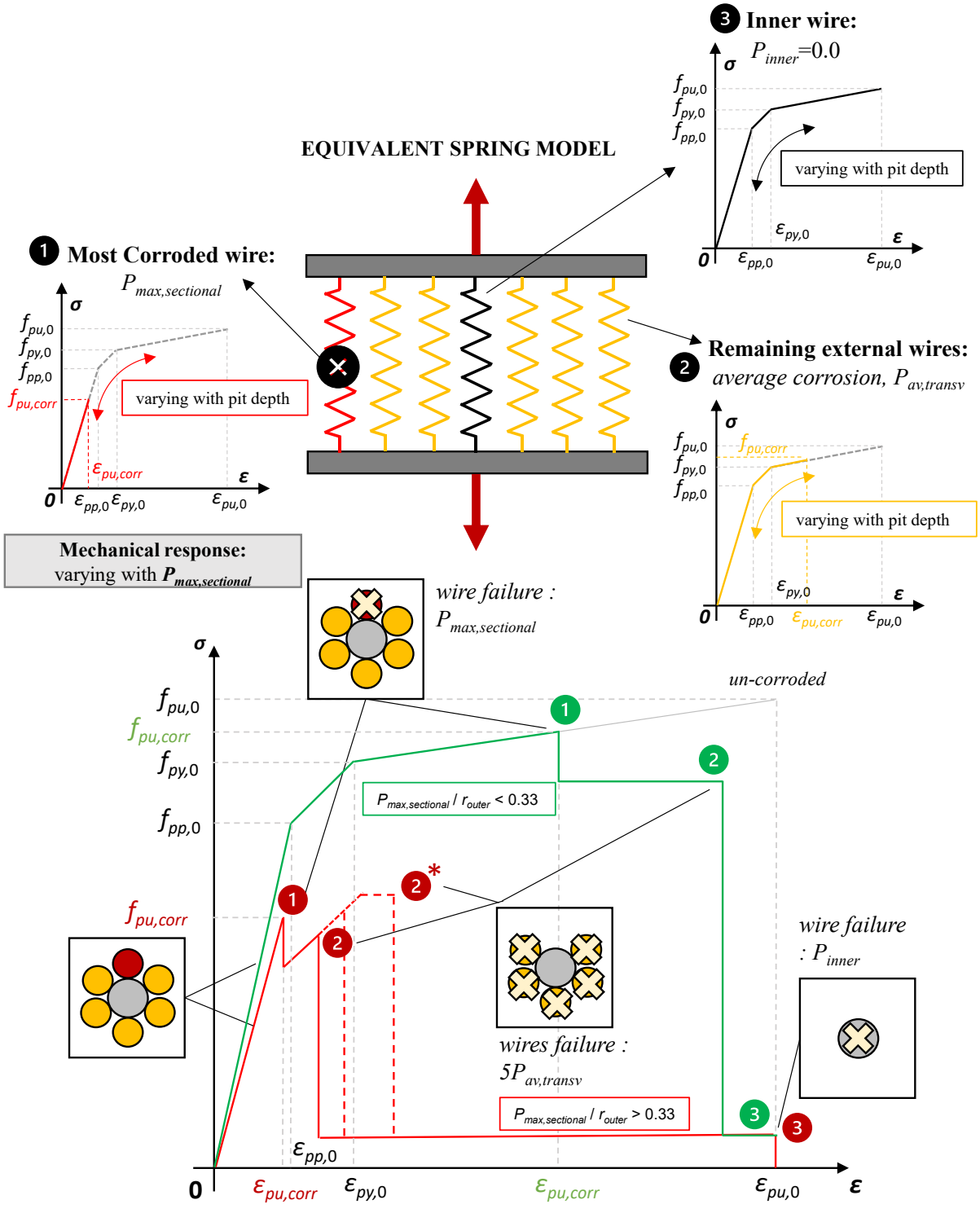

Figure 7-22 Equivalent spring model: residual mechanical response of a corroded strand considering different corrosion levels.

7.5.3 Simplified expressions for daily engineering practice application

In order to provide a useful tool for the accurate and time-saving assessment of the residual mechanical response of a corroded strand to be used by engineers in the daily practice, simplified relationships were proposed for the estimation of: (i) the failure stage of the most corroded wire, referred to as "Failure 1", and (ii) the failure stage of the remaining external wires, denoted as "Failure 2".

The following is a summary of the step-by-step procedure to be applied for the evaluation of the two failure stages of the residual stress-strain response of a corroded strand, as previously shown graphically in Figure 7-22.

1) **Step 1**: *Preliminary evaluation of un-corroded mechanical properties and geometrical features of the investigated wires/strand*.

   Based on in-situ inspection or referring to design drawings, the un-corroded mechanical properties of the investigated strand must be measured in terms of: (i) modulus of elasticity,($E_{p,0}$), (ii) ultimate strength ($f_{p,0}$), and (iii) ultimate strain ($\varepsilon_{p,0}$). Similarly, the geometrical dimensions of the un-corroded radius of external (r_{outer}) and internal wires (r_{inner}) must be defined. The corresponding un-corroded cross-sectional areas of outer ($A_{w,outer,0}$) and inner ($A_{w,inner,0}$) wires are then calculated according to Eq. 7-26. Once the cross-sectional areas of all wires are known, the un-corroded cross-sectional area of the entire strand, $A_{p,0}$, is established by summing the different contributions.

$$A_{w,outer,0} = \frac{\pi\left(2r_{outer}\right)^2}{4} = \frac{\pi\left(\phi_{outer}\right)^2}{4}$$
$$A_{w,inner,0} = \frac{\pi\left(2r_{inner}\right)^2}{4} = \frac{\pi\left(\phi_{inner}\right)^2}{4} \qquad 7\text{-}26$$

2) **Step 2**: *Estimation of the stress-strain relationship of un-corroded wires*

   According to Eq. 7-5, the tri-linear stress-strain relationship for un-corroded wires is defined based on the un-corroded mechanical properties evaluated in Step 1. The simplified relationship consists of:

   (a) An elastic phase ranging from initial coordinates (0; 0) to the proportional limit ($\varepsilon_{pp,0}$; $f_{pp,0}$);

   (b) A yielding phase from the proportional limit ($\varepsilon_{pp,0}$; $f_{pp,0}$) to the yielding point ($\varepsilon_{py,0}$; $f_{py,0}$);

(c) A hardening phase from the yielding point ($\varepsilon_{py,0}$; $f_{py,0}$) and the failure point ($\varepsilon_{pu,0}$; $f_{pu,0}$).

In detail, the strength ($f_{pp,0}$) and the strain ($\varepsilon_{pp,0}$) in correspondence to the proportional limit are evaluated through Eqs. 7-8 and 7-9; while the yielding strength and strain are calculated by adopting Eq. 7-10 and fixed at 1%, respectively. Moreover, the yielding ($E'_{p,0}$) and hardening ($E''_{p,0}$) modulus are estimated according to Eq. 7-6 and Eq. 7-7.

3) **Step 3**: *Measurement of the maximum penetration depth of the most corroded wire*
The location of the critical section is initially determined implementing non-destructive techniques. A local removal of the concrete cover must then be performed. At last, the maximum penetration depth of the most corroded wire, $P_{max,sectional}$, is measured by means of a pit depth gauge instrument or a more accurate portable laser scanner.

4) **Step 4**: *Estimation of the average sectional penetration depth*
Taking into account the analysis of the pitting morphology and the variability of the transversal pitting factor (Ω_i), an average penetration depth, $P_{av,transv}$, is attributed to the external wires, except for the most corroded one, as a function of the $P_{max,sectional}$ – previously measured in step 3 – by adopting Eq. 7-18. Based on experimental evidence, the corrosion level of the inner wire must be determined. In the present research, the penetration depth of the inner wire, P_{inner}, was assumed to be null.

5) **Step 5**: *Prediction of the ultimate corroded strain of corroded wires*
Assuming $P_{max,sectional}$ and $P_{av,transv}$ values, previously calculated in steps 3 and 4, the related ultimate corroded strains ($\varepsilon_{pu,corr}$) of the most corroded wire and the remaining five external wires are evaluated through Eq. 7-20.

6) **Step 6**: *Residual mechanical response of a corroded strand*
Once the residual stress-strain response of each corroded wire has been predicted through Eq. 7-24, it is necessary to adopt the equivalent spring model to evaluate the mechanical response of the entire strand by summing the wires' contributions, according to Eq. 7-25. For the sake of clarity, Eq. 7-27 and Eq. 7-28 report the expressions for estimating the residual ultimate stress of the most corroded wire ($\sigma_{w,max}(\varepsilon)$) and the remaining external wires ($\sigma_{w,av}(\varepsilon)$), respectively.

$$\sigma_{w,\max}(\varepsilon)=\begin{cases}0.00\le\dfrac{P_{\max,sectional}}{r_{outer}}<0.33 & f_{py,0}+E''_{p,0}\left(\varepsilon_{pu,corr}-\varepsilon_{py,0}\right) \quad \varepsilon_{py,0}<\varepsilon_{pu,corr}\le\varepsilon_{pu,0}\\ 0.33\le\dfrac{P_{\max,sectional}}{r_{outer}}<0.86 & f_{pp,0}+E'_{p,0}\left(\varepsilon_{pu,corr}-\varepsilon_{pp,0}\right) \quad \varepsilon_{pp,0}<\varepsilon_{pu,corr}\le\varepsilon_{py,0}\\ 0.86\le\dfrac{P_{\max,sectional}}{r_{outer}}\le 2.00 & E_{p,0}\varepsilon_{pu,corr} \quad \varepsilon_{pu,corr}<\varepsilon_{pp,0}\end{cases} \qquad 7\text{-}27$$

$$\sigma_{w,av}(\varepsilon)=\begin{cases}0.00\le\dfrac{P_{av,transv}}{r_{outer}}<0.33 & f_{py,0}+E''_{p,0}\left(\varepsilon_{pu,corr}-\varepsilon_{py,0}\right) \quad \varepsilon_{py,0}<\varepsilon_{pu,corr}\le\varepsilon_{pu,0}\\ 0.33\le\dfrac{P_{av,transv}}{r_{outer}}<0.86 & f_{pp,0}+E'_{p,0}\left(\varepsilon_{pu,corr}-\varepsilon_{pp,0}\right) \quad \varepsilon_{pp,0}<\varepsilon_{pu,corr}\le\varepsilon_{py,0}\\ 0.86\le\dfrac{P_{av,transv}}{r_{outer}}\le 2.00 & E_{p,0}\varepsilon_{pu,corr} \quad \varepsilon_{pu,corr}<\varepsilon_{pp,0}\end{cases} \qquad 7\text{-}28$$

7) **Step 7**: *Failure 1, rupture of the most corroded wire*

Since the conventional failure mode of the entire strand was associated with the rupture of the most corroded wire, a simplified expression is provided for the assessment of the latter key point. For this purpose, the reduced ultimate strength, $f_{pu,corr,an2}$, and the related residual tensile resistance, $T_{pu,corr,\mathrm{an2}}$, of the entire strand are predicted by simplifying Eq. 7-25, as expressed in Eq. 7-29 and Eq. 7-30, respectively:

$$\begin{aligned}&\sigma(\varepsilon)=f_{pu,corr,an2}=\\ &=\frac{\sigma_{w,\max}(\varepsilon,P_{\max})A_{w,outer,corr}(P_{\max})+5\cdot\ \sigma_{w,av}(\varepsilon,P_{av})A_{w,outer,corr}(P_{av})+\sigma_{w,0}(\varepsilon)A_{w,inner,corr}(P_{inner})}{\sum_{i=1}^{6}\left(A_{w,outer,0,i}\right)+A_{w,inner,0}}=\\ &=\sigma_{w,\max}(\varepsilon,P_{\max})\frac{\left(A_{w,outer,corr}(P_{\max})+5\cdot\ A_{w,outer,corr}(P_{av})+A_{w,inner,0}\right)}{A_{p,0}}=\\ &=\sigma_{w,\max}(\varepsilon,P_{\max})\alpha_{Acorr}\end{aligned} \qquad 7\text{-}29$$

$$T_{pu,corr,an2}=\sigma_{w,\max}(\varepsilon)\alpha_{Acor}A_{p,0} \qquad 7\text{-}30$$

where, α_{Acorr} is a corrosion parameter that estimates the normalized residual cross-sectional area of the entire strand through Eq. 7-31 as a function of the usual input parameter $P_{max,sectional}/r_{outer}$.

$$\alpha_{Acorr} = \begin{cases} \dfrac{P_{\max,sectional}}{r_{outer}} \le 0.33 & \dfrac{A_{w,inner,0} + A_{w,outer,0}\left[\left(1 - 0.303\dfrac{P_{\max}}{r_{outer}}\right) + 5\left(1 - 0.303\left(0.378\dfrac{P_{\max}}{r_{outer}}^2 + 0.25\dfrac{P_{\max}}{r_{outer}}\right)\right)\right]}{A_{p,0}} \\ 0.33 < \dfrac{P_{\max,sectional}}{r_{outer}} \le 0.66 & \dfrac{A_{w,inner,0} + A_{w,outer,0}\left[\left(0.9 - 0.539\left(\dfrac{P_{\max}}{r_{outer}} - 0.33\right)\right) + 5\left(1 - 0.303\left(0.378\dfrac{P_{\max}}{r_{outer}}^2 + 0.25\dfrac{P_{\max}}{r_{outer}}\right)\right)\right]}{A_{p,0}} \\ \dfrac{P_{\max,sectional}}{r_{outer}} > 0.66 & \dfrac{A_{w,inner,0} + A_{w,outer,0}\left[\left(0.9 - 0.539\left(\dfrac{P_{\max}}{r_{outer}} - 0.33\right)\right) + 5\left(0.9 - 0.539\left(\left(0.378\dfrac{P_{\max}}{r_{outer}}^2 + 0.25\dfrac{P_{\max}}{r_{outer}}\right) - 0.33\right)\right)\right]}{A_{p,0}} \end{cases}$$

7-31

8) **Step 8**: *Failure 2, simultaneously rupture of the remaining external wire*s

Similarly to Failure 1, the reduced ultimate strength, $f_{pu,corr,an2,2}$, and the relative residual tensile resistance, $T_{pu,corr,an2.2}$, of the entire strand are estimated in correspondence to the simultaneous failure of the remaining external wires (Failure 2). To this aim, Eq. 7-29 and Eq. 7-30 are simplified by neglecting the contribution of the most corroded wire previously broken, as highlighted in Eq. 7-32 and Eq. 7-33, respectively:

$$\begin{aligned} &\sigma(\varepsilon) = f_{pu,corr,an2,2} = \\ &= \frac{5\cdot\ \sigma_{w,av}(\varepsilon, P_{av})A_{w,outer,corr}(P_{av}) + \sigma_{w,0}(\varepsilon)A_{w,inner,corr}(P_{inner})}{\sum_{i=1}^{6}\left(A_{w,outer,0,i}\right) + A_{w,inner,0}} = \\ &= \sigma_{w,av}(\varepsilon, Pav)\frac{\left(5\cdot\ A_{w,outer,corr}(P_{av}) + A_{w,inner,0}\right)}{A_{p,0}} = \\ &= \sigma_{w,av}(\varepsilon, P_{av})\alpha'_{Acorr} \end{aligned} \qquad 7\text{-}32$$

$$T_{pu,corr,an2,2} = \sigma_{w,av}(\varepsilon)\alpha'_{Acorr}A_{p,0} \qquad 7\text{-}33$$

where, α'_{Acorr} is the modified corrosion parameter that estimates the normalized residual cross-sectional area of the entire strand through Eq. 7-34 on the basis of the usual input parameter $P_{max,sectional}/r_{outer}$ by neglecting the cross-sectional area of the most corroded wire ($A_{w,outer,corr}$), which failed after "Failure 1".

$$\alpha'_{Acorr} = \begin{cases} \dfrac{P_{\max,sectional}}{r_{outer}} \le 0.66 & \dfrac{A_{w,inner,0} + 5A_{w,outer,0}\left(1 - 0.303\left(0.378\left(\dfrac{P_{\max}}{r_{outer}}\right)^2 + 0.25\dfrac{P_{\max}}{r_{outer}}\right)\right)}{A_{p,0}} \\ \dfrac{P_{\max,sectional}}{r_{outer}} > 0.66 & \dfrac{A_{w,inner,0} + 5A_{w,outer,0}\left(0.9 - 0.539\left(\left(0.378\left(\dfrac{P_{\max}}{r_{outer}}\right)^2 + 0.25\dfrac{P_{\max}}{r_{outer}}\right) - 0.33\right)\right)}{A_{p,0}} \end{cases}$$

7-34

7.5.4 Model validation

To validate the simplified version of the proposed model, a comparison between the experimental outcomes and the analytical predictions of stress-strain relationships of the corroded strands coming from the present research and the study conducted by Jeon et al. (2019) was performed by adopting both the CPS and the SCPS models, as shown in Figure 7-23 and Figure 7-24, respectively.

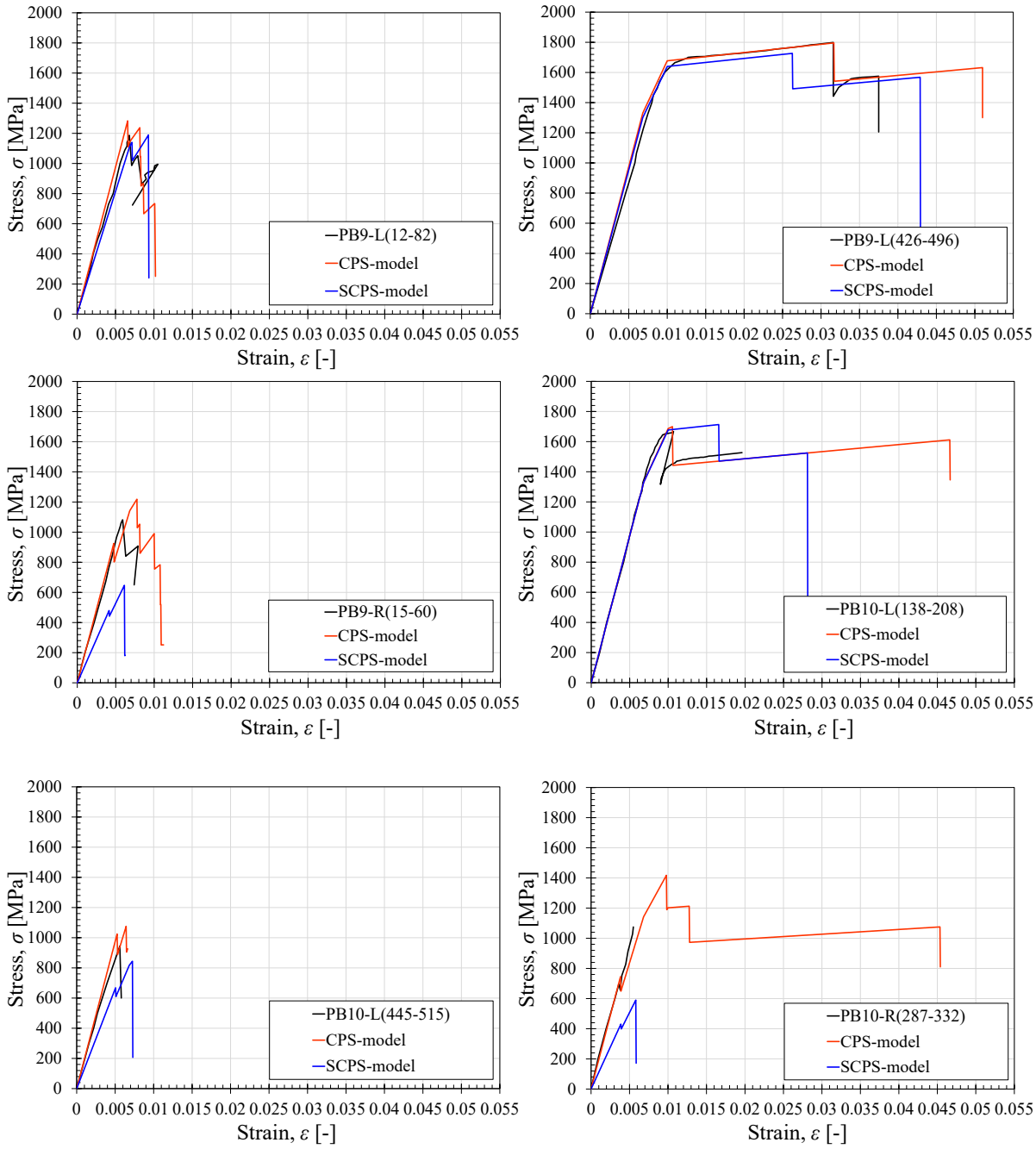

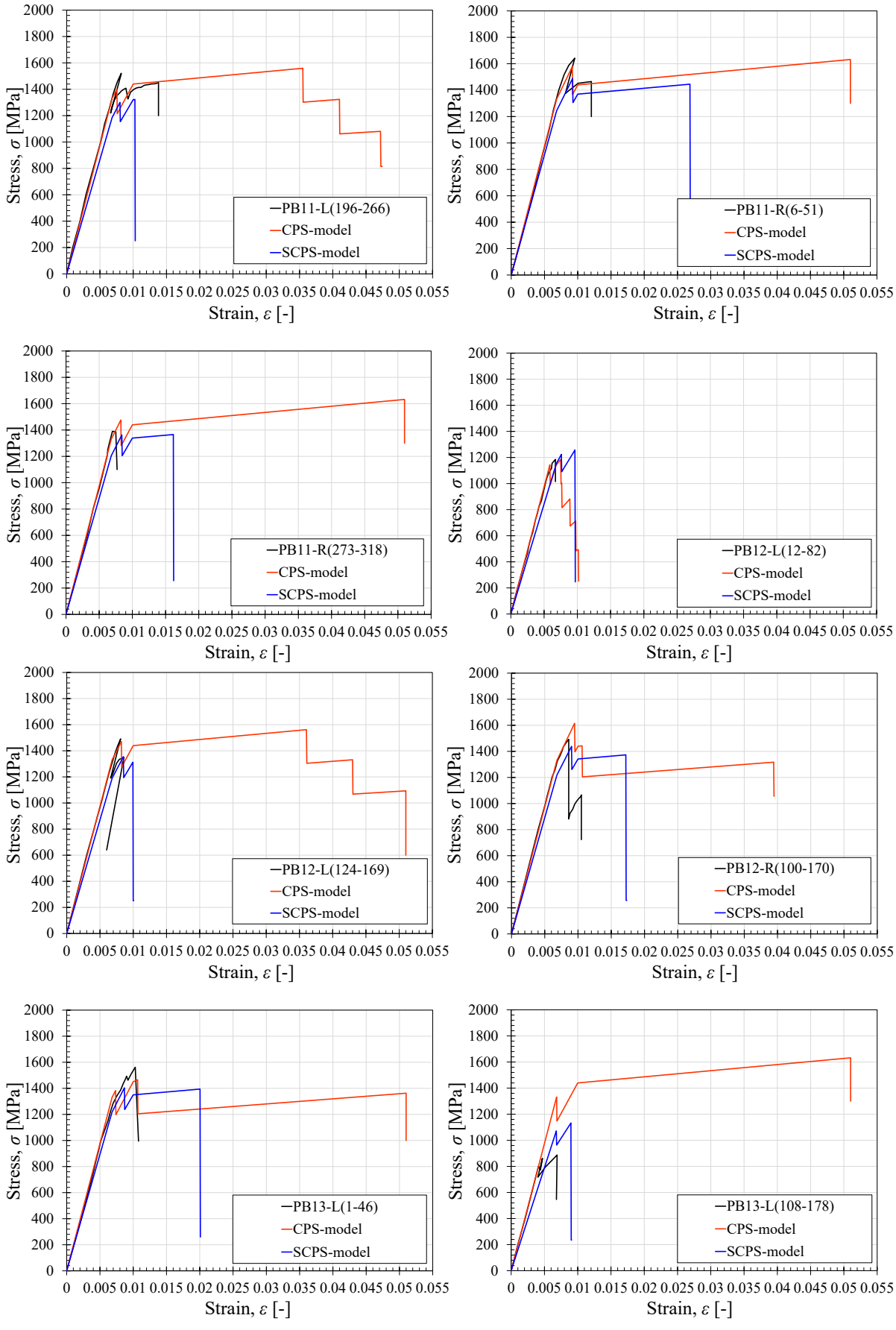
Stress, σ [MPa]
Strain, ε [-]
PB11-L(196-266)
PB11-R(6-51)
PB11-R(273-318)
PB12-L(12-82)
PB12-L(124-169)
PB12-R(100-170)
PB13-L(1-46)
PB13-L(108-178)
CPS-model
SCPS-model

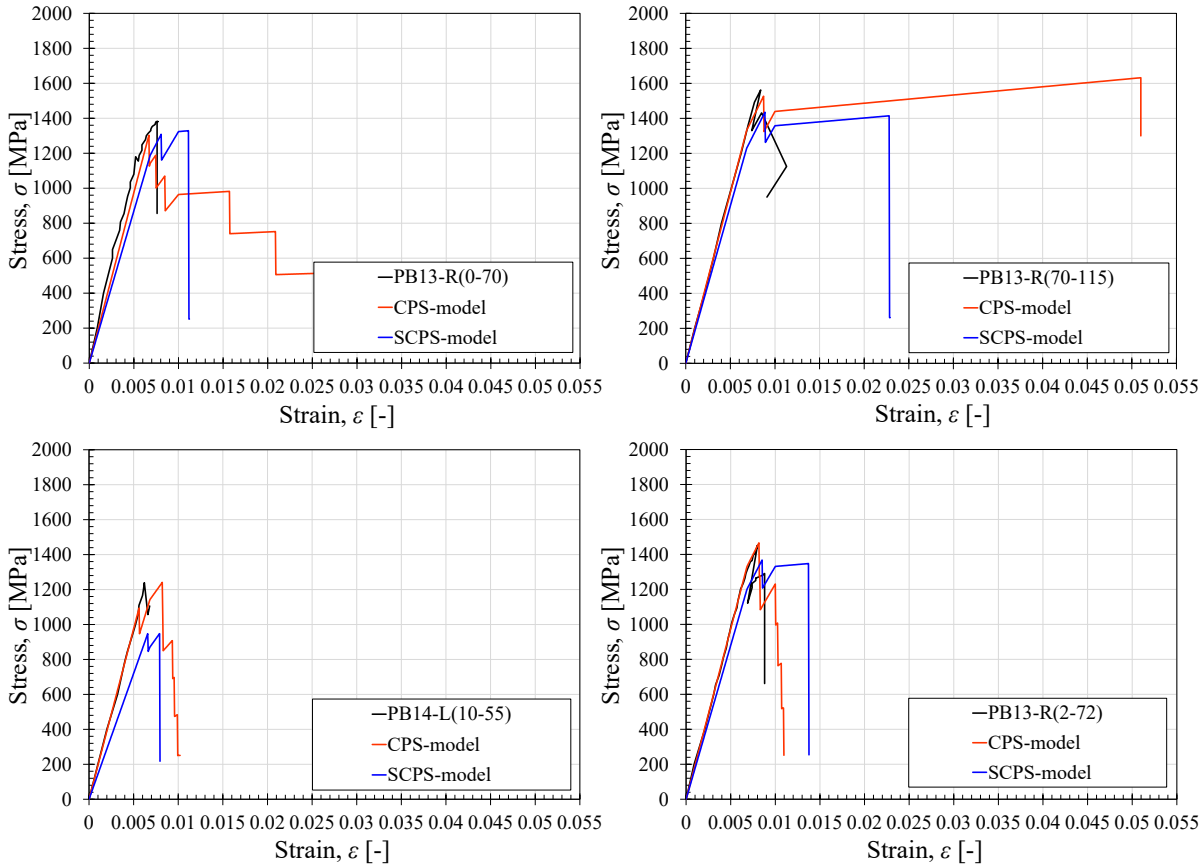

Figure 7-23 Comparison between experimental and analytical predictions – by adopting both the CPS- and SCPS-models – of the corroded strands belonging to the present research tensile tests outcomes.

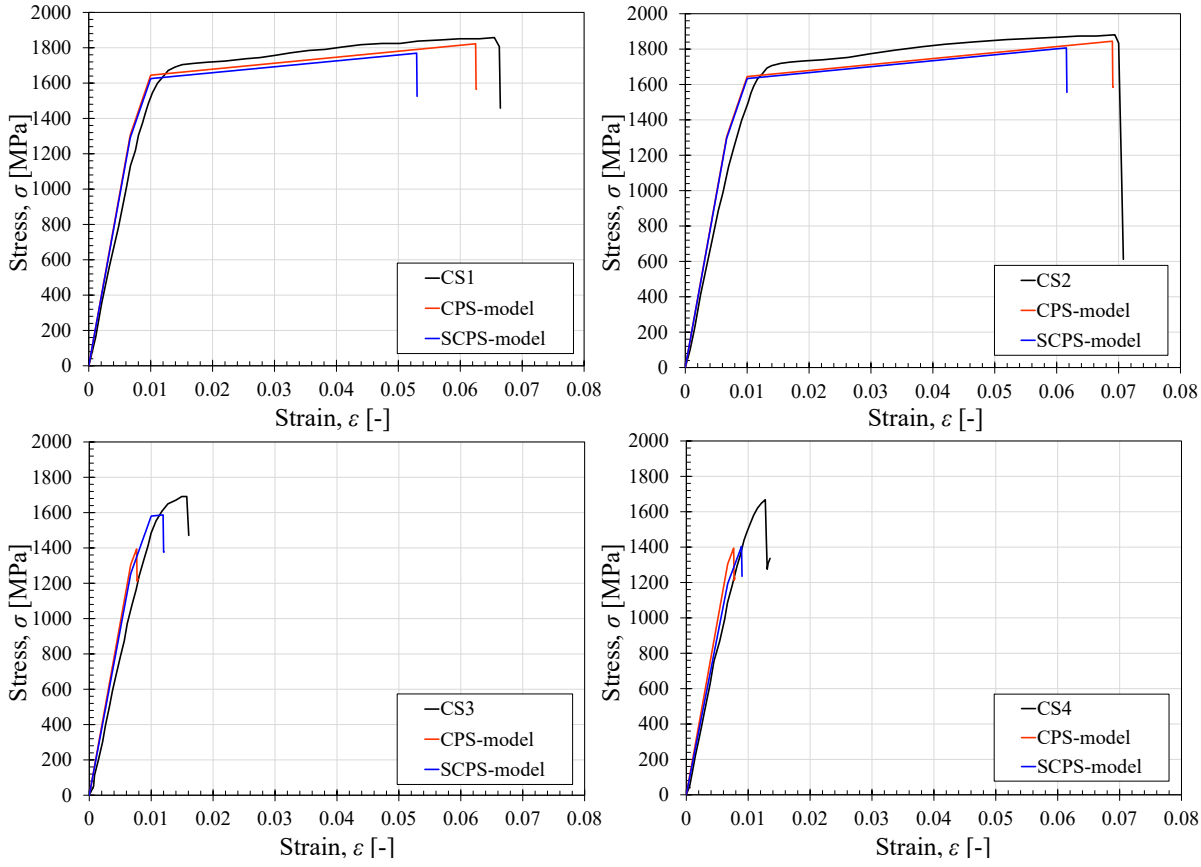

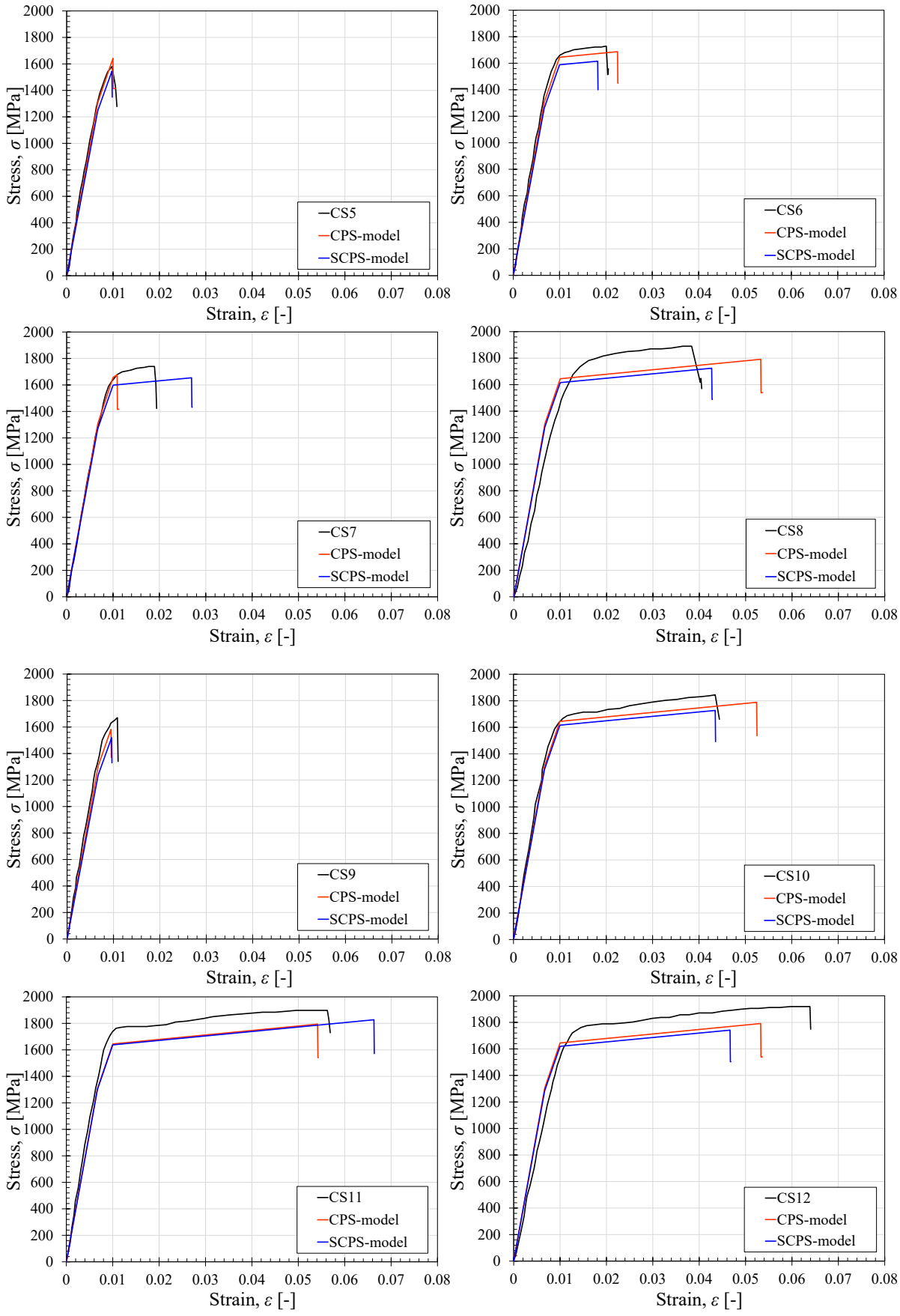

Figure 7-24 Comparison between experimental and analytical predictions – by adopting both the CPS- and SCPS-models – of the corroded strands belonging Jeon et al. (2019) experimental activity.

Despite the simplifications introduced to simulate the complex chloride-induced corrosion process of prestressing strands embedded in concrete, the obtained results revealed that the SCPS-model ensures a significant agreement between analytical predictions and experimental stress-strain relationships. To this end, Figure 7-25 compares the analytical predictions obtained by using the two proposed models in terms of normalized ultimate corroded strength, $f_{pu,corr,exp}/f_{pu,corr,an}$, and normalized ultimate corroded strain, $\varepsilon_{pu,corr,exp}/\varepsilon_{pu,corr,an}$. In detail, the ratios were calculated by dividing the experimental outcomes measured at the conventional failure mode of the corroded strand by the related analytical predictions; whereas the dashed black line represents the perfect match between experimental outcomes and analytical predictions. As a result, more conservative analytical predictions were generally obtained by adopting the SCPS-model instead of the CPS-model, especially in terms of ultimate corroded strength, $f_{pu,corr,an}$, as reported in Figure 7-25(a). Moreover, a significant scatter between analytical and experimental results was observed for highly corroded strands, such as PB9-R(15-60) and PB10-R(287-332). Nevertheless, the introduction of the new regression trend for estimating the ultimate strain decay, $\varepsilon_{pu,corr}$, resulted in more accurate predictions when compared to CPS-model outcomes, as evidenced by Figure 7-25(b). Furthermore, the sectional pitting morphology analysis of corroded strands allowed for a better interpretation of the relationships existing between the maximum penetration depth of the most corroded wire and the relative corrosion level of the remaining external wires, expressed in terms of average penetration depth.

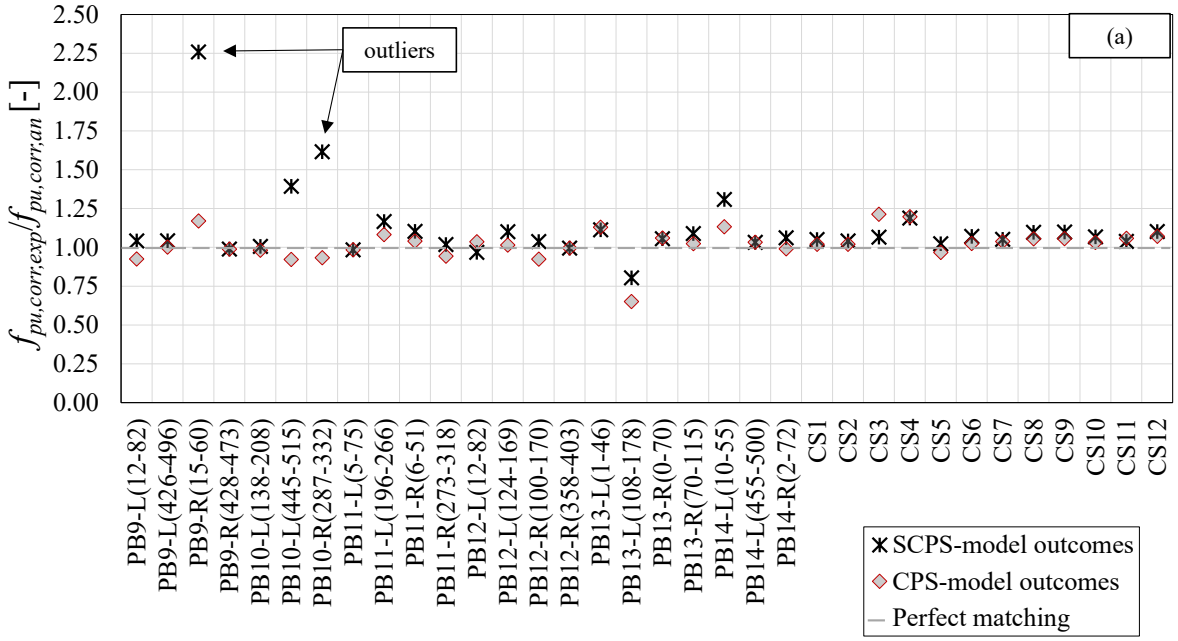

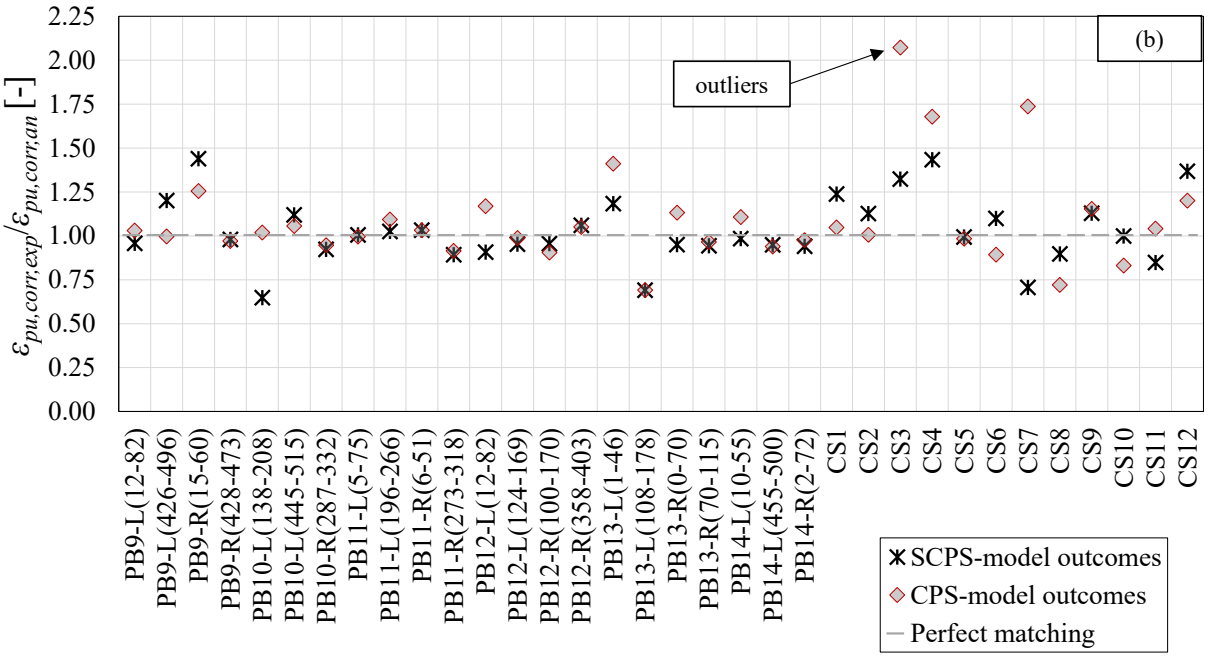

Figure 7-25 Comparison of experimental and analytical results by adopting the CPS- and SCPS-models – in terms of : (a) ultimate strength, $f_{pu,corr,exp}/f_{pu,corr,an}$, and (b) ultimate strain, $\varepsilon_{pu,corr,exp}/\varepsilon_{pu,corr,an}$.

Similar to the CPS model analysis, the performance of the SCPS-model was investigated by conducting a statistical analysis on the 34 corroded and un-corroded samples in terms of the normalized ratios of experimental outcomes and analytical predictions in the form $f_{pu,corr,exp}/f_{pu,corr,an2}$ and $\varepsilon_{pu,corr,exp}/\varepsilon_{pu,corr,an2}$, as reported in Table 7-4. As previously mentioned, the SCPS-model predictions were generally more conservative than the CPS results, as confirmed by the average value of ultimate corroded strength ratio, $f_{pu,corr,exp}/f_{pu,corr,an2}$, which was 1.09 instead of the CPS-model 1.02. On the contrary, adopting the SCPS-model resulted in a better estimation of ultimate corroded strain, as highlighted by the average value of ultimate corroded strain ratio, $\varepsilon_{pu,corr,exp}/\varepsilon_{pu,corr,an2}$, which was 1.02 instead of 1.06 for the CPS-model. Furthermore, the SCPS-model was affected by a higher and lower dispersion of predicted ultimate corroded strength and strain if compared to the CPS-model as confirmed by a standard deviation of 0.13 (0.10 for the CPS-model) and 0.17 (0.21 for the CPS-model), respectively. Finally, the effectiveness of the proposed SCPS-model was highlighted by the evaluation of the Coefficient of Correlation, CoC, and the calculation of the Coefficient of Variation, CV. The first statistical parameter (CoC) resulted equal to 0.94 and 0.97 for the normalized ratios of ultimate corroded strength, $f_{pu,corr,exp}/f_{pu,corr,an2}$, and ultimate corroded strain, $\varepsilon_{pu,corr,exp}/\varepsilon_{pu,corr,an2}$, respectively. The second parameter (CV) resulted equal to 11.79% and 16.54% for the ultimate corroded strength and the ultimate corroded strain ratios, respectively.

Table 7-4 SCPS-model predictions in terms of ultimate strength, $f_{pu,corr,an2}$, ultimate strain, $\varepsilon_{pu,corr,an2}$, normalized strength, $f_{pu,corr,exp}/f_{pu,corr,an2}$, and normalized strain, $\varepsilon_{pu,corr,exp}/\varepsilon_{pu,corr,an2}$. The reported data consider also the un-corroded samples.

Sample ID	$f_{pu,corr,an2}$ [MPa]	$\varepsilon_{pu,corr,an2}$ [-]	$f_{pu,corr,exp}/f_{pu,corr,an2}$ [-]	$\varepsilon_{pu,corr,exp}/\varepsilon_{pu,corr,an2}$ [-]
PB9-L(12-82)	1140.00	0.0071	1.04	0.96
PB9-L(426-496)	1726.60	0.0263	1.04	1.20
PB9-R(15-60)	479.18	0.0041	2.26	1.44
PB9-R(428-473)	1901.75	0.051	0.99	0.98
PB10-L(138-208)	1656.89	0.0165	1.01	0.65
PB10-L(445-515)	677.84	0.005	1.39	1.12
PB10-R(32-102)	-	-	-	-
PB10-R(287-332)	430.85	0.0039	1.62	0.92
PB11-L(5-75)	1901.75	0.051	0.98	1.01
PB11-L(196-266)	1299.90	0.008	1.17	1.03
PB11-R(6-51)	1488.90	0.0092	1.10	1.03
PB11-R(273-318)	1362.60	0.0084	1.02	0.89
PB12-L(12-82)	1224.00	0.0076	0.97	0.91
PB12-L(124-169)	1354.70	0.0085	1.10	0.95
PB12-R(100-170)	1438.20	0.009	1.04	0.96
PB12-R(358-403)	1901.75	0.051	1.00	1.06
PB13-L(1-46)	1403.50	0.0087	1.11	1.18
PB13-L(108-178)	1071.40	0.0068	0.80	0.69
PB13-R(0-70)	1308.10	0.0081	1.06	0.95
PB13-R(70-115)	1435.10	0.0089	1.09	0.94
PB14-L(10-55)	947.02	0.0063	1.31	0.98
PB14-L(455-500)	1901.75	0.051	1.03	0.95
PB14-R(2-72)	1368.00	0.0085	1.06	0.94
PB14-R(77-122)	-	-	-	-
CS1	1769.1	0.0529	1.05	1.24
CS2	1806.9	0.0616	1.04	1.13

CS3	1586.8	0.0119	1.07	1.32
CS4	1403.7	0.0089	1.19	1.43
CS5	1544.55	0.0098	1.02	0.99
CS6	1615.3	0.0182	1.07	1.10
CS7	1654.2	0.0268	1.05	0.71
CS8	1724.1	0.0427	1.10	0.90
CS9	1520.1	0.0096	1.10	1.13
CS10	1727.5	0.0435	1.07	1.00
CS11	1827.4	0.0663	1.04	0.85
CS12	1741.5	0.0467	1.10	1.37
		Mean Value:	1.09	1.02
		Standard Deviation:	0.13	0.17
		CoC [-]:	0.94	0.97
		CV [%]:	11.79	16.54

*Samples PB9-R(15-60) and PB13-L(108-178) neglected in the statistical analysis since considered as outliers.

7.5.5 Main observations

In the present section, a simplified version, named SCPS-model, of the previously defined constitutive law, named CPS-model, for the prediction of the residual stress-strain relationship of corroded prestressing strands was proposed and discussed. To this aim, a total of 34 tensile test outcomes coming from the present research and the experimental activity conducted by Jeon et al. (2019) were considered for the validation of the proposed simplified approach. According to the SCPS-model, the residual tensile response of a corroded prestressing strand is evaluated by adopting the equivalent spring model and its effectiveness lies in its dependence on a single input parameter, which is the maximum penetration depth of the most corroded wire. The model results to be therefore independent from the usual parameters of the mass loss of the corroded strand or the cross-sectional loss of each corroded wire. Since the maximum penetration depth can be measured during in-situ inspection without destructive techniques but by locally removing the concrete cover, the application of the SCPS-model in the daily engineering practice is highly encouraged. In this context, a maximum penetration depth equal to 1/6 of the external wire diameter was established as the critical

threshold value at which the mechanical response of the corroded wire turns from ductile to brittle.

Based on the obtained results and considering the adopted simplifications, the SCPS-model can predict the residual mechanical response of a corroded prestressing strand in terms of stress-strain relationship and tensile force-strain relationships with a higher margin of safety if compared to the CPS-model. The accuracy and the effectiveness of the simplified model was underlined by the statistical analysis outcomes conducted in terms of ultimate corroded strength and ultimate corroded strain ratios of experimental results and analytical predictions, which revealed a mean value and a standard deviation of 1.09 – 0.13 and 1.02 – 0.17 for the first and second analyzed ratios, respectively.

To support the use of the proposed model during engineering practice, future studies should address the identification of an operative procedure for sampling and measuring along the corroded length of the strand; the study of innovative instrumentation, such as micro portable laser scanners complemented by software for maximum pit and wire radius estimation, should also be promoted.

Furthermore, additional corroded prestressing strands should be tested and analyzed for refining and improving the proposed simplified relationships. Particular attention should be paid to high corroded strands, showing corroded inner wire, in order to define a supplementary relationship that correlates $P_{max,sectional}$ and P_{inner}.

Finally, similarly to the CPS-model, further efforts should be devoted to the quantification of the overall residual mechanical response of multiple corroded strands, characterized by different corrosion levels at the analyzed section.

7.6 Partial safety factor for the design tensile strength of corroded strands

As pointed out by Blomfors et at. (2019), the application of simplified models for the assessment of existing structures must be accomplished with a sufficient margin of safety, especially if the interested structures exhibit corrosion damage. Moreover, the assessment of existing structures often differs from the design of new ones because of the different importance of the involved variables. In this regard, Caspeele et al. (2013) proposed a Design Value Method (DVM) for adjusted partial safety factors for the evaluation of existing structures allowing to account for different variabilities of the basic variables, a different target safety level, expressed by the reliability index β_{target}, and a different reference period (1 year) compared to the values usually adopted for design (i.e. 50 years). The assumption of a 1-year reference period is determined by the variability of the corrosion process over time, which requires a more targeted structure verification over a limited life-time span. Although DVM is already considered in codes and guidelines, such as the *fib* Bulletin 80 (2016), the evaluation of partial safety factors for existing RC and PC structures does currently not take into account reduced material characteristics. To fill this gap, the present section discusses the evaluation of a new partial safety factor, $\gamma_{m,corr}$, for the prediction of the design tensile strength of corroded prestressing strands, $f_{pu,corr,des}$, while accounting for the model uncertainties associated with the adoption of the SCPS-model, according to Eq. 7-35:

$$f_{u,corr,des} = \frac{f_{u,corr,an2}}{\gamma_{m,corr}} \tag{7-35}$$

where $f_{u,corr,an2}$ is the ultimate corroded strength predicted via the SCPS-model adoption. It is worth noting that the discussion follows the approach proposed by the latest draft of the future *fib* Model Code 2020 prescriptions. In more details, uncertainties related to material properties, geometry and failure mode were also defined according to the latest draft of the future *fib* Model Code 2020 prescriptions by considering both assessment and design scenarios.

7.6.1 Description of adopted procedure

The proposed partial safety factor was calculated through the definition of Eq. 7-36:

$$\gamma_{m,corr} = \frac{\exp(-1.645V_s)}{\mu_{\mathrm{mod}}\mu_a\mu_{\vartheta R}\cdot \exp\left(-\alpha\beta_{t\arg et}\sqrt{V_{\mathrm{mod}}^2+V_a^2+V_s^2+V_{\vartheta R}^2}\right)} \tag{7-36}$$

where the meaning and the quantification of the adopted parameters are given below:

- V_s is the coefficient of variation (COV) of un-corroded strength of prestressing steel, which is assumed equal to 0.025 according to JCSS recommendations (2001).
- α is the sensitivity factor, assumed equal to 0.7 for a 1-year reference period according to the latest draft of the future Model Code 2020, (R. Caspeele, 2021).
- β_{target} is the annual target reliability index and is defined as a function of (i) the consequence class and (ii) the relative cost of safety measure. Since EN1990 (2015) generally provides over-conservative annual target reliability indexes by assuming yearly independence between failure probabilities, β_{target} for the assessment of existing concrete structures was estimated according to JCSS (2001) and ISO 2394 (2015) recommendations, (R. Caspeele, 2021). In particular, considering the assessment or the design of a structure characterized by a consequence class CC2 and a predefined relative cost of safety measures, a β_{target} equal to 3.3 or 4.2 was respectively assumed in Eq. 7-36 based on economic optimization, as clearly shown in Table 7-5.

Table 7-5. β_{target} evaluation based on economic optimization.

Cost of safety measures	***Consequence class***		
	CC1	**CC2**	**CC3**
Large (A)	3.1	**3.3**	3.7
Normal (B)	3.7	**4.2**	4.4
Small (C)	4.2	4.4	4.7

- μ_a and V_a are, respectively, the mean value and the COV related to geometrical properties. In case of existing concrete structures, the latter uncertainty should be evaluated by means of in-situ analysis. However, in the lack of available measurements, the latest draft of the future Model Code 2020 proposes μ_a and V_a values equal to 1.0 and 0.01 or 0.95 and 0.05 for the assessment or design scenarios, respectively.
- $\mu_{\theta R}$ and $V_{\theta R}$ are, respectively, the mean value and the COV of the resistance model uncertainty. For the sake of clarity, the latest draft of the future Model Code 2020 distinguishes between failure modes associated with bending (reinforcement properties are mostly dominating) or crushing of columns (concrete compressive

strength is dominating) to provide indicative values of resistance model uncertainty. Nevertheless, the suggested values are for non-deteriorating RC members, while no recommendations are provided for existing PC members subjected to chloride-induced corrosion. Considering the absence of specific provisions, $\mu_{\theta R}$ and $V_{\theta R}$ are assumed to be equal to 1.09 and 0.045, valid for members failing in bending.

- μ_{mod} and V_{mod} represent the mean value and the COV related to the analytical predictions of the residual ultimate strength of corroded strands obtained by using the SCPS-model. These latter values are strongly related to corrosion effects and their evaluation and quantification is thoroughly explored in the following paragraph (7.6.2).

It is worth noting that a PSF value, $\gamma_{m,un\text{-}corr}$, of $0.994 \approx 1$ and $1.145 \approx 1.15$ is estimated for the un-corroded scenario in the case of assessment or design conditions, respectively, by substituting the assumed uncertainty values in Eq. 7-37 and by initially neglecting the corrosion effects associated with the SCPS-model uncertainty, i.e. μ_{mod} and V_{mod} factors. Since the present *Thesis* deals with the assessment of corroded prestressing strands, only the related scenario is discussed in the following paragraphs.

Assessment Scenario

$$\gamma_{m,un-corr} = \frac{\exp(-1.645 V_s)}{\mu_a \mu_{\vartheta R} \cdot \exp\left(-\alpha \beta_{target} \sqrt{V_a^2 + V_s^2 + V_{\vartheta R}^2}\right)} = \frac{\exp(-1.645 \cdot 0.025)}{1.0 \cdot 1.09 \cdot \exp\left(-0.7 \cdot 3.3 \sqrt{0.01^2 + 0.025^2 + 0.045^2}\right)} = 0.994 \quad \text{7-37}$$

Design Scenario

$$\gamma_{m,un-corr} = \frac{\exp(-1.645 V_s)}{\mu_a \mu_{\vartheta R} \cdot \exp\left(-\alpha \beta_{target} \sqrt{V_a^2 + V_s^2 + V_{\vartheta R}^2}\right)} = \frac{\exp(-1.645 \cdot 0.025)}{0.95 \cdot 1.09 \cdot \exp\left(-0.7 \cdot 4.2 \sqrt{0.05^2 + 0.025^2 + 0.045^2}\right)} = 1.145$$

7.6.2 SCPS-model uncertainty quantification

As previously discussed, the SCPS-model is a simplified constitutive law that allows the prediction of the residual mechanical properties of corroded prestressing strands. To apply the SCPS-model, the maximum penetration depth of the most corroded wire ($P_{max,sectional}$) must be measured. Subsequently, simplified expressions derived from the pitting morphology

analysis are adopted to estimate the average penetration depth of the remaining external wires ($P_{av,transv}$) and to predict the ultimate corroded strain of a corroded strand ($\varepsilon_{pu,corr,an2}$) as a function of the previously measured maximum penetration depth. Finally, based on $P_{max,sectional}$ and $\varepsilon_{pu,corr,an2}$, the ultimate corroded strength ($f_{pu,corr,an2}$) of the entire strand is predicted.

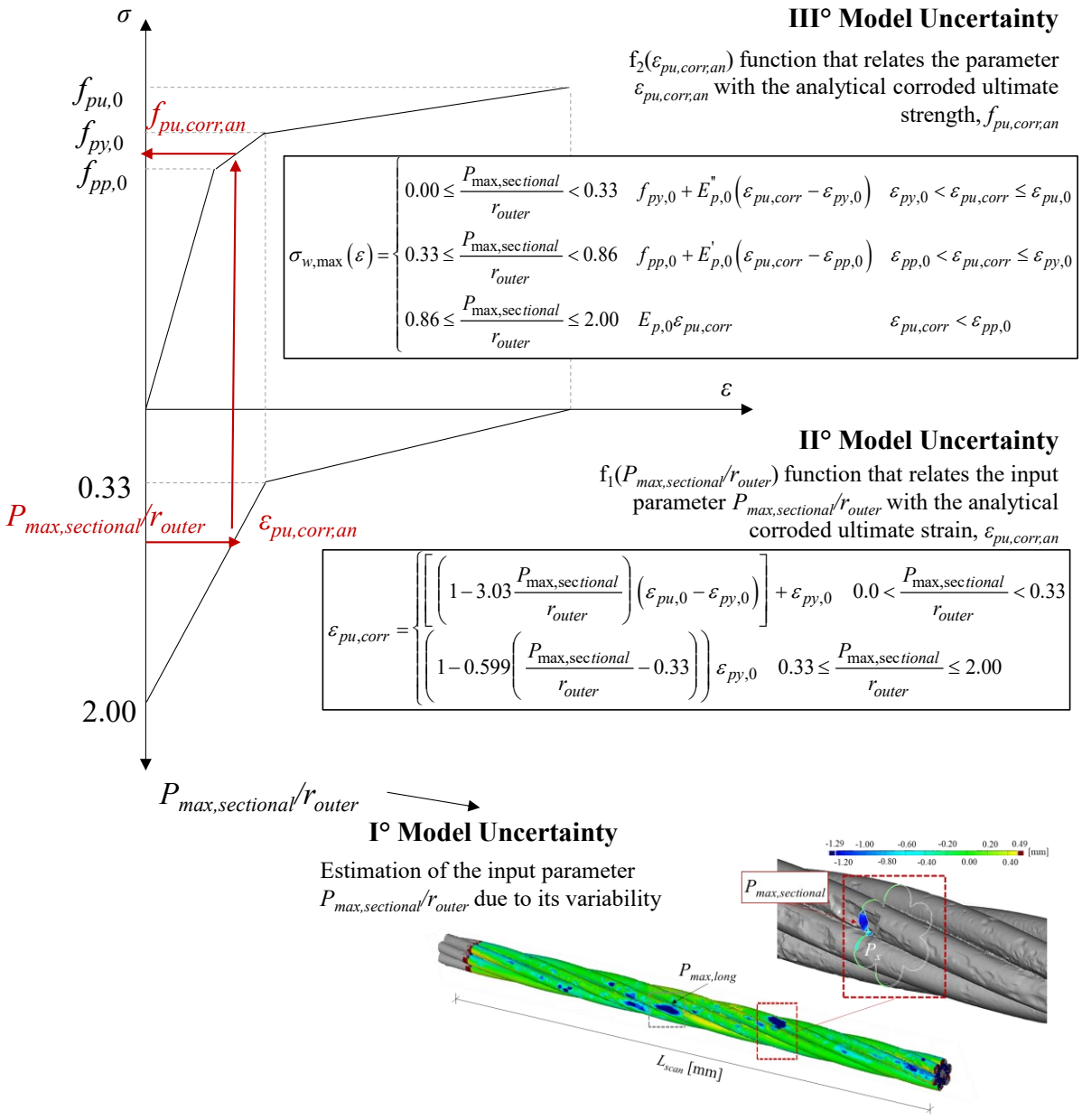

Figure 7-26 Focus on the SCPS-model uncertainties.

Although the SCPS-model was proved to be a simplified but accurate tool for the prediction of the residual mechanical properties of a corroded strand, several uncertainties inherently connected to the proposed model are present, Figure 7-26, such as:

I. The uncertainty related to the maximum penetration depth measurement;
II. The uncertainty related to the ultimate corroded strain and strength predictions through the adoption of Eq. 7-20;
III. The uncertainty related to the estimation of the average penetration depth attributed to the remaining external wires via Eq. 7-18.

7.6.2.1 Procedure for the probabilistic estimation of the maximum penetration depth

To quantify the SCPS-model uncertainty associated with the maximum penetration depth evaluation, the pitting morphology analysis of each available corroded strand was first conducted. To this end, the number of pits, n_{pits}, and the related penetration depths, P_x, were measured as previously described in Chapter 6. Second, the probabilistic analysis of the measured penetration depths of each corroded strand was performed by adopting a Lognormal distribution function, as expressed in Eq. 6-16. As a result, the mean value (λ_x) and the standard deviation (ζ_x) of each obtained distribution were determined, as reported in Table 6-4. Afterwards, for each corroded strand inspected, the fractile value, $\xi_{max,i}$, was calculated in correspondence to the maximum penetration depth, $P_{max,sectional}$, previously measured using the GOM Inspect software, according to Eq. 7-38. Indeed, It is assumed that the maximum penetration depth can be estimated in a simplified way as this fractile of the distribution of the individual penetration depth measurements.

$$\xi_{\max,i} = \Phi\left(\frac{\ln\left(P_{\max,sectional}\right) - \lambda_{x,i}}{\zeta_{x,i}}\right) \qquad 7\text{-}38$$

Since the investigated corroded prestressing strands were characterized by different scanned lengths, L_{scan}, of 250 mm and 500 mm, respectively, the proposed procedure for the maximum penetration depth evaluation was conducted by distinguishing two groups of corroded samples. For the sake of clarity, Table 7-6 reports the obtained fractile values, $\xi_{max,i}$, for each analyzed sample. Afterwards, the mean value, $\mu_{\xi max}$, the standard deviation, $\sigma_{\xi max}$, and the coefficient of variation, $V_{\xi max}$, of the fractile values, $\xi_{max,i}$, were calculated for the two groups. In detail, these latter parameters resulted equal to 0.9859, 0.0134 and 0.0136 for the group of samples with L_{scan} of 250 mm and equal to 0.9770, 0.0274 and 0.0281 for the group of samples with L_{scan} of 500 mm, respectively. Finally, by assuming a Lognormal distribution for the maximum penetration depth, a relationship was defined between the mean of the maximum penetration depth, $\mu_{Pmax,sectional,i}$, and the mean, $\lambda_{x,i}$, and standard deviation, $\zeta_{x,i}$, of the measured pits, as expressed in Eq. 7-39:

$$\mu_{P_{\max,sectional,i}} = \exp\left(\lambda_{x,i} + \zeta_{x,i}\Phi^{-1}\left(\mu_{\xi_{\max}}\right)\right) \quad 7\text{-}39$$

where Φ^{-1} is the inverse distribution function of the mean of the fractile values $\xi_{max,i}$, previously calculated for samples having different scanned lengths. In detail, the estimated $\mu_{Pmax,sectional,i}$ corresponds to the updated maximum penetration depth, $P_{max,sectional,i}$, of each strand to be considered as the input parameter for the prediction of the ultimate corroded strength, $f_{pu,corr,an2}$, of the strand. For the sake of completeness, the updated values in the form of normalized maximum penetration depths, $P_{max,sectional}/r_{outer}$, as well as the related predicted $f_{pu,corr,an2}$ obtained by using Eq. 7-27 are reported in Table 7-6 for each analyzed sample. Furthermore, the ratios between experimental and analytical ultimate corroded strengths, denoted as θ_i, were calculated and reported in Table 7-6.

Table 7-6 Main parameters of the probabilistic evaluation of the maximum penetration depth to be used as input parameter of the SCPS-model and updated $f_{pu,corr,an2}$ predictions.

Sample ID	L_{scan} [mm]	$\xi_{max,i}$ [-]	$\mu_{Pmax} = P_{max,sectional,i}$ [mm]	$P_{max,sectional}/r_{outer}$ [-] updated	$f_{pu,corr,an2}$ [MPa]	θ_i [-]
PB9-R(15-60)	250	0.9984	1.893	0.889	1037.16	1.04
PB10-R(287-332)	250	0.9988	1.655	0.777	1171.50	0.59
PB11-R(6-51)	250	0.9600	1.353	0.635	1323.98	1.24
PB11-R(273-318)	250	0.9750	1.540	0.723	1230.84	1.13
PB12-L(124-169)	250	0.9910	1.089	0.511	1439.35	1.04
PB13-L(1-46)	250	0.9948	1.202	0.564	1389.73	1.12
PB13-R(70-115)	250	0.9799	1.212	0.569	1385.50	1.13
PB14-L(10-55)	250	0.9970	1.701	0.799	1147.63	1.08
PB14-R(77-122)	250	0.9780	0.592	0.278	1656.11	-
	$\mu_{\xi max}$ =	0.9859				
	$\sigma_{\xi max}$ =	0.0134				
	$\delta_{\xi max}$ =	0.0136				
Sample ID	L_{scan} [mm]	$\xi_{max,i}$ [-]	$\mu_{Pmax} = P_{max,sectional}$ [mm]	$P_{max,sectional}/r_{outer}$ [-] updated	$f_{pu,corr,an2}$ [MPa]	θ_i [-]
PB9-L(12-82)	500	0.9933	1.380	0.648	1312.62	0.90
PB9-L(426-496)	500	0.9330	0.577	0.271	1662.47	1.08
PB10-L(138-208)	500	0.9205	0.743	0.349	1591.29	1.05
PB10-L(445-515)	500	0.9944	1.564	0.734	1218.30	0.77
PB11-L(196-266)	500	0.9954	0.912	0.428	1517.35	1.00
PB12-L(12-82)	500	0.9945	1.200	0.564	1390.55	0.85
PB12-R(100-170)	500	0.9855	0.902	0.423	1521.71	0.98
PB13-R(0-70)	500	0.9949	1.075	0.505	1445.45	0.96
PB13-L(108-178)	500	0.9760	1.862	0.874	1058.89	0.81
PB14-R(2-72)	500	0.9824	1.160	0.544	1408.35	1.03
	$\mu_{\xi max}$ =	0.9770				
	$\sigma_{\xi max}$ =	0.0274				
	$\delta_{\xi max}$ =	0.0281				

7.6.2.2 Estimation of the resistance model uncertainty

Once the updated $P_{max,sectional}/r_{outer}$ values were identified, the last step consisted in the evaluation of the resistance model uncertainty associated to the ultimate corroded strength predictions, denoted as μ_{mod} and V_{mod} in Eq. 7-36. To this end, the resistance model uncertainty for corroded strands was estimated according to the procedure provided in the Annex D of EN1990 by referring to the ratios, θ_i, evaluated in paragraph 7.6.2.1 and shown in Figure 7-27.

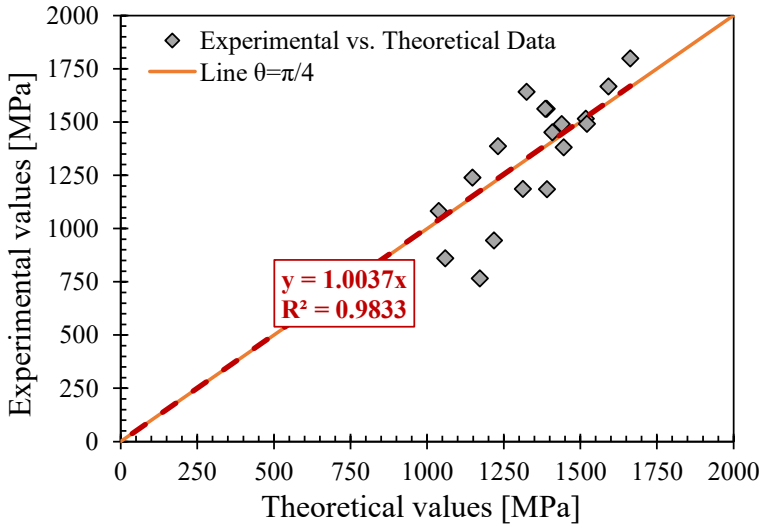

Figure 7-27 θ_i values for investigated corroded strands; orange line represents the perfect matching between experimental outcomes and analytical predictions.

In detail, a Lognormal distribution function was adopted to describe the SCPS-model uncertainty and a graphical examination of θ_i values was performed by analyzing the corresponding quantile plot, as shown in Figure 7-28. As a result, the majority of the SCPS-model predictions (11 out of 18) underestimated experimental results, as confirmed by θ_i values higher than 1.0. Moreover, referring to quantile plot outcomes, the Lognormal distribution function seemed to adequately represent the analyzed random variable.

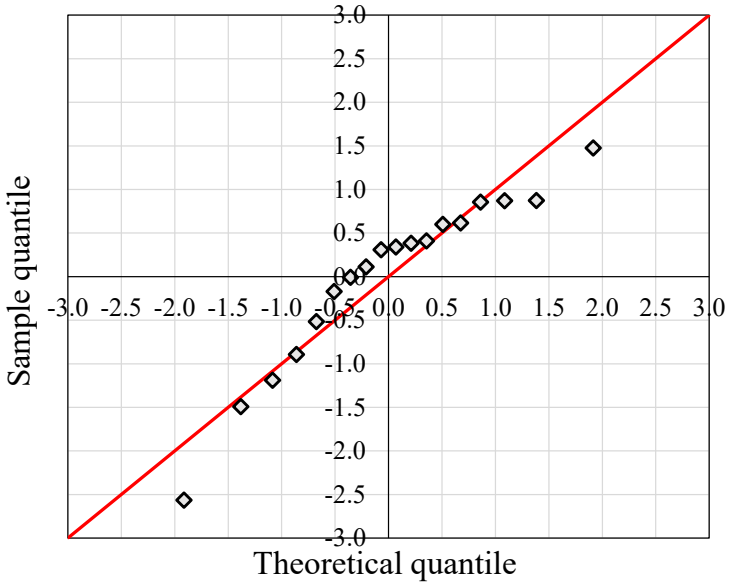

Figure 7-28 Quantile plot by considering θ_i values for investigated corroded strands – adopting a Lognormal distribution function.

As extensively discussed by Engen et al. (2017), the probability distribution of model uncertainty is generally unknown; however, it can be represented as a lognormally distributed random variable as suggested by the EN1990 (2015). This latter distribution was also selected based on the investigated variable fitting showed by the quantile plot reported in Figure 7-28.

According to Annex D of EN1990, once the $P_{max,sectional,i}$ values were evaluated, the SCPS-model uncertainty characteristics, denoted as μ_{mod} and V_{mod} in Eq. 7-36, can be calculated based on the natural logarithm of the parameter δ_i (denoted with Δ_i), which represent the error term associated with each experimental value $f_{pu,corr,exp,i}$. The δ_i values were first evaluated through Eq. 7-40:

$$\delta_i = \frac{f_{pu,corr,\exp,i}}{b \cdot f_{pu,corr,an2,i}} \qquad 7\text{-}40$$

where b – calculated in Eq. 7-41 – stands for the "Least Squares" best-fit of the slope correlating the theoretical and experimental values of the investigated variable, as shown in Figure 7-27.

$$b = \frac{\sum f_{pu,corr,\exp,i} f_{pu,corr,an2,i}}{\sum f_{pu,corr,an2,i}^2} = 1.0037 \qquad 7\text{-}41$$

Second, the mean value ($\bar{\Delta}$), the variance (s_Δ^2), the standard deviation (s_Δ), and the COV (V_δ) of the term Δ were estimated according to Eqs. 7-42 to 7-44, where n is the number of available observations. It is worth noting that $\bar{\Delta}$, s_Δ, and V_δ correspond to the mean value

(μ_{ln}), the standard deviation (σ_{ln}), and the COV (V_{ln}) of the analyzed lognormal distribution function, respectively.

$$\bar{\Delta} = \frac{1}{n}\sum_{1}^{n}\Delta_i = -0.0221 = \mu_{\ln} \qquad 7\text{-}42$$

$$s_{\Delta}^2 = \frac{1}{n-1}\sum_{i=1}^{n}\left(\Delta_i - \bar{\Delta}\right)^2 = 0.025 \qquad 7\text{-}43$$

$$s_{\Delta} = \sqrt{s_{\Delta}^2} = 0.1585 = \sigma_{\ln}$$

$$V_{\delta} = \sqrt{\exp\left(s_{\Delta}^2\right) - 1} = 0.1595 = V_{\ln} \qquad 7\text{-}44$$

Afterwards, considering the relationships between lognormal and normal distribution function parameters – Eqs. 7-45 and 7-46 – the mean value, μ_{mod}, and the standard deviation, σ_{mod}, of the SCPS-model uncertainty were calculated, resulting in the values 0.9905 and 0.1580, respectively; whereas the COV, V_{mod}, of 0.1595 (15.95%) was estimated as the ratio between σ_{mod} and μ_{mod}.

$$\mu_{\ln} = \ln \mu_{\mathrm{mod}} - \frac{1}{2}\ln\left({V_{\mathrm{mod}}}^2 + 1\right) \qquad 7\text{-}45$$

$$\sigma_{\ln} = \sqrt{\ln\left({V_{\mathrm{mod}}}^2 + 1\right)} \qquad 7\text{-}46$$

In addition, to verify the selected distribution type, the Shapiro-Wilk test of normality was performed and compared to a 5% level of significance, Shapiro & Wilk (1965). The test, conducted on $\Delta_i = \ln(\delta_i)$ values provided a Shapiro-Wilk test statistic for normality, W, and a related P-value equal to 0.9069 and 0.0715, respectively, as highlighted in Table 7-7. Based on the obtained results, the test was successful if compared to a 5% level of significance, which means that the Δ_i observations can be reasonably treated as a lognormally distributed random variable, as previously graphically confirmed by the quantile plot in Figure 7-28.

Table 7-7 SCPS-model: Shapiro-Wilk test of normality outcomes.

variable [-]	***W***	***P-value (5% of significance)***	***P-value>0.05 ?***
Δ_i	0.9069	0.0715	Yes

As a result, by introducing the estimated SCPS-model uncertainty – characterized by a mean (μ_{mod}) of 0. 0.9905 and a coefficient of variation (V_{mod}) of 0.1595 – into Eq. 7-36, the proposed partial safety factor, $\gamma_{m,corr}$, equal to 1.31 was determined for the prediction of the design tensile strength of corroded prestressing strands (assessment scenario), $f_{pu,corr,des}$, according to Eq. 7-35, as shown in Eq. 7-47.

$$\gamma_{m,corr} = \frac{\exp(-1.645 V_s)}{\mu_{\mathrm{mod}} \mu_a \mu_{\vartheta R} \cdot \exp\left(-\alpha \beta_{target} \sqrt{V_{\mathrm{mod}}^2 + V_a^2 + V_s^2 + V_{\vartheta R}^2}\right)} = \frac{\exp(-1.645 \cdot 0.025^2)}{0.9905 \cdot 1.0 \cdot 1.09 \cdot \exp\left(-0.7 \cdot 3.3 \sqrt{0.1595^2 + 0.01^2 + 0.025^2 + 0.045^2}\right)} = 1.31 \qquad 7\text{-}47$$

The proposed partial safety factor represents the first attempt available in the scientific literature to properly define a simplified procedure for the prediction of the design ultimate corroded strength of a prestressing strand. The proposed procedure considers several uncertainties related to:

- Geometrical properties;
- Un-corroded mechanical properties for prestressing steel;
- Failure mode of PC member;
- Resistance model uncertainty.

Although the proposed partial safety factor, $\gamma_{m,corr}$, should be regarded as a valuable tool for daily engineering practice to be implemented in future codes and guidelines for the assessment of existing corroded PC members, its effectiveness required further investigation. In particular, to improve the accuracy of the proposed $\gamma_{m,corr}$, additional experimental tests on corroded prestressing strands should be conducted in order to extend the statistical population to be analyzed.

8 Analytical approach for the assessment of corroded PC beams

8.1 Highlights

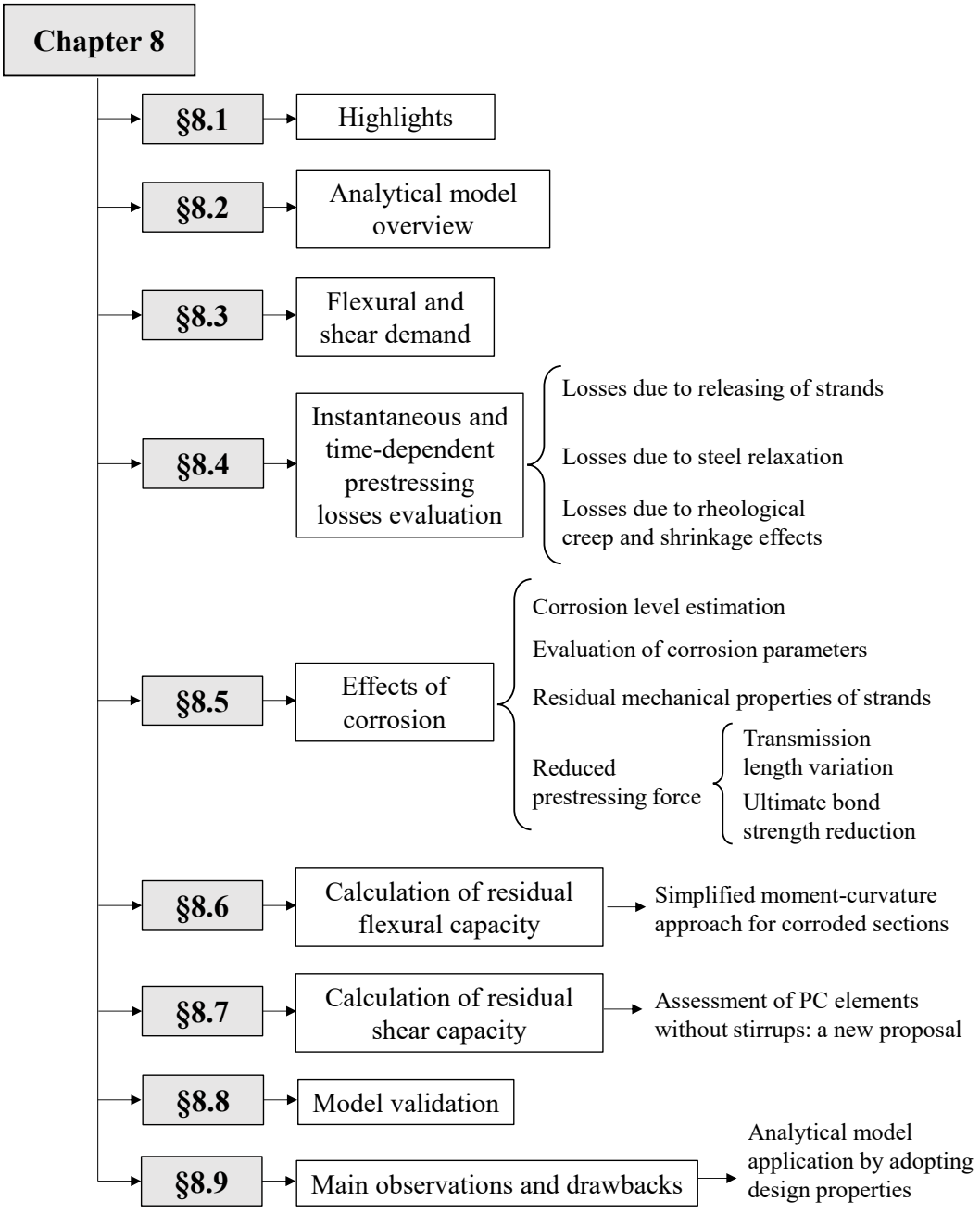

8.2 Analytical model overview

Based on the obtained results, an analytical approach for the assessment of the residual flexural and shear capacity of corroded PC beams without transversal reinforcements was proposed and implemented in a MATLAB code. As highlighted by the flowchart reported in Figure 8-1, the analytical model can be divided into five main phases:

- Evaluation of instantaneous and time-dependent prestressing losses;
- Quantification of corrosion effects;
- Calculation of the residual flexural capacity;
- Calculation of the residual shear capacity;
- Model validation consisting in the prediction of the failure mode and the ultimate load of the investigated corroded PC member.

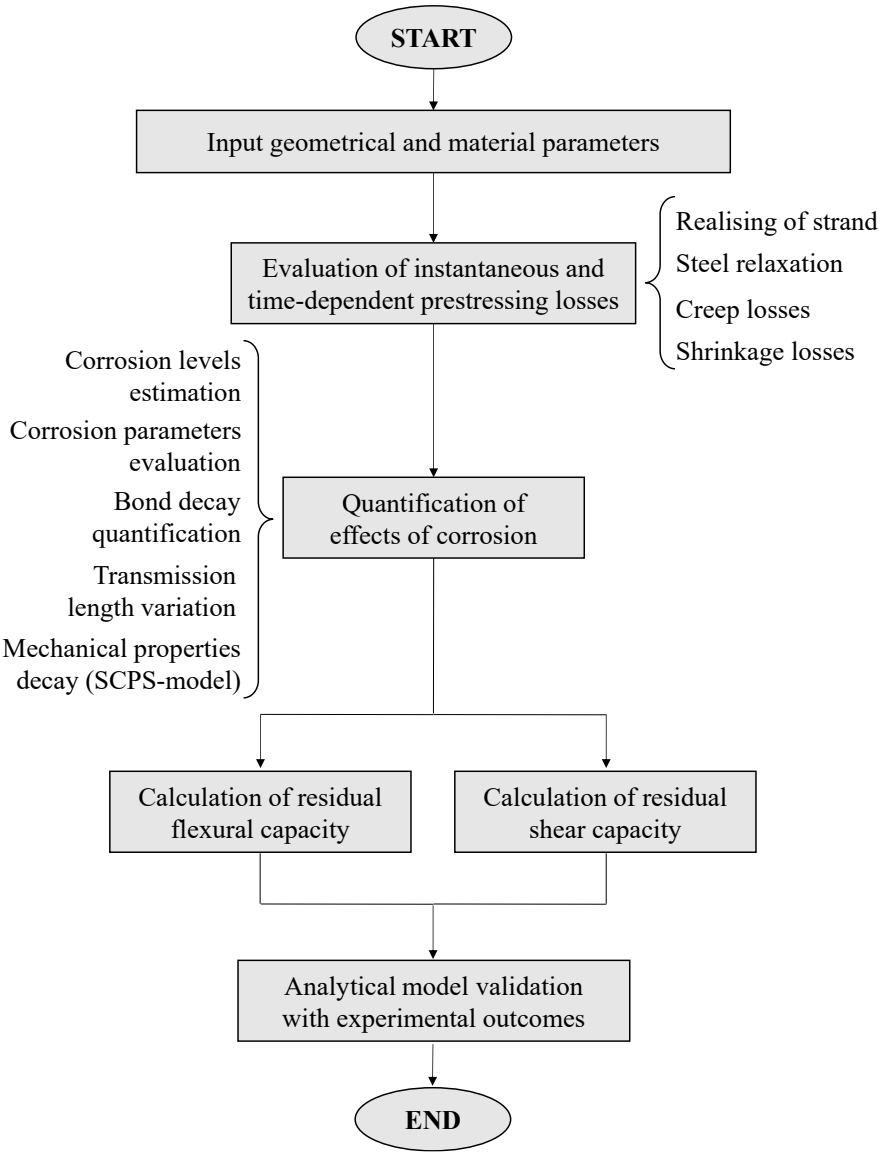

Figure 8-1 Flowchart of the main phases of the proposed analytical model.

The analytical model input parameters are:

- Geometrical and load input parameters:
  - (i) The cross-sectional width, b, and height, h, of the investigated PC element;
  - (ii) The concrete cover thickness, c, and the distance from the centroid of prestressing strand to the extreme compression fibre, $d_{p;}$
  - (iii) The span length, L, and the cantilever parts at beam edges, d_1 and d_2;
  - (iv) The un-corroded radius of inner, r_{inner}, and outer, r_{outer}, wires composing the strand;
  - (v) The un-corroded area of the prestressing strand, $A_{p,0}$;
  - (vi) The cross-section number of strands, n_{strand};
  - (vii) The prestressing strand eccentricity, e;
  - (viii) The concentrated applied load, P, and/or the distributed load, q.
- Mechanical properties of un-corroded reinforcements:
  - (ix) The initial prestressing stress, $\sigma_{p,0}$;
  - (x) The ultimate strength, $f_{pu,0}$, the ultimate strain, $\varepsilon_{pu,0}$, and the modulus of elasticity, $E_{p,0}$, of the prestressing reinforcement;
  - (xi) The average compressive strength of concrete, f_{cm}, and the concrete modulus of elasticity, E_c.
- Corrosion damage parameter:
  - (xii) The maximum penetration depth of the most corroded wire, P_{max};

The effects of corrosion are evaluated through a single input parameter, which is the maximum penetration depth of the most corroded wire, P_{max}. This parameter was established through probabilistic analyses on experimental measurements conducted on available corroded strands by distinguishing between four different scenarios: (a) un-corroded, (b) low, (c) intermediate, and (d) high corrosion. Once the corrosion pattern of the analyzed PC beam is established via visual inspection, the corrosion parameters in terms of (i) average penetration depth of the remaining external wires, P_{av}, (ii) mass loss, η, and (iii) cross-sectional loss, μ, are quantified. Afterwards, the SCPS-model is adopted to determine the residual mechanical properties of corroded strands. Furthermore, analytical models for the evaluation of the transmission length variation, $L_{t,corr}$, and the ultimate bond strength decay induced by corrosion over time are introduced. Finally, the residual flexural and shear capacity of the investigated PC element are determined by using equilibrium and compatibility conditions. Specifically, the Model Code 2010 Level II of approximation expression is adopted for the shear capacity assessment of structural PC members without transversal reinforcement, opportunely modified

to account for corrosion effects. The analytical load at failure, $P_{failure,an}$, and the observed failure mode are adopted as the governing output data for the model validation. To this end, the accuracy and the efficiency of the proposed analytical model is verified by analyzing the ratio, $P_{failure}/P_{failure,an}$, between the experimental and the analytical capacities. Finally, the ultimate load at failure of each analyzed PC beam is investigated through the analytical approach by adopting un-corroded and corroded (mean and design) mechanical properties of prestressing strands to quantify the corrosion effects on the load-bearing capacity decay.

As pointed out by Yu et al. (2022) and ASCE-ACI 426 (1973), a corroded RC or PC beam can fail in bending or shear by showing different failure modes:

- Bending Failure Modes:
    1. Due to compression concrete crushing;
    2. Due to longitudinal rebars rupture;
    3. Due to prestressing reinforcements rupture.
- Combined or Shear Failure Modes:
    4. Combined shear-flexural failure;
    5. Due to transversal reinforcements rupture;
    6. Due to compression failure;
    7. Due to anchorage failure;
    8. Due to compression strut failure;
    9. Due to diagonal tension failure;
    10. Due to shear compression failure.

Considering the absence of transversal reinforcements as well as longitudinal ordinary rebars, the corresponding failure modes are not considered for the validation of the available corroded PC beams. Furthermore, although the bond decay due to severe corrosion can significantly affect the residual capacity of pre-tensioned corroded PC beams, the failure mode associated to anchorage failure is not currently implemented in the proposed analytical approach, where the evaluation of residual flexural and shear capacities are the main focus. Therefore, the anchorage failure evaluation requires further research efforts. Nevertheless, anchorage failure effects on deteriorated PC structures and formulations for the anchorage resistance estimation in the case of corrosion can be found in Franceschini et al. (2021).

The basic assumptions for the flexural and shear capacity of corroded PC beams are that: (i) the sectional resisting contribution is attributed to prestressing reinforcements, and the contribution provided by ordinary rebars in compression is neglected; (ii) Euler-Bernoulli beams with plane sections is assumed.

8.3 Flexural and shear demand

To compare experimental outcomes and analytical predictions, two different loading set-up are considered: (i) the three-point bending configuration and (ii) the four-point bending configuration, as shown in Figure 8-2 and Figure 8-3. The tested PC beams are isostatic structurers simply supported at beam edges and therefore statically determined. The three-point bending loading configuration consists in the application of a concentrated load, P, at mid-span at a distance equal to $L/2$ from the support, whereas the four-point bending configuration involves the application of two concentrated load, P, at a distance equal to $L/3$. The analytical model allows to consider a distributed load, q, applied along the overall PC beam length, as highlighted in Figure 8-2. Nevertheless, it is worth noting that the self-weight contribution is neglected in the following comparisons to properly reproduce the experimental campaign conditions; thus, the load contribution q is assumed to be null.

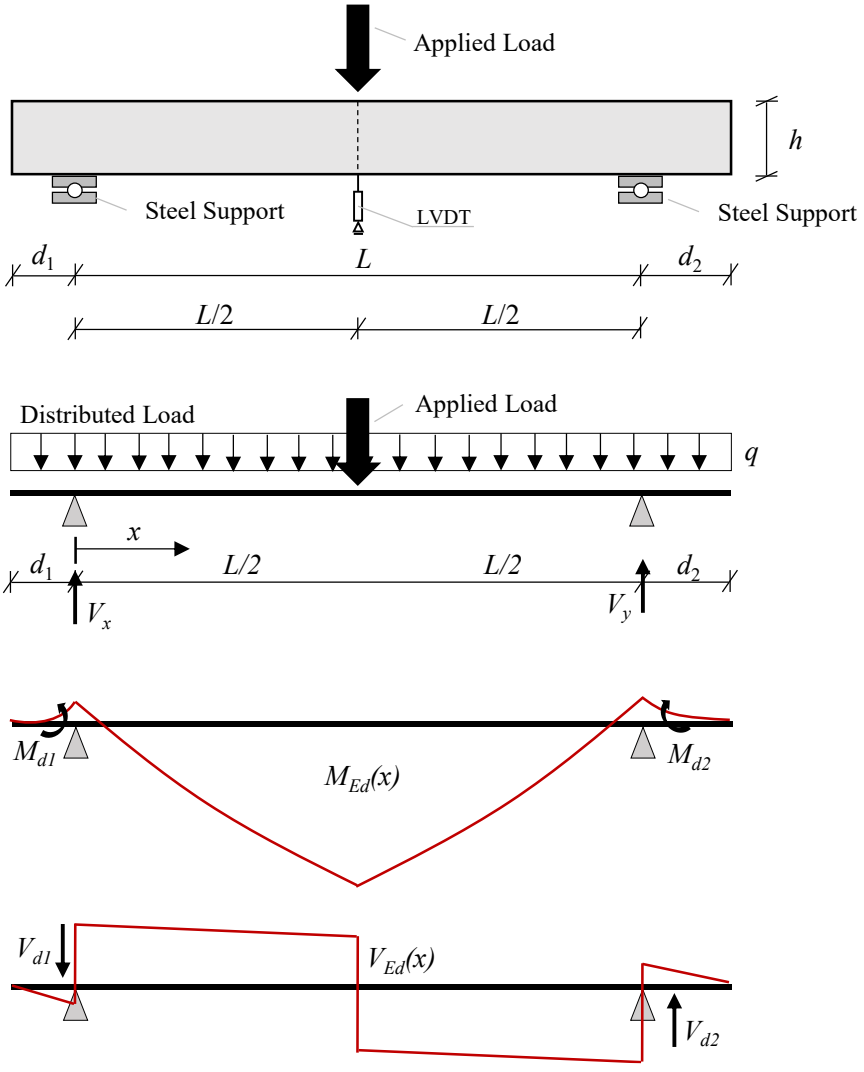

Figure 8-2 Flexural and shear demand evaluation for three-point bending loading configuration.

Specifically, the flexural and shear demand of corroded and un-corroded PC beams tested by adopting a three-point bending configuration can be defined through Eq. 8-1 and Eq. 8-2, respectively, as graphically shown in Figure 8-2:

$$V_{Ed}(x)=\begin{cases} V_x - V_{d_1} - qx & 0 \le x < \dfrac{L}{2} \\ V_x - V_{d_1} - qx - P & \dfrac{L}{2} \le x \le L \end{cases} \quad 8\text{-}1$$

$$M_{Ed}(x)=\begin{cases} V_x x - V_{d_1} x - M_{d_1} - \dfrac{qx^2}{2} & 0 \le x < \dfrac{L}{2} \\ V_x x - V_{d_1} x - M_{d_1} - \dfrac{qx^2}{2} - P\left(x - \dfrac{L}{2}\right) & \dfrac{L}{2} \le x \le L \end{cases} \quad 8\text{-}2$$

where, V_{d1} and V_{d2} are the shear contributions of left and right beam cantilevers – calculated according to Eq. 8-3 and Eq. 8-4 –, whereas M_{d1} and M_{d2} are the related bending moments – evaluated through to Eq. 8-5 and Eq. 8-6. Moreover, V_x is the shear reaction evaluated at left support, which is determined from equilibrium conditions through Eq. 8-7.

$$V_{d_1} = -qd_1 \quad 8\text{-}3$$

$$V_{d_2} = qd_2 \quad 8\text{-}4$$

$$M_{d_1} = -\frac{qd_1^2}{2} \quad 8\text{-}5$$

$$M_{d_2} = -\frac{qd_2^2}{2} \quad 8\text{-}6$$

$$V_x = \frac{M_{d_1}}{L} - \frac{M_{d2}}{L} + \frac{P}{2} + \frac{qL}{2} + V_{d_1} \quad 8\text{-}7$$

The flexural and shear demand of a four-point bending configuration is evaluated through Eq. 8-8 and Eq. 8-9, as graphically shown in Figure 8-3.

$$V_{Ed}(x)=\begin{cases} V_x - V_{d_1} - qx & 0 \le x < \dfrac{L}{3} \\ V_x - V_{d_1} - qx - \dfrac{P}{2} & \dfrac{L}{3} \le x < \dfrac{2}{3}L \\ V_x - V_{d_1} - qx - P & \dfrac{2}{3}L \le x \le L \end{cases} \quad 8\text{-}8$$

$$M_{Ed}(x)=\begin{cases} V_x x - V_{d_1} x - q\dfrac{x^2}{2} - M_{d_1} & 0 \le x < \dfrac{L}{3} \\ V_x x - V_{d_1} x - q\dfrac{x^2}{2} - M_{d_1} - \dfrac{P}{2}\left(x - \dfrac{L}{3}\right) & \dfrac{L}{3} \le x < \dfrac{2}{3}L \\ V_x x - V_{d_1} x - q\dfrac{x^2}{2} - \dfrac{P}{2}\left(x - \dfrac{L}{3}\right) - \dfrac{P}{2}\left(x - \dfrac{2L}{3}\right) - M_{d_1} & \dfrac{2}{3}L \le x \le L \end{cases} \quad 8\text{-}9$$

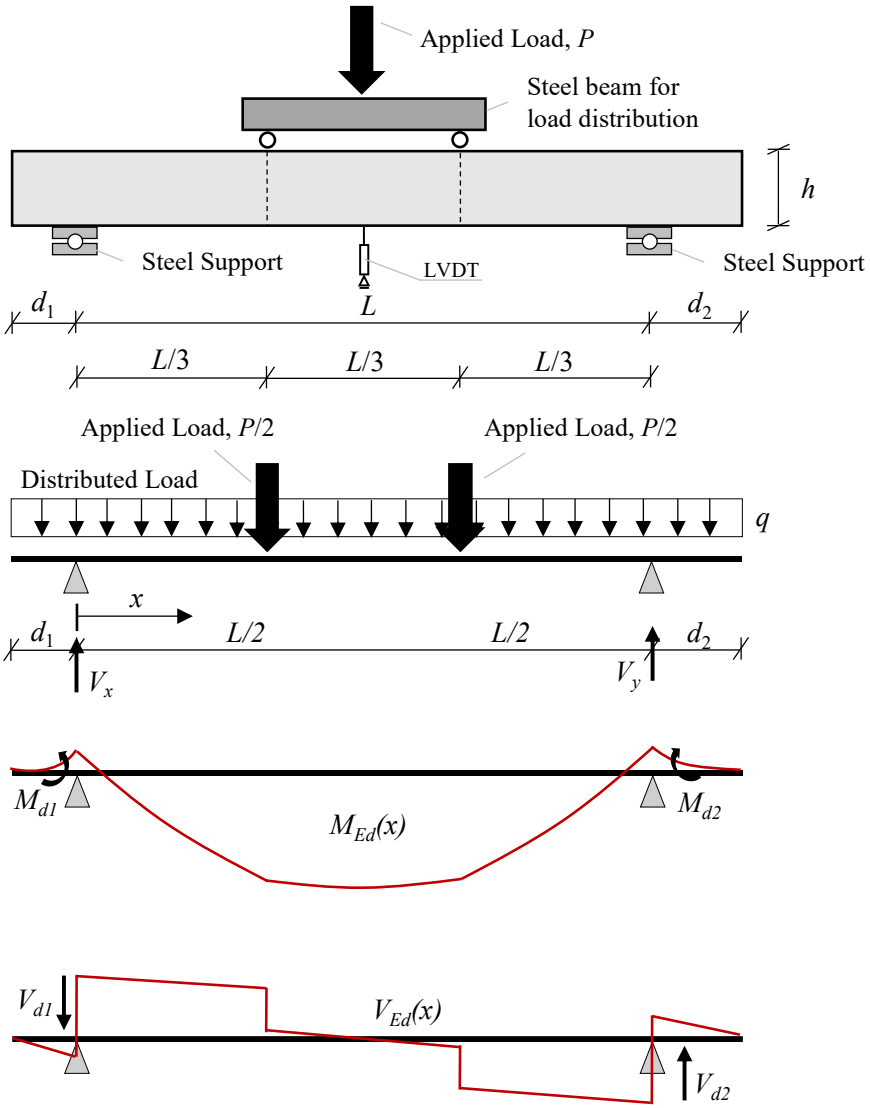

Figure 8-3 Flexural and shear demand evaluation for four-point bending loading configuration.

8.4 Instantaneous and time-dependent prestressing losses evaluation

The existing PC structures generally suffer by a reduction in the initial prestressing stress, $\sigma_p(t)$, over time even though they are unaffected by corrosion. Indeed, the prestressing losses are: (i) instantaneous due to the concrete elastic contraction caused by the releasing of strand, $\Delta\sigma_{p,el}$, and (ii) time-dependent due to the steel relaxation phenomenon, $\Delta\sigma_{p,rel}(t)$, and the rheological effects of creep, $\Delta\sigma_{p,cr}(t)$, and shrinkage, $\Delta\sigma_{p,shr}(t)$. Therefore, the residual prestressing stress, $\sigma_p(t)$, at a time, t, can be calculated according to Eq. 8-10.

$$\sigma_p(t) = \sigma_{p,0} - \Delta\sigma_{p,el} - \Delta\sigma_{p,rel}(t) - \Delta\sigma_{p,cr}(t) - \Delta\sigma_{p,shr}(t) \qquad 8\text{-}10$$

8.4.1 Losses due to releasing of strands

The instantaneous loss due to strands releasing, $\Delta\sigma_{p,el}$, induced by the concrete elastic contraction, is evaluated based on the steel-concrete strain compatibility, as depicted in Figure 8-4. Neglecting the prestressing strands eccentricity, the concrete strain, ε_c, can be first evaluated through Eq. 8-11, and the related stress, σ_c, can be derived by multiplying ε_c by the concrete modulus of elasticity, E_c, as reported in Eq. 8-12.

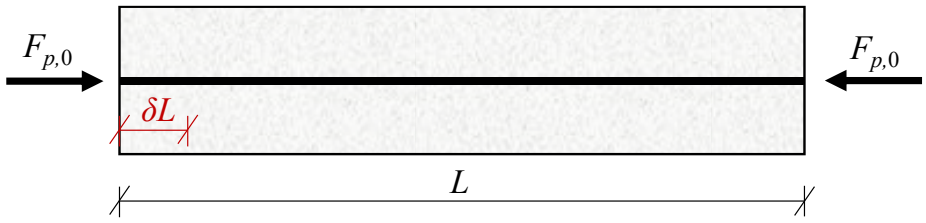

Figure 8-4 Focus on the prestressing losses due to releasing of strands.

$$\varepsilon_c = \frac{\delta L}{L} = \frac{\dfrac{F_{p,0}L}{\left(E_c A_c + E_{p,0}A_{p,0}n_{strand}\right)}}{L} = \frac{F_{p,0}}{\left(E_c A_c + E_{p,0}A_{p,0,tot}\right)} = \frac{F_{p,0}}{\left(E_c\left(A_c + \dfrac{E_{p,0}}{E_{c,i}}A_{p,0,tot}\right)\right)} = \frac{F_{p,0}}{\left(E_c A_i\right)} \qquad 8\text{-}11$$

$$\sigma_c = E_c\varepsilon_c = \frac{F_{p,0}}{A_i} \qquad 8\text{-}12$$

The corresponding prestressing reinforcement stress, $\sigma_{p,s}$, is then estimated through Eq. 8-13.

$$\sigma_{p,s} = \sigma_{p,0} - \frac{E_{p,0}}{E_c}\sigma_c = \sigma_{p,0} - \alpha_e\sigma_c \qquad 8\text{-}13$$

Afterwards, by substituting Eq. 8-12 into Eq. 8-13, the instantaneous loss due to strand releasing, $\Delta\sigma_{p,el}$, is obtained through Eq. 8-14:

$$\left|\Delta\sigma_{p,el}\right| = \alpha_e\sigma_c = \alpha_e\frac{F_{p,0}}{A_i} = \alpha_e\frac{F_{p,0}}{A_c + n_p A_{p,0,tot}} = \frac{F_{p,0}}{\frac{A_c}{\alpha_e} + A_{p,0,tot}} \qquad 8\text{-}14$$

where, α_e is the ratio between $E_{p,0}$ and E_c, which in turn is defined in Eq. 8-15.

$$E_c = E_{c0}\alpha_E\left(\frac{f_{cm}}{10}\right)^{1/3} = 21.5\cdot 10^3\alpha_E\left(\frac{f_{cm}}{10}\right)^{1/3} \qquad 8\text{-}15$$

Considering eccentric strands, the relationships of concrete and prestressing strand stresses should be modified for accounting of eccentric pressure, as reported in Eq. 8-16 and Eq. 8-17, respectively. Hence, the final instantaneous loss due to eccentric strands releasing, $\Delta\sigma_{p,el}$, is calculated through Eq. 8-18.

$$\sigma_c = \frac{F_{p,0}}{A_i} \pm \frac{F_{p,0}\cdot e}{I_i} y \qquad 8\text{-}16$$

$$\sigma_{p,s} = \sigma_{p,0} - \alpha_e\sigma_c = \frac{F_{p,0}}{A_{p,0,tot}} - \alpha_e\left[\frac{F_{p,0}}{A_i} \pm \frac{F_{p,0}\cdot e^2}{I_i}\right] \qquad 8\text{-}17$$

$$\left|\Delta\sigma_{p,el}\right| = \alpha_e\sigma_c = \alpha_e\left[\frac{F_{p,0}}{A_i} \pm \frac{F_{p,0}\cdot e^2}{I_i}\right] = \alpha_e\frac{F_{p,0}}{A_i}\left(1 + \frac{A_i\cdot e^2}{I_i}\right) = \alpha_e\frac{F_{p,0}}{A_i}k = \frac{F_{p,0}}{\frac{A_c}{k\alpha_e} + \frac{A_p}{k}} \qquad 8\text{-}18$$

8.4.2 Losses due to steel relaxation and rheological creep and shrinkage effects

The time-dependent prestressing loss due to steel relaxation, $\Delta\sigma_{p,rel}(t)$, is estimated according to the Eurocode 2 provision (CEN, 2004), as expressed in Eq. 8-19, under the hypothesis of infinite relaxation time:

$$\frac{\Delta\sigma_{p,rel}(t)}{\sigma_{p,0}} = 0.66\rho_{1000}e^{9.1\mu_p}\left(\frac{t}{1000}\right)^{0.75(1-\mu_p)}10^{-5} \qquad 8\text{-}19$$

where, ρ_{1000} is assumed equal to 2.5% for pre-tensioned prestressing strands, t is the time from the strands releasing, which is assumed equal to the PC beam service life (10 years = 3650 days), and μ_p is defined as the ratio between the initial prestressing stress, $\sigma_{p,0}$, and the un-corroded prestressing reinforcement ultimate strength, $f_{pu,0}$.

The rheological effects related to creep and shrinkage are estimated by adopting the Model Code 2010 recommendations (Ceb-Fip, 2013), as reported in Eq. 8-20 and Eq. 8-21, respectively.

$$\Delta\sigma_{p,cr}(t)=\left|\varepsilon_{cc}(t,t_0)E_{p,0}\right| \quad 8\text{-}20$$

$$\Delta\sigma_{p,shr}(t)=\left|\varepsilon_{cs}(t,t_s)E_{p,0}\right| \quad 8\text{-}21$$

Analyzing creep effect, the creep strain, $\varepsilon_{cc}(t,t_0)$, is calculated through Eq. 8-22:

$$\varepsilon_{cc}(t,t_0)=\frac{\sigma_c(t,t_0)}{E_c}\varphi(t,t_0) \quad 8\text{-}22$$

where, $\sigma_c(t,t_0)$, E_c and $\varphi(t,t_0)$, which stand for the concrete compressive stress, the concrete modulus of elasticity at the age of 28 days and the creep coefficient, respectively, are evaluated according to Eq. 8-16, Eq. 8-15 and Eq. 8-23.

$$\varphi(t,t_0)=\varphi_{bc}(t,t_0)+\varphi_{dc}(t,t_0) \quad 8\text{-}23$$

The creep coefficient, $\varphi(t,t_0)$, is then evaluated by summing the contributions provided by the basic creep coefficient, $\varphi_{bc}(t,t_0)$, and the drying creep coefficient, $\varphi_{dc}(t,t_0)$, which are calculated according to Eq. 8-24 and Eq. 8-25, respectively:

$$\varphi_{bc}(t,t_0)=\beta_{bc}(f_{cm})\beta_{bc}(t,t_0)=\left(\frac{1.8}{f_{cm}^{0.7}}\right)\left(\ln\left(\left(\frac{30}{t_{0,adj}}+0.035\right)^2(t-t_0)+1\right)\right) \quad 8\text{-}24$$

$$\varphi_{dc}(t,t_0)=\beta_{dc}(f_{cm})\beta(RH)\beta_{dc}(t_0)\beta_{dc}(t,t_0) \quad 8\text{-}25$$

where, $t_{0,adj}$ is the adjusted age at loading in days calculated through Eq. 8-26 by assuming: (a) the coefficient α_c, which is a coefficient representing the type of cement, equal to 1.0, and (b) by evaluating the age of concrete at loading in days, $t_{0,T}$, through Eq. 8-27. In detail, the number of days where the temperature T prevails, Δt_i, and the mean temperature during the period Δt_i, are assumed equal to 14 days and 22 °C, respectively, for the determination of $t_{0,T}$.

$$t_{0,adj}=t_{0,T}\left[\frac{9}{2+t_{0,T}^{1.2}}+1\right]^{\alpha_c} \quad 8\text{-}26$$

$$t_{0,T}=\Delta t_i\exp\left[13.65-\frac{4000}{273+T(\Delta t_i)}\right] \quad 8\text{-}27$$

Conversely, the contributions $\beta_{dc}(f_{cm})$, $\beta(RH)$, $\beta_{dc}(t_0)$ and $\beta_{dc}(t,t_0)$ for the estimation of the drying creep coefficient are calculated according to Eq. 8-28, Eq. 8-29, Eq. 8-30 and Eq. 8-31, respectively, by assuming a relative humidity of the ambient environment equal to 65% and a perimeter, u, of the member in contact with the atmosphere of 900 mm.

$$\beta_{dc}\left(f_{cm}\right)=\frac{412}{\left(f_{cm}\right)^{1.4}} \tag{8-28}$$

$$\beta\left(RH\right)=\frac{1-\frac{RH}{100}}{\sqrt[3]{0.1\frac{h}{100}}}=\frac{1-\frac{RH}{100}}{\sqrt[3]{0.1\frac{\frac{2A_c}{u}}{100}}}=\frac{1-\frac{65}{100}}{\sqrt[3]{0.1\frac{\frac{2\left(bh\right)}{900}}{100}}} \tag{8-29}$$

$$\beta_{dc}\left(t_0\right)=\frac{1}{0.1+t_{0,adj}^{0.2}} \tag{8-30}$$

$$\beta_{dc}\left(t,t_0\right)=\left[\frac{\left(t-t_0\right)}{\beta_h+\left(t-t_0\right)}\right]^{\gamma\left(t_0\right)}=\left[\frac{\left(t-t_0\right)}{\left(1.5\frac{2\left(bh\right)}{u}+250\alpha_{cm}\right)+\left(t-t_0\right)}\right]^{\gamma\left(t_0\right)}=$$

$$=\left[\frac{\left(t-t_0\right)}{\left(1.5\frac{2\left(bh\right)}{u}+250\left(\frac{35}{f_{cm}}\right)^{0.5}\right)+\left(t-t_0\right)}\right]^{\frac{1}{2.3+\frac{3.5}{\sqrt{t_{0,adj}}}}} \tag{8-31}$$

Considering shrinkage effect, the total shrinkage strain, $\varepsilon_{cs}(t,t_s)$, is calculated through Eq. 8-32 by summing the contributions provided by the basic shrinkage, $\varepsilon_{cbs}(t)$, and the drying shrinkage, $\varepsilon_{cds}(t,t_s)$. Specifically, the variable t and t_s stand for the concrete age in days and the concrete age at the beginning of drying days, which is set equal to 7 days.

$$\varepsilon_{cs}\left(t,t_s\right)=\varepsilon_{cbs}\left(t\right)+\varepsilon_{cds}\left(t,t_s\right) \tag{8-32}$$

The basic shrinkage, $\varepsilon_{cbs}(t)$, is evaluated through Eq. 8-33 multiplying the basic notional shrinkage coefficient, $\varepsilon_{cbs0}(f_{cm})$, – calculated according to Eq. 8-34 by fixing the coefficient α_{bs} equal to 600 – and the time function, $\beta_{bs}(t)$ – estimated via Eq. 8-35.

$$\varepsilon_{cbs}\left(t\right)=\varepsilon_{cbs0}\left(f_{cm}\right)\beta_{bs}\left(t\right) \tag{8-33}$$

$$\varepsilon_{cbs0}\left(f_{cm}\right)=-\alpha_{bs}\left(\frac{0.1f_{cm}}{6+0.1f_{cm}}\right)^{2.5}10^{-6} \tag{8-34}$$

$$\beta_{bs}\left(t\right)=1-\exp\left(-0.2\sqrt{t}\right) \tag{8-35}$$

The drying shrinkage, $\varepsilon_{cds}(t,t_s)$, is calculated through Eq. 8-36 multiplying the notional shrinkage coefficient, $\varepsilon_{cds0}(f_{cm})$, the coefficient β_{RH}(RH), and the function $\beta_{ds}(t\text{-}t_s)$. These latter

factors are evaluated through Eq. 8-37, Eq. 8-38 and Eq. 8-39, respectively, by assuming the coefficients α_{ds1} and α_{ds2} dependent on the cement type equal to 6 and 0.012. In detail, the coefficient β_{RH}(RH) considers the effect associated to the ambient relative humidity, while the function $\beta_{ds}(t\text{-}t_s)$ describes the time-development.

$$\varepsilon_{cds}(t,t_s)=\varepsilon_{cds0}(f_{cm})\beta(RH)\beta_{ds}(t-t_s) \tag{8-36}$$

$$\varepsilon_{cds0}(f_{cm})=\left[(220+110\alpha_{ds1})\exp(-\alpha_{ds2}f_{cm})\right]10^{-6} \tag{8-37}$$

$$\beta(RH)=\begin{cases}-1.55\left[1-\left(\dfrac{RH}{100}\right)^3\right] & 40\le RH<99\% \\ 0.25 & RH\ge 99\%\end{cases}\left(\frac{35}{f_{cm}}\right)^{0.1} \tag{8-38}$$

$$\beta_{ds}(t-t_s)=\left(\frac{(t-t_s)}{0.035h^2+(t-t_s)}\right)^{0.5} \tag{8-39}$$

8.5 Effects of corrosion

8.5.1 Corrosion levels estimation

The proposed analytical model is designed to be dependent on a single sectional input parameter, which is the maximum penetration depth of the most corroded wire, P_{max}. In this context, the main steps for the quantification of the corrosion effects are highlighted in Figure 8-5.

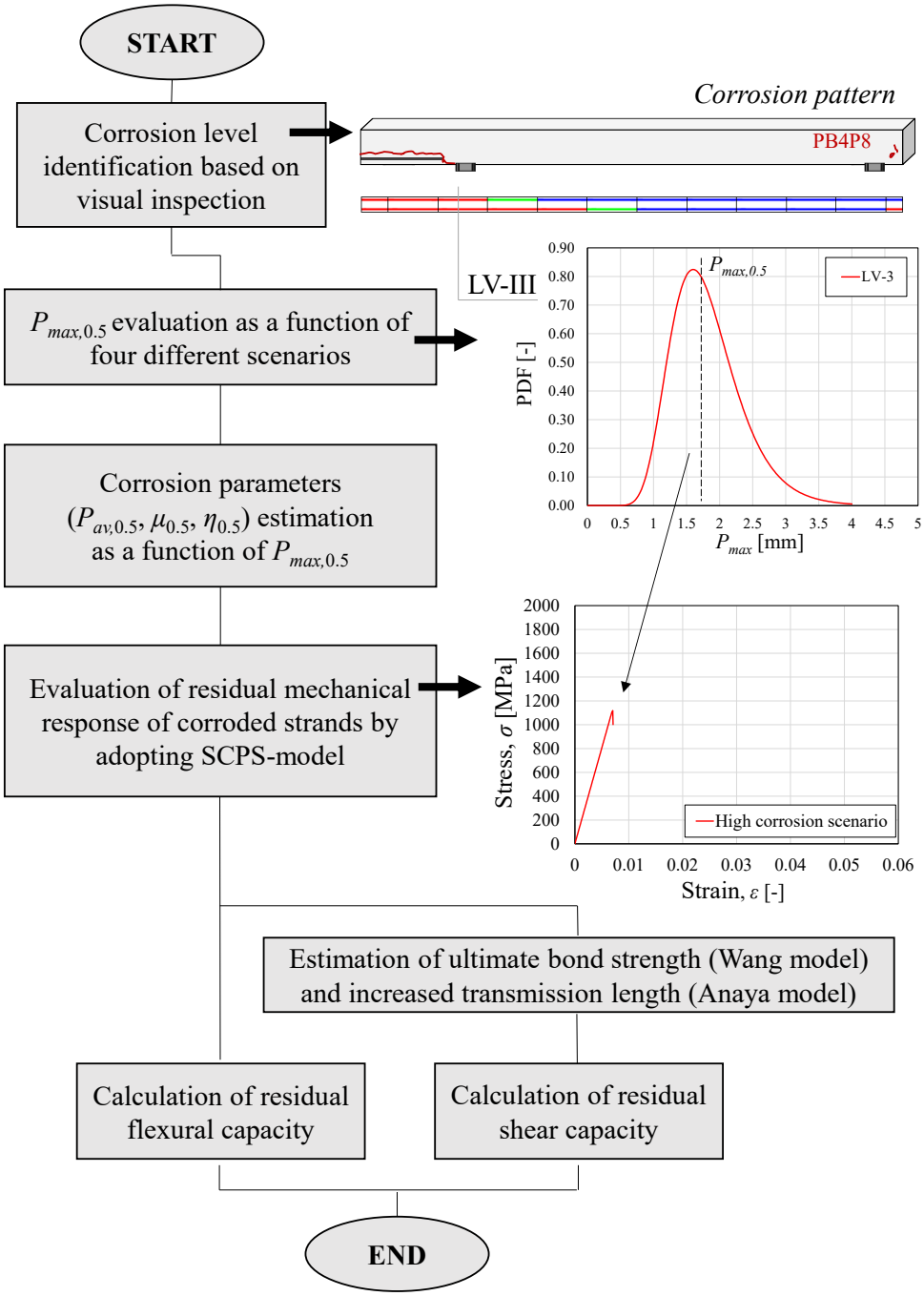

Figure 8-5 Flowchart for the quantification of corrosion effects.

At each section of analysis, a corrosion scenario is first determined based on the corrosion pattern of the analyzed PC beam. In detail, four different scenarios are defined:

- The un-corroded scenario: denoted with LV-0;
- The low corrosion scenario: represented with blue colour in the corrosion pattern and denoted with LV-I in Table 8-1;
- The intermediate corrosion scenario: represented with green colour in the corrosion pattern and denoted with LV-II in Table 8-1;
- The high corrosion scenario: represented with red colour in the corrosion pattern and denoted with LV-III in Table 8-1.

Once the corrosion scenario is defined, the related maximum penetration depth is attributed by assuming the fractile value at 50%, $P_{max,0.5}$, of the maximum penetration depth derived by the Lognormal distribution function of the associated corrosion level. To this end, the available corroded prestressing strands were preliminary divided into one of the four corrosion levels. Afterwards, for each corrosion scenario, the measured maximum penetration depths were statistically analyzed by adopting a Lognormal distribution function, resulting in the PDF and CDF distribution functions reported in Figure 8-6. Finally, the mean value (fractile value at 50%) was assumed as the conventional maximum penetration depth of the corresponding corrosion level. For the sake of clarity, the maximum penetration depth, $P_{max,0.5}$, and the relative normalized value, $P_{max,0.5}/r_{outer}$ are listed in Table 8-1 for the different corrosion scenarios considered. It is worth noting that different maximum penetration depth values, P_{max}, can be adopted as input parameters of the analytical approach without altering the effectiveness of the proposed procedure.

Table 8-1. Maximum and average pit depths for the different corrosion scenarios considered.

Corrosion geometrical features	***Corrosion scenarios***			
	LV-0	**LV-I**	**LV-II**	**LV-III**
$P_{max,0.5}$	0.00	0.052	1.13	1.75
$P_{max,0.5}/r_{outer}$	0.00	0.024	0.53	0.82
$P_{av,0.5}/r_{outer}$	0.00	0.006	0.24	0.47

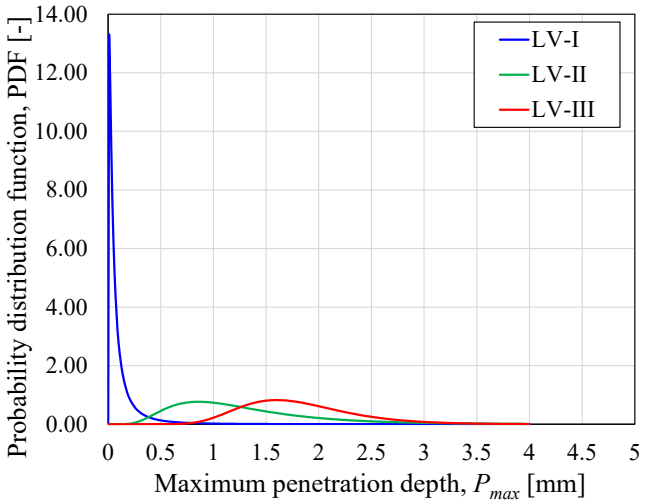

(a)

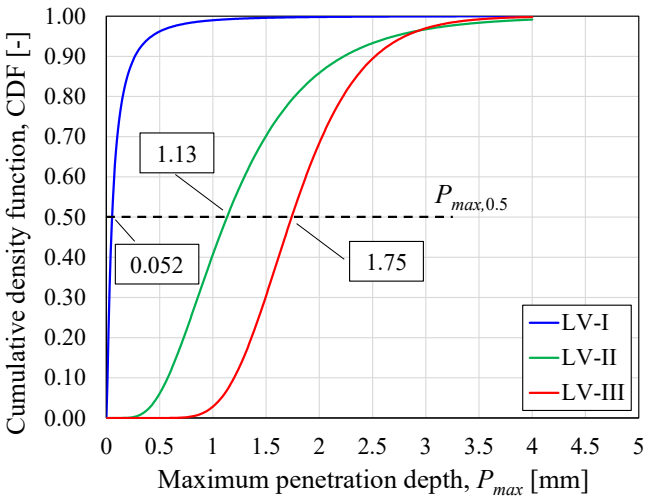

(b)

Figure 8-6 Lognormal distribution function of maximum penetration depths for different corrosion scenarios: (a) PDF and (b) CDF with a focus on fractile value at 50%, $P_{max,0.5}$.

8.5.2 Evaluation of corrosion parameters

Once the normalized maximum penetration depth is known, $P_{max,0.5}/r_{outer}$, the related corrosion parameters in terms of cross-sectional loss, $\mu_{0.5}$, and mass loss, $\eta_{0.5}$, are evaluated as a function of the residual cross-sectional area of the corroded wires composing the strand. To this end, a sectional normalized average penetration depth, $P_{av,0.5}/r_{outer}$, is first assigned to the external wires, except for the most corroded one, based on transversal pitting spatial morphology outcomes through Eq. 8-40. The obtained $P_{av,0.5}/r_{outer}$ values for the different analyzed corrosion scenarios are reported in Table 8-1. Referring to the inner wire, the proposed analytical approach generally allows to input a maximum penetration depth, $P_{inner,0.5}$. However, based on the experimental evidence – previously highlighted in Chapter 6 –, no corrosion signs

were detected for the inner wires of the analyzed corroded samples. Therefore, in the following model validation, $P_{inner,0.5}$ is assumed to be null.

$$\frac{P_{av,0.5}}{r_{outer}} = 0.387\left(\frac{P_{\max,0.5}}{r_{outer}}\right)^2 + 0.25\frac{P_{\max,0.5}}{r_{outer}} \qquad 8\text{-}40$$

Second, the residual cross-sectional areas, $A_{w,outer,corr,0.5}$, of the most corroded wire and the remaining external wires are evaluated through Eq. 8-41 and Eq. 8-42, respectively, as a function of $P_{max,0.5}/r_{outer}$ and $P_{av,0.5}/r_{outer}$; whereas the cross-sectional area of the inner wire is assumed equal to the un-corroded area, $A_{w,inner,0}$.

$$A_{w,outer,corr,\max,0.5} = \begin{cases} \left(1 - 0.303\frac{P_{\max,0.5}}{r_{outer}}\right) A_{w,outer,0} & 0.0 < \frac{P_{\max,0.5}}{r_{outer}} < 0.33 \\ \left[0.9 - 0.539\left(\frac{P_{\max,0.5}}{r_{outer}} - 0.33\right)\right] A_{w,outer,0} & 0.33 \le \frac{P_{\max,0.5}}{r_{outer}} \le 2.00 \end{cases} \qquad 8\text{-}41$$

$$A_{w,outer,corr,av,0.5} = \begin{cases} \left(1 - 0.303\frac{P_{av,0.5}}{r_{outer}}\right) A_{w,outer,0} & 0.0 < \frac{P_{av,0.5}}{r_{outer}} < 0.33 \\ \left[0.9 - 0.539\left(\frac{P_{av,0.5}}{r_{outer}} - 0.33\right)\right] A_{w,outer,0} & 0.33 \le \frac{P_{av,0.5}}{r_{outer}} \le 2.00 \end{cases} \qquad 8\text{-}42$$

Thereafter, substituting Eq. 8-40 into Eq. 8-42, the residual cross-sectional area of the entire strand, $A_{p,corr,0.5}$, is estimated through Eq. 8-43, as a function of $P_{max,0.5}/r_{outer}$ only.

$$A_{p,corr,0.5} = \begin{cases} A_{w,inner,0} + A_{w,outer,0}\left[\left(1 - 0.303\frac{P_{\max,0.5}}{r_{outer}}\right) + 5\left(1 - 0.303\left(0.378\frac{P_{\max,0.5}}{r_{outer}}^2 + 0.25\frac{P_{\max,0.5}}{r_{outer}}\right)\right)\right] & \frac{P_{\max,0.5}}{r_{outer}} \le 0.33 \\ A_{w,inner,0} + A_{w,outer,0}\left[\left(0.9 - 0.539\left(\frac{P_{\max,0.5}}{r_{outer}} - 0.33\right)\right) + 5\left(1 - 0.303\left(0.378\frac{P_{\max,0.5}}{r_{outer}}^2 + 0.25\frac{P_{\max,0.5}}{r_{outer}}\right)\right)\right] & 0.33 < \frac{P_{\max,0.5}}{r_{outer}} \le 0.66 \\ A_{w,inner,0} + A_{w,outer,0}\left[\left(0.9 - 0.539\left(\frac{P_{\max,0.5}}{r_{outer}} - 0.33\right)\right) + 5\left(0.9 - 0.539\left(\left(0.378\frac{P_{\max,0.5}}{r_{outer}}^2 + 0.25\frac{P_{\max,0.5}}{r_{outer}}\right) - 0.33\right)\right)\right] & \frac{P_{\max,0.5}}{r_{outer}} > 0.66 \end{cases}$$

8-43

Third, the cross-sectional loss, $\mu_{0.5}$, of the corroded strands can be immediately estimated by adopting Eq. 8-44:

$$\mu_{0.5} = \frac{A_{p,0} - A_{p,corr,0.5}}{A_{p,0}} = \frac{A_{p,loss,0.5}}{A_{p,0}} \qquad 8\text{-}44$$

where $A_{p,\mathrm{loss}}$ is the prestressing strand cross-sectional area loss due to pitting.

Since the corrosion levels of prestressing reinforcements are assigned via visual inspection and are assumed constant along a fixed length, $L_{inspected}$, – equal to 500 mm for the investigated PC beams –, a homogeneous corrosion can be assumed along this length, as highlighted in Figure 8-7. Consequently, the same normalized maximum penetration depth,

$P_{max,0.5}/r_{outer}$, is assumed along $L_{inspected}$. Hence, by adopting a steel density, ρ_{steel}, equal to 7850 kg/m^3 for both corroded and un-corroded prestressing strands, the cross-sectional loss, $\mu_{0.5}$, and the mass loss, $\eta_{0.5}$, values coincide and an univocal decay trend can be adopted, as shown in Figure 8-7 and as expressed in Eq. 8-45.

$$\eta_{0.5} = \frac{m_{p,0} - m_{p,corr,0.5}}{m_{p,0}} = \frac{\rho_{steel} L_{inspected} A_{p,0} - \rho_{steel} L_{inspected} A_{p,corr,0.5}}{\rho_{steel} L_{inspected} A_{p,0}} = \\ = \frac{\rho_{steel} L_{inspected} \left(A_{p,0} - A_{p,corr,0.5} \right)}{\rho_{steel} L_{inspected} A_{p,0}} = \frac{\left(A_{p,0} - A_{p,corr,0.5} \right)}{A_{p,0}} = \mu_{0.5} \quad \text{8-45}$$

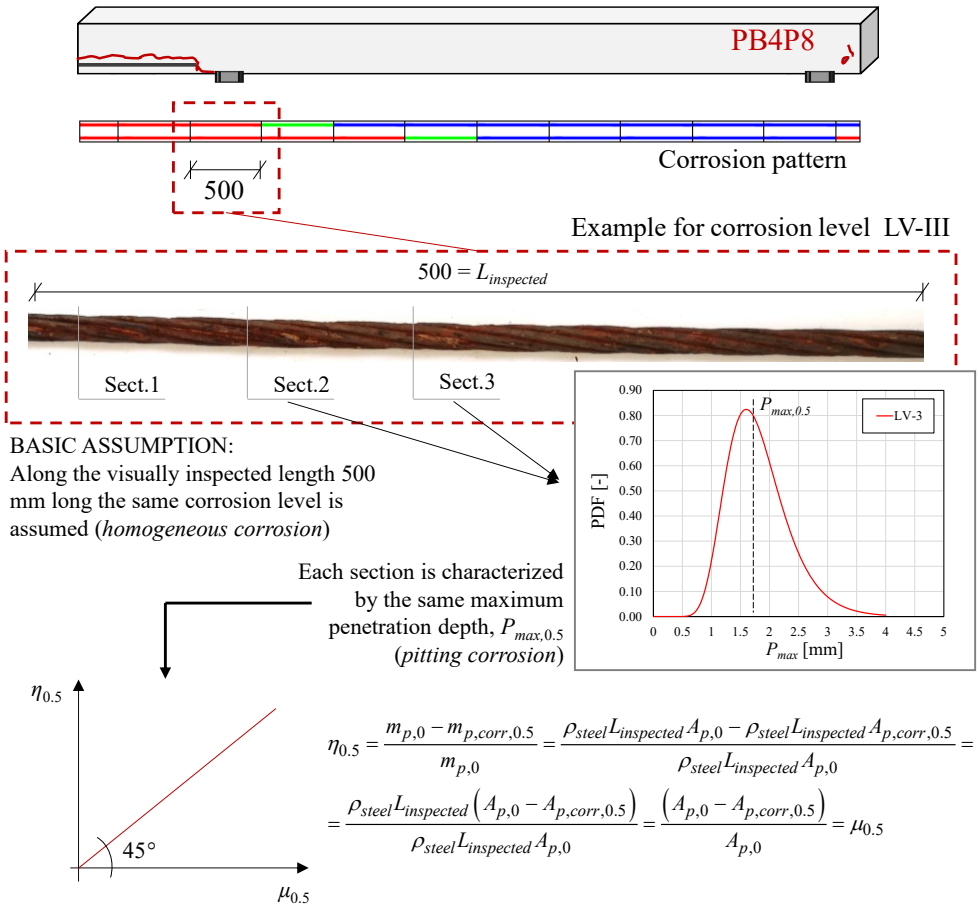

Figure 8-7 Focus on the correspondence between cross-sectional loss and mass loss of a corroded strand along the visually inspected length, $L_{inspected}$.

Although the proposed relationship might seem too conservative in reproducing the real in-service PC beam condition, especially in the case of localized corrosion, it should be considered as a preliminary approach to evaluate the corrosion effects of PC elements subjected to chloride-induced corrosion. Of course, by conducting more accurate visual inspections and a more discretized strand corrosion level assessment, the corrosion level approximation can be improved and a more efficient mass loss vs cross-sectional loss relationship can be defined.

8.5.3 Residual mechanical properties of corroded prestressing strands

The SCPS-model is adopted to predict the sectional residual mechanical behaviour of corroded prestressing strands.

Referring to the maximum penetration depths associated to the selected corrosion scenarios, defined in Section 8.5.1, different stress-strain relationships are evaluated, as reported in Figure 8-8. For the sake of completeness, the expression for the prediction of the residual mechanical response of the entire corroded prestressing strand by adopting the equivalent spring model can be found in Eq. 7-25.

Afterwards, a residual stress-strain relationship is sectionally assigned to prestressing reinforcements as a function of the corrosion pattern of the analyzed corroded PC beam. Although the prestressing strands may exhibit variable corrosion levels at the analyzed section, the analytical approach conservatively attributes the highest sectional recorded corrosion level to all strands. Moreover, since the effective stress redistribution of corroded strands, having different corrosion levels, cannot be determined a priori, the latter assumption is considered reasonable. This conservative assumption is also confirmed by the research conducted by Haefliger & Kaufmann (2022), who pointed out that an average sectional corrosion level attribution does not correctly approximate the residual mechanical response of a corroded element. Indeed, the corrosion level variability associated with the effective combination of number of corroded or un-corroded strands play a key role in the structural element assessment. Hence, the need of a specific and accurate detection of the strands corrosion spatial distribution along the overall element length is further underlined. For the sake of clarity, Figure 8-9 shows the residual mechanical response attribution process in the case of beam PB3P11.

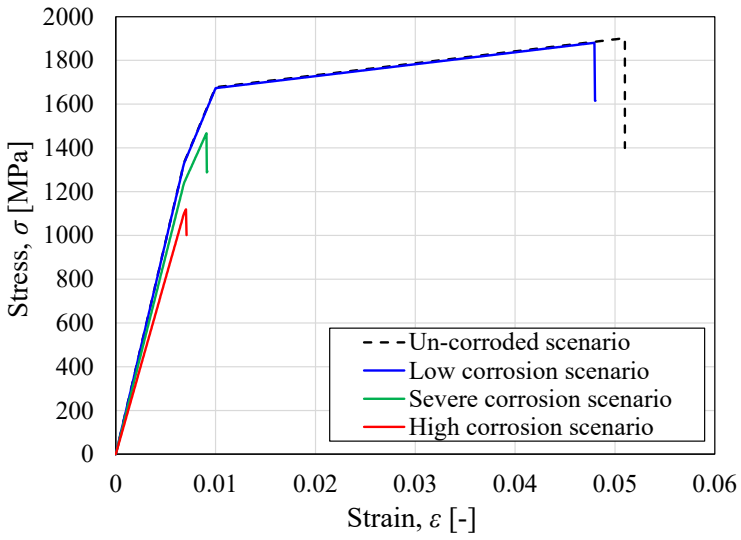

Figure 8-8 Residual mechanical response of corroded strands having different corrosion levels.

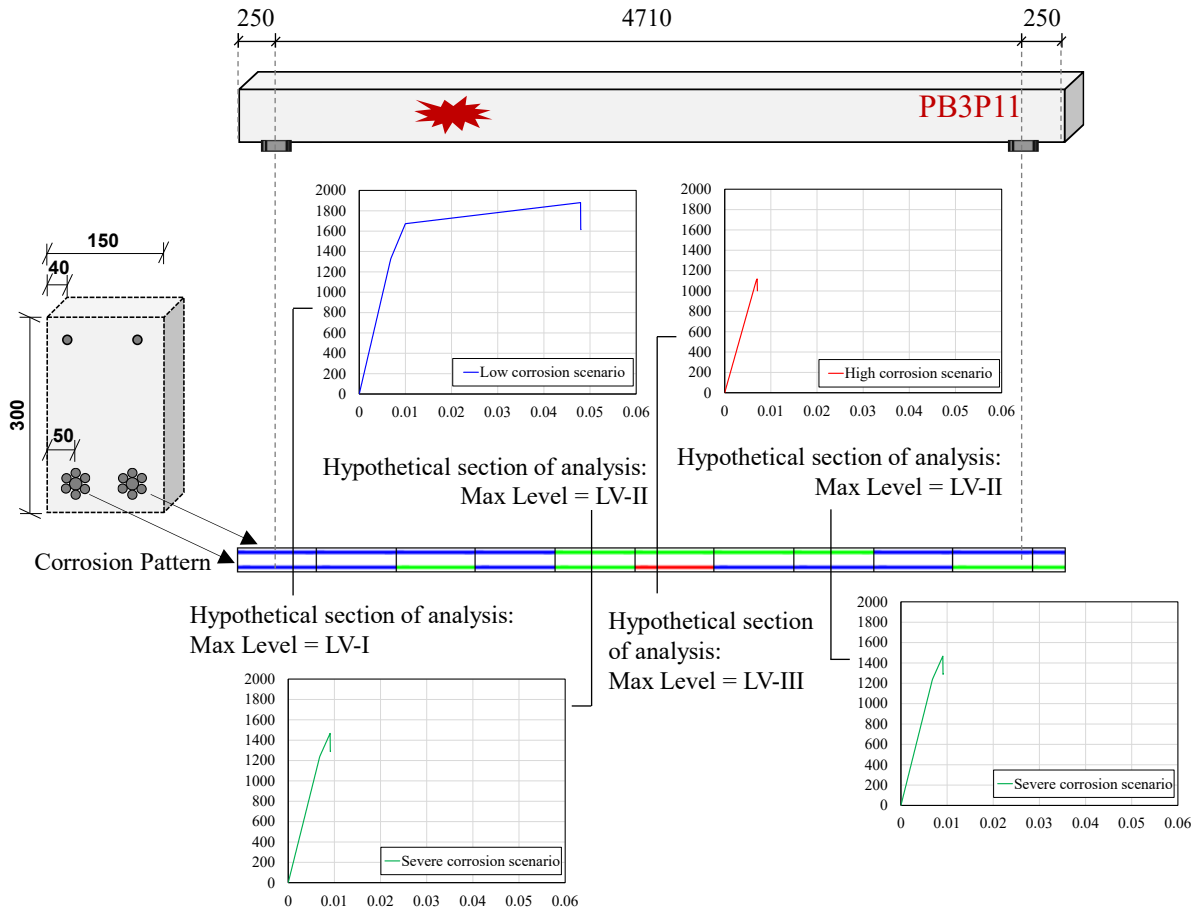

Figure 8-9 Sectional residual mechanical response assignment to corroded strands as a function of PC beam corrosion pattern: example for beam PB3P11.

8.5.4 Reduced prestressing force

In existing PC structures exposed to aggressive environments over service time, the reduction of prestressing stress and, therefore, of the relative prestressing force, $F_{p,0}$, due to chloride-induced corrosion has been documented. In the case of corroded pre-tensioned PC elements, particular attention should be addressed in the evaluation of two distinct occurrences:

- The ultimate bond strength reduction, τ_b, caused by the prestressing steel-concrete interface properties degradation;
- The transmission length increase, L_t, due to reduction of surrounding concrete confinement.

Indeed, bond decay as well as transmission length variation due to corrosion process have a key role in the residual shear capacity of a corroded PC beam. In particular, their rapid degradation may lead to a premature and unexpected failure over time, characterized by the absence of warning signs.

8.5.4.1 Transmission length variation

According to the Eurocode 2 (CEN-EC2, 2004), the transmission length, also known as transfer length, is defined as the distance from the free-end of the beam necessary to transmit the fully effective prestressing-force to the surrounding concrete. Conversely, the ACI Committee 318 (2019) identifies the transmission length in a pre-tensioned member as the length of embedded pretensioned strand necessary to transfer the effective prestress to concrete through bond mechanism from the edge of the beam at the section where the effective prestress is fully developed.

Neglecting corrosion, several provisions for the transmission length quantification, $L_{t,0}$, have been proposed in design codes and guidelines. The most adopted formulations refer to the simplified expressions provided by AASHTO LRFD (2017) and the Korean design code for highways bridges (KDCHB) (2015), which estimate $L_{t,0}$ equal to 60 times and 50 times the un-corroded diameter of the prestressing strand, $\phi_{eq,0}$, respectively. More refined formulations, provided by other codes or guidelines such as Eurocodes, can be found in Jeon S. et al. (2019).

In the case of pre-tensioned structures, the transmission length is a crucial parameter for identifying bond properties. Indeed, as pointed out in the Eurocode 2 (CEN-EC2, 2004) and in the Model Code 2010 (Ceb-Fip, 2013), $L_{t,0}$ can be considered as inversely proportional to the average bond stress, τ_b, which in turn is defined as a function of the radial stress existing at the interface and the friction coefficient between concrete and steel. In this context, the Hoyer effect, which is the mechanism allowing the prestressing force to be transferred to the concrete, play a fundamental role. In fact, a variation of the original radial stress is caused by the strand releasing, resulting in an alteration of prestressing stress. As highlighted by Anaya et al. (2022), after the strand releasing, the initial prestressing stress reduces and the prestressing strand tends to expand laterally to recover its original state. As a result, the friction mechanism between steel and concrete is activated by the combination of the prestressing strand expansion mechanism and the opposite mechanism performed by the surrounding concrete.

The extensive experimental campaigns carried out in the last decades highlighted that the material and geometrical parameters in terms of concrete strength, f_{cm}, concrete cover, c, strand and wire diameter, $\phi_{eq,0}$, and initial prestressing stress, $\sigma_{p,0}$, are the most relevant parameters affecting the transmission length of pre-tensioned PC elements, (Balazs, 1992; Mitchell et al., 1993; Oh et al., 2014). Referring to these latter parameters, Anaya et al. (2022) proposed a simplified expression, calibrated on experimental outcomes, for the evaluation of the un-corroded transmission length, $L_{t,0}$, as expressed in Eq. 8-46. Considering the properties

of the investigated PC beams, i.e. a concrete cover thickness equal to 50 mm, a concrete compressive strength equal to 45.4 MPa, an initial prestressing stress of 1408 MPa, and an equivalent strand diameter equal to 12.9 mm, $L_{t,0}$ results equal to 726 mm that is equivalent to approximately 56 times $\phi_{eq,0}$.

$$L_{t,0} = 30 \frac{\phi_{eq,0} \left(\sigma_{p,0}\right)^{\frac{1}{2}}}{\left(\frac{c}{\phi_{eq,0}}\right)^{\frac{1}{3}} f_{cm}^{\frac{2}{3}}} \qquad 8\text{-}46$$

Considering the corrosion process, the transmission length is primarily affected by the expansion pressure induced by the rust products formation. Indeed, for severe corrosion levels, the expansion pressure increase may lead to concrete damages such as longitudinal splitting cracks formation even to concrete cover spalling, which directly impact the surrounding concrete confinement effect. Therefore, increasing the expansion pressure, the concrete confinement proportionally reduces, resulting in a relevant increase in the transmission length, $L_{t,corr}$. Nevertheless, limited studies have been conducted to analyze and quantify the transmission length in the case of corroded scenarios. Belluco et al. (2021) proposed an analytical model for the evaluation of $L_{t,corr}$ by taking into account the contribution of the corrosion products pressure in the estimation of the total radial pressure and a modified friction coefficient dependent on the depth of corrosion attack. However, as pointed out by the authors, no results are available in scientific literature to provide a relationship between the friction coefficient and the depth of corrosion attack in the case of tensioned strands. Consequently, the model assumed a simplified law based on an arbitrary coefficient. Because of the significant results variability due to this arbitrary assumption, the previous model was not considered sufficiently reliable for the prediction of the corroded transmission length, $L_{t,corr}$.

Anaya et al. (2022), conversely, proposed an analytical approach for the evaluation of the corroded transmission length calibrated and validated on experimental outcomes on corroded wires. Moreover, simplified expressions were provided based on a parametric analysis carried out by varying the mechanical and geometrical variables governing the formulations. Although the authors highlighted that the predictive ability of the expressions must be further validated due to the absence of experimental activities investigating the topic, the proposed simplified approach was considered as an appropriate preliminary starting point for quantifying the corroded transmission length, $L_{t,corr}$, of prestressing reinforcements.

According to the model, $L_{t,corr}$ is evaluated by adopting Eq. 8-47:

$$L_{t,corr} = \kappa L_{t,0} \qquad 8\text{-}47$$

where κ is a dimensionless coefficient that counts for corrosion effects and it is estimated through Eq. 8-48 as function of (i) the prestressing strand cross-sectional loss, $\mu_{0.5}$, (ii) the threshold cross-sectional loss, $\mu_{lim,Lt}$, and (iii) the parameter V_{det}, as graphically highlighted in Figure 8-10. The coefficient V_{det} represents the rate of growth of the transmission length, and it is assumed to remain constant through the corrosion process, as reported in Eq. 8-49. This parameter was found to increase with the increase of the initial prestressing stress and the concrete compressive strength, and with the decrease in the cover / diameter ratio. The threshold cross-sectional loss, $\mu_{lim,Lt}$, is estimated by adopting Eq. 8-50 and it was demonstrated to increase with the increase of the cover / diameter ratio, and with the decrease in the initial prestressing stress, (Anaya et al., 2022). According to Eq. 8-48, the transmission length remains constant until the threshold cross-sectional loss, $\mu_{lim,Lt}$, is exceeded. Thereafter, $L_{t,corr}$ linearly increases with a slope equal to V_{det} based on the difference between the actual corrosion level – represented by $\mu_{0.5}$ value – and the threshold cross-sectional loss, $\mu_{lim,Lt}$.

$$\kappa = 1 + \left(\mu_{0.5} - \mu_{\text{lim},Lt}\right) V_{\text{det}} \geq 1.0 \qquad 8\text{-}48$$

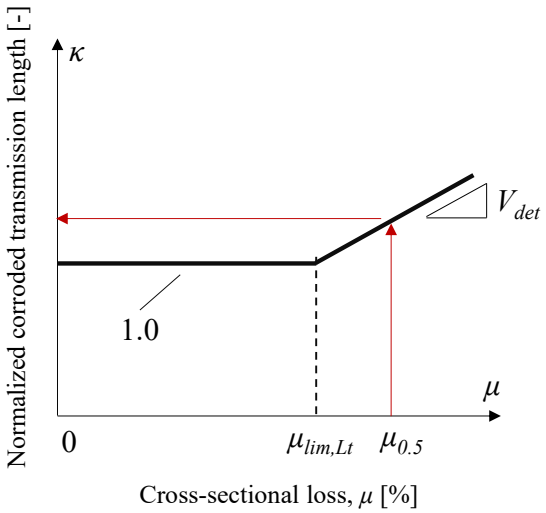

Figure 8-10 Normalized corroded transmission length according to the simplified approach proposed by Anaya et al. (2022).

$$V_{\det} = 0.004 \frac{\sigma_{p,0} \left(f_{cm}\right)^{\frac{1}{9}}}{\left(\phi_{eq,0}\right)^{\frac{1}{3}} \left(\frac{c}{\phi_{eq,0}}\right)^{3}} \quad 8\text{-}49$$

$$\mu_{\lim,Lt} = 2250 \frac{\left(\phi_{eq,0}\right)^{\frac{1}{3}} \left(\frac{c}{\phi_{eq,0}}\right)^{2}}{\left(\sigma_{p,0}\right)^{\frac{5}{4}}} \quad 8\text{-}50$$

8.5.4.2 Ultimate bond strength reduction

Bond resistance at steel-concrete interface is a crucial contribution for the durability and the ultimate capacity of RC and pre-tensioned PC beams, whereas the transmission of prestressing force in post-tensioned PC beams is mostly governed by end anchorage systems, (L. Wang et al., 2018). The bond resistance in RC and pre-tensioned PC elements is attributed to three contributions: (i) adhesion, (ii) friction, and (iii) mechanical interlock. Adhesion contribution commonly disappears as soon as the reinforcements start to slip, while friction and mechanical interlock become the governing factors.

Although several studies have been conducted in the last years on the quantification of the corrosion effects on the ordinary reinforcement bond resistance, (Lin et al., 2019; Tondolo, 2015), a limited number of works focused on corroded prestressing reinforcements, (Dai et al., 2020; L. Wang et al., 2016, 2017, 2018). For low corrosion levels, the available models agree in defining a first increase in bond resistance induced by the beneficial friction contribution, which is enhanced by the greater roughness of deteriorated prestressing steel as well as by a higher confinement provided by the increased concrete pressure. For high corrosion levels, on the contrary, the bond resistance decreases. The available models, conceived on experimental outcomes, differ from each other for the critical mass loss, η_{lim}, value at which the bond stress starts to decrease. Wang et al. (2017) first proposed a simplified model to describe the progressive bond degradation at steel-concrete interface by analyzing the experimental outcomes of 10 pull-out tests, characterized by corrosion level variability. As shown by the black curve in Figure 8-11, the normalized bond strength, R, results unaffected by corrosion until the critical mass loss equal to 6% is not exceeded, thereafter, an exponential decay law is assumed, as expressed in Eq. 8-51.

$$R = \begin{cases} 1.0 & \eta_{0.5} \le 6\% \\ 2.03e^{-0.118\eta_{0.5}} & \eta_{0.5} > 6\% \end{cases} \quad 8\text{-}51$$

The same authors successively performed beam tests on nine corroded pre-tensioned PC beams, (L. Wang et al., 2018). Based on the obtained results, an updated simplified model was defined as in Eq. 8-52. The new normalized bond strength, R_1, is unaffected by corrosion until the η_{lim} value equal to 4.4% is not exceeded, thereafter, a linear decay law was introduced, as highlighted by the orange curve in Figure 8-11. Differently from Wang et al. (2017), the modified model can be applied up to a mass loss value, $\eta_{0.5}$, approximately to 24%.

$$R_1 = \begin{cases} 1.0 & \eta_{0.5} \le 4.4\% \\ 1 - 0.0512\left(\eta_{0.5} - \eta_{\text{lim}}\right) & 4.4\% < \eta_{0.5} \le 24\% \end{cases} \quad 8\text{-}52$$

Nevertheless, the effect of corrosion-induced crack and the confinement role of stirrups significantly impact the bond resistance at steel-concrete interface. As pointed out by Wang et al. (2018), before the reaching of cracking load, corrosion marginally affects the bond stress, thereafter, the bond decay is severely impacted by both concrete cracking and strand corrosion level. The confinement role of stirrups, on the other hand, is crucial for delaying the bond decay induced by concrete cracking, (L. Wang et al., 2017). In this context, it is worth nothing that three types of failure mode can be observed during pull-out tests: (a) strand pull-out failure, (b) strand fracture failure, or (c) splitting of concrete failure. The presence of an appropriate concrete cover thickness (having a cover / strand diameter ratio higher than 4.5) and the presence of stirrups with regular spacing are generally sufficient to provide the strand confinement during pull-out testing and to avoid splitting failure mode. For PC elements without stirrups, the bond stiffness and strength decrease immediately after concrete cracking, since the strand confinement is provided by the deteriorated concrete only, resulting in a high probable premature splitting failure mode. As a result, the analytical approaches – previously introduced – fail in predicting the residual bond strength, leading to unconservative outcomes.

To fill the gap, the present *Thesis* proposes an analytical model for the estimation of the normalized residual bond strength for PC elements without stirrups, R_2. To this end, the experimental data from the pull-out tests performed by Wang et al. (2017) are considered. According to the proposed model, a single exponential decay law is provided as reported in Eq. 8-53 and graphically shown by the red curve in Figure 8-11.

$$R_2 = e^{-0.133\eta_{0.5}} \quad 8\text{-}53$$

As it is visible through the comparison with the other approaches, the main novelty consists in the absence of a critical mass loss value, η_{lim}. Indeed, as previously pointed out, for PC elements without the confinement contribution provided by stirrups, the bond stiffness and strength start to decrease immediately after the concrete cracking. Considering corrosion, it is reasonable to assume that the contribution of the deteriorated concrete is marginal, as confirmed from the visual inspection of the available naturally corroded PC beams analyzed in the present research, which were characterized by longitudinal splitting cracks formed during in service conditions.

Finally, once the normalized residual bond strength is known, R_i, the related effect on prestress loss, $\sigma_{p,corr}(t)$, is considered by reducing the effective prestress, $\sigma_p(t)$, proportionally to the decrease in ultimate bond strength, according to Eq. 8-54.

$$\sigma_{p,corr}(t) = \begin{cases} R\sigma_p(t) & pull-out-test(stirrups) \\ R_1\sigma_p(t) & beam-test \\ R_2\sigma_p(t) & pull-out-test(no-stirrups) \end{cases} \quad 8\text{-}54$$

Although this assumption should be further validated by means of ad-hoc experimental activities, considering the lack of available works in the scientific literature dealing with this issue, the proposed approach can be considered as a preliminary simplified relationship useful to determine the corrosion-induced prestress loss in PC elements and to address the issue to scientific community attention. As a result, the reduced prestressing force, $F_{p,corr}(t)$, can be quantified through Eq. 8-55.

$$F_{p,corr}(t) = \sigma_{p,corr}(t) n_{strand} A_{p,0} \quad 8\text{-}55$$

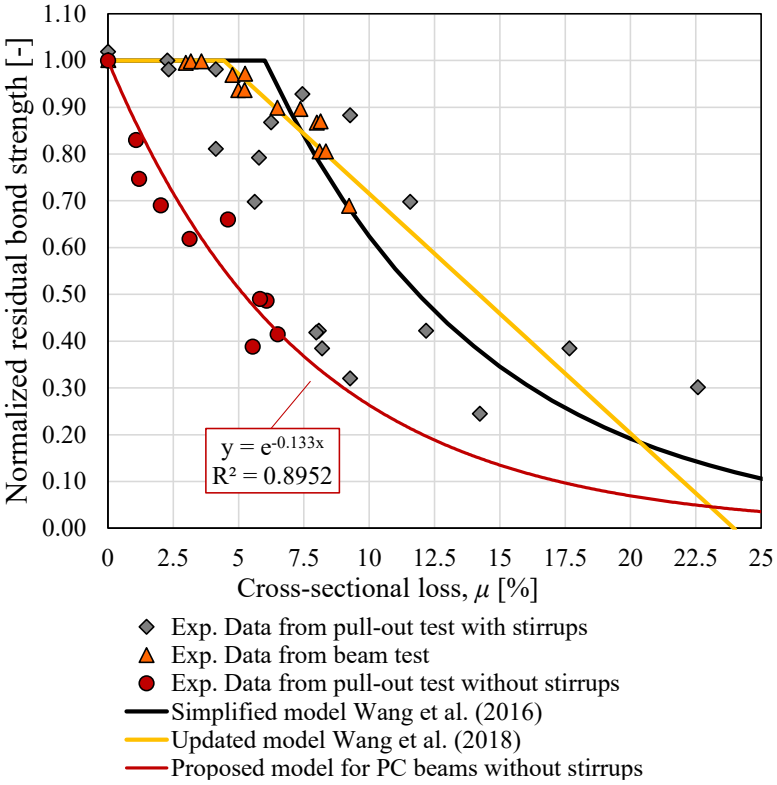

Figure 8-11 Normalized bond strength decay laws.

For the sake of clarity, it is worth noting that each of the analytical approaches introduced for estimating the residual bond strength are implemented in the proposed analytical model for the assessment of corroded PC beams. Nevertheless, since the model validation is conducted on the naturally corroded PC beams without transversal reinforcement previously investigated, the normalized reduced bond strength, R_2, reported in Eq. 8-53 is assumed.

8.6 Calculation of the residual flexural capacity

The residual flexural capacity of un-corroded and corroded PC beams is analyzed through the definition of a simplified moment-curvature approach. In detail, the following constitutive laws are adopted in the proposed simplified model:

- The concrete compressive mechanical properties in terms of average compressive strength, f_{cm}, strain at peak load, ε_{c0}, ultimate compressive strain, ε_{cu}, and modulus of elasticity, E_c, are defined according to the bi-linear relationship (triangular-rectangular trend) provided by the Eurocode 2 (CEN-EC2, 2004) and the Model Code 2010 (2013), as expressed in Eqs. 8-15 and 8-56, and graphically reported in Figure 8-12.

$$\varepsilon_{c0} = \begin{cases} \frac{f_{cm}}{E_c}‰ & for \le C50 \\ \frac{f_{cm}}{E_c}‰ + 0.55\left[\left(f_{cm}-58\right)/40\right]‰ & for > C50 \end{cases} \quad 8\text{-}56$$

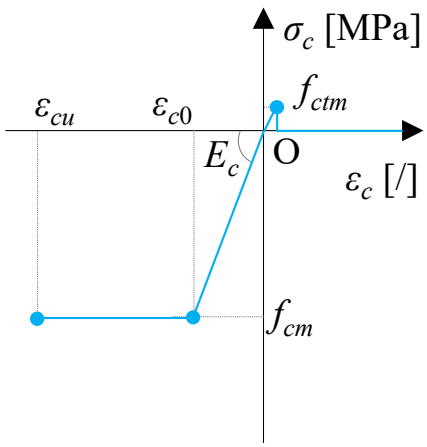

Figure 8-12 Simplified constitutive law for concrete in compression and in tension.

- The concrete tensile mechanical properties in terms of average concrete tensile strength, f_{ctm}, is evaluated according to the expression provided by the Eurocode 2 (CEN-EC2, 2004) and the Model Code 2010 (2013), as expressed in Eq. 8-57.

$$f_{ctm} = \begin{cases} 0.3\left(f_{ck}\right)^{2/3} & c.grades \le C50 \\ 2.12\log\left(1+0.1f_{cm}\right) & c.grades > C50 \end{cases}$$
$$f_{ck} = f_{cm} - 8 \qquad \text{8-57}$$

- The mechanical properties of prestressing strands are estimated by adopting the SCPS-model. For the sake of clarity, the stress-strain relationship in the case of un-corroded scenario is graphically reported in Figure 8-13.

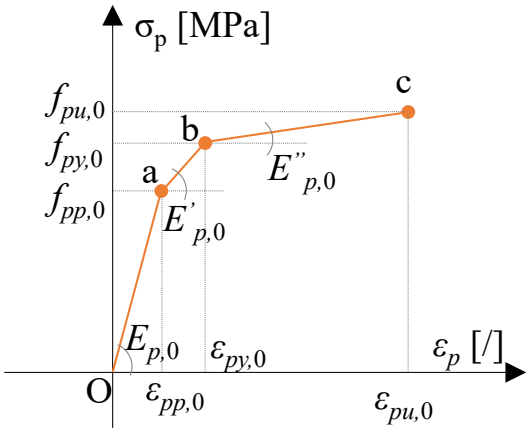

$$f_{pp,0} = 0.7f_{pu,0}$$
$$f_{py,0} = 0.882f_{pu,0}$$
$$\varepsilon_{pp,0} = \frac{0.7f_{pu,0}}{E_p}$$
$$\varepsilon_{py,0} = 1\ \%$$
$$E'_{p,0} = \frac{f_{py,0} - f_{pp,0}}{\varepsilon_{py,0} - \varepsilon_{pp,0}}$$
$$E''_{p,0} = \frac{f_{pu,0} - f_{py,0}}{\varepsilon_{pu,0} - \varepsilon_{py,0}}$$

Figure 8-13 SCPS-model for un-corroded prestressing strands.

8.6.1 Simplified moment-curvature approach

8.6.1.1 Basic assumptions

The simplified moment-curvature approach consists in the definition of a quadrilinear trend, as shown in Figure 8-14, characterized by five critical points, denoted as A' – A – B – C and D, which stand for the following conditions:

1. Point A': reaching of the full prestressing stress;
2. Point A: reaching of the tensile concrete strength;
3. Point B: reaching of the proportional limit in the stress-strain relationship of prestressing strands ($\varepsilon_{pp,0}$;$f_{pp,0}$);
4. Point C: reaching of the yielding point in the stress-strain relationship of prestressing strands ($\varepsilon_{py,0}$;$f_{py,0}$);
5. Point D: reaching of the ultimate limit state in the stress-strain relationship of prestressing strands ($\varepsilon_{pu,0}$;$f_{pu,0}$) or concrete crushing (ε_{cu};f_{cm}).

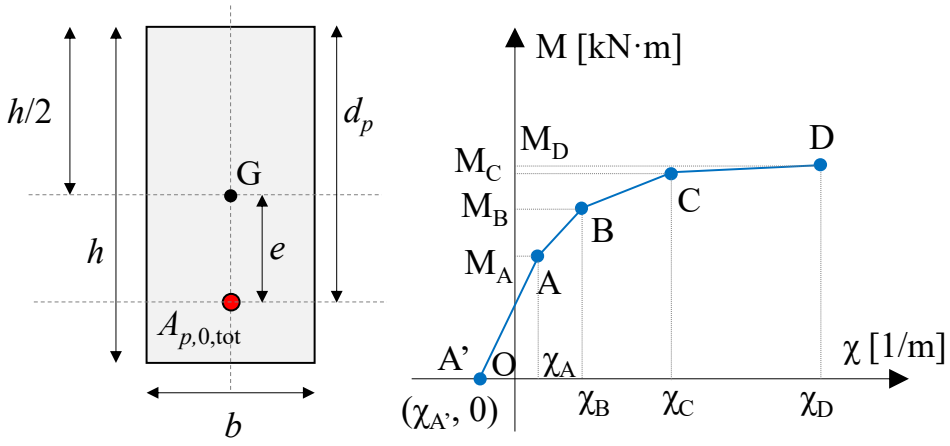

Figure 8-14 Simplified quadrilinear trend for the definition of the sectional moment-curvature diagram of a prestressed concrete beam.

To completely define the sectional moment-curvature diagram highlighted in Figure 8-14, simplified assumptions are made:

- The geometrical centre of gravity, G, is assumed to be coincident with the mechanical centre of gravity, i.e. G is assumed equal to $h/2$ where h is the cross-sectional height. Therefore, the eccentricity of prestressing reinforcement, e, can be evaluated as the difference between d_p, which is the effective depth of reinforcement, and $h/2$;

- The tension-stiffening effect is roughly considered by connecting the events A, B and by taking into account the concrete tensile strength;
- The resistance contribution provided by ordinary longitudinal reinforcements in tension and compression is neglected, since it is assumed that the major resistance contribution is due to prestressing reinforcement;
- The hypothesis that plain sections remain plain is considered through the compatibility relationship reported in Eq. 8-58 (Eulero-Bernoulli behaviour):

$$\varepsilon_c = \frac{\left(\varepsilon_p - \varepsilon_{p,0}\right)x}{\left(d_p - x\right)} = \frac{\Delta\varepsilon_p x}{\left(d_p - x\right)} \qquad 8\text{-}58$$

  where, x is the neutral axis, ε_p is the prestressing strand strain (or concrete strain), while $\varepsilon_{p,0}$ is the strain due to prestressing stress;
- The self-weight of the structural element is neglected;
- The ductility can be estimated once the ultimate and yielding curvatures are known. When the prestressing reinforcement are in their elastic branch, the ductility is assumed to be null;
- The corrosion effect is introduced by predicting the residual mechanical properties of corroded strands in terms of ultimate corroded strength, $f_{pu,corr}$, and ultimate corroded strain, $\varepsilon_{pu,corr}$, by using the SCPS-model. As previously pointed out, according to the corrosion level, three corrosion scenarios can occur:
  - Low corrosion, where the hardening phase of the stress-strain relationship is reduced. In this case, the point c in Figure 8-13 is defined by the pair-value ($\varepsilon_{pu,corr}$;$f_{pu,corr}$), as highlighted in Figure 8-15(a);
  - Intermediate corrosion, where the hardening phase cannot develop, and the stress-strain relationship of corroded strands reduces to a bi-linear trend. In this case, points b and c of the stress strain relationship coincide and are equal to the pair-value ($\varepsilon_{pu,corr}$;$f_{pu,corr}$), as highlighted in Figure 8-15(b);
  - High corrosion, where only the linear elastic phase in the stress-strain relationship of corroded strand develops. In this case, the point a, b, and c coincide and are equal to the pair-value ($\varepsilon_{pu,corr}$;$f_{pu,corr}$), as highlighted in Figure 8-15(c).

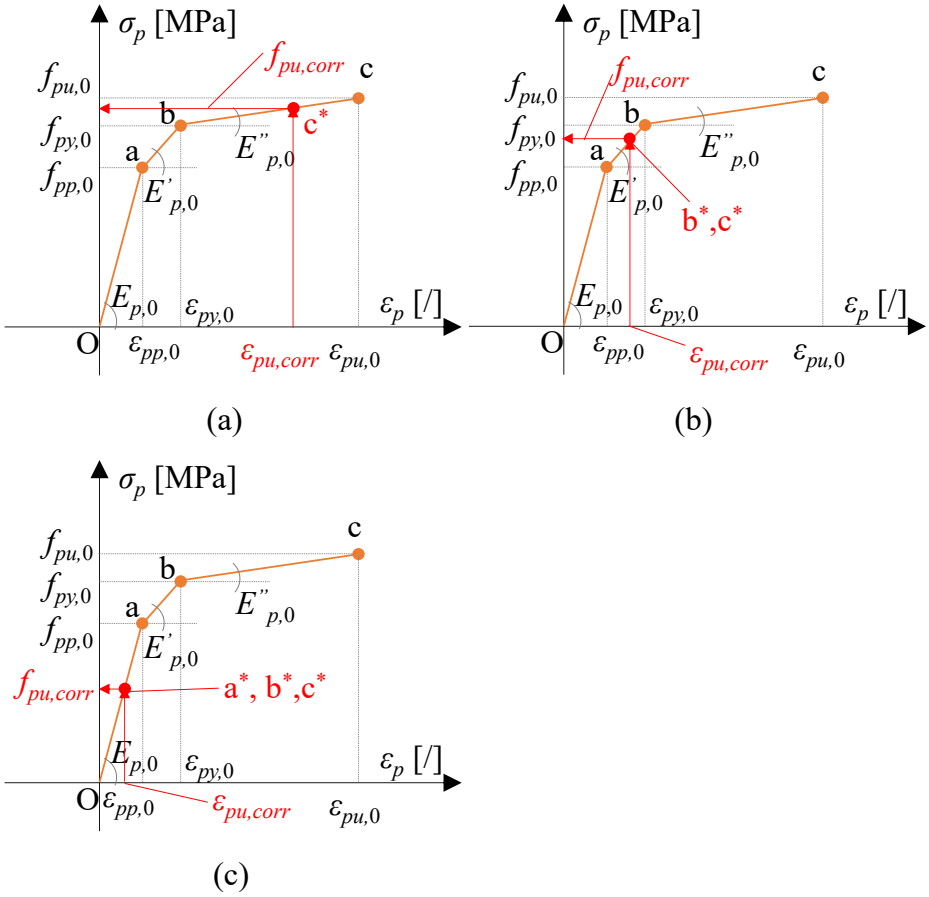

Figure 8-15 Corrosion scenarios and residual mechanical response of corroded strands by adopting SCPS-model: (a) low corrosion, (b) intermediate corrosion, and (c) high corrosion.

8.6.1.2 Critical mechanical reinforcements ratios and cross-sectional failure cases

The ductile or brittle failure mode of the analyzed cross-section is determined as a function of the critical mechanical reinforcement ratios, which play a key role in the definition of the possible failure cases:

- Failure Case "1": Cross-section with low reinforcement level (under-reinforced section). The failure mode is associated to the achievement of the prestressing reinforcement ultimate strain, whereas the concrete compressive ultimate strain is not yet reached. This type of failure mode can occur in the case of (i) a cross-section with a low reinforcement percentage and/or (ii) a cross-section characterized by a significant corrosion level, resulting in a sensible reduction in the prestressing reinforcement ultimate strain, $\varepsilon_{pu,corr}$, Figure 8-16(a);
- Failure Case "2": Cross-section with intermediate reinforcement level (balanced section). The failure mode is balanced and is characterized by the reaching of the

concrete compressive ultimate strain with plasticized prestressing reinforcement, Figure 8-16(b);

- Failure Case "3": Cross-section with high reinforcement level (over-reinforced section). The failure mode is characterized by the reaching of the concrete compressive ultimate strain with prestressing reinforcement in the elastic phase, Figure 8-16(c).

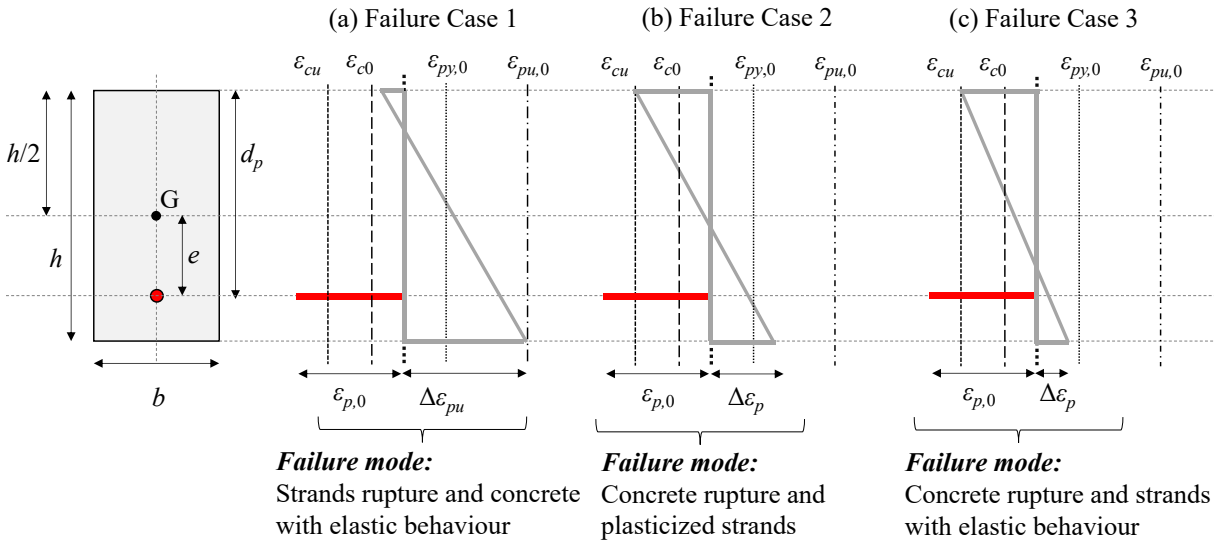

Figure 8-16 Identification of the cross-sectional failure cases: (a) Failure Case 1, (b) Failure Case 2, and (c) Failure Case 3.

The failure cases identification depends on the evaluation of the critical mechanical reinforcement ratios, which are defined as a function of the reinforcement percentages and the critical strain values. The prestressing reinforcement mechanical reinforcement ratio, ω_p, – to be compared with the critical mechanical reinforcement ratios associated to the different failure cases – is calculated according to Eq. 8-59.

$$\omega_p = \frac{A_{p,0,tot} f_{py,0}}{f_{cm} b d_p} \qquad 8\text{-}59$$

The critical mechanical reinforcement ratios that identify the threshold limits between the failure case 1 and 2, ω_1, and between the failure case 2 and 3, ω_3, can be quantified through Eq. 8-60 and Eq. 8-61, respectively:

$$\omega_1 = \frac{\lambda\varepsilon_{cu}}{\left(\varepsilon_{pu,0} - \varepsilon_{p,0} + \varepsilon_{cu}\right)}\frac{f_{pu,0}}{f_{py,0}} = \frac{\lambda\varepsilon_{cu}}{\left(\varepsilon_{pu,0} - \dfrac{\sigma_p(t)}{E_{p,0}} + \varepsilon_{cu}\right)}\frac{f_{pu,0}}{f_{py,0}} \qquad 8\text{-}60$$

$$\omega_3 = \frac{\lambda\varepsilon_{cu}}{\left(\varepsilon_{py,0} - \varepsilon_{p,0} + \varepsilon_{cu}\right)} \qquad 8\text{-}61$$

where λ is assumed equal to 0.8 and corresponds to the reduction parameter associated to the concrete compression "stress-block", and the prestressing stress, $\sigma_p(t)$, is calculated by subtracting the prestressing losses, according to Eq. 8-10.

It is worth noting that the actual simplified moment-curvature diagram needs to be determined based on the expected failure case, which is estimated through the comparison between the prestressing reinforcement mechanical reinforcement ratio, ω_p, and the critical mechanical reinforcement ratios ω_1 and ω_3, as follows:

- If $\omega_p \leq \omega_1$, the Failure Case 1 is expected;
- If $\omega_1 \leq \omega_p \leq \omega_3$, the Failure Case 2 is expected;
- If $\omega_p \geq \omega_3$, the Failure Case 3 is expected.

Considering corrosion, the previous expression must be modified to identify the correct Failure Case. Indeed, for the low corrosion scenario where the stress-strain relationship of the corroded strands is still characterized by the development of a reduced hardening phase, the expressions remain almost unaffected, except for the prestressing stress reduction. For intermediate and high corrosion scenarios, on the contrary, the hardening phase in the stress-strain relationship cannot develop. Therefore, the un-corroded values of yield strength and strength in correspondence of the proportional limit should be assumed equal to the corroded ultimate strength, $f_{pu,corr}$, resulting in a $f_{pu,0}/f_{py,0}$ ratio equal to 1.0.

8.6.1.3 Analytical approach for the un-corroded scenario

In the following paragraphs, the theoretical expressions for the definition of the sectional moment-curvature diagram are illustrated for the different failure cases. Note that the analytical formulations for points A' and A of the moment-curvature diagram are the same for the different failure cases considered.

8.6.1.4 Failure Case "1"

The failure mode of Failure Case "1" is ductile. The first point of the simplified moment-curvature diagram, denoted as point A', corresponds to the achievement of the full prestressing stress with the development of the related negative deflection at beam-span. The

corresponding moment, $M_{p,0}$, due to prestressing force, $F_{p,0}$, can be, therefore, evaluated according to Eq. 8-62:

$$M_{p,0} = F_{p,0}e = \left(n_{strand}A_{p,0}\sigma_p(t)\right)e = \left(A_{p,0,tot}\sigma_p(t)\right)e \quad 8\text{-}62$$

where $A_{p,0}$ is the un-corroded area of a strand, n_{strand} is the number of prestressing strands at the analyzed cross-section, and $A_{p,0,tot}$ is the overall un-corroded area of prestressing reinforcements. Since the self-weight is neglected, the bending moment in correspondence of point A', $M_{A'}$, is assumed to be null, whereas, the related curvature, $\chi_{A'}$, is evaluated through Eq. 8-63, by assuming a cross-sectional linear-elastic behaviour:

$$\chi_{A'} = -\frac{F_{p,0}e}{E_c I_i} = -\frac{\left(A_{p,0,tot}\sigma_p(t)\right)e}{E_c I_i} \quad 8\text{-}63$$

where I_i is the second moment of inertia of the concrete cross-section, estimated through Eq. 8-64, by adopting the coefficient α_e equal to the ratio $E_{p,0}/E_c$.

$$I_i = \frac{bh^3}{12} + A_{p,0,tot}\alpha_e\left(d_p - 0.5h\right)^2 \quad 8\text{-}64$$

The total cross-sectional area, A_i is evaluated according to Eq. 8-65, where the concrete cross-sectional area, A_c, is the product between the beam width, b, and the beam height, h, respectively.

$$A_i = A_c + A_{p,0,tot}\alpha_e = bh + A_{p,0,tot}\alpha_e \quad 8\text{-}65$$

Thereafter, by assuming the general linear-elastic expression for a cross-section subjected to combined compressive and bending stress, the concrete stress at bottom, $\sigma_{c,b}$, and top, $\sigma_{c,t}$, layer are calculated according to Eq. 8-66 and Eq. 8-67, respectively.

$$\sigma_{c,b} = -\frac{F_{p,0}}{A_i} - \frac{M_{p,0}}{I_i}\frac{h}{2} \quad 8\text{-}66$$

$$\sigma_{c,t} = -\frac{F_{p,0}}{A_i} + \frac{M_{p,0}}{I_i}\frac{h}{2} \quad 8\text{-}67$$

As highlighted in Figure 8-17, the first term corresponds to the constant contribution provided by axial force due to prestressing, while the second one stands for the contribution induced by the prestressing strands eccentricity, e.

Finally, once $\sigma_{c,t}$ and $\sigma_{c,b}$ are known, the longitudinal strain at mid-height of the effective shear depth, $\varepsilon_{x,A'}$, at point A' can be estimated by adopting Eq. 8-68.

$$\varepsilon_{x,A'} = \frac{\left(\sigma_{c,b} + \sigma_{c,t}\right)}{2E_c} = -\frac{F_{p,0}}{E_c A_i} \qquad 8\text{-}68$$

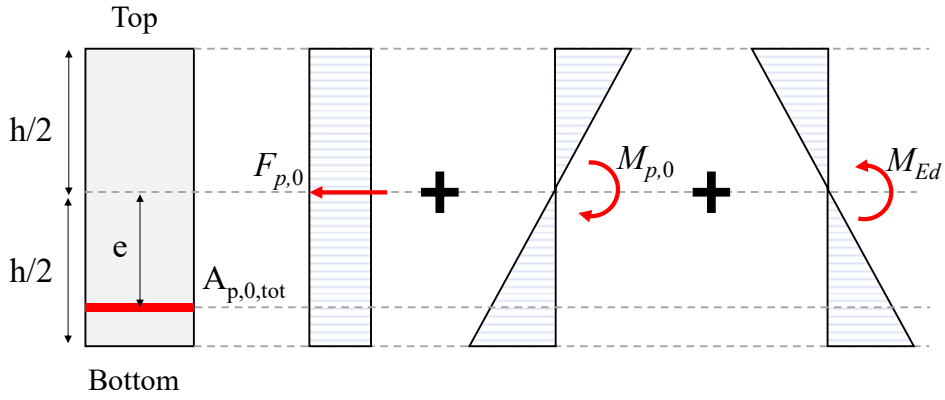

Figure 8-17 Principle of superimposition: sectional contributions due to (i) prestressing force, (ii) moment due to prestressing and eccentricity of strands, and (iii) acting bending moment.

For point A evaluation, the additional contribution provided by the concrete tensile strength, f_{ctm}, should be considered. In detail, the concrete stress at the bottom layer can be quantified through Eq. 8-69, by adding the contribution of the acting bending moment, M_{Ed}.

$$\sigma_{c,b} = -\frac{F_{p,0}}{A_i} - \frac{M_{p,0}}{I_i}\frac{h}{2} + \frac{M_{Ed}}{I_i}\frac{h}{2} \qquad 8\text{-}69$$

Thus, the corresponding bending moment at point A, M_A, at the achievement of a concrete stress at bottom layer, $\sigma_{c,b}$, equal to the concrete tensile resistance, f_{ctm}, is calculated by reversing Eq. 8-69, as reported in Eq. 8-70.

$$M_A = \frac{2I_i}{h}\left[f_{ctm} + \frac{F_{p,0}}{A_i} + \frac{M_{p,0}}{I_i}\frac{h}{2}\right] \qquad 8\text{-}70$$

Finally, once M_A is known, the related curvature, χ_A, and the longitudinal strain at mid-height of the effective shear depth, $\varepsilon_{x,A}$, can be estimated through Eq. 8-71 and Eq. 8-72, respectively.

$$\chi_A = \frac{M_A}{E_c I_i} \qquad 8\text{-}71$$

$$\varepsilon_{x,A} = -\frac{F_{p,0}}{E_c A_i} \qquad 8\text{-}72$$

On the contrary, the point B corresponds to the achievement of the proportional limit in the stress-strain relationship of prestressing strands ($\varepsilon_{pp,0;}\, f_{pp,0}$). It is worth noting that a

concrete linear behaviour is assumed. From the equilibrium condition of the concrete cross-section, Eq. 8-73 is derived.

$$\frac{1}{2} b x_{1,B} \varepsilon_c E_c = A_{p,0,tot} f_{pp,0} \tag{8-73}$$

Afterwards, by expressing ε_c through Eq. 8-58 based on strain compatibility, Eq. 8-73 becomes equal to Eq. 8-74:

$$\frac{1}{2} b E_c \Delta\varepsilon_{pp,0} x_{1,B}^2 + A_{p,0,tot} f_{pp,0} x_{1,B} - A_{p,0,tot} f_{pp,0} d_p = 0 \tag{8-74}$$

where $\Delta\varepsilon_{pp,0}$ is equal to the difference between the strain corresponding to the proportional limit, $\varepsilon_{pp,0}$, and the strain due to prestressing, $\varepsilon_{p,0}$. Once Eq. 8-74 is defined, the corresponding neutral axis, $x_{1,B}$, is calculated as expressed in Eq. 8-75.

$$x_{1,B} = \frac{A_{p,0,tot} f_{pp,0} \left(-1 + \sqrt{1 + \frac{2 b E_c \Delta\varepsilon_{pp,0} d_p}{A_{p,0,tot} f_{pp,0}}} \right)}{b E_c \Delta\varepsilon_{pp,0}} \tag{8-75}$$

Then, the bending moment at point B, $M_{1,B}$, the curvature, $\chi_{1,B}$, as well as the longitudinal strain at mid-height of the effective shear depth, $\varepsilon_{x,1,B}$, are calculated through Eqs. 8-76 to 8-78, respectively:

$$M_{1,B} = A_{p,0,tot} f_{pp,0} \left(d_p - \frac{x_{1,B}}{3} \right) \tag{8-76}$$

$$\chi_{1,B} = \frac{\varepsilon_c + \Delta\varepsilon_{pp,0}}{d_p} \tag{8-77}$$

$$\varepsilon_{x,1,B} = \frac{\varepsilon_c}{x_{1,B}} \left(z^* - x_{1,B} \right) = \Delta\varepsilon_{pp,0} \frac{\left(z^* - x_{1,B} \right)}{\left(d_p - x_{1,B} \right)} \tag{8-78}$$

where z^* is the equivalent shear depth, evaluated from the top concrete compressive layer, as shown in Figure 8-18 and as summarized in Eq. 8-79.

$$z^* = \frac{x}{2} + \frac{z}{2} = \frac{x}{4} + \frac{d_p}{2} \tag{8-79}$$

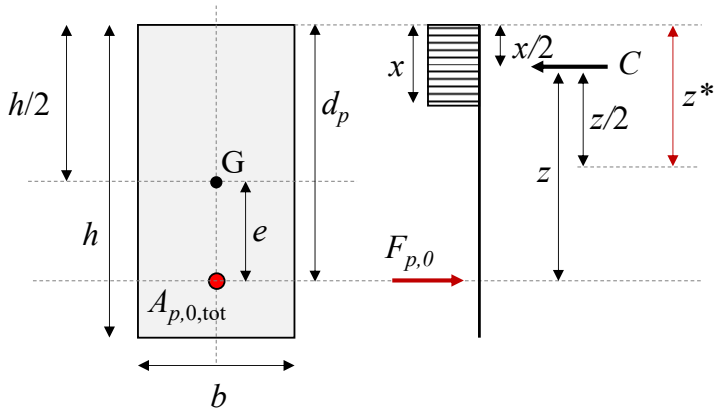

Figure 8-18 Geometrical definition of the equivalent shear depth, z^*.

The point C of the simplified moment-curvature diagram corresponds to the reaching of the yielding point in the simplified stress-strain relationship of prestressing strands ($\varepsilon_{py,0}$; $f_{py,0}$). It is worth noting that the same formulations provided for the point B are valid with the care of replacing the values $f_{pp,0}$ and $\varepsilon_{pp,0}$ with the new values ($\varepsilon_{py,0}$;$f_{py,0}$), respectively. For the sake of completeness, the expression of the bending moment, $M_{1,C}$, the related curvature, $\chi_{1,C}$, and the longitudinal strain at mid-height of the effective shear depth, $\varepsilon_{x,1,C}$, are reported in Eqs. 8-80 to 8-82, respectively.

$$M_{1,C} = A_{p,0,tot} f_{py,0} \left(d_p - \frac{x_{1,C}}{3} \right) \quad 8\text{-}80$$

$$\chi_{1,C} = \frac{\varepsilon_c + \Delta\varepsilon_{py,0}}{d_p} \quad 8\text{-}81$$

$$\varepsilon_{x,1,C} = \frac{\varepsilon_c}{x_{1,C}} \left(z^* - x_{1,C} \right) = \Delta\varepsilon_{py,0} \frac{\left(z^* - x_{1,C} \right)}{\left(d_p - x_{1,C} \right)} \quad 8\text{-}82$$

Finally, to completely characterize the simplified moment-curvature diagram for the Failure Case “1”, the point D, which corresponds to the reaching of the ultimate limit state in the simplified stress-strain relationship of prestressing strands ($\varepsilon_{pu,0}$;$f_{pu,0}$), needs to be estimated. Contrary to the assumption of concrete elastic behaviour at points B and C, the concrete strain at point D is assumed to be higher than the concrete strain at peak load, ε_{c0}, but lower than the compressive ultimate concrete strain, ε_{cu}. Indeed, the corresponding failure mode is attributed to the rupture of prestressing reinforcements. As a result, the neutral axis, $x_{1,D}$, is estimated based on the equilibrium conditions, as expressed in Eq. 8-83.

$$x_{1,D} = \frac{A_{p,0,tot} f_{pu,0}}{0.8 b f_{cm}} \quad 8\text{-}83$$

Thereafter, by adopting Eq. 8-58 for the quantification of ε_c, the bending moment at point D, $M_{1,D}$, is derived through Eq. 8-84, by assuming the elastic behaviour of concrete.

$$M_{1,D} = A_{p,0,tot} f_{pu,0} \left(d_p - \frac{x_{1,D}}{3} \right) \quad 8\text{-}84$$

The associated curvature, $\chi_{1,D}$, and the longitudinal strain at mid-height of the effective shear depth, $\varepsilon_{x,1,D}$, are, then, reported in Eqs. 8-85 to 8-86, respectively.

$$\chi_{1,D} = \frac{\varepsilon_c + \Delta\varepsilon_{pu,0}}{d_p} = \frac{\varepsilon_c + \left(\varepsilon_{pu,0} - \varepsilon_{p,0}\right)}{d_p} = \frac{\varepsilon_c}{x_{1,D}} \quad 8\text{-}85$$

$$\varepsilon_{x,1,D} = \Delta\varepsilon_{pu,0} \frac{\left(z^* - x_{1,D}\right)}{\left(d_p - x_{1,D}\right)} = \chi_{1,D} \left(z^* - x_{1,D}\right) \quad 8\text{-}86$$

8.6.1.5 Failure Case "2"

Hereafter, the analytical expressions, governing the Failure Case "2", are threated. The failure mode related to the analyzed failure case is characterized by the reaching of the concrete compressive ultimate strain with plasticized prestressing reinforcements.

As previously stated, points A' and A of the simplified moment-curvature diagram are characterized by the same analytical expressions of the Failure Case "1", therefore, detailed information can be found in the previous section.

Referring to point B, the effect induced by prestressing stress is considered for the strain compatibility, but it does not directly affect the ultimate bending moment value. First, the neutral axis is estimated through Eq. 8-87 based on the translational equilibrium.

$$x_{2,B} = \frac{A_{p,0,tot} f_{pp,0}}{0.8 b f_{cm}} \quad 8\text{-}87$$

Afterwards, a check on the concrete compressive strain is performed, as expressed in Eq. 8-88.

$$\varepsilon_c = \frac{x \Delta\varepsilon_{pp,0}}{\left(d_p - x_{2,B}\right)} = \frac{x\left(\varepsilon_{pp,0} - \varepsilon_{p,0}\right)}{\left(d_p - x_{2,B}\right)} \geq \left|\varepsilon_{c,0}\right| ? \quad 8\text{-}88$$

If the concrete compressive strain, ε_c, is lower than the concrete strain at the peak load, ε_{c0}, the translational equilibrium of the analyzed section can be evaluated by considering the concrete elastic response. Furthermore, assuming the strain compatibility relationship of Eq. 8-58, the neutral axis can be calculated according to Eq. 8-89.

$$\frac{1}{2}bE_c\Delta\varepsilon_{pp,0}x_{2,B}^2 + A_{p,0,tot}f_{pp,0}x_{2,B} - A_{p,0,tot}f_{pp,0}d_p = 0$$

$$x_{2,B} = \frac{A_{p,0,tot}f_{pp,0}\left(-1+\sqrt{1+\frac{2bE_c\Delta\varepsilon_{pp,0}d_p}{A_{p,0,tot}f_{pp,0}}}\right)}{bE_c\Delta\varepsilon_{pp,0}} \quad 8\text{-}89$$

As a result, the corresponding curvature, $\chi_{2,B}$, as well as the bending moment, $M_{2,B}$, and the longitudinal strain at mid-height of the effective shear depth, $\varepsilon_{x,2,B}$, resulted equal to Eq. 8-90 – Eq. 8-91, and Eq. 8-92, respectively.

$$\chi_{2,B} = \frac{\Delta\varepsilon_{pp,0}}{\left(d_p - x_{2,B}\right)} \quad 8\text{-}90$$

$$M_{2,B} = A_{p,0,tot}f_{pp,0}\left(d_p - \frac{x_{2,B}}{3}\right) \quad 8\text{-}91$$

$$\varepsilon_{x,2,B} = \frac{\varepsilon_c}{x_{2,B}}\left(z^* - x_{2,B}\right) = \Delta\varepsilon_{pp,0}\frac{\left(z^* - x_{2,B}\right)}{\left(d_p - x_{2,B}\right)} \quad 8\text{-}92$$

Conversely, if the condition in Eq. 8-88 is fulfilled, thus, the concrete compressive strain, ε_c, is higher than the concrete strain at the peak load, ε_{c0}, the neutral axis value to be adopted for the quantification of the curvature, bending moment and longitudinal strain is equal to the one previously estimated through Eq. 8-87. Moreover, the bending moment, $M_{2,B}$, can be calculated as expressed in Eq. 8-93.

$$M_{2,B} = A_{p,0,tot}f_{pp,0}\left(d_p - 0.4x_{2,B}\right) \quad 8\text{-}93$$

As stated for the point C of the Failure Case "1", it is worth noting that the same formulations provided for the point B are valid with care of replacing the values $f_{pp,0}$ and $\varepsilon_{pp,0}$ with the values $f_{py,0}$ and $\varepsilon_{py,0}$, respectively.

The point D corresponds to the reaching of the concrete compressive ultimate strain, ε_{cu}. This latter point is completely characterized once the related neutral axis, $x_{2,D}$, and the prestressing reinforcement strain, ε_p, are defined. To this end, the equilibrium condition can be written as in Eq. 8-94.

$$0.8f_c x_{2,D} = A_{p,0,tot}\left[f_{py,0} + E''_{p,0}\left(\varepsilon_p - \varepsilon_{p,0}\right)\right] \quad 8\text{-}94$$

Thereafter, by explicating ε_p through Eq. 8-58 and assuming a strand condition where the point *b* of the stress-strain relationship is overcome, the second-degree expression of the neutral axis, $x_{2,D}$, is derived, as expressed in Eq. 8-95:

$$0.8f_{cm}x_{2,D}^2 + A_{p,0,tot}\left[-f_{py,0} + E''_{p,0}\left(\varepsilon_{cu} + \Delta\varepsilon_{py,0}\right)\right] x_{2,D} - A_{p,0,tot}E''_{p,0}\varepsilon_{cu}d_p = 0 \quad \text{8-95}$$

where $f^*_{p,2,D}$ can be expressed as in Eq. 8-96.

$$f^*_{p,2,D} = \left[-f_{py,0} + E''_{p,0}\left(\varepsilon_{cu} - \Delta\varepsilon_{py,0}\right)\right] \quad \text{8-96}$$

Then, the neutral axis, $x_{2,D}$, is calculated according to Eq. 8-97 and the strain, ε_p, can be estimated through Eq. 8-58. Moreover, the expression of the bending moment at point D, $M_{2,D}$, the curvature, $\chi_{2,D}$, and the longitudinal strain at mid-height of the effective shear depth, $\varepsilon_{x,2,D}$, are reported in Eqs. 8-98 to 8-100, respectively.

$$x_{2,D} = \frac{-A_{p,0,tot}f^*_{p,2,D} + \sqrt{\left(A_{p,0,tot}f^*_{p,2,D}\right)^2 + 3.2bf_{cm}A_{p,0,tot}E''_{p,0}\varepsilon_{cu}d_p}}{1.6bf_{cm}} \quad \text{8-97}$$

$$M_{2,D} = A_{p,0,tot}\left(f_{py,0} + E''_{p,0}\left(\varepsilon_p - \varepsilon_{p,0}\right)\right)\left(d_p - 0.4x_{2,D}\right) \quad \text{8-98}$$

$$\chi_{2,D} = \frac{\varepsilon_{cu}}{x_{2,D}} \quad \text{8-99}$$

$$\varepsilon_{x,2,D} = \frac{\varepsilon_{cu}}{x_{2,D}}\left(z^* - x_{2,D}\right) \quad \text{8-100}$$

8.6.1.6 Failure Case "3"

The analytical expressions, governing the Failure Case "3", are reported in the following. This is characterized by the reaching of the concrete compressive ultimate strain with prestressing reinforcements in the elastic phase.

As for the Failure Case "2", points A' and A of the simplified moment-curvature diagram are identified through the analytical expressions reported in the Failure Case "1", therefore, detailed information can be found in the related section.

The neutral axis of point B, $x_{3,B}$, can be determined through Eqs. 8-101 to 8-103 under the following hypothesis:

- The concrete has reached the strain at peak load, ε_{c0};
- The prestressing reinforcements are in the elastic phase;
- The strain compatibility is ensured by Eq. 8-58.

$$\frac{1}{2}bf_{cm}x_{3,B} = A_{p,0,tot}\left[\varepsilon_{p,0} + \frac{\varepsilon_{c0}\left(d_p - x_{3,B}\right)}{x_{3,B}}\right] \quad 8\text{-}101$$

$$\frac{1}{2}bf_{cm}x_{3,B}^2 + \left[A_{p,0,tot}E_{p,0}\left(\varepsilon_{c0} - \varepsilon_{p,0}\right)\right]x_{3,B} - A_{p,0,tot}E_{p,0}\varepsilon_{c0}d_p = 0 \quad 8\text{-}102$$

$$x_{3,B} = \frac{-f_{p,3,B}^* + \sqrt{\left(f_{p,3,B}^*\right)^2 + 2bf_{cm}A_{p,0,tot}E_{p,0}\varepsilon_{c0}d_p}}{bf_{cm}} \quad 8\text{-}103$$

$$f_{p,3,B}^* = \left[A_{p,0,tot}E_p\left(\varepsilon_{c0} - \varepsilon_{p,0}\right)\right]$$

Once the neutral axis, $x_{3,B}$, is known, the prestressing reinforcement strain, ε_p, can be directly derived from the strain compatibility of Eq. 8-58, then, the corresponding prestressing reinforcement strength, f_p, is obtained through the SCPS-model. Afterwards, the bending moment, $M_{3,B}$, the curvature, $\chi_{3,B}$, and the longitudinal strain at mid-height of the effective shear depth, $\varepsilon_{x,3,B}$, are calculated by adopting Eq. 8-104 – Eq. 8-105 and Eq. 8-106, respectively.

$$M_{3,B} = A_{p,0,tot}f_p\left(d_p - \frac{x_{3,B}}{3}\right) \quad 8\text{-}104$$

$$\chi_{3,B} = \frac{\varepsilon_{c0}}{x_{3,B}} \quad 8\text{-}105$$

$$\varepsilon_{x,3,B} = \frac{\varepsilon_{c0}}{x_{3,B}}\left(z^* - x_{3,B}\right) \quad 8\text{-}106$$

The point C of the simplified moment-curvature diagram corresponds to the reaching of the concrete compressive ultimate strain. Similar expressions, illustrated for point B, can be adopted by replacing the concrete strain and strength at peak load, ε_{c0}, and, f_{cm}, with the concrete compressive ultimate strain and strength, ε_{cu}, and, f_{cm}.

In this case the equilibrium condition is reported in Eq. 8-107, and the following passages are the same of the previous case analyzed.

$$0.8bf_{cm}x_{3,B} = A_{p,0,tot}\left[\varepsilon_{p,0} + \frac{\varepsilon_{cu}\left(d_p - x_{3,B}\right)}{x_{3,B}}\right] \quad 8\text{-}107$$

Finally, since the concrete has already reached its ultimate condition at point C, it worth noting that points C and D coincide and, therefore, analogous analytical formulations can be adopted.

8.6.1.6.1 Simplified moment-curvature model validation: un-corroded scenario

The validation of the simplified moment-curvature diagram on experimental outcomes investigating the behaviour of un-corroded PC beams is presented. Both low and high prestressing level scenarios are reproduced to highlight the suitability and effectiveness of the proposed simplified approach.

From an experimental work in literature (Billet, 1953; Dong Lee, 2022), several scaled PC beams without transversal reinforcement were tested.

Hereafter, the specimens B5, B7, B9 and B12 were considered for the analytical model validation. The specimens had a rectangular cross-section, which geometrical features are reported in Table 8-2, and were reinforced with two types of steel strand, which mechanical properties are reported in Table 8-3. Furthermore, the specimens were characterized by different: (i) amount of prestressing reinforcements, $A_{p,0}$, (ii) initial effective stress in prestressed reinforcement at release, σ_p, and (iii) variable average concrete compressive strength, f_{cm}, as shown in Table 8-3. Specifically, all specimens were tested by adopting four-point bending tests with a shear span length of 914.4 mm, as highlighted in Figure 8-19(a).

Table 8-2 Test set-up and geometrical features, Billet (1953).

Specimen	b [mm]	h [mm]	d_p [mm]	Shear span [mm]
B5	154.90	306.30	237.00	914.40
B7	155.70	308.10	205.50	914.40
B9	154.90	306.30	234.40	914.40
B12	155.70	308.10	211.60	914.40

Table 8-3 Mechanical properties of B5, B7, B9, and B12 specimens, Billet (1953).

Specimen	f_{cm} [MPa]	$A_{p,0}$ [mm^2]	$f_{py,0}$ [MPa]	$f_{pu,0}$ [MPa]	σ_p [MPa]
B5	39.00	160.60	1538.00	1697.00	823.40
B7	40.80	301.30	1538.00	1697.00	815.20
B9	43.70	151.00	1428.00	1655.00	140.70
B12	38.30	283.20	1428.00	1655.00	139.30

The comparisons between experimental outcomes and analytical predictions in terms of full moment-curvature response are reported in Figure 8-19(b) to Figure 8-19(e) for specimen B5, B7, B9 and B12, respectively. A good agreement with the experimental tests is observed, where the moment-curvature diagrams for all specimens are well reproduced and predicted.

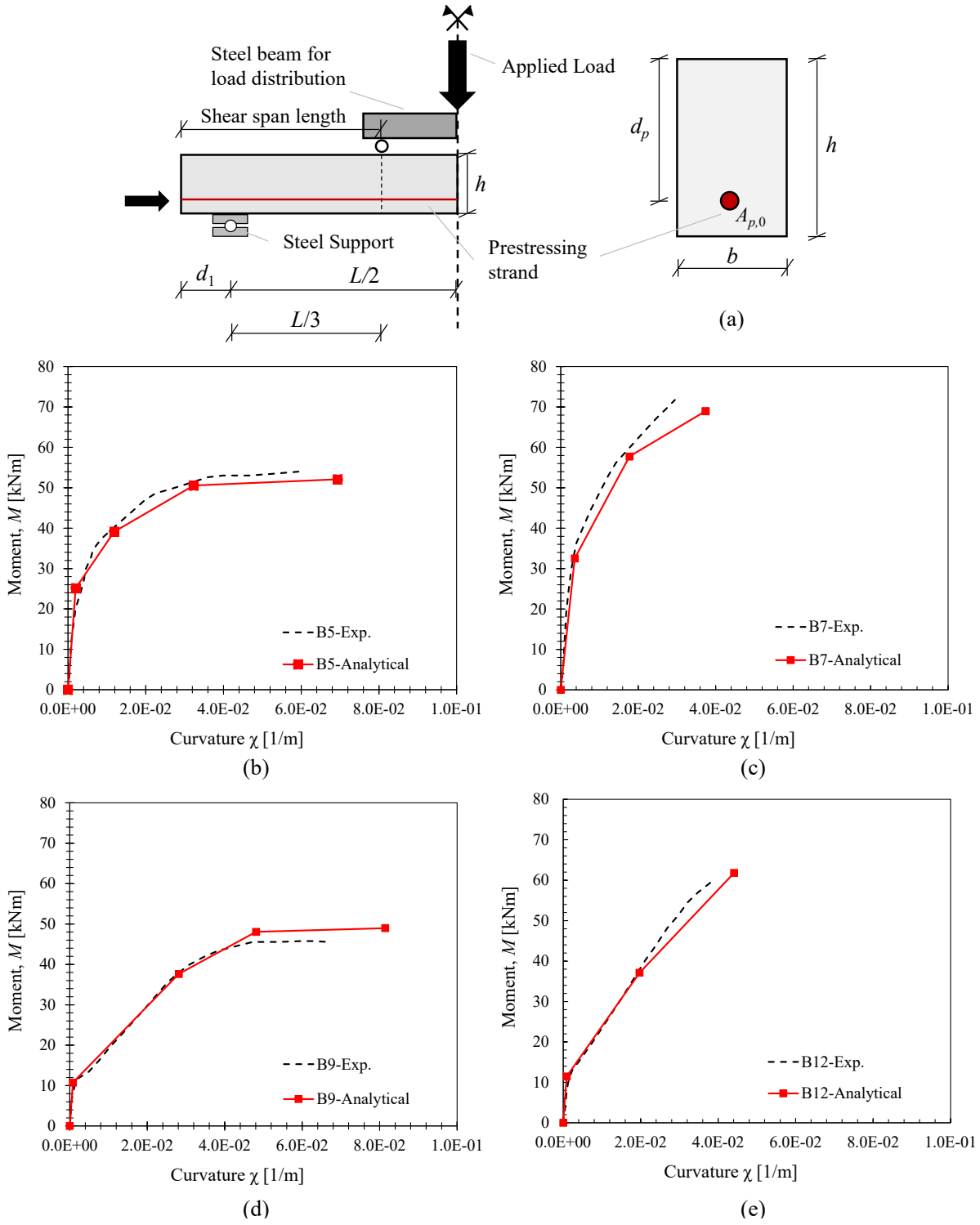

Figure 8-19 Simplified moment-curvature diagram validation on experimental outcomes available in literature: (a) test set-up from Billet (1953), (b)-(e) specimens B5 to B12.

8.6.1.7 Analytical approach modification due to corrosion

The simplified moment-curvature diagram for prestressed sections in the case of corroded strands is discussed. First, the selection of the appropriate Failure Case should be determined as a function of the prestressing reinforcement mechanical properties reduction, $\varepsilon_{pu,corr}$ and $f_{pu,corr}$, which are predicted by using the SCPS-model. Specifically, due to corrosion, the reduced mechanical prestressing reinforcements ratio, $\omega_{p,corr}$, is calculated through Eq. 8-108.

$$\omega_{p,corr} = \frac{A_{p,0} f_{pu,corr}}{f_{cm} b d_p} \tag{8-108}$$

Second, the critical mechanical reinforcement ratios, $\omega_{1,corr}$ and $\omega_{3,corr}$, also decrease as the corrosion level increases, according to Eq. 8-109 and Eq. 8-110, respectively:

$$\omega_{1,corr} = \frac{\lambda \varepsilon_{cu}}{\left(\varepsilon_{pu,corr} - \varepsilon_{p,corr} + \varepsilon_{cu}\right)} \frac{f_{pu,corr}}{f_{py,corr}} \tag{8-109}$$

$$\omega_{3,corr} = \frac{\lambda \varepsilon_{cu}}{\left(\varepsilon_{py,corr} - \varepsilon_{p,corr} + \varepsilon_{cu}\right)} \tag{8-110}$$

where $\varepsilon_{p,corr}$ is the corroded strain due to prestressing evaluated as the ratio between $\sigma_{p,corr}(t)$, which is the residual prestressing stress calculated as expressed in Eq. 8-54, and the modulus of elasticity $E_{p,0}$.

Finally, the updated limits for the selection of the appropriate failure case are:

- If $\omega_{p,corr} \leq \omega_{1,corr}$, the Failure Case 1 is expected;
- If $\omega_{1,corr} \leq \omega_{p,corr} \leq \omega_{3,corr}$, the Failure Case 2 is expected;
- If $\omega_{p,corr} \geq \omega_{3,corr}$, the Failure Case 3 is expected.

It is worth noting that the Failure Case "3" can be neglected in the case of corrosion. Indeed, the corrosion effects mainly promote the transition from Failure Case "2" to Failure Case "1" due to a significant reduction in the mechanical properties of the corroded strands.

For a low corrosion level, LV-I, the stress-strain relationship of corroded prestressing strands is characterized by a residual hardening phase. Therefore, the expected failure mode is related to the reaching of the concrete compressive ultimate strain. If $\omega_{p,corr}$ is included between $\omega_{1,corr}$ and $\omega_{3,corr}$, the analytical model previously proposed for the Failure Case "2", in the case of un-corroded scenario, can be adopted by replacing the un-corroded mechanical properties of prestressing reinforcements with the reduced ones. On the contrary, if $\omega_{p,corr}$ is lower than $\omega_{1,corr}$ the analytical expressions, reported hereafter for intermediate (LV-II) and high (LV-III) corrosion levels, should be used.

For intermediate and high corrosion levels, a non-ductile behaviour of corroded prestressing strands characterized by a bi-linear or an elastic residual stress-strain response is defined, respectively. Therefore, the expected failure mode is associated to the strands rupture.

The simplified moment-curvature diagram for the intermediate corrosion level is defined by the following main points:

1. Point A': reaching of the full prestressing stress, resulting in the development of the negative deflection at beam mid-span;
2. Point A: reaching of the tensile concrete cracking;
3. Point B: reaching of the proportional limit in the stress-strain relationship of prestressing strands ($\varepsilon_{pp,0;}f_{pp,0}$);
4. Point C coincident with Point D: reaching of the ultimate point in the stress-strain relationship of corroded prestressing strands ($\varepsilon_{pu,corr;}$ $f_{pu,corr}$).

In the case of the high corrosion level, the main points of the simplified moment-curvature diagram remain the same, with the only exception that the ultimate point in the stress-strain relationship of corroded prestressing strands ($\varepsilon_{pu,corr;}$ $f_{pu,corr}$) is reached at point B instead of point C. Therefore, the analytical expressions of points C and D can be neglected, since these later points are assumed to be coincident with point B.

For the sake of completeness, the analytical expressions for the definition of the points A', A, B, and C of the simplified moment-curvature diagram for corroded prestressed sections are reported.

- Point A':

The curvature, $\chi_{A',corr}$, is estimated through Eq. 8-111 by assuming a sectional linear-elastic behaviour.

$$\chi_{A',corr} = -\frac{F_{p,0,corr}e}{E_c I_i} = -\frac{\left(A_{p,0,tot}\sigma_{p,corr}(t)\right)e}{E_c I_i} \qquad 8\text{-}111$$

The corresponding bending moment, $M_{A',corr}$, is assumed to be null and the longitudinal strain at mid-height of the effective shear depth, $\varepsilon_{x,A',corr}$, is evaluated through Eq. 8-112.

$$\varepsilon_{x,A',corr} = -\frac{F_{p,0,corr}}{E_c A_i} \qquad 8\text{-}112$$

- Point A:

The bending moment, $M_{A,corr}$, the curvature, $\chi_{A,corr}$, and the longitudinal strain at mid-height of the effective shear depth, $\varepsilon_{x,A,corr}$, are calculated as expressed in Eq. 8-113 – Eq. 8-114 and Eq. 8-115, respectively.

$$M_{A,corr} = \frac{2I_i}{h}\left[f_{ctm} + \frac{F_{p,0,corr}}{A_i} - \frac{F_{p,0,corr}e}{I_i}\frac{h}{2}\right] = \frac{2I_i}{h}\left[f_{ctm} + \frac{F_{p,0,corr}}{A_i} - \frac{M_{p,0,corr}}{I_i}\frac{h}{2}\right] \quad 8\text{-}113$$

$$\chi_{A,corr} = \frac{M_{A,corr}}{E_c I_i} \quad 8\text{-}114$$

$$\varepsilon_{x,A,corr} = -\frac{F_{p,0,corr}}{E_c A_i} \quad 8\text{-}115$$

- Point B:

The neutral axis, $x_{B,corr}$, is evaluated based on equilibrium conditions according to Eq. 8-116. Afterwards, the bending moment, $M_{B,corr}$, the curvature, $\chi_{B,corr}$, and the longitudinal strain at mid-height of the effective shear depth, $\varepsilon_{x,B,corr}$, are calculated as expressed in Eq. 8-117 – Eq. 8-118 and Eq. 8-119, respectively. Specifically, $\Delta\varepsilon_{pp,0}$ is defined as the difference between $\varepsilon_{pp,0}$ and $\varepsilon_{p,0}$.

$$x_{B,corr} = \frac{A_{p,0,tot} f_{pp,0}\left(-1 + \sqrt{1 + \frac{2bE_c \Delta\varepsilon_{pp,0} d_p}{A_{p,0,tot} f_{pp,0}}}\right)}{bE_c \Delta\varepsilon_{pp,0}} \quad 8\text{-}116$$

$$M_{B,corr} = A_{p,0,tot} f_{pp,0}\left(d_p - \frac{x_{B,corr}}{3}\right) \quad 8\text{-}117$$

$$\chi_{B,corr} = \frac{\varepsilon_c + \Delta\varepsilon_{pp,0}}{d_p} \quad 8\text{-}118$$

$$\varepsilon_{x,B,corr} = \frac{\varepsilon_c}{x_{B,corr}}\left(z^* - x_{B,corr}\right) = \Delta\varepsilon_{pp,0}\frac{\left(z^* - x_{B,corr}\right)}{\left(d_p - x_{B,corr}\right)} \quad 8\text{-}119$$

- Point C (severe corrosion) and point B (high corrosion)

Assuming the concrete elastic behaviour, Point C and point B for the intermediate and high corrosion scenarios, respectively, correspond to the achievement of the corroded strands ultimate mechanical properties ($\varepsilon_{pu,corr}$; $f_{pu,corr}$), resulting in strands rupture. In this context, The neutral axis, $x_{C,corr}$ ($x_{B,corr}$), is evaluated based on equilibrium conditions according to Eq. 8-120, whereas the bending moment, $M_{C,corr}$ ($M_{B,corr}$), the curvature, $\chi_{C,corr}$ ($\chi_{B,corr}$), and the longitudinal strain at mid-height of the effective shear depth, $\varepsilon_{x,C,corr}$ ($\varepsilon_{x,B,corr}$), are calculated as expressed in Eq. 8-121 – Eq. 8-122 and Eq. 8-123, respectively. The factor $\Delta\varepsilon_{pu,corr}$ is defined as the difference between $\varepsilon_{pu,corr}$ and $\varepsilon_{p,0}$.

$$x_{C,corr} = x_{B,corr} = \frac{A_{p,0,tot} f_{pu,corr} \left(-1 + \sqrt{1 + \frac{2bE_c \Delta\varepsilon_{pu,corr} d_p}{A_{p,0,tot} f_{pu,corr}}} \right)}{bE_c \Delta\varepsilon_{pu,corr}} \quad 8\text{-}120$$

$$M_{C,corr} = M_{B,corr} = A_{p,0,tot} f_{pu,corr} \left(d_p - \frac{x_{C,corr}}{3} \right) \quad 8\text{-}121$$

$$\chi_{C,corr} = \chi_{B,corr} = \frac{\varepsilon_c + \Delta\varepsilon_{pu,corr}}{d_p} \quad 8\text{-}122$$

$$\varepsilon_{x,C,corr} = \varepsilon_{x,B,corr} = \frac{\varepsilon_c}{x_{C,corr}} \left(z^* - x_{C,corr} \right) = \Delta\varepsilon_{pu,corr} \frac{\left(z^* - x_{C,corr} \right)}{\left(d_p - x_{C,corr} \right)} \quad 8\text{-}123$$

For the sake of clarity, Figure 8-20 and Figure 8-21 show the reduced moment-curvature diagrams and the longitudinal strain at mid-height of the effective shear depth trends, $\varepsilon_{x,corr}$, for the several corrosion levels considered. In detail, Figure 8-20(a) reports the M-χ responses, where the reduction of both ultimate moment and curvature, as well as cracking moment, is observed; whereas Figure 8-20(b) shows both strand and concrete strains at failure, where it is evident the failure mode transition from concrete crushing to steel fracture with increasing corrosion level. It is worth noting that in the following calculations the equivalent shear depth, z^*, is assumed for simplicity equal to $0.9d_p$ as suggested by the Model Code 2010.

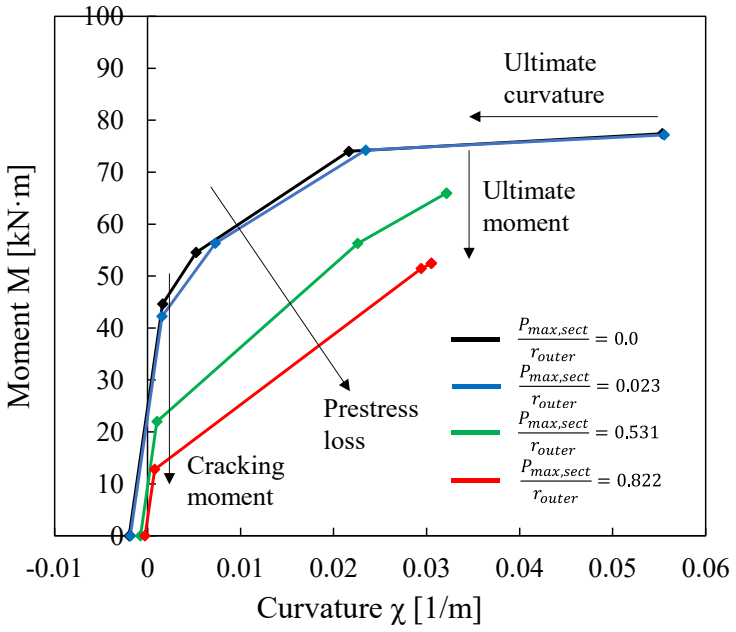

(a)

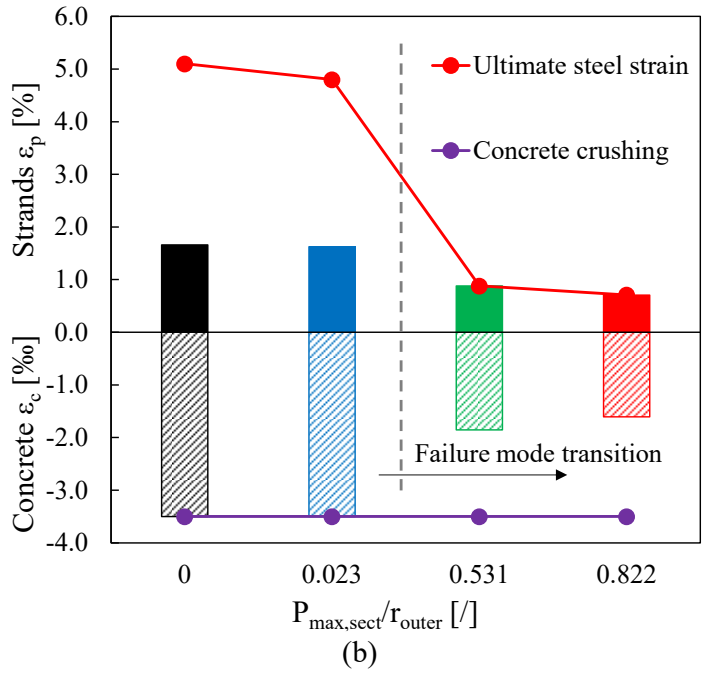

Figure 8-20 Simplified moment-curvature diagrams for corroded and un-corroded scenarios: (a) M-χ responses, and (b) strands and concrete strains vs corrosion levels.

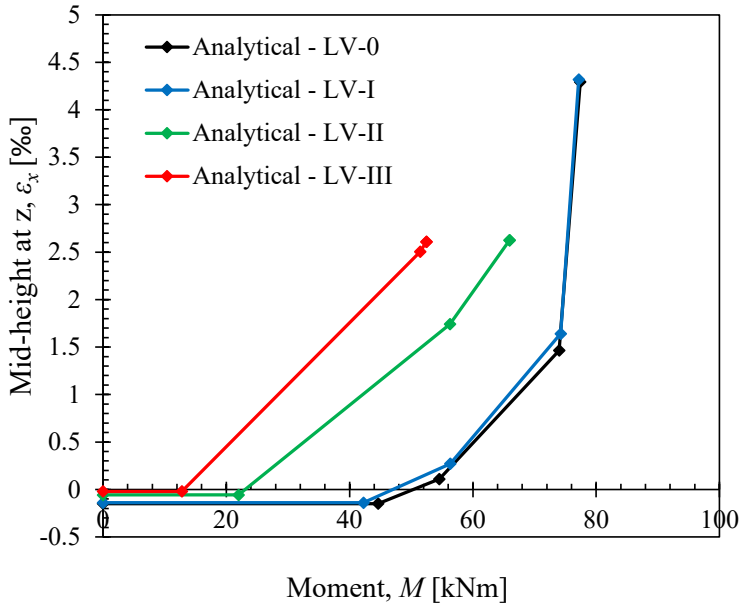

Figure 8-21 Longitudinal strain at mid-height of the effective shear depth trend for corroded and un-corroded scenarios.

In the context of the different corrosion levels, the reduction in terms of cracking and ultimate moments is shown in Figure 8-22, together with the prestressing level reduction in the case of splitting failure mode. A considerable reduction of ultimate (cracking) moment is observed ranging from 77.4 (44.6) kNm of LV-0 to 52.5 (12.8) kNm of LV-III, and of prestress level, especially from LV-I to LV-II and III.

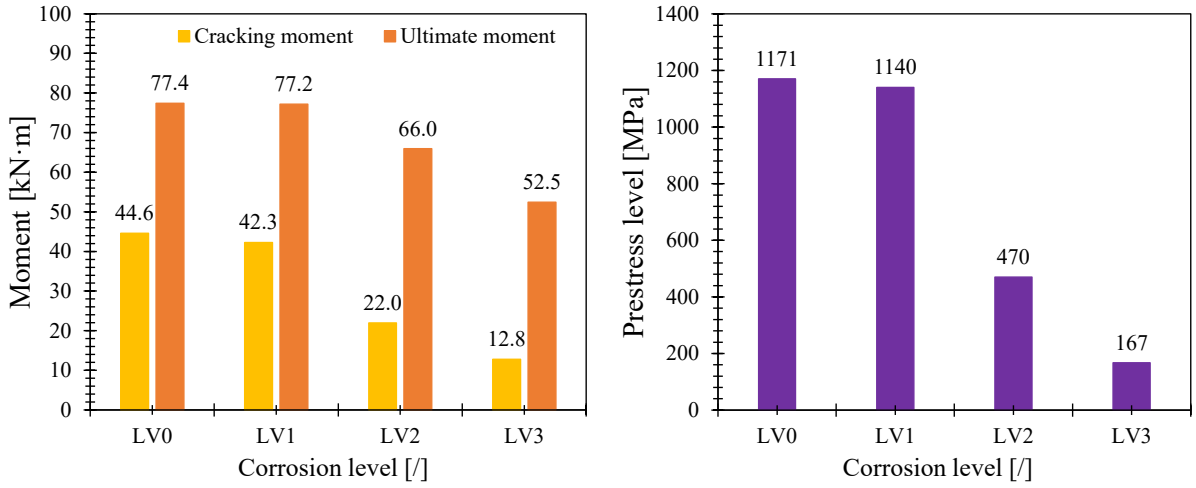

Figure 8-22 (a) Ultimate moment and cracking moment reduction, and (b) prestress level reduction for the different corrosion scenarios considered.

8.7 Calculation of residual shear capacity

Although shear resistance plays a crucial role in the bearing capacity of corroded existing structures, a lack of validated analytical models addressing the prediction of the residual shear capacity of corroded existing PC beams with and without transversal reinforcement is available in the scientific literature.

8.7.1 Assessment of PC elements without stirrups: a new proposal

According to the Model Code 2010 (Ceb-Fip, 2013), the shear resistance of un-corroded PC elements without shear reinforcement, V_{Rd}, is evaluated by quantifying the concrete contribution, $V_{Rd,c}$, as expressed in Eq. 8-124:

$$V_{Rd} = V_{Rd,c} = k_v \frac{\sqrt{f_{ck}}}{\gamma_c} bz \qquad 8\text{-}124$$

where γ_c is the concrete partial safety factor, b is the beam width, f_{ck} is the concrete characteristic compressive strength, z is the overall effective shear depth (internal level arm), and k_v is a crucial coefficient dependent on the longitudinal strain at mid-height of the effective shear depth, ε_x. For the sake of clarity, two approximation levels, denoted as level I and level II, are defined in the Model Code 2010 for determining the shear resistance of PC members without shear reinforcement. Moreover, assessing existing PC structures, the partial safety factor γ_c can be set equal to 1.0, whereas the concrete characteristic compressive strength, f_{ck}, can be assumed equal to the average concrete compressive strength, f_{cm}.

In detail, the effective shear depth, z, is evaluated through Eq. 8-125:

$$z = \frac{z_s^2 A_{s,0} + z_p^2 n_{strands} A_{p,0}}{z_s A_{s,0} + z_p n_{strands} A_{p,0}} \qquad 8\text{-}125$$

where z_s and z_p stand for the distances between the centreline of the compressive chord and the longitudinal reinforcement and strand axes, respectively, whereas the longitudinal strain at mid-height of the effective shear depth, ε_x, is calculated according to Eq. 8-126:

$$\varepsilon_x = \frac{\left(\frac{M_{Ed}}{z} + V_{Ed} + N_{Ed} \frac{\left(z_p - e\right)}{z} \right)}{2\left(\frac{z_s}{z} E_{s,0} A_{s,0} + \frac{z_p}{z} E_{p,0} n_{strands} A_{p,0} \right)} \qquad 8\text{-}126$$

where M_{Ed}, V_{Ed} and N_{Ed} denote the acting bending moment, the shear force and the normal force (axial force), respectively. In the absence of longitudinal reinforcement, $A_{s,0}$, Eq. 8-126 can be further simplified, as expressed in Eq. 8-127.

$$\varepsilon_x = \frac{\left(\frac{M_{Ed}}{z} + V_{Ed} + N_{Ed} \frac{\left(z_p - e\right)}{z} \right)}{2\frac{z_p}{z} E_{p,0} n_{strands} A_{p,0}} = \frac{\left(\frac{M_{Ed}}{z} + V_{Ed} + N_{Ed} \frac{\left(z_p - e\right)}{z} \right)}{2E_{p,0} n_{strands} A_{p,0}} \qquad 8\text{-}127$$

It is worth noting that a lower and upper boundaries equal to 0.0 and 0.003 for the parameter ε_x are provided by the Model Code 2010.

Once the coefficient ε_x is known, the parameter k_v is subsequently determined according to Eq. 8-128 and Eq. 8-129 for the Model Code 2010 level I and level II of approximation (*LoA*), respectively:

$$k_v = \frac{180}{1000 + 1.25z} \qquad 8\text{-}128$$

$$k_v = \frac{0.4}{1 + 1500\varepsilon_x} \frac{1300}{1000 + k_{dg} z} \qquad 8\text{-}129$$

where the coefficient k_{dg} can be set equal to 1.0 by providing that the size of the maximum aggregate particles is not less than 16 mm.

To account for corrosion effects, the present *Thesis* proposes modifications to the Model Code 2010 level II of approximation analytical expression for evaluating the residual shear capacity, $V_{Rd,corr}$, of corroded PC beams without shear reinforcement. According to the proposed model, the following assumptions are introduced for the estimation of $V_{Rd,corr}$:

- Adoption of the un-corroded cross-sectional area of prestressing reinforcement, $A_{p,0}$, to be consistent with the SCPS-model assumption.
- Estimation of a reduced axial force, $N_{Ed,corr}$, which corresponds to a reduced prestressing force, $F_{p,corr}(t)$, calculated through Eq. 8-130 as the product between $A_{p,0}$ and the residual prestressing stress, $\sigma_{p,corr}(t)$.

$$N_{Ed,corr} = -F_{p,corr}(t) = \sigma_{p,corr}(t) n_{strand} A_{p,0} \qquad 8\text{-}130$$

- Evaluation of the modified longitudinal strain at mid-height of the effective shear depth, $\varepsilon_{x,corr}$, by adopting the expressions previously defined in paragraph 8.6. In detail, the sectional $\varepsilon_{x,corr}$ values are derived from the application of the simplified moment-curvature approach, which outcomes are obtained as a function of: (i) the residual mechanical properties of corroded prestressing

strands – evaluated by adopting the SCPS-model –, (ii) the reduced prestressing force, $F_{p,corr}(t)$ – evaluated through Eq. 8-130 –, and (iii) the sectional acting bending moment, M_{Ed}.

- Introduction of an amplification factor $(1+\beta)$ applied to the modified longitudinal strain at mid-height of the effective shear depth, $\varepsilon_{x,corr}$, in order to consider the shifting of moment diagram and the shear demand, as expressed by Eq. 8-131and shown in Figure 8-23.

$$\varepsilon_{x,corr}^{MV} = \varepsilon_{x,corr}\left(1+\beta\right) = \varepsilon_{x,corr}\left[1+\frac{V_{Ed}}{M_{Ed}}\frac{z}{2}\left(\cot g\left(\theta\right)+\cot g\left(\alpha\right)\right)\right] \qquad 8\text{-}131$$

Since for the analyzed PC beams no transversal reinforcements were provided, $\theta=45°$ and $\cot g(\alpha)=0.0$ are assumed.

To the author best knowledge, the analytical approach proposed by the Model Code 2010 level II of approximation is the only model available to date in the scientific literature for the same purpose. Therefore, this latter analytical procedure – defined for un-corroded PC members – is modified for evaluating the residual shear capacity, $V_{Rd,corr}$, of corroded PC elements without shear reinforcement. To this end, the longitudinal strain at mid-height of the effective shear depth, $\varepsilon_{x,corr}$, that changes due to corrosion process, is calculated with Eq. 8-132, where corrosion effects are introduced via:

- A reduced cross-sectional area of longitudinal reinforcement, $A_{s,corr}$, and prestressing strands, $A_{p,corr}$, respectively;
- A reduced axial force, $N_{Ed,red}$, which is evaluated through Eq. 8-133 as the product between the corroded area of prestressing reinforcements and the residual prestressing stress, $\sigma_p(t)$, considering the losses induced by (a) elastic contraction, (b) releasing of strands, (c) creep, and (d) shrinkage effects.

$$\varepsilon_{x,corr} = \frac{\left(\frac{M_{Ed}}{z}+V_{Ed}+N_{Ed,red}\frac{\left(z_p-e\right)}{z}\right)}{2\left(\frac{z_s}{z}E_{s,0}A_{s,corr}+\frac{z_p}{z}E_{p,0}n_{strands}A_{p,corr}\right)} \qquad 8\text{-}132$$

$$N_{Ed,red} = \sigma_p\left(t\right)n_{strand}A_{p,corr} \qquad 8\text{-}133$$

A comparison between the longitudinal strains at mid-height of the effective shear depth, $\varepsilon_{x,corr}$, evaluated by considering Eq. 8-131 and Eq. 8-132 is shown in Figure 8-23 as a function of the bending moment for the beams PBN3P1 (black lines – un-corroded scenario) and PB3P11 (red lines – corroded scenario). Moreover, Figure 8-23 is also useful to highlight the effect associated with the additional contribution provided by the amplification factor $(1+\beta)$ to the estimation of longitudinal strain at mid-height of the effective shear depth, $\varepsilon_{x,corr}^{MV}$, of the proposed approach. For the un-corroded scenario, the positive strains result similar for both approaches until the event C, where the strands' yielding starts. Conversely, for corroded members, the proposed approach returns lower strains if compared to the modified MC 2010 approach.

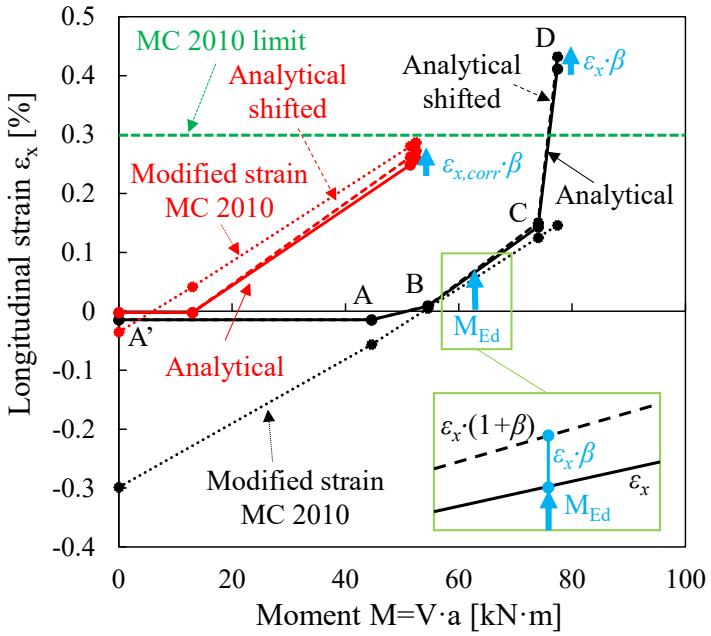

Figure 8-23 Comparison between longitudinal strains at mid-height of the effective shear depth for corroded and un-corroded scenarios.

To determine the reliability and accuracy of the two analytical approaches, a validation is performed in paragraph 8.8 by comparing the experimental outcomes and the analytical predictions of the previously investigated naturally corroded PC beams without transversal reinforcement in terms of observed failure mode and ultimate load at failure, $P_{failure}$.

8.7.1.1 Check on shear capacity at beam edges

The sectional shear resistance of the PC beam is evaluated along its overall length by adopting the expression provided in Eq. 8-124. In addition, the Eurocode 2 (CEN-EC2, 2004) provides the expression reported in Eq. 8-134 for predicting the residual shear strength, $V_{Rd,c,end}$, which should be compared to the resistant contribution, $V_{Rd,c}$, estimated through Eq. 8-124:

$$V_{Rd,c,end} = \frac{Ib}{S}\sqrt{f_{ctm}^2 + \alpha_I \sigma_{cp} f_{ctm}} \quad 8\text{-}134$$

where:

- f_{ctm} is evaluated according to the Model Code 2010 provisions through Eq. 8-57;
- b is the beam cross-section width;
- S and I are respectively the first and the second moment of inertia of the rectangular cross-section and they are evaluated according to Eq. 8-135 and Eq. 8-136, respectively;

$$S = \frac{bh^2}{6} \quad 8\text{-}135$$

$$I = \frac{bh^3}{12} \quad 8\text{-}136$$

- σ_{cp} is the compressive stress due to prestressing force contribution and it is estimated as reported in Eq.8-137 by assuming $F_{p,corr}$ as expressed in Eq. 8-55;

$$\sigma_{cp} = \frac{N_{Ed,corr}}{A_c} = \frac{F_{p,corr}(t)}{A_c} = \frac{\sigma_{p,corr}(t) n_{strand} A_{p,0}}{A_c} \quad 8\text{-}137$$

- α_I is the coefficient that identifies the effect related to prestressing force transmission in pre-tensioned PC elements. The latter is sectionally evaluated according to Eq.8-138 as the ratio between the abscissa of the analyzed section with respect to the beam edge, L_x, and the corroded transmission length, $L_{t,corr}$, previously estimated through Eq. 8-47.

$$\alpha_I = \frac{L_x}{L_{t,corr}} \quad 8\text{-}138$$

This latter expression is valid for the un-cracked PC beam zones, where the tensile stress is lower than $f_{ctk,0.05}/\gamma_c$. In those zones, it is recommended that the shear resistance is limited to the reaching of the concrete tensile stress. Therefore, for the beam sections where the stress allows the application of Eq. 8-134, the residual shear capacity is assumed equal to the minimum value between the shear resistance $V_{Rd,c,corr}$ and $V_{Rd,c,end}$.

8.8 Model validation

The un-corroded and corroded PC beams without transversal reinforcement investigated in the present *Thesis* were adopted to validate the proposed analytical approach. To this end, the procedure depicted in the flowchart of Figure 8-1 is considered.

The comparison between experimental outcomes and analytical predictions in terms of both (i) failure mode and (ii) ultimate load capacity is reported in Table 8-4. In this context, the effectiveness of the proposed analytical approach is further verified through the comparison with the analytical predictions obtained by adopting the modified Model Code 2010 approach, as shown in Table 8-5. It is worth noting that the shear failure of the investigated PC beam is estimated at a critical section with distance d_p from supports or applied loads.

Based on the obtained results, it is possible to state that:

- The proposed analytical model can successfully predict the experimental failure mode of both corroded and un-corroded PC beams, previously recorded during three- and four-point bending tests.
- The model accuracy and the applicability of the proposed approach is determined through the experimental versus analytical ultimate failure load ratio, $P_{failure}/P_{failure,an}$. As reported in Table 8-4, all the analytical predictions underestimated the experimental ultimate load, providing that the adoption of the proposed approach results in the conservative assessment of the residual flexural and shear load carrying capacity of corroded PC beams without transversal reinforcement. To support the statement, the mean value, the standard deviation, and the coefficient of variation, CV, of the ratio $P_{failure}/P_{failure,an}$ of un-corroded and corroded PC beams result equal to 1.29, 0.17, and 12.87%, respectively. Considering the predicted behaviour of corroded PC beams only, the obtained statistical parameters become equal to 1.33, 0.17, and 12.51%, respectively.
- Considering the modified Model Code 2010 proposal, the failure mode of the investigated corroded and un-corroded PC beams is correctly predicted. Referring to the ultimate failure load predictions, a significant underestimation of experimental outcomes is observed. In detail, the over-conservative outcomes are confirmed by the mean value, the standard deviation, and the coefficient of variation, CV, of the ratio $P_{failure}/P_{failure,an}$ of un-corroded and

corroded PC beams, which result equal to 1.58, 0.31, and 19.38%, as reported in Table 8-5.

- Finally, the effectiveness of the proposed analytical approach for the prediction of the shear failure mode of corroded PC beams, is additionally confirmed by the modelling uncertainties given by current guidelines in the case of shear failure mode prediction of un-corroded members. In this context, the Netherland guidelines for nonlinear finite element analysis of concrete structures, (Belletti et al., 2017), pointed out that the shear failure mode of un-corroded members is the most difficult failure mode to be predicted due to the complex nature of the involved mechanisms. Referring to the latter modelling uncertainties, a mean value, and a coefficient of variation equal to 1.39 and 0.10 were provided, respectively. Although the proposed analytical model additionally considers corrosion effects, the model uncertainties (1.33 and 0.17), reported in Table 8-4, are in line with the guidelines' provisions in the case of NLFE predictions of un-corroded members, (Belletti et al., 2017). However, it is worth noting that, due to insufficient references concerning a similar subject, it is difficult to compare and verify the obtained results. Therefore, additional experimental and analytical studies are needed on corroded PC members to further validate and calibrate the proposed analytical approach.

Finally, Figure 8-25-Figure 8-26, Figure 8-27, Figure 8-28, and Figure 8-29 highlight the flexural and shear analytical predictions for un-corroded beams PBN3P1 and PBN4P2, beam PB3P11 failing in bending, beam PB4P6 failing in Shear I mode, and beam PB4P7 failing in Shear II mode, respectively. As it is visible, the analytical approach correctly reproduces the experimental failure mode of the investigated PC beams and the assumption of a critical shear section at a distance d (d=d_p=250 mm) from the applied load is in good agreement with the recorded experimental outcomes. In fact, the location of the critical shear section at a distance d for un-corroded RC beams without transverse reinforcement with pinned supports under point loads was already noticed by Khuntia & Stojadinovic (2001), as shown in Figure 8-24.

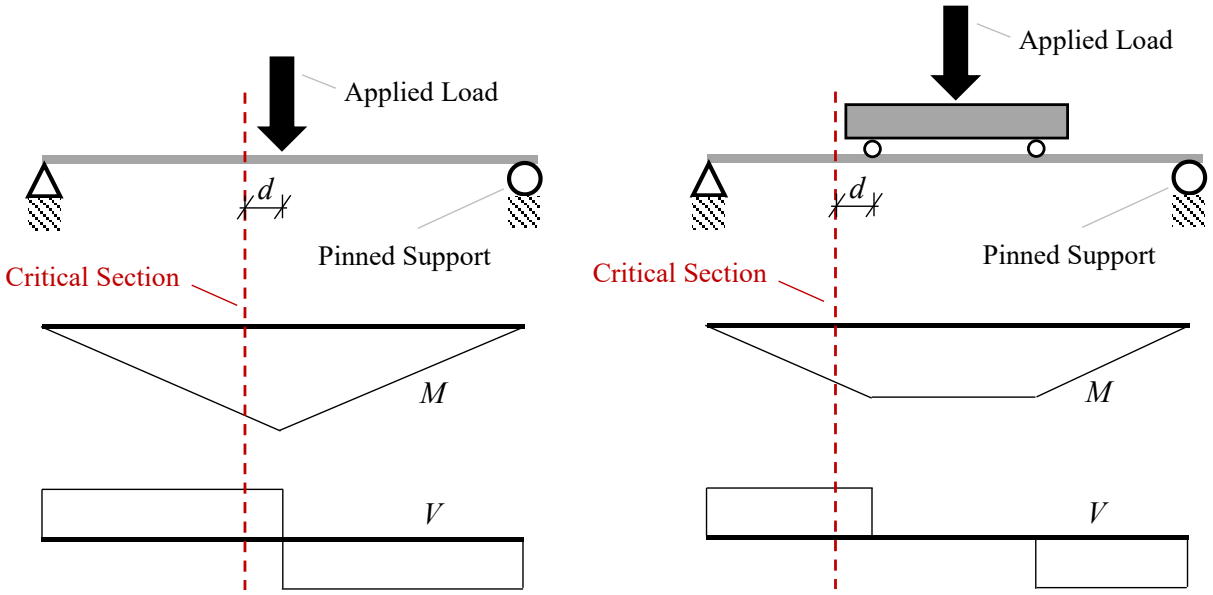

Figure 8-24 Location of critical section for beams with pinned and fixed supports under point and uniform loading.

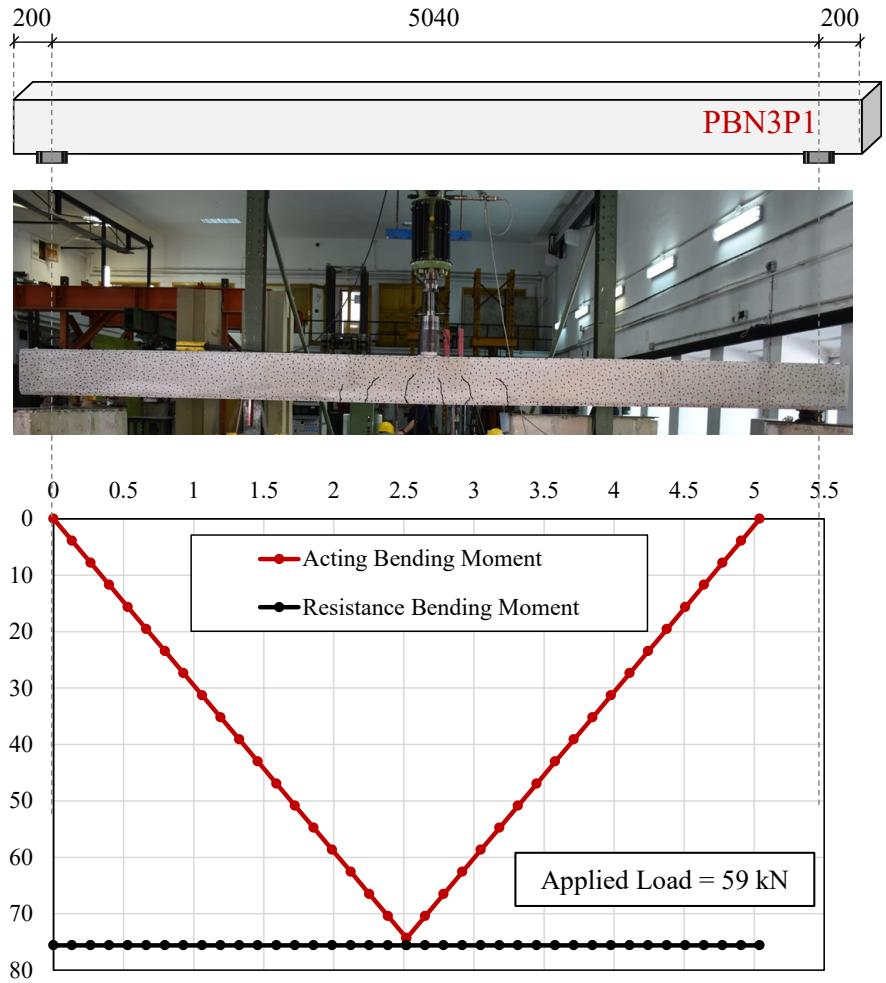

Figure 8-25 Failure mode and analytical prediction for the un-corroded beam PBN3P1.

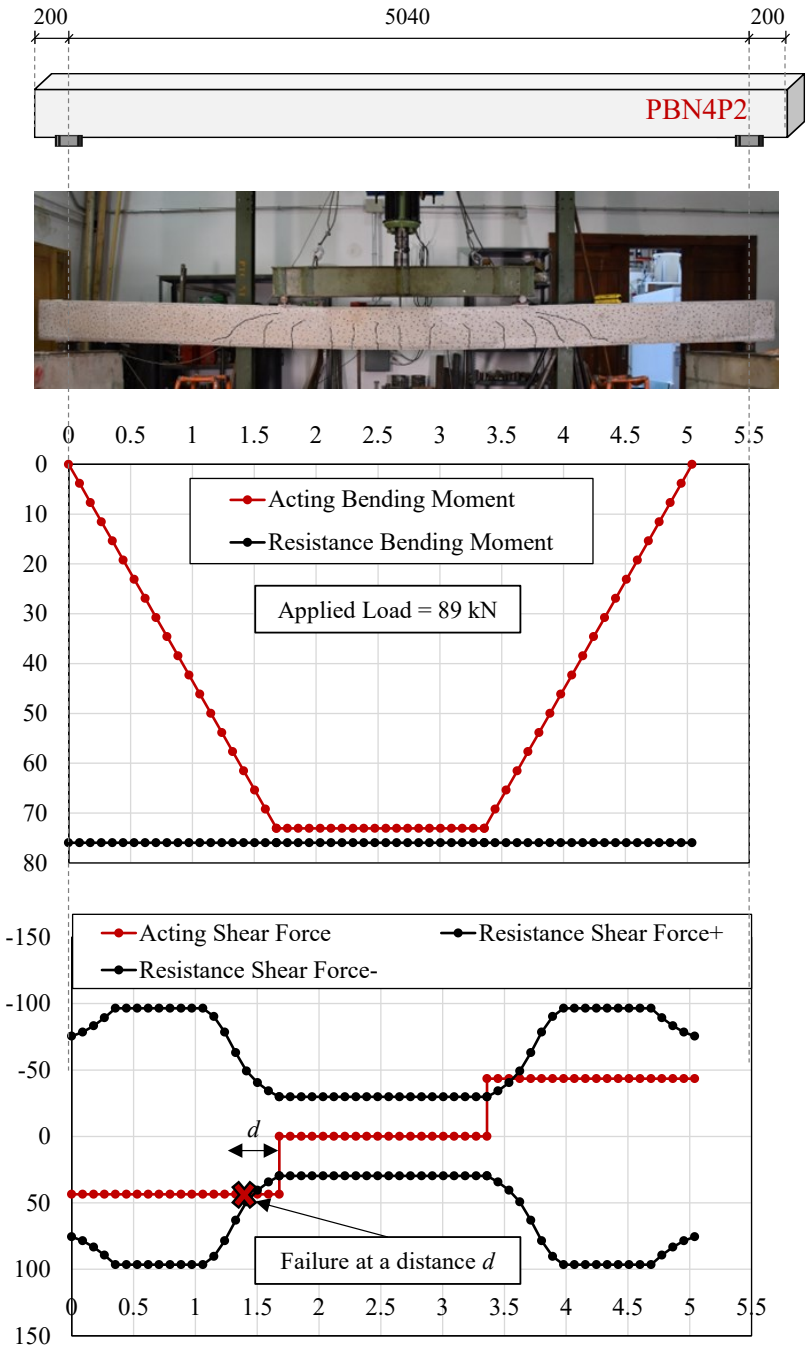

Figure 8-26 Failure mode and analytical prediction for the un-corroded beam PBN4P2.

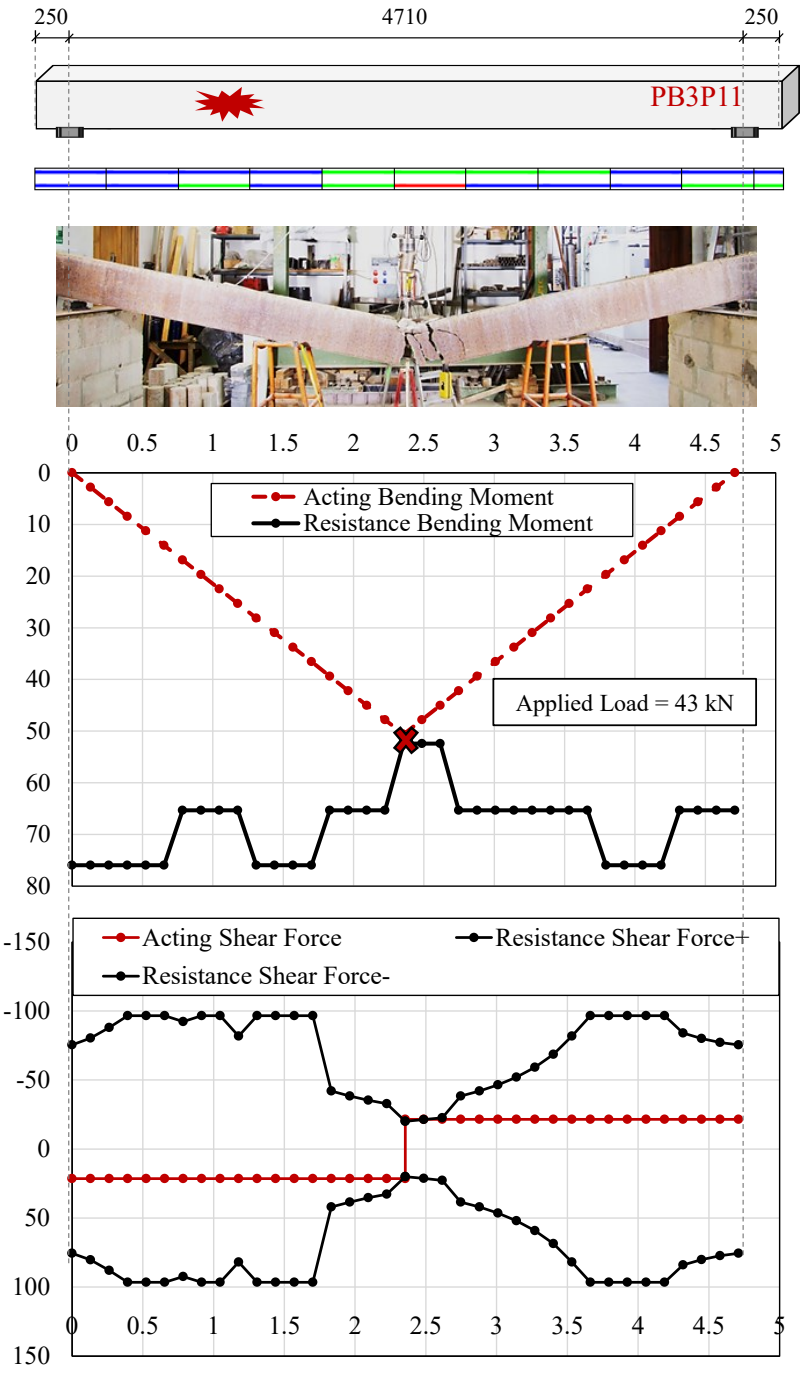

Figure 8-27 Failure mode and analytical prediction for the corroded beam PB3P11.

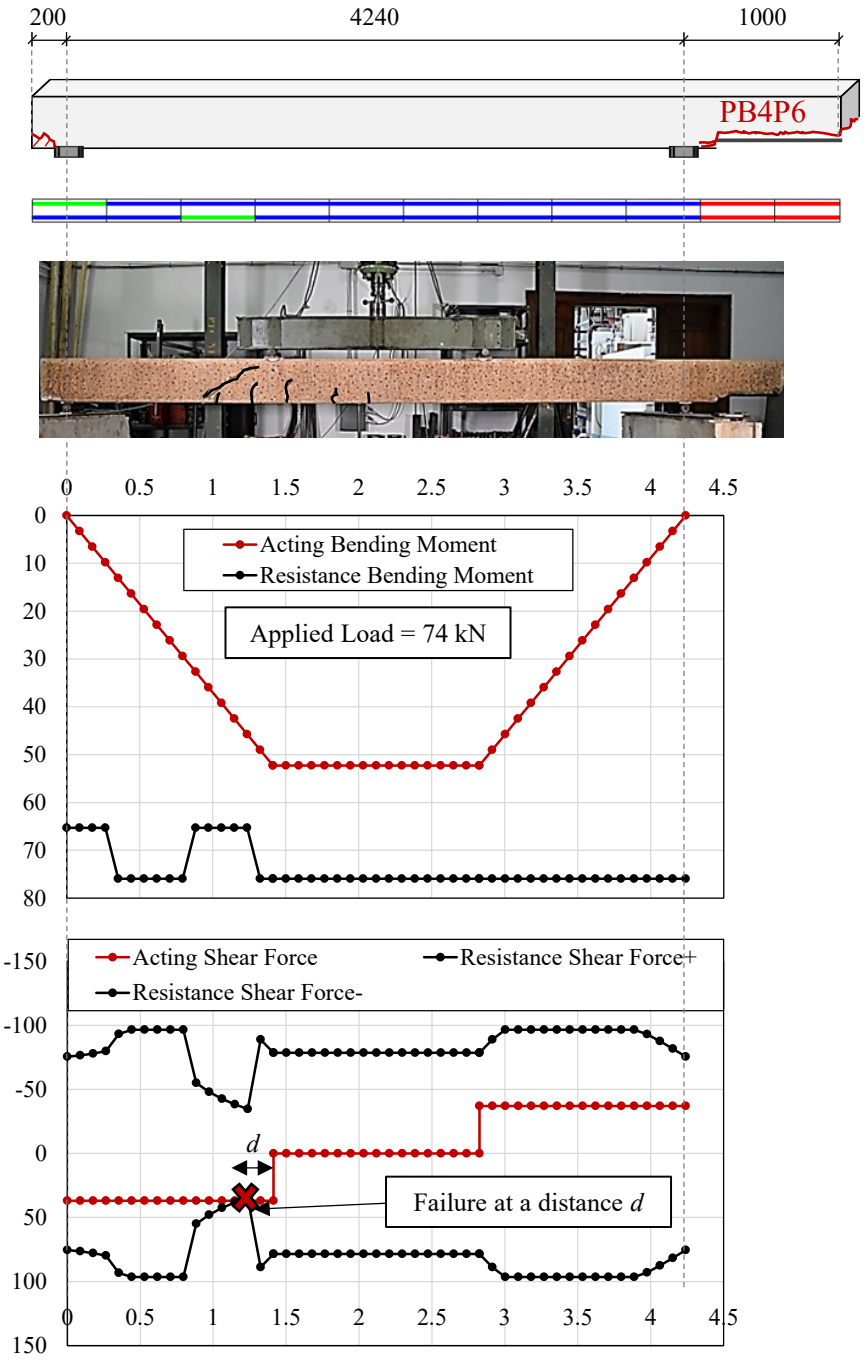

Figure 8-28 Failure mode and analytical prediction for the corroded beam PB4P6.

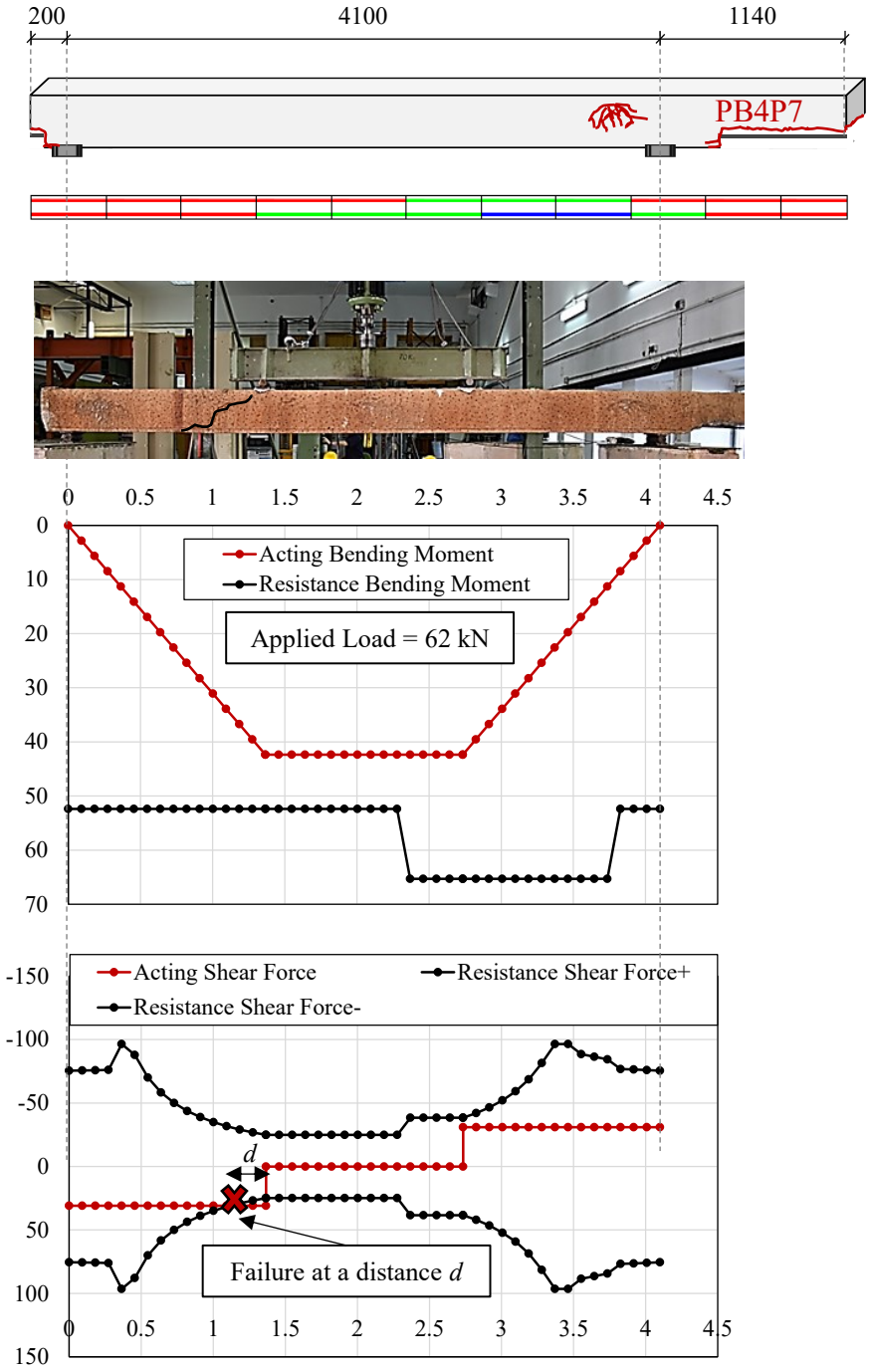

Figure 8-29 Failure mode and analytical prediction for the corroded beam PB4P7.

Table 8-4 Comparison between experimental outcomes and analytical predictions obtained by adopting the proposed analytical model.

Beam Specimen	$P_{failure}$ [kN]	$P_{failure,an}$ [kN]	Failure mode experimental	Failure mode analytical	$P_{failure}/P_{failure,an}$ [-]
PBN3P1	70.14	59.00	Bending	Bending	1.19
PBN4P2	98.47	89.00	Shear I	Shear	1.11
PB4P5	90.21	74.00	Shear I	Shear	1.22
PB4P6	89.39	74.00	Shear I	Shear	1.21
PB4P7	81.74	62.00	Shear II	Shear	1.32
PB4P8	100.06	69.00	Shear I	Shear	1.45
PB4P9	80.00	77.00	Shear II	Shear	1.04
PB3P11	62.00	43.00	Bending	Bending	1.44
PB4P13	127.45	91.00	Shear I	Shear	1.40
PB4P14	145.90	94.00	Shear I	Shear	1.55
				Mean Value:	1.29
				Standard Deviation:	0.17
				CV [%]:	12.87

Table 8-5 Comparison between experimental outcomes and analytical predictions obtained by adopting the analytical approach proposed by Walraven (2020).

Beam Specimen	$P_{failure}$ [kN]	$P_{failure,an}$ [kN]	Failure mode experimental	Failure mode analytical	$P_{failure}/P_{failure,an}$ [-]
PBN3P1	70.14	59.00	Bending	Bending	1.19
PBN4P2	98.47	88.00	Shear I	Shear	1.12
PB4P5	90.21	58.00	Shear I	Shear	1.56
PB4P6	89.39	59.00	Shear I	Shear	1.52
PB4P7	81.74	49.00	Shear II	Shear	1.67
PB4P8	100.06	54.00	Shear I	Shear	1.85
PB4P9	80.00	60.00	Shear II	Shear	1.33
PB3P11	62.00	37.00	Bending	Bending	1.68
PB4P13	127.45	69.00	Shear I	Shear	1.85
PB4P14	145.90	70.00	Shear I	Shear	2.08

A summary of the previous results is shown in Figure 8-30. As it is visible, a tangible improvement in the experimental ultimate load prediction is obtained through the adoption of the proposed analytical approach if compared to the modified Model Code 2010 proposal. As expected, analyzing un-corroded beams, the two models work analogously.

Since the experimental tests did not present the same span length, L, and a/d ratio, an evident decrease in the failure loads cannot be observed. For these reasons, the analytical method was re-applied to all beams by considering the un-corroded properties. The percentage ratio between corroded and un-corroded loads for the tested beams by using the analytical method is shown in Figure 8-31. As a result, the decrease of load-bearing capacity becomes evident ranging from LV-0 (un-corroded) to LV-II and III. Indeed, LV-II and III exhibit approximately a residual bearing capacity of 67.50 % and 61.18 %, respectively, confirming the detrimental effect of corrosion.

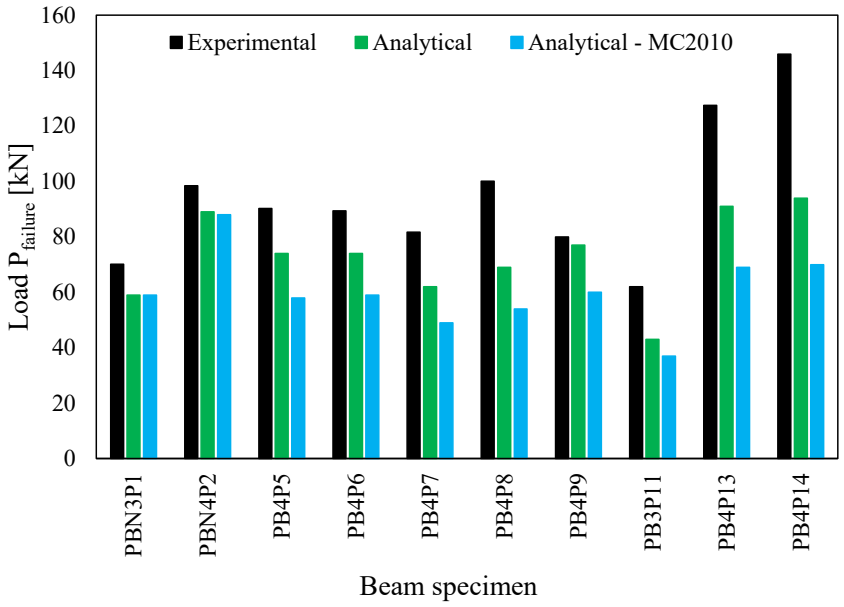

Figure 8-30 Comparison of ultimate load from experimental tests and analytical methods.

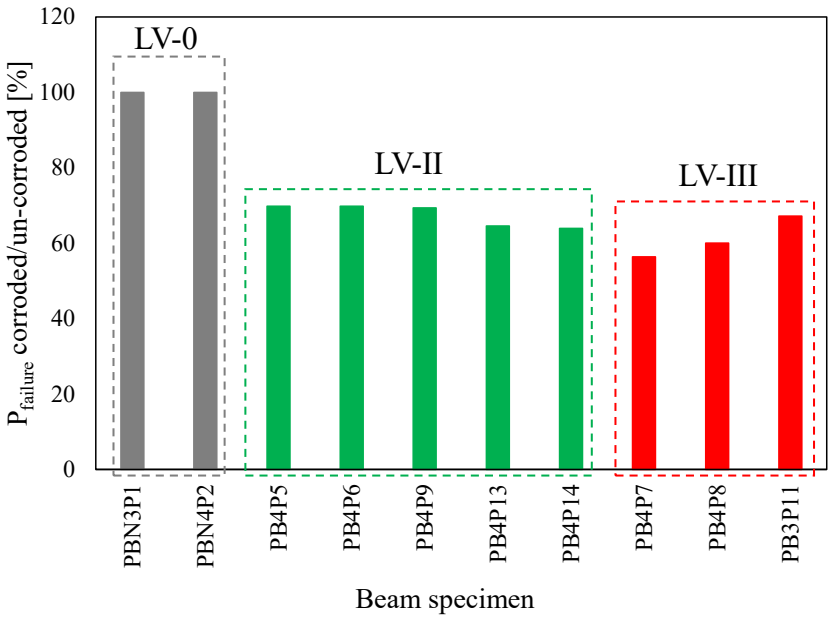

Figure 8-31 Analytical ultimate load percentage ratio (corroded/un-corroded) considering different corrosion levels.

8.9 Main observations and drawbacks

An analytical approach concerning the assessment of corroded PC beams without transversal reinforcement is proposed. The sectional model is based on a single input parameter, which is the maximum penetration depth of the most corroded wire. Four scenarios are considered, referred to as (i) un-corroded, (ii) low corroded, (ii) intermediate corroded, and (iv) high corroded. Each scenario involves a maximum penetration depth, $P_{max,0.5}$, estimated via the probabilistic analysis of the maximum penetration depths of the available corroded strand samples belonging to the investigated corrosion level. First, a simplified moment-curvature diagram is proposed to determine the flexural capacity as well as the longitudinal strain at mid-height of the effective shear depth, ε_x. In this context, the prestressing stress reduction and the prestressing reinforcement mechanical properties decay are introduced to consider the corrosion effects on the residual flexural capacity of corroded PC elements. The first contribution is assumed to be consistent with the ultimate bond strength decay via the introduction of a coefficient R_2, derived from the pull-out tests on corroded specimens without transversal reinforcements. The second contribution is estimated through the adoption of the SCPS-model. The shear capacity is predicted by using the Model Code 2010 Level II of approximation formulation, opportunely modified to consider the corrosion effects. To this end, the modified longitudinal strain at mid-height of the effective shear depth value, $\varepsilon_{x,corr}$, is determined through the simplified moment-curvature diagram for each corrosion level

analyzed, and the prestressing force reduction, $F_{p,corr}(t)$, is evaluated through the twofold effect of (i) the transmission length variation, $L_{t,corr}$, and the prestressing stress reduction, respectively estimated by adopting the model proposed by Anaya et al. (2022) and the coefficient R_2. Furthermore, the cross-sectional area of the prestressing reinforcement is assumed to be unaffected by corrosion to be consistent with the SCPS-model assumption. Finally, the comparison between experimental and analytical outcomes of the previously analyzed corroded and un-corroded PC beams in terms of (a) observed failure mode and (b) ultimate load at failure is performed to validate the model.

Based on the obtained results, the proposed analytical model can successfully predict the experimental failure mode of both corroded and un-corroded PC beams. Moreover, although conservative results, the effectiveness of the analytical approach is observed. Specifically, the mean value, the standard deviation and the coefficient of variation, CV, of the ratio $P_{failure}/P_{failure,an}$ of un-corroded and corroded PC beams result equal to 1.29, 0.17, and 12.87%, respectively.

Although the proposed analytical model can be considered as a useful tool to be applied in the daily engineering practice for preliminary assessing the residual flexural and/or shear capacity of corroded PC beams, the model applicability is currently limited to PC members without transversal reinforcement. Furthermore, the adopted relationships for the prestressing stress reduction as well as the simplified model for the quantification of the corroded transmission length should be verified through ad-hoc experimental campaigns. Additionally, due to the absence of experimental outcomes on corroded PC elements, the simplified moment-curvature approach has been validated only against experimental outcomes from un-corroded PC members.

8.9.1 Analytical model application by adopting design properties

The assessment of the tested PC beams is performed herein by adopting the design properties for concrete and prestressing steel. Since the concrete was considered unaffected by corrosion, the partial safety factor γ_c equal to 1.49 suggested in the Appendix B of the *fib* Bulletin 80 (2016) is used, by assuming a consequence class (CC) equal to 2. In addition, the design strength of corroded strands is evaluated via the partial safety factor (PSF), $\gamma_{m,corr}$, equal to 1.31, previously discussed in paragraph 7.6. In Table 8-6 are summarized the adopted average and design material properties.

In addition, Figure 8-32(a) reports the design stress-strain behaviour of prestressing steel as function of corrosion levels, while Figure 8-32(b) shows the corresponding reduced moment-curvature responses, resulting in an evident decrease in terms of both ultimate and cracking moments by adopting the design values.

Table 8-6 Mechanical properties and partial safety factors assumed for concrete and prestressing steel.

Material	f_{cm} **[MPa]**	$f_{pu,0}$ **[MPa]**	***PSF*** **[-]**	$f_{cd} = f_{ck}/\gamma_c$ **[MPa]**
Concrete	45.40	/	1.49	25.10
Prestressing steel	/	1901.75	1.31	/

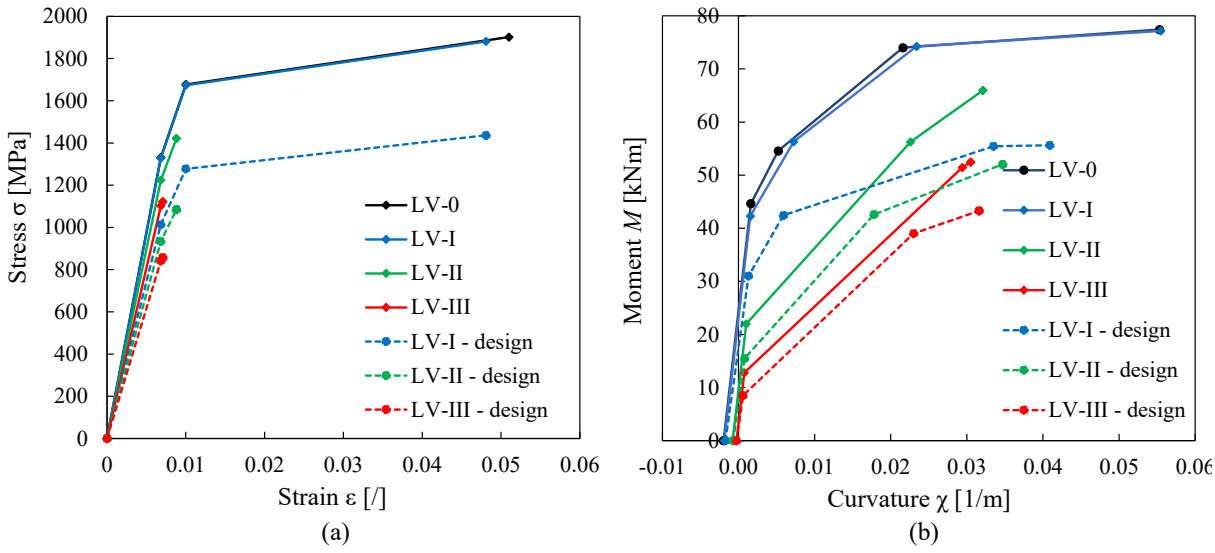

Figure 8-32 Average vs design: (a) stress-strain of prestressing steel, (b) moment-curvature response.

Table 8-7 summarizes the analytical loads at failure for each beam analyzed with un-corroded, $P_{failure,an,uncorr}$, and corroded (mean and design) properties, $P_{failure,an,mean}$ - $P_{failure,an,des}$.

Table 8-7 Comparison between analytical load at failure for beams with un-corroded and corroded (mean and design) properties.

Beam Specimen	$P_{failure,\ un\text{-}corroded}$ **[kN]**	$P_{failure,\ corroded\ mean}$ **[kN]**	$P_{failure,\ corroded\ des}$ **[kN]**	$P_{failure,des} / P_{failure,mean}$ **[%]**
PB4P5	106.00	74.00	60.00	81.1
PB4P6	106.00	74.00	61.00	82.4
PB4P7	110.00	62.00	50.00	81.4
PB4P8	115.00	69.00	56.00	79.1
PB4P9	111.00	77.00	62.00	80.6
PB3P11	64.00	43.00	35.00	78.7
PB4P13	141.00	91.00	72.00	81.2
PB4P14	147.00	94.00	74.00	80.5

Furthermore, Figure 8-33 graphically shows the comparison between the ultimate loads evaluated by adopting the different mechanical properties, showing a more conservative prediction in the case of design properties adoption. Indeed, considering the ratio $P_{failure,an,des}/P_{failure,an,mean}$, a 20% reduced ultimate load is predicted by adopting design properties, as shown in Figure 8-34.

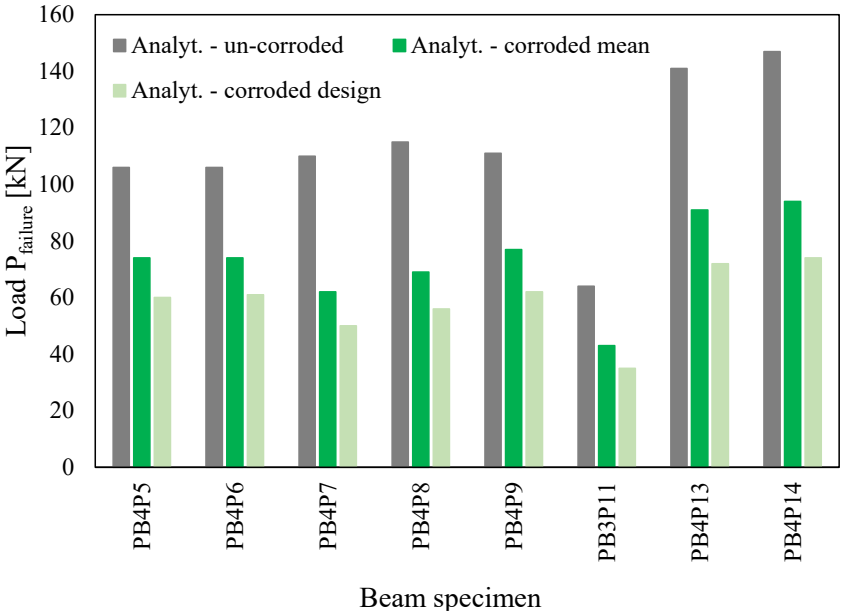

Figure 8-33 Average vs design: predicted loads at failure of beams with un-corroded and corroded (mean and design) properties.

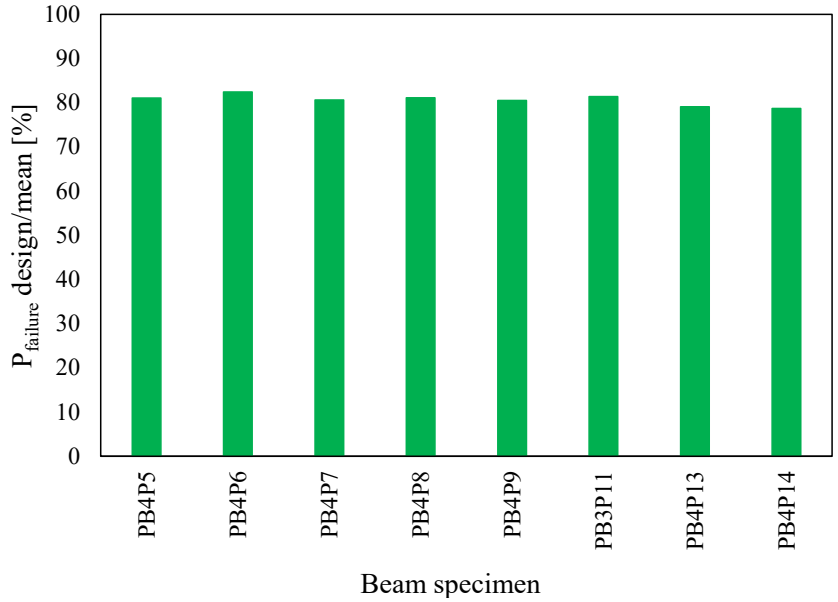

Figure 8-34 Ratio between design and mean loads at failure.

This section collects the main proposals and findings of the present *Thesis*: (i) the application of the proposed SCPS-model, (ii) the use of the preliminary partial safety factor for corroded strands, and (iii) the application of the analytical model procedure for the assessment of deteriorated PC beams without transversal reinforcement. Based on the obtained result, further research efforts should be devoted to the definition and refinement of simplified procedure for the assessment and design of corroded structures.

9 General conclusions and Future research

9.1 Conclusions and observations

In the present work, the issue of chloride-induced corrosion on naturally corroded PC beams subjected to wet-dry cycles using sea water was investigated. The aims of the research were to assess the residual structural capacity of such members and to propose useful constitutive laws for predicting the reduced mechanical response of corroded strands as well as to provide an analytical method for assessing the residual life of corroded PC beams without transversal reinforcements. Both flexural and shear capacity were considered in the analytical model, while the mechanical properties decay of corroded prestressing strands was estimated by adopting the proposed SCPS-model. The present *Thesis* was divided into the following sections:

- *State of the Art*: the available scientific literature was thoroughly reviewed and the lacunae of the current codes and guidelines provisions for the assessment of corroded structures were highlighted. After reporting a detailed timeline of PC bridge and building collapses from 1960 to the present day, available experimental tests conducted on corroded PC beams to assess their residual bending and shear resistance were analyzed. The main corrosion parameters in terms of mass loss and cross-sectional loss for mechanical properties decay were then introduced. In this context, a detailed analysis of the possible pit type morphological configurations was outlined. Finally, the experimental tensile test activities conducted on corroded prestressing reinforcements were investigated.
- *Residual structural capacity evaluation*: via visual inspection, the concrete surface defects of each corroded PC beam were detected in terms of splitting longitudinal cracks, spalling of concrete cover, and swelling. Outcomes revealed that concrete damage was often located at the beam edges, where the presence of a construction practice deficiency consisting in the prestressing strands unprotection promoted a severe corrosion. Concurrently, corrosion potential mapping was performed along the entire length of each investigated PC beam, while ohmic drop and corrosion rate were

measured at the beam edges and at mid-span, respectively. From corrosion potential results, a high probability of corrosion was expected along PC beams length, whereas the corrosion rate outcomes obtained adopting the linear polarization technique revealed I_{corr} values above the established corrosion activation threshold of 0.1 $\mu A/cm^2$. Additionally, chloride test results showed high chloride concentration levels exceeding the standard threshold value set at 0.6%cem. In particular, exceptionally high values equal to 8%cem were recorded in correspondence to longitudinal splitting cracks at the beam edge of beam PB9 and at mid-span of beam PB10. Following indirect corrosion measurements, three- and four-point bending tests were carried out on corroded and un-corroded beams to assess their flexural and shear residual structural capacity. During the mechanical tests, Digital Image Correlation (DIC) was performed to investigate the strain field evolution of each tested beam. From the flexural resistance point of view, the un-corroded beam PBN3P1 showed the best mechanical performance, while corroded beams PB3P10 and PB3P11 showed a significant corrosion-induced reduction in terms of ultimate bending moment (load-carrying capacity), deflection, and ductility. From the shear resistance point of view, the strain localization induced by prestressing strands deterioration led to premature beam failure. For corroded PC beams with similar a/d ratios, the residual shear resistance also decreased with increasing strand corrosion levels in terms of ultimate load-carrying capacity, ultimate deflection, and ductility. Although tested PC beams were characterized by different shear span-to-depth ratios, two primary failure modes, denoted as Shear I and Shear II, were defined. Shear I mode was characterized by a shear-bending interaction prior to failure. Bending vertical cracks indeed developed before the appearance of a diagonal shear crack that led to beam collapse. Shear II mode showed the presence of a single diagonal crack formed from the loading steel plate towards the prestressing reinforcement. Nevertheless, bond decay due to chloride-induced corrosion at prestressing steel–concrete interface might have played a relevant role in the shear failure mode of severely corroded PC beams, as evidenced by the sudden drops visible in the vertical displacement diagrams of beams PB4P5, PB4P7 and PB4P9.

- *Constitutive laws proposal*: following the mechanical tests, a refined and a simplified stress-strain relationship, named CPS- and SCPS-model, respectively, were proposed to predict the residual mechanical response of prestressing strands subjected to chloride-induced corrosion. To this end, the pitting morphology spatial variability was

first investigated by analyzing 3D models of corroded strands using the GOM Inspect software. Useful correlations between the corrosion parameters of mass loss, cross-sectional loss and maximum penetration depth of the most corroded wire were proposed and discussed. Moreover, the effect of concrete surface defects on the longitudinal pitting spatial variability as well as the role played by the presence of possible construction practice deficiencies were analyzed. Outcomes revealed that preferential pathways developed, enhancing the chloride ions attack through direct contact with external agents and prestressing reinforcements, resulting in a more aggressive chloride-induced corrosion at the beam edges, characterized by deeper and widespread pits. Furthermore, the pitting factor of naturally corroded prestressing strands was investigated for the first time by considering both longitudinal and transversal (sectional) variability. Following tensile tests on corroded and un-corroded strand samples, two constitutive laws were defined. Although the models were based on different assumptions, both used the equivalent spring material approach to predict the overall response of a corroded strand by summing the wires' contributions. The CPS-model adopted the cross-sectional loss of each wire as the main input parameter for the prediction of ultimate strength and ultimate strain decay and considered different decay laws as a function of three pit type morphological configurations – hemispherical, half-moon, and planar shape –. The SCPS, on the other hand, was a simplified version of the CPS-model. This latter was based on a single input parameter, namely the maximum penetration depth of the most corroded wire, and was designed for the daily engineering practice. The SCPS-model, which is independent from the possible pit type morphology configurations, adopted a single decay law for ultimate strain and estimated an average sectional penetration depth for the remaining external wires as a function of the maximum penetration depth of the most corroded wire. Both constitutive laws were successfully validated against experimental tensile test results from the present research and from data available in the literature. In addition, a preliminary partial safety factor for the estimation of the design ultimate strength of corroded prestressing strands was proposed. The procedure considered several uncertainties related to: (i) geometrical properties, (ii) un-corroded mechanical properties of prestressing steel, (iii) failure mode of PC members, and (iv) resistance model uncertainty.

- *Analytical proposal*: in addition to the definition of constitutive laws for corroded strands, a simplified analytical approach was proposed for the assessment of the

residual structural performance of corroded PC beams without transversal reinforcements in terms of both flexural and shear capacity. The input model parameter is the maximum penetration depth of the most corroded wire. Four scenarios were considered by distinguishing between: un-corroded, and low, intermediate, and high corrosion. The instantaneous and time-dependent prestressing losses over time due to strand release, steel relaxation and creep and shrinkage effects were considered. Furthermore, the transmission length variation and the prestressing loss decay due to chloride-induced corrosion were introduced. The analytical model assumed the SCPS-model for the reduced mechanical properties decay of prestressing reinforcements. Moreover, a simplified moment-curvature diagram was proposed as a function of the different corrosion levels for the definition of the flexural capacity and the evaluation of the strain at mid-depth of the beam cross-section, which was found to be a fundamental parameter for the evaluation of the shear resistance according to the Model Code 2010 level II of approximation expression. The analytical model was finally validated by comparing the experimental outcomes and the analytical predictions of the investigated PC beams in terms of both ultimate load and failure mode.

9.2 Future research and recommended improvements

In light of the obtained results, the needed research and future works on the corrosion issue in prestressed concrete structures are briefly outlined below in the form of a bulleted list.

9.2.1 Corrosion measurements and experimental tests on corroded PC elements

- Concrete surface defects revealed to be crucial for the development of preferential pathways for chloride ion diffusion. Nevertheless, further efforts should be devoted to the measurement of crack width opening in the case of longitudinal splitting crack formation. To fill this gap, useful correlations should be provided for the prediction of the corrosion level of prestressing reinforcements embedded in concrete starting from the rapid crack width measurement.
- The present research highlighted the deteriorating effect on the chloride ion diffusion process induced by the presence of a particular construction practice deficiency (prestressing reinforcements unprotected at beam edges). Nevertheless, other deficiencies were commonly pointed out during in-situ inspection, such as (i) moist spots, (ii) water retention due to inadequate water-proofing systems, (iii) unsealed anchor headers, (iv) use of poor construction materials or (v) presence of voids next to reinforcements due to improper vibration of concrete, the effects of which need to be analyzed in depth.
- Experimental campaigns on naturally corroded PC members, instead of artificially accelerated ones, are still required to further understand the actual behaviour of deteriorated structures. Specific experimental tests on PC elements under static, dynamic, and cyclic loading are still required for the evaluation of the residual structural performance, particularly when considering different environmental exposure conditions. Furthermore, additional experimental activities should be planned to investigate the debonding effect induced by the corrosion process (anchorage failure).
- The issues related to experimental tests are:
    a) Definition of common test set-up and loading conditions. Due to the spalling of concrete cover, the analyzed beams were tested with different span-to-depth-ratios, as a result, the residual load carrying capacity could not be directly compared. To facilitate the estimation and quantification of corrosion

effects, corroded and un-corroded PC beam specimens should be tested under the same test set-up conditions and shear-to-depth-configuration;

b) In order to correlate the residual structural capacity of the analyzed PC member with the actual corrosion level, the corrosion pattern along the overall length of the investigated specimen needs to be accurately evaluated.

9.2.2 Pitting morphology analysis of corroded prestressing strands

- The present work investigated several corroded strand samples in order to evaluate the effects of chloride-induced corrosion on prestressing reinforcements. Although useful correlations between the main corrosion parameters were proposed, further corroded prestressing strands under similar and/or different exposure conditions should be investigated to further validate the accuracy and reliability of the proposed relationships, taking into account the concurrent presence of the concrete surface defects.
- The proposed relationships were defined based on the analysis of pre-tensioned corroded strands embedded in concrete. Therefore, the efficiency as well as the applicability of the proposed formulations in the case of post-tensioned prestressing reinforcements must be further verified. Indeed, post-tensioned reinforcements are commonly inserted in a protective duct, which leads to different interface conditions if compared to pre-tensioned strands embedded in concrete. Therefore, the pitting morphology spatial variability of those reinforcement types may differ from the ones investigated, requiring additional research efforts. To this end, supplementary experimental tests on corroded post-tensioned strands are necessary.
- Several corrosion parameters proved to be crucial for the assessment of the residual mechanical properties of corroded prestressing strands, such as the cross-sectional loss or the maximum penetration depth of the most corroded wire. To further investigate the effect of these latter parameters, additional studies should focus on the variability of the penetration depth from a probabilistic point of view, by conducting Monte-Carlo analyses.

9.2.3 Constitutive laws for the residual mechanical response of corroded strands

- The accuracy and applicability of both the CPS- and SCPS-models were verified based on available experimental outcomes. However, due to the limited number of studies available in the scientific literature, further experimental tensile tests need to be conducted to increase the data population, improving and refining the proposed decay relationships.
- Additional severely corroded prestressing strands, showing a corroded inner wire, should be tested and analyzed to define an experimental relationship that allows to estimate the penetration depth of the inner wire starting from a single measurement of the maximum penetration depth of the most corroded wire in the same analyzed section.
- Although the proposed models are useful tools for accurate and conservative predictions of the residual mechanical properties of a corroded strand, an operational procedure – based on in-situ sampling and measuring of corrosion parameters – needs to be established. Otherwise, the operational application of the proposed models in the assessment of in service corroded prestressed elements may be hindered. Towards this aim, the scientific literature has highlighted possible non-destructive techniques to be applied for the measurement of corrosion parameters directly during in-situ inspections. Nevertheless, non-destructive methods were not considered in the present work and require additional scientific forces to determine the best cost-benefit solution.
- Both proposed models were limited to the prediction of the residual mechanical response of a single corroded prestressing strand. Further research efforts should be devoted to providing a simplified model able to estimate the sectional residual mechanical properties of multiple corroded strands, characterized by different corrosion levels. Indeed, in the case of existing structures, such as bridges or tanks, several prestressing strands are generally present in the same section, each of which provides a key contribution to the overall load-carrying capacity of the structural PC element. Therefore, a simplified model based on an equivalent spring approach might be adopted to evaluate corroded strand contributions separately and to successively estimate the overall residual sectional response without leading to overconservative predictions.

- For the first time, a preliminary attempt was made to define a partial safety factor for the prediction of the ultimate design strength of a corroded prestressing strand. Although the proposed partial safety factor should be considered as a useful tool for the daily engineering practice to be implemented in future codes and guidelines for the evaluation of existing corroded PC members, its effectiveness needs to be further verified. In particular, to improve the accuracy of the proposed factor, additional experimental tests on corroded prestressing strands should be conducted in order to extend the statistical data population available to date. Furthermore, additional studies are required for the proper evaluation of both resistance model and failure mode uncertainties.

9.2.4 Analytical model for the assessment of the residual capacity of PC beams

- The proposed analytical model is an instrument to evaluate the residual life and capacity of corroded PC beams without shear reinforcement. However, although the effectiveness of the analytical model was validated against naturally corroded PC beams, most PC elements in existing structures are commonly characterized by the presence of transversal reinforcement, thus, further research should be devoted to extend the proposed analytical model.
- Additional experimental data on corroded PC beams without stirrups are welcomed to further validate the proposed analytical approach.
- The analytical model for assessing the residual capacity of corroded PC beams with transversal reinforcements should take the following factors into account:
    a) A different corrosion level for prestressing reinforcement and stirrups. To this end, an ad-hoc stress-strain relationship must be provided for the prediction of the residual mechanical properties of corroded transversal reinforcement;
    b) Analysis of the interaction between the decay mechanisms developing in prestressing reinforcement and stirrups. In particular, changes in failure mode may occur after severe deterioration of stirrups;
    c) Evaluation of the bond decay associated with the confinement contribution provided by the presence of transversal reinforcements;

9.2.5 Improvements of current codes and guidelines

- The existing guidelines and codes, except for the CONTECVET manual, are either lacking or have non-uniform provisions concerning RC and PC structures and infrastructures against corrosion, therefore, a significant research effort is needed.
- Further studies are needed to cover the gap in the current Eurocodes, in particular with regard to specific strategies to be adopted for the assessment of existing structures in terms of mechanical properties decay and required analyses.
- Reliable and rigorous maintenance protocols, monitoring systems and simplified analytical models capable of assessing the residual structural capacity of deteriorating PC members must be introduced in new codes and guidelines to enhance the durability of existing structures and infrastructures.

References

ACI Committee 201. (1994). *Guide to Durable Concrete, Manual of Concrete Practice, Part 1*.

ACI Committee 222. (1994). *Corrosion of metals in concrete, Manual of Concrete Practice, Part 3*.

ACI Committee 318. (2019). *Building code requirements for structural concrete*.

ACI Committee 357. (1994). *Guide for design and construction of fixed off-shore concrete structures, Manual of Concrete Practice, Part 4*.

Ahmad, S., & Kamran. (2018). Residual flexural capacity of corroded reinforced concrete beams. *IOP Conference Series: Materials Science and Engineering*, *377*(1). https://doi.org/10.1088/1757-899X/377/1/012121

Akpanyung, K. V., & Loto, R. T. (2019). Pitting corrosion evaluation: A review. *Journal of Physics: Conference Series*, *1378*(2). https://doi.org/10.1088/1742-6596/1378/2/022088

Al-Harthy, A. S., Stewart, M. G., & Mullard, J. (2011). Concrete cover cracking caused by steel reinforcement corrosion. *Magazine of Concrete Research*, *63*(9), 655–667. https://doi.org/10.1680/macr.2011.63.9.655

Al-Mashgari, H. A. Y., Hejazi, F., & Alkhateeb, M. Y. (2021). Retrofitting of corroded reinforced concrete beams in flexure using CFRP rods and anchor bolt. *Structures*, *29*(November 2019), 1819–1827. https://doi.org/10.1016/j.istruc.2020.12.047

Al-Sulaimani, G. J., Kaleemullah, M., Basunbul, I. A., & Rasheeduzzafar. (1990). Influence of Corrosion and Cracking on Bond Behavior and Strength of Reinforced Concrete Members. *ACI Structural Journal*, *87*.

Alexopoulos, N. D., Apostolopoulos, C. A., Papadopoulos, M. P., & Pantelakis, S. G. (2007). Mechanical performance of BStIV grade steel bars with regard to the long-term material degradation due to corrosion damage. *Construction and Building Materials*, *21*(6), 1362–1369. https://doi.org/10.1016/j.conbuildmat.2005.09.008

Almusallam, A. A. (2001). Effect of degree of corrosion on the properties of reinforcing steel bars. *Construction and Building Materials*, *15*(8), 361–368. https://doi.org/10.1016/S0950-0618(01)00009-5

Almusallam, A. A., Al-Gahtani, A. S., Aziz, A. R., & Rasheeduzzafar. (1996). Effect of reinforcement corrosion on bond strength. *Construction and Building Materials*, *10*(2), 123–129. https://doi.org/10.1016/0950-0618(95)00077-1

Almusallam, T. H. (1997). Effect of corrosion on flexural behavior of ferrocement. *Journal of Ferrocement*, *25*(2), 105–113.

Alonso, C. Andrade;C.J. Gulikers, R. Polder, R. Cigna, O. Vennesland, M. Salta, A. R. and B. E. (2004). Recommendations of RILEM TC-154-EMC: "Electrochemical techniques for measuring metallic corrosion" Test methods for on-site corrosion rate measurement of steel reinforcement in concrete by means of the polarization resistance method. *Materials and Structures*, *37*(273), 623–643.

Alonso, C., Andrade, C., Rodriguez, J., & Diez, J. M. (1998). Factors controlling cracking of concrete affected by reinforcement corrosion. *Materials and Structures/Materiaux et Constructions*, *31*(211), 435–441. https://doi.org/10.1007/bf02480466

American Association of State Highway and Transportation Officials. (2017). *AASHTO LRFD bridge design specifications*.

Anania, L., Badalà, A., & D'Agata, G. (2018). Damage and collapse mode of existing post tensioned precast concrete bridge: The case of Petrulla viaduct. *Engineering Structures*, *162*(January), 226–244. https://doi.org/10.1016/j.engstruct.2018.02.039

Anaya, P., Martín-Pérez, B., Rodríguez, J., & Andrade, C. (2022). Transfer length of corroded wires in prestressed concrete members. *Structural Concrete*, *23*(1), 154–171. https://doi.org/10.1002/suco.202100265

Andrade, C. (2021). Approach to the residual strength of steel bars due to corrosion. *Fib CACRCS DAYS 2021 - Capacity Assessment of Corroded Reinforced Concrete Structures*, 13–17.

Andrade, C., Alonso, C., & Molina, F. J. (1993). Cover cracking as a function of bar corrosion: Part I-Experimental test. *Materials and Structures*, *26*(8), 453–464. https://doi.org/10.1007/BF02472805

Andrade, C., & Gonzalez, J. A. (1978). Quantitative Measurements of Corrosion Rate of Reinforcing Steels Embedded in Concrete Using Polarization Resistance Measurements. *Werkstoffe Und Korrosion*, *29*(8), 515–519.

Angst, U. M. (2018). Challenges and opportunities in corrosion of steel in concrete. *Materials and Structures/Materiaux et Constructions*, *51*(1), 1–20. https://doi.org/10.1617/s11527-017-1131-6

Angst, U., & Vennesland. (2009). Critical chloride content in reinforced concrete - State of the art. *Concrete Repair, Rehabilitation and Retrofitting II - Proceedings of the 2nd International Conference on Concrete Repair, Rehabilitation and Retrofitting, ICCRRR*, 149–150. https://doi.org/10.1201/9781439828403.ch41

Angst, Ueli, Elsener, B., Larsen, C. K., & Vennesland, Ø. (2009). Critical chloride content in reinforced concrete - A review. *Cement and Concrete Research*, *39*(12), 1122–1138. https://doi.org/10.1016/j.cemconres.2009.08.006

Ann, K. Y., & Song, H. W. (2007). Chloride threshold level for corrosion of steel in concrete. *Corrosion Science*, *49*(11), 4113–4133. https://doi.org/10.1016/j.corsci.2007.05.007

Apostolopoulos, C. A., & Papadakis, V. G. (2008). Consequences of steel corrosion on the ductility properties of reinforcement bar. *Construction and Building Materials*, *22*(12), 2316–2324. https://doi.org/10.1016/j.conbuildmat.2007.10.006

Apostolopoulos, C. A., & Papadopoulos, M. P. (2007). Tensile and low cycle fatigue behavior of corroded reinforcing steel bars S400. *Construction and Building Materials*, *21*(4), 855–864. https://doi.org/10.1016/j.conbuildmat.2005.12.012

Apostolopoulos, Ch Alk. (2007). Mechanical behavior of corroded reinforcing steel bars S500s tempcore under low cycle fatigue. *Construction and Building Materials*, *21*(7), 1447–1456. https://doi.org/10.1016/j.conbuildmat.2006.07.008

Apostolopoulos, Ch Alk, Papadopoulos, M. P., & Pantelakis, S. G. (2006). Tensile behavior of corroded reinforcing steel bars BSt 500s. *Construction and Building Materials*, *20*(9), 782–789. https://doi.org/10.1016/j.conbuildmat.2005.01.065

Apostolopoulos, Charis A., Demis, S., & Papadakis, V. G. (2013). Chloride-induced corrosion of steel reinforcement - Mechanical performance and pit depth analysis. *Construction and Building Materials*, *38*, 139–146. https://doi.org/10.1016/j.conbuildmat.2012.07.087

Apostolopoulos, Charis Alk, Koulouris, K. F., & Apostolopoulos, A. C. (2019). Correlation of Surface Cracks of Concrete due to Corrosion and Bond Strength (between Steel Bar and Concrete). *Advances in Civil Engineering*, *2019*. https://doi.org/10.1155/2019/3438743

Asami, K., & Kikuchi, M. (2003). In-depth distribution of rusts on a plain carbon steel and weathering steels exposed to coastal-industrial atmosphere for 17 years. *Corrosion Science*, *45*(11), 2671–2688. https://doi.org/10.1016/S0010-938X(03)00070-2

ASTM G1-03. Standard practice for preparing, cleaning, and evaluating corrosion test specimens. (2017).

Audenaert, K., De Schutter, G., & Marsavina, L. (2009). Influence of cracks and crack width on penetration depth of chlorides in concrete. *European Journal of Environmental and Civil Engineering*, *13*(5), 561–572. https://doi.org/10.1080/19648189.2009.9693134

Azad, A. K., Ahmad, S., & Al-Gohi, B. H. A. (2010). Flexural strength of corroded reinforced concrete beams. *Magazine of Concrete Research*, *62*(6), 405–414. https://doi.org/10.1680/macr.2010.62.6.405

Azad, Abul K., Ahmad, S., & Azher, S. A. (2007). Residual strength of corrosion-damaged reinforced concrete beams. *ACI Materials Journal*, *104*(1), 40–47. https://doi.org/10.14359/18493

Balazs, G. L. (1992). Transfer Control of Prestressing Strands. *PCI Journal*, *37*(6), 60–71. https://doi.org/10.15554/pcij.11011992.60.71

Bastidas-Arteaga, E., Chateauneuf, A., Sánchez-Silva, M., Bressolette, P., & Schoefs, F. (2010). Influence of weather and global warming in chloride ingress into concrete: A stochastic approach. *Structural Safety*, *32*(4), 238–249. https://doi.org/10.1016/j.strusafe.2010.03.002

Bastidas-Arteaga, Emilio, Schoefs, F., Stewart, M. G., & Wang, X. (2013). Influence of global warming on durability of corroding RC structures: A probabilistic approach. *Engineering Structures*, *51*, 259–266. https://doi.org/10.1016/j.engstruct.2013.01.006

Battelle Columbus Laboratories and National Institute of Standards and Technologies (NIST). (1995). *Economic Effects of Metallic Corrosion in the United States*.

Bažant, Z. P., & Panula, L. (1978). Practical prediction of time-dependent deformations of concrete. *Material and Structures*, *4*(11), 425–434. https://doi.org/10.1007/BF02473872

Bazzucchi, F., Restuccia, L., & Ferro, G. A. (2018). Considerations over the Italian road bridge infrastructure safety after the polcevera viaduct collapse: Past errors and future perspectives. *Frattura Ed Integrita Strutturale*, *12*(46), 400–421. https://doi.org/10.3221/IGF-ESIS.46.37

Belletti, B., Damoni, C., Hendriks, M. A. N., & de Boer, A. (2017). *Rijkswaterstaat Technisch Document (RTD): Validation of the Guidelines for Nonlinear Finite Element Analysis of Concrete Structures*.

Belluco, S., Fabris, N., & Faleschini, F. (2021). Analytical modelling of transmission and anchorage length in corroded pre-tensioned concrete elements. *Proceedings of the 1st Conference of the European Association on Quality Control of Bridges and Structures*, 903–911.

Belluco, S., Fabris, N., Faleschini, F., & Caprili, S. (2021). Mechanical behavior of corroded strands: a review of constitutive models. *Proceedings of the Fib CACRCS DAYS 2021 - Capacity Assessment of Corroded Reinforced Concrete Structures Venue: On-Line 30th November- 3rd December 2021*, 69–72.

Benenato, A., Ferracuti, B., Imperatore, S., Kioumarsi, M., & Spagnuolo, S. (2020). Behaviour of prestressed concrete beams damaged by corrosion. *Proceedings of the Fib CACRCS DAYS 2020 - Capacity Assessment of Corroded Reinforced Concrete Structures*, 221–228.

Billet, D. F. (1953). *Study of prestressed concrete beams failing in flexure*. University of Illinois.

Blaber, J., Adair, B., & Antoniou, A. (2015). Ncorr: Open-Source 2D Digital Image Correlation Matlab Software. *Experimental Mechanics*, *55*(6), 1105–1122. https://doi.org/10.1007/s11340-015-0009-1

Blomfors, M., Larsson Ivanov, O., Honfi, D., & Engen, M. (2019). Partial safety factors for the anchorage capacity of corroded reinforcement bars in concrete. *Engineering Structures*, *181*(October 2018), 579–588. https://doi.org/10.1016/j.engstruct.2018.12.011

British Standards Institute. (1985). *British Standard 8110: Part 1, Structural use of concrete – code of practice for design and construction*.

Bruce, S., McCarten, P., Freitag, S., & Hasson, L. (2008). Deterioration of Prestressed Concrete Bridge Beams in New Zealand. In *Land transport New Zealand REsearch Report 337*.

Caines, S., Khan, F., & Shirokoff, J. (2013). Analysis of pitting corrosion on steel under insulation in marine environments. *Journal of Loss Prevention in the Process Industries*, *26*(6), 1466–1483. https://doi.org/10.1016/j.jlp.2013.09.010

Cairns, J., Dut, Y., & Law, D. (2008). Structural performance of corrosion-damaged concrete beams. *Magazine of Concrete Research*, *60*(5), 359–370. https://doi.org/10.1680/macr.2007.00102

Cairns, J., Plizzari, G. A., Du, Y., Law, D. W., & Franzoni, C. (2005). Mechanical properties of corrosion-damaged reinforcement. *ACI Materials Journal*, *102*(256–264).

Calvi, G. M., Moratti, M., O'Reilly, G. J., Scattarreggia, N., Monteiro, R., Malomo, D., Calvi, P. M., & Pinho, R. (2019). Once upon a Time in Italy: The Tale of the Morandi Bridge. *Structural Engineering International*, *29*(2), 198–217. https://doi.org/10.1080/10168664.2018.1558033

Campana, S., Ruiz, M. F., Anastasi, A., & Muttoni, A. (2013). Analysis of shear-transfer actions on one-way RC members based on measured cracking pattern and failure kinematics. *Magazine of Concrete Research*, *65*(6), 386–404. https://doi.org/10.1680/macr.12.00142

Cao, J., Liu, L., & Zhao, S. (2020). Relationship between Corrosion of Reinforcement and Surface Cracking Width in Concrete. *Advances in Civil Engineering*, *2020*. https://doi.org/10.1155/2020/7936861

Capozucca, R., & Cerri, M. N. (2003). Influence of reinforcement corrosion-in the compressive zone-on the behaviour of RC beams. *Engineering Structures*, *25*(13), 1575–1583. https://doi.org/10.1016/S0141-0296(03)00119-6

Caprili, S., & Salvatore, W. (2015). Cyclic behaviour of uncorroded and corroded steel

reinforcing bars. *Construction and Building Materials*, *76*, 168–186. https://doi.org/10.1016/j.conbuildmat.2014.11.025

Caprili, S., & Salvatore, W. (2018). Mechanical performance of steel reinforcing bars in uncorroded and corroded conditions. *Data in Brief*, *18*, 1677–1695. https://doi.org/10.1016/j.dib.2018.04.072

Caspeele, R. (2021). Partial factor based assessment of existing concrete structures: new developments and applications. *Proceedings of the Fib CACRCS DAYS 2021 - Capacity Assessment of Corroded Reinforced Concrete Structures Venue: On-Line 30th November-3rd December 2021*, 3–6.

Caspeele, Robby, Sykora, M., Allaix, D. L., & Steenbergen, R. (2013). The design value method and Adjusted Partial Factor Approach for existing structures. *Structural Engineering International: Journal of the International Association for Bridge and Structural Engineering (IABSE)*, *23*(4), 386–393. https://doi.org/10.2749/101686613X13627347100194

Castel, A., François, R., & Arliguie, G. (2000a). Mechanical behaviour of corroded reinforced concrete beams - Part 1: experimental study of corroded beams. *Materials and Structures/Materiaux et Constructions*, *33*(9), 539–544. https://doi.org/10.1007/bf02480533

Castel, A., François, R., & Arliguie, G. (2000b). Mechanical behaviour of corroded reinforced concrete beams - Part 2: bond and notch effects. *Materials and Structures/Materiaux et Constructions*, *33*(9), 545–551. https://doi.org/10.1007/bf02480534

Castel, Arnaud, Coronelli, D., & François, R. (2012). Response of corroded prestressed beams with bonded strands. *Proceedings of the Institution of Civil Engineers: Structures and Buildings*, *165*(5), 233–244. https://doi.org/10.1680/stbu.10.00023

Cavagnis, F., Fernández Ruiz, M., & Muttoni, A. (2018). An analysis of the shear-transfer actions in reinforced concrete members without transverse reinforcement based on refined experimental measurements. *Structural Concrete*, *19*(1), 49–64. https://doi.org/10.1002/suco.201700145

Ceb-Fip. (2013). *fib Model Code for Concrete Structures 2010*.

CEB-fip. (2006). *fib Bulletin 34 - Model code for service life design*.

CEB-fip. (2011). *fib Bulletin 59: Condition control and assessment of reinforced concrete structures*.

CEB-fip. (2015). *fib bulletin 76: Benchmarking of deemed-tosatisfy provisions in standards: Durability of reinforced concrete structures exposed to chlorides*.

CEB-fip. (2016). *fib Belletin 80: Partial factor methods for existing concrete structures*.

CEB. (1989). *Durable Concrete Structures - CEB Design Guide, Bulletin D'Information No.182*.

CEN-EC2. (2004). *EN 1992: Eurocode 2: Design of concrete structures - Part 1-1: General rules and rules for buildings*.

CEN. (2014). *European Standard: EN-206: Concrete-Specification, performance, production and confirmity*.

CEN. (2015). *Eurocode 0 - Basis of structural design*.

Chen, E., Berrocal, C. G., Fernandez, I., Löfgren, I., & Lundgren, K. (2020). Assessment of the mechanical behaviour of reinforcement bars with localised pitting corrosion by Digital Image Correlation. *Engineering Structures*, *219*(June), 110936. https://doi.org/10.1016/j.engstruct.2020.110936

Chen, E., Berrocal, C. G., Löfgren, I., & Lundgren, K. (2020). Correlation between concrete cracks and corrosion characteristics of steel reinforcement in pre-cracked plain and fibre-reinforced concrete beams. *Materials and Structures/Materiaux et Constructions*, *53*(2). https://doi.org/10.1617/s11527-020-01466-z

Chen, J., Fu, C., Ye, H., & Jin, X. (2020). Corrosion of steel embedded in mortar and concrete under different electrolytic accelerated corrosion methods. *Construction and Building Materials*, *241*, 117971. https://doi.org/10.1016/j.conbuildmat.2019.117971

Chernin, L., Val, D. V., & Stewart, M. G. (2012). Prediction of cover crack propagation in RC structures caused by corrosion. *Magazine of Concrete Research*, *64*(2), 95–111. https://doi.org/10.1680/macr.10.00108

Chinchón-Payá, S., Torres Martín, J., Silva Toledo, A., & Sanchez, J. (2021). Quantification of Chlorides and Sulphates on Concrete Surfaces Using Portable X-ray Fluorescence. Optimization of the Measurement Method Using Monte Carlo Simulation. *Materials*, *14*.

Cobo, A., Moreno, E., & Cánovas, M. F. (2011). Mechanical properties variation of B500SD high ductility reinforcement regarding its corrosion degree. *Materiales de Construccion*, *61*(304), 517–532. https://doi.org/10.3989/mc.2011.61410

Colajanni, P., Recupero, A., Ricciardi, G., & Spinella, N. (2016). Failure by corrosion in PC bridges: a case history of a viaduct in Italy. *International Journal of Structural Integrity*.

Collins, M. P., & Mitchel, D. (1997). *Prestressed Concrete Structures*. Englewood Cliffs: Prentice Hall.

CONTECVET IN30902I. A validated user's manual for assessing the residual life of concrete structures. (2001). DG Enterprise, CEC.

Coronelli, D., Castel, A., Vu, N. A., & François, R. (2009). Corroded post-tensioned beams with bonded tendons and wire failure. *Engineering Structures*, *31*(8), 1687–1697. https://doi.org/10.1016/j.engstruct.2009.02.043

Coronelli, D., François, R., Dang, H., & Zhu, W. (2019). Strength of Corroded RC Beams with Bond Deterioration. *Journal of Structural Engineering*, *145*(10), 04019097. https://doi.org/10.1061/(asce)st.1943-541x.0002358

Cosenza, E., Sessa, M., Losanno, D., & Bilotta, A. (2020). Application of the new Italian guidelines for existing bridges: an early case-study. *Proceedings of the Fib CACRCS DAYS 2020 - Capacity Assessment of Corroded Reinforced Concrete Structures Venue: On-Line 1st- 4th December 2020*, 231–234.

Costa, A., & Appleton, J. (2002). Case studies of concrete deterioration in a marine environment in Portugal. *Cement and Concrete Composites*, *24*(1), 169–179. https://doi.org/10.1016/S0958-9465(01)00037-3

Dai, L., Bian, H., Wang, L., Potier-Ferry, M., & Zhang, J. (2020). Prestress Loss Diagnostics in Pretensioned Concrete Structures with Corrosive Cracking. *Journal of Structural Engineering*, *146*(3), 04020013. https://doi.org/10.1061/(asce)st.1943-541x.0002554

Dai, L., Chen, Y., Wang, L., & Ma, Y. (2021). Secondary anchorage and residual prestressing force in locally corroded PT beams after strand fracture. *Construction and Building Materials*, *275*, 122137. https://doi.org/10.1016/j.conbuildmat.2020.122137

Dang, V. H., & François, R. (2013). Influence of long-term corrosion in chloride environment on mechanical behaviour of RC beam. *Engineering Structures*, *48*, 558–568. https://doi.org/10.1016/j.engstruct.2012.09.021

Darmawan, M. S., & Stewart, M. G. (2007). Effect of pitting corrosion on capacity of prestressing wires. *Magazine of Concrete Research*, *59*(2), 131–139. https://doi.org/10.1680/macr.2007.59.2.131

Dasar, A., Hamada, H., Sagawa, Y., & Yamamoto, D. (2017). Deterioration progress and performance reduction of 40-year-old reinforced concrete beams in natural corrosion environments. *Construction and Building Materials*, *149*, 690–704. https://doi.org/10.1016/j.conbuildmat.2017.05.162

Dasar, A., Irmawaty, R., Hamada, H., Sagawa, Y., & Yamamoto, D. (2016). Prestress loss and bending capacity of pre-cracked 40 year-old PC beams exposed to marine environment. *MATEC Web of Conferences*, *47*. https://doi.org/10.1051/matecconf/20164702008

Davis, J. R. (2000). Corrosion: understanding the basics. In *ASM International*. https://doi.org/10.5860/choice.37-6294

Deng, L., Wang, W., & Yu, Y. (2016). State-of-the-Art Review on the Causes and Mechanisms of Bridge Collapse. *Journal of Performance of Constructed Facilities*, *30*(2), 1–13. https://doi.org/10.1061/(asce)cf.1943-5509.0000731

Department of Transportation. (1993). *BA38/98 - assessment of the fatigue life of corroded or damaged reinforcing bars*.

Di Carlo, F., Isabella, P., Rinaldi, Z., & Spagnuolo, S. (2021). Influence of corrosion on the flexural behaviour of corroded reinforced concrete beams. *Fib CACRCS DAYS 2021 - Capacity Assessment of Corroded Reinforced Concrete Structures*.

Dong Lee, J. (2022). The effect of tension stiffening in moment-curvature responses of prestressed concrete members. *Engineering Structures*, *257*(February), 114043. https://doi.org/10.1016/j.engstruct.2022.114043

Dong, W., Ye, J., Murakami, Y., Oshita, H., Suzuki, S., & Tsutsumi, T. (2016). Residual load capacity of corroded reinforced concrete beam undergoing bond failure. *Engineering Structures*, *127*, 159–171. https://doi.org/10.1016/j.engstruct.2016.08.044

El-Sayed, A. K. (2017). Shear capacity assessment of reinforced concrete beams with corroded stirrups. *Construction and Building Materials*, *134*, 176–184. https://doi.org/10.1016/j.conbuildmat.2016.12.118

El Maaddawy, T. A., & Soudki, K. A. (2003). Effectiveness of Impressed Current Technique to Simulate Corrosion of Steel Reinforcement in Concrete. *Journal of Materials in Civil Engineering*, *15*(1), 41–47. https://doi.org/10.1061/(asce)0899-1561(2003)15:1(41)

El Maaddawy, T., Soudki, K., & Topper, T. (2005). Long-term performance of corrosion-damaged reinforced concrete beams. *ACI Structural Journal*, *102*(5), 649–656. https://doi.org/10.14359/14660

El Menoufy, A., & Soudki, K. (2014). Flexural behavior of corroded pretensioned girders repaired with CFRP sheets. *PCI Journal*, *59*(2), 129–143. https://doi.org/10.15554/pcij.03012014.129.143

ElBatanouny, M. K., Nanni, A., Ziehl, P. H., & Matta, F. (2015). Condition assessment of prestressed concrete beams using cyclic and monotonic load tests. *ACI Structural Journal*, *112*(1), 81–90. https://doi.org/10.14359/51687181

Elices, M., Valiente, A., Caballero, L., Iordachescu, M., Fullea, J., Sánchez-Montero, J., & López-Serrano, V. (2012). Failure analysis of prestressed anchor bars. *Engineering Failure Analysis*, *24*, 57–66. https://doi.org/10.1016/j.engfailanal.2012.03.007

Engen, M., Hendriks, M. A. N., Köhler, J., Øverli, J. A., & Åldstedt, E. (2017). A quantification of the modelling uncertainty of non-linear finite element analyses of large concrete

structures. *Structural Safety*, *64*, 1–8. https://doi.org/10.1016/j.strusafe.2016.08.003

Federal Highway Administration. (2006). *Status of the Nation's Highways, Bridges, and Transit: Condition and Performance*.

Federation international du beèton. (2006). *Model Code for Service Life Design, fib Bulletin 34*.

Feng, W., Tarakbay, A., Ali Memon, S., Tang, W., & Cui, H. (2021). Methods of accelerating chloride-induced corrosion in steel-reinforced concrete: A comparative review. *Construction and Building Materials*, *289*, 123165. https://doi.org/10.1016/j.conbuildmat.2021.123165

Fernandez, I., Bairán, J. M., & Marí, A. R. (2015). Corrosion effects on the mechanical properties of reinforcing steel bars. Fatigue and σ-ε behavior. *Construction and Building Materials*, *101*, 772–783. https://doi.org/10.1016/j.conbuildmat.2015.10.139

Fernandez, I., Herrador, M. F., Marí, A. R., & Bairán, J. M. (2018). Ultimate Capacity of Corroded Statically Indeterminate Reinforced Concrete Members. *International Journal of Concrete Structures and Materials*, *12*(1). https://doi.org/10.1186/s40069-018-0297-9

fib Model Code 2010. Model Code for Concrete Structures. (2013).

Finozzi, I., Saetta, A., & Budelmann, H. (2018). Structural response of reinforcing bars affected by pitting corrosion: experimental evaluation. *Construction and Building Materials*, *192*, 478–488. https://doi.org/10.1016/j.conbuildmat.2018.10.088

Fraczek, J. (1987). Review of Electrochemical Principles as Applied to Corrosion of Steel in a Concrete or Grout Environment. In F.W. Gibson (Ed.), *ACI SP-102, Corrosion, Concrete and ChloridesSteel Corrosion in Concrete: Causes and Restraints* (pp. 13–24). American Concrete Institute.

Franceschini, L., Vecchi, F., Tondolo, F., Belletti, B., & Montero, S. J. (2022). Mechanical Behaviour of Corroded Strands under Chloride Attack: A New Constitutive Law. *Construction and Building Materials*, *316*.

Franceschini, Lorenzo, Vecchi, F., Belletti, B., Andrade, C., & Peiretti, H. (2021). Analytical method for the evaluation of the residual service life of prestressed concrete beams subjected to corrosion deterioration. *Structural Concrete*, 1–17. https://doi.org/10.1002/suco.202100245

François, R., & Arliguie, G. (1999). Effect of microcracking and cracking on the development of corrosion in reinforced concrete members. *Magazine of Concrete Research*, *51*(2), 143–150. https://doi.org/10.1680/macr.1999.51.2.143

Geng, C., Xu, Y., & Weng, D. (2008). A new method to quickly assess the inhibitor efficiency. *Journal Wuhan University of Technology, Materials Science Edition*, *23*(6), 950–954.

https://doi.org/10.1007/s11595-007-6950-9

Giriraju, R., Sengupta, A. K., & Pillai, R. G. (2022). Tensile Behaviour of Corroded Strands in Prestressed Concrete Systems. *Journal of The Institution of Engineers (India): Series A*, *103*(3), 867–879. https://doi.org/10.1007/s40030-022-00656-y

González, J. A., Andrade, C., Alonso, C., & Feliu, S. (1995). Comparison of rates of general corrosion and maximum pitting penetration on concrete embedded steel reinforcement. *Cement and Concrete Research*, *25*(2), 257–264. https://doi.org/10.1016/0008-8846(95)00006-2

Haefliger, S., & Kaufmann, W. (2022). Corroded Tension Chord Model: Load-deformation behavior of structures with locally corroded reinforcement. *Structural Concrete*, *23*(1), 104–120. https://doi.org/10.1002/suco.202100165

Han, S. J., Lee, D., Yi, S. T., & Kim, K. S. (2020). Experimental shear tests of reinforced concrete beams with corroded longitudinal reinforcement. *Structural Concrete*, *21*(5), 1763–1776. https://doi.org/10.1002/suco.201900248

Hansson, C. M. (2011). The impact of corrosion on society. *Metallurgical and Materials Transactions A: Physical Metallurgy and Materials Science*, *42*(10), 2952–2962. https://doi.org/10.1007/s11661-011-0703-2

Hansson, C. M., Poursaee, A., & Laurent, A. (2006). Macrocell and microcell corrosion of steel in ordinary Portland cement and high performance concretes. *Cement and Concrete Research*, *36*(11), 2098–2102. https://doi.org/10.1016/j.cemconres.2006.07.005

Hariche, L., Ballim, Y., Bouhicha, M., & Kenai, S. (2012). Effects of reinforcement configuration and sustained load on the behaviour of reinforced concrete beams affected by reinforcing steel corrosion. *Cement and Concrete Composites*, *34*(10), 1202–1209. https://doi.org/10.1016/j.cemconcomp.2012.07.010

Hartt, W. H., & Lee, S. K. (2016). Projecting corrosion induced bridge tendon failure resulting from deficient grout: Part I - Model Development and Example Results. *NACE - International Corrosion Conference Series*, *1*(8), 448–459.

Helland, S., Maage, M., & Fluge, F. (2003). *Duranet: service life design of concrete structures*.

Helmerich, R., & Zunkel, A. (2014). Partial collapse of the Berlin Congress Hall on May 21st, 1980. *Engineering Failure Analysis*, *43*, 107–119. https://doi.org/10.1016/j.engfailanal.2013.11.013

Higgins, C., & Farrow, W. C. (2006). Tests of reinforced concrete beams with corrosion-damaged stirrups. *ACI Structural Journal*, *103*(1), 133–141. https://doi.org/10.14359/15094

Hope, B. B., Page, J. A., & Poland, J. S. (1985). The Deterioration of the Chloride Content of Concrete. *Cement and Concrete Research*, *15*, 863–870.

Hou, J., & Song, L. (2015). Numerical Investigation on Stress Concentration of Tension Steel Bars with One or Two Corrosion Pits. *Advances in Materials Science and Engineering*, *2015*. https://doi.org/10.1155/2015/413737

Huang, L., Ye, H., Jin, X., Jin, N., & Xu, Z. (2020). Corrosion-induced shear performance degradation of reinforced concrete beams. *Construction and Building Materials*, *248*, 118668. https://doi.org/10.1016/j.conbuildmat.2020.118668

Huber, P., Huber, T., & Kollegger, J. (2016). Investigation of the shear behavior of RC beams on the basis of measured crack kinematics. *Engineering Structures*, *113*, 41–58. https://doi.org/10.1016/j.engstruct.2016.01.025

Hunkeler, F. (2005). Corrosion in reinforced concrete: Processes and mechanisms. In *Corrosion in Reinforced Concrete Structures* (Issue December 2005). https://doi.org/10.1533/9781845690434.1

Imam, A., & Azad, A. K. (2016). Prediction of residual shear strength of corroded reinforced concrete beams. *International Journal of Advanced Structural Engineering*, *8*(3), 307–318. https://doi.org/10.1007/s40091-016-0133-x

Imhof, D. (2004). *Risk Assessment of Existing Bridge Structures*.

Imperatore, S., & Rinaldi, Z. (2016). Strength decay of RC sections for chloride attack. *International Journal of Structural Integrity*, *7*(2), 194–212.

Imperatore, Stefania, Rinaldi, Z., & Drago, C. (2017). Degradation relationships for the mechanical properties of corroded steel rebars. *Construction and Building Materials*, *148*, 219–230. https://doi.org/10.1016/j.conbuildmat.2017.04.209

IPCC. (2013). *Climate Change 2013: The Physical Science Basis- Contribution of Working Group I to the Fifth Assessment Report of the Intergovernmental Panel on Climate Change*.

IPCC. (2014). *Climate Change 2014-Impacts, Adaptation, and Vulnerability-Part A: Global and Sectoral Aspects-Working Group II Contribution to the Fifth Assessment Report of the Intergovernmental Panel on Climate Change*.

ISO. (2015). *ISO 2394:2015: General principles on reliability for structures*.

ISO 8044 Standard. (2020). *Corrosion of metals and alloys - Vocabullary*.

Iuliano, L., & Minetola, P. (2009). Enhancing moulds manufacturing by means of reverse engineering. *International Journal of Advanced Manufacturing Technology*, *43*(5–6), 551–562. https://doi.org/10.1007/s00170-008-1739-3

Jafar Mazumder, M. A. (2020). Global Impact of Corrosion: Occurrence, Cost and Mitigation. *Global Journal of Engineering Sciences*, *5*(4), 0–4. https://doi.org/10.33552/gjes.2020.05.000618

Javaherdashti, R. (2017). Microbiologically influenced corrosion. In B. Derby (Ed.), *British Corrosion Journal* (II°, Vol. 29, Issue 3). Springer. https://doi.org/10.1179/000705994798267674

JCSS. Probabilistic Model Code - Part 3: Resistance Models, Chapter 3.04: pp.1 (2001).

Jeon, C.H., Nguyen, D., & Shim, C. S. (2020). Assessment of Mechanical Properties of Corroded Prestressing Strands. *Applied Sciences*, *10*(4055), 1–19. https://doi.org/10.3390/app10124055

Jeon, Chi Ho, Lee, J. Bin, Lon, S., & Shim, C. S. (2019). Equivalent material model of corroded prestressing steel strand. *Journal of Materials Research and Technology*, *8*(2), 2450–2460. https://doi.org/10.1016/j.jmrt.2019.02.010

Jeon, Chi Ho, Nguyen, C. D., & Shim, C. S. (2020). Assessment of mechanical properties of corroded prestressing strands. *Applied Sciences (Switzerland)*, *10*(12). https://doi.org/10.3390/APP10124055

Jeon, Chi Ho, & Shim, C. S. (2020). Flexural behavior of post-tensioned concrete beams with multiple internal corroded strands. *Applied Sciences (Switzerland)*, *10*(22), 1–17. https://doi.org/10.3390/app10227994

Jeon, S. J., Shin, H., Kim, S. H., Park, S. Y., & Yang, J. M. (2019). Transfer Lengths in Pretensioned Concrete Measured Using Various Sensing Technologies. *International Journal of Concrete Structures and Materials*, *13*(1). https://doi.org/10.1186/s40069-019-0355-y

Jia, J., Yu, F., Yao, D., & Zhu, W. (2011). Strain analysis of corrosed prestressed concrete beams on fatigue test. *Advanced Materials Research*, *255–260*, 355–359. https://doi.org/10.4028/www.scientific.net/AMR.255-260.355

Jiang, C., Wu, Y. F., & Dai, M. J. (2018a). Degradation of steel-to-concrete bond due to corrosion. *Construction and Building Materials*, *158*(October), 1073–1080. https://doi.org/10.1016/j.conbuildmat.2017.09.142

Jiang, C., Wu, Y. F., & Dai, M. J. (2018b). Degradation of steel-to-concrete bond due to corrosion. *Construction and Building Materials*, *158*, 1073–1080. https://doi.org/10.1016/j.conbuildmat.2017.09.142

Joint ASCE-ACI Task Committee 426 on Shear and Diagonal Tension of the Committee on Masonry and Reinforced Concrete of the Structural Division, A. (1973). The Shear

Strength of Reinforced Concrete Members. *Journal of Structure Division*, *June*(6), 1091–1187.

Juarez, C. A., Guevara, B., Fajardo, G., & Castro-Borges, P. (2011). Ultimate and nominal shear strength in reinforced concrete beams deteriorated by corrosion. *Engineering Structures*, *33*(12), 3189–3196. https://doi.org/10.1016/j.engstruct.2011.08.014

Jung, J. S., Lee, B. Y., & Lee, K. S. (2019). Experimental Study on the Structural Performance Degradation of Corrosion-Damaged Reinforced Concrete Beams. *Advances in Civil Engineering*, *2019*(2). https://doi.org/10.1155/2019/9562574

Kani, G. N. J. (1966). Basic Facts Concerning Shear Failure. *ACI Journal*, *63*(6), 675–692. https://doi.org/10.14359/7644

Kashani, M. M., Alagheband, P., Khan, R., & Davis, S. (2015). Impact of corrosion on low-cycle fatigue degradation of reinforcing bars with the effect of inelastic buckling. *International Journal of Fatigue*, *77*, 174–185. https://doi.org/10.1016/j.ijfatigue.2015.03.013

Kashani, M. M., Crewe, A. J., & Alexander, N. A. (2013). Nonlinear cyclic response of corrosion-damaged reinforcing bars with the effect of buckling. *Construction and Building Materials*, *41*, 388–400. https://doi.org/10.1016/j.conbuildmat.2012.12.011

Kashani, M. M., Maddocks, J., & Dizaj, E. A. (2019). Residual Capacity of Corroded Reinforced Concrete Bridge Components: State-of-the-Art Review. *Journal of Bridge Engineering*, *24*(7), 1–34. https://doi.org/10.1061/(asce)be.1943-5592.0001429

Kearsley, E. P., & Joyce, A. (2014). Effect of corrosion products on bond strength and flexural behaviour of reinforced concrete slabs. *Journal of the South African Institution of Civil Engineering*, *56*(2), 21–29.

Khan, I., François, R., & Castel, A. (2014). Experimental and analytical study of corroded shear-critical reinforced concrete beams. *Materials and Structures/Materiaux et Constructions*, *47*(9), 1467–1481. https://doi.org/10.1617/s11527-013-0129-y

Khan, M. U., Ahmad, S., & Al-Gahtani, H. J. (2017). Chloride-Induced Corrosion of Steel in Concrete: An Overview on Chloride Diffusion and Prediction of Corrosion Initiation Time. *International Journal of Corrosion*, *2017*. https://doi.org/10.1155/2017/5819202

Khuntia, M., & Stojadinovic, B. (2001). Shear strength of reinforced concrete beams without transverse reinforcement. *ACI Structural Journal*, *98*(5), 648–656.

Kioumarsi, M., Benenato, A., Ferracuti, B., & Imperatore, S. (2021). Residual flexural capacity of corroded prestressed reinforced concrete beams. *Metals*, *11*(3), 1–22. https://doi.org/10.3390/met11030442

Koch, G., Varney, J., Thompson, N., Moghissi, O., Gould, M., & Payer, J. (2016). *International measures of prevention, application, and economics of corrosion technologies study*.

Korean Road and Transportation Association (KRTA). (2015). *Design code for highway bridges (Limit state design)*.

Koteš, P. (2013). Influence of corrosion on crack width and pattern in an RC beam. *Procedia Engineering*, *65*, 311–320. https://doi.org/10.1016/j.proeng.2013.09.048

Kruger, J. (2011). Cost of Metallic Corrosion. *Uhlig's Corrosion Handbook: Third Edition*, 15–20. https://doi.org/10.1002/9780470872864.ch2

Kumar, P., & Imam, B. (2013). Footprints of air pollution and changing environment on the sustainability of built infrastructure. *Science of the Total Environment*, *444*, 85–101. https://doi.org/10.1016/j.scitotenv.2012.11.056

Lachemi, M., Al-Bayati, N., Sahmaran, M., & Anil, O. (2014). The effect of corrosion on shear behavior of reinforced self-consolidating concrete beams. *Engineering Structures*, *79*, 1–12. https://doi.org/10.1016/j.engstruct.2014.07.044

Lee, G. C., Mohan, S. B., Huang, C., & Fard, B. N. (2013). A study of US bridge failures (1980–2012). In *MCEER Technical Report*.

Lee, H. S., & Cho, Y. S. (2009). Evaluation of the mechanical properties of steel reinforcement embedded in concrete specimen as a function of the degree of reinforcement corrosion. *International Journal of Fracture*, *157*(1–2), 81–88. https://doi.org/10.1007/s10704-009-9334-7

Leondardt, F. (1965). Reducing the shear reinforcement in reinforced concrete beams and slabs. *Magazine of Concrete Research*, *17*(53), 187–198. https://doi.org/10.1680/macr.1965.17.53.187

Li, D., Wei, R., Du, Y., Guan, X., & Zhou, M. (2017). Measurement methods of geometrical parameters and amount of corrosion of steel bar. *Construction and Building Materials*, *154*, 921–927. https://doi.org/10.1016/j.conbuildmat.2017.08.018

Li, D., Wei, R., Li, L., Guan, X., & Mi, X. (2019). Pitting corrosion of reinforcing steel bars in chloride contaminated concrete. *Construction and Building Materials*, *199*, 359–368. https://doi.org/10.1016/j.conbuildmat.2018.12.003

Li, F., Luo, X., Wang, K., & Ji, Y. (2017). Pitting Damage Characteristics on Prestressing Steel Strands by Combined Action of Fatigue Load and Chloride Corrosion. *Journal of Bridge Engineering*, *22*(7), 1–12. https://doi.org/10.1061/(asce)be.1943-5592.0001057

Li, F., & Yuan, Y. (2013). Effects of corrosion on bond behavior between steel strand and concrete. *Construction and Building Materials*, *38*, 413–422.

https://doi.org/10.1016/j.conbuildmat.2012.08.008

Li, F., Yuan, Y., & Li, C. Q. (2011). Corrosion propagation of prestressing steel strands in concrete subject to chloride attack. *Construction and Building Materials*, *25*(10), 3878–3885. https://doi.org/10.1016/j.conbuildmat.2011.04.011

Li, S., Tang, H., Gui, Q., & John Ma, Z. (2017). Corrigendum to "Fatigue behavior of naturally corroded plain reinforcing bars" [Construction and Building Materials 152 (2017) 933–942](S0950061817313144)(10.1016/j.conbuildmat.2017.06.173)). *Construction and Building Materials*, *155*, 1256–1257. https://doi.org/10.1016/j.conbuildmat.2017.09.011

Li, S., Tang, H., Gui, Q., & Ma, Z. J. (2017). Fatigue behavior of naturally corroded plain reinforcing bars. *Construction and Building Materials*, *152*, 933–942. https://doi.org/10.1016/j.conbuildmat.2017.06.173

Lin, H., Zhao, Y., Feng, P., Ye, H., Ozbolt, J., Jiang, C., & Yang, J. Q. (2019). State-of-the-art review on the bond properties of corroded reinforcing steel bar. *Construction and Building Materials*, *213*, 216–233. https://doi.org/10.1016/j.conbuildmat.2019.04.077

Lin, H., Zhao, Y., Ožbolt, J., & Hans-Wolf, R. (2017). The bond behavior between concrete and corroded steel bar under repeated loading. *Engineering Structures*, *140*, 390–405. https://doi.org/10.1016/j.engstruct.2017.02.067

Liu, X., Zhang, W., Gu, X., Asce, M., & Ye, Z. (2023). Assessment of Fatigue Life for Corroded Prestressed Concrete Beams Subjected to High-Cycle Fatigue Loading. *Journal of Structural Engineering*, *149*(2). https://doi.org/10.1061/JSENDH.STENG-11663

Liu, X., Zhang, W., Gu, X., & Zeng, Y. (2017). Degradation of Mechanical Behavior of Corroded Prestressing Wires Subjected to High-Cycle Fatigue Loading. *Journal of Bridge Engineering*, *22*(5), 04017004. https://doi.org/10.1061/(asce)be.1943-5592.0001030

Liu, Y., Fan, Y., & Apostolopoulos, C. (2019). Experimental study on flexural behavior of prestressed concrete beams reinforced by CFRP under chloride environment. *Advances in Civil Engineering*, *2019*. https://doi.org/10.1155/2019/2424518

Lopes, S. M. R., & Simões, L. M. L. P. (1999). Influence of corrosion on prestress strands. *Canadian Journal of Civil Engineering*, *26*(6), 782–788. https://doi.org/10.1139/l99-043

Lu, C., Yuan, S., Cheng, P., & Liu, R. (2016). Mechanical properties of corroded steel bars in pre-cracked concrete suffering from chloride attack. *Construction and Building Materials*, *123*, 649–660.

Lu, Z. H., Li, F., & Zhao, Y. G. (2016). An investigation of degradation of mechanical behaviour of prestressing strands subjected to chloride attacking. *International Conference on Durability of Concrete Structures, ICDCS 2016*, 57–65.

https://doi.org/10.5703/1288284316111

Ma, Y., Guo, Z., Wang, L., & Zhang, J. (2017). Experimental investigation of corrosion effect on bond behavior between reinforcing bar and concrete. *Construction and Building Materials*, *152*, 240–249. https://doi.org/10.1016/j.conbuildmat.2017.06.169

Mak, M. W. T., Desnerck, P., & Lees, J. M. (2019). Corrosion-induced cracking and bond strength in reinforced concrete. *Construction and Building Materials*, *208*, 228–241. https://doi.org/10.1016/j.conbuildmat.2019.02.151

Mancini, G., & Tondolo, F. (2014). Effect of bond degradation due to corrosion - A literature survey. *Structural Concrete*, *15*(3), 408–418. https://doi.org/10.1002/suco.201300009

Mangat, P. S., & Elgarf, M. S. (1999). Flexural strength of concrete beams with corroding reinforcement. *ACI Structural Journal*, *96*(1), 149–158. https://doi.org/10.14359/606

Meda, A., Mostosi, S., Rinaldi, Z., & Riva, P. (2014). Experimental evaluation of the corrosion influence on the cyclic behaviour of RC columns. *Engineering Structures*, *76*, 112–123. https://doi.org/10.1016/j.engstruct.2014.06.043

Minh, H., Mutsuyoshi, H., & Niitani, K. (2007). Influence of grouting condition on crack and load-carrying capacity of post-tensioned concrete beam due to chloride-induced corrosion. *Construction and Building Materials*, *21*(7), 1568–1575. https://doi.org/10.1016/j.conbuildmat.2005.10.004

Ministero delle Infrastrutture e della Mobilità Sostenibili. (2022). *Linee guida per la classificazione e gestione del rischio, la valutazionedella sicurezza ed il monitoraggio dei ponti esistenti*.

Ministry of Public of Works. (2008). *Code on Structural Concrete (EHE-08)*.

Mircea, D., Ioani, A., Filip, M., & Pepenar, I. (1994). Long-term durability of reinforced and prestressed elements in aggressive environments. *ACI Materials Journal*, *91*(2), 135–140. https://doi.org/10.14359/4564

Mitchell, D., Cook, W. D., & Tham, T. (1993). Influence of High Strength Concrete on Transfer and Development Length of Pretensioning Strand. *PCI Journal*, *38*(3), 52–66. https://doi.org/10.15554/pcij.05011993.52.66

Mondoro, A., Frangopol, D. M., & Liu, L. (2018). Bridge Adaptation and Management under Climate Change Uncertainties: A Review. *Natural Hazards Review*, *19*(1), 1–12. https://doi.org/10.1061/(asce)nh.1527-6996.0000270

Montemor, M. F., Simões, A. M. P., & Ferreira, M. G. S. (2003). Chloride-induced corrosion on reinforcing steel: From the fundamentals to the monitoring techniques. *Cement and Concrete Composites*, *25*(4-5 SPEC), 491–502. https://doi.org/10.1016/S0958-

9465(02)00089-6

Moreno, E., Cobo, A., Palomo, G., & González, M. N. (2014). Mathematical models to predict the mechanical behavior of reinforcements depending on their degree of corrosion and the diameter of the rebars. *Construction and Building Materials*, *61*, 156–163. https://doi.org/10.1016/j.conbuildmat.2014.03.003

Morgese, M., Ansari, F., Domaneschi, M., & Cimellaro, G. P. (2020). Post-collapse analysis of Morandi's Polcevera viaduct in Genoa Italy. *Journal of Civil Structural Health Monitoring*, *10*(1), 69–85. https://doi.org/10.1007/s13349-019-00370-7

Murer, N., & Buchheit, R. G. (2013). Stochastic modeling of pitting corrosion in aluminum alloys. *Corrosion Science*, *69*, 139–148. https://doi.org/10.1016/j.corsci.2012.11.034

Naderpour, H., Ghasemi-Meydansar, F., & Haji, M. (2022). Experimental study on the behavior of RC beams with artificially corroded bars. *Structures*, *43*(June), 1932–1944. https://doi.org/10.1016/j.istruc.2022.07.005

Nakicenovic, N., Alcamo, J., Grubler, A., Riahi, K., Roehrl, R., Rogner, H. H., & Victor, N. (2000). *Special report on emissions scenarios (SRES), a special report of Working Group III of the intergovernmental panel on climate change*.

Nasr, A., Björnsson, I., Honfi, D., Larsson Ivanov, O., Johansson, J., & Kjellström, E. (2019). A review of the potential impacts of climate change on the safety and performance of bridges. *Sustainable and Resilient Infrastructure*, *6*(3–4), 192–212. https://doi.org/10.1080/23789689.2019.1593003

Nasser, H., Van Steen, C., Vandewalle, L., & Verstrynge, E. (2021). An experimental assessment of corrosion damage and bending capacity reduction of singly reinforced concrete beams subjected to accelerated corrosion. *Construction and Building Materials*, *286*, 122773. https://doi.org/10.1016/j.conbuildmat.2021.122773

National Physical Laboratory. (2020). *The Corrosion of Steel in Concrete – Basic Understanding , Monitoring and Corrosion Control Methods*.

Nogal, M., Bastidas-arteaga, E., & Dos Santos Gervasio, H. M. (2021). Consideration of climate change-induced corrosion by structural codes. *IABSE Congress, Christchurch 2021: Resilient Technologies for Sustainable Infrastructure*, 1064–1070.

Nürnberger, U. (2002). Corrosion induced failure mechanisms of prestressing steel. *Materials and Corrosion*, *53*(8), 591–601. https://doi.org/10.1002/1521-4176(200208)53:8<591::AID-MACO591>3.0.CO;2-X

Nuti, C., Briseghella, B., Chen, A., Lavorato, D., Iori, T., & Vanzi, I. (2020). Relevant outcomes from the history of Polcevera Viaduct in Genova, from design to nowadays failure. *Journal*

of Civil Structural Health Monitoring, *10*(1), 87–107. https://doi.org/10.1007/s13349-019-00371-6

Oh, B. H., Lim, S. N., Lee, M. K., & Yoo, S. W. (2014). Analysis and prediction of transfer length in pretensioned, prestressed concrete members. *ACI Structural Journal*, *111*(3), 549–559. https://doi.org/10.14359/51686571

Ou, Y. C., Susanto, Y. T. ., & Roh, H. (2016). Tensile behavior of naturally and artificially corroded steel bars. *Construction and Building Materials*, *103*, 93–104.

Oyado, M., Kanakubo, T., Sato, T., & Yamamoto, Y. (2011). Bending performance of reinforced concrete member deteriorated by corrosion. *Structure and Infrastructure Engineering*, *7*(1), 121–130. https://doi.org/10.1080/15732471003588510

Papadopoulos, M. P., Apostolopoulos, C. A., Alexopoulos, N. D., & Pantelakis, S. G. (2007). Effect of salt spray corrosion exposure on the mechanical performance of different technical class reinforcing steel bars. *Materials and Design*, *28*(8), 2318–2328. https://doi.org/10.1016/j.matdes.2006.07.017

Papadopoulos, M. P., Apostolopoulos, C. A., Zervaki, A. D., & Haidemenopoulos, G. N. (2011). Corrosion of exposed rebars, associated mechanical degradation and correlation with accelerated corrosion tests. *Construction and Building Materials*, *25*(8), 3367–3374. https://doi.org/10.1016/j.conbuildmat.2011.03.027

Pape, T. M., & Melcher, R. E. (2013). Performance of 45-year-old corroded prestressed concrete beams. *Proceedings of the Institution of Civil Engineers: Structures and Buildings*, *166*(10), 547–559. https://doi.org/10.1680/stbu.11.00016

Park, R., & Paulay, T. (1975). *Reinforced Concrete Structures*. John Wiley & Sons, Inc.

Parrott, L. J. (1990). Damage caused by carbonation of reinforced concrete. *Materials and Structures*, *23*(3), 230–234. https://doi.org/10.1007/BF02473023

Pedrosa, F., & Andrade, C. (2017). Corrosion induced cracking: Effect of different corrosion rates on crack width evolution. *Construction and Building Materials*, *133*, 525–533. https://doi.org/10.1016/j.conbuildmat.2016.12.030

Pillai, R. G., Gardoni, P., Hueste, M. D., Reinschmidt, K., & Trejo, D. (2010). Flexural Reliability of Corroding Segmental Post-tensioned Bridges. *Safety, Reliability and Risk of Structures, Infrastructures and Engineering Systems*, *April 2018*, 1920–1927.

Plank, A., Struck, W. T., & Zschätzsch, M. (1981). *Causes of the partial failure of the Congress Hall in Berlin-Tiergarten*.

Podolny, W. (1992). Corrosion of Prestressing Steels and Its Mitigation. *PCI Journal*, *37*(5), 34–55. https://doi.org/10.15554/pcij.09011992.34.55

Polder, R. B., Peelen, W. H. A., & Courage, W. M. G. (2012). Non-traditional assessment and maintenance methods for aging concrete structures - Technical and non-technical issues. *Materials and Corrosion*, *63*(12), 1147–1153. https://doi.org/10.1002/maco.201206725

Popovics, S., Simeonov, Y., Bozhinov, G., & Barovsky, N. (1983). *Durability of Reinforced Concrete in Sea Water, Chapter 2* (Corrosion of Reinforcement in Concrete Construction (Ed.)). Ellis Horwood.

Recupero, A., & Spinella, N. (2019). Experimental tests on corroded prestressed concrete beams subjected to transverse load. *Structural Concrete*, *20*(6), 2220–2229. https://doi.org/10.1002/suco.201900242

Rinaldi, Z., Imperatore, S., & Valente, C. (2010). Experimental evaluation of the flexural behavior of corroded P/C beams. *Construction and Building Materials*, *24*(11), 2267–2278. https://doi.org/10.1016/j.conbuildmat.2010.04.029

Roberge, P. R. (2008). Corrosion Engineering - Principles and Practice. In The McGraw-Hill Companies (Ed.), *CEA, Chemical Engineering in Australia* (Vol. ChE9, Issue 2).

Rodriguez, J., Ortega, L. M., & Casal, J. (1997). Load carrying capacity of concrete structures with corroded reinforcement. *Construction and Building Materials*, *11*(4), 239–248. https://doi.org/10.1016/S0950-0618(97)00043-3

Rodríguez, P., Ramirez, E., Feliu, S., Gonzalez, J. A., & Lopez, W. (1999). Significance of coplanar macrocells to corrosion in concrete-embedded steel. *Corrosion*, *55*(3), 319–325. https://doi.org/10.5006/1.3283994

Rogers, R. A., Wotherspoon, L., Scott, A., & Ingham, J. M. (2012). Residual strength assessment and destructive testing of decommissioned concrete bridge beams with corroded pretensioned reinforcement. *PCI Journal*, *57*(3), 100–118. https://doi.org/10.15554/pcij.06012012.100.118

Saha, M., & Eckelman, M. J. (2014). Urban scale mapping of concrete degradation from projected climate change. *Urban Climate*, *9*, 101–114. https://doi.org/10.1016/j.uclim.2014.07.007

Sahmaran, M., Anil, O., Lachemi, M., Yildirim, G., Ashour, A. F., & Acar, F. (2015). Effect of corrosion on shear behavior of reinforced engineered cementitious composite beams. *ACI Structural Journal*, *112*(6), 771–782. https://doi.org/10.14359/51687749

Salem, H. M., & Helmy, H. M. (2014). Numerical investigation of collapse of the Minnesota I-35W bridge. *Engineering Structures*, *59*, 635–645. https://doi.org/10.1016/j.engstruct.2013.11.022

Sanchez, J., Fullea, J., & Andrade, C. (2017). Corrosion-induced brittle failure in reinforcing

steel. *Theoretical and Applied Fracture Mechanics*, *92*(September), 229–232. https://doi.org/10.1016/j.tafmec.2017.08.006

Schiebl, P., & Mayer, T. F. (2007). *Schlussberichte zur ersten Phase des DAfStb/BMBF-Verbundforschungsvorhabens "Nachhalting Bauen mit Beton", (German)*.

Schiessl, P., & Raupach, M. (1997). Laboratory Studies and Calculations on the Influence of Crack Width on Chloride-Induced Corrosion of Steel in Concrete. *ACI Materials Journal*, *94*(1), 56–62.

Schmitt, G. a., Schütze, M., Hays, G. F., Burns, W., Han, E., Pourbaix, A., & Jacobson, G. (2009). Global Needs for Knowledge Development in Materials Deterioration and Corrosion Control in cooperation with. In *Word Corrosion Organization: Vol. FHWA-RD-01* (Issue May).

Schreier H, J-J, O., & MA, S. (2009). *Image correlation for shape, motion and deformation measurements: Basic concepts, theory and applications.* (Springer (Ed.)).

Schupack, M., & Suarez, M. G. (1982). Some Recent Corrosion Embrittlement Failures of Prestressing Systems in the United States. *Journal - Prestressed Concrete Institute*, *27*(2), 38–55. https://doi.org/10.15554/pcij.03011982.38.55

Shapiro, A. S. S., & Wilk, M. B. (1965). An Analysis of Variance Test for Normality (Complete Samples). *Biometrika*, *52*(3), 591–611. https://pdfs.semanticscholar.org/1f1d/9a7151d52c2e26d35690dbc7ae8098beee22.pdf

Shen, J., Gao, X., Li, B., Du, K., Jin, R., Chen, W., & Xu, Y. (2019). Damage evolution of RC beams under simultaneous reinforcement corrosion and sustained load. *Materials*, *12*(4), 1–16. https://doi.org/10.3390/ma12040627

Soltani, M., Safiey, A., & Brennan, A. (2019). A state-of-the-art review of bending and shear behaviors of corrosion-damaged reinforced concrete beams. *ACI Structural Journal*, *116*(3), 53–64. https://doi.org/10.14359/51714481

Sousa, M. L., Dimova, S., Athanasopoulou, A., Rianna, G., Mercogliano, P., Villani, V., Nogal, M., Gervasio, H., Neves, L., Bastidas-Arteaga, E., & Tsionis, G. (2020). *JRC Technical Report: expected implications of climate change on the corrosion of structures*. https://doi.org/10.2760/05229

Stern, M., & Geary, A. L. (1957). Electrochemical Polarization: I . A Theoretical Analysis of the Shape of Polarization Curves. *Journal of The Electrochemical Society*, *104*(1), 56–63.

Su, X., Ma, Y., Wang, L., Guo, Z., & Zhang, J. (2022). Fatigue life prediction for prestressed concrete beams under corrosion deterioration process. *Structures*, *43*(August), 1704–1715. https://doi.org/10.1016/j.istruc.2022.07.043

Sun, X., Kong, H., Wang, H., & Zhang, Z. (2018). Evaluation of corrosion characteristics and corrosion effects on the mechanical properties of reinforcing steel bars based on three-dimensional scanning. *Corrosion Science*, *142*(November 2017), 284–294. https://doi.org/10.1016/j.corsci.2018.07.030

Taha, N. A., & Morsy, M. (2016). Study of the behavior of corroded steel bar and convenient method of repairing. *HBRC Journal*, *12*(2), 107–113. https://doi.org/10.1016/j.hbrcj.2014.11.004

Tahershamsi, M., Fernandez, I., Lundgren, K., & Zandi, K. (2017). Investigating correlations between crack width, corrosion level and anchorage capacity. *Structure and Infrastructure Engineering*, *13*(10), 1294–1307. https://doi.org/10.1080/15732479.2016.1263673

Tahershamsi, M., Lundgren, K., Plos, M., & Zandi, K. (2014). Anchorage of naturally corroded bars in reinforced concrete structures. *Magazine of Concrete Research*, *66*(14), 729–744. https://doi.org/10.1680/macr.13.00276

Talukdar, S., Banthia, N., Grace, J. R., & Cohen, S. (2012). Carbonation in concrete infrastructure in the context of global climate change: Part 2 - Canadian urban simulations. *Cement and Concrete Composites*, *34*(8), 931–935. https://doi.org/10.1016/j.cemconcomp.2012.04.012

Tanaka Y., Kawano H., Watanabe H., & T., K. (2001). Chloride-induced deterioration and its influence on load carrying capacity of post-tensioned concrete bridges. *Third Int. Conf. Concrete under Severe Conditions — Environment and Loading*, 495–502.

Tang, F. J., Chen, G. Da, & Yi, W. J. (2014). Corrosion-induced concrete cracking, steel-concrete bond loss, and mechanical degradation of steel bars. *Advanced Materials Research*, *919–921*, 1760–1770. https://doi.org/10.4028/www.scientific.net/AMR.919-921.1760

Tang, F., Lin, Z., Chen, G., & Yi, W. (2014). Three-dimensional corrosion pit measurement and statistical mechanical degradation analysis of deformed steel bars subjected to accelerated corrosion. *Construction and Building Materials*, *70*, 104–117. https://doi.org/10.1016/j.conbuildmat.2014.08.001

Tariq, F., Gaikwad, M., & Bhargava, P. (2021). Analysis of behaviour of corroded RC beams exposed to elevated temperatures. *Journal of Building Engineering*, *42*(July 2020), 102508. https://doi.org/10.1016/j.jobe.2021.102508

The European Union - BriteEuRam III. (2000). *DuraCrete Final Technical Report*.

The National Academy of Science. (2000). *Durability of Precast Segmental Bridges, NCHRP Web Doc 15*.

Tondolo, F. (2015). Bond behaviour with reinforcement corrosion. *Construction and Building Materials*, *93*, 926–932. https://doi.org/10.1016/j.conbuildmat.2015.05.067

Torres-Acosta, A. A., Fabela-Gallegos, M. J., Munoz-Noval, A., Vásquez-Vega, D., Hernandez-Jimenez, J. R., & Martínez-Madrid, M. (2004). Influence of corrosion on the structural stiffness of reinforced concrete beams. *Corrosion*, *60*(9), 862–872. https://doi.org/10.5006/1.3287868

Torres-Acosta, Andrés A., & Castro-Borges, P. (2013). Corrosion-induced Cracking of Concrete Elements Exposed to a Natural Marine Environment for Five Years. *Corrosion*, *69*(11), 1122–1131.

Torres-Acosta, Andrés A., & Martnez-Madrid, M. (2003). Residual Life of Corroding Reinforced Concrete Structures in Marine Environment. *Journal of Materials in Civil Engineering*, *15*(4), 344–353. https://doi.org/10.1061/(asce)0899-1561(2003)15:4(344)

Torres-Acosta, Andrés A., Navarro-Gutierrez, S., & Teran-Guillen, J. (2007). Residual Flexure Capacity of Corroded Reinforced Concrete Beams. *Engineering Structures*, *29*(6), 1145–1152.

Trejo, D., Hueste, M. B. D., Gardoni, P., Pillai, R. G., Reinschmidt, K., Im, S. B., Kataria, S., Hurlebaus, S., Gamble, M., & Ngo, T. T. (2009). *Effect of Voids in Grouted, Post-Tensioned Concrete Bridge Construction: Volume 1 - Electrochemical Testing and Reliabililty Assessment* (Vol. 7, Issue 2). http://tti.tamu.edu/documents/0-4588-1-Vol1.pdf%0Ahttp://www.ntis.gov

Tuutti, K. (1982). *Corrosion of steel in concrete*. Swedish Cement and Concrete Research Institute, Stockholm.

United Nations Office for Disaster Risk Reduction. (2019). *GAR: Global Assessment Report on Disaster Risk Reduction*.

United Nations Office for Disaster Risk Reduction. (2020). *Making Critical Infrastructure Resilient: Ensuring continuity of service policy and regulations in Europe and central Asia*.

Val, D. V. (2007). Deterioration of Strength of RC Beams due to Corrosion and Its Influence on Beam Reliability. *Journal of Structural Engineering*, *133*(9), 1297–1306. https://doi.org/10.1061/(asce)0733-9445(2007)133:9(1297)

Val, V., & Melchers, E. R. (1997). RELIABILITY OF DETERIORATING RC SLAB BRIDGES. *Journal of Structural Engineering*, *123*(12), 1638–1644.

Valiente, A. (2001). Stress corrosion failure of large diameter pressure pipelines of prestressed concrete. *Engineering Failure Analysis*, *8*(3), 245–261. https://doi.org/10.1016/S1350-

6307(00)00010-8

Valor, A., Caleyo, F., Rivas, D., & Hallen, J. M. (2010). Stochastic approach to pitting-corrosion-extreme modelling in low-carbon steel. *Corrosion Science*, *52*(3), 910–915. https://doi.org/10.1016/j.corsci.2009.11.011

Vanama, R. K., & Ramakrishnan, B. (2020). Improved degradation relations for the tensile properties of naturally and artificially corroded steel rebars. *Construction and Building Materials*, *249*, 118706. https://doi.org/10.1016/j.conbuildmat.2020.118706

Vandamme, M., Zhang, Q., Ulm, F. J., Le Roy, R., Zuber, B., Gartner, B., & Termkhajornkit, P. (2013). Creep Properties of Cementitious Materials from Indentation Testing: Significance, Influence of Relative Humidity, and Analogy Between C-S-H and Soils. *Proceding of the Ninth International Conference on Creep, Shrinkage, and Durability Mechanics*, 48–61.

Vereecken, E., Botte, W., Lombaert, G., & Caspeele, R. (2021). Assessment of corroded prestressed and posttensioned concrete structures: A review. *Structural Concrete*, *22*(5), 2556–2580. https://doi.org/10.1002/suco.202100050

Vu, H. H., Vu, N. A., & François, R. (2014). Effect of corrosion of tensile rebars and stirrups on the flexural stiffness of reinforced concrete members. *European Journal of Environmental and Civil Engineering*, *18*(3), 358–376. https://doi.org/10.1080/19648189.2014.881759

Walraven, J. (2020). Significance of reinforcement corrosion for modelling the behaviour of existing concrete structures. *Proceedings of the Fib CACRCS DAYS 2020 - Capacity Assessment of Corroded Reinforced Concrete Structures*, 239–249.

Wang, L., Hu, Z., Yi, J., Dai, L., Ma, Y., & Zhang, X. (2020). Shear Behavior of Corroded Post-Tensioned Prestressed Concrete Beams with Full/Insufficient Grouting. *KSCE Journal of Civil Engineering*, *24*(6), 1881–1892. https://doi.org/10.1007/s12205-020-1777-4

Wang, L., Li, C., & Yi, J. (2015). An Experiment study on behavior of corrosion RC beams with different concrete strength. *Journal of Coastal Research*, 259–264. https://doi.org/10.2112/SI73-046.1

Wang, L., Li, T., Dai, L., Chen, W., & Huang, K. (2020). Corrosion morphology and mechanical behavior of corroded prestressing strands. *Journal of Advanced Concrete Technology*, *18*(10), 545–557. https://doi.org/10.3151/jact.18.545

Wang, L., Yi, J., Zhang, J., Floyd, R. W., & Ma, Y. (2018). Bond behavior of corroded strand in pretensioned prestressed concrete beams. *ACI Structural Journal*, *115*(6), 1803–1812.

https://doi.org/10.14359/51706892

Wang, L., Yi, J., Zhang, J., Jiang, Y., & Zhang, X. (2017). Effect of corrosion-induced crack on the bond between strand and concrete. *Construction and Building Materials*, *153*, 598–606. https://doi.org/10.1016/j.conbuildmat.2017.07.113

Wang, L., Zhang, X., Zhang, J., Yi, J., & Liu, Y. (2016). Simplified Model for Corrosion-Induced Bond Degradation between Steel Strand and Concrete. *Journal of Materials in Civil Engineering*, *29*(4), 04016257. https://doi.org/10.1061/(asce)mt.1943-5533.0001784

Wang, X. H., Gao, X. H., Li, B., & Deng, B. R. (2011). Effect of bond and corrosion within partial length on shear behaviour and load capacity of RC beam. *Construction and Building Materials*, *25*(4), 1812–1823. https://doi.org/10.1016/j.conbuildmat.2010.11.081

Weizhong, G., Raupach, M., & Wei-Liang, J. (2010). Korrosionsprodukte und Deren Volumenfaktor bei der Korrosion von Stahl in Beton. *Beton- Und Stahlbetonbau*, *105*(9), 572–578. https://doi.org/10.1002/best.201000036

Woodward, R. J., & Williams, F. . (1988). Collapse of Ynys-y-Gwas bridge, West Glamorgan. *Proc. Instn Civ. Engrs*, 635–669.

Xia, J., Jin, W. L., & Li, L. Y. (2012). Effect of chloride-induced reinforcing steel corrosion on the flexural strength of reinforced concrete beams. *Magazine of Concrete Research*, *64*(6), 471–485. https://doi.org/10.1680/macr.10.00169

Xia, J., Jin, W. liang, Zhao, Y. xi, & Li, L. yuan. (2013). Mechanical performance of corroded steel bars in concrete. *Proceedings of the Institution of Civil Engineers: Structures and Buildings*, *166*(5), 235–246. https://doi.org/10.1680/stbu.11.00048

Xie, H. B., Wang, Y. F., Gong, J., Liu, M. H., & Yang, X. Y. (2018). Effect of Global Warming on Chloride Ion Erosion Risks for Offshore RC Bridges in China. *KSCE Journal of Civil Engineering*, *22*(9), 3600–3606. https://doi.org/10.1007/s12205-018-1547-8

Xu, S., Zhang, Z., Li, R., & Qiu, B. (2017). Experimental study on the shear behavior of RC beams with corroded stirrups. *Journal of Advanced Concrete Technology*, *15*(4), 178–189. https://doi.org/10.3151/jact.15.178

Xue, X., Seki, H., & Song, Y. (2014). Shear behavior of RC beams containing corroded stirrups. *Advances in Structural Engineering*, *17*(2), 165–178. https://doi.org/10.1260/1369-4332.17.2.165

Yang, Jincheng, Haghani, R., Blanksvärd, T., & Lundgren, K. (2021). Experimental study of FRP-strengthened concrete beams with corroded reinforcement. *Construction and Building Materials*, *301*, 124076. https://doi.org/10.1016/j.conbuildmat.2021.124076

Yang, Jun, Guo, T., & Li, A. (2020). Experimental investigation on long-term behavior of

prestressed concrete beams under coupled effect of sustained load and corrosion. *Advances in Structural Engineering*, *23*(12), 2587–2596. https://doi.org/10.1177/1369433220919067

Yang, R., Yang, Y., Liu, P., & Wang, X. (2022). Experimental Study on Shear Performance of Post-Tensioning Prestressed Concrete Beams with Locally Corroded Steel Strands. *Coatings*, *12*(9). https://doi.org/10.3390/coatings12091356

Yang, X., Wu, T., & Chen, Y. (2018). Relationship of corrosion of concrete reinforcement to accelerated corrosion current. *Construction Materials*, *172*(5), 263–268. https://doi.org/10.1680/jcoma.17.00083

Yang, Y., Nakamura, H., Miura, T., & Yamamoto, Y. (2019). Effect of corrosion-induced crack and corroded rebar shape on bond behavior. *Structural Concrete*, *20*(6), 2171–2182. https://doi.org/10.1002/suco.201800313

Ye, Z., Zhang, W., & Gu, X. (2018). Deterioration of shear behavior of corroded reinforced concrete beams. *Engineering Structures*, *168*(February), 708–720. https://doi.org/10.1016/j.engstruct.2018.05.023

Yoo, C.-H., Chul Park, Y., & Kim, H.-K. (2018). Modeling Corrosion Progress of Steel Wires in External Tendons. *Journal of Bridge Engineering*, *23*(12), 04018098. https://doi.org/10.1061/(asce)be.1943-5592.0001331

Yoo, C. H., Park, Y. C., & Kim, H. K. (2020). Section loss in naturally corroded 7-wire steel strands in external tendons. *Structure and Infrastructure Engineering*, *16*(11), 1593–1603. https://doi.org/10.1080/15732479.2020.1714668

Yoon, S., Wang, K., Weiss, W. J., & Shah, S. P. (2000). Interaction between loading, corrosion, and serviceability of reinforced concrete. *ACI Structural Journal*, *97*(6), 637–644. https://doi.org/10.14359/9977

Youn, S.-G., & Kim, E.-K. (2006). Deterioration of Bonded Post-Tensioned Concrete Bridges and Research Topics on the Strength Evaluation in Isarc. *HBRC Journal*, *46*(2), 151–163.

Yu, F., Jia, J., Yao, D., & Zhu, W. (2011). Fatigue behavior of prestressed concrete beams under corrosion. *Advanced Materials Research*, *255–260*, 360–364. https://doi.org/10.4028/www.scientific.net/AMR.255-260.360

Yu, L., François, R., Dang, V. H., L'Hostis, V., & Gagné, R. (2015a). Development of chloride-induced corrosion in pre-cracked RC beams under sustained loading: Effect of load-induced cracks, concrete cover, and exposure conditions. *Cement and Concrete Research*, *67*, 246–258. https://doi.org/10.1016/j.cemconres.2014.10.007

Yu, L., François, R., Dang, V. H., L'Hostis, V., & Gagné, R. (2015b). Distribution of corrosion

and pitting factor of steel in corroded RC beams. *Construction and Building Materials*, *95*, 384–392. https://doi.org/10.1016/j.conbuildmat.2015.07.119

Yu, Q.-Q., Gu, X.-L., Zeng, Y.-H., & Zhang, W.-P. (2022). Flexural behavior of Corrosion-Damaged prestressed concrete beams. *Engineering Structures*, *272*(August), 114985. https://doi.org/10.1016/j.engstruct.2022.114985

Yu, Q. Q., Gu, X. L., Zeng, Y. H., & Zhang, W. P. (2022). Flexural behavior of Corrosion-Damaged prestressed concrete beams. *Engineering Structures*, *272*(April), 114985. https://doi.org/10.1016/j.engstruct.2022.114985

Yuan, Y., Ji, Y., & Shah, S. P. (2007). Comparison of two accelerated corrosion techniques for concrete structures. *ACI Structural Journal*, *104*(3), 344–347. https://doi.org/10.14359/18624

Zeng, Y. H. (2013). Resaerch on bending behavior of corroded PC beams. *Applied Mechanics and Materials*, *351–352*, 1662–1668. https://doi.org/10.4028/www.scientific.net/AMM.351-352.1662

Zhan, Y., Zhao, R., Ma, Z. J., Xu, T., & Song, R. (2016). Behavior of prestressed concrete-filled steel tube (CFST) beam. *Engineering Structures*, *122*(September), 144–155. https://doi.org/10.1016/j.engstruct.2016.04.050

Zhang, S. F., Lu, C. H., & Liu, R. G. (2011). Experimental determination of chloride penetration in cracked concrete beams. *Procedia Engineering*, *24*, 380–384. https://doi.org/10.1016/j.proeng.2011.11.2661

Zhang, W., Liu, X., & Gu, X. (2016). Fatigue behavior of corroded prestressed concrete beams. *Construction and Building Materials*, *106*, 198–208. https://doi.org/10.1016/j.conbuildmat.2015.12.119

Zhang, W. P., Li, C. K., Gu, X. L., & Zeng, Y. H. (2019). Variability in cross-sectional areas and tensile properties of corroded prestressing wires. *Construction and Building Materials*, *228*, 1–11. https://doi.org/10.1016/j.conbuildmat.2019.116830

Zhang, W., Song, X., Gu, X., & Li, S. (2012). Tensile and fatigue behavior of corroded rebars. *Construction and Building Materials*, *34*, 409–417. https://doi.org/10.1016/j.conbuildmat.2012.02.071

Zhang, W., Zhang, H., Gu, X., & Liu, W. (2018). Structural behavior of corroded reinforced concrete beams under sustained loading. *Construction and Building Materials*, *174*, 675–683. https://doi.org/10.1016/j.conbuildmat.2018.04.145

Zhang, X., Wang, L., Zhang, J., & Liu, Y. (2017a). Corrosion-induced flexural behavior degradation of locally ungrouted post-tensioned concrete beams. *Construction and*

Building Materials, *134*, 7–17. https://doi.org/10.1016/j.conbuildmat.2016.12.140

Zhang, X., Wang, L., Zhang, J., & Liu, Y. (2017b). Corrosion-induced flexural behavior degradation of locally ungrouted post-tensioned concrete beams. *Construction and Building Materials*, *134*, 7–17. https://doi.org/10.1016/j.conbuildmat.2016.12.140

Zhang, X., Wang, L., Zhang, J., Ma, Y., & Liu, Y. (2017). Flexural behavior of bonded post-tensioned concrete beams under strand corrosion. *Nuclear Engineering and Design*, *313*, 414–424. https://doi.org/10.1016/j.nucengdes.2017.01.004

Zhao, Y., Hu, B., Yu, J., & Jin, W. (2011). Non-uniform distribution of rust layer around steel bar in concrete. *Corrosion Science*, *53*(12), 4300–4308. https://doi.org/10.1016/j.corsci.2011.08.045

Zhao, Y., Xu, X., Wang, Y., & Dong, J. (2020). Characteristics of pitting corrosion in an existing reinforced concrete beam exposed to marine environment. *Construction and Building Materials*, *234*, 117392. https://doi.org/10.1016/j.conbuildmat.2019.117392

Zhao, Y., Yu, J., Hu, B., & Jin, W. (2012). Crack shape and rust distribution in corrosion-induced cracking concrete. *Corrosion Science*, *55*, 385–393. https://doi.org/10.1016/j.corsci.2011.11.002

Zhou, Y., Gencturk, B., Willam, K., & Attar, A. (2015). Carbonation-Induced and Chloride-Induced Corrosion in Reinforced Concrete Structures. *Journal of Materials in Civil Engineering*, *27*(9). https://doi.org/10.1061/(asce)mt.1943-5533.0001209

Zhu, W. (2014). *Effect of corrosion on the mechanical properties of the corroded reinforcement and the residual structural performance of the corroded beams*.

Zhu, W., & François, R. (2014). Corrosion of the reinforcement and its influence on the residual structural performance of a 26-year-old corroded RC beam. *Construction and Building Materials*, *51*, 461–472. https://doi.org/10.1016/j.conbuildmat.2013.11.015

Zhu, W., François, R., Cleland, D., & Coronelli, D. (2015). Failure mode transitions of corroded deep beams exposed to marine environment for long period. *Engineering Structures*, *96*, 66–77. https://doi.org/10.1016/j.engstruct.2015.04.004

Zhu, W., François, R., Coronelli, D., & Cleland, D. (2013). Effect of corrosion of reinforcement on the mechanical behaviour of highly corroded RC beams. *Engineering Structures*, *56*, 544–554. https://doi.org/10.1016/j.engstruct.2013.04.017

Zhu, W., François, R., Fang, Q., & Zhang, D. (2016). Influence of long-term chloride diffusion in concrete and the resulting corrosion of reinforcement on the serviceability of RC beams. *Cement and Concrete Composites*, *71*, 144–152. https://doi.org/10.1016/j.cemconcomp.2016.05.003

Zona, A., Ragni, L., & Dall'Asta, A. (2008). Finite element formulation for geometric and material nonlinear analysis of beams prestressed with external slipping tendons. *Finite Elements in Analysis and Design*, *44*(15), 910–919. https://doi.org/10.1016/j.finel.2008.06.005

Zou, Z., & Yang, G. (2021). Experimental Study on Shear Behavior of Fiber Reinforced Concrete Beams with Corroded Stirrups. *IOP Conference Series: Earth and Environmental Science*, *719*(2). https://doi.org/10.1088/1755-1315/719/2/022071

Appendix

A.1. Mechanical performance of corroded RC beams

Table A-1 provides a general overview of the experimental tests conducted worldwide on corroded RC beams from 1990 to 2022, thereby extending the survey carried out by Soltani et al. (2019), to investigate the flexural and shear behaviour of corroded RC beams available in scientific literature. Specifically, Table A-1 reports: (i) the Reference of the analyzed experimental campaign, (ii) the number of corroded specimens with in brackets the number of the reference un-corroded specimens, (iii) the test set-up, by distinguishing between four-point (FPBT) and three-point (TPBT) bending test, (iv) the observed failure mode, and (v) the adopted corrosion process, where IC, ACE and NAT stand for Impressed Current, Artificial Climate Environment, and Natural corrosion, respectively.

Table A-1 State-of-the-Art on flexural and shear experimental behaviour of corroded RC beams.

Reference	N° of tested corroded beams, (un-corroded)	Test set-up	Failure mode	Corrosion process
Al-Sulaimani et al. (1990)	21 (3)	FPBT	Bending	IC (200 μA/cm^2)
Almusallam et al. (1997)	7 (1)	DIST	Bending	IC (-μA/cm^2)
Rodriguez et al. (1997)	21 (10) tested in bending 20 (10) tested in shear	FPBT	Bending Shear	IC (100 μA/cm^2)
Mangat & Elgarf (1999)	103 (8)	FPBT	Bending	IC (1000 up to 4000 μA/cm^2)
Yoon et al. (2000)	7 (3)	FPBT	Sustained Load	IC (different voltage)
Castel et al. (2000a)	2 (2)	TPBT	Bending	ACE (wet-dry cycles)
Capozucca & Cerri (2003)	2 (1)	FPBT	Bending	ACE (wet-dry cycles)
Torres-Acosta et al. (2004)	10 (2)	TPBT	Bending	IC (80 μA/cm^2)
El Maaddawy et al. (2005)	8 (1)	FPBT	Bending	IC (215 μA/cm^2)
Higgins and Farrow (2006)	9 (5)	FPBT	Shear	IC (600 μA/cm^2)
Azad et al. (2007)	52 (4)	FPBT	Bending	IC (250 μA/cm^2)
Torres-Acosta et al. (2007)	11 (1)	TPBT	Bending	IC (80 μA/cm^2)

Cairns et al. (2008)	10 (4)	TPBT	Bending	IC (60 μA/cm^2)
Azad et al. (2010)	42 (6)	TPBT	Bending	IC (1780 μA/cm^2)
Oyado et al. (2011)	11 (2)	FPBT	Bending	IC (350 up to 1330 μA/cm^2) + ACE
Wang et al. (2011)	8 (2)	FPBT	Shear	IC (- μA/cm^2)
Juarez et al. (2011)	8 (8)	FPBT	Shear	IC (100 μA/cm^2)
Xia et al. (2012)	18 (2)	FPBT	Bending	IC (- μA/cm^2)
Zhu et al. (2013)	2 (2)	TPBT	Bending	ACE (wet-dry cycles)
Dang & Francois (2013)	1 (1)	TPBT	Bending	ACE (wet-dry cycles) for 27 years
Tahershamsi et al. (2014)	11 (2)	FPBT	Bending	NAT
Khan et al. (2014)	1 (1)	TPBT	Sustained Load	ACE (wet-dry cycles) for 26 years
Vu et al. (2014)	2 (1)	TPBT	Bending	ACE (wet-dry cycles)
Zhu and Francois (2014)	1 (1)	TPBT	Bending	ACE (wet-dry cycles)
Khan et al. (2014)	2 (1)	TPBT	Sustained Load & Shear	ACE
Lachemi et al. (2014)	12 (4)	FPBT	Shear	IC (200 μA/cm^2)
Xue et al. (2014)	8 (2)	TPBT	Shear	IC (1000 μA/cm^2)
Kearsley and Joyce (2014)	11 (1)	FPBT	Bending	IC (1087 μA/cm^2)
Yu et al. (2015)	2 (1)	TPBT	Bending	ACE (wet-dry cycles)
Zhu et al. (2015)	2 (2)	TPBT	Bending	ACE (wet-dry cycles)
Wang et al. (2015)	14 (8)	FPBT	Bending	IC (1800 μA/cm^2)
Sahmaran et al. (2015)	8 (2)	FPBT	Shear	IC (200 μA/cm^2)
El-Sayed et al. (2017)	6 (3)	FPBT	Shear	IC (400 μA/cm^2)
Imam and Azad (2016)	13 (2)	FPBT	Shear	IC (400 μA/cm^2)
Zhu et al. (2016)	1 (1)	TPBT	Bending	ACE (wet-dry cycles)
Dong et al. (2016)	15 (6)	FPBT	Bending	IC (- μA/cm^2)
Xu et al. (2017)	18 (3)	FPBT	Shear	IC (800 μA/cm^2)
Dasar et al. (2017)	2	FPBT	Bending	NAT

				(20 years of marine env.)
Ye et al. (2018)	12 (1)	FPBT	Bending & Shear	IC (100 μA/cm^2)
Ahmad & Kamran (2018)	4	FPBT	Bending	IC (-μA/cm^2)
Zhang et al. (2018)	5 (3)	FPBT	Sustained Load	IC (25, 50, 100 μA/cm^2)
Fernandez et al. (2018)	9 (3)	TPBT	Bending	IC (350 μA/cm^2)
Shen et al. (2019)	3 (1)	FPBT	Sustained Load	IC (200 μA/cm^2) + ACE (wet-dry cycles)
Jung et al. (2019)	14 (2)	FPBT	Bending & Shear	IC (- μA/cm^2)
Huang et al. (2020)	9 (3)	FPBT	Bending & Shear	IC (0.3 up to 0.8 μA/cm^2)
Han et al. (2020)	6 (2)	TPBT	Shear	IC (1000 μA/cm^2)
Al-Mashgari et al. (2021)	4	FPBT	Bending	IC (800 mA)
Tariq et al. (2021)	27	FPBT	Bending	IC (0.01 μA/cm^2)
Yang et al. (2021)	8 (2)	FPBT	Bending	IC (220 μA/cm^2)
Nasser et al. (2021)	12 (5)	TPBT	Bending	IC (100 μA/cm^2)
Zou & Yang (2021)	27	FPBT	Shear	IC (1000 μA/cm^2)
Di Carlo et al. (2021)	4 (2)	FPBT	Bending	IC (600 for 38 days + 400 for 85 days)
Naderpour et al. (2022)	4 (1)	FPBT	Bending & Shear	Turning

A total of 794 beams were analyzed; 81.61% (648 beams) were corroded at different levels, while the remaining 18.39% (146 beams) were un-corroded and used as reference beams for corrosion quantification and evaluation. Referring to the fifty-three scientific papers reviewed, 62% studied the corrosion influences on the flexural structural behaviour of RC beams, 29% analysed the shear structural performance, whereas the remaining 9% investigated the coupled effect of corrosion and applied sustained load, as shown graphically in Figure A-1.

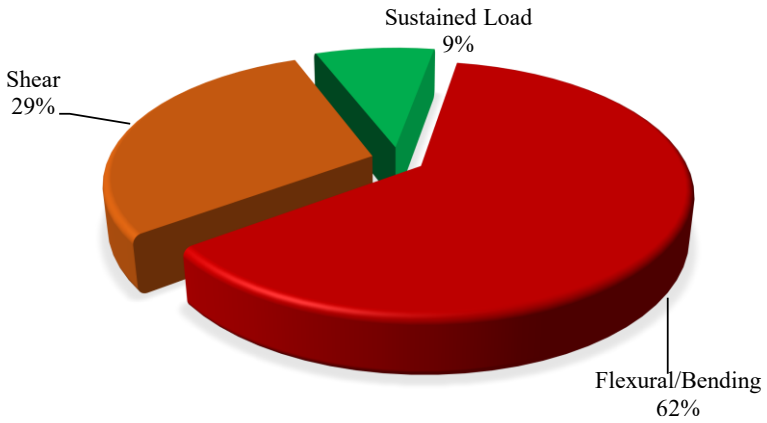

Figure A-1 Analysis of the mechanical behaviour investigated through experimental campaigns.

As highlighted in Figure A-2(a), the majority of experimental tests were conducted by adopting the impressed current (IC) method – 39 experimental programs –, whereas a limited number of studies were performed by adopting the artificial climate environment method (ACE) – 13 experimental programs. In addition, a lack of experimental tests analyzing specimens coming from natural environments was observed. Indeed, only the experimental research carried out by Tahershamsi et al. (2014) and Dasar et al. (2017) estimated the residual flexural response and the pre-cracking effect on twelve and two naturally corroded RC beams, respectively. Considering the IC method, 27.50% of the experimental campaigns using the impress current technique, adopted current density, I_{corr}, values ranging between 100 μA/cm^2 and 400 μA/cm^2, whereas 30% used I_{corr} values higher than 400 μA/cm^2, as well represented in Figure A-2(b). Although the latter recreated corrosion-induced damage in a reasonable amount of time, allowing for shorter experimental campaigns, they resulted ineffective in replicating the natural corrosion process. The remaining 25% adopted I_{corr} values lower than 100 μA/cm^2, as suggested by Rodriguez et al. (1997) and Alonso et al. (1998). Unfortunately, as shown in Figure A-2(b), 17.50% of the available experimental research did not provide the I_{corr} values adopted.

Due to the discrepancy in available outcomes caused by significant differences in the assumptions of exposure condition, specimen dimensions, reinforcement ratio and adopted accelerated method, it is difficult to draw common conclusions. However, referring to the obtained results, it is evident how, by increasing the corrosion level, a significant decrease in terms of flexural and shear load-carrying capacity, ultimate ductility, stiffness and bond resistance occurred for both longitudinal and transversal reinforcements. Moreover, several authors highlighted that as the corrosion level increases, the failure mode of corroded RC beams shifts from ductile (bending failure) to brittle (shear or anchorage failure). Finally, some studies

showed that the use of Carbon Fiber Reinforced Polymers (CFRP) or FRP strengthening systems can be viable techniques for improving the load-carrying capacity of corroded RC structural elements.

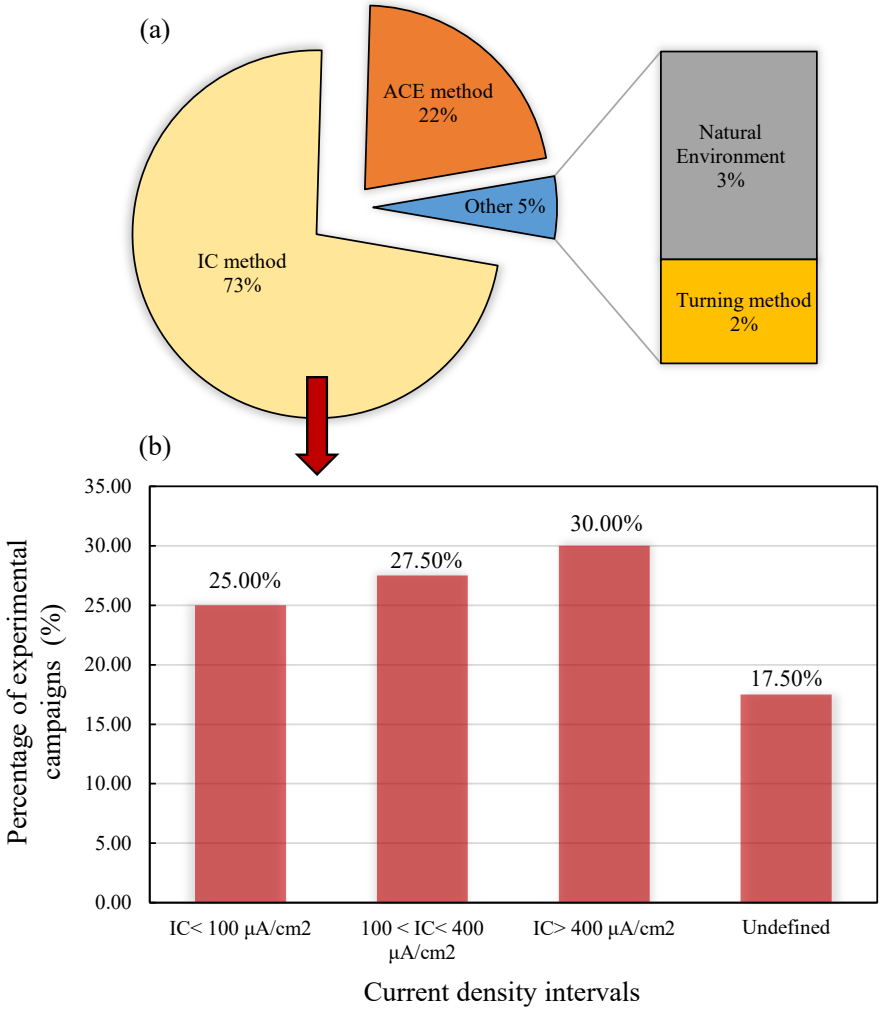

Figure A-2 Analysis of the corrosion methods adopted in experimental campaigns to investigate the corrosion effects: (a) percentage subdivision and (b) range of current density in the case of IC method.

For the sake of completeness, further State-of-the Art surveys have been conducted by Zhou et al. (2015), Mancini & Tondolo (2014) and Kashani et al. (2019), respectively, on the variation of the mechanical properties of concrete members, the bond decay at the steel-concrete interface, the nonlinear behaviour of RC beams under cyclic loading and the available numerical models for structural performance evaluation of corroded RC components.

A.2. Mechanical behaviour of corroded ordinary reinforcements

To analyze the issue related to the mechanical property reduction of reinforcements caused by corrosion, Table A-2 reports a general overview of the experimental tensile tests performed globally, as well as the most used analytical models for corroded ordinary reinforcements. The current State-of-the-Art intends to highlight all scientific works undertaken in the prediction of the residual stress-strain response of corroded rebars by presenting a comprehensive list of the research realized from 2000 to 2022, thus extending the survey conducted by Vanama & Ramakrishnan (2020).

Table A-2 State-of-the-Art on tensile tests and residual mechanical response of corroded rebars.

Reference	**N° of tested rebars, (un-corroded)**	**Tensile loading type**	**Corrosion target**	**Corrosion process**
Almusallam (2001)	19 (3): D6; 23 (3): D12	M	η 0.88%-75%: D6 2.11%-80%: D12	IC (2 μA/cm^2), Bars in concrete
Cairns et al. (2005)	25: D16 and D20	M	μ: Up to 72%	IC (0.01 – 0.05 μA/cm^2), Bars in concrete
Apostolopoulos et al. (2006)	18 (4): D8 (tempcore) BST500s	M	η:up to 35%	Artificial (salt spray) Bare bars
Papadopoulos et al. (2007)	36 (6) + 36 (6): D12 (tempcore) S500s and B500C	M	η: 1%-8.96%	Artificial (salt spray) Bare bars
Apostolopoulos & Papadopoulos (2007)	30 (5) + 18 (3) D10 S400	M & C	η: 1.58%-8.48%	Artificial (salt spray) Bare bars
Apostolopoulos (2007)	9 (3): D12 (tempcore) S500s	C	η: 1.35%-10.4%	Artificial (salt spray) Bare bars
Alexopoulos et al. (2007)	48 (40): D12 BStIV	M	-	Artificial (salt spray) Bare bars
Apostolopoulos & Papadakis (2008)	25 (NAT) + 5 (artificial) D10, BSt 420	M	η: 0.25%-16%	NAT (chloride) Bars in concrete + Artificial (salt spray) Bare bars
Lee & Cho. (2009)	SD 295A: D13 SD 345: D13	M	η: up to 35%	Artificial carbonation and chloride (salt spray)
Papadopoulos et al. (2011)	98 (NAT) from 64 different sites: D8 and D10	M	η: up to 16%	NAT (chloride) Bars in concrete Artificial (salt spray) Bare bars
Cobo et al. (2011)	39 (1) D16 B500SD steel 46 (1) D20 B500SD steel	M	η: 2.1%-15.3%	IC (10 μA/cm^2) Bars in concrete

Zhang et al. (2012)	44 (1): R6.5 Serie-A 20 (1): D12 Serie-B	M & C	*η:* 15.6%-31.3% (Serie-A) *η:* 4.5%-39.7% (serie-B)	NAT (carbonation) Bars in concrete & IC (100 μA/cm^2)
Xia et al. (2013)	120 bare Bars + 212 Bars in concrete R6, R8, R12; (HPB235) D12, D14, D16, D20; (HRB335, 400, 500)	M	*η:* 0.0-14% (embedded) *η:* 0.2%-58% (bare bars)	Artificial IC (200 μA/cm^2) ACE (wet & dry)
Kashani et al. (2013)	39 (1): D12, B500	C	*η:* 8.59%-47.4%	IC (1.1 μA/cm^2) Bars in concrete
Apostolopoulos et al. (2013)	7 (1): Bare bars + 10: Bars in concrete D8, B500C	M	*η:* 1.33%-13.55% Bare bars *η:* 0.75%-4.2% Bars in concrete	IC (-μA/cm^2) Bars in concrete Artificial (salt spray) Bare bars
Moreno et al. (2014)	25 (1): D16, D20 B500SD	M	*η:* 4.01%-15.21%	IC (10 μA/cm^2) Bars in concrete
Meda et al. (2014)	6 (3): D16, B500C (tempcore) + 16: D16	M	*η:* 11.9%-22.1% Bare bars *η:* 14.76%-23.4% Bars in concrete	IC (50 μA/cm^2) Bare bars Bars in concrete
Kashani et al. (2015)	48: D12, B500	C	*η:* 11%-38%	IC (-μA/cm^2) Bars in concrete
Fernandez et al. (2015)	38 (2) (M) + 140 (C) D10 & D12, B500SD (tempcore)	M & C	*η* (M): 8.4%-21.5% *η* (C): 8.6%-27.6%	IC (-μA/cm^2) Bars in concrete
Caprili et al. (2015)	30 B500A, B400C, B450, B500B, B400C, B450C	M & C	*η:* 1.2%-44.86%	Artificial (salt spray) Bare bars
Taha & Morsy. (2016)	48 (3): D10, D12, D16	M	*η:* 10%-30%	IC (-μA/cm^2) Bare bars
Ou et al. (2016)	18: D13, D16, D19 + 13: D16, 16 D29 (IC) Steel A706	M	*η:* 5.9%-82.4%	NAT (building from coastline of northern Taiwan) & IC (600 μA/cm^2) Bars in concrete
Lu et al. (2016)	10 (1): D16, HRB400	M	*η:* 1.87%-5.77%	NAT (1 year) & Artificial (wet & dry) Bars in concrete
Li et al. (2017a; 2017b)	34 (3): R12	C	*η:* 2.80%-9.40%	NAT (carbonation 35 years) Bars in concrete
Imperatore et al. (2017)	13 (1): D8 14 (1): D12 20 (1): D16 18 (1): D20	M	*η:* 4.4%-53.21%	IC (-μA/cm^2) Bare bars

Caprili et al. (2018)	D8, D12, D16, D20, D25 Steel B400, B450, B500A, B500B, B500C	M & C	*η:* 0.3%-18.5%	Artificial (salt spray) Bare bars
Finozzi et al. (2018)	8 (1 pit), 3 (2 pits), (3): D16, B550B	M	*μ:* Up to 56.5%	Artificial (turning) Bare bars
Chen et al. (2020)	56 (5): D10, B500B (tempcore)	M	*μ:* 1.56%-33.65%	Artificial (wet & dry) Bars in concrete
Vanama & Ramakrishnan (2020)	38: R12.7 MS250 – MS350 + 15: D16, Fe500D	M	*η:* 0.81%-79.64% (NAT) *η:* 9.95%-50.51% (IC)	NAT (54-year-old) Bars in concrete IC (4421 μA/cm^2) Bare bars

IC = Impressed Current method, ACE = Artificial Climate Environment method, NAT = natural corrosion, M = monotonic test, C = cyclic test, D = deformed/ribbed rebar, R = round rebar, ϕ = rebar diameter.

From a general point of view, the rebars tested in scientific works were corroded in different ways:

- Through the impressed current technique: by applying a current density, I_{corr}, ranging between 0.01 μA/cm^2 to 100 μA/cm^2, except for the experimental works conducted by Xia et al. (2013), Ou et al. (2016), and Vanama & Ramakrishnan (2020), who adopted I_{corr} values equal to 200 μA/cm^2, 600 μA/cm^2 and 4421 μA/cm^2, respectively;
- Through artificial climate environment (the ACE technique): by applying salt spray;
- Through the samples exposure to wetting and dry conditions;
- Through natural deterioration: by retrieving samples from existing structures subjected to aggressive natural environments for several years.

In particular, the mechanical behaviour of both bare bars and bars embedded in concrete was experimentally investigated.

Referring to the quantification of corrosion effects, the two main analyzed corrosion parameters were the mass loss, η, and the maximum cross-sectional loss, μ_{max} (i.e. minimum cross-sectional area, A_{min}) of the corroded reinforcement. Nevertheless, the maximum penetration depth, P_{max}, was also recognized as a relevant corrosion parameter in the prediction of the residual stress-strain response of corroded rebars, Taha & Morsy (2016) and Lu et al. (2016). However, a great variability of experimental results was observed due to different factors, such as (i) the different testing conditions, (ii) the corrosion methods adopted, and (iii) the different mechanical properties of the un-corroded tested samples.

Based on the obtained outcomes, the scientific community agrees in affirming that corrosion primarily deteriorates: (i) yield, f_y, and ultimate strength, f_u, (ii) ductility, and ultimate strain, ε_u, and (iii) fatigue life of rebars. It was also observed that an increase in the corrosion level results in a decrease in the elasticity modulus, E_s, and a transition from ductile to brittle failure mode, associated to a significant reduction in yielding plateau.

A.3. Maximum pits features and area loss due to pitting classification

Considering the 24 collected samples Table A-3 reports the geometrical description of the maximum pit of each external wire (*six for each sample*) composing the strand and the additional classification of the corresponding area loss due to pitting through the comparison with three different pit type morphology configurations: (1) hemispherical, (2) half-moon and (3) planar. The core wire was assumed as un-corroded.

Table A-3 Geometrical description of the maximum pit for each external wire and additional classification of the corresponding area loss due to pitting.

Identifying Code		P_x [mm]	P_y [mm]	P_z [mm]	A_p [mm^2]	$A_{p,1}$ [mm^2]	$A_{p,2}$ [mm^2]	$A_{p,3}$ [mm^2]	Final classification
PB9-L(12-82)	W_1	1.198	20.29	1.98	3.87	2.44	5.03	3.28	3
	W_2	1.336	27.03	2.36	3.98	2.86	5.59	3.82	3
	W_3	1.421	20.80	2.06	4.25	3.12	5.93	4.16	3
	W_4	1.144	6.52	2.81	2.45	2.28	4.81	3.08	1
	W_5	1.410	5.89	2.38	3.15	3.09	5.89	4.12	1
	W_6	1.711	25.63	2.28	5.76	4.08	7.08	5.35	3
PB9-L(426-496)	W_1	-	-	-	-	-	-	-	-
	W_2	-	-	-	-	-	-	-	-
	W_3	0.414	1.22	1.16	0.57	0.51	1.76	0.71	1
	W_4	0.424	0.73	0.83	0.51	0.53	1.80	0.74	1
	W_5	-	-	-	-	-	-	-	-
	W_6	0.377	1.95	1.31	0.49	0.44	1.60	0.62	1
PB9-R(15-60)	W_1	1.574	18.97	2.33	5.46	3.62	6.54	4.78	3
	W_2	1.620	12.84	2.41	5.83	3.77	6.72	4.97	2
	W_3	1.432	15.26	2.06	3.97	3.16	5.98	4.20	3
	W_4	2.785	13.78	2.87	9.21	8.09	10.94	9.86	3
	W_5	1.393	13.41	2.81	3.84	3.03	5.82	4.05	3
	W_6	1.202	8.93	1.42	3.53	2.45	5.05	3.30	3
PB9-R(428-473)	W_1	-	-	-	-	-	-	-	-
	W_2	-	-	-	-	-	-	-	-
	W_3	-	-	-	-	-	-	-	-
	W_4	0.170	1.86	0.65	0.11	0.14	0.72	0.19	1
	W_5	-	-	-	-	-	-	-	-
	W_6	-	-	-	-	-	-	-	-
PB10-L(138-208)	W_1	-	-	-	-	-	-	-	-
	W_2	0.317	3.52	1.43	0.52	0.34	1.35	0.48	3
	W_3	0.591	5.87	2.56	1.35	0.91	2.50	1.19	3
	W_4	0.405	4.76	1.68	0.68	0.41	1.72	0.69	3
	W_5	-	-	-	-	-	-	-	-
	W_6	-	-	-	-	-	-	-	-
PB10-L(445-515)	W_1	0.889	5.32	2.23	2.16	1.58	3.75	2.15	3
	W_2	1.166	4.16	2.08	3.59	2.35	4.90	3.16	3
	W_3	1.110	5.11	2.09	2.25	2.18	4.67	2.95	1
	W_4	2.447	8.39	3.56	7.78	6.76	9.80	8.46	3
	W_5	2.050	10.20	2.93	6.15	5.28	8.37	6.78	3
	W_6	2.566	15.03	3.69	7.36	7.23	10.22	8.96	1
PB10-R(32-102) (NEGLECTED)	W_1	-	-	-	-	-	-	-	-
	W_2	-	-	-	-	-	-	-	-
	W_3	-	-	-	-	-	-	-	-
	W_4	-	-	-	-	-	-	-	-
	W_5	-	-	-	-	-	-	-	-
	W_6	-	-	-	-	-	-	-	-
PB10-R(287-332)	W_1	1.529	8.93	2.77	4.00	3.47	6.36	4.60	1
	W_2	1.360	6.32	2.87	4.51	2.93	5.69	3.92	3
	W_3	0.727	1.68	0.91	1.36	1.17	3.08	1.61	1
	W_4	1.426	7.22	2.96	3.94	3.14	5.95	4.18	3
	W_5	2.880	10.17	2.95	8.41	8.47	11.24	10.24	1
	W_6	1.127	7.31	1.69	1.85	2.23	4.74	3.01	1
PB11-L(5-75) **Un-corroded**	W_1	-	-	-	-	-	-	-	-
	W_2	-	-	-	-	-	-	-	-
	W_3	-	-	-	-	-	-	-	-
	W_4	-	-	-	-	-	-	-	-

	W_5	-	-	-	-	-	-	-	-
	W_6	-	-	-	-	-	-	-	-
PB11-L(196-266)	W_1	0.521	3.01	1.78	0.60	0.72	2.21	1.00	1
	W_2	0.898	5.99	2.90	2.30	1.60	3.79	2.19	3
	W_3	1.402	8.75	3.09	4.38	3.06	5.86	4.08	3
	W_4	0.505	2.66	1.08	0.35	0.68	2.14	0.95	1
	W_5	0.555	2.77	1.46	0.53	0.79	2.36	1.09	1
	W_6	0.437	1.09	1.42	0.52	0.55	1.86	0.77	1
PB11-R(6-51)	W_1	0.976	4.24	2.11	2.15	1.81	4.11	2.46	3
	W_2	-	-	-	-	-	-	-	-
	W_3	0.196	1.35	0.71	0.19	0.17	0.83	0.24	1
	W_4	-	-	-	-	-	-	-	-
	W_5	0.349	2.51	1.27	0.62	0.40	1.48	0.55	3
	W_6	0.274	2.41	0.76	0.25	0.28	1.17	0.39	1
PB11-R(273-318)	W_1	-	-	-	-	-	-	-	-
(NEGLECTED)	W_2	-	-	-	-	-	-	-	-
	W_3	1.152	14.22	3.40	2.91	2.30	4.84	3.11	3
	W_4	-	-	-	-	-	-	-	-
	W_5	-	-	-	-	-	-	-	-
	W_6	-	-	-	-	-	-	-	-
PB12-L(12-82)	W_1	1.549	15.47	3.89	4.82	3.54	6.44	4.68	3
	W_2	0.814	23.38	2.05	2.11	1.39	3.44	1.90	3
	W_3	1.075	10.32	1.97	2.39	2.08	4.52	2.82	1
	W_4	0.974	4.13	1.22	2.51	1.80	4.11	2.45	3
	W_5	0.734	6.51	2.00	2.94	1.19	3.11	1.64	2
	W_6	1.251	41.21	2.47	5.88	2.60	5.25	3.49	2
PB12-L(124-169)	W_1	0.645	2.61	1.70	1.53	0.98	2.73	1.36	3
	W_2	0.865	3.90	1.12	1.58	1.52	3.66	2.07	1
	W_3	0.958	13.25	3.28	2.12	1.76	4.04	2.40	3
	W_4	0.478	3.19	1.12	0.61	0.63	2.03	0.88	1
	W_5	0.599	4.91	1.63	0.66	0.88	2.54	1.22	1
	W_6	1.227	10.84	2.88	3.17	2.53	5.15	3.40	3
PB12-R(100-170)	W_1	0.894	4.68	1.52	1.96	1.59	3.77	2.17	3
	W_2	1.001	6.80	2.26	2.81	1.88	4.22	2.55	3
	W_3	0.766	2.67	2.67	1.40	1.27	3.24	1.74	1
	W_4	0.866	2.83	1.62	1.62	1.52	3.66	2.08	1
	W_5	0.782	11.03	1.74	1.20	1.31	3.31	1.79	1
	W_6	0.677	4.40	2.02	0.90	1.06	2.87	1.46	1
PB12-R(358-403)	W_1	-	-	-	-	-	-	-	-
Un-corroded	W_2	-	-	-	-	-	-	-	-
	W_3	-	-	-	-	-	-	-	-
	W_4	-	-	-	-	-	-	-	-
	W_5	-	-	-	-	-	-	-	-
	W_6	-	-	-	-	-	-	-	-
PB13-L(1-46)	W_1	0.792	7.26	2.95	2.17	1.33	3.35	1.83	3
	W_2	0.724	8.68	2.00	1.72	1.17	3.07	1.61	3
	W_3	0.883	4.90	1.55	1.12	1.56	3.73	2.13	1
	W_4	1.462	7.52	1.62	2.06	3.25	6.10	4.32	1
	W_5	1.162	6.44	2.23	2.50	2.33	4.88	3.15	1
	W_6	0.972	5.77	1.41	2.97	1.80	4.10	2.45	3
PB13-L(108-178)	W_1	1.595	15.16	2.55	4.68	3.69	6.62	4.87	3
	W_2	1.286	21.60	2.90	2.60	2.70	5.39	3.62	1
	W_3	1.840	12.09	3.00	3.79	4.53	7.58	5.89	1
	W_4	1.327	8.21	3.60	3.69	2.83	5.55	3.78	3
	W_5	1.285	13.38	2.70	2.49	2.70	5.38	3.62	1
	W_6	1.645	15.23	3.36	4.12	3.86	6.82	5.07	1
PB13-R(0-70)	W_1	1.147	19.22	1.63	3.18	2.29	4.82	3.09	3
	W_2	1.297	4.57	1.91	2.82	2.74	5.43	3.67	1
	W_3	1.294	10.42	2.32	2.90	2.73	5.42	3.66	1
	W_4	1.141	9.53	1.74	2.44	2.27	4.80	3.07	1
	W_5	1.380	10.39	2.39	3.19	2.99	5.77	4.00	1
	W_6	0.908	6.81	1.39	3.12	1.63	3.83	2.22	2
PB13-R(70-115)	W_1	0.876	25.39	2.93	2.53	1.54	3.70	2.11	3
	W_2	1.008	12.01	2.84	2.80	1.90	4.25	2.58	3
	W_3	0.779	7.85	2.33	2.16	1.30	3.30	1.78	3
	W_4	0.465	4.27	1.86	0.92	0.61	1.97	0.84	3
	W_5	0.634	2.58	1.39	1.02	0.96	2.69	1.32	1
	W_6	0.353	3.63	1.61	0.53	0.40	1.50	0.56	1
PB14-L(10-55)	W_1	2.229	34.19	2.97	7.58	5.94	9.03	7.54	3
	W_2	1.099	5.79	1.73	2.92	2.15	4.62	2.91	3
	W_3	1.290	10.91	2.16	3.08	2.72	5.40	3.64	1
	W_4	2.237	17.51	3.43	5.92	5.97	9.06	7.57	1
	W_5	0.837	16.38	2.40	2.93	1.44	3.54	1.98	2
	W_6	1.106	3.51	2.45	3.88	2.17	4.65	2.93	2
PB14-L(455-500)	W_1	-	-	-	-	-	-	-	-

Un-corroded	W_2	-	-	-	-	-	-	-	-
	W_3	-	-	-	-	-	-	-	-
	W_4	-	-	-	-	-	-	-	-
	W_5	-	-	-	-	-	-	-	-
	W_6	-	-	-	-	-	-	-	-
PB14-R(2-72)	W_1	1.201	16.49	1.76	1.93	2.45	5.04	3.30	1
	W_2	1.055	17.58	2.42	3.08	2.03	4.44	2.75	3
	W_3	1.228	10.19	2.32	2.63	2.53	5.15	3.40	3
	W_4	1.180	5.26	1.20	2.91	2.38	4.95	3.21	3
	W_5	1.095	19.40	2.23	3.64	2.14	4.61	2.90	3
	W_6	1.217	27.04	2.24	3.04	2.50	5.11	3.36	3
PB14-R(77-122)	W_1	0.481	3.35	1.40	0.58	0.64	2.04	0.88	1
	W_2	0.424	3.58	1.28	0.40	0.53	1.80	0.74	1
	W_3	0.413	0.94	0.61	0.38	0.51	1.75	0.71	1
	W_4	0.329	1.99	1.38	0.52	0.36	1.40	0.51	3
	W_5	0.443	5.45	1.06	0.62	0.56	1.88	0.78	1
	W_6	0.541	2.53	0.96	0.71	0.76	2.30	1.05	1

** Where W stands for wire and the number ranging from 1 to 6 identifies the different external wires

A.4. Cross-sectional loss evaluation of corroded external wire

Considering the 24 collected samples, Table A-4 reports the cross-sectional loss, μ, of each external wire (*six for each sample*) at the section where the longitudinal maximum pit depth, $P_{max,long}$, was measured. The core wire was assumed as un-corroded.

Table A-4 Cross-sectional loss, μ, of each external wire at the section where the longitudinal maximum pit depth, $P_{max,long}$, was measured.

Sample ID°	wire	μ [%]	Sample ID°	wire	μ [%]
PB9-L(12-82)	W_1	24.23	**PB9-R(15-60)**	W_1	7.18
	W_2	21.02		W_2	6.59
	W_3	11.19		W_3	27.40
	W_4	11.42		**W_4**	69.21
	W_5	23.42		W_5	18.63
	W_6	37.59		W_6	10.46
PB9-L(426-496)	W_1	-	**PB9-R(428-473)**	W_1	-
	W_2	-	**Un-corroded**	W_2	-
	W_3	-		W_3	-
	W_4	3.67		W_4	-
	W_5	-		W_5	-
	W_6	-		W_6	-
PB10-L(138-208)	W_1	-	**PB10-R(32-102)**	W_1	-
	W_2	-	**(NEGLECTED)**	W_2	-
	W_3	8.39		W_3	-
	W_4	1.22		W_4	-
	W_5	-		W_5	-
	W_6	-		W_6	-
PB10-L(445-515)	W_1	1.30	**PB10-R(287-332)**	W_1	13.26
	W_2	-		W_2	-
	W_3	-		W_3	-
	W_4	59.61		W_4	7.48
	W_5	29.94		**W_5**	59.58
	W_6	-		W_6	1.58
PB11-L(5-75)	W_1	-	**PB11-R(6-51)**	**W_1**	17.41
Un-corroded	W_2	-		W_2	-
	W_3	-		W_3	-
	W_4	-		W_4	-
	W_5	-		W_5	-
	W_6	-		W_6	-
PB11-L(196-266)	W_1	-	**PB11-R(273-318)**	W_1	-
	W_2	4.41		W_2	-
	W_3	28.66		**W_3**	23.52
	W_4	2.81		W_4	-
	W_5	-		W_5	-
	W_6	1.06		W_6	-
PB12-L(12-82)	W_1	19.19	**PB12-R(100-170)**	**W_1**	15.18
	W_2	21.14		W_2	3.26
	W_3	13.74		W_3	-
	W_4	11.20		W_4	-
	W_5	21.73		W_5	-
	W_6	36.86		W_6	8.97
PB12-L(124-169)	W_1	-	**PB12-R(358-403)**	W_1	-
	W_2	2.23	**Un-corroded**	W_2	-

	W_3	-		W_3	-
	W_4	-		W_4	-
	W_5	4.24		W_5	-
	W_6	23.96		W_6	-
PB13-L(1-46)	W_1	-	**PB13-R(0-70)**	W_1	3.11
	W_2	-		W_2	7.78
	W_3	-		W_3	6.58
	W_4	22.85		W_4	16.71
	W_5	7.78		W_5	22.03
	W_6	-		**W_6**	27.02
PB13-L(108-178)	**W_1**	34.38	**PB13-R(70-115)**	W_1	-
	W_2	-		**W_2**	20.23
	W_3	-		W_3	-
	W_4	-		W_4	-
	W_5	-		W_5	-
	W_6	-		W_6	-
PB14-L(10-55)	**W_1**	53.06	**PB14-R(2-72)**	W_1	18.19
	W_2	12.10		W_2	6.40
	W_3	17.60		W_3	7.98
	W_4	14.94		W_4	10.31
	W_5	17.89		W_5	9.86
	W_6	12.80		**W_6**	23.69
PB14-L(455-500)	W_1	-	**PB14-R(77-122)**	W_1	-
Un-corroded	W_2	-		W_2	-
	W_3	-		**W_3**	4.99
	W_4	-		W_4	-
	W_5	-		W_5	-
	W_6	-		W_6	-

Acknowledgements

The writing of this *Thesis* would not have been possible without the support and guidance of incredibly special people.

First of all, I would like to thank my supervisor Professor Beatrice Belletti: your expertise and work ethic have been a source of inspiration. I'm also grateful for the constant guidance and excellent supervision during my "journey".

Thanks for giving me the opportunity to work on a stimulating topic of research.

Throughout this "journey" I have spent many hours working with amazing people who shared their knowledge and experience with me: in particular Professor Javier Sanchez, Professor Francesco Tondolo, Professor Carmen Andrade, and Professor Robby Caspeele. Without your help I would never have been able to reach my final goal. Moreover, thanks to Professor Emanuela Cerri for her significant contribution concerning the chemical part review of Chapter 2.

A big thanks goes to my old friends – Riccardo, Stefano, and Enrico – and to my colleagues, Francesca, Simone and Biagio, your friendship and support have been a rescue anchor in the stormy days.

Finally, a heartfelt thanks to my family – Paolo, Simona, and Elisa, and to my girlfriend, Gaia, for your constant support during these years and the assiduous encouragement to never give up.

Lorenzo Franceschini

25th December 2022

Ringraziamenti

La stesura di questa Tesi non sarebbe stata possibile senza il supporto e la guida di persone davvero speciali.

Prima di tutto, vorrei ringraziare il mio supervisore la Professoressa Beatrice Belletti: la sua esperienza e la sua etica del lavoro sono state una fonte di ispirazione. Le sono grato anche per la costante guida e l'eccellente supervisione del lavoro svolto durante il mio "viaggio". Grazie per avermi dato la possibilità di lavorare su un argomento di ricerca a me stimolante. Lungo tutto questo cammino ho passato molte ore lavorando con persone fantastiche le quali hanno condiviso la loro conoscenza ed esperienza con me: in particolare il Professore Javier Sanchez, il Professore Francesco Tondolo, la Professoressa Carmen Andrade e il Professore Robby Caspeele. Senza il vostro aiuto non sarei mai stato in grado di raggiungere il mio obiettivo finale. Inoltre, ringrazio la Professoressa Emanuela Cerri per il suo prezioso contributo di revisione al Capitolo 2 inerente alle formulazioni chimiche.

Un grande ringraziamento va ai miei vecchi amici – Riccardo, Stefano, ed Enrico – e ai miei colleghi di lavoro – Francesca, Simone e Biagio – la vostra amicizia e supporto sono stati un'ancora di salvezza nei giorni tempestosi.

Infine, un sentito ringraziamento alla mia Famiglia – Paolo, Simona, ed Elsia – e alla mia ragazza, Gaia, per il vostro costante supporto durante questi tre anni e il continuo incoraggiamento a non arrendermi mai.

Lorenzo Franceschini

25th Dicembre 2022

Curriculum Vitae (CV)

Personal information

Name: **Lorenzo Franceschini**

Emails: lorenzo.franceschini@unipr.it

Date of Birth: 15 May 1994

Nationality: Italian

Work experience and education

Nov 2019 - Dic 2022	Ph.D. student in Civil Engineering Department of Engineering and Architecture (DIA) University of Parma, Italy
Dic 2021 - up to now	Member of the Organizing Committee of the CACRCS DAYS Conference: Capacity Assessment of Corroded Reinforced Concrete Structures – from research to daily engineering evaluation.
Nov 2019 - up to now	*fib* (Federation International du Béton) Young Member
Aug 2019 - Nov 2019	Research fellowship Department of Engineering and Architecture (DIA) University of Parma, Italy
Mar 2017 - Jul 2019	Master's degree in Civil Engineering Department of Engineering and Architecture (DIA) University of Parma, Italy
Sep 2013- Mar 2017	Bachelor's degree in Civil Engineering Department of Engineering and Architecture (DIA) University of Parma, Italy
Sep 2008 - June 2013	Scientific High School Istituto di Istruzione Superiore "Guglielmo Marconi", Parma (PR), Italy

Additional work formation

Oct 2022	Specialized engineer for post-earthquake assessment Corso AeDes - Agenzia Regionale per la Sicurezza Territoriale e la Protezione Civile, Parma (PR), Italy
Jan 2020	Professional Practice Exam (Esame di Stato) Ordine degli ingegneri di Parma, Parma (PR), Italy

List of Publications

Journal Publications

1. **Franceschini L.**, Belletti B., Ferretti F., Sirico A., Ravasini S. & Pagliari F. (2023). *Experimental investigation on anti-falling protection system for reinforced concrete-brick composite floors*. Engineering Structures 276, 115361. https://doi.org/10.1016/j.engstruct.2022.115361
2. **Franceschini L.**, Belletti B., Tondolo F. & Sanchez J. (2022). *Study on the probability distribution of pitting for naturally corroded prestressing strands accounting for surface defects*. Buildings 12, 1732. https://doi.org/10.3390/buildings12101732
3. Michelini E., Belletti B., **Franceschini L.** & Martinelli E. (2022). *Time-dependent seismic fragility curves for existing RC core-wall buildings exposed to corrosion*. Structural Concrete. https://doi.org/10.1002/suco.202200373
4. **Franceschini L.**, Belletti B., Tondolo F. & Sanchez J. (2022). *A simplified stress-strain relationship for the mechanical behaviour of corroded prestressing strands: the SCPS-model*. Structural Concrete. https://doi.org/10.1002/suco.202200170
5. **Franceschini L.**, Vecchi F., Tondolo F., Belletti B. & Sanchez J. (2022). *Mechanical behaviour of corroded strands under chloride attack: a new constitutive law*. Construction and Building Materials, 316: 125872. https://doi.org/10.1016/j.conbuildmat.2021.125872
6. Vecchi F.; **Franceschini L.** & Belletti B. (2021). *Modelling of Time-Dependent Behaviour of Corroded Reinforced Concrete Elements*. Materials Proceedings 2021, 6, 4. https://doi.org/10.3390/CMDWC2021-09957
7. **Franceschini L.**, Vecchi F., Belletti B., Andrade C. & Peiretti H.-C. (2021). *Analytical method for the evaluation of the residual service life of prestressed concrete beams subjected to corrosion deterioration*. Structural Concrete. pp. 1–17. https://doi.org/10.1002/suco.202100245
8. Ravasini S., Sio J., **Franceschini L.**, Izzuddin B. A. & Belletti, B. (2021). *Validation of simplified tying force method for robustness assessment of RC framed structures*. Engineering Structures, 249(October), 113291.
9. **Franceschini L.**, Vecchi F. & Belletti B. (2021). *The PARC_CL 2.1 Crack Model for NLFEA of Reinforced Concrete Elements Subjected to Corrosion Deterioration*.

Corrosion and Materials Degradation, 2, pp. 474-492. https://doi.org/10.3390/cmd2030025

10. Vecchi F., **Franceschini L.**, Tondolo F., Belletti B., Sanchez J. & Minetola P. (2021). *Corrosion morphology of prestressing steel strands in naturally corroded PC beams*. Construction and Building Materials, 296, pp. 1-20. https://doi.org/10.1016/j.conbuildmat.2021.123720
11. Belletti B., Rodriguez J., Andrade C., **Franceschini L.**, Sanchez J. & Vecchi F. (2020). *Experimental tests on shear capacity of naturally corroded prestressed beams*. Structural Concrete, pp. 1-17. https://doi.org/10.1002/suco.202000205

Conference Publications

1. Ravasini S., **Franceschini L.** & Belletti B. (2023). *Simplified analytical method for moment-curvature response of corroded prestressed concrete beams*. Proceedings of the 8th International Symposium on Life-Cycle Civil Engineering (IALCEE2023), 11th – 15th 2023, Milan, Italy. *paper accepted*.
2. **Franceschini L.**, Botte W., Caspeele R., Belletti B., Tondolo F. & Sanchez J. (2023). *Partial safety factor for the design strength prediction of naturally corroded prestressing strands*. Proceedings of the 14th International Conference on Application of Statistics and Probability in civil engineering (ICASP14), 9th – 13th July 2023, Dublin, Ireland. *abstract accepted & paper submitted*.
3. Belletti B., Ravasini S., Sirico A., **Franceschini L.**, Vitali A. & De Berardinis P. (2022). *Experimental and Analytical Study of a Welded Steel Wire Mesh for Anti-Falling Debris Protection System*. Proceedings of the Italian Concrete Conference (ICC), 12th – 15th October 2022, Naples.
4. **Franceschini L.**, Belletti B., Sanchez J. & Tondolo F. (2022). *Dependency of pitting corrosion spatial variability on crack pattern of prestressed concrete members*. Proceedings of the 14th *fib* PhD Symposium, 5th – 7th September 2022, Rome, Italy.
5. Vecchi F., **Franceschini L.** & Belletti B. (2022). *PARC_CL 2.1: Modelling of the Time-Dependent Behaviour of Reinforced Concrete Slabs*. Proceedings of the EURO-C Conference: Computational Modelling of Concrete and Concrete Structures – Meschke, Pichler & Rots (Eds), ISBN:978-1-032-32724-2, 23th – 26th May 2022, Vienna, Austria, pp:624-633.

6. **Franceschini L.**, Belletti B. & Violi B. (2021). *Service Life Prediction of Corroded Prestressed Concrete Beams based on Probabilistic Assumptions*. Proceedings of the *fib* CACRCS Days 2021: *Capacity Assessment of Corroded Reinforced Concrete Structures*, 30th November – 3rd December 2021, venue on-line, Italy, pp: 151-155.
7. Vecchi F., **Franceschini L.**, Belletti B. & Calcavecchia B. (2021). *Capacity assessment of existing RC Columns taking into account bi-axial shear failure*. Proceedings of the *fib* CACRCS Days 2021: *Capacity Assessment of Corroded Reinforced Concrete Structures*, 30th November – 3rd December 2021, venue on-line, Italy, pp: 173-176.
8. **Franceschini L.**, Vecchi F., Belletti B., Tondolo F. & Sanchez J. (2021). *SCPS-Model: a Simplified Stress-strain Model for Corroded Prestressing Strands*. Proceedings of the *fib* CACRCS Days 2021: *Capacity Assessment of Corroded Reinforced Concrete Structures*, 30th November – 3rd December 2021, venue on-line, Italy, pp: 73-77.
9. Belletti B., **Franceschini L**., Martinelli E., Michelini E. & Vecchi F. (2021). *Seismic fragility assessment for an existing RC frame-wall dual system building with corroded bars*. Proceedings of the *fib* CACRCS Days 2021: *Capacity Assessment of Corroded Reinforced Concrete Structures*, 30th November – 3rd December 2021, venue on-line, Italy, pp: 185-188.
10. **Franceschini L.**, Sirico A., Ravasini S., Belletti B., Vitali A. & De Bernardinis P., (2021). *Numerical and Analytical Assessment of a Galvanized Welded Steel Wire Mesh: an Anti-Falling Debris Protection System for Ceiling*. Proceedings of the 2nd *fib* Symposium on Concrete and Concrete Structures, Nov. 18th -19th 2021, Sapienza University, Rome, Italy.
11. **Franceschini L.**, Vecchi F., Tondolo F., Belletti B., Sanchez, J. & Minetola, P. (2021). *Variability in section loss and maximum pit depth of corroded prestressing wires*. 1st Conference of the European Association on Quality Control of Bridges and Structures – EUROSTRUCT2021, 29th August – 1st September, Padova, Italy.
12. **Franceschini L.**, Belletti B., & Vecchi F. (2021). *The PARC-CL 2.1 crack model for reinforced concrete elements subjected to corrosion and long-term effects*. Book of abstracts of the EM4SS'21 Conference: Engineered Materials for Sustainable Structures. 26th – 28th April 2021, venue on-line.
13. Vecchi F., Belletti B., **Franceschini L.**, Andrade C., Rodriguez J. & Sanchez J. (2020). *Flexural test on prestressed beams exposed to natural chloride action*. Proceedings of the

fib CACRCS Days 2020: *Capacity Assessment of Corroded Reinforced Concrete Structures*, 1st – 4th December 2020, venue on-line, Italy, pp: 205-212.

14. Belletti B., Corres Peiretti H., Andrade C., Ghiretti M., **Franceschini L.** & Vecchi F. (2020). *Evaluation of the residual life of corroded prestressed concrete beams*. Proceedings of the *fib* CACRCS Days 2020: *Capacity Assessment of Corroded Reinforced Concrete Structures*, 1st – 4th December 2020, venue on-line, Italy, pp: 429-437.
15. Belletti B., **Franceschini L.** & Ravasini S. (2019). *Tie force method for reinforced concrete structures*. Proceedings of the International *fib* Symposium on Conceptual Design of Structures, 1(1), 57–64.